Development of the Miniature Seismic Reflection (MSR) System for Nondestructive Evaluation of Concrete Shaft and Tunnel Linings

by

Afshin Sadri

A thesis submitted to the Faculty of Graduate Studies and Research
in partial fulfillment of requirements for the
Degree of Doctor of Philosophy

Department of Mining and Metallurgical Engineering
McGill University
Montreal, Canada

December, 1996

0-612-70192-1

ABSTRACT

Nondestructive evaluation of the structural integrity of shaft and tunnel concrete linings is the focus of this thesis. A nondestructive testing system was assembled based on the principle of miniature seismic reflection (MSR). The MSR system consists of spherical tip impactors and a pair of vertical and tangential displacement transducers. Mechanical impact causes generation of stress P- and S-waves in the test object. The elastic waveforms undergo multiple reflections between the top and bottom of the testing layer. The surface displacements are captured by a vertical and tangential displacement transducer. The signals are transformed from time domain waveforms to frequency spectra. The vertical displacement transducer is sensitive to normal surface displacements and the highest amplitude peak on the computed frequency spectrum is related to the resonance of the P-wave between the top and the bottom layer. Similarly, the tangential displacement transducer is sensitive to the horizontal surface displacements, and the maximum peak value in the generated frequency spectrum corresponds to the resonance of the S-wave between the two layers of the testing object. Thus, knowing the thickness of the given layer, as well as the measured frequencies, allows P- and S-wave velocities to be calculated. Alternatively, if the thickness is unknown, the time-distance graph of the primary surface wave arrivals can be used to calculate the P-wave velocities and, subsequently, the thickness of the layer. The MSR response depends on the material properties of the testing object. The elastic wave velocities can be used to calculate directly the dynamic elastic properties of the test object. In this study, simulated fractures and steel reinforcement bars were detected and located using the reflected P-waves. In addition, the changes in elastic properties of various types of concrete mixes were monitored for a 28-day curing period. The MSR elastic constants were then compared with dynamic and static values obtained by standard methods in order to assess their accuracy. For the field trial, various sections of two concrete shaft linings at different elevations were investigated and the dynamic elastic properties of the linings were evaluated. Also, the thickness of a concrete tunnel lining was computed using the MSR system. Finally, the MSR system was used to compute the dynamic elastic properties of different rock types. The system was used to monitor changes in elastic properties of rock cores as a uniaxial load was applied on them. For the field trial, the MSR system was used to detect the position of discontinuities in a rock mass and to evaluate the rock's dynamic elastic properties in an underground mining environment.

RÉSUMÉ

L'évaluation non destructive de l'intégrité structurale de puits et de tunnels en béton est le but de cette thèse. Le principe MSR (réflexion sismique à petite échelle) est à la base d'un système non destructif construit pour les études effectuées. Le système MSR consiste en une source d'impact mécanique muni d'un bout sphérique et de capteurs à déplacements verticaux et tangentiels. L'impact de la boule sphérique sur une surface génère des ondes de contraintes de types P et S. Ces ondes subissent de multiples réflexions entre deux limites de l'échantillon d'essai. Les déplacements à la surface sont décelés à l'aide des capteurs. Par la suite, les signaux sont transformés du domaine du temps au domaine de fréquence par l'intermédiaire d'un logiciel spécialisé. Le capteur à déplacement vertical est sensible aux déplacements normaux à la surface. L'amplitude maximale dans la gamme fréquentielle calculée par le logiciel correspond à la résonance de l'onde P entre les surfaces inférieure et supérieure de l'échantillon. Le capteur tangentiel est sensible aux mouvements horizontaux sur la surface d'essai et la résonance de l'onde S correspond à l'amplitude maximale de la gamme fréquentiel trouvée. Les vitesses de propagation des ondes P et S peuvent être calculées à l'aide des fréquences observées si l'épaisseur de l'échantillon est connue. Si l'épaisseur n'est pas connue, le diagramme temps-distance des arrivées primaires des ondes de surface est utilisé pour déterminer la vélocité des ondes P ainsi que l'épaisseur du matériau d'essai. La réponse du système MSR dépend en grande partie des propriétés des matériaux qui composent le spécimen d'essai. Les vélocités des ondes élastiques sont utilisées pour calculer les propriétés élastiques dynamiques de l'échantillon. Lors de l'étude présenté dans ce document, des fissures artificielles ainsi que des aciers d'armatures ont été détectés et localisés. De plus, le changement des propriétés élastiques de plusieurs mélanges de béton à été observé pendant les premiers 28 jours de cure. Les constantes élastiques déterminées à l'aide du système MSR ont été comparées à des résultats statiques et dynamiques obtenus par des méthodes classiques. Des essais in situ on été effectués sur des revêtements en béton à différentes élévations dans une mine. Lors de ces essais, les propriétés dynamiques ainsi que l'épaisseur du revêtement ont été évaluées. Finalement, le système MSR a été employé pour évaluer les propriétés dynamiques élastiques de plusieurs types de roches. Le système MSR a été utilisé pour observer le changement des propriétés élastiques de carottes soumises à des contraintes uni-axiales. Des essais in situ ont été effectués pour déceler la position de discontinuités dans le rock et pour en déterminer ses propriétés dynamiques.

ACKNOWLEDGEMENTS

I would like to express my gratitude to my thesis supervisor, Professor Ferri P. Hassani for his invaluable support and inspiration throughout the course of this research. My deep gratitude also goes to my friend and colleague, Dr. Mohammed Momayez-zadeh, for his continual guidance and encouragement throughout this research project.

Special thanks are extended to Professor Malcolm J. Scoble, Professor Hani Mitri, Professor Michel L. Bilodeau, Professor Bibhu Mohanty, Professor Saeed Mirza, Dr. Parviz Mottahed, Dr. Kaveh Saleh, Dr. Arnfinn Prugger, Dr. Kayvan Fotoohi and Mr. John Mossop for their constructive comments and fruitful and kind exchanges of information. Appreciation is extended to Mr. T.M. Proctor Jr. for his support and permission to build the tangential displacement transducers.

Thanks are extended to the Jamieson Structures Laboratory staff: Dr. William D. Cook and Mr. Ron Sheppard, and Mr. AliReza Majdzadeh of the Geomechanics Laboratory at McGill University for their assistance in preparation and testing of the specimens. The french translation of the abstract by Mr. Phillippe Guevremont is greatly appreciated.

Many thanks to Mr. Moe Molavi and Mr. Mark Hout, the Chief Engineers of Allan and CCP Mines in Saskatchewan and Mr. Bu Livan of the S.T.C.U.M. in Montreal for their invaluable support.

The author is grateful to his parents and fiance, Shahnaz Jafarzadeh, for their invaluable encouragement and love, without which the completion of this project would not have been possible.

Last but not least, I would also like thank Purnima Mujumdar and Marina Rosati for their support when needed.

Table of Contents

List of Figures

List of Tables

List of Plates

List of Symbols

σ	= stress
F	= force
A	= area
ϵ	= strain
E	= Young's modulus
G	= shear modulus
τ	= shear stress
γ	= shear strain
υ	= Poisson's ratio
K	= bulk modulus
P	= pressure
V	= volume
ρ	= density
C_p	= P-wave velocity
C_s	= S-wave velocity
C_R	= R-wave velocity
R_p	= reflected P-wave
R_s	= reflected S-wave
r_p	= refracted P-wave
r_s	= refracted S-wave
Z	= acoustic impedance
A_T	= amplitude of the stress in the reflected wave
A_I	= amplitude of motion in the incidence waveform
A_R	= amplitude of reflected waveform
α_p	= angle of reflected P-wave
α_s	= angle of reflected S-wave
R_{pp}	= reflection coefficient for reflected P-wave
R_{ss}	= reflection coefficient for reflected S-wave
n	= final amount of nodes
λ	= wavelength
f	= frequency
V	= velocity of standing wave

l	= length
L	= length of a pile
U	= shape correction factor
R	= shape factor depending on the cross section
Δt	= reflected travel time
t	= time
T	= thickness
Δf	= difference between two mobility peaks
X	= distance between to receivers
ϕ	= phase difference
$C_{R(f)}$	= velocity of component frequency
Δt_f	= travel time between two receivers
f_p	= frequency of resonated P-wave
f_s	= frequency of resonated S-wave
t_c	= contact-time
m_s	= mass of sphere
T_d	= depth of the flaw from the top of overlay
C_{pc}	= P-wave velocity in concrete
C_{po}	= P-wave velocity in the overlay
T_o	= thickness of overlay
W	= unit weight of concrete
f'_c	= concrete strength
f'_c	= average concrete 28-day compressive strength
E_c	= concrete elastic moduli
D	= diameter
I	= moment of inertia
y	= deflection measured from the center
x	= pressure generator constant
M_r	= pressure-volume relationship
Δu	= radial deformation
Δt_p	= period of P-wave arrival
Δt_s	= period of P-wave arrival

CHAPTER 1

THESIS DESCRIPTION

1.1 INTRODUCTION

The purpose of the research presented in this thesis is to develop and evaluate a new nondestructive testing (NDT) system for monitoring the integrity of concrete structures in an underground mining environment. The system function is based on miniature seismic reflection (MSR) principles. To evaluate the capabilities of the new system, comprehensive laboratory and field studies are carried out on concrete samples and structures with different dimensions and specifications. Experimental studies are also conducted on rock samples and structures to evaluate the capability of the MSR system in conducting tests on materials other than concrete.

This chapter presents the needs for research, reviews the research objectives, summarizes the organization of this thesis and finally presents a statement of originality for this research work.

1.2 RESEARCH NEEDS

The integrity of a structure depends in great part on the physical properties of its constituent materials. In the case of concrete structures, at the design stage, compressive strength is used as the main functional material representative. However, depending on service and exposure conditions, properties other than strength influence the integrity of the structure. Initially, the quality of the concrete structure depends on good mixing, pouring and casting operations. Later, during the life cycle of the structure, concrete properties may change as a result of its exposure to hostile environmental conditions. This infrastructure decay is reflected by the development of fractures and voids within the concrete, the reduction of the thickness which may reduce and effect its load bearing capacity, and steel corrosion of the reinforcement bars which may cause structural failure.

To assure that a finished concrete element is structurally adequate for the purpose it was designed, it has to be monitored periodically. In practice, cylindrical samples of concrete are cast and tested for the 28-day compression test, to obtain an indication of concrete quality. However, the test specimens may not truly represent the quality of concrete in a structure, that may vary due to the operator's carelessness resulting in differences in compaction and curing conditions.

As an alternative, in situ nondestructive testing (NDT) techniques have been developed which provide very useful information as a means of quality control of in-place concrete. The use of NDT techniques for inspection of concrete is relatively new and they can not fully substitute for direct strength tests. However, when applied systematically and periodically on large concrete structures, NDT techniques provide an excellent means of monitoring concrete quality rapidly, nondestructively and at a lower cost than core strength tests.

The in situ nondestructive testing techniques provide information on many aspects of concrete structures. The NDT techniques are used to estimate mechanical properties, measure thickness, and locate delaminations, voids and cracks.

In general, shaft and tunnel linings are like hollow cylindrical or hollow half-cylindrical concrete structures that are in contact with the surrounding rock and soil. In cross section, shafts are exclusively circular or elliptical and tunnel linings are circular and/or elliptical. Concrete shaft and tunnel linings are constructed to support the shaft and tunnel equipment and the walls of the excavation. For shafts, concrete is used as a lining material since the placement is mechanized, the rate of excavation is high, and it can be installed at low cost. For tunnels, concrete is used as a means of long-term support. However, the most decisive elements for the selection of concrete for shaft and tunnel linings are hydrogeological conditions and ground pressure. Concrete strength is adjusted according to need, and is set between 20 and 50 MPa. Watertightness of the lining can be achieved within aquifers with moderate head. In difficult ground with high water pressure, cast iron tubbings with concrete mantle are applied. The shafts and tunnels may be fully or partially lined with concrete rings. Concrete thickness for the lining is generally between 0.31 m and 0.61 m, with a minimum thickness of 0.25 m. To be more specific, the thickness of lining varies with depth throughout the length of the shaft and tunnels to accommodate the increased pressure.

The assessment of the condition of concrete shaft and tunnel linings in underground excavations is difficult since most of the deterioration process takes place at the rock-side or blind-side (at the rock/concrete interface) of the lining. Groundwater and variations in stress conditions are the main cause for deterioration and damage to the concrete lining. Presently, visual inspection is the most common method of monitoring used for detecting damaged areas in shafts. Visual inspection is not a reliable method due to the fact that most of the degradation begins from the rock-side and by the time the damaged area is visible on the air-side, repair is costly. The traditional method of evaluating concrete condition is to extract core samples from the structure and measure the thickness, locate the existing delaminations and test for strength and elastic properties. To prevent the problems associated with coring, nondestructive testing (NDT) techniques could be used to provide the necessary information.

There are a number of NDT techniques in use, capable of detecting voids and delaminations in concrete shaft and tunnel lining; these include: pulse-echo, impact-echo, impulse-response, Spectral Analysis of Surface Wave (SASW), and Ground Probing Radar (GPR) techniques. The advantage of these techniques is their ability to operate from the air-side of the concrete lining and provide the necessary information regarding the state of the concrete for maintenance purposes. However, none of the currently available NDT techniques can determine thickness, detect voids and delaminations, and evaluate concrete quality at the same time.

1.3 RESEARCH OBJECTIVES

Among the NDT techniques, the impact-echo technique was found to be the most promising system to be adopted for evaluating the integrity of concrete linings in a mining environment. The impact-echo method was developed in the mid-1980's for the purpose of detection and location of defects in concrete structures. The impact-echo technique is based on transient stress P-wave propagation and reflection in concrete, where the stress pulse is generated by a mechanical impact (Carino and Sansalone, 1988).

The main objective of this research project is to enhance the impact-echo technique by adding an S-wave transducer and a variable size impact source to the system. Knowledge of P- and S-wave parameters can provide information about the material properties of the concrete structure.

The most important of these physical properties are their elastic properties. These are Young's modulus of elasticity E, the modulus of rigidity G, the bulk modulus K, and Poisson's Ratio υ, which are known as elastic constants. The theory of elasticity is an accepted scientific and engineering principle. Concrete, after curing, acts as an elastic material and the theory of elasticity can be used in determining its elastic constants.

For concrete, E, G and υ are commonly calculated from the results of standard static tests. A load is applied by a compression machine and the resulting strain on the sample is measured by a strain gauge. The calculated stress and strain values are used to measure Young's modulus and Poisson's ratio. According to the same principle, the shear modulus can be calculated by changing the direction of stress. K is commonly computed using E, G and υ values.

The elastic constants can also be calculated by dynamic methods. In one such method the velocity of propagation of stress waves in concrete is related to its elastic behavior. The theory is based on the assumption that concrete behaves elastically due to applied transient stresses which results in a very low level of strain. The stresses applied in dynamic methods are insignificant.

A systematic, periodic inspection of concrete structures based on their dynamic elastic properties helps in monitoring the quality of the structure. Any change in the quality of the concrete can be detected and further damage can be prevented ahead of time. None of the available nondestructive testing techniques are capable of evaluating dynamic elastic properties of concrete directly from one available face. In most of the field or laboratory testing methods, P-wave velocity and density can be determined within 1% accuracy. However, other parameters for calculating dynamic elastic moduli are assumed (i.e. Poisson's ratio and/or S-wave velocity) due to the fact that the existing methods are not capable of determining these factors from one face of the structure. The fact that an absolute error of 0.05 in estimating Poisson's ratio will lead to about 7% total error in the computed dynamic modulus of elasticity (Naik and Malhotra, 1991) suggests that a high precision in situ NDT system, capable of determining all the necessary parameters, is the solution to the problem of concrete quality control. The NDT system presented in this thesis directly measures P- and S-wave parameters which are principally sensitive to the physical properties of the tested materials.

The new system functions based on the seismic reflection principle. Because of the range of frequencies used, the new technique is defined as a "Miniature Seismic Reflection" (MSR) system for evaluation of concrete structures. The MSR system is nondestructive, simple to operate, less costly, mobile, and can function in a mining environment as well as in the laboratory. The MSR system is designed to detect and locate cavities, voids, delaminations and discontinuities in concrete structures. In addition to detection and location of defects, the MSR system can also be used to evaluate the dynamic elastic properties of concrete. The system is capable of testing concrete structures or specimens from one direction. The MSR system uses measurements of the compressive and shear wave velocities. The elastic wave velocities are extracted from the signals by the fast Fourier transform (FFT) technique. The FFT of the signals offers precise and rapid measurement of wave velocities and reduces human judgement errors, which are common in waveform analysis.

Two broad band vertical and tangential displacement transducers, suitable for capturing reflected compressive and shear waves of the desired frequencies, are the receiving sensors of the MSR system. The MSR system has a series of spherical tip impact devices. Each impact device contains a ball-bearing of a certain diameter which controls the range of frequencies generated by the impact on the material. The impact devices are designed to cover a range of frequencies between 10 and 20 kHz. Each device is able to generate repeatable impacts with the same energy in any orientation with respect to the testing surface.

1.4 METHODOLOGY

Following the equipment assembly, a comprehensive laboratory testing program is carried out for evaluating the MSR system.

Laboratory experiments are arranged in order to evaluate the capability of the MSR system in detecting simulated flaws and fractures in concrete blocks and slabs. Also, the behavior of propagated transient P- and S-waves in relationship with different reflecting surfaces is studied.

The MSR system is used to monitor concrete cylinders of various strengths at daily intervals from the time of casting up to the 28-day standard curing period. Different concrete mix ratios are selected in order to model the type of concrete used in structures such as shaft and tunnel linings. Concretes are tested daily for their elastic moduli, shear modulus, bulk modulus, and Poisson's ratio. The results are compared with the standard dynamic and static testing methods. This experiment is conducted to study the sensitivity of the MSR system to the physical and chemical changes caused by different elements affecting the curing and hardening of concrete. Since curing causes an increase in elastic properties, the stiffening of concrete can be monitored quantitatively through changes in elastic constants. The effect of cement type and aggregate size on the changes in wave velocities and elastic constants is also studied. Finally, the relationship between increasing strength and elastic moduli is illustrated.

Different rock types are tested by the MSR system in laboratory conditions. The purpose of this study is to investigate the capability of the MSR system to evaluate other heterogeneous materials such as rocks. The cored and block specimens are tested by the MSR system to evaluate the effect of size and dimension on wave propagation. The results are compared with standard dynamic and static testing techniques.

The MSR system is also used to study the relationship between increasing stress on rock samples and stress wave velocities, and subsequently dynamic elastic constants. The results of this study are compared with the changes in ultrasonic wave velocities. The purpose of this study is to evaluate the capability of the new system for monitoring the dynamic changes in a mining environment and to illustrate the relationship between the increase in stress and the changes in P- and S-wave velocities and elastic constants.

The MSR system is also used to measure quality and thickness of concrete shaft and tunnel linings. The behavior of the reflected signals in relationship with the reflecting interfaces is studied. The main emphasis is the concrete/rock interface and the effect of rocks with different acoustic stiffness on the reflected signals. The findings are compared with the available in situ and laboratory data.

Finally, the MSR system is used to evaluate the thickness and dynamic elastic properties of a rock mass in an underground mining environment. The findings are compared with extracted and tested cores in the laboratory.

1.5 THESIS ORGANIZATION

Chapter 2 presents an overview of nondestructive testing techniques.

Chapter 3 describes the fundamental principles of elastic behavior of solids and elastic waves.

Chapter 4 describes the available laboratory and field techniques capable of evaluating dynamic elastic constants of concrete and rocks.

Chapter 5 presents the available laboratory and field techniques used for evaluating static elastic properties. This chapter also includes a comparison between dynamic and static elastic properties.

Chapter 6 describes the MSR system.

Chapter 7 presents the laboratory experiments regarding P-wave measurement, propagation behavior of elastic waves from different reflecting surfaces, and detection and location of simulated planar and vertical discontinuities and reinforcement bars in concrete.

Chapter 8 describes the investigation carried out by the MSR system and the standard dynamic and static systems in order to monitor the curing and stiffening of various types of concrete cylinders and laboratory-made structures.

Chapter 9 presents the results of the field testing of the MSR system on concrete shaft and tunnel linings.

Chapter 10 describes the results of laboratory and field testing by the MSR system carried out on several rock types with different dimensions.

Chapter 11 summarizes important conclusions and suggest further developments.

1.6 STATEMENT OF ORIGINALITY

The original contributions described in this thesis relate to:

a) The assembly of an NDT system capable of evaluating concrete specimens and structures based on their dynamic elastic properties for the purpose of quality control. The assembly included manufacturing of a tangential displacement transducer and a series of impact devices. One important aspect of the system is its capability of conducting tests from only one face of the tested object.

b) The first application of an NDT system based on the miniature seismic reflection principle to measure S-wave parameters and dynamic elastic properties of concrete directly.

c) The first application of an NDT system to monitor the setting time and curing of concrete elements by their dynamic elastic properties based on the miniature seismic reflection principle.

d) Measuring dynamic elastic properties of a shaft lining, directly based on the miniature seismic reflection principle.

e) The first application of an NDT system to measure dynamic elastic properties of rocks both in the laboratory and in the field, from one available face and based on the miniature seismic reflection principle.

CHAPTER 2

NONDESTRUCTIVE TESTING METHODS

2.1 INTRODUCTION

According to applications, there are three general categories of nondestructive testing methods used in the mining industry.

The first category includes the tests which estimate the in situ strength indirectly, such as surface hardness, and directly, such as penetration resistance and pullout techniques. The second category includes the tests which measure the material properties of concrete and rock, such as moisture, density, compressive wave velocity, modulus of elasticity, thickness, and temperature. Ultrasonic, nuclear and electrical methods are in this category. The third category includes the tests which are used to detect and locate the problem areas within concrete structures and rock masses such as honeycombing, fractures, flaws and delaminations. Impact-echo, ground penetrating radar, pulse-echo, infrared thermography and acoustic emission methods are in this category.

This chapter presents an overall review of available nondestructive testing methods in the fields of quality control and maintenance of excavated rock masses and concrete support systems in mining. The techniques presented in this chapter are not the only ones used, but they are the most common that are used by the concrete industry and some have been approved by the standard committees of the professional associations such as American Concrete Institute (ACI), American Society for Testing and Materials (ASTM) and geotechnical engineering such as International Society for Rock Mechanics (ISRM), and ASTM.

2.2 TRADITIONAL TESTING METHODS

2.2.1 Concrete

Concrete technology encompasses many specific types of mixtures and designs which are arranged to provide adequate structural support for various purposes. Once the concrete structure is completed, it must be verified that the finished strength and modulus of elasticity are those required for the specific purpose they were designed for. Another area of concern would be the effect time has on these structures, effects such as the generation of cavities or the development of fractures, as well as changes in elastic properties and strength. A traditional method is to test 28-day cured cylindrical or prismatic samples for their compressive strength. In this method, concrete mixes have been prepared with the same concrete specifications as those of structure. Compressive and tensile strength values can provide information on elastic behavior and service performance.

The main disadvantage regarding testing of precast samples is the fact that the test specimen may not be representative of concrete used in the structure. The curing conditions, moisture content and mixing might not be the same for the laboratory made specimen and the concrete used in the structure. Furthermore, the in situ stress on the behavior of concrete would be neglected in the precast samples. Continuous or radically changing stress conditions have various effects on the compressive and tensile strength of an elastic medium. Therefore the precast samples do not truly represent the conditions the structure is in. Other testing techniques are applied by extracting cylindrical core samples from the structures and by evaluating these samples directly in laboratories. Using this method, tests are not repeatable and the procedure causes damage to the structures (Hassani, Momayez, and Wang, 1989; Malhotra, 1984). In case of concrete structures barricading water reservoirs or aquifers, such as dams and shaft and tunnel liners, coring might cause permanent damage to the entire structure. Figure 2-1 illustrates schematic drawings of concrete shaft and tunnel linings.

2.2.2 Rocks

The understanding of rocks as engineering material depends upon the understanding of their behavior under various stress conditions. Nevertheless, there are many types of rock and many variants of each type, as well as numerous dynamic changes that occur as a result of alteration of their natural condition. Laboratory and in situ tests are the tools needed for a better understanding of rock behavior.

Detailed information about the mechanical properties of rock masses such as the strength and elastic constants could guide maintenance personnel to prevent further structural damages. Furthermore, detection of discontinuities, loose and separated rocks is important to maintaining a safe working environment for mine personnel. A traditional method for determining the thickness, mechanical properties and quality assessment has been based upon the extraction of several core samples from the rock masses and evaluations done indirectly later in laboratories. In the case of separations and loose rocks, scaling has been used to solve immediate problems. However, high costs, safety problems and time limitations require the use and further development of less costly, nondestructive and faster devices. Figure 2-1 illustrates schematic drawings of a rock mass.

2.3 NONDESTRUCTIVE TESTING AND EVALUATION METHODS

A series of methods and instruments have been developed to evaluate concrete structures and excavated rock masses in situ and nondestructively. Nondestructive testing techniques are rapid and less costly alternatives to the traditional methods. Table 2-1 shows a summary of nondestructive testing and evaluation techniques for concrete and rocks and their use. Nondestructive testing equipment is divided into three general types:

The first category includes equipment that is able to estimate the strength, durability, hardness, elastic parameters and quality of concrete and rock. It is noteworthy to point out that nondestructive techniques only provide an estimated value for the above mentioned parameters. A true value can only be attained by using direct methods, where the specimen has to be loaded to failure. In the second category, tests are performed in order to measure concrete and rock properties such as elastic wave velocity, temperature, density, moisture and elastic properties. The third category of in situ nondestructive testing equipment is used to locate the reinforcement steel bars or rock bolts, particularly important in the case of corroded bars in concrete, and cracks and discontinuities, thickness, and honeycombing structures in concrete and rock masses.

Based on the literature review, the major in situ nondestructive techniques can be divided into eight broad sections according to their fundamental principles. They are presented in the following sections.

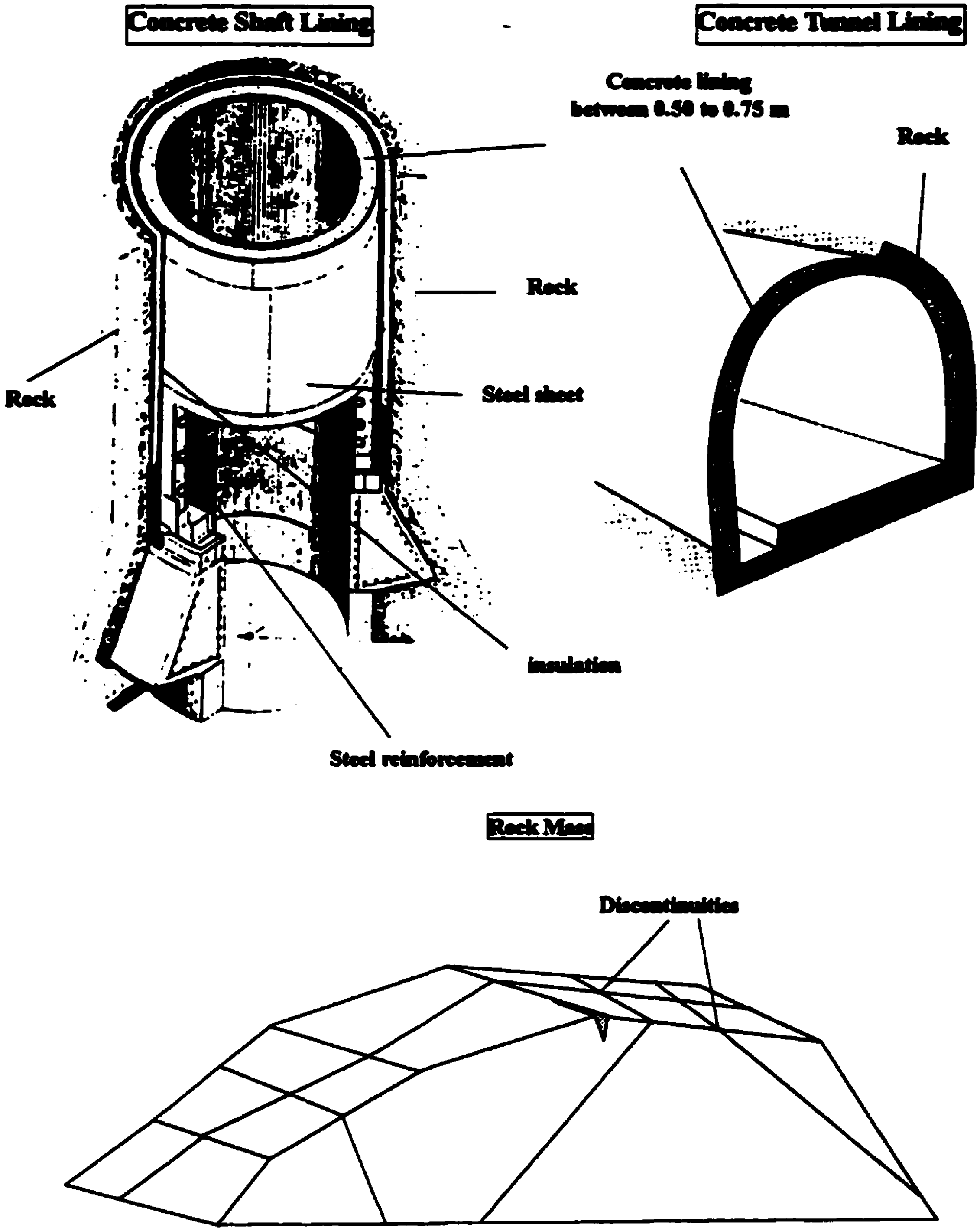

Figure 2-1 Schematic drawings of concrete shaft and tunnel lining and rock mass, three main areas of concern for application of NDT & E in mining and geotechnical engineering.

Table 2-1 Summary of nondestructive testing and evaluation techniques for concrete and rocks and their use.

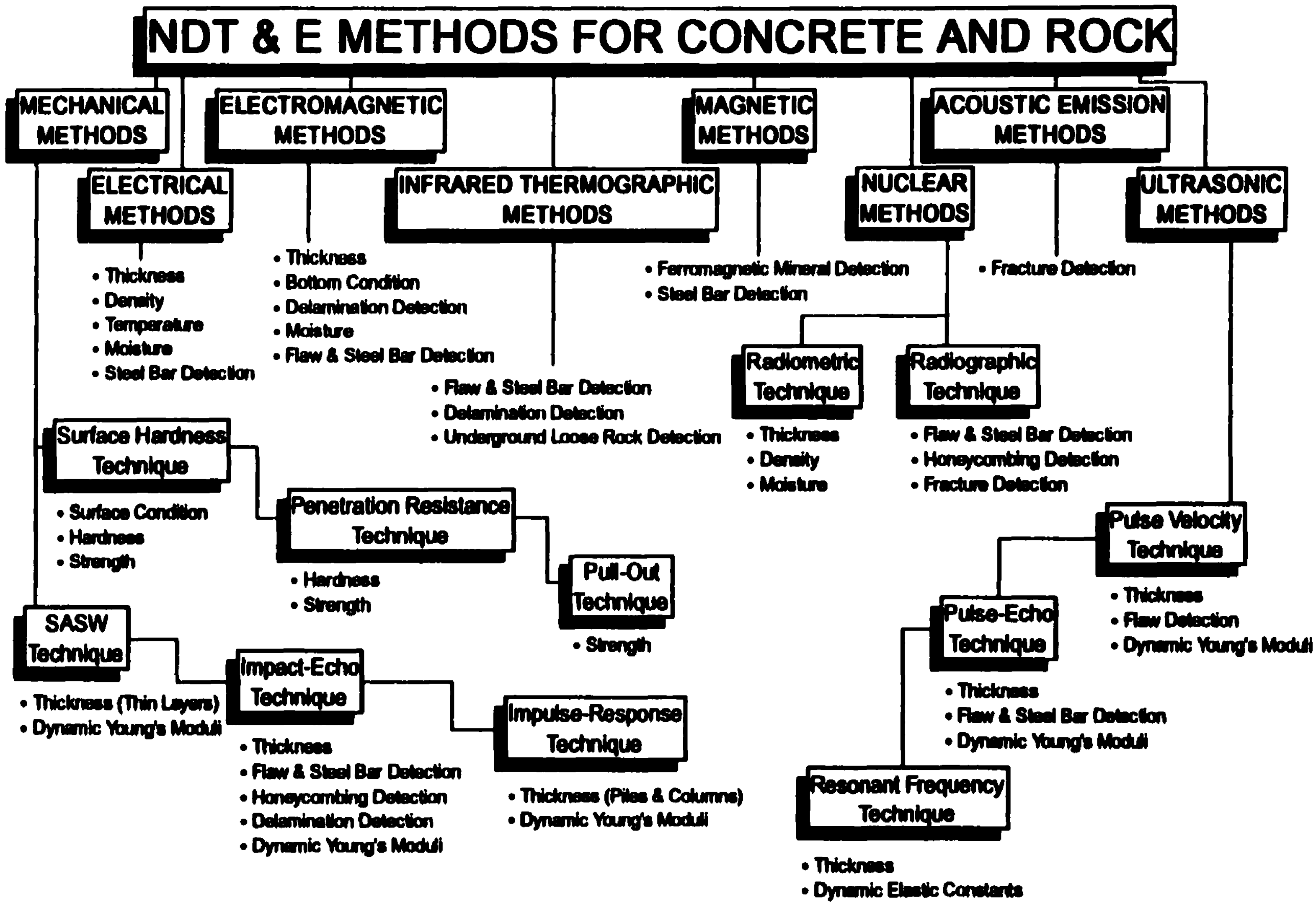

2.4 MECHANICAL METHODS

Some of the mechanical devices, that are currently available, can be used to measure strength or hardness of materials. Other types of mechanical devices are used to detect defects or properties of materials by use of stress wave propagation techniques. Mechanical methods are divided into six major techniques:

2.4.1 Surface Hardness Equipment

Available equipment is capable of estimating the concrete and rock hardness by impacting the surface and measuring the indentation or rebound value. Further correlation curves to the rock and concrete's compressive strength have been constructed by various investigators (Schmidt, 1954, and Kolek, 1958). Conventional techniques are inexpensive and fast. The Schmidt hammer testing system and the EQUITIP hardness tester are the two most widely used concrete and rock hardness testing equipment. The performance of both devices is based on the rebound of their impact body as it comes in contact with the concrete or rock surface. In the case of the Schmidt hammer, attempts have been made by various researchers to obtain empirical correlations between strength properties and the number of rebounds (Schmidt, 1954; Kolek, 1958; and Arni, 1972). The new Schmidt hammer is equipped with digital displays which enhance data collection. The EQUITIP hardness tester includes an impact device and a processing unit with digital display. For various materials, different impact devices with variable heads are used. The number of rebounds from the surface of the specimen generates a voltage value which is calibrated for a certain surface hardness. This value is displayed on the processing unit. For both the Schmidt hammer and the EQUITIP hardness tester, the hardness values must be corrected if the impact direction is different from the vertical direction. Conversion tables are used for this purpose. The other factors that may influence the results for concrete are: the moisture content, surface conditions, and aggregate size and type. For rocks, complex mineralogy has to be taken into consideration. Although the use of surface hardness testing equipment is simple and straightforward, the accuracy of the results are highly dependent on the correct positioning of the devices on the specimen surface.

2.4.2 Penetration Resistance and Pullout Systems

Both systems are semi-destructive, but since in some literature they are classified as nondestructive techniques (Malhotra, 1984) they will be briefly discussed.

The penetration technique essentially uses a powder-actuated gun or driver which fires a hardened alloy probe into the concrete. Later, the exposed length of the probe can be used as a measure of the concrete hardness and of the compressive strength of the specimen. The Windsor probe testing system is the most widely known penetration resistance device available for both laboratory and in situ measurements. The variation of the aggregate size, shape and hardness affects the results (Malhotra, 1991).

The pullout system entails pulling out a steel rod from the hardened concrete. A steel rod is placed in the concrete at the time of construction. When it is pulled, a dynamometer measures and registers the force. The pullout test is mainly used during the early construction phase in order to estimate the in situ strength of concrete. The main drawback to this technique is that the tests cannot be repeated and the steel rods have to be pre-planted. The maximum size and shape of the coarse aggregates has a large influence on the final results (Malhotra, 1984).

Both penetration and pullout methods are techniques for measuring compressive strength at early stages of concrete curing. The two systems are used strictly for concrete testing and there is no published records of the use of these methods to measure rock qualities (note: rock bolt pullout test is not considered in this category).

2.4.3 Petite Sismique Technique

The petite sismique method has been designed to estimate the rock's static modulus of elasticity. The principle of petite sismique is based on the refraction seismic technique. It emphasizes the determination of the shear wave parameters, with the most critical parameter being the frequency for the subsequent empirical correlation with the static modulus of elasticity. The system consists of an impact source (preferably a horizontally oriented surface force), a signal enhancement seismograph, and a few (minimum three) receivers (moving coil geophones or accelerometers). The orientation of the receivers is selected in a way to detect the shear wave arrivals. Later, signal analysis is performed in the frequency domain instead of the traditional time domain which makes the data processing more accurate (Bieniawski, 1978). Despite the successful results obtained by the petite sismique method, it has not been tried on concrete structures.

2.4.4 Impact-Echo Technique

Impact-echo is a technique developed for thickness measurement and delamination location in concrete (Sansalone and Carino, 1986; Sadri, 1992). The system is based on a high resolution seismic reflection survey on concrete structures using an impact source, a broad band unidirectional receiver and a waveform analyzer.

The mechanical impact generates stress pulses in the structure. The stress pulses undergo multiple reflections between the top and the bottom concrete layer. The surface displacements are recorded and the frequency of the successive arrivals of the reflected pulses is determined. P-wave reflections are used for detection of discontinuities and voids in concrete and rock structures. Discontinuities, defects and reinforcements could be identified in the resulting frequency spectra, as the P-wave reflects from their surfaces. Thus, knowing the thickness of a given layer, together with the derived frequencies, compression and shear wave velocities can be calculated. If, on the other hand, the thickness is unknown, the time-distance graph of the primary surface stress wave is used to calculate the thickness. The main drawback of the impact-echo system is the thickness limitation of the structures undergoing testing. Since, the impact source cannot provide high frequency signals above 20 kHz, accurate detection of defects in structures less than 10 cm thick is near impossible.

2.4.5 Impulse-Response Technique

The impulse-response method follows a principle similar to that of the impact-echo. A stress pulse is generated by a mechanical impact on the surface of the object. The force-time function of the hammer is recorded. A transducer records the vibration response of the surface as the reflected waves arrive. The processing of the recorded waveforms of the force and the arriving reflected waveforms reveals information about the condition of the structure. The impulse response of the structure is calculated by dividing the Fourier transform of the reflected wave by the Fourier transform of the force-time function of the impact. The technique is used to evaluate the dynamic stiffness of the concrete piles (Higgs, 1979). Discontinuities, voids and the base material affect the impulse-response evaluation. The main drawback of the system is the size and shape limitation of the structure undergoing testing.

2.4.6 Spectral Analysis of Surface Waves (SASW) Technique

The SASW method uses the Rayliegh wave (R-wave) to determine the stiffness profile and layer thickness of thin concrete layers. The SASW system includes an impact device, two receiving transducers, and a two-channel waveform analyzer. The characteristics of the impact device and the relative positioning of the transducers are determined by the stiffness and thickness of the layers. The R-wave produced by impact contains a range of frequencies, or components of different wavelengths. This range depends on the contact time of impact; the shorter the contact time, the broader the range of frequencies or wavelengths. The velocity of the individual frequency components are called phase velocity. For the component frequency of the impacts, a plot of phase velocity versus wavelength is obtained. This curve is used to calculate the stiffness profile of the test object. The experimental results are compared with theoretical curves until the results match (Nazerian and Stokoe, 1983). The main drawbacks of SASW are the limitation on the maximum layer thickness of the two media, and the matching of theoretical and experimental data.

2.5 ULTRASONIC METHODS

Ultrasonic equipment is constructed to operate based on two different principles: resonant frequency and pulse velocity method (Blitz, 1971). Almost all of the field and laboratory instruments for concrete and rock evaluation make use of pulse velocity systems. This method operates by measuring the average time taken for the ultrasonic wave to travel between the source and the receiver. The distance between the two points is divided by the travel time, which gives the average velocity of compressive wave propagation in the material. This method is used for measuring uniformity and in some cases the compressive strength. In addition to quality evaluation, ultrasonic waves can be used for determining fractures and voids within structures. This is known as the pulse-echo technique, which makes use of reflected waveforms from the interfaces to locate defects or measure thickness from only one direction. Ultrasonic equipment (pulse velocity) is capable of locating discontinuities, of quality evaluation and of thickness measurements. PUNDIT is the most commonly used ultrasonic instrument utilized for both field and laboratory testing. The main drawbacks are problems caused by wave scattering and unwanted noise, which are mainly due to the heterogeneous nature of concrete and rocks.

The principle of the resonant frequency method is based on the relation between the natural frequency of vibration of an elastic medium and its dynamic elastic properties. For a vibrating beam of known dimensions, the natural frequency of vibration is related to the elastic properties and the density of the medium. Therefore, the dynamic elastic modulus of the material can be calculated by measuring the natural frequency of vibration of the samples. In addition to the dynamic elastic properties of the concrete, moisture content and the strength of the samples could also be evaluated by using the mathematical relationships between the damping constant and the physical properties of the specimen. This is mainly a laboratory testing procedure and representative samples from the structures are tested for quality control purposes. However, field tests have been recorded on concrete columns (Gaidis and Rosenberg, 1986). The main limitations involve the shape and size of the samples, which effect the testing procedures (Malhotra, 1991; Lama 1978).

2.6 ELECTRICAL METHODS

The change in the electrical properties of the concrete and rocks such as electrical resistance, dielectric constant and polarization resistance can be monitored in order to evaluate thickness, moisture content, density and temperature variations. Electrical resistivity has been used to measure concrete and rock thickness by using the dialectic difference between the concrete and the base material and two different layers of rocks. A change in the slope of the resistivity versus depth curve is used to estimate the depth of a concrete slab or a rock layer. The dielectric constant of concrete and rock increases with any increase in the moisture content. Capacitance instruments are used to measure the in situ moisture content of the concrete and rocks. Linear polarization is used to calculate the corrosion rate of steel reinforcement bars in concrete slabs and pavements. Problems may occur due to variability of moisture content and temperature in the concrete and rock. The main drawback of the electrical methods is the assumption that the resistivity of each layer is constant and varies slightly with depth, which is far from reality (Hassani et al., 1989; Malhotra, 1984).

2.7 MAGNETIC METHODS

Magnetic devices are available for detecting ferromagnetic materials. For concrete structures these devices are used for detecting the position of the reinforcing bars, prestressing tendons, and metal ducts within the concrete, and can also be used for identification of the corrosion of the bars. In the case of rock formations, magnetic devices are used to determine ferromagnetic minerals within the rock mass.

Three main techniques using different magnetic principles are available for nondestructive testing purposes: a) Magnetic Induction, b) Flux Leakage Theory, and c) Nuclear Magnetic Resonance (NMR).

a) The Magnetic Induction systems operate based on the fact that steel rods or any other ferromagnetic objects within the specimen affect and in fact distort the primary field generated by the instrument (Malhotra, 1984). The instrument consists of a U-shaped magnetic core with two mounted coils. An alternating current is passed through one coil and the induced current is measured in the other coil. The presence and distance of steel reinforcement bars and ferromagnetic mineralized zones can be located by their effect on the induced current.

b) Other magnetic devices use the Flux Leakage methodology. These instruments are sensitive to changes in magnetic lines of force (flux) flowing through the materials. When a ferromagnetic material is magnetized, magnetic flux flows through and completes a path between the poles. However, if the pathway is disturbed by a crack or discontinuity, its magnetic permeability will be disturbed and this results in a flux leakage. The intensity of flux leakage can be used to characterize the various discontinuities and their shapes.

c) Nuclear Magnetic Resonance (NMR) systems use the interaction between nuclear magnetic dipole moments and a magnetic field. This interaction can be used to measure the moisture content of the material by detecting the signals from the hydrogen nuclei present in water molecules (Gorbanpoor and Shew, 1991).

The main drawback of these systems is that they cannot be used in heavily reinforced concrete elements or in tunnels with steel culvert supports, since the effect of a secondary field cannot be eliminated as a result of the intense presence of ferromagnetic alloys and detection and positioning of the targets is very difficult.

2.8 ELECTROMAGNETIC METHODS

Short-pulse or Ground Penetration (or Probing) Radar (GPR) is an electromagnetic equivalent of ultrasonic and stress-wave reflection techniques. An antenna transmits the EM pulses into the object. The energy travels through different materials with different velocities. This variation of velocity has a direct relationship to the material quality, which is controlled by the material's dielectric properties. A change in the material's dielectric constant, which occurs at interfaces such as concrete and air, or between two different rock types, causes a change in wave shape. The reflected signals are received by the receiving antenna, separate from the transmitting antenna, or in the same casing. Signals are positive when they are traveling from a lower to a higher dielectric material (e.g., air to concrete) and are negative when they are traveling from higher to lower dialectical material (e.g., concrete to air). Electromagnetic waves are also known as microwaves or centimeter waves. An EM wave which has a range of wavelengths between 0.3 and 30 cm corresponds to frequencies in the range of 1 to 100 GHz. The commercially available GPR systems operate with the frequencies ranging from 20 MHz to 2 GHz.

The radar system operates by a transmitting antenna and a receiving antenna that collects the reflected waveforms. The control unit controls the functions of the GPR system such as scanning speed, signal filters, amplifications and time measurements. Ground Penetrating Radar could be used for detection of delaminations, cracks, voids, and reinforcing steel bars within the concrete with reasonable accuracy (Momayez, Sadri, and Hassani, 1994). The GPR has been demonstrated to be an effective tool in measuring the thickness and geometry of pillar structures, in addition to locating faults and shear zones in underground coal, salt and gold mines (Momayez et al., 1994; Fenner, 1995)

The resolution of the survey can be accurately set by using various antenna-signal frequency combinations (Hassani et al., 1989; Momayez et al., 1994). The GPR could be used for inspection of underground concrete linings, shafts and dams. The system could also be used to map the cavities and fracture patterns behind the linings, particularly in the case of shafts and subway tunnels.

2.9 INFRARED THERMOGRAPHIC METHODS

Infrared thermography, or infrared scanning, is a technique which operates based on the capability of various materials to absorb heat. Solar radiation is the main source of heat for surface structures. As the solar ray flows through a structure, air voids and fracture openings absorb a larger percentage of heat than the surrounding material. This can be monitored and registered by an infrared camera. The same principle holds for steel reinforcement but at a different intensity (Weil, 1991).

Using infrared thermography, it is possible to locate voids, delaminations, fractures and steel reinforcing bars. However, it is not possible to locate their exact position. Test results are highly affected by the surrounding conditions such as time of day or seasonal changes. Moisture content of the concrete or rocks also affects the readings (Weil, 1991). As for the underground openings and shaft linings, an artificial primary source of heat is needed. In the tunnels, a convectional heating of the air and lining surfaces can be achieved with diesel or gas machinery exhaust. Loose rocks in underground excavations were successfully detected by discriminating the loose from the rock mass using the insulating factor of the air in the fracture or parting behind the loose rocks and the contrast between the heat absorption between the rock and the air (Yu, Henning and Croxall, 1983). The release of toxic fumes as a result of engine exhaust is the main drawback and it is not practical to use a infrared thermography system in a closed environment (Yu, Henning and Croxall, 1983).

2.10 ACOUSTIC EMISSION METHODS

Acoustic emission or stress emission is a general term used for any transient waveform released from a solid which is under stress. In concrete structures, the main source of wave emission would be crack development or the slip between the concrete and the reinforcing bars. In a rock mass fracture developments, slipping along rock planes, or closure of voids or cavities are the main source of stress-wave emissions. On the concrete surface a number of transducers receive and later register these low amplitude stress waves. The variation of arrival time of waveforms registered by each transducer is used to locate the source. Later interpretations can be performed using the intensity of wave emission. Rock bursts, rate of subsidence, and rate of movements along the faults and fracture zones can be detected by placing receiving transducers with various patterns along the excavated openings (Kat, 1988; Franklin, 1990). An increase in wave emission in a structure could be analyzed as an unsafe condition; however, this is not considered as a satisfactory deduction (Ghorbanpoor, 1991; Mindess, 1991; Franklin, 1990). In rock masses, the same principle applies.

2.11 RADIOACTIVE METHODS

Radioactive methods are mainly used in the concrete industry. In mining, applications are limited to detection of radioactive minerals. Radioactive systems are classified into two main subgroups:

2.11.1 Radiography Technique

Using a radioactive source, this technique provides a photographic image of the concrete which makes it possible to locate the reinforcement bars, voids, fractures, and honeycombing. High costs associated with the source, dangerous high voltage equipment, and safety factors make this technique undesirable for field use (Malhotra, 1984).

2.11.2 Radiometry Technique

Because gamma rays are capable of passing through concrete, various types of radioisotopes are used and pre-planted within the structures at the time of construction. Using calibrated charts the thickness, moisture content, and density of concrete can be measured. This can be done as a result of change in the emerging intensity of gamma rays, which are collected with the aid of a scintillometer or geigercounters. Similarly, high operational costs and safety factors have limited the use of radiometry in the field of nondestructive testing (Hassani et al., 1989; Malhotra, 1984).

2.12 CONCLUSIONS

In situ nondestructive testing techniques provide a great deal of information about maintenance and support of concrete and excavated rock mass structures at relatively low cost. In case, extra information is needed about the quality of a structure or if the damaged areas are not visible, nondestructive testing becomes a useful tool for the field engineers. One appealing factor about the nondestructive testing methods is that the tests could be repeated in situ for the same area, for a majority of the cases. An overview of nondestructive testing methods suggests that at present no <u>truly</u> nondestructive testing technique is currently available for determining quality and thickness at the same time as detecting voids and delaminations, both in concrete and rocks. A number of reliable nondestructive testing techniques exist for measuring material properties and strength of concrete and rock. Some other nondestructive testing methods have been used to detect and measure the delaminations, voids and thickness.

CHAPTER 3

FUNDAMENTAL PRINCIPLES OF ELASTIC BEHAVIOR OF SOLIDS AND ELASTIC WAVES

3.1 INTRODUCTION

This chapter presents background information on elastic wave generation, and its propagation, and detection. The theory of elasticity for solids and the interrelationship between elastic constants is illustrated. The principles that effect the velocity of elastic waves and the reasons behind signal reflection, refraction, diffraction, and radiation pattern as an effect of the source and material quality are also discussed.

3.2 FUNDAMENTALS OF ELASTIC WAVE PROPAGATION

To understand the behavior of the travelling waves in elastic medium, it is necessary to define the quantities that describe the elastic properties of a medium.

3.2.1 Stress and Strain

As the elastic waves travel through a media, there are two principal changes experienced by the material: first, the redistribution of internal forces and second, the deformation of the geometrical shape. These effects are best explained in terms of the concepts of stress and strain.

Stress is the measure of the force, F, per unit area across a surface element, A, within the material. In other words, the stress is defined as a limiting value of the ratio F/A when A tends to be infinitely small (Sharma, 1986). Therefore stress could be expressed as:

$$\sigma = \lim_{A \to 0} \frac{F}{A} \qquad (3-1)$$

When F is normal to the stress element, the stress is called normal stress; it is called tensile stress or compressive stress if it is directed away or into the material at the point of application. If F is tangential to the area element, the stress is a shearing stress and is defined by two mutually perpendicular components that are in the plane of the area element. The stress at a point within a body is defined if the normal stress and two shearing stresses are determined for three mutually perpendicular area elements which intersect at a point. Strain is a measure of the relative deformation of a body when it is subjected to stress. The change in size or shape characterizes strain. Strain causing only a change in shape and no change in volume is called shear strain, whereas a change in volume without change in shape is called dilatation or contraction. The strains associated with the relative change in length in the direction of respective stress are called normal strains.

$$\epsilon = \frac{\Delta l}{l} \tag{3-2}$$

where Δl is the change in length and l is the original length. In this case strain is expressed as change in length.

3.2.2 Elastic Behavior

For safe and economical design of a structure within an excavated rock mass or on the surface, adequate knowledge of physical properties of both the rock and the structure is indispensable. Elastic behavior is one of the important properties that should be taken into consideration. All materials undergo deformation when they are subjected to load. Excessive load results in structural failure of the material. Most of the materials regain their original size and shape after the removal of the load when the temperature is constant. Elasticity is the terminology used for the ability of a material to regain its original shape and size. The return of the body to its original shape is known as elastic deformation. When the material completely recovers its shape it is said to be perfectly elastic and if it does not fully regain its original shape it is said to be partially elastic.

The elastic constants quantify specific relationships between different types of stresses and strains (Sharma, 1986):

1. Modulus of elasticity
2. Shear modulus
3. Poisson's ratio
4. Bulk modulus

3.2.3 Elastic Constants

In 1678 the British mathematician, Robert Hooke (1635-1703) established a relationship between elastic deformation and load. In general, Hooke's law states that stress, σ, is proportional to strain, ϵ. According to Hooke's law a perfectly elastic body exhibits a linear relationship between stress and strain.

$$\sigma \propto \epsilon \tag{3-3}$$

In 1807, Thomas Young (1773-1829), British scientist, introduced a constant of proportionality, E, known as the modulus of elasticity or Young's modulus and is a measure of a material's stiffness. A large value of E implies a stiff material like granite, and a small value indicates flexible materials such as talc. In a practical situation when a material is under tensile or compressive load within its elastic strain range, the ratio of the stress to the strain in the direction of the applied stress is called modulus of elasticity.

$$E = \frac{\sigma}{\epsilon} \tag{3-4}$$

Since the strain is a dimensionless quantity and unitless, the modulus of elasticity is expressed by the same units as stress; in the SI system it would be Pascals.

For the shear stresses, τ, and the shear strains, γ, the constant of proportionality, G is called shear modulus or modulus of rigidity. The shear strain is the resulting deformation without change of volume. The strain in this case could be expressed by the angle of deformation. The shear modulus for liquid and gas media is zero. In SI system, shear modulus is expressed in Pascals.

$$G = \frac{\tau}{\gamma} \tag{3-5}$$

In most metals, E and G are almost constant regardless of the quality of the material; however, this is not true in case of rocks and concrete. The E value varies with strength and material content within the elastic range of the sample because the stress and strain relationship is not linear. In this case, the value of E is calculated for a specific stress and the corresponding strain.

In 1811 the French mathematician Simon Poisson (1781-1840) identified the relationship between the axial strain ϵ_a and the lateral strain ϵ_l. The ratio of the lateral strain to the axial strain is known as Poisson's ratio, υ, which is a dimensionless quantity. Poisson's ratio is a measure of geometric change in the shape of an elastic body. The value of Poisson's ratio is always positive and varies between 0.0 and 0.5. The value of Poisson's ratio remains constant within elastic straining of the materials.

$$\upsilon = \frac{\epsilon_l}{\epsilon_a} \tag{3-6}$$

If a body of volume V is subjected to uniform compressive stress, such as hydrostatic pressure, P, its volume will be decreased an amount ΔV. The bulk modulus, K, is the ratio of the pressure to the volumetric strain $\frac{\Delta V}{V}$. Bulk modulus is a reciprocal of compressibility. In SI system bulk modulus is expressed in Pascals.

$$K = -\frac{P}{\frac{\Delta V}{V}} \tag{3-7}$$

Although no rock or concrete is perfectly elastic, it is often convenient to assume quasi-elasticity, and apply elastic theory to the behavior of the rocks or concretes. All the elastic constants are interrelated when the material is continuous, isotropic, homogeneous and perfectly elastic. Rock masses are anisotropic, which means their behavior is directional. The directional behavior is controlled by bedding, jointing, microstructures and fabric orientation for rocks. Nevertheless, the elasticity in rocks is affected by the rock type, porosity, particle size, and water content. In the case of concrete, which is a heterogeneous and multiphase material, bulk porosity, porosity of the aggregates, cement paste matrix, and the transition zone are the important factors affecting the modulus of elasticity. The known elastic constant values of rocks and concrete suggest that the chemical composition and bonding are the main factors for variation in the elasticity values. However, in routine engineering work, rocks and concrete are assumed to be isotropic. In extreme anisotropic cases, orthotropic symmetry directions could be added to the equations and orthotropic constants can be calculated.

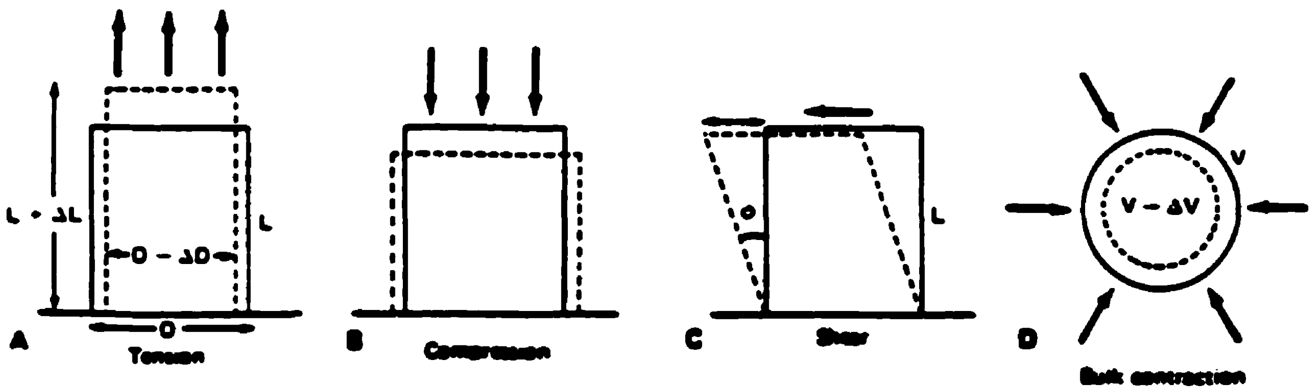

Figure 3-1 Common types of elastic strain. (after Sharma, 1986)

Table 3-1 Illustrates the interrelationship between the four elastic constants (Telford, 1990).

Young's Modulus (GPa)	Shear Modulus (Rigidity) (GPa)	Poisson's Ratio	Bulk Modulus (GPa)
$E = 2G(1+\upsilon)$	$G = \frac{E}{2(1+\upsilon)}$	$\upsilon = \frac{(3K-2G)}{2(3K+G)}$	$K = \frac{E}{3(1-2\upsilon)}$
$E = \frac{9Gk}{(G+3k)}$	$G = \frac{3EK}{(9K-E)}$	$\upsilon = \frac{(3K-E)}{6K}$	$K = \frac{EG}{3(3G-E)}$
$E = 3K(1-2\upsilon)$	$G = \frac{3K(1-2\upsilon)}{2(1+\upsilon)}$	$\upsilon = \frac{(E-2G)}{2G}$	$K = \frac{2G(1+\upsilon)}{3(1-2\upsilon)}$

3.3 ELASTIC WAVES

A wave is defined as a disturbance which travels through a medium. When a stress is suddenly applied (transient stress) to an elastic body, the corresponding displacement is propagated outwards as an elastic wave. Elastic waves are also referred to as stress waves. The ultrasonic waves traveling within an elastic body are elastic waves. There are two principal types of elastic waves: body and surface waves. Body waves travel across and surface waves travel along the surface of an elastic medium.

As a result of release of stress, an elastic medium undergoes two types of deformations: compression and shear. In primary mode, three main types of elastic waves may be observed as a result of a mechanical shock to a solid:

1) Compression, longitudinal or primary (P) waves.
2) Shear, transverse or secondary (S) waves.
3) Rayleigh or (R) waves.

Compression (P) waves are characterized by particle motion being longitudinal. This means that while the wave is passing through a medium, particles will vibrate about an equilibrium position, in the same direction as the P-wave is travelling. These waves involve compression and rarefaction, but no rotation of the material while they are passing through an elastic medium (Mooney, 1980; Telford, 1990).

Shear (S) waves are characterized by particle motion being transverse. This means that while the wave is passing through a medium, particle displacement will be perpendicular to the direction of propagation and motion of S-waves. These waves involve shearing and rotation, but no volume change while they are passing through an elastic medium (Mooney, 1980; Telford, 1990; and Helbig, 1987).

Rayleigh (R) waves are surface waves which move with marginal attenuation in the direction of wave propagation. In R-waves the particle motion is more or less a combination of longitudinal and transverse vibration. Characteristically, their energy level drops rapidly as the wave penetrates below the surface (Mooney, 1980; Telford, 1990).

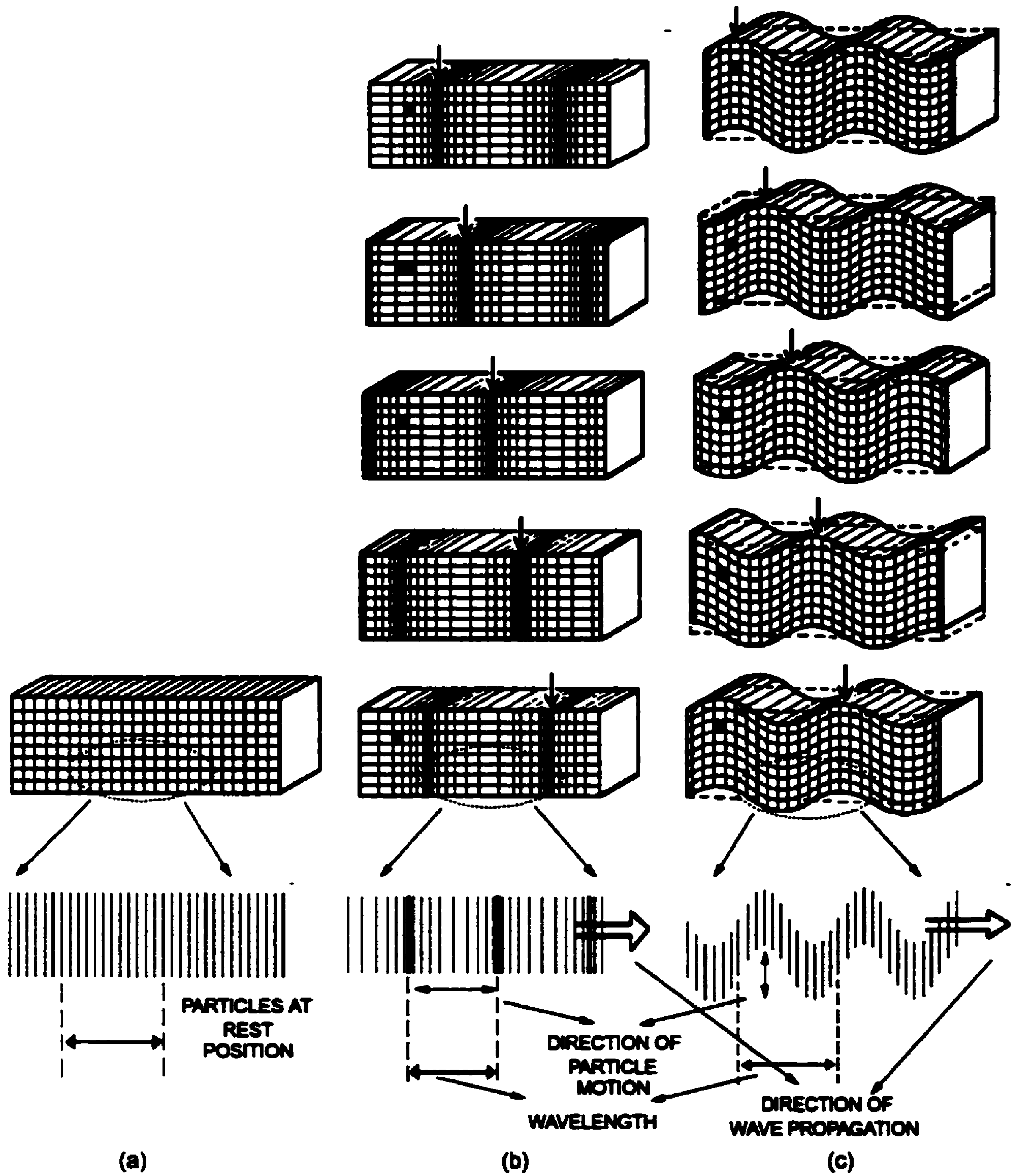

Figure 3-2 Successive stages in the deformation of a block of a material by compressive waves and shear waves and their particle motion. The sequences in progress with time from top to bottom. (modified after Phillips 1968).

a) The block of material, b) compressive waves, and c) Shear waves.

Each of these waves result in a momentary displacement in the specimen it traverses. P-waves have a back-and-forth (compression) motion that is parallel to the direction the wave propagates. S-waves have a to-and-fro (shear) motion which is perpendicular to the direction of propagation (see Figure 3-2). R-waves have a retrograde elliptical type of particle motion which is in part perpendicular and in part parallel to the surface. As a result R-waves have both horizontal and vertical components (Mooney, 1974 and 1980; Telford, 1990). The shape of P-, S-, and R-wavefronts depends on the characteristics of the source that is used to generate the waves. There are three idealized types of wavefronts: planer, cylindrical and spherical. In the case of a point source (spherical-tipped impact source) normal to the surface of the media, the resulting P- and S-wavefronts are spherical and the R-wavefront is circular.

3.3.1 Wave Velocity

P-wave velocity, C_P, is a function of Poisson's ratio, υ, Young's modulus, E, and mass density, ρ, of the material it is traversing (Telford, 1990).

$$C_P = \sqrt{\frac{E(1-\upsilon)}{(1+\upsilon)(1-2\upsilon)\rho}} \tag{3-8}$$

In bonded media, the dimensions of the specimen effect the wave velocity. In the case of rods and thin plates, P-wave velocity can vary depending on the dimensions of the specimen relative to the component wavelength of the propagating wave. For rod-like specimen, the P-wave velocity is independent of the Poisson's ratio, if the diameter of the rod is much smaller than the component wavelength(s) of the propagated wave (Sansalone, 1985). In this situation, P-wave velocity is calculated by the following equation (Banks, 1962):

$$C_P = \sqrt{\frac{E}{\rho}} \tag{3-9}$$

S-wave velocity, C_S, is calculated by the equation (Sharma, 1986):

$$C_S = \sqrt{\frac{E}{2\rho(1+\upsilon)}} \tag{3-10}$$

The relation between S- to P- wave velocity can be calculated as (Sharma, 1986):

$$\frac{C_S}{C_P} = \sqrt{\frac{(1-2\upsilon)}{2(1-\upsilon)}} \tag{3-11}$$

R-wave velocity, C_R, can be related to the shear wave by the following equation (Sansalone, 1985):

$$C_R = \frac{0.87+1.12\upsilon}{1+\upsilon} \times C_S \tag{3-12}$$

The P- and R-wave velocities are related by the following equation (Sansalone, 1985):

$$C_R = \frac{0.87+1.12\upsilon}{1+\upsilon}\sqrt{\frac{(1-2\upsilon)}{2(1-\upsilon)}}C_P \tag{3-13}$$

Each of the three waves travel with different velocities. P-waves have the highest velocity. S-wave velocities are between 0.65 and 0.45 of the P-wave velocities, depending on the stiffness of the material. As the material stiffness increases the ratio between the S- and P-wave velocities increases. For a Poisson ratio ,υ, of 0.2, the C_S to C_P ratio would be 0.61 (Sansalone, 1985). The R-wave is the slowest of the three. R-waves have a velocity of roughly 92% of the S-waves (for a Poisson ratio of 0.2) and 56% of P-waves (Mooney, 1974; Sansalone, 1985). They are easy to recognize because they have large amplitudes, low frequencies and appear last. In most of the seismological studies the main work has been done on P-waves, since they arrive prior to other waves and can be recognized without interference from other wave types. P-waves travel through all three types of media: solids, liquids and gases. The most familiar type of P-wave is sound. Available nondestructive testing equipment that employs P-waves as the principle of their operation are ultrasonic and impact-echo equipment. On the other hand, S-waves can only pass through solids. They are often generated by the same sources generating P-waves. In a simple comparison between P- and S-waves of the same frequency, S-waves have smaller wavelengths and amplitudes than P-waves. Fundamentally, shear waves are subdivided based on their polarization characteristics to radial (SV) and transverse (SH) components (see Figure 3-3). SH-waves have their particle displacements parallel to the boundary surface, and SV-waves have their particle displacements lying in the incident plane. SV-waves are not easily recognizable on a time domain spectrum, since they are coupled with P-waves and the receivers are sensitive to both P-waves and to SV-waves. On the other hand, SH-waves are self-consistent in a sense that they do not interact with P- and SV-waves. This means that they do not convert into P- and/or SV-waves nor do P- and/or SV-waves convert into SH-waves (Helbig, 1987). As a result, when a pure SH-wave is generated, a seismic section can be obtained only with SH-wave reflections. R-waves can be easily recognized by their distinguished large-amplitude low-frequency signals arriving almost immediately after S-waves (Helbig, 1987).

Elastic waves represent a large and diverse subject matter. In this study our focus will mainly be on body waves generated as a result of electro-acoustic transducers and point source mechanical impact sources.

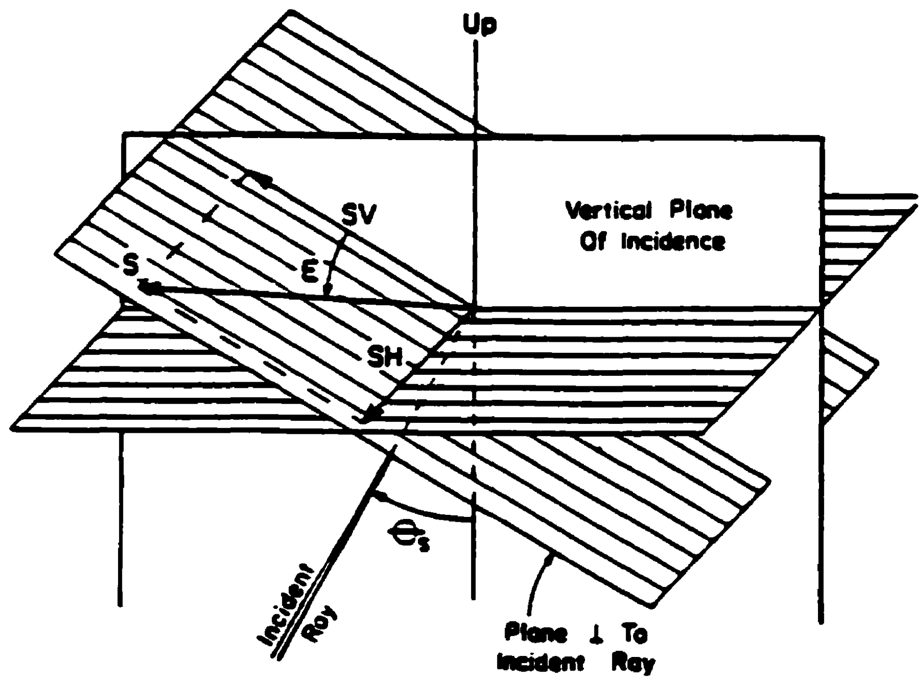

Figure 3-3 Resolution of shear wave motion into SV and SH components. (after Stauder, 1962 and Mooney, 1981).

Table 3-2 The relationship between elastic wave velocities and dynamic elastic moduli (Telford, 1990):

Young's Modulus (GPa)	Shear Modulus (Rigidity) (GPa)	Poisson's Ratio	Bulk Modulus (GPa)
$E = C_p^2 \rho \frac{(1+\upsilon)(1-2\upsilon)}{1-\upsilon}$	$G = \rho C_s^2$	$\upsilon = \frac{\left(\frac{C_p}{C_s}\right)^2 - 2}{2\left(\frac{C_p}{C_s}\right)^2 - 2}$	$K = \rho\left(C_p^2 - \frac{4}{3}C_s^2\right)$
$E = C_s^2 2\rho(1+\upsilon)$	$G = \frac{K}{\left(\frac{C_p^2}{C_s^2} - \frac{4}{3}\right)}$		$K = G\left(\frac{C_p^2}{C_s^2} - \frac{4}{3}\right)$

Where:
Compressional Wave velocity = C_p (m/s)
Shear wave velocity = C_s (m/s)
Density = ρ (kg/m^3)

3.3.2 Reflection, Refraction and Diffraction

When a P- or S-wavefront extends from the source of disturbance uniformly in all directions, its energy declines with the square of the distance and the wave amplitude reduces directly in proportion to the distance traveled. As the wavefront reaches a second boundary, part of the elastic waves are reflected and part of it penetrates to the second medium (refracted). The concept governing the reflection and refraction of elastic waves is the same as that of the reflection of light from a mirror. Nevertheless, despite the similarities, elastic wave reflections and refractions are slightly more complicated than those of light from a mirror. In general, any body wave (P- and S-waves) striking a boundary will generate two reflected P- and S-wave and two refracted P- and S-waves. This phenomena is called mode conversion and is controlled by the angle of incidence. The reflection and refraction are governed by Snell's Law:

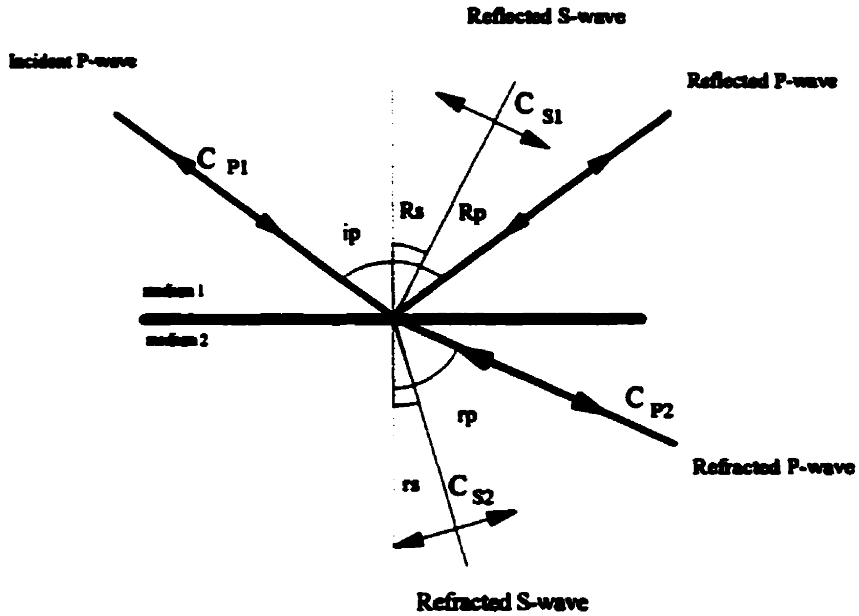

Figure 3-4 Behavior of an incident P-wave at a boundary separating two media with different velocities; reflection, refraction and mode conversion. (Sharma, 1986)

$$\frac{\sin i_p}{C_{p1}} = \frac{\sin R_p}{C_{p1}} = \frac{\sin R_s}{C_{s1}} = \frac{\sin r_p}{C_{p2}} = \frac{\sin r_s}{C_{s2}} \qquad (3-15)$$

where R is the angle of reflection, i is the angle of incidence, r is the angle of refraction, C_p is the velocity of P-wave and C_s is the velocity of S-wave.

Snell's law is used for the determination of the reflected wave path (see Figure 3-4). The amplitude of reflected signals depends upon the interface's boundary condition and the acoustic impedance, the angle of incidence, the distance of the interface to the source, and the signal's attenuation rate.

The reflection of a signal from an interface between two media with different density or elastic moduli depends on the specific acoustic impedance of the two media.

The corresponding equation in terms of amplitudes was given by Zoeppritz (1919), where in this case the Z is the specific acoustic impedance of a medium, ρ is the density, and W_v is any elastic wave velocity (i.e. the equation is valid for P- or S-waves).

$$Z = \rho . C_p \tag{3-16}$$

For P-wave velocity, C_p acoustic impedance could be rewritten as (Telford, 1990):

$$Z = \sqrt{E . \rho} \tag{3-17}$$

this equation changes for S-wave to:

$$Z = \sqrt{G . \rho} \tag{3-18}$$

equations 3-17 and 3-18 apply only to rod waves.

For P-waves, the amplitude of particle motion, A_R, is maximum when the angle of incidence of the waveform is normal to the interface. The amplitude of particle motion for the reflected wave (A_R) is calculated by (Telford, 1990):

$$A_R = A_I \frac{Z_1 - Z_2}{Z_1 + Z_2} \tag{3-19}$$

where A_I is the amplitude of motion in the incidence waveform. Z_1 is the acoustic impedance of the first layer and Z_2 is acoustic impedance of the reflecting layer or the second layer.

The amplitude of the stress in the refracted wave (A_T) is given by the following equation (Telford, 1990):

$$A_T = A_I \frac{2Z_2}{Z_1 + Z_2} \tag{3-20}$$

Another important property provides information on the relative size of the amplitude of each reflected wave compared to the incident wave. The amplitude ratios of the reflected P-wave (A_p / A_l) and the reflected S-wave (A_s / A_l) compared to the incident wave amplitude are called reflection coefficients. The reflection coefficients at a stress-free boundary (i.e. air) are found to be (McIntire, Birks, and Green, 1987):

$$R_{pp} = \frac{\sin 2\alpha_l \sin 2\alpha_s - \left(\frac{c_p}{c_s}\right)^2 \cos^2 2\alpha_s}{\sin 2\alpha_l \sin 2\alpha_s + \left(\frac{c_p}{c_s}\right)^2 \cos^2 2\alpha_s} \qquad (3-21)$$

$$R_{ss} = \frac{2\left(\frac{c_s}{c_p}\right)^2 \sin 2\alpha_l \cos 2\alpha_s}{\sin 2\alpha_p \sin 2\alpha_s + \left(\frac{c_s}{c_p}\right)^2 \cos^2 2\alpha_s} \qquad (3-22)$$

where α_p and α_s are the angles of reflected P- and S-waves respectively. For the reflected S-wave the same formula applies. In this equation R_{pp} signifies the reflection coefficient for the reflected P-wave referred to an incident P-wave energy and R_{ss} is a reflection coefficient for the reflected S-wave.

For an SV-wave incident at all angles below the critical angle, both a reflected P mode (SP) and a reflected SV mode (SS) generally occur. Depending on the value of the Poisson's ratio, there are for some materials specific values of incident angles when the amplitude of the reflected SV mode is zero (SS=0). In all cases there is always a reflected P mode (SP) for this range of incident angles. With stress-free boundary conditions, there is a set of reflection coefficients for this problem as follows (McIntire, Birks, and Green, 1987):

$$R_{pp} = \frac{2\left(\frac{c_s}{c_p}\right)^2 \cos 2\alpha_S \sin 2\alpha_s}{2\sin 2\alpha_p \sin 2\alpha_s + \left(\frac{c_s}{c_p}\right)^2 \cos^2 2\alpha_s} \qquad (3-23)$$

$$R_{ss} = \frac{2\sin 2\alpha_p \sin 2\alpha_s - \left(\frac{C_p}{C_s}\right)^2 \cos^2 2\alpha_s}{2\sin 2\alpha_p \sin 2\alpha_s + \left(\frac{C_p}{C_s}\right)^2 \cos^2 2\alpha_s} \quad (3-24)$$

All parameters have the same definitions as given before for the reflected P mode. This problem, with the exception of the appearance of the critical angle phenomenon, is symmetric in results to the reflected P mode discussed earlier. For the SV-wave incident on a stress-free boundary at incident angles greater than the critical angle, a reflected longitudinal P mode (PP) cannot occur (McIntire, Birks, and Green, 1987).

Figure 3-5 shows the partition of energy for an incident longitudinal and transverse waves and for several values of Poisson's ratio. To calculate the energy reflection coefficients for incident waves, the following should be known: the unit area of the incident waves, the amplitude of reflection waves, and the energy of the incident waves.

Various combinations of the horizontal and vertical source and receivers have a strong influence on the enhancement of the receiving signals and their amplitude. Initially, White (1965) found the relationship between the angle of incidence of the generated wave at a stress-free surface, the angle of reflected wave, and the displacements at the surface as a function of C_p / C_s and hence Poisson's ratio, υ (see Figure 3-6). The radiation characteristics of a surface (horizontal or vertical) point source are identical to the receiving characteristics of a (horizontal or vertical) receiver. Kahler (1988) states that the influence of Poisson's ratio on the source and receiver is specially large for horizontal sources and receivers, both for P- and SV-waves, while SH-waves are not affected by Poisson's ratio. For a horizontal source there is no component of P in the z-direction. The pattern for SV-waves is complicated whereas the SH-wave pattern is simple, for it has no components in the x-direction. For a vertical source, the radiation patterns are symmetrical around the z-axis and there are no components of SV-waves in vertical and horizontal directions and at the critical angle; also there is no SH-wave.

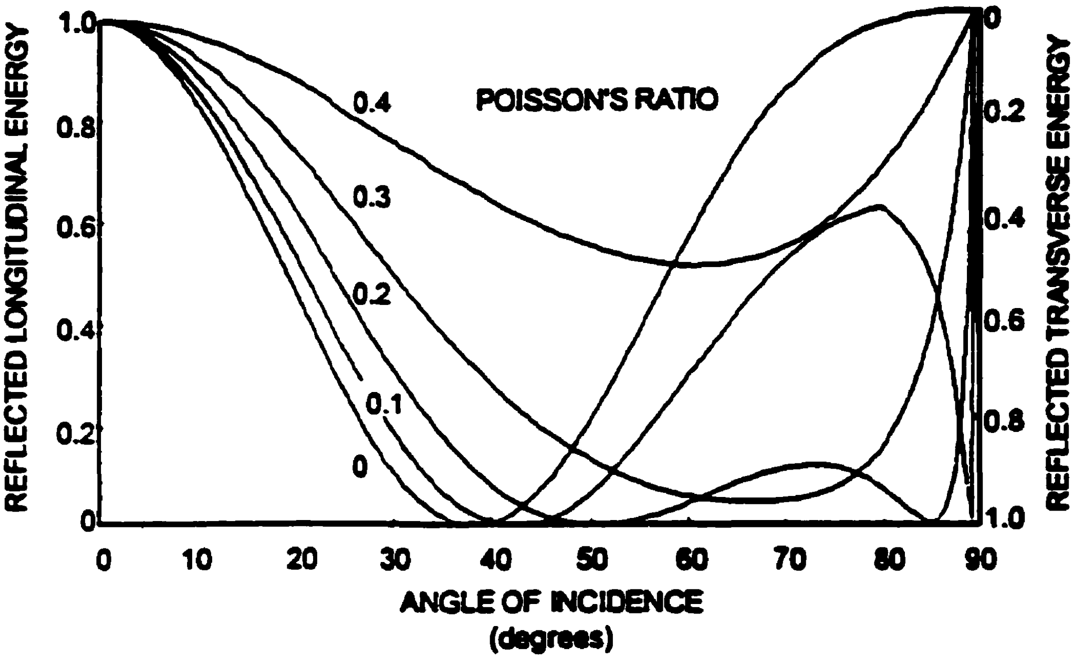

(a)

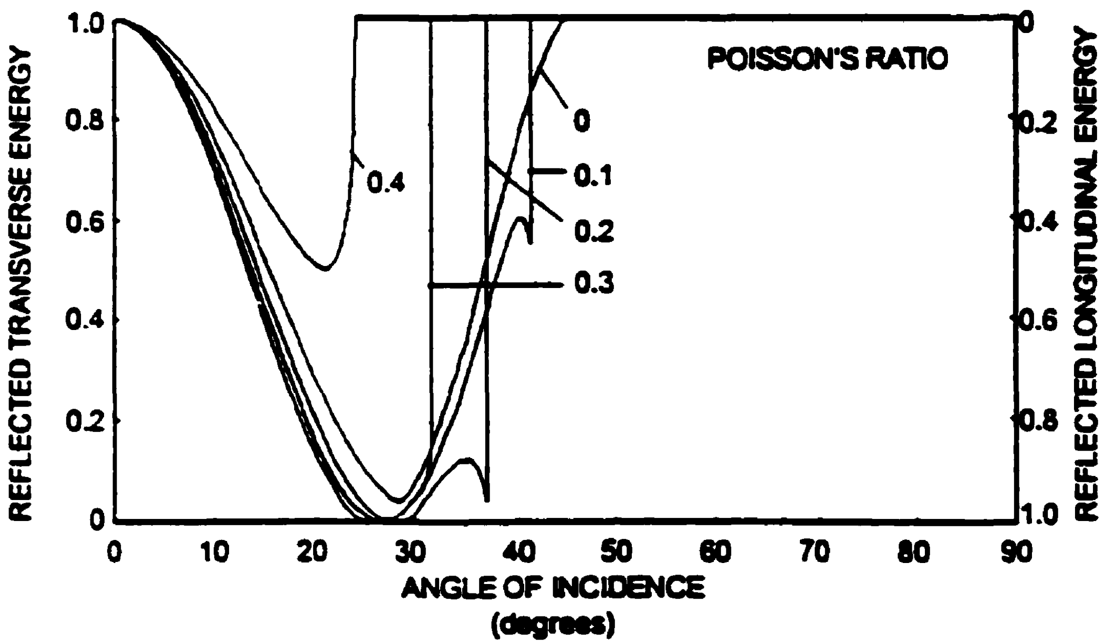

Figure 3-5 Energy reflection coefficient for incident a) longitudinal energy and b) transverse energy (after Miller and McIntire, 1987.

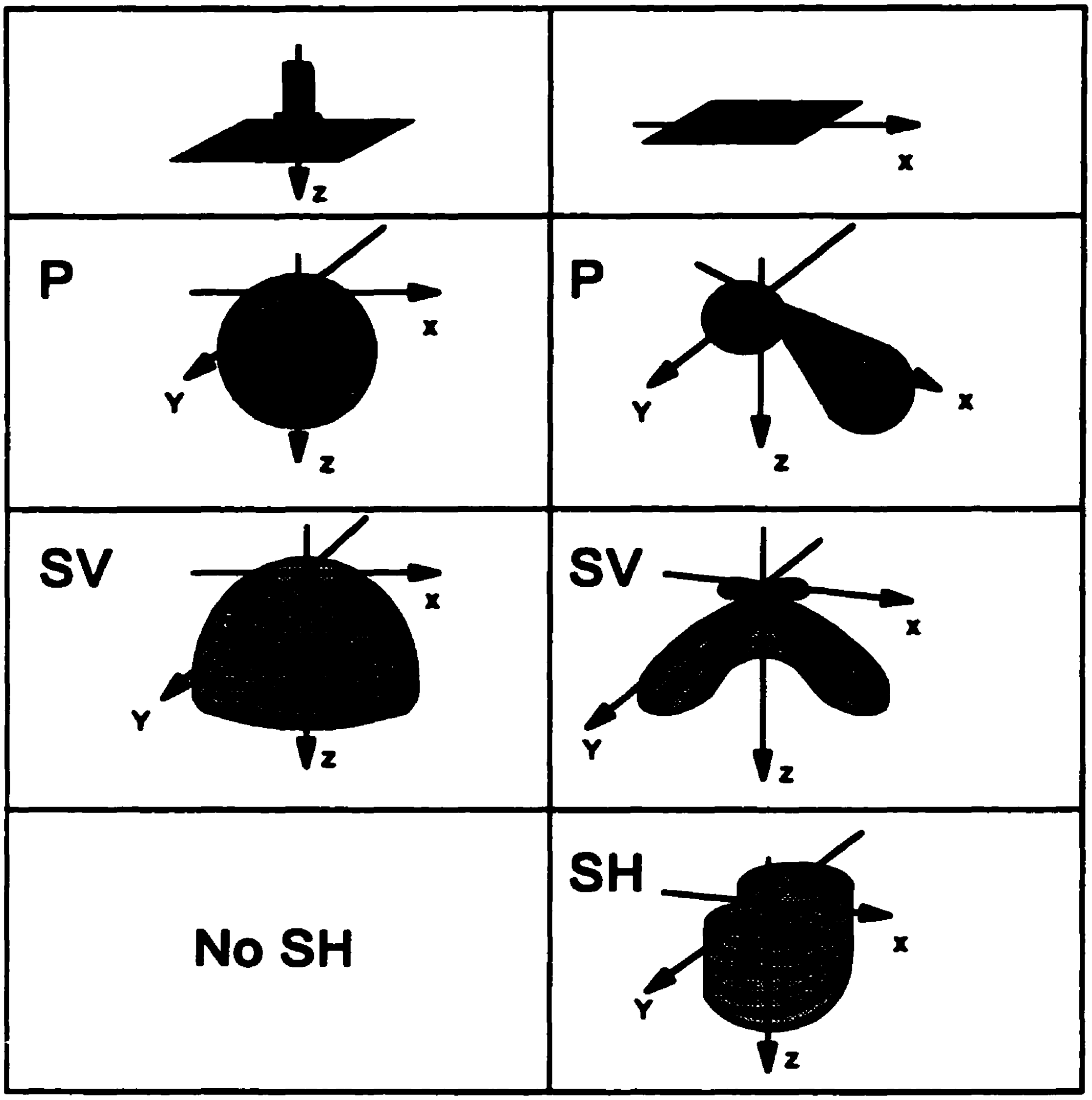

Figure 3-6 Schematic drawing of the radiation pattern of a horizontal and vertical surface point source. Left: vertical; right: horizontal source, Poisson's ratio is about 0.25.
(modified after Kahler and Meissner, 1983)

Diffraction occurs when an elastic wave is incident upon a sharp edge of a discontinuity (i.e. crack tip). The sharp corner serves as a center of scattering waves. These waves have spherical wavefronts, originating from the sharp edge (Sansalone, 1985). Mode conversion (transformation of one wavetype to another, e.g., P-wave to S-wave) also happens at the sharp edge (see Figure 3-7).

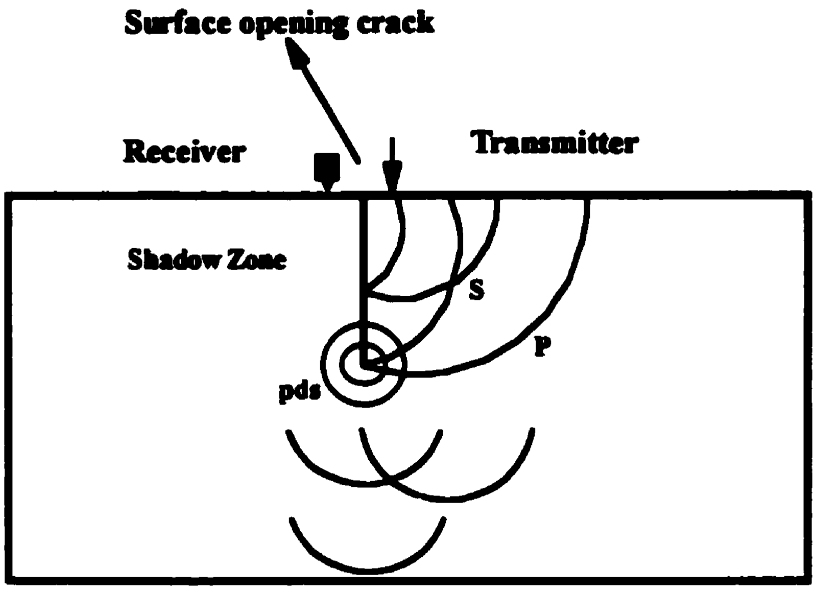

Figure 3-7 Wave diffraction as a result of surface opening crack edge and the position of the transmitter and the receiver with respect to the crack for measuring the depth of it.

3.3.3 The Elastic Wave (Body Waves) Generators

Electro-acoustic transducers are common means of generating body waves, particularly P-waves. Continuous, short-duration pulses are generated by an electro-acoustic transducer which is coupled to the specimen. The signals are usually picked by a receiving transducer (Mooney, 1974).

To use surface sources for generation of elastic waves, a direct force, either horizontal or vertical, is used. A vertical impact source generates P-, SV-, and R-waves. A horizontal impact source generates P-, SV-, SH-, and R-waves (Mooney, 1974).

For a horizontal impact surface source the radiation pattern of SH-waves is at maximum when perpendicular to the force, and decreases to zero in the direction of the force. The P- and SV-wave radiation will be zero in a plane perpendicular to the force (see Figure 3-6). For observation in a vertical plane which contains the force, P-wave radiation is at maximum at an angle of about 60° and decreases to zero in both vertical and horizontal directions. SV-wave radiation is large in the vertical direction and remains large out to the critical angle given by $\sin\theta_s = C_s/C_p$. Beyond that the amplitude decreases and reaches zero for the horizontal direction (Mooney, 1974; Helbig, 1987).

For a vertical impact surface source, the maximum P-wave propagates in a vertical direction beneath the impact source, and decreases to zero in the horizontal direction along the surface (see Figure 3-6). The SV-wave amplitudes are strong at a particular angle from the source (45° from the source, for a Poisson's ratio of 0.25). This maximum amplitude is related to the complicated radiation pattern of the SV-waves. Zero amplitudes occur at the critical angle given by $\sin\theta_s = C_s/C_p$ (which is 35.2° for a Poisson's ratio of 0.25) (see Figure 3-8). At small angles, close to vertical, particle motion is rectilinear but becomes elliptically polarized for larger angles (Mooney, 1974; Helbig, 1987).

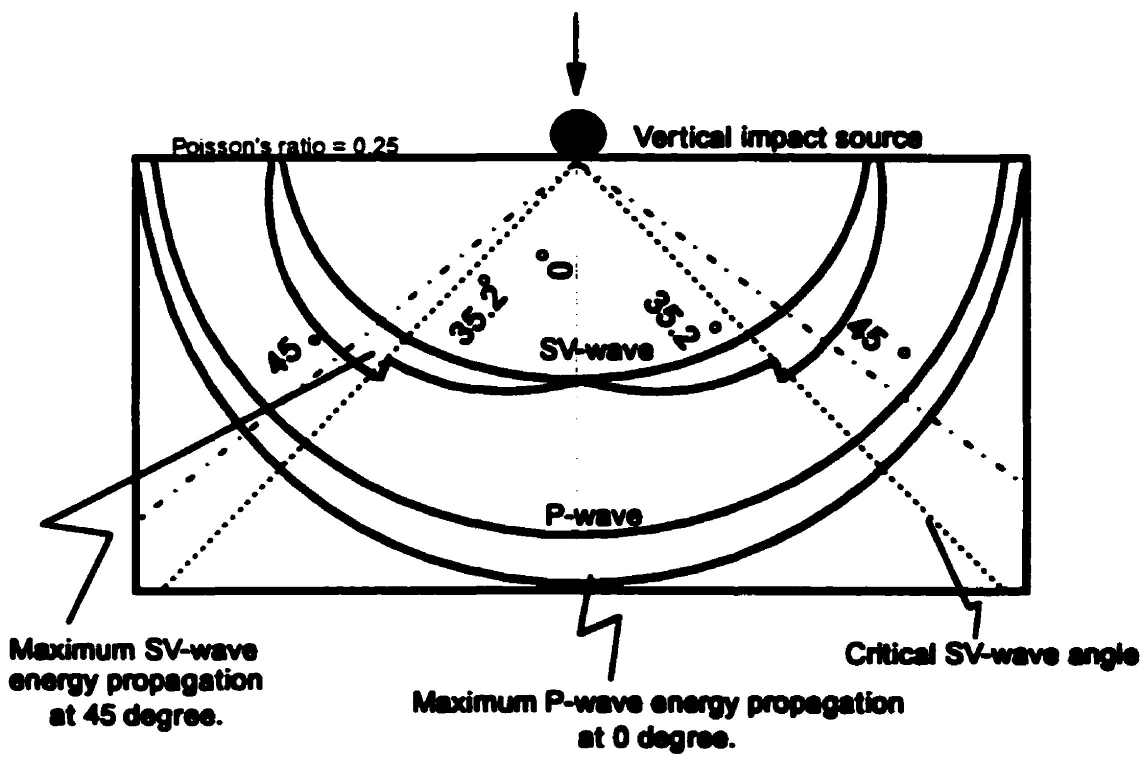

Figure 3-8 The resulting energy propagation of P- and SV-waves from a vertical impact source having spherical wavefronts.

For the electro-acoustic transducers and mechanical-impact sources (both horizontal and vertical), the generation of elastic waves in solids depends on the dimensions of the generators. From the curves of Figure 3-9, it can be seen that the radiation pattern and shape of the ultrasonic field is a function of the ratio of the diameter of the transducer to the wavelength ($2a/\lambda$) (Filipczynski, Pawlowski, and Wehr, 1966). For ultrasonic transducers, when the wavelength is much greater than the diameter of the transducer ($\lambda \gg 2a$) P-, S- and R-waves are generated. When the $\lambda \sim 2a$, both S- and R-waves decrease with respect to the P-wave radiation field. With further decrease in the wavelength ($\lambda \gg 2a$), the S- and R-waves disappear, and the P-wave field gradually increases (Filipczynski, Pawlowski, and Wehr, 1966) and changes its wavefront shape. The same case applies for mechanical-impact devices. The diameter and the time duration of the impact tip (i.e. sphere) controls the frequency (and wavelength) ranges of the input signal (Goldsmith, 1965). Nevertheless, since the frequencies generated by an impact source are lower than the ultrasonic range (20 kHz), all three types of elastic wave are generated as a result of the mechanical impact on a solid's surface (see Figure 3-10).

Explosive sources are rich generators of P- and S-waves. The proportion of shear wave can be increased by deliberately introducing asymmetry (Geyer and Martner, 1969; Kisslinger, 1961; and Nicholls, 1961). Explosive sources are mainly used in a bore hole for evaluating rock masses.

In a borehole, a mass falling to the bottom of the hole is also effective. In such cases the radiation pattern of the P-wave is at maximum both downward and upward from the point of impact. For SV-waves, the radiation pattern is at maximum in a direction 30° from horizontal, and in general SV-waves are stronger in the horizontal direction (Mooney, 1975; Helbig, 1987).

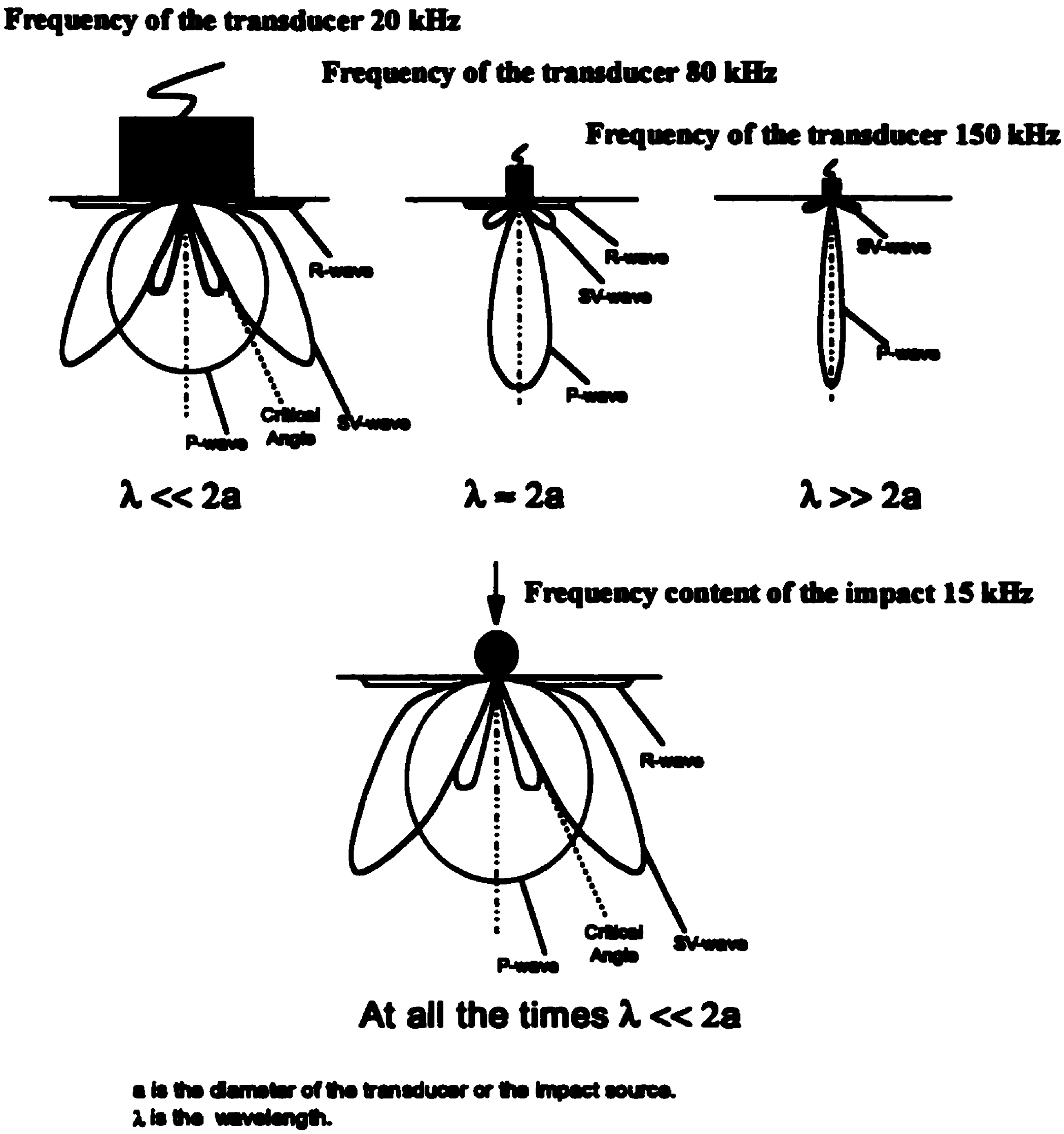

Figure 3-9 Schematic drawing of resulting radiation pattern of P-and SV-wave due to ultrasonic transducers and vertical impact source on a solid. There is a relationship between the diameter of the ultrasonic transducer and the frequency of input signal and the radiation patterns for the body waves.

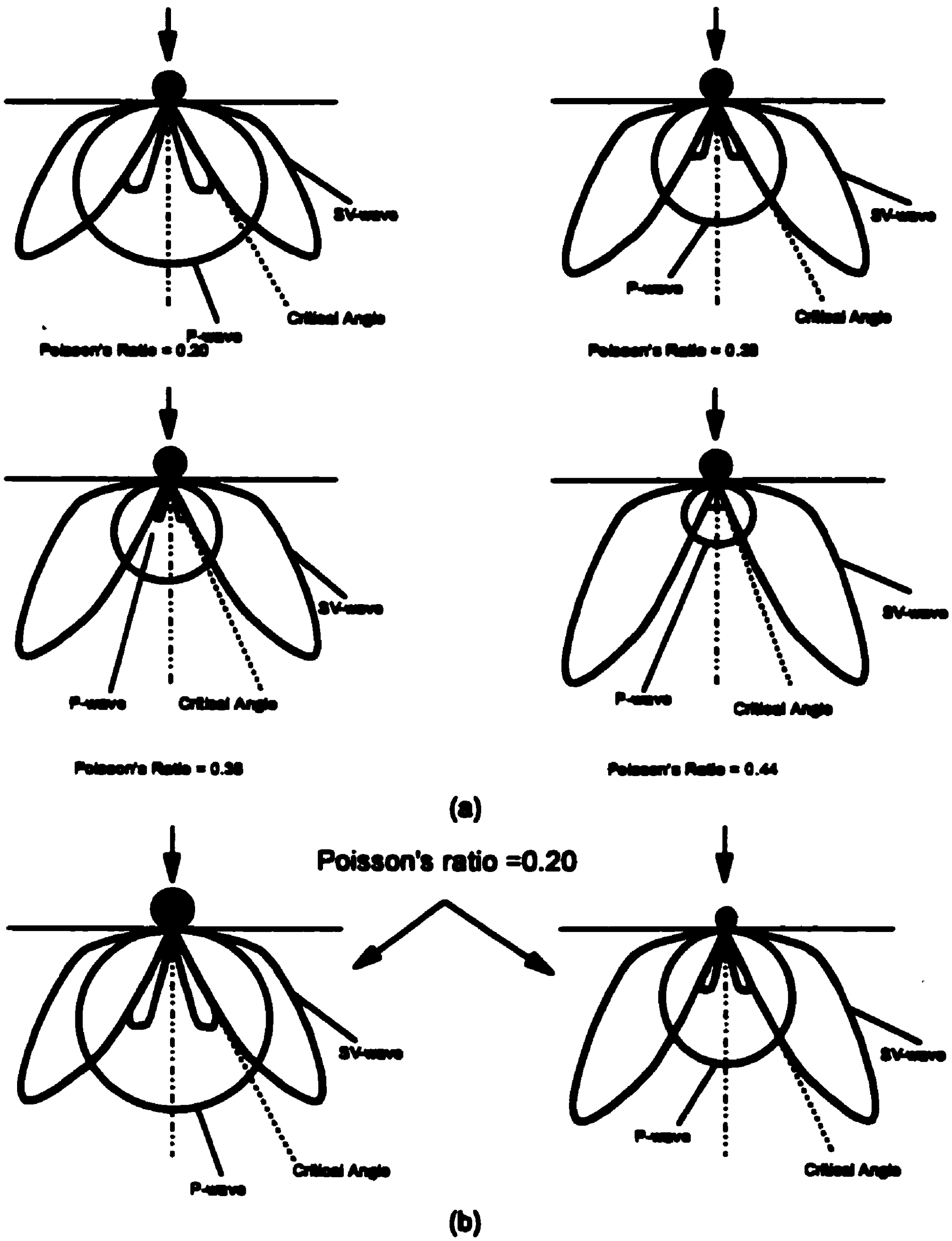

Figure 3-10 Schematic drawing of resulting radiation pattern of P-and SV-waves due to the spherical tipped vertical impact source on a solid. a) The radiation patterns are effected by the Poisson's ratio of the medium, the spherical balls with the same diameter, b) the diameter of the spheres effect the frequency content of the impact and the radiation pattern.

The selection of the source depends on the specific application. For concrete structures with limited thickness, electro-acoustic transducers and mechanical-impact sources are most efficient. For rock masses, depending on the dimensions, explosive sources, borehole-adopted sources, electro-acoustic transducers, and mechanical-impact devices are used to generate body waves. Since the explosive and borehole sources are destructive and are used in limited applications, they are not feasible for evaluation purposes. As for electro-acoustic transducers, no commercial unit exists with satisfactory performance on concrete and rocks. On the other hand, vertical-impact source generators have sufficient elastic energy to overcome the effects of the attenuation and divergence. They are easy to use. They are nondestructive and the tests are repeatable. Therefore, the mechanical-impact devices are the most efficient mean of generating body waves in concrete and rock.

3.3.4 Elastic Wave (Body Waves) Receivers

Geophones are velocity-sensitive elastic wave detectors, that respond to the particle velocity shifts of the testing medium. Geophones could be used for detection of P- and S-waves. Special units are available that are sensitive to either vertical or horizontal vibrations. Geophones are typically moving coils suspended in a magnetic field. The coils are free to move relative to the magnetic structure that is attached to the detector case. A movement of the surface to which the geophone is coupled, causes it to produce a small output voltage proportional to the particle motion in the medium. Geophones are mainly used for low-frequency elastic wave detections (Sharma, 1986; Telford, 1990).

Accelerometers are detection devices that respond to an acceleration-type impulse. They tend to compensate for attenuation of high frequency signals travelling in the medium. Their range can be from 1 kHz to 25 kHz. Accelerometers are sensitive to horizontal, vertical and inclined vibrations (Mooney, 1974).

Piezoelectric transducers (such as quartz, barium titanite, lithium sulfate monohydride, and polarized ceramics) convert mechanical deformations into electrical pulses. Their use is restricted to high-frequency, low-power applications due to their fragile nature. Both P- and S-wave piezoelectric transducers with various band widths and frequency ranges exist for detection purposes (Hassani, Momayez and Wang, 1989).

The selection of elastic wave detectors is mainly determined by the specific application. Detection of low-frequency, high-power elastic waves is commonly achieved by the geophones and accelerometers. For detection of high-frequency, low-power elastic pulses, piezoelectric transducers are more suitable. Different types of piezoelectric crystals are used in transducers according to the required sensitivity criteria for each application.

CHAPTER 4

METHODS OF DETERMINING DYNAMIC ELASTIC CONSTANTS

4.1 INTRODUCTION

The dynamic elastic constants can be calculated from the elastic wave velocity measurements. In General, there are two ways to measure the elastic behavior of rocks and concrete under dynamic loading, namely, laboratory methods and field methods. Laboratory methods require precast or extracted concrete samples with restricted dimensions for measurements of the elastic constants. In laboratory testing, representative rock samples are extracted from the rock mass and dimensionally prepared for measurements of the dynamic modulus of elasticity. Most of the in situ testing methods for concrete evaluation are at early stages of development. Current nondestructive testing techniques use theoretical models (SASW) or assumed elasticity parameters such as Poisson's ratio or shear wave velocities (impact-echo, pulse velocity, pulse-echo, and impulse-response) for calculating other elastic parameters such as Young's modulus. Seismic wave propagation methods are used for in situ testing of rocks. The resonant frequency (RF) and ultrasonic pulse velocity (UPV) techniques are the traditional techniques used for laboratory determination of dynamic elastic constants of rocks. This chapter contains a comprehensive review of the various techniques and instrumentation used for measurements of dynamic elastic moduli for rocks and concrete. Because of the importance of some standard techniques such as resonant frequency and pulse velocity, and due to particular interest on the impact-echo technique, the details are reviewed in more depth in this chapter.

4.2 RESONANT FREQUENCY (RF) TECHNIQUE

In 1877, Lord Rayleigh published "The Theory of Sound", and described the resonant frequency testing procedures. The first practical applications were made by Quimby in 1925, who generated longitudinal vibrations in metal bar specimens. In 1928, Pierce calculated for the first time, the modulus of elasticity of various alloys using cylindrical samples. Muzzey used a device in 1930, creating magnetostrictive effects for generating longitudinal vibrations and tested the theoretical relationship between natural longitudinal frequency and the dimensions of a vibrating specimen. In 1935, Grime generated longitudinal vibrations in building materials by tapping on one end and recording the vibrations on the other end. In 1937, Grime and Eaton carried out further investigations on building materials by measuring their transverse resonance frequency. In this investigation, piezoelectric quartz crystal was used for the first time as the detecting device. Powers, Obert, Hornibrook, and Thomson were the first to conduct extensive research using vibrational techniques on concrete specimens in the 1930s. In 1938, Powers was the first researcher to establish a standard testing system of the resonant frequency (RF) method. In 1936, Ide used rock cylinders as integral parts of condensers by cementing foil to the base of the cylinder, and then placing the cylinder on a steel disc with a mica strip, separating the steel from the foil. A variable frequency was applied to the condenser thus formed until the natural longitudinal frequency of the specimen was attained. This value was used to calculate the elastic constants of the rock being tested. The results showed that for rock of low porosity such as granite and other intrusive igneous rocks, the static and dynamic values compared favorably. However, for porous media such as sandstone, the difference between static and dynamic elastic moduli was up to 30%. Obert in 1946 and the U.S. Bureau of Reclamation in 1953 developed methods for determining the fundamental resonant frequencies of rock cylinders. In 1954, Mitchell determined transverse and torsional resonance frequencies of various diamond drilling cores and measured the Young's and shear modului; Sutherland (1965) compared the static and dynamic elastic constants of eight different rock types.

4.2.1 Principle of Resonant Frequency (RF) Technique

In a vibrating test object, the natural frequency of vibration is related to the dynamic modulus of elasticity and the density of the material. Therefore, the dynamic modulus of elasticity could be calculated knowing the natural frequency of vibration of cylindrical or prismatic bars.

The RF method is based on the standing wave phenomenon. The RF method requires the determination of longitudinal, flexural and torsional wave velocities. When the stress waves are generated in a specimen in the form of torsional or longitudinal vibrations, the reflected waves on the surface of the specimen occur as superposition of the two waves. Since the generated and reflected waves have the same amplitude, superposition of these entities can result in standing waves if they are in phase. In this case, nodes will appear where the waves cancel each other, and peaks will occur when waves combine to produce maximum amplification. When the standing waves are present in a medium, there is a number of nodes defined as n. The following relationship can therefore be established:

$$l = n.\frac{\lambda}{2} \tag{4-1}$$

where l is the length of the sample, λ is wavelength, and n is the number of nodes. Since the wave velocity can be expressed as:

$$V = \lambda.f \tag{4-2}$$

therefore the velocity of the standing wave could be expressed as:

$$V = \lambda.f = \frac{2lf}{n} \tag{4-3}$$

where f is the frequency at which the vibrations are introduced.

As mentioned before, waves can be generated in three ways: which are longitudinal, flexural, and torsional. The longitudinal and flexural vibrations are functions of the modulus of elasticity, and torsional vibrations are functions of the modulus of rigidity of the material. Continuous waves are introduced in the test objects by a transmitter or a mechanical oscillator. The frequency of these waves is systematically varied until a resonance condition is created in the test object. Resonance occurs when the driving frequency is equal to the frequency of the fundamental mode of vibration of the test object. The response of the test object is monitored by a receiving transducer at a close distance from the transmitter. A significant increase in the amplitude of the measured response indicates the presence of resonance condition. The fundamental mode of vibration is identified using the frequency at which this increase occurs. For longitudinal waves, the transmitter and the receiver are placed at the two ends of a cylindrical or prismatic specimen, so that the standing wave travels from one end to the other. In the case of flexural vibrations, waves are generated from the center of the sample, which is mounted on two supports, and received at one end of the sample. Finally, in the case of the torsional resonance frequency, the transmitter and the receiver are placed opposite to each other so that the vibrations twist and untwist the sample. An oscilloscope is used to determine the orientation of the standing wave in the sample, and therefore to identify the vibration mode and the number of nodes n (see Figure 4-1).

4.2.2 Longitudinal Vibrations

Longitudinal vibrations could be used to determine the dynamic Young's modulus of elasticity of cylindrical and prismatic rock and concrete specimens. The relationship between the modulus of elasticity and frequency is described as:

$$E = \frac{V_l^2}{U} . \rho = \frac{1}{U}\left[\frac{2 l f_l}{n}\right]^2 . \rho \tag{4-4}$$

where V_l and f_l are the velocity of the longitudinal standing wave frequency, respectively, l is the length of the sample that the wave travels, ρ is the density of the sample, n is the number of nodes, and U is a correction factor for the shape of the sample.

4.2.3 Flexural Vibrations

Flexural vibrations are more widely used to determine the dynamic Young's modulus of elasticity since they are easier to generate. The relationship between modulus of elasticity and flexural wave frequency f_f is given by:

$$E = \left[\frac{2\pi l^2 f_f}{K m^2}\right]^2 . \rho T \tag{4-5}$$

where m is a constant depending on the mode of vibration and T is a shape factor.

4.2.4 Torsional Vibrations

The following equation is used to relate the torsional resonance frequency, f_t, and the dynamic modulus of rigidity, G.

$$G = \frac{4\rho R l^2 f_t^2}{n^2} \qquad (4-6)$$

In this equation, R is the shape factor depending on the cross section of the sample, and the n is an integer that identifies the oscillation mode. The resonant frequency testing apparatus and method for concrete has been described by ASTM C 215-85 and is considered as a standard measurement technique.

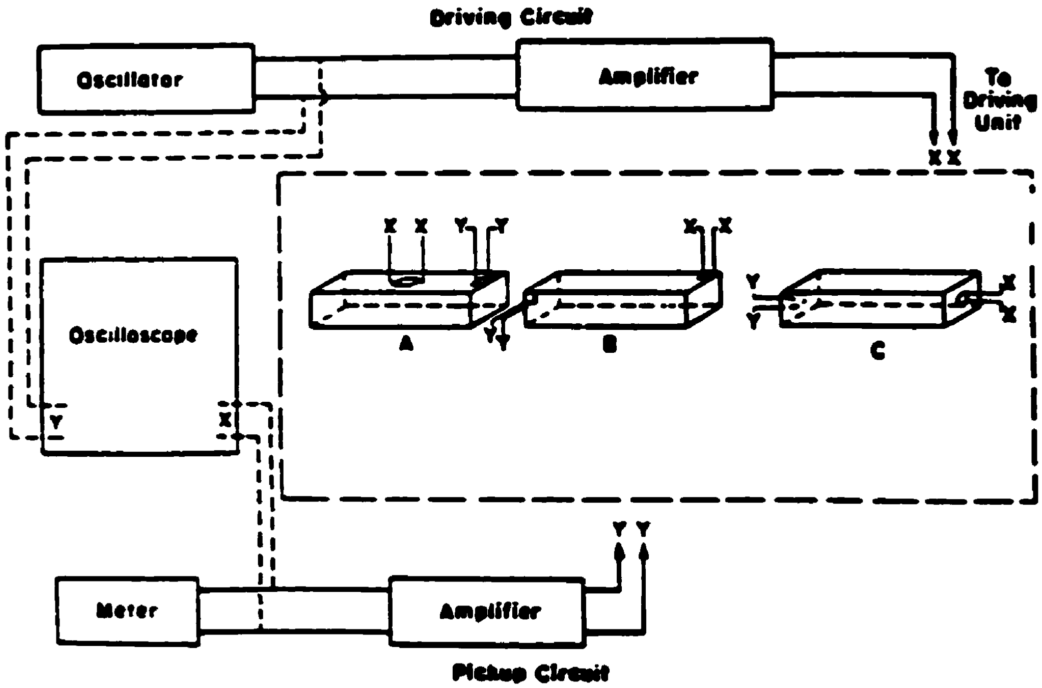

Figure 4-1 Schematic diagram of a typical apparatus showing driver and pick-up positions for the three types of vibrations. A) Transverse resonance. B) Torsional resonance. C) Longitudinal resonance. (Adapted from ASTM C 215-85).

4.2.5 Other Techniques of Resonant Frequency (RF) Testing

In 1986, a new method of RF measurement was proposed by Gaidis and Rosenberg for concrete samples. In this method the specimen is struck by a hammer which causes the specimen to vibrate at its natural frequency. The amplitude of the waves is obtained by a waveform analyzer and the component frequencies are determined by the fast Fourier transform technique. The amplitude of the specimen response is displayed against the frequency, and the frequency of the major peaks can be read directly.

In the experimental setup, the receiving transducer is coupled at one end of the sample with microcrystalline wax, and at the other end the specimen is struck by a hammer. The signals are recorded to obtain the frequency response of the sample. The advantage of this method is the greater speed of testing and the freedom of the tested specimen to have a wider range of dimensions.

4.2.6 Factors Affecting Resonant Frequency (RF) Technique Regardless of Media

4.2.6.1 Size and Length of the Specimen

Obert and Duvall (1941) demonstrated that for a given concrete, the value of dynamic elastic moduli varies depending on the size of the specimen. Larger specimens have lower resonance frequencies because of their weight and size. Kesler and Higuchi (1954) found that longer beams with less resonance frequency give a higher dynamic modulus of elasticity. Jones (1962) recorded no difference between the dynamic modulus of elasticity for different specimens having a frequency range of 70 to 10000 Hz. Thornton and Alexander (1987) recorded an increase in the resonant frequency of the fundamental flexural mode with increase of thickness or with decrease in the length.

4.3 ULTRASONIC PULSE VELOCITY (UPV) TECHNIQUE

The development of the ultrasonic pulse velocity (UPV) technique started in Canada and England at the same time after the Second World War. The first instrument was developed by Leslie and Cheesman in Canada and was called the soniscope. At the same time in England, an ultrasonic tester was developed by Jones. Both instruments were similar, apart from minor details. Since the 1960's, UPV techniques have been used extensively in laboratories and in the field for testing both concrete and rocks. The main application of the ultrasonic testing equipment is to detect flaws and discontinuities in the medium. However, since the velocity of the ultrasonic waves depends on the material quality of the medium, the ultrasonic velocities are used to characterize the quality and elastic properties of solids. ASTM C 597-83 describes the standard apparatus and testing technique for pulse velocity through concrete.

4.3.1 Principle of Ultrasonic Technique

All frequencies above 20000 cycles per second (cps) (20 kHz) can be considered as an ultrasonic frequency, or above the audible sound range. In practice, ultrasonic instrument functions in the range of 20 kHz to 50 MHz for nondestructive testing purposes. The ultrasonic waves propagate as waves of particle vibrations. Ultrasonic waves travel freely through the uniform solids and low-viscosity liquids; they are rapidly attenuated by voids in the media. The difference in the frequency of vibration effects the attenuation rate and the wavelength of the signal. For a high frequency of vibration, the attenuation rate is high and the wavelength is small. For a low frequency of vibration, the attenuation rate is small and the wavelength is large. In practice, test frequencies are selected depending the sensitivity and sound penetration. In the case of rocks and concretes, suitable frequencies are between 20 kHz to 250 kHz, with 50 kHz being appropriate for the field instruments. The relationship between frequency, wavelength and velocity is given by:

$$velocity(cm/s) = wavelength(cm) x frequency(cps) \qquad (4-7)$$

It is noted from this equation that the velocity varies directly with the frequency and the wavelength. However, wavelength and frequency vary inversely with respect to one another. Velocity is measured using the time at which the propagated ultrasonic vibrations move from point A to point B in a material, and depends on the elastic properties of the material and the mode of vibration. The ultrasonic velocity of a material is determined by its modulus of elasticity and density, by the following equation:

$$V = \sqrt{\frac{E}{\rho}} \qquad (4-8)$$

Note: Equation 4-8 applies only to "rod" specimen (causing a "rod wave"), where the testing object has a diameter much less than the length (D<<L).

The velocity of ultrasonic pulses travelling in a solid depends on the density and elastic property of the material. Therefore, the elastic quality of solids could be evaluated by measuring the ultrasonic wave velocity and density of such materials.

The methods of generating ultrasonic pulses are by electro-acoustic transducers. The electro-acoustic transducers operate in two ways: a) by radio-frequency (RF) wave trains driving the crystal at a controlled frequency and precise time; and b) by a shock pulse that allows the crystal in the ultrasonic transducer to resonate at its natural frequency thus establishing the vibrational frequency. By driving the piezoelectric crystal at its fundamental resonant frequency, maximum sensitivity is achieved. There are three main types of ultrasonic transducers: sonic, magnetostrictive, and piezoelectric. Among the three types of transducers the piezoelectric transducers are the most commonly used transducers in the ultrasonic testing equipment. Selection of the transducers depends upon the specific application and characteristics of the test medium.

In the UPV testing method, an ultrasonic pulse is created by a transmitting transducer. The pulse travels through the test object with a known length and is collected by a receiving transducer. The delay (travel) time is recorded by the apparatus. From the travel time and the known distance (path length) between the transducers, the apparent pulse velocity is calculated (see Figure 4-2).

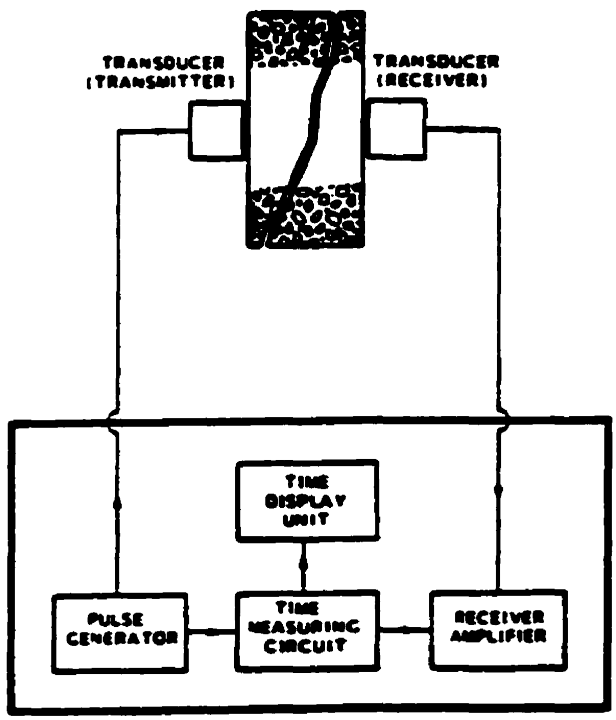

Figure 4-2 Schematic diagram of UPV test circuit. (Adapted after Naik, 1979)

$$Pulse\ \ Velocity = \frac{Path\ \ Length}{TransitTime} \qquad (4-9)$$

The active areas of transmitting and receiving transducers are coupled to the test specimen by a coupling fluid such as oil, water or glycerine. The transmitting and receiving transducers are designed to generate and receive a straight beam or an angular beam where it is appropriate for the test procedure.

4.3.2 Applications

In 1964, Bradfield and Gatfield of England developed the a pulse-echo system for measuring the thickness of concrete pavements. The transducers operated at 100 kHz and arranged as a pitch-catch system for measuring 0.3 m thick concrete specimen in the laboratory. In 1968, Howkins et al. developed a catch-pitch system for measuring concrete thicknesses of 0.18 m and 0.25 m in the laboratory. The error of margin of the measurements was up to 2% in both cases. In 1976, Weber et al. used a pitch-catch system with a 200 kHz transmitter, developed by the Ohio State University, to conduct field tests on concrete pavements. The error margin of results was up to 3%, however they concluded that the system needed more adjustments for field testing. In 1977, Forrest reported the use of pulse-echo for measuring the length of concrete piles. His efforts were successful in using a 12 kHz transmitter to measure 24 m long piles. In 1983, Thorton and Alexander developed a pitch-catch system with a 190 kHz transmitter and PZT receiver. Their efforts were mainly focused on equipment development. Slab thickness measurements up to 0.25 m were reported.

4.3.3 Ultrasonic Testing Equipment

Ultrasonic pulse velocity instruments generate and introduce an ultrasonic signal into the test specimen. Later, the transmitted signal is collected by a receiving transducer. The instrument displays the delay time for the signal to travel through the specimen. The time measurements are displayed on the instrument, in microseconds. The transducers are usually placed on two sides of the specimen for direct measurements. There are two other transducer arrangements: semi-direct and indirect (see Figure 4-3). However, better results can be expected from the direct transducer arrangements. The transducers are coupled to the surface of the specimen by acoustic couplants such as petroleum jelly or grease.

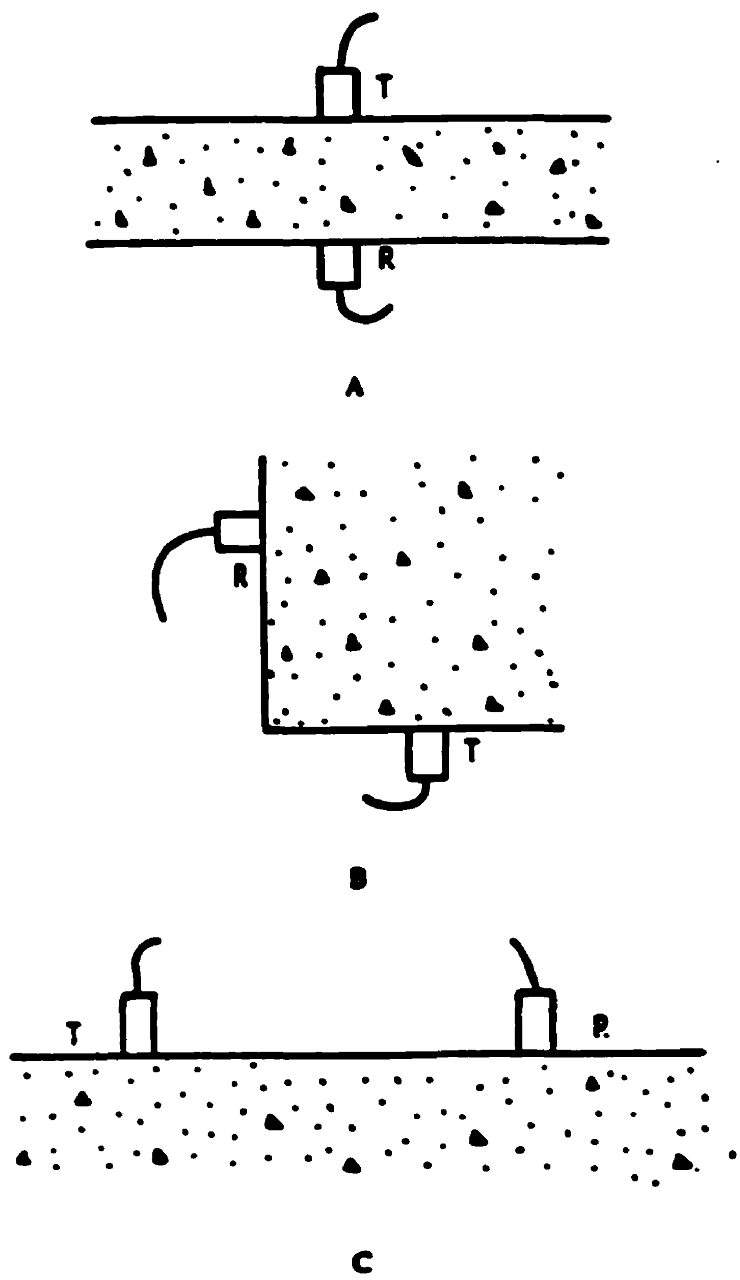

Figure 4-3 Methods of UPV arrangement: A) direct, B) semi-direct, and C) indirect. (Adapted from PUNDIT manual, 1981). Note: T = transmitter and R = receiver.

Pulse-echo instruments create a burst or pulse of sound when a piezoelectric crystal is activated with an electrical pulse. The generated pulse travels through the transducer, its couplant agent, and into the material under test. The sound pulse continues its path until it encounters a sudden change in the properties of the material. The change could be caused by material property or a discontinuity, and in this case sound signal echos or returns back. Depending on the path length, many signals are reflected, later processed by the electronic circuitry, and displayed as a single reading. The reflected signals are monitored by the transmitter acting as a receiver (true pulse-echo) or by a second transducer located near the pulse source (pitch-catch). The true pulse-echo instruments consist of a shock-pulse generator, variable attenuator, amplifier, filter, and spectrum analyzer or oscilloscope with marker, delay, and various gating circuits (see Figure 4-4). The sensitivity of the equipment is controlled by the transducers, pulser, and the amplifier. The transmitting and receiving transducer(s) mainly utilize piezoelectric elements such as lead zirconate titanate (PZT) for generating and receiving the signals. The shock-pulse generator produces a burst of energy for the transmitting transducer. A pulse-repetition device controls the number of pulses generated per unit time, which controls the scanning speed. The receiving transducer is preceded by a variable attenuator to increase the dynamic range of the instrument. It also prevents amplifier saturation that would result in a nonlinear output with respect to the input voltage. The receiving amplifier circuits amplify the returning signals and modify them for display. After the amplification, the ultrasonic pulses are sent to a spectrum analyzer or an oscilloscope for measurement and discrimination of the pulse amplitudes. Using the time base of the display, the pulse travel time is determined. If the velocity of the longitudinal wave is known, the travel time can be used to determine the depth of the reflecting surface:

$$T = \frac{1}{2}.(\Delta t).C_p \qquad (4-10)$$

where Δt is the reflected travel time, T is the depth, and C_p is the P-wave velocity. The equation could also be used for the pitch-catch system only if the distance between the transmitter and receiver is small.

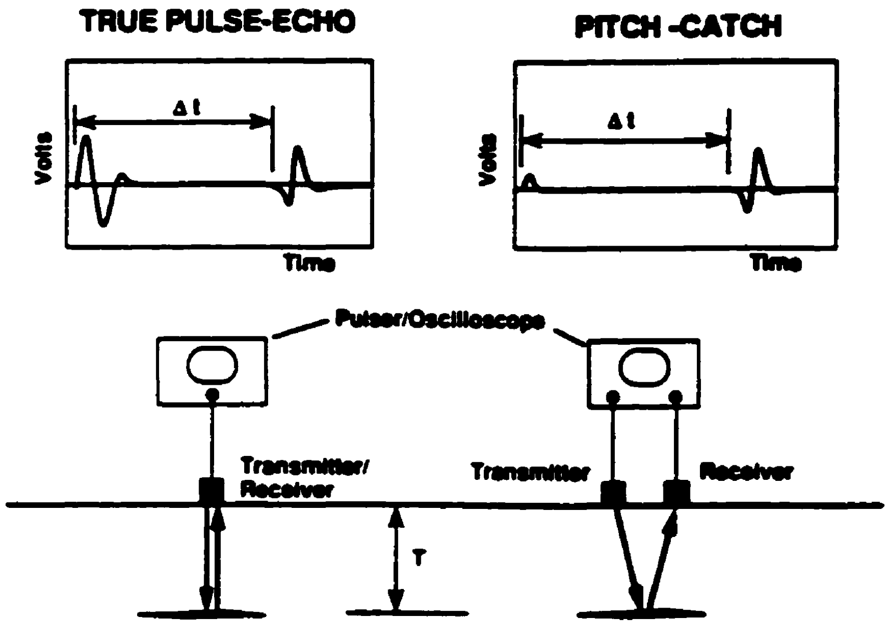

Figure 4-4 Schematic of pulse-echo and pitch-catch techniques. (After Sansalone, 1991).

The time domain analysis has been used in both true pulse-echo and catch-pitch.

4.3.4 Factors Affecting Pulse Velocity Measurements and Dynamic Elastic Constants

The factors affecting the elastic constants can be divided into two categories: the survey condition (regardless of the media) and the media effect.

4.3.4.1 Factors Affecting Pulse Velocity Measurements Regardless of Media

a) Acoustic Contact

Improper acoustic contact might result in wrong pulse velocity readings. A good contact between the transducers and the media is usually induced by grease or other couplants.

b) Temperature of Specimen

Temperature variations between 5° to 30°C in the media (concrete or rock) have been found to have insignificant effects on the pulse velocity (Jones and Facaoaru, 1969). For other temperatures in concrete, RILEM recommended a correction table.

c) Moisture Condition of Specimen

The moisture condition has little to no effect on pulse velocity. However, it was recorded by Jones (1969) that saturated concrete has a higher pulse velocity than dry concrete.

d) Path Length of Specimen

Theoretically, the path length of the specimen should not have any effect on the pulse velocity. However, in practice a shorter path length gives higher pulse velocity than a longer path length specimen. This is mainly affected by the aggregate size and the frequency range of the transducers, which control the attenuation rate of the signal. For concrete, RILEM has recommended the following maximum path lengths for direct UPV testing:

a) 100 mm for concrete with a maximum aggregate size of 30 mm.
b) 150 mm for concrete with a maximum aggregate size of 45 mm.

e) Size and Shape of Specimen

Usually the size and shape of the specimen has no effect on the pulse velocity. However, the lateral dimension of the specimen should be greater than the wavelength of the pulse, otherwise the resulting pulse velocity will not be accurate. In the case of the concrete, the wavelength of the pulse must be larger than the maximum aggregate size in the mix. In the case of rocks, the wavelength of the signal has to be larger than the maximum size of the minerals in the rock matrix.

4.3.4.2 Media Effect

a) Concrete

i) Aggregate Size, Grading, Type and Content

It has been established by many researchers that the compressive strength of the concrete and UPV is affected by the aggregate characteristics (Jones, 1962; Facaoaru, 1970; Bullock, et al., 1959; Sturrup, et al., 1984; Swamy, and Al-Ahmad, 1984; Anderson, and Seals, 1981). In 1954, Jones reported that for the same concrete mix proportions with the same compressive strength, the rounded coarse aggregates of limestone give lower pulse velocity values than of crushed limestone, while crushed granite give an intermediate velocity value between the two. Jones (1962), Kaplan (1959) and Bullock and Whitehurst (1959) established that for the same strength level, mixes with higher aggregate content have higher pulse velocity values. In 1962, Jones illustrated that a higher aggregate-cement ratio causes lower compressive strength in concrete. The dynamic modulus of elasticity of the concrete is affected by the modulus of elasticity of the constituent materials and their relative proportions. In 1962, Jones stated that for a given composition of cement paste, that is the w/c ratio, the elastic modulus of the concrete increases with an increase in the percentage of the total aggregates.

ii) Cement Type and Admixtures

In 1954, Jones reported that type of cement does not influence the pulse velocity. However, the rate of hydration has a direct effect on the pulse velocity. As the rate of hydration increases, pulse velocity and strength also increase. In 1970, Facaoaru found that use of rapid-hardening cement results in an increase in the pulse velocity and the strength of the concrete. The use of admixtures such as calcium chloride have similar effects. Admixtures increase the setting time of the concrete and will increase the early age strength and pulse velocity. In a CANMET study (Malhotra and Sivasundaram, 1991), it was illustrated that incorporation of low calcium fly ashes in a concrete mix increases the dynamic and static moduli of elasticity in relation to the strength.

iii) Water-to-Cement Ratio

In 1959, Kaplan reported that as the w/c ratio increases, the density, compressive strength, flexural strength and the pulse velocity decrease. In 1962, Jones reported that an increase in w/c ratio reduces the modulus of elasticity.

iv) Degree of Compaction

The hand-compacted or inadequately vibrated concrete is less dense than well compacted concrete. Pulse velocity depends on density. Therefore poorly compacted concrete, honeycombed, and less dense concrete result in a decrease in the pulse velocity. In 1962, Jones recorded a decrease in the modulus of elasticity as the volume of entrapped air increased in a concrete mix.

v) Curing Conditions and Age of Concrete

The effect of curing and age of the concrete on pulse velocity is similar to the strength development in concrete. Kaplan reported in 1959 that pulse velocity is higher in the laboratory-cured sample than in site-cured specimen. In 1962, Jones recorded the pulse velocity relationship with the age of concrete. He showed that the pulse velocity increases rapidly and later flattens out, similar to the response of strength versus age. In 1958, Kesler and Higuchi stated that for the same curing conditions, the dynamic modulus of elasticity increases with strength. Obert and Duvall (1941) have shown that the change in dynamic elastic moduli is rather small after 3 to 4 days of air drying. However, it has been recorded by Malhotra (1983) that oven drying of the specimen over the first 48 hours of curing causes a reduction in the dynamic modulus of elasticity. A possible explanation given by Malhotra blames the shrinkage and microfracturing for the drop in the modulus of elasticity. The effects of curing on the modulus of elasticity and wave velocities are rather crucial.

b) Rocks

i) Rock Type

Generally, as the degree of compaction increases, the velocity of wave propagation and the modulus of elasticity increases. For example, velocity of wave propagation in limestone varies between 2000 m/s and 6000 m/s, depending on the degree of compaction (Lama, 1978).

ii) Texture

The velocity of a wave in a rock may be related to the mineral constituents of the rock and their preferred orientations (Ramana, 1973). The velocity of waves is also influenced by the size of the grains. The velocities are recorded to be generally higher in fine-grained rock than in coarse-grained rocks (Lama, 1978).

iii) Density

The pulse velocity increases as the density and the mean atomic weight of the rocks increases. The relationship may be linear or curvilinear (Birch, 1960, 1961). Youash (1970) and Ramana (1973) reported an increase in the modulus of elasticity as the rock density increases.

iv) Porosity

In general as the porosity of the rock increases, the pulse velocity decreases (Ramana, 1973; Lama, 1978). Between the various types of porosity in rocks, inter-granular and interagranular, the latter has the highest influence on the wave velocity variations (Gregory and Gardner, 1958). Youash (1970) recorded a decrease in the modulus of elasticity as porosity increases.

v) Anisotropy

The pulse velocity is different along and across layered rocks. The pulse velocity parallel to the layers is higher than the pulse velocity perpendicular to the layers. Youash (1970) recorded higher values of modulus of elasticity for foliated sandstone cores, when the readings were taken parallel to the foliations. Ramana's (1973) tests on shistose rocks illustrated that S-wave anisotropy is of the same order as P-wave anisotropy.

vi) Stress

Both longitudinal and shear ultrasonic pulse velocities in rocks increase with increasing pressure. Tocher (1957), and Wyllie, Gregory and Gardner (1958) reported that when a specimen is under uniaxial load, the pulse velocities increase when the measurements are in direction of load. There is a rapid increase in the wave velocity at low pressure due to closure of the voids and microfractures and increase of contact between the mineral constituents. Under uniaxial loading the pulse velocity decreases when the sample reaches over 65% of its maximum strength due to formation of microfractures.

vii) Water Content

The increase in water content of the rocks results in an increase in longitudinal wave velocity. However, the longitudinal wave velocities in completely saturated porous rocks is lower than in slightly porous rocks since the velocity of waves in water is lower than that in mineral constituents. For transverse wave velocities, the velocity remains constant regardless of the degree of water content since transverse waves do not pass through water.

viii) Temperature

The wave velocities and elastic constants drop with an increase of temperature in rocks (Lama, 1978).

4.3.5 Comparison Between Pulse Velocity and Resonant Frequency Techniques

The main difference between the two methods is the range of frequencies within which the wave velocity is determined in the medium. For rocks and concretes, the RF instruments operate in the frequency range of 1 to 30 kHz and the pulse method operates in the range of 20 kHz to 250 kHz. However, most researchers believe that in this range of frequencies, elastic constants are independent of the frequency variations.

Another difference between the two methods was pointed out by LeComte (1963), who focused on the way the stress and strain is imposed on the sample. The RF method generates standing waves, whereas the pulse method generates transient waves. However, since the stress and strain values in the samples are small, they behave elastically and semi-elasticly, so that the elastic constants are not effected.

4.4 SEISMIC WAVE PROPAGATION TECHNIQUE

Dynamic elastic constants of rock masses are measured in situ based upon the computation of seismic wave velocities through the medium. Seismic wave velocities can be measured by swinging a sledge hammer against an outcrop or by detonating explosives in a shallow drilled hole and observing the travel time to the geophones (or accelerometers) placed at several distances from the source. The zero time shot is determined in addition to the travel times to the geophones and is recorded in a waveform analyzer. P-waves are detected mainly using vertical oriented receivers and S-waves are detected using transversely oriented receivers. The velocities are computed by dividing the source to receiver distance by the arrival times of the signals from the source to the receivers (see Figure 4-5).

Utilizing the rock density and velocities, the dynamic elastic constants can be calculated from the equations in Table 3-2. Using the reflection and refraction methods, depth of the various rock beds as well as the thickness of overburden soil can also be calculated. The seismic wave propagation technique can also be applied between drill holes. Both downhole hammers and explosives are used for such measurements. The location of the boreholes is selected according to the shape of the rock mass and its structure. Detection of the shear waves and problems associated with the mode convergence are the main problems associated with this technique.

Figure 4-5 Schematic diagram for apparatus arrangement of seismic propagation technique. (After Goodman, 1989)

4.5 PETITE SISMIQUE TECHNIQUE

In 1967, Schneider developed a new in situ technique known as petite sismique. This method is capable of estimating the static modulus of the rock mass. The petite sismique method uses a seismic refraction over a distance of 2 to 10 meters, and focuses mainly on the determination of the shear wave arrival. The petite sismique system consists of a signal enhancement seismograph, a horizontally oriented surface source, and directional, moving coil geophones with a frequency range between 1 to 1000 Hz (see Figure 4-6). Both horizontal and vertical displacement units are used, thus providing superior flexibility in the geophone arrangement. For a wide frequency range such as 200 to 1500 Hz, proper receivers must be chosen to eliminate resonance disturbance. A horizontal surface source is used to generate shear wave polarizing traits to advantage and to propagate SH-waves which are theoretically free of the P-wave energy (Belesky, 1984). The signal enhancement seismograph is used; the ability to store and sum the individual signals this way reduces the random background nose and improves the arrival of the shear wave signal (Bieniawski, 1976).

4.5.1 Application

The original work by Schneider (1967) emphasizes shear wave parameters such as frequency, attenuation, wavelength, and velocity. He used plate load tests to measure the static modulus of elasticity and correlated the results with the shear wave frequencies obtained by the petite sismique method. To evaluate the petite sismique method in a mining environment, Heuze (1981) tested pillars in an underground limestone mine. This experiment was accomplished using receivers mounted on one side of a pillar and a source placed on the opposite end. The results indicated that a surface refraction survey is the optimum approach for observing shear waves. It was also concluded that two main factors affect the shear wave frequencies: 1) the force-time function of the source, and 2) the transfer function between the source and the geophone.

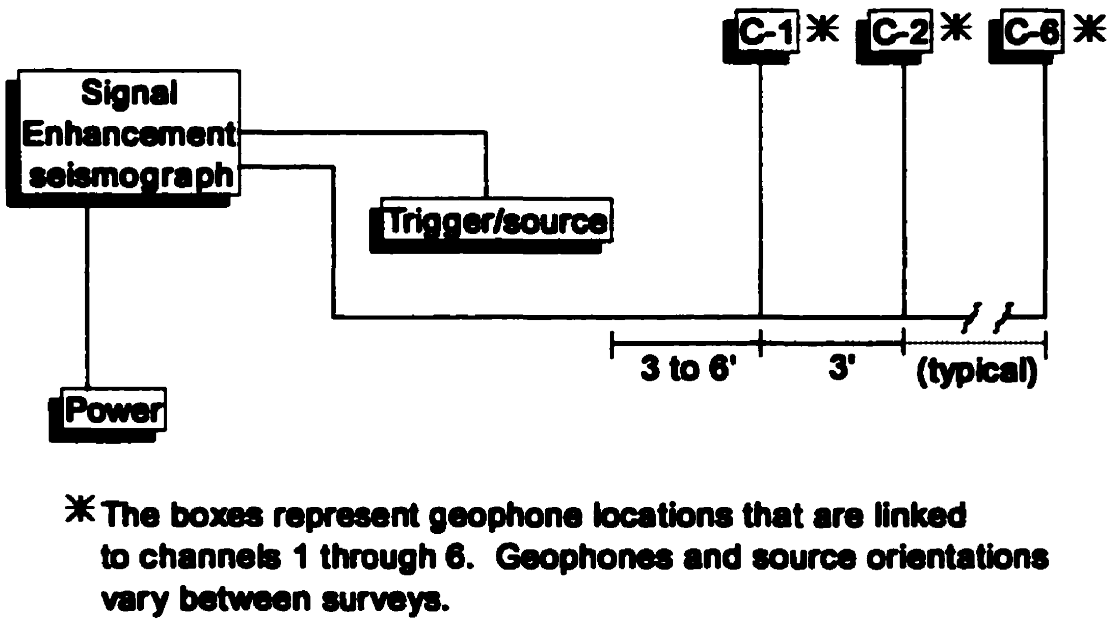

Figure 4-6 Block diagram of petite sismique field survey with linear array of receivers. (Modified after Belesky, 1984)

4.6 IMPULSE-RESPONSE TECHNIQUE

4.6.1 Principle

A mechanical impact is generated on the surface of the specimen. The force-time function of the impact is recorded. A transducer located near the impact source records the reflected waves from the bottom surface of the sample. The time history of the impact force and the time history of the structure's response are recorded, and the impulse response is calculated. This can be accomplished by deconvolution or, in the frequency domain, by dividing the Fourier transform of the response waveform by the Fourier transform of the impact force-time function. The changes in geometry and the existence of flaws affect the impulse response of a structure. In the frequency domain, the resultant response of the structure is a function of the frequency component input. Digital signal processing techniques are used to obtain the impulse response function, which is also known as the transfer function. The procedure to calculate the transfer function is outlined by Higgs (1979). For analysis purposes, the velocity is measured and the resulting impulse-response spectrum has units of velocity/force which are referred to as "mobility", and the spectrum is called "mobility plot". In the mobility plot, at the frequencies corresponding to the resonance frequency of the structure, the mobility values are at maximum. The difference between any two mobility peaks, Δf, is equal to the natural longitudinal frequency. The length L of the pile can be calculated by using the following equation:

$$L = \frac{C_p}{2(\Delta f)} \tag{4-11}$$

where the C_p is the P-wave velocity. At low frequencies, where the pile and the soil are vibrating together, the impulse-response provides information about the dynamic stiffness of the soil-pile structure. At low frequencies, the initial slope of the mobility plot is approximately a straight line and the slope of this line represents the dynamic flexibility of the pile head (see Figure 4-7). The dynamic stiffness is the inverse of the dynamic flexibility.

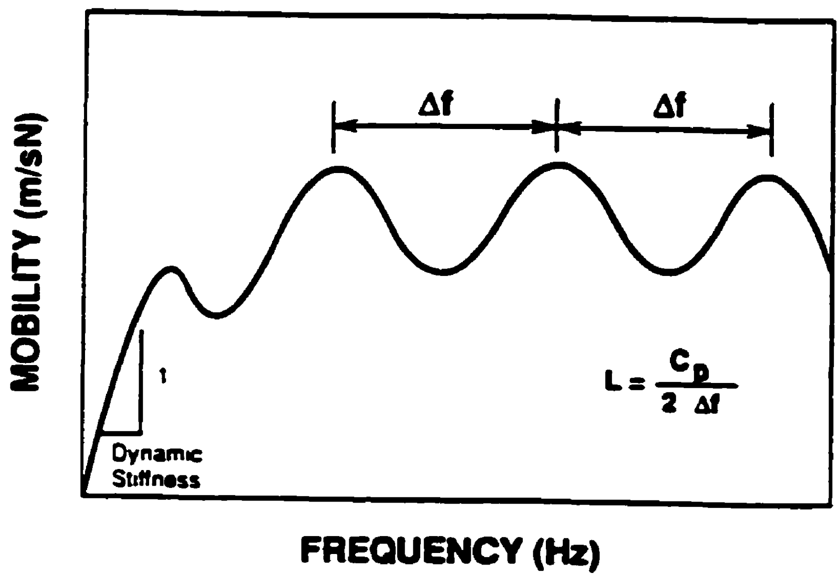

Figure 4-7 Idealized mobility plot for a concrete pile. (Adapted from Sansalone, 1991).

4.6.2 Applications

The impulse-response technique is used mainly to calculate the thickness of concrete piles over 10.0 meters long and their dynamic stiffness characteristics in the soil. However, if the longitudinal frequency response of the specimen and the P-wave velocity are known, the dynamic modulus of elasticity of the medium can be calculated. In 1974, Davis and Dunn outlined the factors affecting the impulse-response technique to be: the diameter of the pile, the quality of the concrete, and the damping characteristics of the support or the soil. Higgs (1979) stated that for a L/D (length/diameter) greater than 20, the test results are not reliable unless the pile passes through a very soft soil deposit into a rigid stratum. Olson et al. (1995) used the impulse-response technique to evaluate a concrete shaft lining in Saskatchewan. The technique was not successful in providing information on the depth of voids and could not differentiate between the back-side voids and the near-surface delamination cracks.

4.7 SPECTRAL ANALYSIS OF SURFACE WAVES (SASW) TECHNIQUE

4.7.1 Principle

The SASW method is a technique used to measure the dynamic elastic moduli and thickness of thin concrete layers such as pavements. The method is based on the dispersion of R-waves in layered systems. A transient stress pulse is generated mechanically by an impact source on the surface of the specimen. Two receivers placed a certain distance apart monitor the surface displacements as the wavefront passes through them. The R-wave is the principal stress wave used in the signal analysis. This is due to the fact that the R-wave amplitudes are larger than the P- and S-wave amplitudes on the surface. The generated R-wave contains a range of frequencies. The contact time controls this range of frequencies; the shorter the contact time, the broader the range of frequencies. The amplitude of R-wave decays exponentially with depth. The longer the wavelength, the deeper is the penetration of the R-wave. The impact source plays an important role in the success of the SASW method. The impact is chosen so that the high frequency components of the impact, particularly the R-wave, travel only through the top layer. Lower frequency components penetrate to the second layer. According to the relationship between the elastic wave velocity and the dynamic modulus of elasticity, the velocity of R-waves in each layer depends on the material properties in each layer. Therefore, the velocity of the R-waves in each layer is different and is called "phase velocity". The phase velocity is calculated by the travel time between the two receivers. The travel time is determined by the phase difference of the frequency components when they arrive at the receivers knowing the distance between the two receivers (see Figure 4-8).

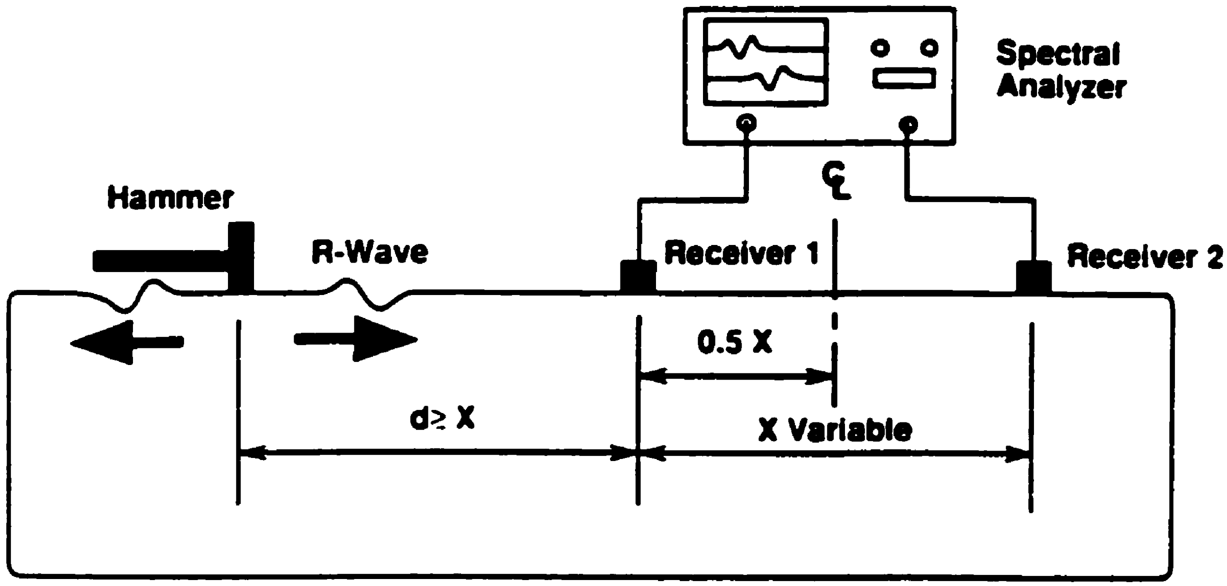

Figure 4-8 Schematic of the SASW technique. (After Sansalone, 1991).

$$C_{R(f)} = \frac{X}{\Delta t_f} = X . \frac{360}{\phi} f \qquad (4-12)$$

In this equation, $C_{R(f)}$ is the velocity of the component frequency, X is the distance between the two receivers, f is the frequency of the sine curve which is the inverse of the period, and ϕ is the phase difference which is calculated from:

$$\phi = \Delta t f (360°) \qquad (4-13)$$

and Δt_f is the travel time between the two receivers and is calculated from the following equation:

$$\Delta t_f = \frac{\phi}{(360°)f} \qquad (4-14)$$

The wavelength, λ_f, corresponding to a component frequency, is calculated from the following equation:

$$\lambda_f = \frac{C_{R(f)}}{f} = X \cdot \frac{360}{\phi} \qquad (4-15)$$

The calculations are repeated for each component frequency and a plot of the wavelength versus phase velocity is obtained; it is known as "dispersion curve". It is used to obtain the dynamic modulus of elasticity. A process called "inversion" is used to approximate the dynamic modulus of elasticity.

In this process, the test site is modeled using layers of varying thickness. Each layer has a different modulus of elasticity depending on the expected values. Each layer is assigned a density, Poisson's ratio, and S-wave velocity. Using this information, the solution for the R-wave propagation is determined and a theoretical dispersion curve is calculated for the assumed layer system. The theoretical curve is compared with the experimental dispersion curve. If the curves match, the problem is solved and the assumed modulus of elasticity is correct. If there are discrepancies, the assumed layered system is changed or a new theoretical curve is calculated. This process is repeated until a match between the theoretical and experimental curves are obtained.

4.7.2 Instruments

The SASW system has three components: an impact source (usually a hammer); two receivers (which can be geophones or accelerometers), and a two channel spectral analyzer for recording and processing the waveforms. The reliable data is calculated only for the components with wavelengths greater than one-half of the receiver spacing and less than three times the spacing. The spacing between the receivers is small at the beginning and the separation increases with repeated tests. The distance between the impact source and the nearest receiver is kept larger than the distance between the two receivers. The distance between the receivers increases as the thickness of the two-layered system increases. The type of impact source is dependent on the thickness of the two-layer system. If the layers are thin, a small hammer is used to generate short duration pulses with shorter wavelengths. The receivers are selected so that they are sensitive to vertical surface displacements.

4.7.3 Applications

The SASW has been successfully used for the evaluation of road profiles where the asphalt-concrete or concrete layer was treated as a single layer (Nazarian and Stokoe, 1984 and 1986; Nazarian et al. 1983 and 1988). Nazarian et al. (1983, 1984, 1986, and 1988) have used SASW by monitoring the surface motion at two points a known distance apart. The information for each wavelength component and wave velocity was extracted, and the elastic properties of the layered materials were calculated. Olson et. al (1995) used the SASW technique to evaluate the condition of the concrete shaft lining in Saskatchewan. The SASW technique successfully provided information about the stiffness of the lining and also the condition of the concrete/rock interface.

4.8 IMPACT-ECHO TECHNIQUE

The impact-echo technique for the detection of flaws and delaminations in plate-like concrete structures was developed in the mid-1980's by Carino and Sansalone in the United States National Institute of Standards and Technology. The method was developed for detecting a variety of defects in concrete structures, including plain and reinforced concrete slabs and walls, concrete slabs with overlays, columns with circular, square, or rectangular cross-sections, as well as square and rectangular beams. Impact-echo is not commonly used for determining the dynamic elastic properties of concrete or rocks. However, assuming an appropriate value for Poisson's ratio or shear wave velocity and using the equations in Table 3-2, the elastic constants can be calculated, with the P-wave velocity obtained by the impact-echo technique.

4.8.1 Principle

As a transient stress pulse is introduced into a test specimen by a spherically tipped mechanical impact source, the P- and S-waves propagate into the object along spherical wavefronts and R-waves propagate along the surface on a circular wavefront, centered at the point of impact. The internal discontinuities, voids and the boundaries of the concrete cause reflections of the P-and S-waves. The reflected waves at the surface cause displacement, which is measured by the receiving transducer. If the receiving transducer is placed close to the impact source, the dominant surface displacements are due to the P-wave arrivals because of the radiation patterns associated with the P- and S-waves. The P-wave is the principle elastic wave used for detection purposes by the impact-echo system. The pulses generated by the impact source are composed of low-frequency waves. The point impact source generates a pulse propagating in all directions rather than a focused beam similar to the one in the pulse-echo technique. The P-wave arriving at the surface is reflected back into the concrete, and a transient resonance condition is created as the multiple reflections occur between the top surface of the concrete and the internal reflections from the interfaces or the bottom surface of concrete. Each P-wave arrival on the top surface produces a characteristic downward displacement. Therefore, the waveform is periodic, and the period is approximately equal to the travel path ($2T$) divided by the P-wave velocity C_p, where T is the depth of the reflected surface (see Figure 4-9). Frequency has an inverse relationship to the period and therefore the frequency corresponds to the multiple reflections of the P-wave between the top surface and the reflecting interface f_p, such that:

$$T = \frac{C_p}{2f_p} \qquad (4-16)$$

The frequency content of the surface displacements is obtained using the fast Fourier transform (FFT) technique. The FFT technique is based on the principle of the Fourier transform, which states that any waveform can be represented as a sum of sine curves, each with a particular amplitude, frequency, and phase shift. The resulting amplitude spectrum contains peaks at frequency values which correspond to the dominant frequencies in the displacement waveforms. The resolution in the frequency spectrum, that is, the frequency difference between adjacent points, is measured by the sampling frequency used to capture the waveform, divided by the number of points in the waveform record. This limits the resolution of the calculated depth, since the frequency and depth have a direct relationship.

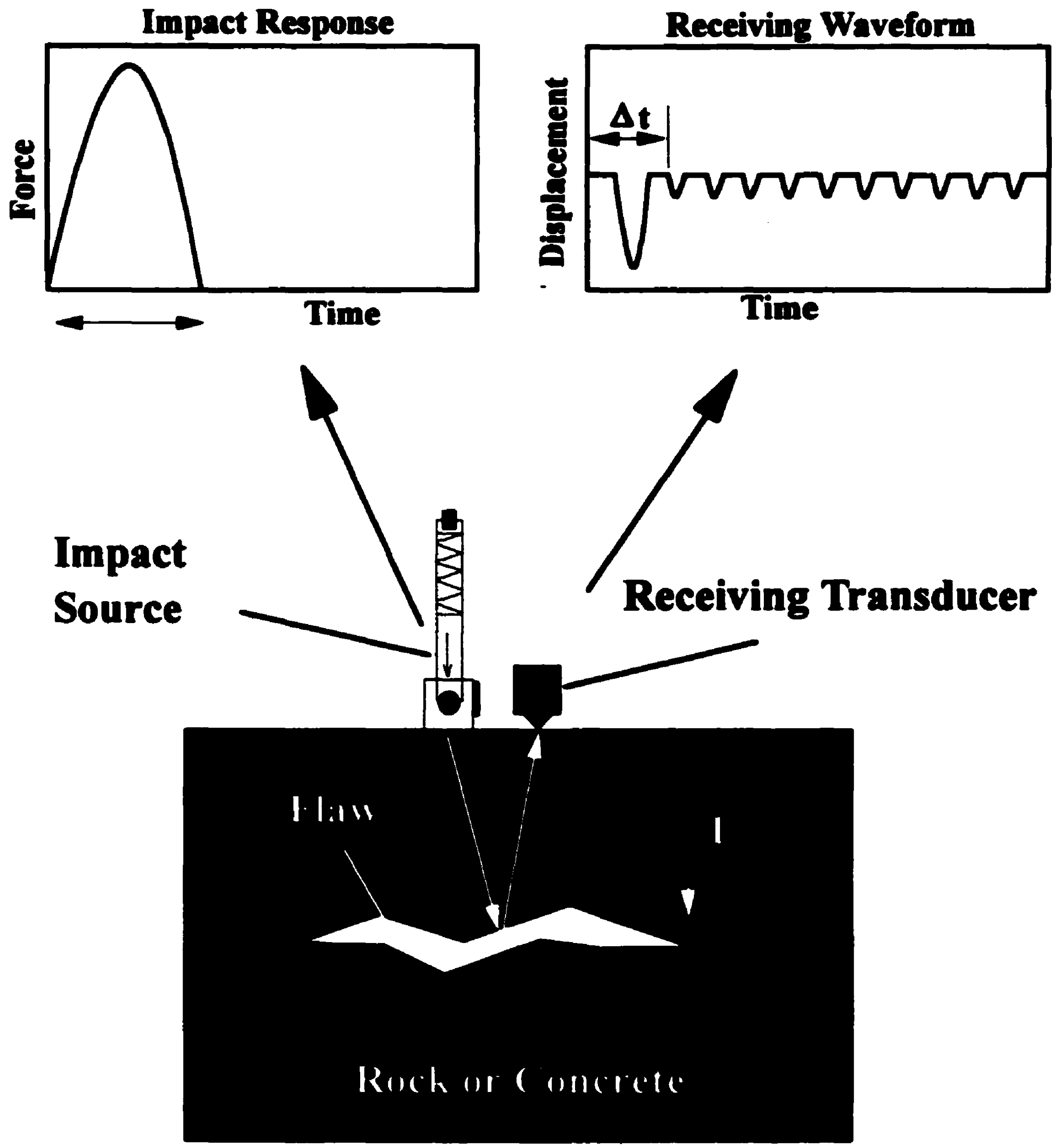

Figure 4-9 Principle of the impact-echo technique.

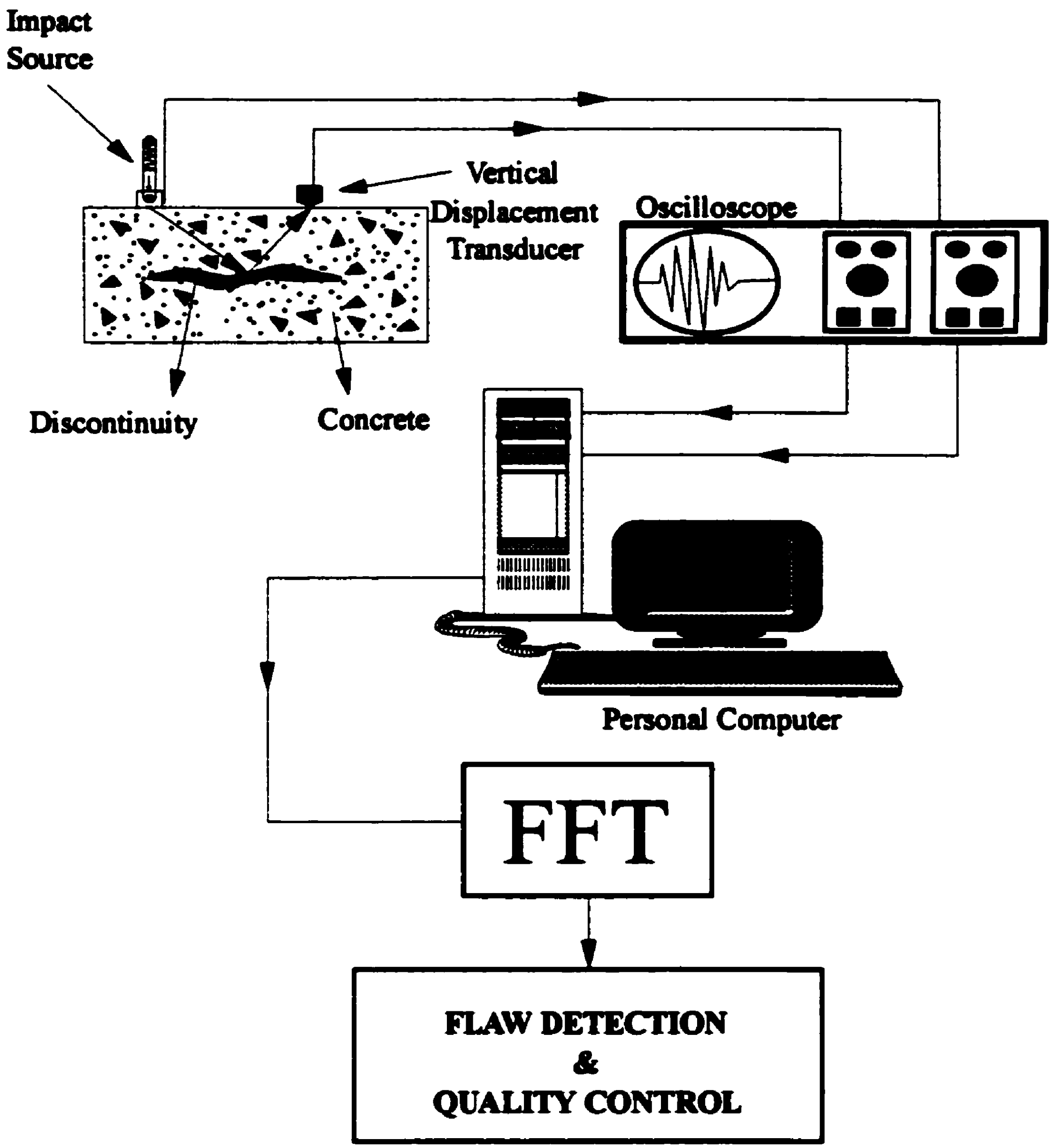

Figure 4-10 The schematic diagram of impact-echo system setup.

4.8.2 Impact-Echo Testing Equipment

An impact-echo system is composed of three main components: an impact source, a receiving transducer, and a digital oscilloscope or a waveform analyzer (see Figure 4-10).

4.8.2.1 Impact Source

The impact source is a critical part of the impact-echo system. A small diameter steel sphere is used as the impact source. The sphere is either dropped, or mechanically shot at the concrete plate. The duration of a free-fall impact of a spherical source is short, ranging between 20 - 90 μs. During impact, part of the energy is transferred into the concrete as elastic wave energy. The force-time history of an impact may be approximated as a half-sine curve, and the duration of the impact is the "contact time" (lead to equation 4-17).

$$F = F_{max} \sin \pi \frac{t}{t_c}$$

$$0 \le t \le t_c \qquad (4-17)$$

where F_{max} is the maximum force (N), and t_c is the contact time of impact (s).

The amplitude of the force-time function F_{max} affects the displacements and stresses in the elastic waves generated by the impact. The contact time determines the frequency content of the stress pulse.

The contact time of an impact produced by a steel sphere as a result of free fall on a concrete plate could be approximated by the Hertz elastic solution (Goldsmith, 1965):

$$t_c = 5.97[\rho_s(\delta_s + \delta_p)]^{0.4} \frac{R}{(h)^{0.1}} \qquad (4-18)$$

$$\delta_p = \frac{1 - \upsilon_p^2}{E_p} \qquad (4-19)$$

$$\delta_s = \frac{1-\upsilon_s^2}{E_s} \qquad (4-20)$$

where

ρ_s is the density of the sphere (kg/m^3);
R is the radius of the sphere (m);
h is the drop height (m);
υ_p is the Poisson's ratio of the concrete plate;
υ_s is the Poisson's ratio of the steel sphere;
E_p is the Young's modulus of elasticity for the concrete plate (N/m^2); and
E_s is the Young's modulus of elasticity for the steel
sphere (N/m^2).

For example, for a concrete plate with Young's modulus of 36 GPa and Poisson's ratio of 0.2, the contact time (in μs) can be written as:

$$t_c = 0.00858\frac{R}{(h)^{0.1}} \qquad (4-21)$$

From this relationship, it is obvious that contact time is a function of the sphere radius and is slightly affected by the drop height.

The maximum force is given by the following equation:

$$F\max = \frac{1.140(\upsilon_0)^2 m_s}{\alpha_m} \qquad (4-22)$$

where

$$\alpha_m = \left[\frac{15\pi\upsilon_0^2}{16(R)^{0.5}}(\delta_s+\delta_p)m_s\right]^{0.4} \qquad (4-23)$$

and m_s is the mass of the sphere (kg) and υ_0 is the velocity of the sphere at impact (m/s).

4.8.2.2 Receiving Transducer

The receiving transducer used in impact-echo testing is a conical-tipped piezoelectric transducer. This transducer is sensitive to the vertical surface displacements over a broad range of frequencies. The transducer consists of a small conical piezoelectric element attached to a large brass backing. The brass backing dampens out undesirable noises. Because of its small contact area, the transducer behaves as a point receiver. A thin metal strip, preferably lead, is used for acoustic coupling between the transducer and the surface of concrete. Therefore, the transducer does not require liquid couplants.

4.8.2.3 Waveform Analyzer

A digital oscilloscope or a waveform analyzer is used to capture the transient output of the transducer, digitize the waveform, and perform signal processing.

4.8.2.4 Signal Acquisition and Processing

The captured waveforms can be studied in the time domain or can be transformed into the frequency domain by the use of the fast Fourier transform (FFT) technique. The initial studies were carried out in the time domain (Steinbeck and Vey, 1975); later it was found that analysis is faster and simpler in the frequency domain (Sansalone, 1985). In time domain analysis, the impact time can be calculated from the distance between the impact source and the receiver and the known velocity of R-waves in the concrete. The reflected P-wave could be identified and its velocity calculated. Later, knowing the thickness of the concrete, according to the time of arrival of the P-wave, flaws can be identified. In the frequency domain, the principle is based on the fact that any waveform can be constructed by superposition of the sine curves of varying amplitudes and frequencies, with appropriate phase shifts. The FFT technique is used to obtain the frequency spectrum of the digital displacement waveform (Stearns, 1975). In sound concrete, the maximum amplitude in the frequency spectrum corresponds to the multiple arrivals of the P-wave reflected from the bottom surface. This statement is true if the impact source and the receiver are close to one another and the transducer is sensitive to the vertical displacements. The reason for this high amplitude is that the

P-wave has the highest wave velocity of all elastic waves and for the same sampling time it creates the most resonance between the two surfaces of concrete. Most of the impact-echo results are based on the frequency spectrum analysis (see Figure 4-11).

4.8.3 Determination of P-Wave Velocity in Concrete

Any impact-echo analysis requires the knowledge of the P-wave velocity in the medium. Different methods were used to determine the P-wave velocity in concrete. When the thickness of the concrete in a sound section is known, the frequency value of the P-wave from the spectrum created by the impact-echo and equation 4-16 can be used to determine P-wave velocity (Sansalone, 1985). Alternatively, if a core is available, P-wave velocity can be calculated by performing impact-echo test on the core. The known length and the measured frequency can be used to compute P-wave velocity using equation 4-16. It was found that P-wave velocities from core samples are 5% slower than the velocities calculated from the structure (Sansalone and Carino, 1986). The direct ultrasonic pulse velocity (UPV) method can be used, when that the two sides of the structure are accessible. It was found that the P-wave velocities calculated by the impact-echo are 10% slower than the velocities measured by the UPV method (Sansalone, 1985). If the two sides of the concrete structure are not accessible and coring is not possible (i.e. in mine shafts), the P-wave velocity is calculated from the surface waves. Using impact-echo to identify the first arrival P-wave in time domain, the P-wave velocity can be calculated. The impact source is fixed on the surface and the receiving transducer is placed on different known intervals on a straight line apart from the source (starting from 200 mm away from the source). The time of P-wave arrivals at each point is calculated for three to five stations. A graph is constructed with the time on the y-axis and the distance from the source on the x-axis. The slope of the constructed graph is used to determine the P-wave velocity (Sadri, 1992). It was found that the P-wave velocities measured by this method are about 5% faster than the impact-echo measurements using the frequency spectrum analysis. The P-wave velocity can be calculated indirectly, using distinct and high amplitude R-wave arrivals in the time domain. In this method, two transducers are used, one placed next to the impact source and the other transducer at a distance away from the first transducer (not more than 100 to 200 mm). The time arrival of the R-wave between the two transducers is determined from the waveform analyzer, and the R-wave velocity is calculated knowing the distance between the first and the second transducers. Assuming the Poisson's ratio of concrete to be 0.2, equation 4-13 is used to estimate P-wave velocity (Lin and Sansalone, 1994).

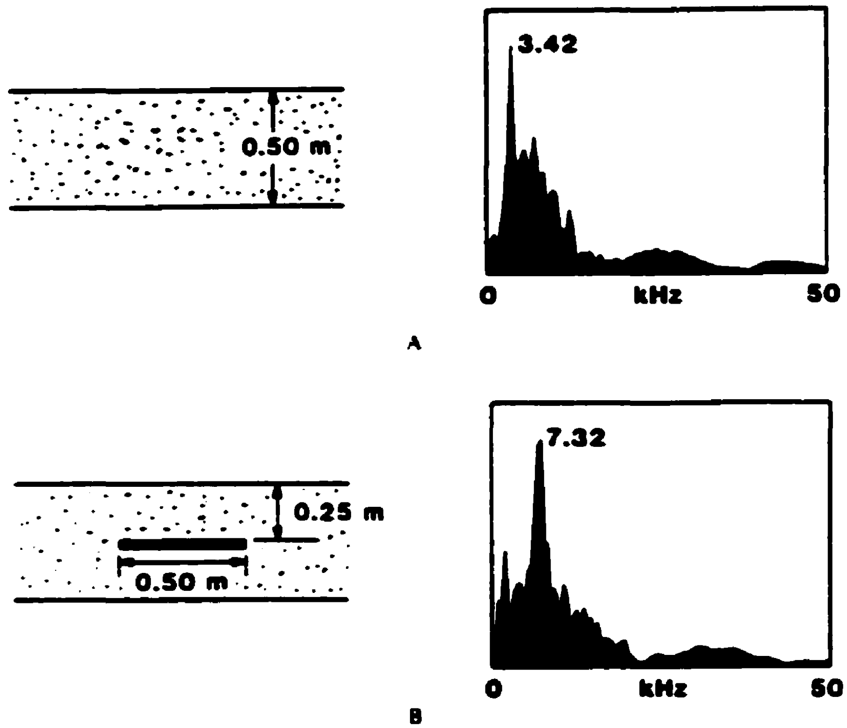

Figure 4-11 Examples of frequency spectra: A) test over a solid portion of concrete slab; B) test over a disk-shaped void. (After Sansalone, 1989).

4.8.4 Effect of the Variables on Impact-Echo Results

4.8.4.1 Spacing Between Impact Source and Receiver

For detection purposes, a small distance between the impact source and the receiver minimizes the complications caused by the R-wave or S-wave arrivals. The separation of the impact source and the receiver (H) are related to the concrete thickness (T). The best impact-echo measurements were taken where the H/T values were less than 0.2. Above H/T value of 0.2, both the displacement waveform and the frequency spectrum become complicated (Sansalone, 1985). For example, at an H/T value of 1, the S-wave arrivals have a significant influence on the displacement response (Sadri, 1992).

4.8.4.2 Time Duration of the Impact (Contact-Time)

The time duration of the impact or the contact-time is a key factor in the impact-echo testing system. The contact-time (t_c) determines the frequency content of the waves generated by the impact. The force-time function of the impact of a sphere on a plate is approximately a half-cycle sine curve. Such an impact contains a range of frequencies. Most of the impact energy is contained in frequencies less than $1.5/t_c$. The short contact-time impacts generate waves with a broader range of frequencies; however, each component frequency has a lower amplitude. A short contact-time pulse contains a higher frequency content and shorter wavelengths; as a result smaller defects can be detected. As an approximation, the highest frequency component of significant amplitude in a pulse equals the inverse of the contact-time. For impact-echo testing of shallow structures, shorter contact-times are preferable. On the other hand, as the contact-times are shorter, the frequency spectra becomes more complicated. The longer-duration impacts generate a narrower band of lower frequency and higher amplitude waves. The low frequency waves (long wavelengths) travel longer (used for thick structures), but they are unable to detect small flaws. The wavelength of the waveform has to be smaller than the dimensions of the flaw in order for it to be detected (Sansalone and Carino, 1986). Also, the waves must have wavelengths equal to the path length of the structure. The appropriate contact-time is determined by computing the required wavelengths, converting the wavelength to frequency and then choosing a contact-time that is short enough to generate required frequencies. It is important to know that the actual contact-time of a spherical source depends on the surface condition of the concrete and the diameter of the sphere. For a given spherical source, the smoother the concrete surface and the smaller the sphere diameter, the shorter the contact-time. Steel spheres or spherical-tipped impact sources are convenient impact sources.

4.8.4.3 Relation Between Flaw Size and Flaw Depth

The larger the ratio is of the lateral dimension of the flaw over its located depth (D/T), the easier it is to be detected. However, the previous work has shown that the flaws with dimensions larger or equal to one half of the depth of the flaw can be easily detected (Sansalone and Carino, 1986; Sadri, 1992), with an appropriate choice of impact source.

4.8.5 Applications of Impact-Echo

Steinbeck and Vey (1975) used impact-echo for evaluating concrete piles. An impact source generated the signal on the top of the piles and an accelerometer was used as the receiver. The signals were analyzed in the time domain. An abrupt change in the cross section was used to mark discontinuities, voids, and delaminations. In the absence of imperfections, the thickness of the piles was calculated. The success of the method relied on the relation between the impact source and the length of the pile and the characteristics of the surrounding materials. In 1983, Carino and Sansalone initiated theoretical and experimental studies to develop impact-echo for testing structures other than piles. In their laboratory studies, impact-echo was used to detect various types of interfaces and defects in concrete slabs and wall structures, with or without reinforcement bars. In most of Carino and Sansalone's experiments, the specimens were constructed containing flaws at known locations.

In conjunction with their experimental studies, Carino and Sansalone have performed numerical studies using the finite element method. The finite element method was used to illustrate the propagation of transient waves in bounded solids and their interaction with flaws.

In the field study, successful results were obtained by monitoring concrete piles and ice-skating rink slabs for flaw detection.

4.8.5.1 Plate-Like Structures

a) Detection of Flaws

Proven applications involving detection of flaws in plate structures include:
- detection of voids
- detection of planar or inclined cracks
- detection of shallow delaminations
- detection of honeycombing (poorly consolidated concrete)
- detection of voids in grouted tendon ducts
- determination of surface opening cracks

b) Shallow Delaminations

Calculations and analysis for disk-shaped voids, planar cracks and inclined cracks in a concrete slab are similar. The impact response of concrete structures (plate, beam, column, ring, etc.) containing shallow cracks or delaminations (less than about 0.1 m deep) is fundamentally different than the response obtained from deeper voids or delaminations. This is due to the fact that the waves generated by the impact source excite one or more flexural modes of vibration of the thin concrete section above the crack. The larger the lateral dimension and/or the shallower the delamination, the lower will be the flexural frequencies. The fundamental flexural mode of vibrations occurs at a frequency that is less than the solid plate thickness frequency. The amplitude of these low frequency flexural vibrations is very large relative to the high frequency reflections from the surface of the shallow delaminations. This large-amplitude, low-frequency vibration is a characteristic feature of waveforms obtained from tests over shallow delaminations, and the frequency spectrum contains one or more large-amplitude, lower-frequency peaks. In this case the frequency correspondence to the depth of the concrete is difficult to distinguish, and as a result locating the depth of the delamination may not be possible (Sansalone, Pratt, Cheng, 1992).

c) Surface Opening Cracks

The impact-echo system has been used to estimate the length of the surface opening cracks (Sansalone and Carino, 1986 and 1988; Sadri 1992). The impact source is placed on one side of the crack and the receiver on the opposite side. As the propagating stress waves strike the tip of the crack, the signals diffract. The diffracted P-wave has spherical wavefronts and the tip of the crack acts as a wave generator. Part of the diffracted P-wave reaches the receiver and the top surface. The diffracted wave reflects back into the plate and part of it is incident upon the crack tip and a new diffracted P-wave is generated. Therefore, a resonant condition is created between the crack tip and the receiver. This condition produces a peak in the amplitude spectrum at a frequency defined by the equation 4-16, where T corresponds to the depth of the surface opening crack. S-waves also diffract from the surface opening cracks and maintain their spherical wavefront. Both P- and S-waves continue to propagate into the plate-like concrete structure and reflect between the top and bottom surfaces of the plate, giving rise to the amplitudes in the frequency spectrum corresponding to the solid thickness frequencies.

d) Voids in Grouted Tendon Ducts

Laboratory studies have been conducted to detect voids in grouted tendon ducts (Sansalone and Carino, 1986, 1988; Sansalone, Lin, and Carino, 1990; Carino and Sansalone, 1991). Presence of a thin layer of higher acoustic impedance between two thick layers of like acoustic impedances does not effect the transmission of stress waves. The metal duct between concrete and grout is an example of such a situation. The results suggest that in case of fully grouted ducts, waves propagate through the ducts and no reflections occur. However, in cases that air or water filled voids are present within the grout, reflections will occur from these voids. Difficulties arise when the grout has a higher acoustic impedance than the surrounding concrete. In such cases grouted tendon ducts affect the transmission of the stress waves, and detection of the voids in the grout is difficult (Sadri, 1995).

e) Honeycombing

Honeycombing refers to unconsolidated or segregated concrete. Impact-echo has been used for detection of honeycombing in concrete (Sansalone and Carino 1988a, b). Reflections and diffractions occur as the stress waves encounter the honeycombing. Also, a part of the signal traverses through the honeycombing, and later as a result of the bottom surface, a part of it reflects back to the surface passing again through the honeycombing. Thus the resulting frequency spectrum contains peaks corresponding to the diffracted and reflected waves from the honeycombing and also reflected waves from the bottom surface. The thickness peak generally is shifted to a value less than the solid thickness frequency peak, because the waves are slower when they pass through the honeycombing. To detect honeycombing, short duration impacts are needed to cause significant reflections.

4.8.5.2 Layered Plates

Layered plate-like structures such as:

- concrete plates with overlays (either asphalt or concrete, or both);
- concrete plates with an embedment (usually a steel layer);
- concrete plates with steel liners;
- concrete liners for rock mines or tunnel shafts; and
- layered pavement systems where the concern is for detecting voids in the sub-

grade beneath the concrete using the impact-echo (Sansalone, Lin and Carino, 1990; Sansalone and Carino, 1989 and 1990; Lin, Sansalone and Carino, 1991). In the case of asphalt overlay on concrete, the acoustic impedance of the concrete is about 1.5 times greater than that of the asphalt, and the amplitude of the reflected wave from the asphalt/concrete interface is about 20% of the incident amplitude, while the amplitude of the refracted wave into the concrete is 120% of the incident amplitude (Sansalone and Carino, 1989). The waves that are refracted into the concrete plate are subsequently reflected and refracted at the bottom surface. The reflection and refraction then will occur at the concrete/asphalt interface as the reflected waves propagate back through the plate. In cases that the overlay is separated from the concrete, a large amplitude occurs in the frequency spectrum as a result of reflection from the free stress interface. If the two layers are perfectly bonded there is a low-amplitude peak on the frequency spectrum corresponding to the depth of the overlay and one large amplitude peak corresponding to the total thickness (Sansalone and Carino, 1989). To determine the depth of the flaw, the velocity of the P-wave in the overlay and in the concrete must be known. The depth of the flaw can be calculated using the following equation (Sansalone and Carino, 1989):

$$T_d = 0.5\left[\frac{C_{po}}{f_d} + \frac{C_{po} - C_{pc}}{f_o}\right] \qquad (4-24)$$

where T_d is the depth of the flaw from the top of the overlay; C_{pc} is the P-wave velocity in the concrete; C_{po} is the P-wave velocity in the overlay; f_o is the frequency value corresponding to the depth of the overlay, and f_d is the frequency value corresponding to the total depth.

If the velocities of the P-wave in the two layers are known, the frequency response of the full thickness could be expressed as:

$$f_t = \frac{1}{\frac{2T_c}{C_{pc}} + \frac{2T_o}{C_{po}}} \qquad (4-25)$$

where T_c and T_o are the thicknesses of the concrete and the overlay respectively.

4.8.5.3 Steel Reinforcing Bars

P-wave reflection from a concrete/steel interface is different from the reflections from concrete/air interface (Sansalone and Carino, 1990; Sadri, 1992), because steel has a higher acoustic impedance than concrete. The reflected waves from the steel interface do not change sign (i.e. from a tension to compressional or vice-versa) as they do when they are incident upon an interface having a lower acoustic impedance. Therefore, the periodicity of the P-wave arriving at the surface is twice that given by equation 4-16. Thus equation 4-16 can be written as:

$$T = \frac{C_p}{4f_p} \qquad (4-26)$$

This equation is valid for calculating the location of reinforcing bars or other objects with higher acoustic impedance than concrete. For steel bars, the accuracy depends upon the relationship between the diameter of the bar and its depth in concrete. Impact-echo can be used for detecting near-surface reinforcement bars (Sansalone and Carino, 1990; Sadri, 1992; Cheng and Sansalone 1992).

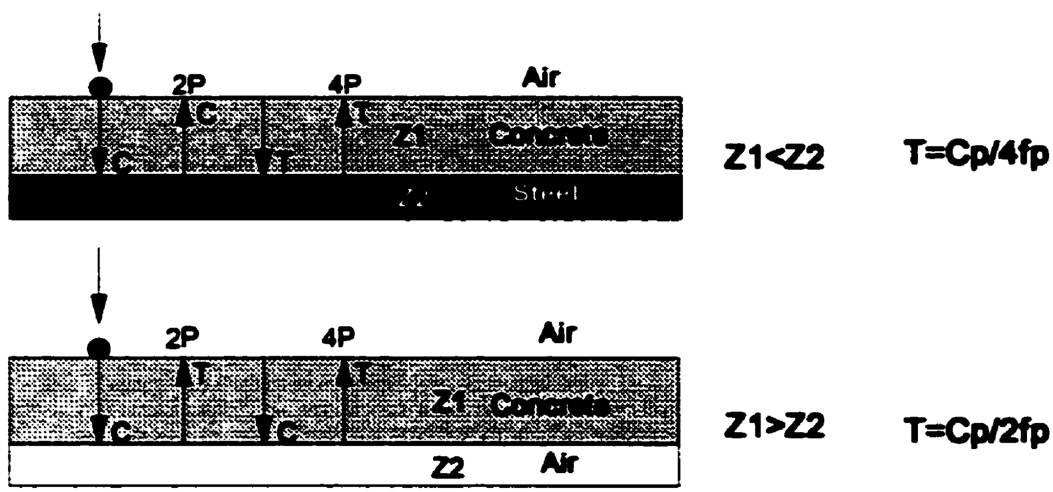

Figure 4-12 Effect of interface: wave reflections from concrete/steel and concrete/air interfaces.

4.8.5.4 Bar-like Structures (Beam and Column)

In the plate-like structures the dominant response of the impact-echo is due to the reflections between the top and bottom surface of the plate, or possible defects. In bar-like structures such as beams and columns, the side boundaries have a significant effect on the wave propagation. When an impact is generated on one side of a structure such as a pile, the resulting wavefront is initially spherical but later becomes planar as the pulse travels down the bar-like structure. The plane wave reflection occurs at the bottom surface, the reflected waves travel through the length and are detected by the receiver. The length of the pile acts as a wave guide. Long-duration impacts are used due to the long length of the piles. The signal analysis is simple and straightforward.

The transverse point impact response on concrete bars having circular, square, and rectangular cross sections is considerably different. When a transverse point impact is generated, the interpretation is more complex. The transient response of a bar subjected to a transverse impact is a combination response of a number of cross sectional modes of vibration which are caused by multiple reflections of waves in the cross section (Lin and Sansalone, 1991a, b, 1992). In this situation, the length of the bar does not effect the results as long as it is greater than about three times the width (Lin and Sansalone, 1991a, b). The geometry and shape of the cross-section controls the shape and the frequency of the cross-sectional mode. The presence of the defects disrupts the frequency pattern created by the cross sectional modes in a solid bar. Once the solid response is understood, the presence of the defects can be determined easily. Equation 4-16 could be used to locate the defects.

4.8.5.5 Hollow Cylindrical Structures

The hollow cylindrical structures such as tunnel concrete liners (i.e subway tunnels) or the concrete shaft lining in underground mines, are surrounded by soil or rock. The response of the stress waves generated by impact-echo is greatly affected by the acoustic properties of the surrounding materials. The impact response is strong where there is a relatively large difference between the acoustic impedances of the concrete lining and the surrounding materials. The experimental work on the concrete shaft lining at Allan potash mine in Saskatchewan by Lin and Sansalone (1994) suggests that the acoustic impedances between the concrete and rock ($|Z_r - Z_c / Z_r + Z_c|$) should be greater than about 0.24. In this study it was shown that when the acoustic impedance of the concrete and surrounding rock is the same, the concrete thickness cannot be measured. If the acoustic impedance of the rock is lower than that of the concrete, equation 4-16 is used when the acoustic impedance of the rock is higher than concrete, equation 4-26 is used to explain the relation between the P-wave velocity and the frequency in the concrete liner with a certain thickness. Delaminations between the concrete lining and the surrounding rock are easily identifiable, independent of the rock's acoustic properties (Lin and Sansalone, 1994). The separations between the concrete/rock interface or fractures within the concrete liner (concrete/air or concrete/water) can be detected and the equation 4-16 can be used to determine their depth.

4.8.5.6 Evaluation of Setting Time, Strength and Dynamic Elastic Constants of Concrete

The impact-echo method was used by Pessiki and Carino (1988) to monitor the development of mechanical properties of the concrete at an early stage. The values of P-wave velocities obtained by the impact-echo method were compared with the standard penetration test for determining the setting time of the concrete. The setting time of the concrete based on the impact-echo results showed excellent correlation between the initial setting times obtained by the penetration resistance tests. It was shown that a strength-velocity relationship for a given concrete mixture could be used subsequently as a reliable means of estimating the strength of a concrete structure.

4.9 SUMMARY

Dynamic elastic constants are calculated from the elastic wave velocities and densities. In this chapter, various techniques used for generation and detection of elastic waves in rocks and concrete have been discussed. The theory, apparatus, applications and limitations of each technique has been given. A summary of advantages and disadvantages of all the wave propagation techniques are presented in Table 4-1.

Table 4-1 A summary of techniques used to measure dynamic modulus of elasticity for rocks and concrete.

Dynamic Modulus of Elasticity Measuring Techniques						
Technique	Concrete		Rock		Advantages	Disadvantages
	Lab.	Field	Lab.	Field		
ResonantFrequency (RF)	X	X	X	-	- Calculates the natural frequency of different vibration modes. - Calculates the elastic moduli. - Relatively inexpensive. - Extensively used.	- The dimensions of the specimen control the testing procedure. - It is not commonly used in the field.
Ultrasonic Pulse Velocity (UPV)	X	X	X	X	- Direct P-wave velocity measurement. - Easy to use. - Fast measurement technique. - Relatively inexpensive. - Extensively used.	- Difficult to measure S-wave parameters. - Usually assumes Poisson's ratio or shear wave velocity for elastic moduli measurement. - Rapid signal attenuation problem.
Seismic Wave Velocity	-	X	-	X	- Direct elastic wave measurement. - Used for large scale measurements. - Could be inexpensive (i.e. hammer seismic). - Extensively used.	- Difficult to recognize S-wave parameters. - Could be expensive (i.e. borehole, and use of explosives).
Petite Sismique	-	-	-	X	- Direct measurement of S-wave parameters. - Comparison of static modulus of elasticity with S-wave parameters.	- Difficulty in generation and detection of S-waves. - Presently in experimental stages. - Can be expensive (i.e. source and receiver).
Impulse-Response	-	X	-	-	- Measures the elastic moduli of the concrete piles and it's base material. - Inexpensive.	- Indirect calculations of modulus values. - It is limited to the piles or columnar structures.
SASW	-	X	-	-	- Capable of measuring modulus of elasticity for thin pavement layers. - Inexpensive.	- Calculates the elastic moduli values by comparing with various models. - Assumes theoretical Poisson's ratio values for calculations. - Rapid R-wave attenuation in thick concrete layers.
Impact-Echo	X	X	-	-	- Direct measurements of P-wave parameters. - Inexpensive.	- Very thin layers (i.e below 15 cm. are difficult evaluate.

CHAPTER 5

METHODS OF DETERMINING STATIC ELASTIC CONSTANTS

5.1 INTRODUCTION

This chapter presents the various laboratory and in situ methods used for measuring the static modulus of elasticity parameters for rocks and concretes. Also, the factors that influence the static modulus values are briefly discussed. Finally, a brief comparison between the dynamic and static modulus of elasticity of rocks and concretes is presented.

5.2 MEASUREMENT OF DEFORMATION

The deformation of concrete or rock samples is measured with the help of three devices, which are mechanical, optical, and electrical gauges. The most widely used are mechanical gauges, most commonly referred to as dial gauges. These dial gauges are made of gears connected to a shaft. When pressure is applied on this shaft, it moves and forces the gears to turn, thereby recording the deformation to the surface on which the shaft is installed. In brief, mechanical gauges work similarly to the micrometers. A precision in the range of 0.01 to 0.001 mm is common.

Optical gauges consist of a short mechanical arm with a small mirror mounted on it which reflects a beam of light falling upon it. Following the law of reflection, the reflected beam moves twice as fast as the short arm, and the magnified angular movement of the reflected beam is measured either at some distance from the pivot point of the system or by using an optical system thereby magnifying the displacement of the end of the short mechanical arm. A large variety of optical instruments is available with magnifications from 10 to 1000 times, and precision ranges from 5 mm to 0.002 mm.

Finally, electrical gauges include linear variable differential transformers (LVDT) and electrical resistance strain gauges. These devices are based on the principle that resistance in an electrical wire changes as it extends lengthwise, or as a movable part (as in a rheostat), or a change in self-inductance or capacitance of a moveable magnetic element occurs.

5.2.1 Stress-Strain Curve

The static modulus of elasticity for a material under tension or compression is given by the slope of the stress-strain curve for the concrete or the rock under uniaxial load. Since the stress-strain curve for the concrete and rocks is not linear, three methods for computation of Young's modulus are used (see Figure 5-1).

a) The tangent modulus is given by the slope of a line drawn tangential to the stress-strain curve at any point on the curve.

b) The secant modulus is given by the slope of a line drawn from the origin to a point on the curve corresponding to a 40% (for rocks it is to the 50%) (ASTM DESIGNATION D 3148-72) of the stress at the failure load.

c) The chord modulus, known as average modulus in rock mechanics, is given by the slope of a line drawn between two points (more or less the straight line portion) on the stress-strain curve.

d) The initial tangent modulus is the tangent modulus of the line drawn at the origin. The initial tangent modulus corresponds to very small instantaneous strains and is compared to the dynamic elastic modulus.

Poisson's ratio could be calculated for the material subjected to the axial load, by measuring the ratio of the lateral strain to the axial strain within the elastic range (usually between 40% to 60% of the maximum strength). For concrete, the Poisson's ratio values range between 0.11 and 0.28, however the average Poisson's ratio for concrete is 0.20 (Fintel, 1985). The Poisson's ratio values tend to be higher at early curing stages, and then due to increase in strength and age, Poisson values decrease (Fintel, 1985; Sadri, 1992).

The stages of a typical stress-strain curve are important to note. In rocks, during the initial application of load on the sample, pores, cracks and joints close and the specimen becomes denser. The stress-strain curve shows an upward concavity (section A). In concrete, below about 30 percent of the ultimate load, the transition zone cracks, that were formed during curing, remain stable; therefore the stress-strain curve remains linear. In rocks, at the intermediate stress level, usually between one-third and two-thirds of the maximum uniaxial strength, most of the rocks and concretes become linearly elastic (section B). At this stage all of the pores, cracks and joints are closed; therefore the strain increments become proportional to the stress values. In concrete, above 30 percent of the ultimate load, the transition zone microcracks increase in length and the curve begins to deviate from the straight line. Until 50% of the ultimate load a stable system of microcracks may be assumed in the transition zone. At 50 to 60 percent of the ultimate load, cracks begin to form in the matrix. With further increase in stress up to about 75% of ultimate load, the cracks in the transition zone become unstable and the stress-strain curve bends considerably toward the horizontal. In rocks, following this stage up to the peak stress value, new intergranular, interagranular and trans-granular microcracks form. In concrete, after 75 to 80 percent of the ultimate load, very high strains are developed, the crack system is becoming continuous and rapid both in the matrix and the transition zone. Finally, the shape of the stress-strain curve becomes concave downward up to failure (see Figure 5-1).

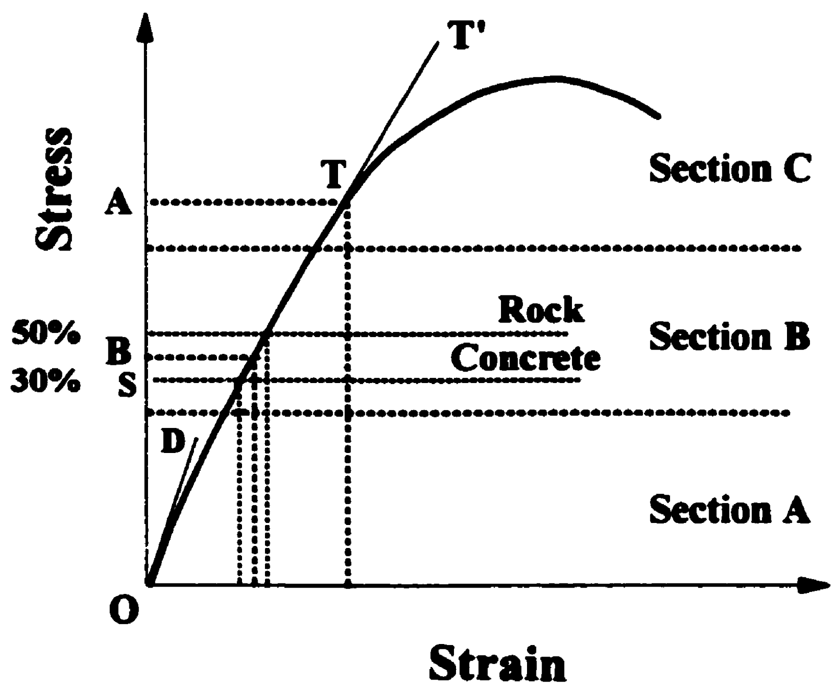

AB is the chord modulus, known as average modulus
OS is secant modulus 30% Max. stress
OD is initial tangent modulus
TT' is tangent modulus
Section A shows pores, cracks and joints are closing.
Section B shows pores, cracks and joints are closed.
Section C shows new cracks and joints are opening.

Figure 5-1 A typical stress-strain curve.

5.3 DETERMINATION OF STATIC ELASTIC MODULUS IN CONCRETE: LABORATORY METHOD

ASTM C 469 describes the method of measuring static modulus of elasticity (chord modulus) and Poisson's ratio of a 6.0 in. (15.0 cm) by 12.0 in. (30.5 cm) concrete cylinder. The samples are loaded in longitudinal compression at a constant loading rate within the range of 35 ± 5 psi. Appropriate deformation (strain) gauges are installed horizontally and vertically (perpendicular and parallel) to the direction of loading for later computation of Poisson's ratio. The generated stress-strain curve is used to compute the static Young's modulus of elasticity.

For structural design purposes, the Young modulus of elasticity values are estimated from empirical equations (Mehta and Monteiro, 1993). These empirical equations assume a direct relationship between the density, strength, and elastic modulus of concrete.

The ACI code (1983) expresses the elastic modulus in terms of the concrete strength:

$$E_c = 0.043(W)^{\frac{3}{2}}(f'_c)^{\frac{1}{2}} \quad for\, f'_c \leq 40 MPa \qquad (5-1)$$

where W is the unit weight of concrete in kg/m^3 and f'_c is concrete compressive strength in MPa.

The ACI committee 363 (1992) and CSA Standard (1994) have expressed modulus of elasticity in the following form:

$$E_c = \left(3320(f'_c)^{\frac{1}{2}} + 6900\right)\left(\frac{\rho_c}{2300}\right) \quad for\, 21 MPa \leq f'_c \leq 83 MPa \quad (5-2)$$

where ρ_c is the concrete density in kg/m^3.

The following empirical equation is introduced by the ACI Building Code 318, for concretes weighting between 90.0 (40.8 kg) and 155.0 (70.3 kg) lb/ft^3.

$$E_c = W_c^{1.5} \times 33 f'_c{}^{1/2} \qquad (5-3)$$

where the E_c is the concrete modulus of elasticity in psi, W_c is the unit weight in lb/ft^3, and f'_c is the 28-day uniaxial compressive strength of the standard cylinders. For a concrete with a density value between 1400 and 2300 kg/m^3 (normal weight concrete) the following equation is used:

$$E_c = 57000\sqrt{f'_c} \tag{5-4}$$

where f'_c, compressive strength of the cylinder is in lb/in^2 and E_c is lb/in^2. When E_c is expressed in GPa and f'_c is expressed in MPa the equation changes to:

$$E_c = 4.73\sqrt{f'_c} \tag{5-5}$$

In the CEB-FIP Code (1990), the modulus of elasticity of normal weight concrete can be estimated from:

$$E_c = 2.5\times 10^4 (f_{cm}/10)^{1/3} \tag{5-6}$$

where the E_c is the modulus of elasticity of 28-day concrete in MPa, and f_{cm} is the average 28-day compressive strength.

5.4 FACTORS AFFECTING STATIC MODULUS OF ELASTICITY AND POISSON'S RATIO OF CONCRETE

The modulus of elasticity of concrete is expressed as a function of concrete compressive strength. Hansen (1956), Gunzler (1970), Lew and Reichard (1978, Byfors (1980), Oluokun et al. (1991), and Mehta (1994) have studied the changes in concrete compressive strength and modulus of elasticity at early ages. The elastic modulus of concrete is affected by aggregate type, water/cement ratio, cement type, temperature, and testing parameters (Byfors (1980), Zia et al. (1991), ACI committee 363 (1984), Collins and Mitchell (1990):

5.4.1 Aggregate

The concretes with dense aggregate have a higher modulus of elasticity. The aggregate porosity seems to be the main factor. This is because the aggregate porosity determines its stiffness, which in turn controls the ability of the aggregate to restrain the matrix strain. Different types of aggregates effect the modulus of elasticity because different aggregate types have different modulus of elasticity and the overall modulus of elasticity of the concrete is a combination of its material constituents. Lightweight rocks such as limestone are more porous than intermediate aggregates such as granite. The modulus of elasticity of the aggregates influences the modulus of elasticity of bulk concrete samples. In two concrete mixes with the same strength, the modulus of elasticity is higher for the mix with granite type aggregate than that with limestone type aggregate. The size, shape, surface texture, grading, and mineralogical composition can influence the microfracturing and influences the stress-strain curve.

5.4.2 Cement Paste Matrix

Porosity controls the modulus of elasticity of the cement paste matrix. The porosity of the cement paste is controlled by the water/cement ratio, air content, mineral admixtures and degree of cement hydration.

5.4.3 Transition Zone

Transition zone is a term used for the boundary between the coarse aggregates and the cement paste. The void spaces, microfractures, and the orientation of the calcium hydroxide crystals are mainly concentrated in the transition zone which influences the stress-strain relationship in concrete.

5.4.4 Testing Parameters

It has been observed that the concrete samples that are tested in wet conditions have approximately 15% higher modulus of elasticity values than those tested in dry conditions. The rate of the applied load influences the stress-strain curve, the rate of crack propagation and hence the modulus of elasticity.

5.4.5 Poisson's Ratio

In 1970, Gunzler reported that there was no change in Poisson's ratio at early hours of curing (15 hours to 30 hours). Perenchio and Kilieger (1978), Carrasquillo et al. (1981), Klink (1985), and NRMCA (1992) reported that Poisson's ratio is affected by age and concrete strength. However, Oluokun et al. (1990) concluded that Poisson's ratio is not affected by the concrete strength or age. Byfors (1980) reported that Poisson's ratio is lower at early ages and increases with increasing age and strength.

5.5 DETERMINATION OF STATIC ELASTIC MODULUS IN ROCKS: LABORATORY METHODS

5.5.1 The Simple Compression Test

An unconfined compression test on a core specimen, with two smooth ends having a length-to-diameter ratio of 2 and 3, and a device to measure strains, yields a stress-strain curve. The sample is loaded between the cylindrical seats in a compression testing machine. The uniaxial stress is increased at a rate of 0.5-1.0 MPa/s. The readings of strains, that is the axial and the circumferential strains, are collected usually using electrical resistance strain gauges. The Young's modulus of elasticity, E , is obtained from the slope of axial stress-strain curve. Poisson's ratio, υ, is obtained by dividing the lateral strain by the axial strain.

5.5.1.1 Applications

As early as 1883, Milne and Grey measured the value of Young's modulus for Japanese rocks in connection with earthquake research and seismology. They used rock beams and calculated the results from the standard beam theory.

Later in 1910, Adams and Coker developed a more comprehensive laboratory testing procedure to measure Young's modulus and Poisson's ratio of marbles and granites. The tests were of the uniaxial type on cubic and cylindrical samples. The stress-strain curves plotted illustrated hysteresis effects. However, the variations of temperature had no measurable effect on the results. In 1930, Phillips conducted a series of experiments on shales, sandstones and siltstones to study the effect of variation of moisture content on Young's modulus and Poisson's ratio. In 1933, Zisman made a study of the elastic constants of rocks as part of a larger study concerning geophysical applications. Cyclic loading tests were made on cylinders, the load, vertical and horizontal strains being measured. From these results, Young's modulus and Poisson's ratio were calculated directly. Static uniaxial loading was used, and the average of the results for loading and unloading was taken. The results showed that both Young's modulus and Poisson's ratio increased with an increasing load. Evans in 1935 did a study of marble, sandstone and concrete cylinders under uniaxial loading conditions. Both elastic and plastic effects were reflected in the results. The rate of loading was varied, but the stress-strain curve proved to be independent of time.

In 1937, a comprehensive survey of one hundred rocks from North America was undertaken by Griffith. The cubic samples were tested for their compressive strength and hardness. Later, their variations with the water content of the rocks were studied. Both compressive strength and hardness of rocks were found to reduce with increasing water content. In this study, it was assumed that the maximum water content was equal to the pore volume of rock. The work was continued by Phillips (1948). The values of Young's modulus and Poisson's ratio were calculated. The results showed that for cyclic loading both Young's modulus and Poisson's ratio increased with load.

5.5.1.2 Factors Affecting Static Modulus of Elasticity of Rocks

a) Specimen Geometry

In homogeneous rocks the height to diameter (h/d) of the cylindrical samples may or may not influence the modulus values (Lama, 1978). In nonhomogeneous rocks, the h/d ratio may influence the stress-strain curve, and hence the modulus values (Lama, 1970). The change in modulus values is more obvious when the h/d ratios increase substantially to 3 and higher (Handin et al., 1972). A low h/d ratio results in an increase of confining pressure; hence the mode of fracture of the specimen decrease and the modulus values increase (Lama and Gonano, 1976).

b) Temperature

Temperature influences the stress-strain curve particularly when there is high lateral pressure. In this case the ductility of the rock increases and affects the modulus values (Lama, 1978, and Goodman, 1989).

c) Fractures, Voids and Rock Structure

Fractures and pores have a great influence on the calculated modulus values. The large number of microfractures and voids results in low modulus values (Lama, 1970). The modulus values for rocks stressed parallel to the beddings and foliations are higher than when the stress is perpendicular to them. Poisson's ratio is greatly influenced by the opening and closing of the fractures and voids (Lama, 1978).

d) Testing Parameters

The type of loading platen (rough, smooth, shape and relative stiffness, rigid or brush, and its diameter relative to the specimen) influences the stress distribution in the sample, and therefore effects the modulus values (Lama, 1978). Smooth, brush platens with their diameters similar to the testing specimen are recommended. The rate of loading is also an important testing parameter which influences the modulus values and particularly the Poisson's ratio. The load must be applied uniformly on the specimen. The rate of loading on rocks is different upon the rock type (Lama, 1978). If the rock does not behave linearly elastic, and a test is conducted at a particular stress rate, the corresponding strain rate shall be different at different stages of strain. It shall increase for a rock with a stress-strain curve being convex towards the stress axis (e.g., shales and limestones) and decrease for a rock with a stress-strain curve being convex towards the strain axis (e.g., coals and rock salt). Nevertheless, most of the machines are capable of giving strain rates between 10^{-3} to 10^{-4}. However, the influence on the modulus values because of changes on the platen condition and rate of loading do not exceed more than 5-10% between the extreme cases (Lama, 1978).

5.5.2 The Brazilian Test

The Brazilian test uses a cylindrical rock or concrete sample (where the length-over-diameter ratio should be approximately 2.5:3.0) to calculate the Poisson's ratio and the Young's modulus. The sample is subjected to an increasing load applied parallel to one of the core diameters. The strain is measured with a 90° strain gauge rosette placed at the center of the sample, and oriented to record both horizontal and vertical strain (ϵ_x and ϵ_y respectively). Knowing the load P, and the horizontal and vertical deformations, it is possible to calculate Poisson's ratio and Young's modulus as following (Hondros, 1959):

$$\upsilon = -\left(\frac{3\epsilon_x + \epsilon_y}{3\epsilon_y + \epsilon_x}\right) \qquad (5-7)$$

$$E = \frac{6P(\upsilon^2 - 1)}{\pi D t(\upsilon \epsilon_x + \epsilon_y)} \qquad (5-8)$$

where D is the diameter, and t is the thickness of the core sample.

5.5.3 Bending Test

The bending test is a very simple method for measuring Young's modulus. A beam or cylindrical sample is placed on two supports, and a load is applied at one or two points. The modulus of elasticity can then be calculated using the following equations:

for one-point loading:

$$E = \frac{WL^3}{48(yI_z)} \qquad (5-9)$$

for two-point loading:

$$E = \frac{WL^3}{56(yI_z)} \qquad (5-10)$$

where W is the load applied;

L is the length of the sample;

y is the deflection measured at the center of the sample, and I_z is the moment of inertia of the section at the centroid.

Depending on whether the cross-sectional shape of the sample is rectangular or circular, the moment of inertia I_z can be found as $bh^3/12$ (for a rectangular beam, where b is width and h is height) or $\pi d^4/64$ (for cylindrical core of diameter d). Since rocks and concretes have different values for the modulus of elasticity when tested in tension or compression, $E_{bending}$ can be related to $E_{compression}$ and $E_{tension}$ (Adler, 1970) (assuming linear stress-strain behavior):

$$E_{bending} = \frac{4(E_{compression} \cdot E_{tension})}{(\sqrt{E_{compression}} + \sqrt{E_{tension}})^2} \quad (5-11)$$

This equation is only applicable to rectangular specimens.

5.5.4 Compression of Square Plates

The modulus of elasticity and Poisson's ratio of rocks or concretes can be calculated (assuming the sample to be linearly elastic) by measuring the horizontal and vertical strains at the center of the square plate and using the following equations (Davis and Stagg, 1970):

$$\upsilon = \frac{\beta - \alpha}{\beta\alpha - 1} \quad (5-12)$$

$$E = \frac{\sigma_h}{\epsilon_h}(1 + \upsilon\alpha) \quad (5-13)$$

where σ_h is the horizontal tensile stress,

ϵ_h is the horizontal strain at center,

α is the ratio of the vertical to the horizontal stress $\left(-\frac{\sigma_v}{\sigma_h}\right)$, and

β is the ratio of the vertical to the horizontal strain $\left(-\frac{\epsilon_v}{\epsilon_h}\right)$.

5.5.5 Triaxial Test (Solid and Hollow Cylinders)

Elastic constants can be determined from triaxial testing, using strain gauges mounted on the exterior surface of the samples and the connections being taken out through specially designed plates.

The relationship between the modulus of elasticity and Poisson's ratio with the applied axial stress, σ_1, the confining pressure, p_3, and the axial strain, ϵ_1, is given by:

$$E = \frac{(\sigma_1 - 2\upsilon p_3)}{\epsilon_1} \quad (5-14)$$

In case of a hollow cylinder, the internal pressure is zero, and the modulus of elasticity is calculated by:

$$E = \frac{1}{\epsilon_1}\left[\sigma_1 - \frac{2\upsilon p_3 b^2}{(b^2 - a^2)}\right] \tag{5-15}$$

where υ is the Poisson's ratio;

b is the outside radius of the cylinder and

a is the radius of the hole.

5.6 DETERMINATION OF STATIC ELASTIC MODULUS IN ROCKS: FIELD METHODS

There are a number of field methods available for measuring the static elastic constants in rocks. In this section, a brief description of these methods and their instrumentation are given.

5.6.1 Dilatometer and Gallery Tests

Dilatometers or pressuremeters are applied in drillholes for measurements of the elastic moduli. The instrument is inserted in a drillhole and is expanded to apply pressure to the drillhole walls (ISRM, 1987). The gallery test is a similar experiment conducted in the bulkheaded section of a tunnel. Dilation of the hole is measured as a function of the pressure, from which the deformability parameters of the ground are calculated. It can also be used to test hollow cylinders of rock in the laboratory for measurement of the elastic moduli.

Using the following equation the shear modulus, G, is calculated as:

$$G = M_r \frac{\pi L D^2}{x} \tag{5-16}$$

where L is the length and D is the diameter of the drillhole test section (in metric units); x is the pressure generator constant (depending on the type of the dilatometer), and M_r is the pressure-volume relationship constant of the rock (M_r is in megapascals, per turn of the screw pump).

In cases that the Poisson's ratio is known and the Young's modulus can be calculated from:

$$E = 2(1 + \upsilon)G \tag{5-17}$$

or

$$E = (1 + \upsilon)\Delta p \frac{a}{\Delta u} \tag{5-18}$$

where p is the applied uniformed pressure;
a is the radius of the borehole, and
Δu is the radial deformation.

5.6.2 Radial Jacking Tests

The radial jacking test is a large scale test for measurement of deformability of tunnels. The loads are applied to the circumference of a tunnel by a series of jacks and the resulting radial expansion is measured.

5.6.3 Flat Jack Test

With the flat jack test, large volume of rocks are loaded to pressures up to 70 MPa or higher using stainless steel flat jacks with special welding details. Typically an area of 600 cm^2 is selected and is cut by a saw in a linear fashion, several flat jacks are placed in the slot, and pressure is applied to the rocks. The slot expansion displacements are measured by electrical transducers. Readings are taken for different pressures as the pressure rises. The results are presented graphically, and the modulus of elasticity, E, is calculated from the graph at any given pressure by:

$$E = k(1 - \upsilon^2)\frac{dp}{dD} \tag{5-19}$$

where k is a coefficient which is determined graphically and depends on the number of jacks and chamber configuration;

υ is the Poisson's ratio which is usually approximated, and

dp/dD is the slope of pressure versus the slot opening at the selected point.

5.6.4 Plate-Bearing Test

The plate-bearing test is the most common and least expensive large-scale in situ test for determining the deformability in rocks (ISRM, 1981). A rigid plate, which is built up from several concentric disks of heavy gauge steel, is pushed against a prepared rock surface, and the settlements are measured at the surface of the plate. As the load is increased at equal increments, the displacements are measured at the plate surface. The load is cycled often to check the nonlinearity and the difference in loading and unloading behavior.

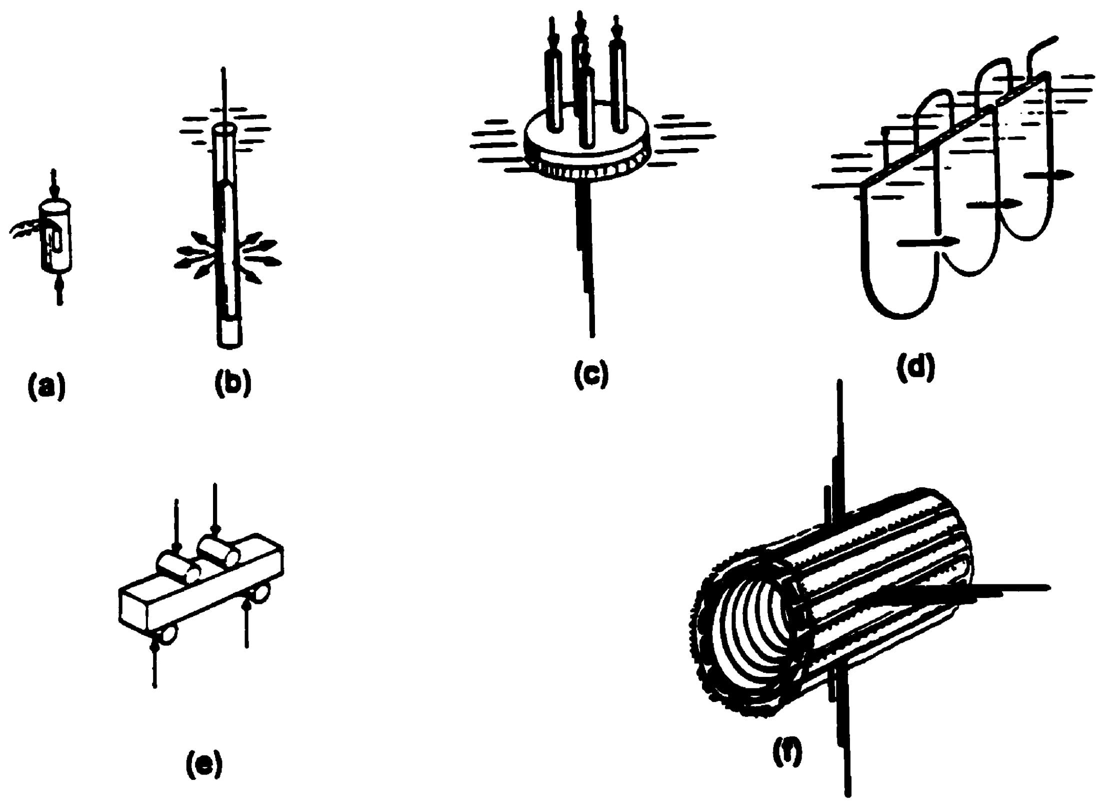

Figure 5-2 Configurations of the methods for measuring static modulus of elasticity: a) uniaxial and triaxial tests, b) dilatometer test, c) plate-loading test, d) large flat-jack test, e) four-point beam-bending test and f) radial jacking or tunnel pressurization test. (Modified after Franklin and Dusseault, 1989).

5.7 COMPARISON BETWEEN DYNAMIC AND STATIC ELASTIC CONSTANTS

In the case of rocks and concrete the values of dynamic elastic moduli are several times greater than the static ones, because of the time lag of the strains behind that of the applied stresses due to the anelasticity of the materials (Blitz, 1996). Lama (1978) made a general comparison between the values of static and dynamic modulus of elasticity of various rock types. He concluded that with the static method, the values of modulus of elasticity are more scattered than values obtain by dynamic methods; however, with the static methods the strain values are as high as 10^{-2} compared with the low strain values of 10^{-5} obtained using the dynamic methods. Since the dynamic methods involve low strains, a comparison of static and dynamic values is possible only if the static values are taken at comparable stress levels. Previous workers have shown that the dynamic values of Young's modulus are found to be significantly greater than the static values. The difference was explained due to the presence of voids, fractures and cavities. Zisman (1933) and Ide (1936) explained this difference with the static yielding being increased by deformation of discontinuities and cavities and the dynamic methods being less influenced. They also concluded that the higher degree of compaction in the rocks leads to better between the dynamic and static results. Other results such as those of the United States Bureau of Reclamation (1948), Dvorak (1957), Sutherland (1962), Chenevert (1964), Youash (1970), Coon (1968), Rzhevsky and Novik (1971), and Ramana (1973) agree with these results. In 1953, the U.S. Bureau of Reclamation reported that the discrepancy between the dynamic and static values is less for rocks with higher values of modulus of elasticity.

In concrete, the dynamic and static modulus of elasticity are different as a result of two major factors: a) the low rate of stress and strain as a result of the dynamic loading compared to the high rate of stress and strain in static loading; and b) nonhomogeneity of the concrete effects the two moduli in different ways (Philleo, 1955). In general, dynamic modulus of elasticity values are appreciably higher than static ones for all concrete types (Neville, 1981). According to the British Code CP 110:1972, the dynamic E_d and static E_c modulus of elasticities in GPa could be expressed by:

$$E_c = 1.25E_d - 4.1 \qquad (5-20)$$

The relation dose not apply for lightweight aggregate concretes and concretes containing more than 500 kg cement per cubic meter of concrete. For light and normal weight concrete it has been suggested that the relationship between the static and dynamic moduli is a function of the density of the concrete (Popovics, 1973). The dynamic Poission's ratios for concrete are higher than static values particularly at early curing stages.

5.8 SUMMARY

In this chapter, the various laboratory and in situ techniques for measuring static elastic moduli for concrete and rocks are described. For each method, the test procedures and the various implications are discussed. The current in situ measurement techniques are used mainly to calculate the deformability of the rocks rather than those of the concrete. Various in situ techniques are designed to measure the static modulus of elasticity of rock masses or concrete structures with different dimensions and scales. A comparison between the static and dynamic elastic moduli for rocks and concrete suggest that in most cases the dynamic values are larger than the static values and that is mainly due to the anelasticity of the materials, the rate of loading, and the strain rates.

CHAPTER 6

MINIATURE SEISMIC REFLECTION (MSR) SYSTEM

6.1 INTRODUCTION

An MSR system was assembled in the Geomechanics Laboratory at McGill University. The hardware was designed in order to be used on circular and arch-shaped concrete structures and rock masses in the field and also laboratory size specimens. A number of impact devices are designed to generate repeatable signals with a wide range of frequencies into the objects. The analysis software program is developed to identify and measure P- and SV-wave frequencies and subsequently their velocities, with the GAUSS mathematical and statistical system using a time series analysis package.

6.2 PRINCIPLE OF MSR SYSTEM

The MSR system functions based on the impact-echo principle. Figure 6-1 shows a schematic representation of the MSR system. In general the MSR nondestructive testing system involves a set of impact sources, two broad-band displacement transducers, an analog-to-digital signal converter card (A/D card) or a digital oscilloscope and a portable computer. As the mechanical switch on the top of the impact device is activated, the impact body is released to cause an impact on the surface of the media. The impact of the spherical tip of the impact body results in the generation of a low frequency stress signal into the medium. The stress signal transforms into the body waves and surface waves. The body waves travel into the testing object and any change in the acoustic properties of the medium results in their reflection toward the source direction. The change in acoustic properties could be the result of any internal cracks or flaws or different material such as rocks. The reflected wavefronts are picked up by the transducers. The vertical displacement transducer is sensitive to the vibrations caused by the P-wavefronts at right angles to the surface. The tangential displacement transducer is sensitive to the vibrations caused by the S-wavefronts parallel to the surface. The signals are amplified and transferred to an A/D card. The sampling rate and number of data points are arranged as required, for each test on the A/D card. Although measuring the time between arrivals of the P- and S-waves at the surface is complicated, the measurements can be converted into a frequency domain spectrum. The time domain waveforms are transferred to a portable computer to be transferred into frequency domain spectra by the fast Fourier transform (FFT) technique. The frequency spectra are generated by signal processing software and displayed by the portable computer for the required analysis. The frequency associated with the stress wave resonance between the two surfaces (e.g. top surface/flaw or top/bottom surfaces) becomes easily identifiable.

In the following sections, the aspects of the MSR system studied in more detail are as follows:

- The instrumentation including impact source, receiving transducers, and signal analysis
- The test configuration between the impact source and the receiver
- The signal processing and analysis technique

6.3 MSR SYSTEM (INSTRUMENTATION)

6.3.1 Impact Source

The impact source controls the energy and the frequency content of the propagating pulse. The force-time function of the impact can be approximated as a half-sine curve (Figure 6-1). The amplitude of the force-time function affects the amplitude of the wave particle motion as it travels through the medium. The contact-time of the impact controls the frequency content of the pulse.

The most suitable source of body wave generation for nondestructive testing of composite solids such as concrete and rocks is a spherical tip impact device. The advantage of using impact generated stress waves is that a heterogeneous material like concrete or rock appears homogeneous to the propagating waves. The impact of a spherical tip impactor on the surface of a solid generates body waves, that have spherical wavefronts with a wide range of frequency components (see Section 3.2.3).

The MSR system requires a set of impact devices. Each impact device has a different diameter spherical tip impact body. The small diameter impact bodies are used for thin slabs or for short length specimens. The large diameter impact bodies are applied where rock or concrete bodies are thick and longer wavelengths are required.

For the design of the impact devices, two main requirements have to be fulfilled. Firstly, the generated impacts have to be repeatable on the exact position with the same intensity. Secondly, the impact source should be able to function on the ceilings, vertical, and arch shaped walls with minimum influence from the gravitational force.

Taking the above into consideration, a series of practical impact devices were designed and produced. Each device consists of a spherical test tip which is housed in an impact body, an impact spring and a loading spring, a catch chuck, a release bottom, a loading tube and a guide tube. Four impact devices with impact head diameters of 1.3, 1.5, 3.0 and 15.0 mm were manufactured (see Plate 6-1). All the impact devices have a 16.5 cm length and a 3.0 cm diameter (see Figure 6-2). Depending on the mass of the impact body, the resulting energy varies (see Table 6-1). The four impact devices in theory are capable of producing impacts having time durations (contact-times) between 16 to 140 μs on smooth concrete and rock surfaces.

Table 6-1 Specifications of MSR impact devices.

Hammer Head Diameter (mm)	Mass of Impact Body (g)	Impact Energy (Nmm)	Impact Strain Rate on the Concrete $\mu\epsilon/s$
1.3	11.1	27.0	0.77×10^{-5}
1.5	10.8	24.0	2.32×10^{-5}
3.0	5.4	11.0	2.75×10^{-5}
15.0	19.2	42.0	3.86×10^{-5}

6.3.1.1 Dynamic and Static Loading

Impact of the impact bodies on the surface of a solid involves very short loading times with transient pulses of only a few μs in duration. The short-duration, low-energy transient impacts are responsible for generating low strains in the range of 10^{-5} $\mu\epsilon/s$ and low stresses in the medium. In the case of the seismic exploration devices, high rates of loading cause strain rates in the range of 10^{+5} $\mu\epsilon/s$ and high stresses in the medium. In dynamic methods, low strains of 10^{-5} mm/mm are involved with high rates of loading. The range of strain properties generated by the impact devices are used to classify MSR system as an apparatus capable of measuring dynamic elastic properties.

Knowing that the static methods are identified by their slow rate of loading, strains are in the range of 10^{-2} mm/mm, strain rates in the range of $10^{-3}\ \mu\epsilon/s$ and high stresses in the medium.

6.3.1.2 Contact-Time

The transient impact of a spherical object on surface of a solid generates P- and S-(body) waves as well as R-(surface) waves. A spherical impact source acts as a point source which is responsible for generating spherical body waves in a solid. The duration of the impact or contact-time, t_c, is an important parameter in MSR testing. The contact-time is mainly controlled by the diameter of the sphere (Sansalone, 1985) and the surface conditions of the testing surface. The smaller is the diameter of the sphere and the smoother is the surface of the testing area, the shorter is the contact-time. The contact-time controls the frequency content of the waves generated by the impact. The notion of frequency content arises from the principle of Fourier series, where the pulse shape can be approximated by the sum of a number of sine functions of different frequencies (Carino, 1986). For a spherical impactor, the force-time function of the impact can be calculated by equation 3-21. However, the force-time function of the impact can be approximated as a half-cycle sine curve (Sansalone, 1985). The width of the curve is the contact-time. The time-history of R-wave produces a vertical surface displacement. The time-history of the R-wave has the shape of the force-time function of the impact. Therefore, the force-time function of the R-wave can be used to estimate the contact-time of an impact. A spherical impact contains a wide range of frequencies. Spherical impacts with short contact-times have a broader range of frequencies, but low amplitude waves. Impacts with longer contact-times have a narrower band of lower frequencies and higher amplitude waves. Low frequencies have longer wavelengths and travel longer and deeper in a medium. Short wavelengths have the advantage of detecting small defects but the disadvantage of having a rapid attenuation and thus shallow penetrations. Large diameter spheres are used to generate impacts with longer contact-times and longer wavelengths, to detect deeper flaws, or to evaluate thicker structures. In order to evaluate the integrity of a medium, at least one full wavelength should travel the path length, back and forth, three full cycles. Thus, the choice of the impactor and its contact-time depends on the thickness of the testing specimen and the size and the depth of the flaw or the reinforcement bars (in the case of concrete). The impact should generate waves having wavelengths smaller than or equal to the thickness of the testing specimen. To detect a flaw within a medium, the wavelengths should be smaller than its dimensions. The contact-time of the impact should always be shorter than PP- or SS-wave arrivals. To use the correct impact source for a specimen, first the required wavelengths should be determined. Later, the wavelengths should be converted to frequency by modifying equation 3-2 to $f = \frac{V}{\lambda}$. In a solid, for a given impact the wavelengths of compressive waves are longer than the shear waves. Therefore, the upper limit of the wavelengths traveling the path length depends on the P-wave. Thus a contact-time that is short enough to generate the required frequencies can be selected. An approximation for the upper limit on the usable frequency range generated by a given impact is given by Sansalone and Carino, 1986 as:

$$\Delta f = \frac{1.25}{t_c} \tag{6-1}$$

Table 6-2 illustrates the relationship between the possible contact-times that can be generated by spherical impact sources, and the range of frequencies, Δf, generated by the impact. The body wave velocities of steel, concrete, and granite were used to calculate the generated wavelengths for each contact-time. It was assumed that the surfaces of the specimens are smooth and the impacts are repeatable. In term of thickness contact-time can be explained to be: $t_c < \frac{2T}{C_p}$.

Table 6-2 A relationship between contact-time, generated frequencies, and wavelengths of body waves produced.

Sphere Diameter (mm)	Contact-Time (t_c) (μs)	Range of Frequencies (Δf) (kHz)	P-wave-length (m) (for a velocity of 6400.0 m/s) Steel	S-wave-length (m) (for a velocity of 4300.0 m/s) Steel	P-wave-length (m) (for a velocity of 4000.0 m/s) Concrete	S-wave-length (m) (for a velocity of 2300.0 m/s) Concrete	P-wave-length (m) (for a velocity of 4600.0 m/s) Granite	S-wave-length (m) (for a velocity of 2200.0 m/s) Granite
1.4	10	0-125.0	0.05	0.03	0.03	0.02	0.04	0.02
2.9	15	0-83.3	0.08	0.05	0.05	0.03	0.06	0.03
4.8	25	0-50.0	0.13	0.09	0.08	0.05	0.09	0.04
6.4	35	0-35.7	0.18	0.12	0.11	0.07	0.13	0.06
7.9	45	0-27.7	0.23	0.16	0.14	0.08	0.17	0.08
9.5	55	0-22.7	0.28	0.19	0.18	0.10	0.20	0.10
11.1	65	0-19.2	0.33	0.22	0.21	0.12	0.24	0.11
12.7	75	0-16.7	0.38	0.26	0.24	0.14	0.28	0.13
13.4	85	0-14.7	0.44	0.29	0.27	0.16	0.31	0.15
14.9	95	0-13.2	0.48	0.33	0.30	0.17	0.39	0.17

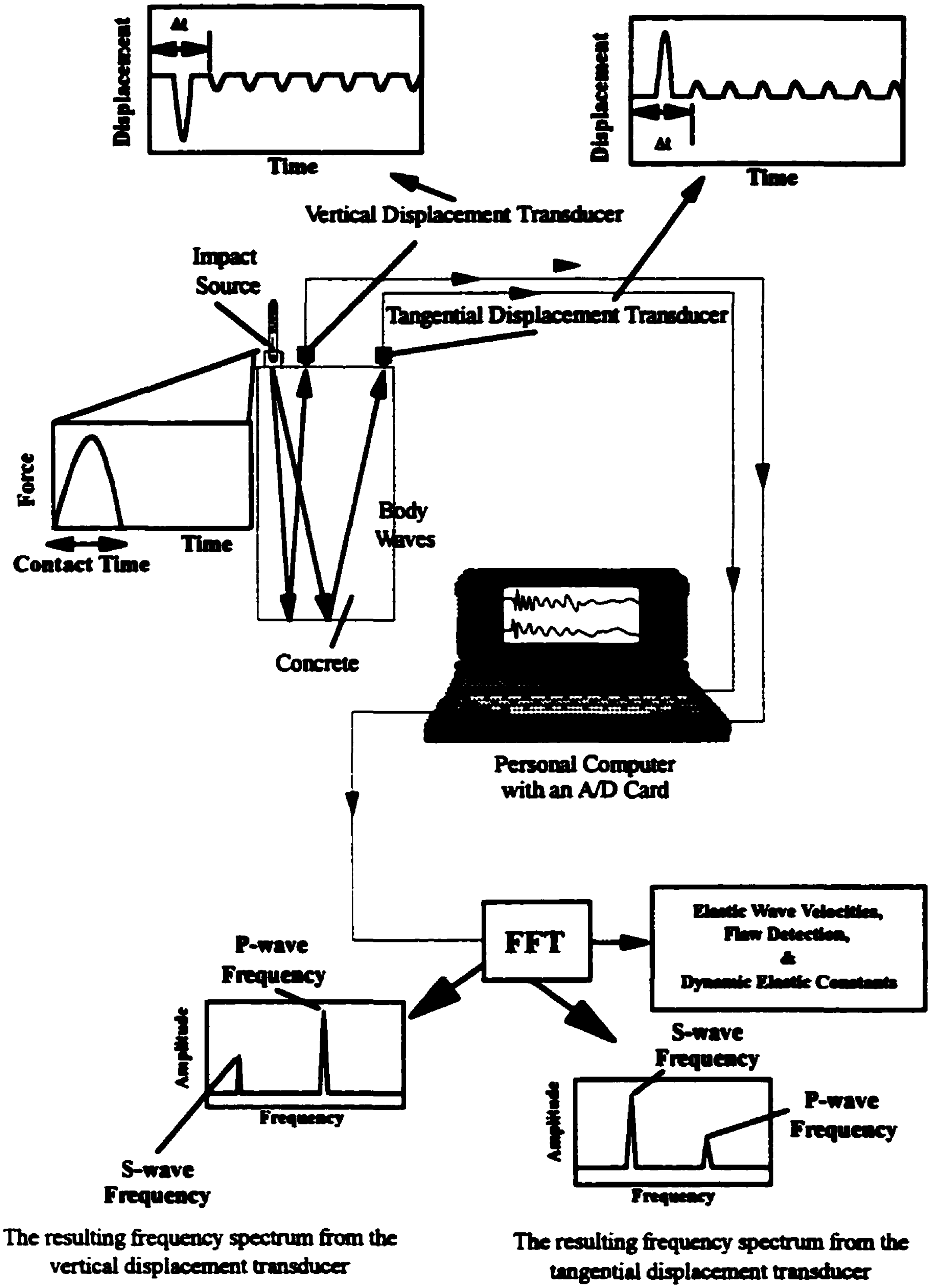

Figure 6-1 The Schematic Diagram of the MSR system.

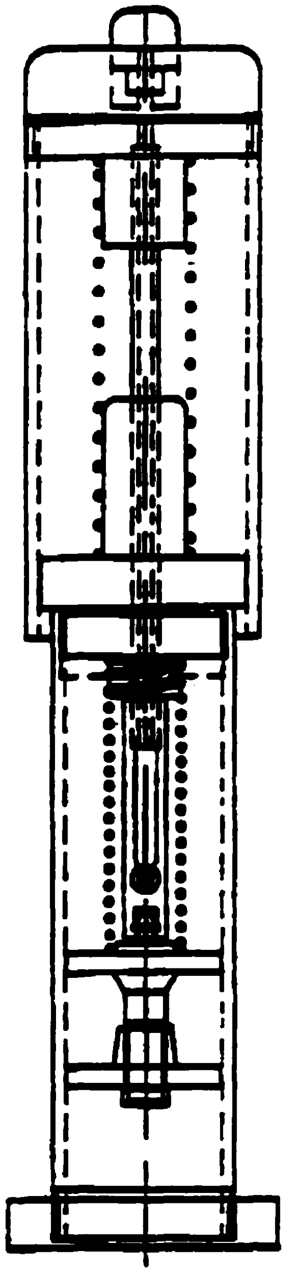

Figure 6-2 Schematic of the hand held impact device assembly, Scale: 1:1.

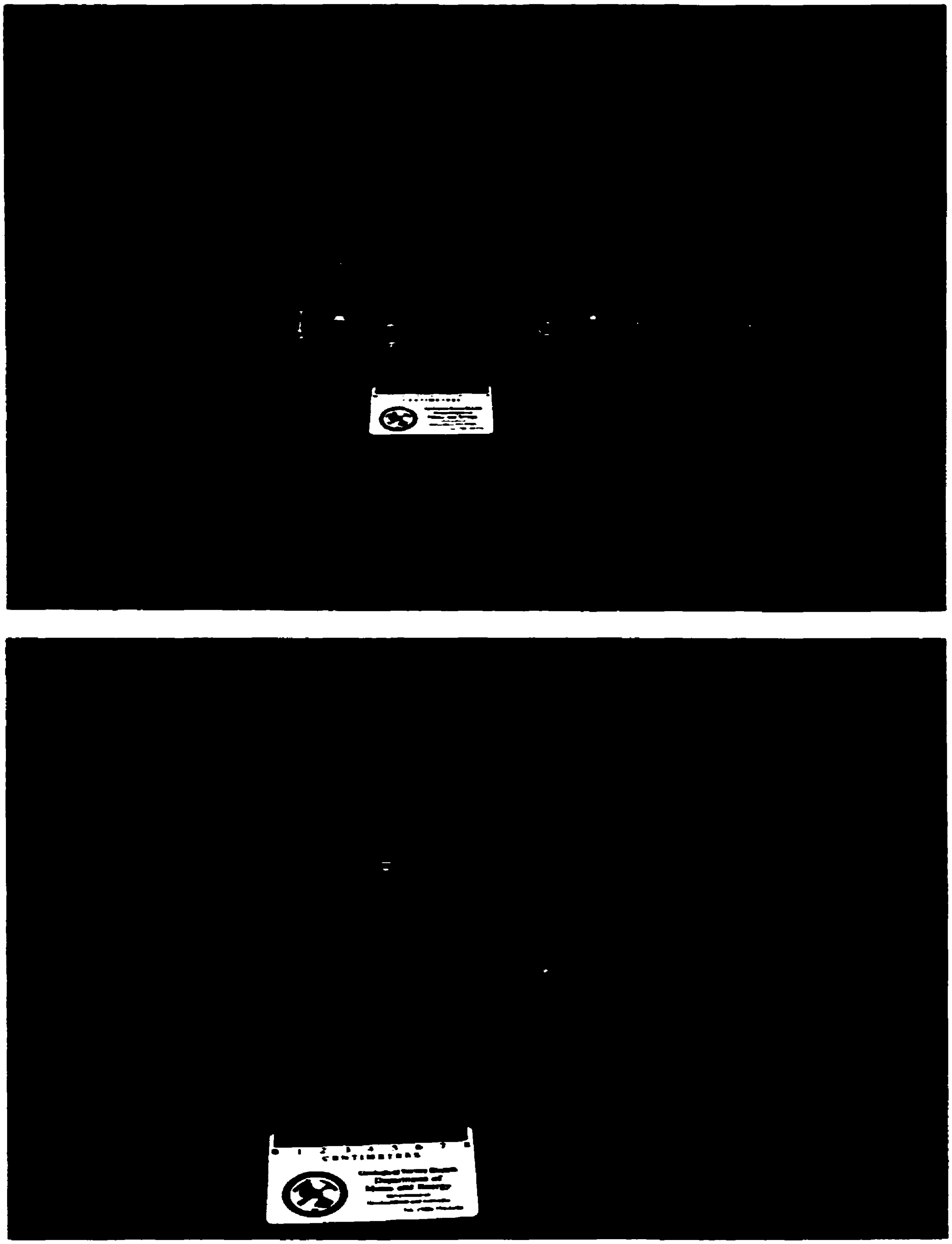

Plate 6-1 The MSR impact devices.

6.3.2 Transducers

Broadband piezoelectric transducers are more suitable for impact testing since the output signals are less tainted with the effects of transducer resonance (Carino, 1986). Also, broadband transducers respond to signals over a wide frequency range.

Vertical displacements are best detected by a sensitive piezoelectric vertical displacement transducer. Horizontal displacements are best detected by a sensitive piezoelectric horizontal displacement transducer. Both P- and S-waves are detected by the two types of transducers. For the vertical displacement transducers, the vertical motion is generated by the P-wave as a result of both displacement and propagation vectors. The S-wave is detected as a result of the vertical displacements generated by the S-wave propagation vector. For the horizontal displacement transducer, the S-wave is detected due to the horizontal displacements caused by the S-wave displacement vector. P-waves are also detected by the horizontal displacement transducer, since every time a P-wave reaches the surface (at epicenter), it disperses along the surface. The P-wave propagation vector along the surface creates a horizontal displacement which is detected by the horizontal displacement transducer.

One set of receivers was used in the MSR system: one vertical displacement piezoelectric transducer and one tangential displacement transducer. Both transducers are broadband and due to their small contact areas behave as point receivers.

The vertical displacement transducer is an IQI Model 501 dynamic piezoelectric transducer, developed by the National Bureau of Standards (NBS) (the name has been changed to the United States National Institute of Standards and Technology). This transducer, which has become known as the NBS-conical transducer, has a response that is uniform over a wide frequency range, is directly related to displacement, and is sensitive almost exclusively to displacement normal to the surface (Proctor, 1982). The NBS-conical transducer has a cone shaped active element made of lead-zirconite-titanate (commonly known as PZT). The aperture of the active element is 1.0 mm in diameter, smaller than any wavelengths of expected frequency ranges. The small contact area of the transducer makes it act as a point receiver (see Figure 6-3 and Plate 6-2a). The Model 501 transducer offers the exceptional feature of very flat frequency response over the range 50 kHz to 1 MHz. Overall, the transducer is 21.0 mm in diameter and 18.4 mm thick. Two ends of the active element are attached to silver electrodes. On one side, the active element is fixed to a cylindrical brass backing filled with tin and tungsten powder epoxy mix. The heavy brass backing causes dampening of undesirable frequencies. The brass backing is connected to a matching amplifier. The matching amplifier is powered up by a 9 volt battery, type NEDA 1604A. The output signal is transferred to a waveform analyzer by a BNC connector (maximum output voltage of ∓ 2 volts, peak to peak).

For the purpose of field and laboratory testings the transducer, amplifier, and the battery were fixed into a cylindrical aluminum casing (see Plate 6-2b). The aluminum casing is used to prevent the effect of electromagnetic disturbances and also to protect the inner contents from the rough field environment. The conical tip of the active element is in contact with a copper plate attached to the casing. The copper plate was used to complete the circuit and also to protect the exposed tip of the transducer. The tip of the transducer is in direct contact with the testing medium. Since the transducer is pressed against the medium, it does not require the use of liquid couplants. The vertical displacement transducer can be placed within a circle, having the impact source at the center of it and the radius as small as the P-wavelength. The smaller the distance between the impact source and the receiver (d_V), the smoother the resulting frequency spectrum will become. For detection purposes, d_V must remain minimal and constant throughout the survey line.

The tangential displacement transducer was originally designed by Proctor (1988). Presently no commercial units are available. Therefore, with the inventor's permission, for the experimental purposes of this project, two units were constructed from the original design (see Plate 6-3). The tangential displacement transducer consists of two pieces: the active PZT element and a component, matched backing. The active element has the form of a truncated pyramid with a 12 mm square base and a 6 mm height. The aperture, which is the truncated end, is 0.5 mm by 2.0 mm with the smaller dimension in the direction of polarization (the direction of maximum tangential sensitivity). The backing is made out of brass and has the overall dimensions of 25.0 mm thick, 65.0 mm long, and 50.0 mm wide. A conical cavity is cut into the rear of the backing and filled with molten tin metal. The backing and the active element were attached by a low temperature tin-indium solder (see Figure 6-4 and Plate 6-4a). The transducer's response was nearly flat and constant over a 1.5 MHz (0 to 1.5 MHz) bandwidth. The transducer captures an output voltage waveform which is proportional to the tangential dynamic displacement. At the same time it has a minimal output when exposed to vertical displacement (see Figure 6-5). The transducer displays directional behavior, having a null signal output when the polarization direction is at a right angle to the direction from the source. The brass backing is connected to the matching amplifier. The matching amplifier is powered by a 9 volt battery, type NEDA 1604A. The output signal is transferred to a waveform analyzer by a BNC connector (maximum output voltage of $\mp$ 2 volts, peak to peak).

For the purpose of field and laboratory testing, the transducer, amplifier, and the battery were housed in a cylindrical metallic casing (see Plate 6-4b). The metallic casing is used to prevent the effect of electromagnetic disturbances and also to protect the inner contents from the rough field environment. The truncated pyramid aperture of the active element is in contact with a copper strip that is fastened to the casing. The tangential displacement transducer must be placed within a circle, with the impact source being at the center of it and the radius being less than the S-wavelength. The distance between the impact source and the receiver (d_t) has to be determined based on the thickness of the plate and material properties. Once the angle of S-wave reflection is selected, the optimum horizontal displacements can be detected by the transducer. The piezoelectric tip of the transducer has a linear contact with the surface. The direction of the PZT linear tip of the transducer must be at right angle to the impact point.

Both transducers were cased in a way that can be functional in underground situations. The small tip of the transducers requires minimum surface preparation of the structures. Figure 6-6 and Plate 6-5 show the test configurations for the MSR transducers in underground hollow circular concrete structure. Plate 6-6 shows the MSR system, including the set of impact devices, transducers, and portable computer.

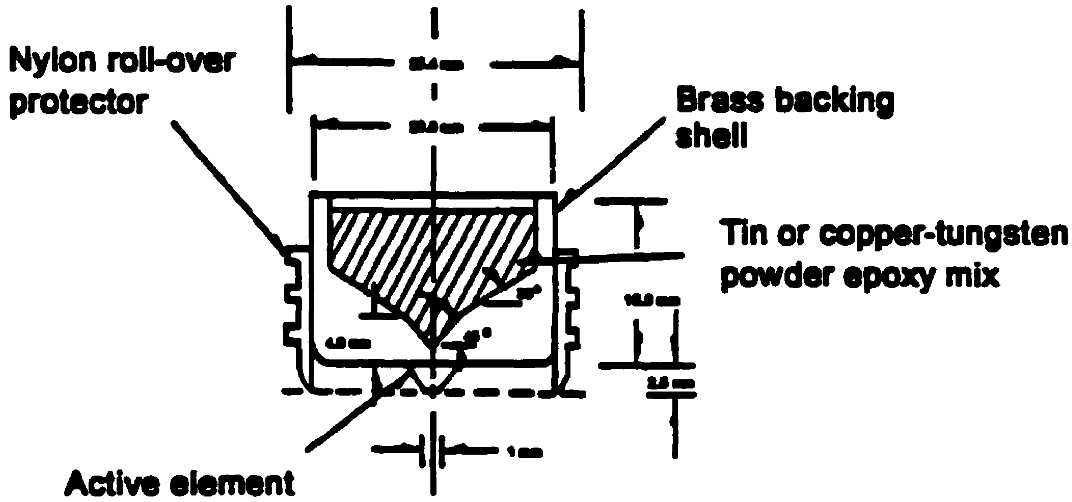

Figure 6-3 Schematic of NBS conical tip vertical displacement transducer (after Proctor, 1986).

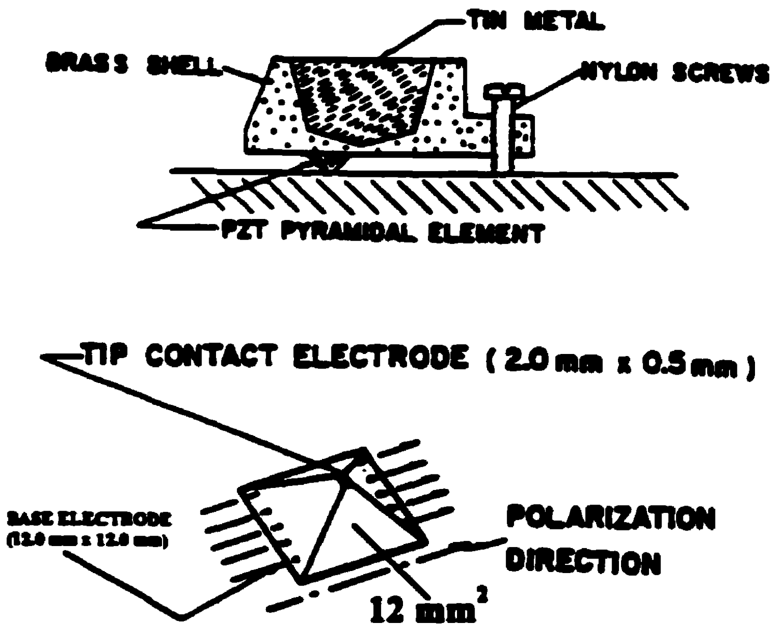

Figure 6-4 Schematic of tangential displacement transducer (after Proctor, 1988).

(a)

(b)

Plate 6-2 The vertical displacement transducer; a) initial casing, b) field casing.

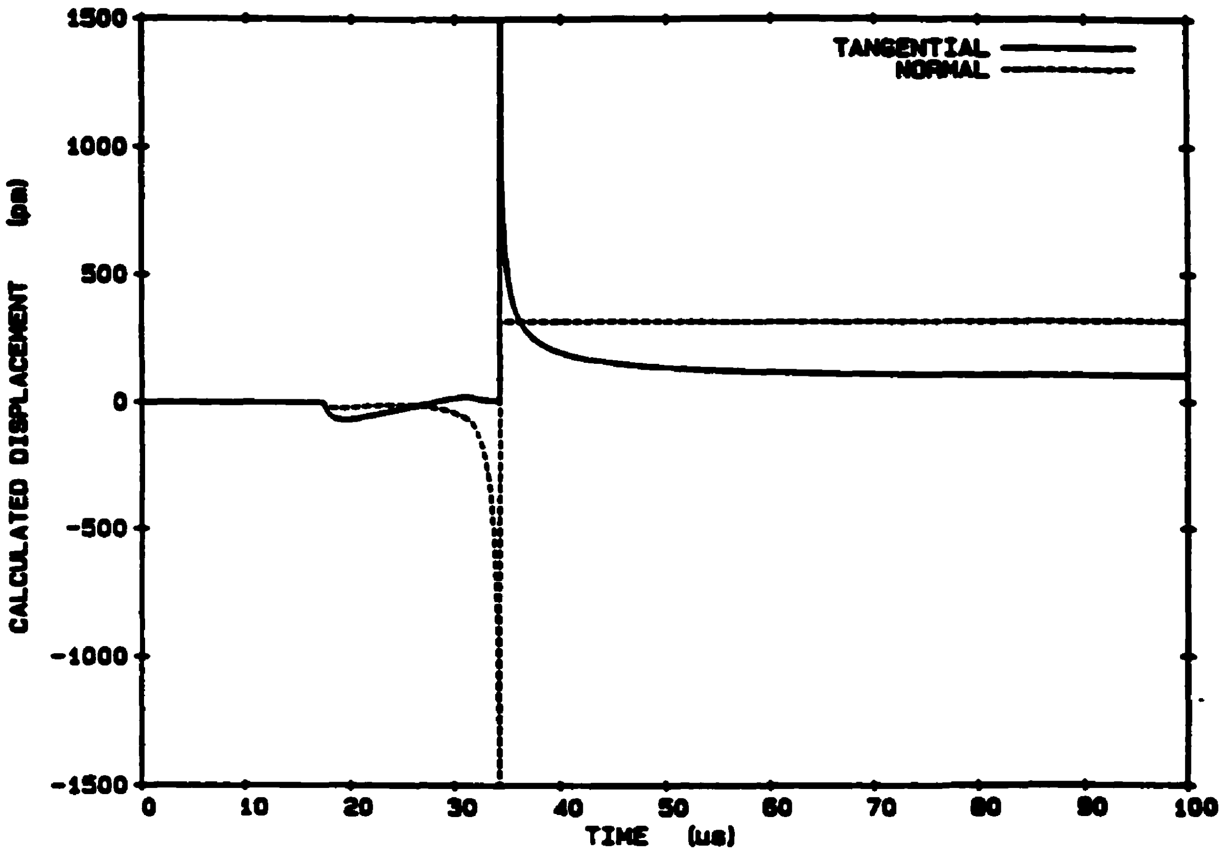

Figure 6-5 The theoretical tangential displacement (solid curve) and vertical displacement (dashed curve) of point on the surface of an infinite half space of steel subjected to a point, unloading step-force of 23.6 N. Distance between source and point of observation is 103 mm (after Proctor, 1988)

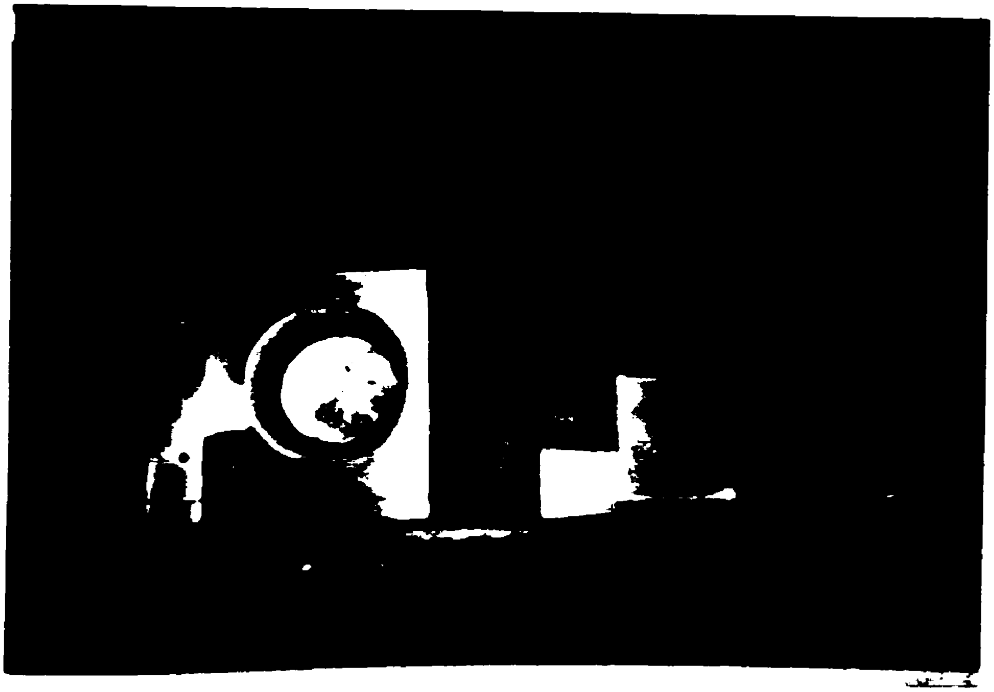

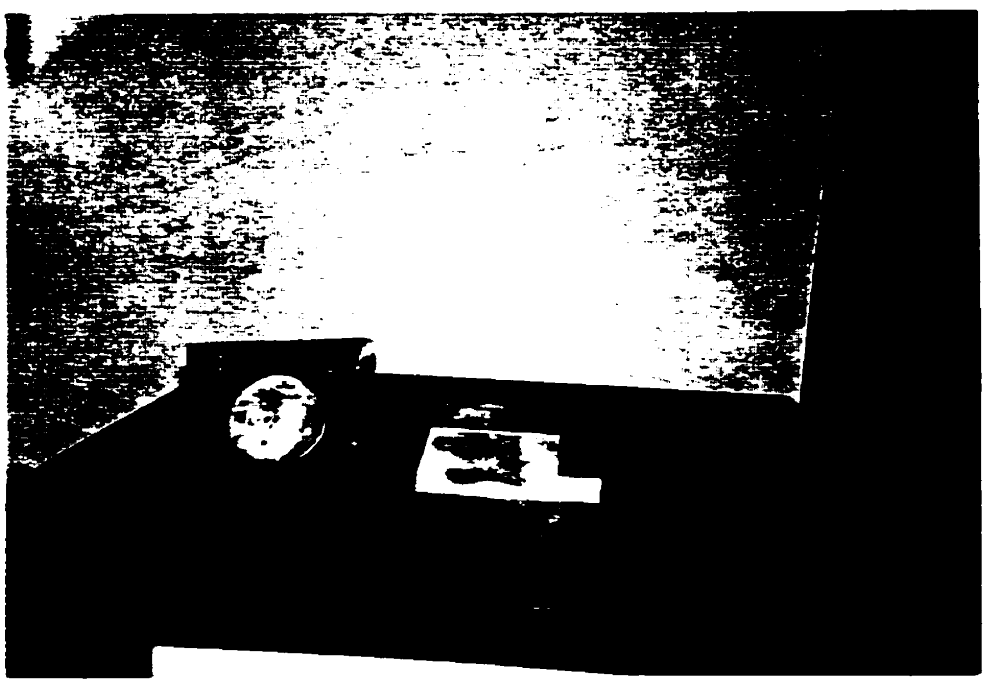

Plate 6-3 The construction of tangential displacement transducer.

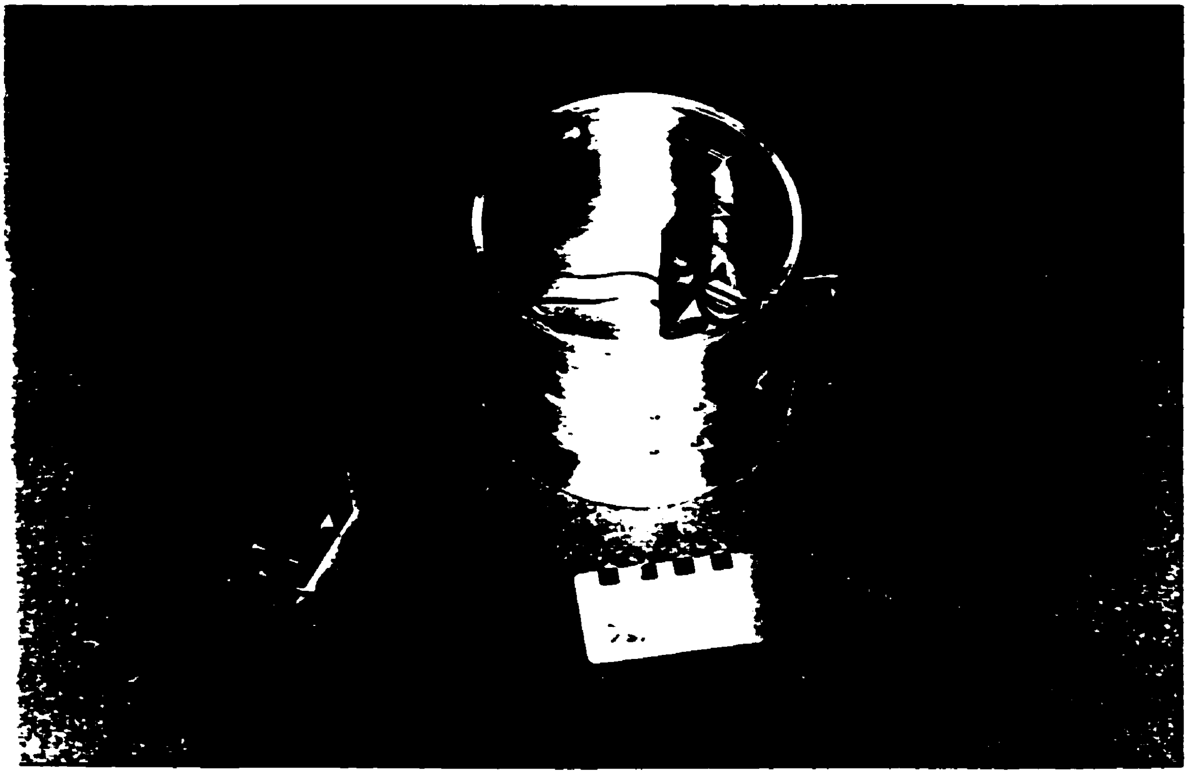

(a)

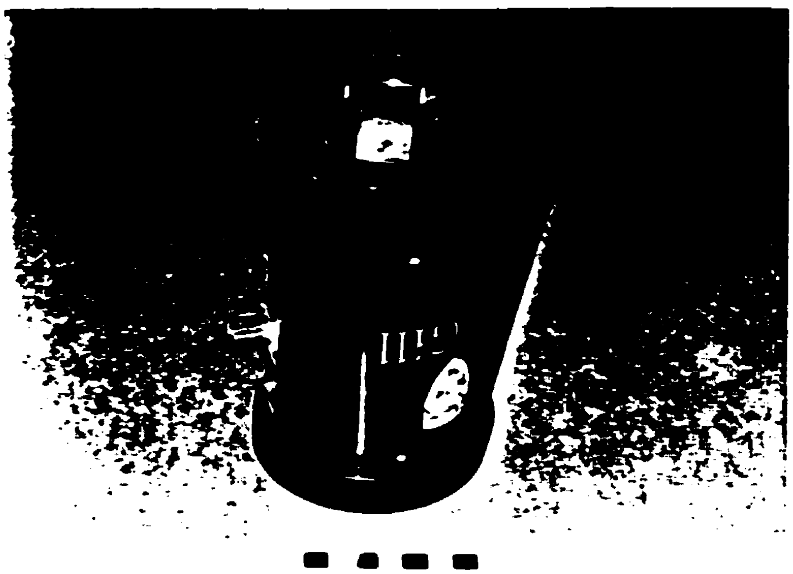

(b)

Plate 6-4 The tangential displacement transducer: a) initial casing, b) field casing.

6.3.2.1 The Configuration of the Impact Source and the Receivers

The MSR technique is designed in order to evaluate the materials by an indirect method, that is, based on the miniature seismic reflection principles, the data can be collected successfully from the same surface from which the signal was generated into the medium. Nevertheless, for the evaluation of the elastic properties of the concrete and rocks, the direct method can also be used. The direct method refers to the arrangement of the impact source and the receiver on two opposite sides of a sample.

The surface displacement waveforms are affected by the test configuration, that is, they are affected by the position of the impact point and the position of the receiving transducers. The distance from the impact source to the vertical displacement transducer will be referred as d_v, and to the tangential displacement transducer, d_t. Here T would refer to the distance between the top surface and the reflecting interface. In the indirect testing method, when d_v/T is small, the incident and the reflected angle for P-wave is small. At this point, based on the P-wave's radiation pattern, reflection coefficient and velocity, the received signal will be dominated by the P-waves. Increasing the d_v/T ratio causes a number of problems. Firstly, the arrival time for the surface wave might interfere with the reflected P-wave. Secondly, the incident and the reflection angles will be different, with respect to the position of the vertical displacement transducer; thus, the mode conversion signals (i.e. PS, SP, etc.) might interfere with the reflected P-wave arrivals and their reflection coefficient. Thirdly, the total path length of the ray path might increase, which will affect the P-wave's velocity values. The d_v must be arranged less than the P-wave's path length.

In the case of d_t, the arrangements are more complicated. The maximum horizontal displacements occur between 35° to 45° of the incident angle at the bottom of the plate. In this case, the exact angle depends on the elastic properties of the medium. For the reflected S-wave, the maximum displacements occur between 35° to 45° of the reflected ray. Here, the thickness of the plate (T) has an important role on detection of maximum horizontal displacement on the surface. In most cases when d_t/T ratio has a value of 1.0 the reflection signals are predominantly S-waves. For example, in cases that the maximum horizontal displacements occurs at 45° of the S-wave path, in a plate having 0.2 m thickness, the tangential displacement transducer has to be placed 0.2 m apart from the impact source, to detect the maximum displacements for the S-waves. It should also be noted that the d_t must be less than the S-wavelength, for the velocity values to be considered reliable.

6.3.3 Signal Processing and Analysis

The reflected waveforms received by the transducers are transferred to a signal analyzer. The recorded displacement waveforms can be analyzed in the time domain. However, this involves the operator's skill and judgement in recognizing the waveforms. Above all, in order to determine the depth of discontinuities or defects, one must know the time of arrival of reflected P-waves from the internal defects and external boundaries. Thus, the time domain analysis is often time consuming and difficult. To overcome this problem, the signal analysis can be carried out in the frequency domain. The frequency content of the digital surface displacement waveforms is obtained using the fast Fourier transform technique (FFT). The resulting frequency spectrum shows the amplitude of the frequencies in the waveform.

6.3.3.1 Signal Analysis

Impact of a spherical mass on top of a free standing solid plate results in generation of a pulse within the plate. Both P- and SV-waves reflect back and forth between the top and bottom of the plate. The successive arrival of the waveforms at the top of the plate results in periodic displacements received by the transducers. The P-wave component of the pulse results mainly in vertical displacements and is received best at close distance to the point impact source. The SV-waves also produce vertical displacements on the surface. At this stage, using a vertical displacement transducer, the collected displacements caused by the P-wave component of the pulse are much larger than those caused by the SV-wave component of the pulse. The arrival of each P-wave (tension waves) causes downward (inward) displacements at the top surface of the plate. Therefore, a displacement waveform collected by the vertical displacement transducer exhibits periodic downward displacements. The time between the successive downward displacements is the time, Δt_p, for the P-wave to propagate to the bottom of the plate and return to the top surface. Δt_p is also known as the period of P-wave arrivals.

$$\Delta t_p = \frac{2T}{C_p} \qquad (6-1)$$

In this equation T is the slab thickness, C_p is the P-wave velocity, and Δt_p is the travel time or the period for P-wave arrivals. The frequency of the P-wave arrivals is the inverse of the travel time or the period and is calculated by the following equation:

$$f_p = \frac{1}{\Delta t} \qquad (6-2)$$

This frequency is related to the thickness of the slab and is known as thickness frequency (Sansalone and Carino, 1986). When Δt is substituted with equation (6-2), the frequency can be expressed in terms of P-wave velocity and thickness:

$$f_p = \frac{C_p}{2T} \qquad (6-3)$$

Also, P-wave velocity can be expressed in term of thickness and frequency of P-wave arrivals:

$$C_p = 2T \cdot f_p \qquad (6-4)$$

Knowing the thickness of the plate, and measuring the frequency of arrival P-waves from the frequency spectrum, the P-wave velocity can be calculated from the above equation. Using the above relationships, the thickness of the plate can be expressed by:

$$T = \frac{C_p}{2f_p} \qquad (6-5)$$

Knowing the P-wave velocity in the plate and the frequency of P-wave arrivals, the thickness of plate can be determined. The same analysis is applicable for detecting internal defects within the plate.

The signal analysis of the SV-wave components of the generated signals by a point impact is quite similar to the analysis of the P-waveforms. Shear waves have the same hemispherical wavefront characteristics as the compression waves. Arrival of shear wave components of the pulse on the surface causes horizontal and vertical displacements. The horizontal displacements are collected by a tangential displacement transducer. The amplitude of horizontal displacements caused by the SV-wave arrivals is larger than the displacements caused by the P-wave arrivals. The arrival of each SV-wave causes a transverse-right displacement at the top surface of the plate, which can be seen as an upward (outward) form in the time domain spectrum. Therefore, a displacement waveform collected by the tangential displacement transducer exhibits periodic outward displacements. The time between the successive outward displacements is the time, Δt_s , for the SV-wave to propagate to the bottom of the plate and return to the top surface. Δt_s is also known as the period of SV-wave arrivals and is given by:

$$\Delta t_s = \frac{2T}{C_s} \qquad (6-6)$$

In this equation T is the slab thickness, C_s is the SV-wave velocity, and Δt_s is the travel time or the period for SV-wave arrivals. The frequency of the SV-wave arrivals is the inverse of the travel time, or the period, and is calculated by the following equation:

$$f_s = \frac{1}{\Delta t} \qquad (6-7)$$

This frequency is related to the thickness of the slab and is known as thickness frequency (Sansalone and Carino, 1986). When Δt is substituted with equation (6-7), the frequency can be expressed in terms of SV-wave velocity and thickness:

$$f_s = \frac{C_s}{2T} \qquad (6-8)$$

Also SV-wave velocity can be expressed in term of thickness and frequency of SV-wave arrivals:

$$C_s = 2T \cdot f_s \qquad (6-9)$$

Knowing the thickness of the plate, and measuring the frequency of arrival SV-waves from the frequency spectrum, the SV-wave velocity can be calculated from the above equation. Using the above relationships, the thickness of plate can be expressed by:

$$T = \frac{C_s}{2f_s} \qquad (6-10)$$

Knowing the SV-wave velocity in the plate and the frequency of SV-wave arrivals, the thickness of plate can be determined. The same analysis is applicable for detecting internal defects within the plate.

6.3.3.2 Analog-to-Digital Signal Converter Card (A/D Card) and the Frequency Analysis

An A/D card was used to acquire the waveforms and store the signals in the time domain. The card was installed in a portable computer. The A/D card contains one input channel. Each signal contains 4000 sampling points per channel. The signals were collected in the time domain by the A/D card and saved in a portable computer. A program was written to transform the time domain signals into frequency domain, using the fast Fourier transform (FFT) technique. The resulting frequency spectrum contains 2048 points.

The record length of a test is determined by the number of sampling points and the time between samples. The relationship between the sampling points and the time interval between samples is used to determine the frequency resolution in the frequency spectra based on the following equation:

$$\Delta f = \frac{1}{nr} \qquad (6-11)$$

where Δf is the frequency interval, n is the number of sampling points, and r is the time interval between the samples. The time interval between the samples, r, is used to calculate the sampling rate.

$$Sampling \quad rate = \frac{1}{r} \qquad (6-12)$$

For example, taking 2048 samples (n) at 10 μ s (r) results in frequency intervals of 4.88×10^{-5} kHz and sampling rate of 100 kHz.

The selection of the r and n is affects the resolution of the frequency spectrum, the sampling rate, and the record length. An increase in r and n values results in longer record length and higher resolution. The frequency interval has a opposite relationship with the sampling rate. Hence, a slow sampling rate improves the resolution in the frequency domain. The calculations are valid as long as the transformation setup follows this rule of thumb: the sampling rate must stay at least twice the highest frequency in the time domain spectrum. For the thin specimen, the time interval between samples, r, was kept small to attain the required sampling rate. In addition, to obtain a correct response in the frequency spectrum, the P- and S-waves need to reflect three times through the thickness of the structure or specimen. This means that the duration of each test should be at least three times the length of each wave traveling in the media. The required time can be calculated by dividing the velocity of the wave by twice the thickness of the medium. For thick structures, such as shaft liner having an average of 0.6 m thickness, the required duration of the recorded signal must be lengthened. For example in the case of shaft lining, 2048 samples at 10 μs have given more accurate results for flaw detections or thickness measurements. For thin structures or small samples the record length can be selected to be small. For small slabs of the order of 0.25 m, 2048 at 5 μs have worked well.

6.3.3.3 Fast Fourier Transform (FFT) Program

The transformation of the digital signals from the time domain to the frequency domain is based on the idea that any waveform can be represented as a sum of sine curves, each with a unique amplitude, frequency, and phase shift (Telford, 1990). This transformation can be carried out by the FFT technique. Figure 6-7 shows a simple transformation of time to the frequency domain by the FFT technique.

In this study, the FFT program was developed in the GAUSS mathematical and statistical system using the time series analysis package.

The algorithm of the developed software is as follows:

Read signal from file.
Select first 2048 points from signal and assign it to vector SIGNAL.
Call SPECTRUM function.

The inputs for SPECTRUM function are:

1) SIGNAL, the time series to be transformed.
2) WF, the windowing flag (e.g. uniform, hamming, etc.).
3) OL, the overlap function for series greater than NPS points.
4) SR, the sampling rate in Hz.
5) NPS, the number of points used in FFT.

The outputs of the SPECTRUM function are:

1) F, the frequency in the signal.
2) POWER, the power spectrum density.
3) PHASE, the phase spectrum.

Plot frequency (F) verses power spectral density (POWER).
Select P-wave or S-wave reflected frequencies.
Use equations 6-4 and 6-9 to measure P-wave and S-wave velocities.
From the velocity values and the bulk density of the medium, use the equations in Table 3-2 to obtain the values for dynamic elastic constants.

The transformed signal is analyzed and saved in a portable computer. The portable computer requires a math co-processor, for the signal processing calculations.

6.4 A COMPARISON BETWEEN THE MSR SYSTEM AND OTHER WAVE PROPAGATION TECHNIQUES

Table 6-3 summarizes the advantages and the disadvantages of NDT elastic wave propagation techniques in comparison with the MSR system. One advantage of the MSR technique over traditional nondestructive methods such as RF, UPV, and impulse-response techniques is that accurate readings may be obtained from a free surface regardless of the dimensions and condition of the concrete structure. The main advantage of the MSR system over the impact-echo technique is the presence of an additional tangential displacement transducer in the system and also the multi-strength/multi-diametrical impact devices. These additional enhancement features provide the MSR system with the capability of measuring direct shear wave parameters and as a result the data can be used to calculate the dynamic elastic constants at every point on the structure. The MSR system in comparison with the pulse-echo technique uses a more accurate and easy to operate interpretation technique (frequency domain verses time domain). In comparison with the SASW technique, the MSR system has the capability of measuring dynamic elastic properties without assuming various models and ratios. The MSR system in comparison with the petite sismique and seismic wave velocity techniques operates at a smaller and more detailed scale.

Table 6-3 A comparison between MSR system and the NDT & E techniques capable of measuring dynamic elastic moduli.

Dynamic Modulus of Elasticity Measuring Techniques						
Technique	Concrete		Rock		Advantages	Disadvantages
	Lab.	Field	Lab.	Field		
Resonance Frequency	X	X	X	-	- Calculates the natural frequency of different vibration modes. - Calculates the elastic moduli. - Relatively inexpensive. - Extensively used.	- The dimensions of the specimen control the testing procedure. - It is not commonly used in the field. - Needs to have access to the specimen from various directions.
Ultrasonic Pulse Velocity	X	X	X	X	- Direct P-wave velocity measurement. - Easy to use. - Fast measurement technique. - Time saving. - Inexpensive. - Extensively used.	- Difficult to measure S-wave parameters. - Usually assumes Poisson's ratio or shear wave velocity for elastic moduli measurement. - Rapid signal attenuation problem. - Best functions if it has two side access to the specimen.
Seismic Wave Velocity	-	X	-	X	- Direct elastic wave measurement. - Used for large scale measurements. - Could be inexpensive (i.e. hammer seismic). - Extensively used.	- Difficult to recognize S-wave parameters. - Could be expensive (i.e. borehole, and use of explosives). - Best functions if it has two side access to the specimen.
Petite Sismique	-	-	-	X	- Direct measurement of S-wave parameters. - Comparison of static modulus of elasticity with S-wave parameters. - It functions from one accessible side to the specimen.	- Difficulty in generation and detection of S-waves. - Presently in experimental stages. - Can be expensive (i.e. source and receiver).
Impulse-Response	-	X	-	-	- Measures the elastic moduli of the concrete piles and it's base material. - It functions from one accessible side to the specimen. - Inexpensive.	- Indirect calculations of modulus values. - It is limited to the piles or columnar structures.
SASW	-	X	-	-	- Capable of measuring modulus of elasticity for thin pavement layers. - It functions from one accessible side to the specimen. - Inexpensive.	- Calculates the elastic moduli values by comparing with various models. - Assumes theoretical Poisson's ratio values for calculations. - Rapid R-wave attenuation in thick concrete layers.
Impact-Echo	X	X	-	-	- Direct measurements of P-wave parameters. - Capable of detecting and locating flaws. - It functions from one accessible side to the specimen. - Inexpensive. - Time saving.	- Very thin layers (i.e below 15 cm. are difficult to detect.
MSR	X	X	X	X	- Direct measurements of P- and S-wave parameters. - Capable of detecting and locating flaws. - It functions from one accessible side to the specimen. - Capable of measuring the elastic constants. - Time saving. - Inexpensive.	- Very thin layers (i.e below 15 cm. are difficult to detect.

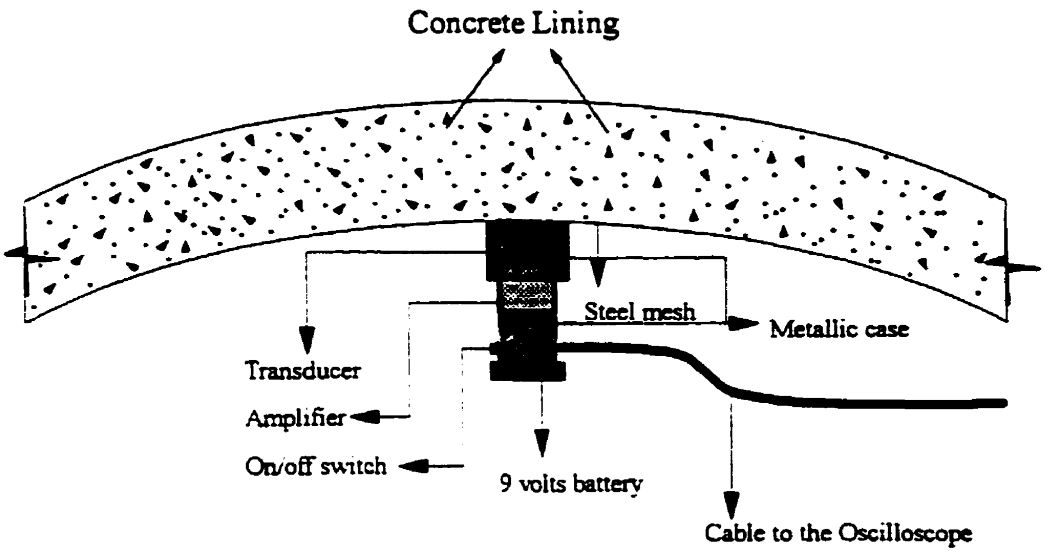

Figure 6-6 The schematic diagram of the MSR transducer setup on an arch-shaped concrete structure.

Plate 6-5 The impact source and the receiver on the concrete tunnel lining.

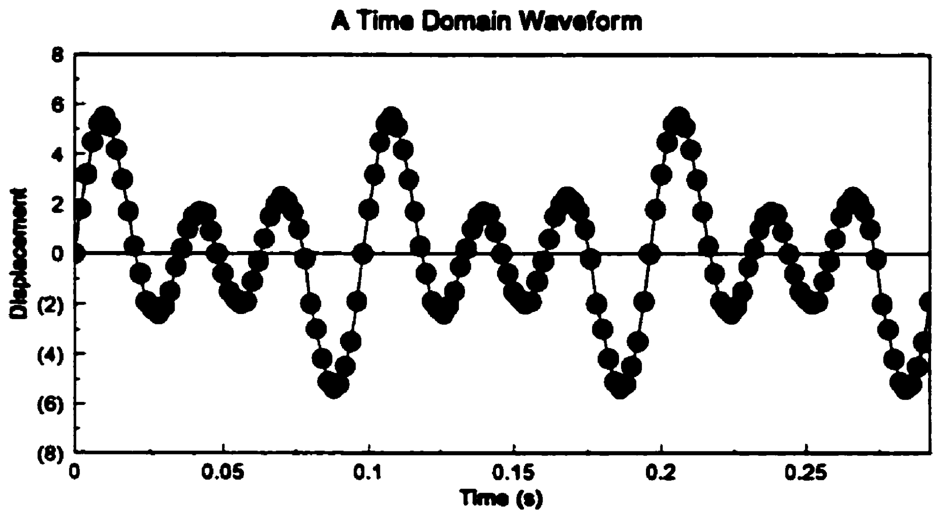

$g(t) = \sin 2\pi (20)t + 2\sin 2\pi (40)t + 3\sin 2\pi (60)t$
where t = time, s.

(a)

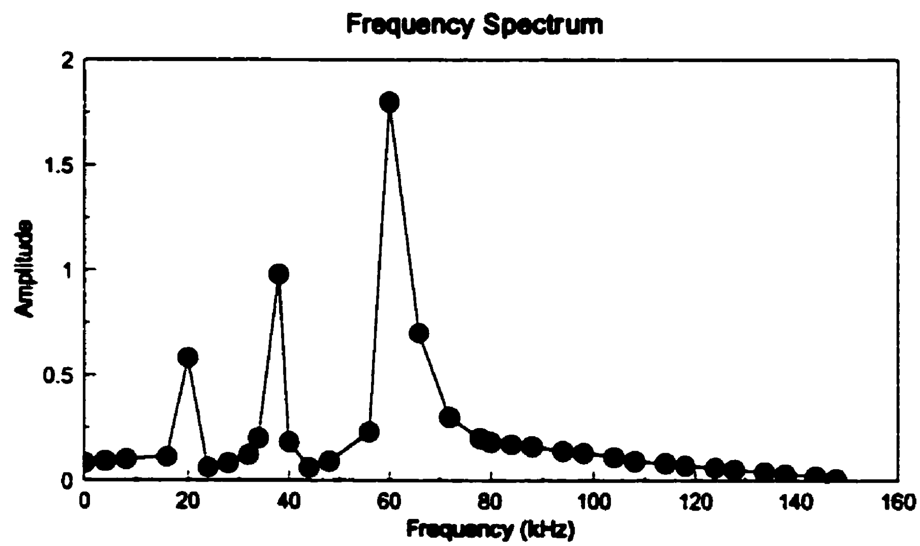

(b)

Figure 6-7 Example of a frequency spectrum obtained from a time domain waveform using the FFT technique. a) digital time domain waveform, and b) frequency spectrum

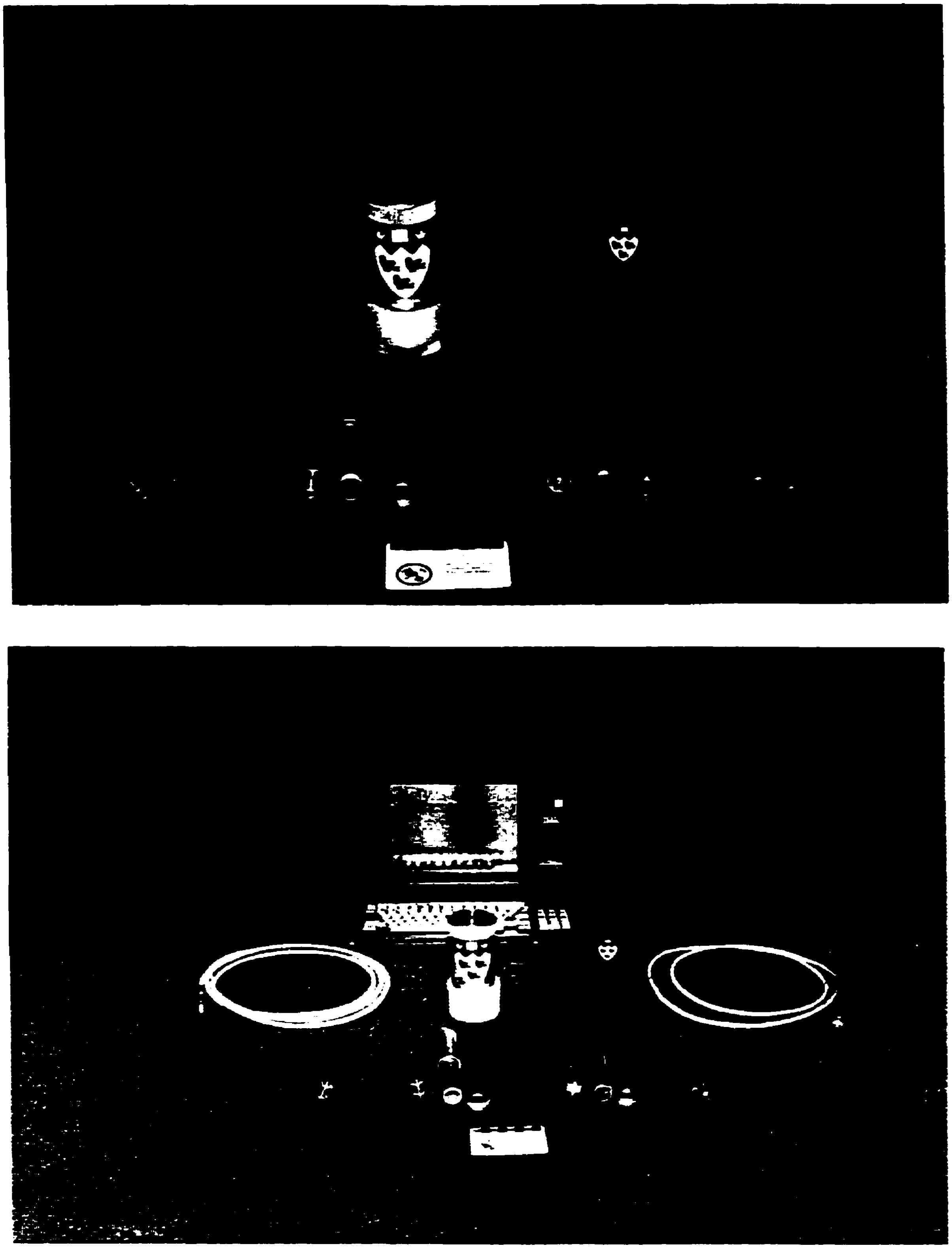

Plate 6-6 The MSR system.

CHAPTER 7

APPLICATION OF MSR SYSTEM FOR DETECTION IN CONCRETE

7.1 INTRODUCTION

A series of laboratory experiments was performed to investigate the capability of the MSR system in the detection and location of delaminations and reinforcement objects in concrete. P-wave velocity is a critical parameter in the determination of thickness and locating flaws in concrete. A number of techniques for evaluation of P-wave velocity of the structures will be studied. To examine the detection capability of the MSR system, buried objects were used to simulate variations in a concrete block. Plexiglas plates were used to simulate the presence of objects with lower acoustic impedance than concrete, such as cracks and voids. Steel plates were used to simulate the presence of objects with higher acoustic impedance than concrete, such as rocks (i.e. concrete/rock interface). Steel bars were used to simulate the presence of reinforcement bars. The second part of this study focuses on actual detection and location of a discontinuity within a concrete slab.

7.2 MEASUREMENT OF P-WAVE VELOCITY

For detection purposes the MSR system requires the determination of one of the two critical parameters: thickness or P-wave velocity. In many applications the P-wave velocity is determined by testing a portion of the structure where the thickness is known. In this case, the known thickness, T, and the measured frequency, f_p, can be used to calculate the P-wave velocity, by using equation 6-4.

Nevertheless, in many cases the P-wave velocity varies from place to place due to the fact that the material quality, either concrete or rock, changes within short intervals. An average of many points (at least five) in a flawless portion of the testing area could provide a good estimate of the P-wave velocity. In cases that the thickness is known, it is important to verify the P-wave velocity at each testing station. In most cases, part of the signal passes through the flaws and reaches the back of the testing object and gets reflected toward the transducer. Consequently, on the frequency spectra the thickness frequency is identifiable; therefore the P-wave velocity can be calculated.

In cases such as mine shaft and tunnel linings where the exact thickness is not known, it is possible to calculate the P-wave velocity by indirect methods. In indirect methods surface waves are used to calculate P-wave velocity. The measurements are done in time domain. One such method is the determination of P-wave velocity by the R-wave velocity (Lin and Sansalone, 1993). In this method two transducer units (two vertical or tangential, or one of each) are arranged on the surface so that the R-wave velocity through a specific distance of concrete could be determined. The impact source should be positioned adjacent to one of the transducers. In fact, one of the transducers could be used as the triggering mechanism of the system. Figure 7-1a shows a schematic drawing of the test configuration, and Figure 7-1b shows typical results which consist of the recorded waveform by each transducer. Since the R-wave has a large amplitude it is easily recognizable. The time difference, Δt, between the arrival of the R-wave at the first transducer and its arrival at the second transducer can be used to calculate the R-wave velocity, C_R:

$$C_R = \frac{d_t}{\Delta t} \tag{7-1}$$

where d_t is the distance between the two transducers. By modifying equation 3-13 to the following equation, P-wave velocity can be estimated:

$$C_p = \frac{1+\upsilon}{0.87+1.12\upsilon}\sqrt{\frac{2(1-\upsilon)}{(1-2\upsilon)}}C_R \tag{7-2}$$

For this technique the value of Poisson's ratio υ has to be assumed. For concrete a Poisson's ratio of 0.2 can be used for the calculations. Hence, equation 7-2 can be rewritten as:

$$C_p = 1.79C_R \tag{7-3}$$

To measure the P-wave velocity by this technique the distance between the two transducers, d_t, should be kept small (i.e. between 10 to 20 cm) since at greater distances the sharp downward displacement that characterizes the beginnings of the R-wave becomes more rounded, and it is difficult to recognize the beginning of the wave.

A portion of a concrete block was tested for evaluation of P-wave velocity, using the R-wave signals. The transducer separations were at 0.2 m and the impact device was placed 0.05 m away from the trigger transducer. The time delay between arrivals of the R-waves was 120 μs. R-wave velocity was calculated to be 1667 m/s. Using Poisson's ratio of 0.2 for concrete in equation 7-3, the P-wave velocity was calculated to be 2983 m/s. To compare the estimated P-wave velocity by the R-wave technique with the P-wave velocity of the concrete block in that area, equation 6-4 was used. On the frequency spectra, a frequency of 3223 Hz was indicative of P-wave reflections from the other end of the concrete block. Knowing the thickness to be 0.55 m, the velocity of the P-wave was calculated to be 3545 m/s. The estimated P-wave velocity by the R-wave technique shows a 16% discrepancy with the thickness P-wave velocity.

Using R-wave velocity to estimate P-wave velocity has two major drawbacks:

a) For the calculations, the value of Poisson's ratio is assumed. A discrepancy between the real and assumed values causes errors which results in errors in location of the objects within the structure.

b) As was discuss before, concrete and rocks are not homogeneous materials. Particularly in the case of concrete, aggregate segregation due to gravity and poor mixing is a common phenomena which causes the wave velocities to be higher at the lower part of the structure. Therefore, estimating the P-wave velocity by the surface R-waves can result in erroneous velocity values.

There is an alternative technique to measure P-wave velocity directly. The technique is based on measurements of the first P-wave arrival. The impact on the surface results in the propagation of the body waves both on the surface and within the solid. Using two transducers and an impact source the velocity of the first P-wave arrival can be calculated.

Figure 7-3a shows a schematic illustration of the test configuration, and Figure 7-2 shows typical results which consist of the waveform recorded at each transducer. In this technique, the impact source remains in one position all the time. Next to the impact source one of the transducers functions as the base transducer and registers the zero time or the time of impact. The position of the second transducer (or the mobile transducer) is changed after each reading. The station intervals for the second transducer is kept constant along a linear array.

The first wave to arrive at the second transducer is that of the direct surface P-wave travelling along the concrete surface. Figure 7-2a shows the recorded waveform for the base transducer. Figures 7-2b to 7-2e illustrate the mobile transducer output as the distance between the impact source and receiver increase. The surface P-wave appears first 0.2 m away from the impact source. Before this distance, the large R-wave amplitude interferes with recognition of the first arrival P-wave. Readings were taken up to 0.5 m distance between the impact source and the receiver.

To calculate the P-wave velocity, the travel-time graph was plotted with station spacing on the abscissa and time of first arrival P-wave on the ordinate (Figure 7-3b). The slope of the best fit line would give the velocity of the P surface wave. Comparing the calculated wave velocity value from the graph (3334 m/s) and the estimated P-wave velocity by the R-wave velocity technique (2983 m/s) with the thickness P-wave velocity (3545 m/s) clearly shows that the wave velocity obtained from the travel-time graph is in better agreement with the thickness P-wave velocity. The P-wave velocity obtained from the travel-time graph is only 6% smaller than the thickness velocity.

Calculation of the P-wave based on first arrival and travel-time graph is a more reliable technique than the R-wave technique. The fact that surface P-wave velocity is 6% slower than the thickness velocity can be explained based on the aggregate segregation that occurs at the time of casting.

Based on the results shown in this section it is evident that P-wave velocity can be calculated even if there is only access to one side of the structure. P-wave velocity calculated from the travel-time graph and the frequency value of the reflected P-wave can be used in equation 6-5 in order to calculate concrete thickness where it is not available.

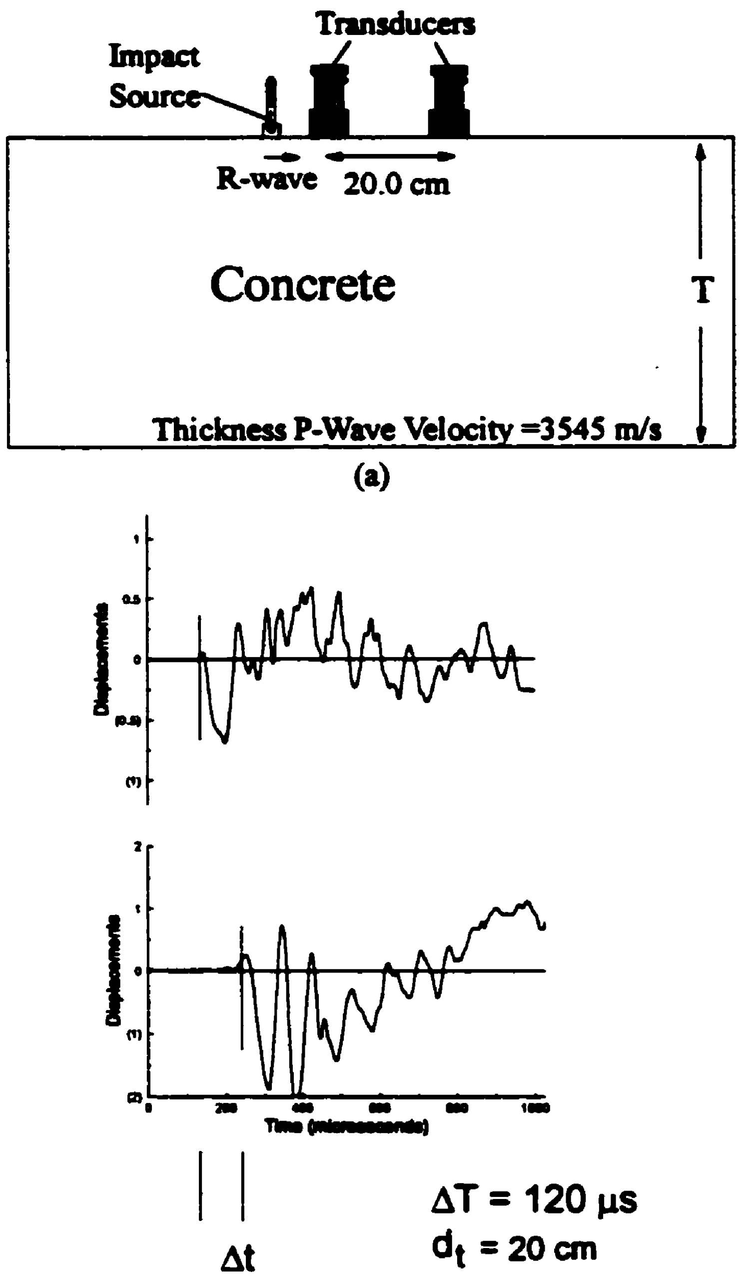

Assumed Poisson's Ratio = 0.2
R-wave Velocity = 1667 m/s
Estimated P-wave Velocity = 2983 m/s

(b)

Figure 7-1 Schematic test configuration for R-wave velocity measurement (a), waveforms captured by the vertical displacement transducer for measuring R-wave velocity (b).

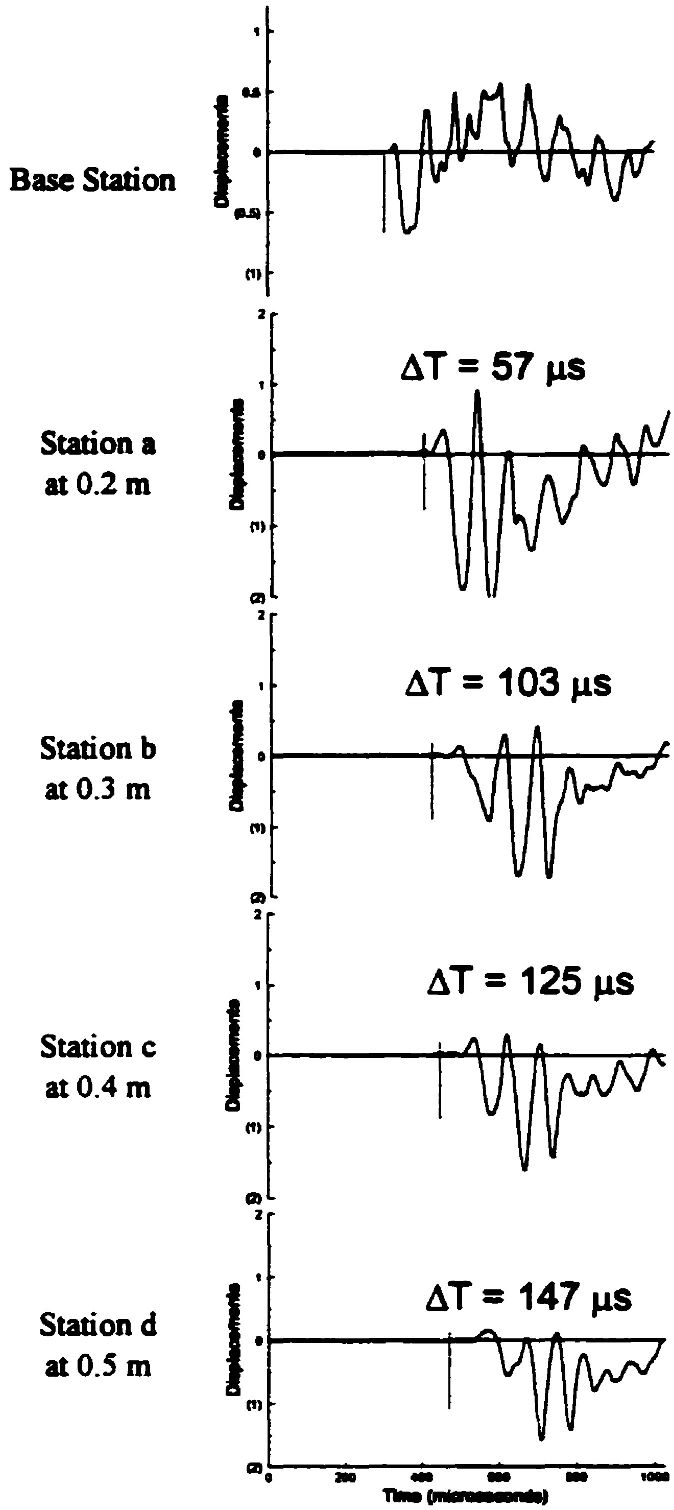

Figure 7-2 Waveforms captured by the vertical displacement transducer for measuring surface first arrival P-wave velocity .

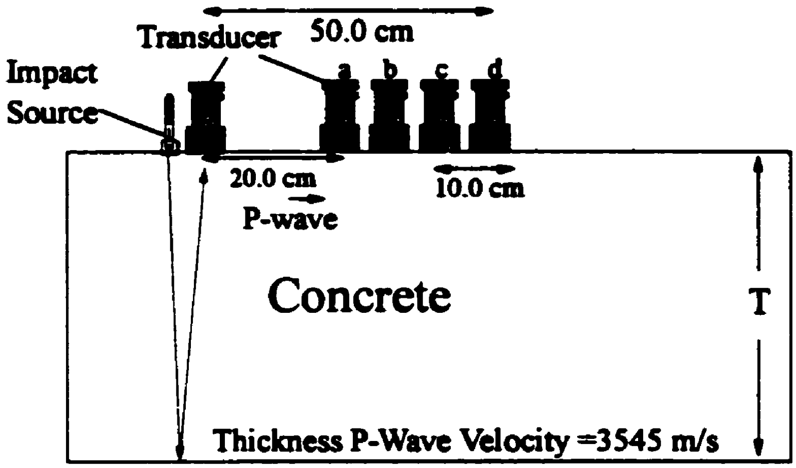

(a)

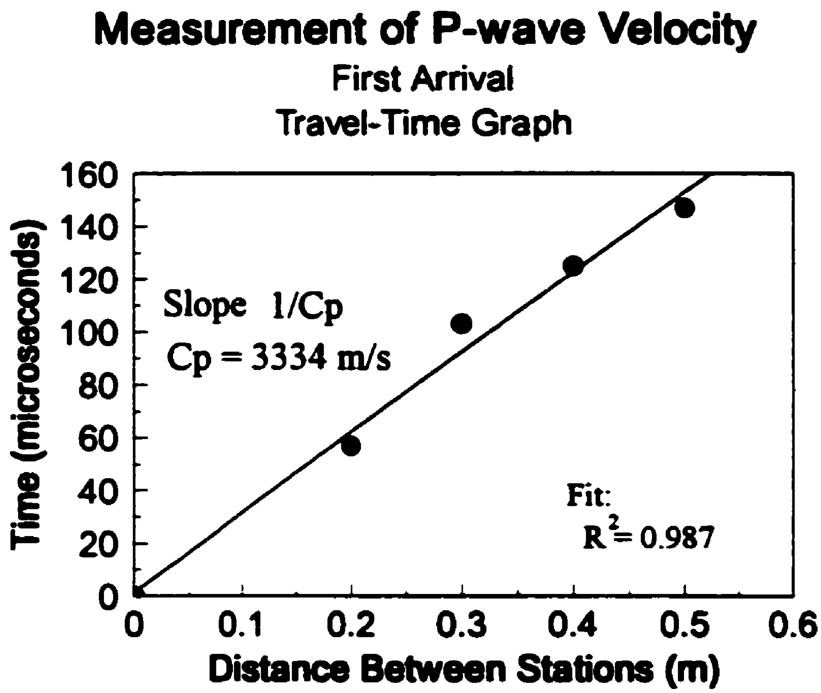

(b)

Figure 7-3 Schematic test configuration for P-wave velocity measurement (a), travel-time graph (b).

7.3 FUNDAMENTAL PRINCIPLES GOVERNING THE MSR SYSTEM

The MSR system functions based on the fundamental principles discussed in Chapter 3. The purpose of this section is to expand on some of the fundamental principles governing the MSR system. Hence the following aspects of MSR system will be considered in more detail:

- The impact response in a solid plate
- The reflections, surface displacement response, and radiation patterns

7.3.1 Impact Response in a Solid Plate

To describe the impact response of a spherical object on the surface of a solid plate, first we assume the plate to have infinite dimensions but a certain thickness (elastic half-space) with a free boundary. In this case, an elastic half-space which adjoins a medium which do not transmit elastic waves, the system of waves consists of course of incident and reflected waves only. The impact results in generation of a stress signal within the plate. In a solid plate, the stress signal will be transferred to multi-component stress waves. In an elastic medium, stress waves behave according to the elastic properties of the medium, and thus can be identified as elastic waves. The two main components of the stress signal are the P- and S-waves. Both waves are generated from the hypocenter of the impact and propagate within the solid. As the body waves (P- and S-waves) propagate into the material along spherical wavefronts, their velocity is affected by the medium's material properties. The material properties affecting the P- and S-wave velocities are elastic modulus of the material E, Poisson's ratio υ, and the material density ρ (see equations 3-8 and 3-10). An abrupt change in the physical properties of the material causes reflection of the body waves. This boundary is known as an acoustic interface and is a boundary between two materials with differing acoustic impedances (density × velocity). Internal cracks, voids and the boundaries of the test object will cause reflection (echos) of the body waves between the two interfaces. A complete description of the propagation of elastic waves in solids can be found in Chapter 3. The arrival of these reflections at the surface where the impact was generated causes displacements.

The displacements are measured by the receiving transducers in successive waveform format. The wave arrivals correspond to impulsive changes in the signal, in the time domain spectra. This response includes the normal surface displacements, caused by the P- and S-wave arrivals, the horizontal surface displacements caused by the S-waves, multiple reflected waves (PP, SS, PPP, SSS, etc.), and mode-converted waves (PS, SP, PSP, SPS, etc.).

In this section the course of incident and reflection for the P-wave and S-wave having spherical waveforms, generated by a transient impact in an elastic half-space adjacent to a free space, and another elastic half-space will be discussed.

7.3.1.1 Reflected P-waves

The P-wave starts its path as a compression wave (having compressive stress at the wavefront), causing a downward displacement. The P-wave has a higher velocity than the S-wave and is characterized by in-line particle motion. This means the P-wave particle motion is in the same direction as the ray path.

The spherical P-wave can also be described by its displacement vector and propagation vector. In the case of the P-wave, both displacement vector and propagation vector move within the same plane.

Figure 4-12 illustrates effect of interface materials on the P-wave reflections. The compression wave reaches the bottom boundary (free surface) and is reflected back as a tension wave (T). The returning P-wave reaches the top surface of the plate as a tension wave (T) and starts the second reflection cycle as a compression wave (C). At this stage the reflected P-wave at the surface is a PP-wave and has gone through a compression/tension (CT) reflection mechanism. This cycle repeats to a point that all the energy is attenuated. On the time domain spectra this phenomena can be seen as the amplitude of the surface reflections caused by the periodic P-wave arrivals decrease.

The CT wave mechanism is true only if both surfaces of the plate have free boundaries, or in case of the bottom boundary, it is in contact with a material with lower acoustic impedance than the solid plate (i.e. concrete/water). In the case that the lower boundary is in contact with a material with higher acoustic impedance than the testing plate (i.e. concrete/steel), reflection mechanism changes. In this case the P-wave enters the plate as a compressional wave (C) but as it reflects back from the lower boundary, the wave mechanism remains compressional (C). Thus, the P-wave reaches the top surface as a compression wave (C) and when it gets reflected from the free surface boundary, its mechanism changes to tensional (T). In this case, the reflection mechanism for the first cycle of the P-wave is compression/compression (CC). At a free boundary (i.e. solid/air), almost all of the incident energy (100%) in a P-wave is reflected back. However, in the case of an interface with a material having higher acoustic impedance than the testing material (i.e concrete/steel), part of the incident energy of the P-wave transmits into the second boundary, part of it refracts, and part of it reflects. The amount of the reflected incident P-wave energy is controlled by the difference in the acoustic impedance of the two materials. The greater the difference in impedances, the greater the amount of reflected energy there is.

7.3.1.2 Reflected S-waves

The shear wave because of its properties of polarization can be subdivided into the SH and SV types, both of which have transverse particle motion and travel with the same velocity. However, as was discussed in Chapter 3 (Section 3.3) the SH-waves cannot be generated by a vertical point impact source and only the SV-wave is generated by a vertical point impact source.

The SV-wave is generated at the time of impact, below the hypocenter and disperses along a spherical wavefront. The shear wave's propagation vector is similar to the P-wave propagation vector. Nevertheless, maximum SV-wave energy propagates diagonally to the incident angle (see Figure 3-8). The SV-wave has no vertical displacement component, but transverse particle motion. In the case of shear wave, the displacement vector and the propagation vector do not act in the same plane, but in two planes perpendicular to one another.

The velocity of the SV-wave is smaller than that of the P-wave and it follows the P-wave along the ray path. Same as the P-wave, the SV-wave's reflection properties are governed by the acoustic characteristics of the reflecting boundary. At first we assume the acoustic properties of the reflection surface are lower than the elastic half-space plate that the wave travels through (e.g. concrete/air). As the SV-wavefront starts its traverse through the solid, the medium is displaced transversely around the direction of propagation. As a result, SV-wave generates particle motion normal to its ray path. Moreover, since the particle motion moves from left to right of the ray path at any given instant, SV-wave is responsible for generating shear stresses as the wave moves along. When the SV-wave reaches the bottom layer of the plate, the transverse motion changes direction from left to right (T_r) or vise versa. The returning SV-wave reaches the top surface of the plate as a transverse-left (T_l). Therefore, the first SV-wave reflection (SS-wave) mechanism is a transverse-left/transverse-right (T_lT_r). At the top the displacement vector creates a tangential displacement to the surface. The polarity of the receiving SV-waveform at the surface is similar to the wave generated by the point impact source.

When the elastic half-space plate is in contact with an elastic half-space plate with acoustic properties stiffer than the initial plate (e.g. concrete/steel), the reflection mechanism of the displacement vectors is different than the earlier case. When the acoustic impedance of the second layer is higher than the first layer, the transverse-left (or right) mechanism (T_l) created by the impact do not change to a transverse-right (T_r), and remains as transverse-left (T_l). Therefore, the first cycle of SV-wave (SS-Wave) creates a mechanism with a transverse-left/transverse-left (T_lT_l). For the displacement mechanism, the polarity of the S-wave remains as it was generated by the impact.

7.3.2 The Resulting Surface Displacements

The displacements on the surface of the elastic half-space are vertical and tangential to the surface. Both P- and SV-wave arrivals generate normal surface displacements as a result of arrival of their propagation vectors. The P-wave arrivals result in vertical displacements as response to its displacement vector. Therefore, both P-waves' propagation and displacement vectors cause vertical displacements on the surface. The SV-wave arrivals result in horizontal displacements caused by its displacement vector but the SV-wave's propagation vector causes surface diagonal displacements.

7.3.3 Displacement Magnitude and Radiation Pattern

The displacement magnitude of the two elastic waves and their radiation pattern are affected by the angle of incident, frequency of the transient pulse, and the elastic properties of the elastic half-space plate. In this case the angle of incident is always at zero degrees. The frequency of the impact pulse has an effect on the displacement magnitude of both P- and SV-waves. The lower the frequency of impact, the higher the displacement magnitude will be. The elastic properties of the medium affect the radiation pattern and displacement magnitude of the body waves (see Figure 3-10).

The displacement magnitudes are different for P- and SV-waves. The displacement magnitude of the P-wave is not uniform along the spherical wavefront. The displacements are maximum below the impact area and along the centerline of the plate, under the hypocenter, and the intensity reduces almost to zero at the top surface of the plate. The horizontal displacements caused by the SV-wave are minimal at the center of the plate, under the hypocenter, becoming larger along rays located at increasing angles from the centerline (see Figure 3-8). Between 35° to 45° from the centerline the SV-wave displacements are at maximum; the intensity reduces to zero at the top surface of the plate. The displacement intensity of the SV-wave is more sensitive to the elastic properties of the medium. Also within the 35° to 45° angles there is a discontinuity (critical angle) in the displacements in the spherical SV-wavefront (see figure 3-8).

For the P-wave the compressive stress is greatest at the centerline and decreases toward the surface of the plate. For the SV-wave, the shear stress is equal to the state of equal biaxial tension and compression. Therefore, the shear stress is lowest at the centerline and increases toward the 35° to 45° angle (depending on the elastic properties of the medium). At this range the shear stress is at maximum and reduces toward the surface.

In general, most of the resulting energy generated by the spherical impact is transferred as a P-wave rather than an SV-wave.

7.4 OBJECT DETECTION AND LOCATION IN CONCRETE

Simulated flaws and fractures in addition to steel reinforcement bars were positioned in known locations within a large concrete block. Figure 7-4 shows the schematic illustration of the concrete block and the object orientations within it. Plate 7-1 shows the casting of the concrete block. The dimensions of the concrete block were 2.24 m × 0.97 m × 0.55 m. After concrete mix was poured in to the cast, it was covered with a plastic sheet for 7 days and kept in the laboratory environment (i.e., ambient temperature of 22 ± 1°C and relative humidity of 50 ± 10%). A concrete vibrator helped the mix to layout uniformly and it also reduced the possibility of additional voids forming within the concrete. The concrete mix specifications were:

Cement type	10
Concrete type	35 MPa
Average aggregate size	14 mm

The maximum aggregate size	80mm ± 20
Air content	5 to 8%
Water/cement ratio	0.36

A number of objects were constructed in the concrete cast to simulate flaws, reinforcement, fracture and concrete/rock interface. The acoustic properties of each object were predetermined by the UPV and RF techniques and are listed in Table 7-1.

Table 7-1 Physical properties and acoustic properties of the objects used in the locating experiment.

Material	Density (kg/m^3)	P-wave velocity (m/s)	Specific acoustic impedance ($kg/m^2.s$)	Young's Modulus of elasticity (GPa)
Air	1.205	343	0.413	----
Wood	371	1579.2	0.58×10^6	3.9
Plexiglas	1214	2396.0	2.9×10^6	5.7
Concrete	2385	4000.0	9.2×10^6	34
Steel	7810	4614.3	36.0×10^6	102

Three main setups were created:

a) A pair of square plates with 12.6 mm thickness were placed next to one another, one made of steel and the other one of plexiglas. Both plates were located 25 cm from the bottom, 30 cm from top, and attached to the bottom through a 4 cm thick wooden stand. The bottom of the plate was connected to the wooden stand through a hollow steel pipe.

Both plates were chosen to have the same exact dimensions, but different materials. The characteristics of the reflected P- and S-waves would be related to second material's specific acoustic properties. In this exercise steel plate simulates rocks having higher acoustic properties than concrete block, and plexiglas plate simulates rocks with lower acoustic properties than concrete.

b) Steel reinforcement bars were placed in three locations. Each bar was 12 mm in diameter. The first set of bars was placed 16.0 cm from the top. The two other sets were placed on top of one another. The second set was placed at 31.0 cm from the top, and the third set was placed at 90° to the second set, having a distance of 16.0 cm from the top.

This design was made to test the performance of MSR in locating the steel bars, even with complex arrangements.

c) A 19.8 cm long and 6 mm thick rectangular shaped piece of plexiglas was placed perpendicularly down from the surface of concrete slab. The plate was placed to simulate an opening or a fracture. The objective of this exercise was to measure the depth of the fracture using the diffracted P-waves from the tip of the plate.

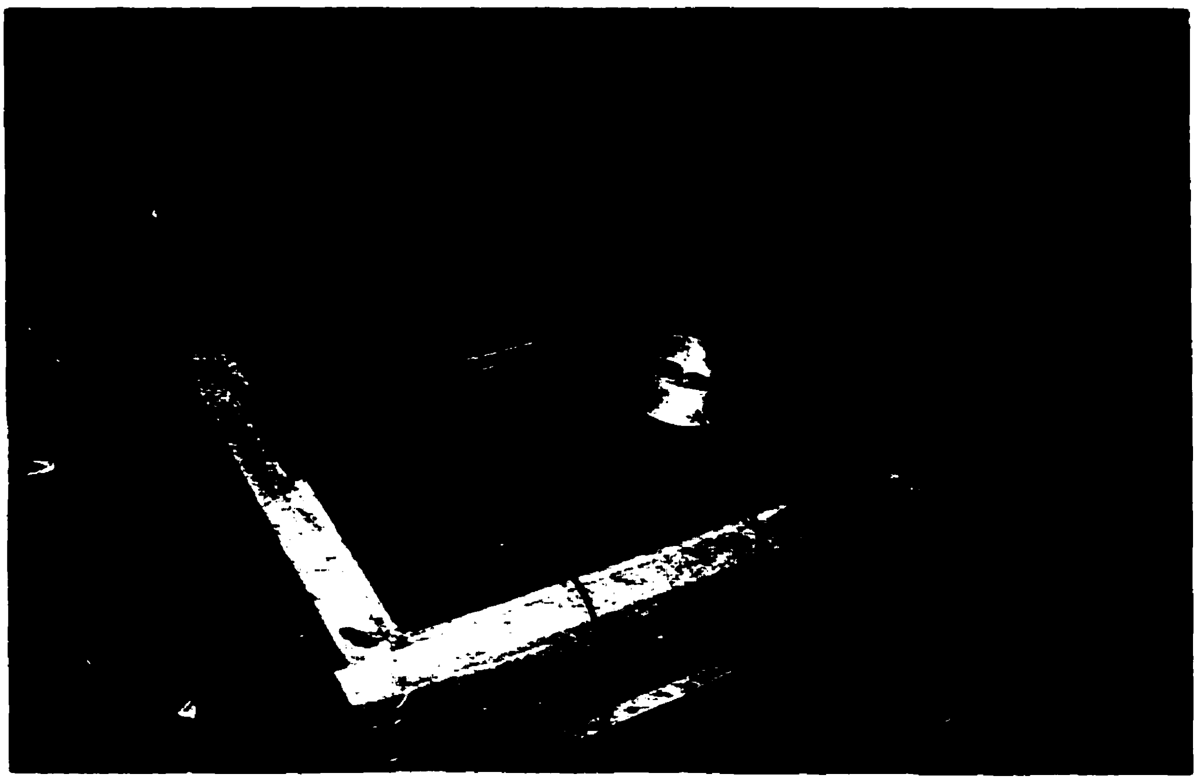

Plate 7-1 Above: casting of the concrete block, below: initial testing by MSR system.

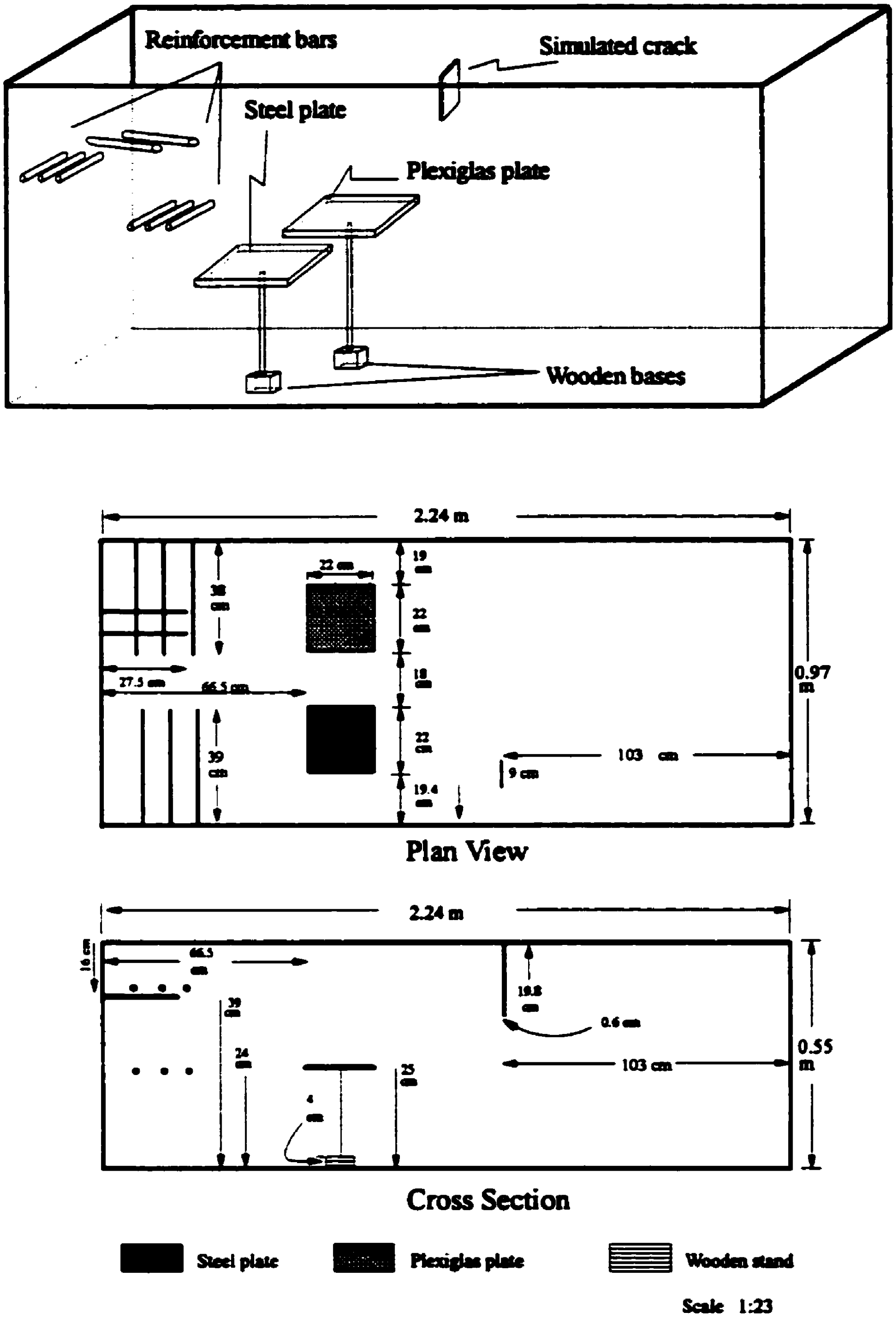

Figure 7-4 The three dimensional, plan view, and cross section of the concrete block with simulated flaws in it.

7.4.1 Steel and Plexiglas Plates in a Concrete Block

Study of planar square plates in a 0.55 m concrete block was carried out. Knowing that any abrupt change in acoustic properties of a material causes body waves to reflect, both P- and S-waves were used to detect the plates. Figure 7-5 shows a typical displacement waveform captured by the vertical displacement transducer and Figure 7-6 shows a typical displacement waveform captured by the tangential displacement transducer, on the 0.55 m thick concrete block. Figure 7-7a and d illustrates the vertical transducer and the impactor's configuration for detecting the steel and plexiglas plates. The distance between the transducer and the impact source was 0.05 m. The P-wave velocity in the concrete was 3920 m/s. Figures 7-7b and c illustrates the waveform and frequency spectra obtained by the vertical displacement transducer on the top of the steel plate. The P-wave velocity in concrete was calculated using equation 6-4 and the distinct amplitude value in the frequency spectra (3564 Hz), and knowing the concrete block's thickness value of 0.55 m. For the S-wave velocity, two different values were obtained for the concrete: one on top of the plexiglas plate having a frequency of 2637 Hz, giving a velocity of 2901 m/s, and one on top of the steel plate with a frequency of 2051 Hz giving a velocity of 2256 m/s.

In this case the concrete is in contact with the plexiglas plate and the acoustic properties of the plexiglas plate is lower than the concrete block (see Table 7-1). The P-wave causes a compression/tension stress characterization as it traverses into an object. The S-wave causes a transverse-right/transverse-left stress characterization as it moves into an object. At an interface where the underlying material has a lower acoustic impedance than concrete (e.g. air), the initial P- and S-waves changes sign, that is, the compression in the case of the P-wave changes to tension and in the case of S-wave the transverse-left reflects as transverse-right or vice versa (see Section 7.3.1 for more details). Figure 7-7a and 7-7a show the sign changes for the P- and S-waves. In this case, for the P-wave every time it reaches the transducer, it is a tension wave. The tension wave causes an inward displacement of the surface which can be seen in the displacement waveform captured by the vertical displacement transducer in Figure 7-7b. The frequency of the tension waves at the surface is $C_p/2T$ (see Section 7.3.1.1). On the resulting frequency spectra in Figure 7-7c, the large amplitude peak at 6689 Hz corresponds to the successive reflection of the P-waves from the plexiglas plate. Using equation 6-5 and P-wave velocity of 3920 m/s, the position of the plate can be calculated to be at 0.29 m from the top.

For the S-wave every time the wave reaches the tangential displacement transducer, it is a transverse-left wave which can be seen as an outward impression in the displacement waveform (Figure 7-8b). The frequency of the transverse-left waves at the surface is $C_s/2T$ (see Section 7.3.1.2). Therefore, equation 6-10 was used to calculate position of the plate in concrete. Figure 7-8c illustrates the resulting frequency spectra from the impact on the top of the plexiglas plate. The large amplitude at 4736 Hz corresponds to the reflection of the successive S-waves from the plexiglas plate. Using the value of 2901 m/s as the velocity of the S-wave from that region (see Figure 7-8c), the position of the plate was calculated at 0.31 m from the top.

In the case that the P- and S-waves incident upon a material with acoustic properties than concrete, their sign do not change (see Section 7.3.1.1 for more detail). Figures 7-7d and 7-8d show the signs of the P- and S-waves as they travel between the steel plate and the top surface of a concrete block. Figure 7-7e shows that the reflected P-wave from the steel plate has an upward displacement upon arrival at the vertical displacement transducer. In the case of the P-wave, the compression wave remains a compression wave upon incident on top of the steel plate. As the compression wave reaches the top, it changes to a tension wave. The tension wave repeats the cycle without changing its sign as it reflects from the concrete/steel boundary. Thus the period of the tension wave arrives at the surface is twice as long as the plexiglas case. The frequency of the tension wave would be:

$$f_p = \frac{C_p}{4T} \qquad (7-4).$$

S-wave follows the same principle as the P-wave when it reflects from a secondary surface with higher acoustic properties than concrete block. It takes twice as long for the transverse-left wave to reach the tangential displacement transducer. Therefore the frequency of the transverse-left wave would be:

$$f_s = \frac{C_s}{4T} \qquad (7-5)$$

To calculate the position of the steel plate in the concrete equations 7-4 and 7-5 can be used with slight modifications. Equation 7-4 was modified by Sansalone (1985) to equation 4-26 for depth calculation of steel bars. However, S-waves can also be used for depth calculation when equation 7-5 is rewritten as:

$$T = \frac{c_s}{4f_s} \tag{7-6}$$

The distinct amplitude peak value of 3271 in the frequency spectra in Figure 7-7f captured by the vertical displacement transducer was used to calculate the position of the steel plate at 0.30 m. Note that the P-wave velocity used for this calculation is 3920 m/s. Using equation 7-5 and S-wave velocity of 2256 m/s, the position of the steel plate was calculated as 0.25 m from the top.

This study was carried out to investigate the behavior of the body waves upon incident on materials with lower and higher acoustic impedance than concrete. The plexiglas was used to artificially simulate the presence of air or rocks with lower acoustic stiffness than concrete and the steel plate was used to simulate the presence of rocks with higher acoustic stiffness than concrete. Overall the results obtained by the vertical displacement transducer are in better agreement with the actual position of the plates in the concrete. Table 7-2 is a summary of the results calculated by the MSR system and the actual position of the objects in the concrete block.

Table 7-2 A comparison between the actual position of the plates and the calculated values by the MSR.

Actual Position of the Plates		Calculated Position of the Plates by MSR			
		By P-wave		By S-wave	
Plexiglas	Steel	Plexiglas	Steel	Plexiglas	Steel
0.3 m	0.3 m	0.29 m	0.30 m	0.31 m	0.25 m

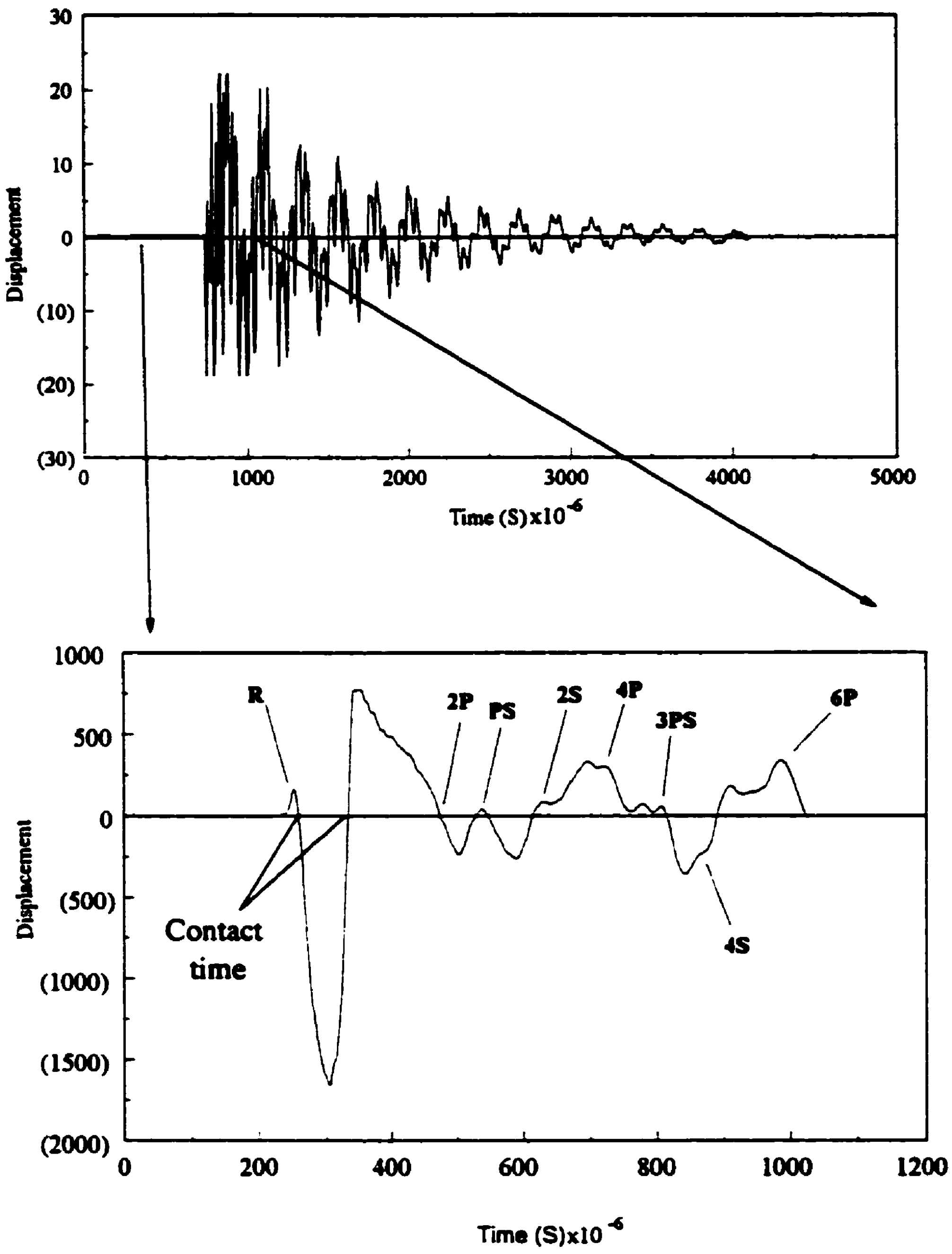

Figure 7-5 Typical waveform collected by the vertical displacement transducer on top of a concrete block having 0.55 m thickness.

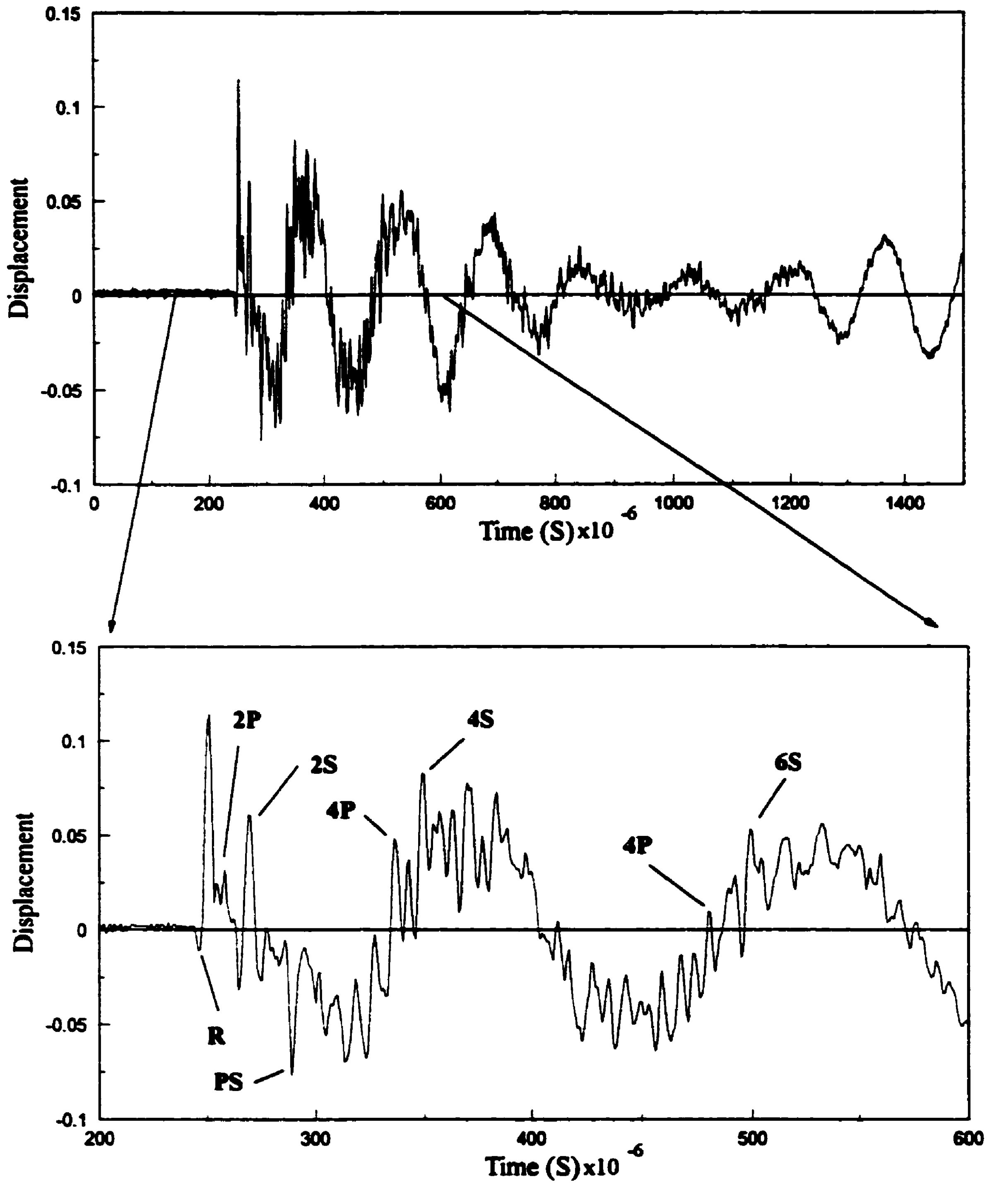

Figure 7-6 Typical waveform collected by the vertical displacement transducer on top of a concrete block having 0.55 m thickness.

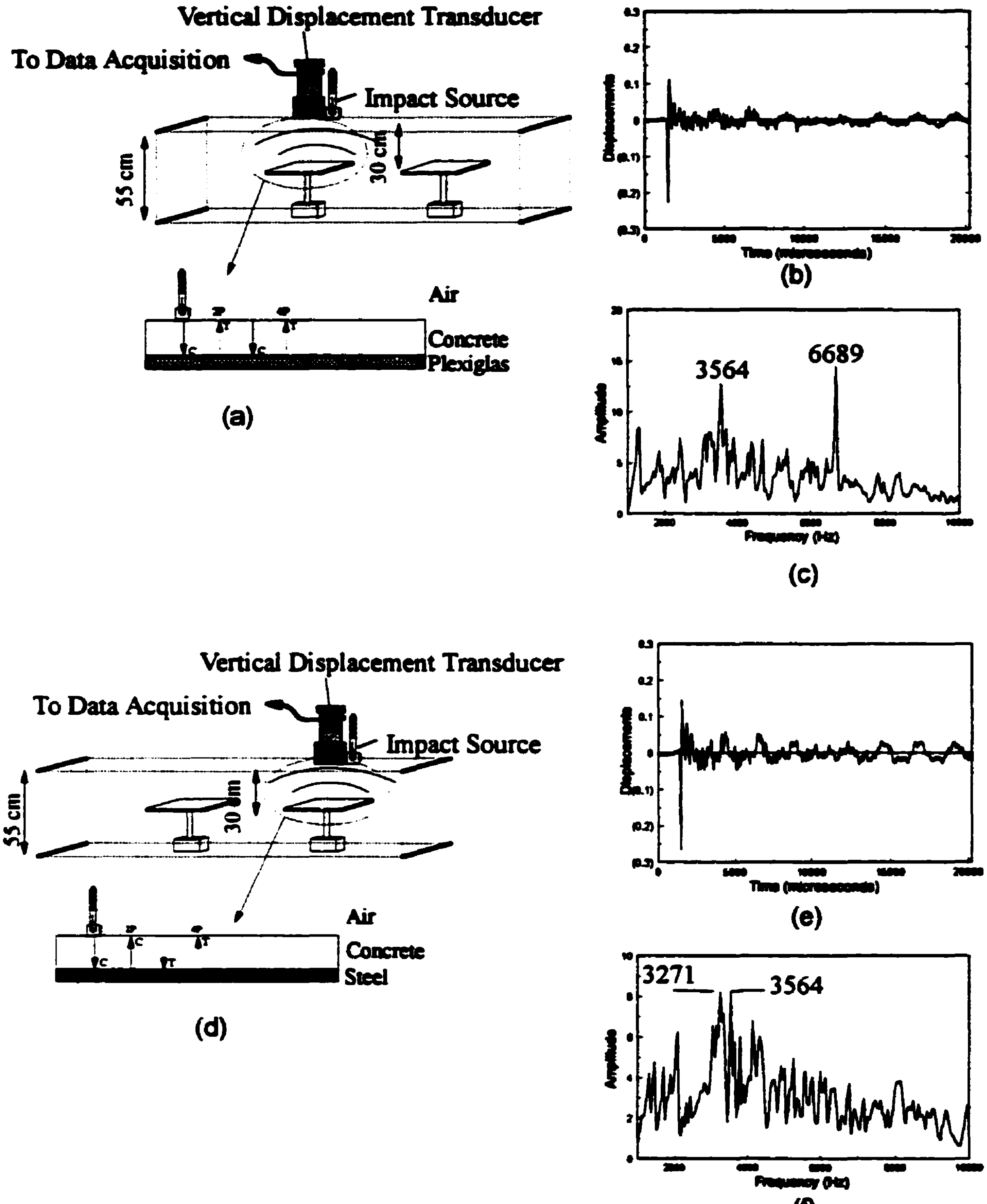

Figure 7-7 Vertical displacement transducer on top of the Plexiglas plate (a) the waveform (b) and frequency spectrum (c), the transducer on top of the steel plate (d) the related waveform (e) and frequency spectrum.

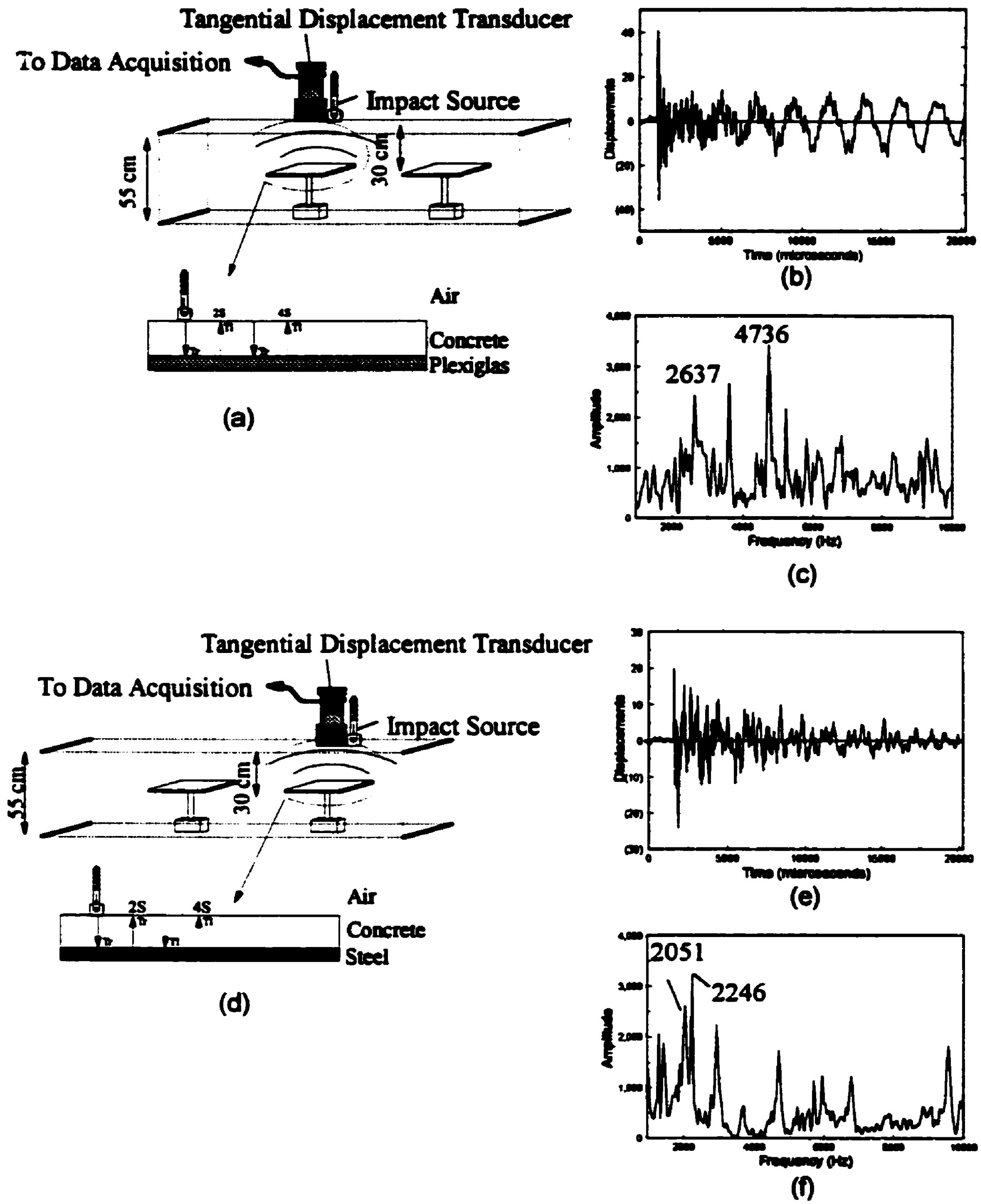

Figure 7-8 Tangential displacement transducer on top of the Plexiglas plate (a) the waveform (b) and frequency spectrum (c), the transducer on top of the steel plate (d) the related waveform (e) and frequency spectrum.

7.4.2 Detection of the Steel Reinforcement Bars

In this section the MSR system was used to detect the position of the steel reinforcement bars in the concrete block. Throughout the tests the vertical displacement transducer was used to detect the P-wave reflected waveforms. Two series of tests were conducted:

a) Three bars were placed at 0.09 m spacing (Figure 7-9a).
b) Two bars were placed at a 90° angle to one another at a corner of the concrete block forming a cross (Figure 7-10a).

The purpose of this survey was to confirm the capability of the MSR system in detecting of the small diameter steel reinforcement bars within concrete.

7.4.2.1 Three Parallel Steel Reinforcement Bars

Three steel reinforcement bars were placed parallel to one another in a linear array (Figure 7-9a). Each bar was 0.39 m long and 0.012 m in diameter. The third bar at position (d) was located 0.13 m away from the edge of the concrete block. The location of the bars from the top of the block varied: at location (b) the steel bar was at 0.170 m, at location (c) it was 0.176, and at location (d) the steel bar was located 0.184 m from the top.

An impact device with a 3.0 mm diameter was used as the impact source, generating impacts with an average of 65 μs contact-time. Figure 7-9b shows the typical waveform captured by the vertical displacement transducer on the top of the steel reinforcement bars. Figure 7-9c is the resulting frequency spectra at position (a) (see Figure 7-9a), where the concrete block has no reinforcement bars. Using the 0.55 m thickness of the block, 3125 Hz as the peak frequency value, the velocity of the P-wave was calculated based on equation 6-4 to be 3438 m/s. Due to the nature and type of the steel bars as the reflection surface (which was discussed in previous sections), equation 4-26 was used to calculate the depth of reinforcement bars. Figure 7-9d is the frequency spectra generated from the MSR results at the top of the first bar, at location (b). The large amplitude value at 5125 Hz is related to the multiple P-wave reflections from the top of the steel bar. The calculated depth of the steel bar is 0.168 from the top. Note that the second peak is related to the position of the steel bar at position (c). Figure 7-9e shows the frequency spectra related to the waveform collected on top of the second steel bar at (c). In this frequency due to the fact that all of the steel bars are positioned at a closed spacing, three distinctive peaks are shown. The second steel bar's position was calculated by using the value of 6445 Hz at 0.174 m from the top surface. The two other frequency values at 4932 Hz and 8300 Hz correspond to the position of the steel bars at points (a) and (d). Figure 7-9f shows the frequency responds of the MSR system on top of the third steel bar at position (d). The velocity of the P-wave at this location is slightly different than the three previous positions. At position (d) the velocity of P-wave is 3491 m/s which is calculated using the peak frequency of 3174 Hz in the frequency spectra. The second frequency peak in the spectra at 4688 Hz is related to the P-wave reflections from the steel bar at location (d). The position of the steel bar at this location was calculated to be 0.186 m. The second distinct peak in the frequency spectra is related to the position of the steel bar at location (c).

In this exercise the steel reinforcement bars were located accurately within the concrete block. The line of survey was selected to be perpendicular to the longitudinal direction of the steel bars. The highest amplitude in the frequency spectra beside the thickness frequency was indicating the shortest distance between the vertical displacement transducer and the upper surface of the buried object. Table 7-3 shows a comparison between the actual position of the reinforcement bars and the calculated values by the MSR.

Table 7-3 A comparison between actual position of the parallel steel bars and the calculated values by the MSR.

Actual Position of the Reinforcement Bars			Calculated Position of the Reinforcement Bars by MSR		
Position (b)	Position (c)	Position (d)	Position (b)	Position (c)	Position (d)
0.170 m	0.176 m	0.184 m	0.168 m	0.174 m	0.186 m

7.4.2.2 Two Crossing Reinforcement Bars

In most of the structures, particularly the concrete shaft linings, complex reinforcements are necessary to secure the integrity of the design. The purpose of this exercise was to study the capability of the MSR system to detect and locate crossed reinforcement bars.

Two sets of steel reinforcement bars were placed in the concrete block, crossing one another at a 90° angle (see Figure 7-10a). The steel bars were 0.38 m long, 0.012 m in diameter and were separated by 0.09 m at each set. The upper set was placed 0.180 m from the top surface and the second set was placed 0.355 m from the top surface (see Figures 7-4 and 7-10a).

In this exercise, two different impact sources were used to generate the stress pulses. In the case of the upper steel bars the impact source with a 3.0 mm diameter was used, generating pulses with 70 μs contact-times. For the steel bars at the lower position a source with higher energy impacts was necessary. Therefore, the impactor with 15.0 mm diameter was used, generating impacts with an average of 95 μs.

Figure 7-10b shows the waveform response captured by the vertical displacement transducer on top of the crossing bars generated by the 3.0 mm diameter impact device. In the corresponding frequency spectra at Figure 7-10c, 3027 Hz is the thickness frequency, 4785 Hz is the reflection from the steel bar that the vertical displacement transducer was placed on top, and 6934 Hz is the reflection from the adjacent steel bar placed 0.09 m away. The position of the steel bar at the top layer was calculated to be at 0.174 m using the P-wave velocity of 3330 m/s. The steel bars at the lower level are invisible to the pulses generated by the high frequency impact source because of the high attenuation rate.

Figure 7-10d shows the waveform response captured by the vertical displacement transducer on top of the crossing bars generated by the 15.0 mm diameter impact device. In the corresponding frequency spectra at Figure 7-10e, 3271 Hz is the thickness frequency and 2539 Hz is the reflection from the steel bar that the vertical displacement transducer was placed on top of it at the lower position. The position of the steel bar at the lower layer was calculated to be at 0.350 m using the P-wave velocity of 3598 m/s. The steel bars on the top layer are invisible to the pulses generated by the low frequency impact device since the wavelength of the pulses are too long. Table 7-4 shows a comparison between the actual position of the reinforcement bars and values calculated by the MSR system.

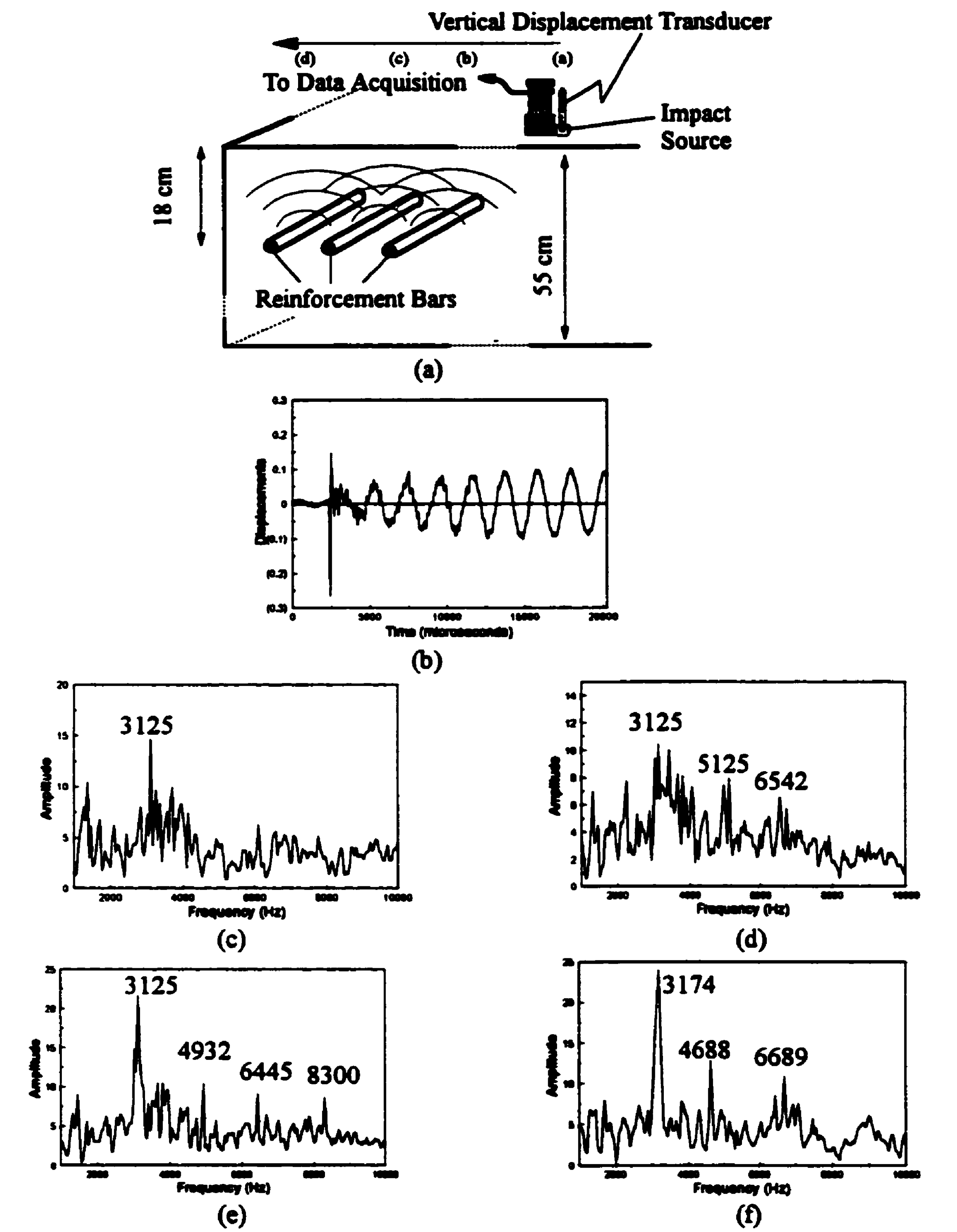

Figure 7-9 The position of the three parallel bars (a), example of displacement waveform on top of the steel bars (b), and frequency spectra related to each position (c), (d), (e), and (f).

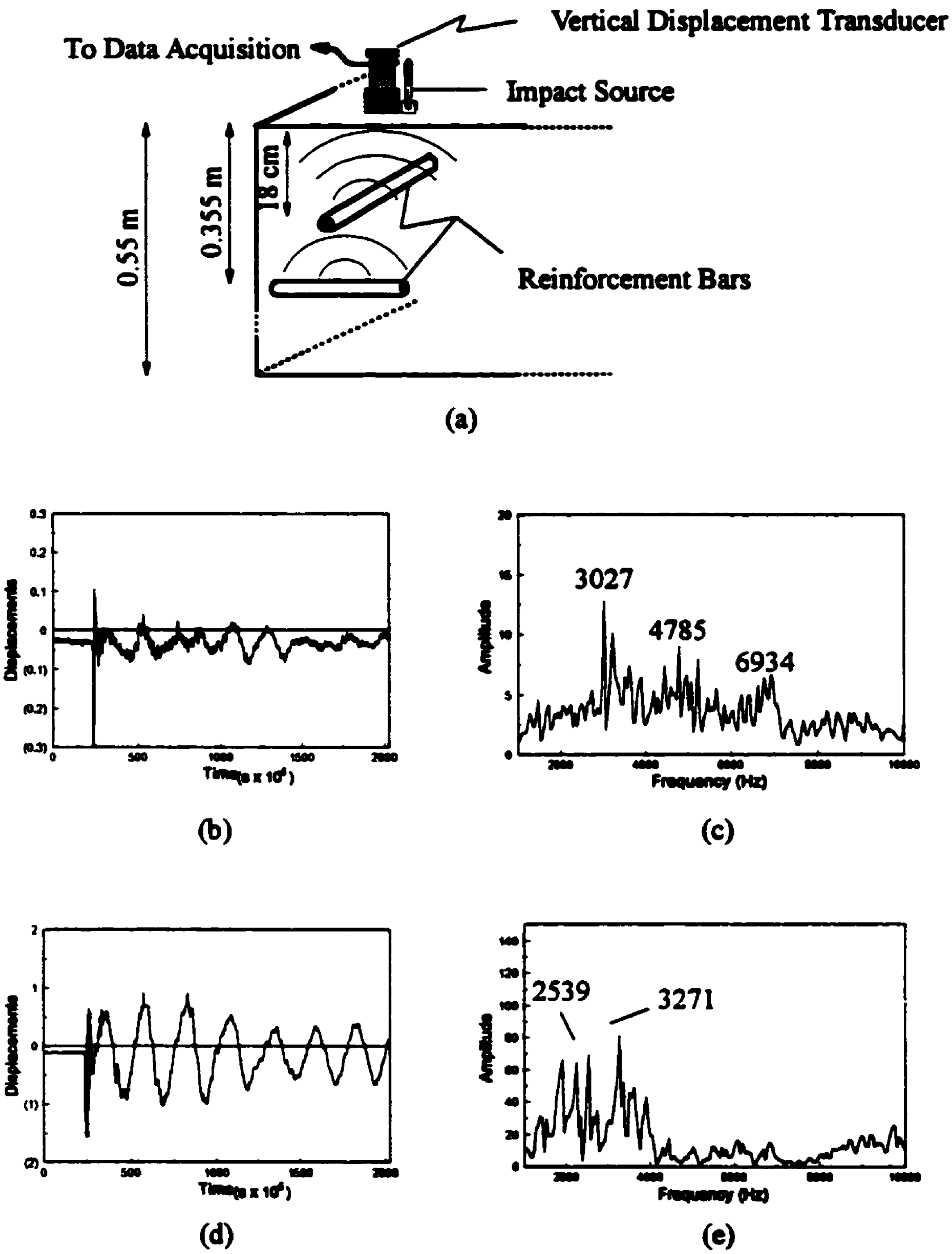

Figure 7-10 Two crossed steel reinforcement bars (a), the waveform obtained by the vertical displacement transducer for the top bar (b), the related frequency spectrum (c), the waveform obtained by the vertical displacement transducer for the bottom bar (d) and the frequency spectrum (e).

Table 7-4 A comparison between actual position of the crossed steel bars and the calculated values by the MSR.

Actual Position of the Reinforcement Bars		Calculated Position of the Reinforcement Bars by MSR	
Top Steel Bar	Lower Steel Bar	Top Steel Bar	Lower Steel Bar
0.180 m	0.355 m	0.174 m	0.350 m

7.4.3 Depth of Simulated Vertical Opening Crack

A vertical opening crack in concrete block was simulated using a 6 mm thick plexiglas plate hung from the top surface at the time of casting (see Figures 7-4 and 7-11a). The plexiglas plate was 0.198 m vertically deep into the concrete block.

The impact source was located on one side of the crack and the vertical displacement transducer was placed on the opposite side (see Figure 7-11a). Both the impact source and the receiver were placed 0.1 m away from the crack. The impact source was 15.0 mm in diameter, generating an average contact-time of 95 μs.

After emission of stress waves by the impact source, diffraction of incident waves occurs at the bottom edge of the plexiglas, which acts as a source for the generation of cylindrical waves (Sansalone, M., 1985). Figure 7-11a shows the diffraction of P- and S-wave at the bottom end of the crack. The diffracted P-wave is the first wave to arrive at the transducer. On the other side of the crack, the incident wave is not capable of penetrating the crack. The only waves capable of penetrating this shadow zone are diffracted waves. The diffracted S-wave is the second wave arriving at the transducer. Both P- and S-waves reflect downward from the surface of the concrete. In their pathway, part of their energy diffracts, back to the surface from the edge of the crack. This cycle repeats itself, which gives rise to a resonance condition with the frequency of the P-wave arrival at the receiver corresponding to the approximate depth of the crack.

In addition to the arrival of the diffracted waves, reflected P-waves generated by the initial pulse generate a resonance with a frequency which is twice the thickness of the slab.

Figure 7-11b illustrates the frequency spectra obtained from the MSR test. There are two distinct high amplitude peaks. The largest amplitude at 3564 Hz is caused by the resonance of the P-wave between the top and bottom of the concrete block. Knowing the thickness of the slab to be 0.55 m the velocity of the P-wave was calculated, using equation 6-4, which was 3920 m/s. A large amplitude frequency peak at 10010 Hz is the frequency which corresponds to the resonance of the P-wave reflection from the top of the slab and the diffraction at the bottom of the crack. This value is twice the distance from the tip of the crack to the surface due to the close approximation of the impactor and receiver. In this case, a frequency value of 10010 Hz corresponded to a depth of 0.196 m, which is close to the measured depth at 0.198 m. Table 7-5 illustrates a comparison between the actual depth of the crack and calculated value using MSR system.

Table 7-5 A comparison between actual position of crack and the calculated values by the MSR.

Actual Position of the Crack	Calculated Position of the Crack by MSR
0.198 m	0.196 m

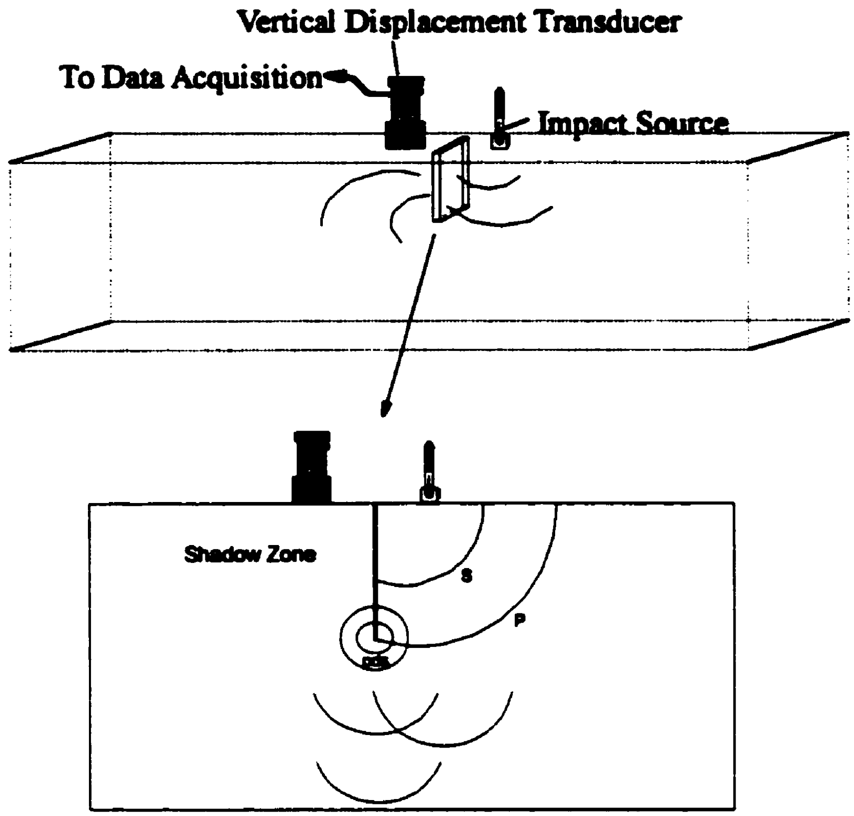

(a)

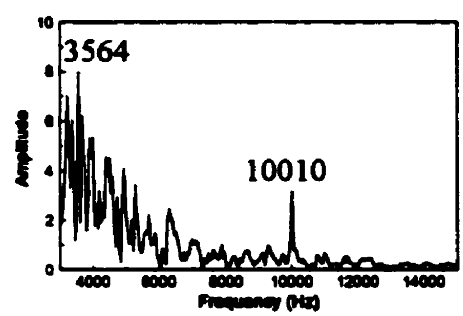

(b)

Figure 7-11 The position of the simulated vertical opening crack in the concrete block (a), and the related frequency spectrum (b) generated by the vertical displacement transducer.

7.5 DETECTION OF A PLANAR FRACTURE IN A CONCRETE SLAB

This laboratory exercise was carried out in order to demonstrate the capability of the MSR system to detect the position of an actual planar fracture within a plate-like concrete slab. In addition the slabs' average dynamic Young's modulus, shear modulus, bulk modulus, and Poisson's ratio were calculated. A 3.0 mm diameter impact source capable of generating an average contact-time of 75 μs was used to generate stress pulses.

7.5.1 Results and Discussion

A plate-like concrete slab having dimensions of 2.6 m × 1.4 m × 4.6 m was cast with three different types of concrete mixes. The poor-strength concrete was sandwiched between the two high-strength concretes, to facilitate formation of a fracture halfway from the top of the slab. The fracture was formed uniformly in the middle of the slab having a zigzag wavy shape with respect to the surface (see Figure 7-12a). The main objective of this exercise was to measure the distance of the fracture from the top surface. To achieve this goal a grid of 0.2 m by 0.2 m was drawn on the top surface of the slab (see Figure 7-12b). The grid was selected in a order for the MSR signals to scan and cover as much of the area as possible. The average velocity of the P-wave velocity in the concrete was found to be 4300 m/s. The P-wave velocity was calculated from the peak value in the frequency spectra, known thickness, and equation 6-4. The vertical displacement transducer was used for this assessment. The thickness variations are presented in longitudinal cross sections of the concrete slab according to each scanning line. Figure 7-13 shows the cross sections of the survey lines with the calculated position of the planar fracture by the MSR.

To measure the dynamic elastic constants of the slab, shear wave velocities were captured on eight different positions by a tangential displacement transducer. An average value of 2561 m/s was calculated for the shear wave velocity.

Knowing the relationship between the stress wave velocities with the density and the elastic moduli (see Table 3-2), the Young's modulus, Poisson's ratio, shear modulus and bulk modulus of the slab was calculated. The average mass density of the concrete was calculated at 2300 kg/m^3.

The Poisson's ratio of the slab was calculated to be 0.23.
The Young's modulus of the slab was calculated to be 37.0 GPa.
The shear modulus of the slab was calculated to be 15.0 GPa.
The Bulk modulus of the slab was calculated to be 22.0 GPa.

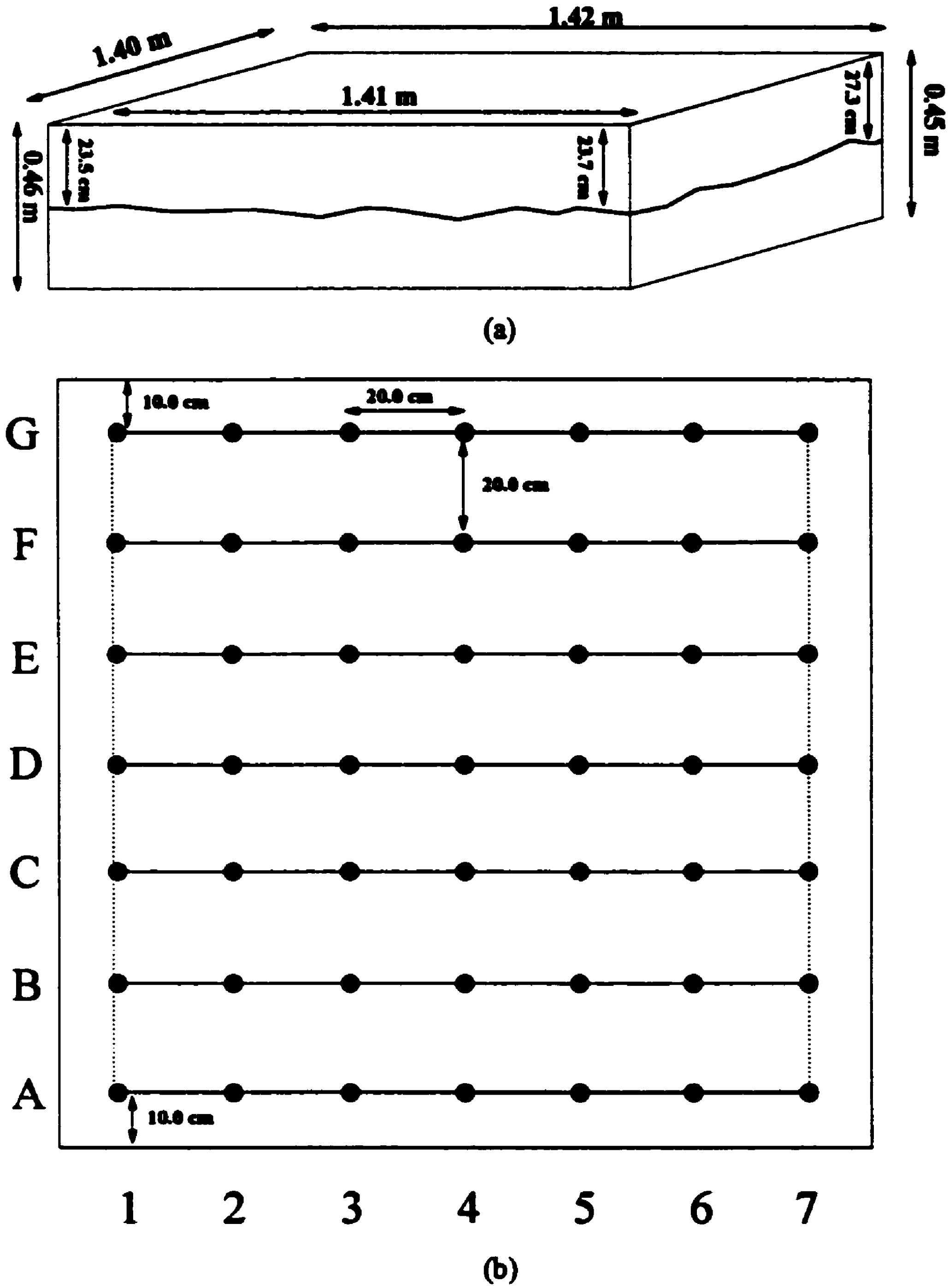

Figure 7-12 a) Schematic drawing of the concrete slab and (b) the plan view of MSR survey lines.

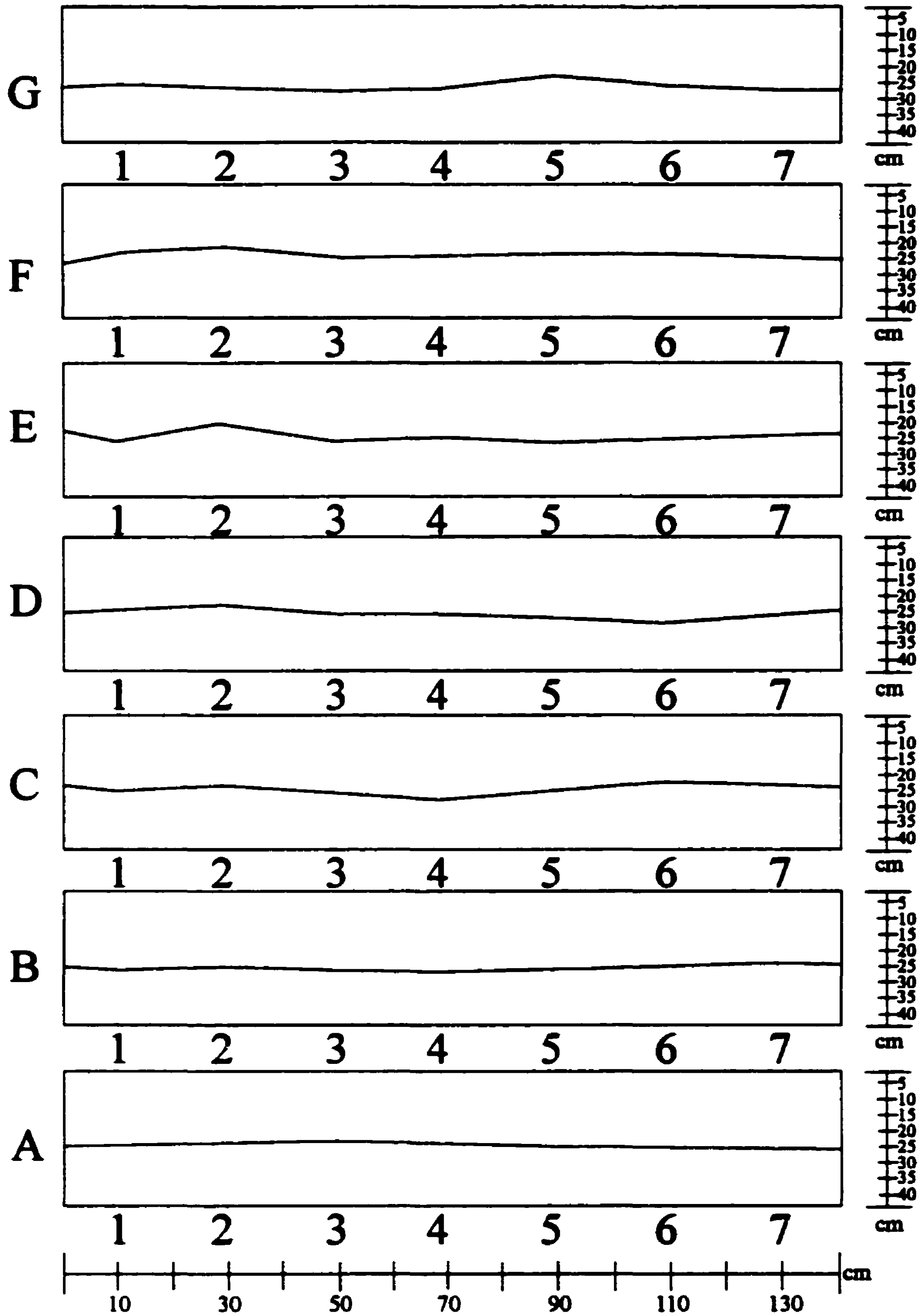

Figure 7-13 Longitudinal slices of the concrete slab with the planar fracture, reproduced by the MSR data.

7.6 SUMMARY AND CONCLUSIONS

This chapter has described the implementation of the MSR system in detecting flaws, steel reinforcement bars, and vertically positioned crack in concrete. The assembled MSR system described in Chapter 6 was used to conduct the experiments in this chapter. The experiments demonstrated that:

1. The function of the MSR system for detection purposes is limited to the knowledge of one of two variables: thickness or P-wave velocity. In the case in which the thickness is known, the velocity can be calculated by the frequency of the P-wave reflections from the back of the plate. Otherwise, the P-wave velocity should be calculated by the indirect methods. The P-wave velocity was estimated indirectly by using surface R-waves. Also the P-wave velocity was indirectly calculated using the first arrival of surface P-wave velocities. The two values of P-wave velocities from the indirect methods were compared with the P-wave velocity obtained by the reflected waveform from the bottom of the block. From the results it can be concluded that there will always be a discrepancy between the velocity of the reflected signals and that of the surface waves due to the heterogeneity of the concrete. However, the velocity obtained by the first surface P-wave arrival is in better agreement with the reflected P-wave in comparison with the estimated P-wave velocity computed from the R-wave velocity.

2. The displacement waveforms and their frequency spectra were used throughout this study in order to detect and locate the simulated flaws and delaminations in the concrete block. The S-wave as well as P-wave were used in order to study the reflection behavior of the body waves from lower and higher acoustic stiff plates than the initial block. Simulated planar flaws were detected by P- and S-wave with great accuracy.

3. Steel bars are normal constituents of a concrete structure, used for reinforcement particularly in underground concrete linings. Two sets of reinforcement bars, one in a tight parallel formation and the second set in a top and bottom crossed formation were imbedded in a concrete block. The position of both sets were detected by the vertical displacement transducer and the P-wave reflections with great accuracy.

4. A simulated vertical opening crack was placed in the concrete block at the time of casting. Using the vertical displacement transducer and the impact device on both sides of the crack on the surface, the depth of the opening crack was calculated with great accuracy.

5. A realistic planar fracture was created half-way across a concrete slab. A chessboard survey grid was marked on top of the slab. The vertical displacement transducer was used to outline the position of the planar fracture in the concrete. The tangential displacement transducer was used to provide shear wave parameters. Having assumed an average density value for the concrete slab, the average values for the elastic constants of the slab were calculated.

The work discussed in this chapter has established the basis of the MSR as a nondestructive testing system for the detection of different types of flaws and delaminations in concrete blocks in laboratory conditions.

CHAPTER 8

APPLICATION OF THE MSR SYSTEM FOR MEASURING THE QUALITY OF CONCRETE

8.1 INTRODUCTION

An investigation was conducted to evaluate the effectiveness of using the MSR system to monitor quality of concrete mixes. Upon initial mixing, fresh concrete is a fluid like material. Through the physical and chemical reactions collectively termed hydration, this fluid like mix changes to a hardened mass. The hardening of concrete occurs during what is known as the setting period. The beginning and the end of concrete's setting period or setting time is not clearly known. The setting time of the concrete is understood by its stiffening. The stiffening of concrete can be quantified by the increase in body wave velocities, gain in elastic constants, and strength.

In this chapter the MSR system will be used to monitor the setting time of concrete. Monitoring of concrete's stiffening is carried out by the MSR system on the cylindrical samples. Six types of concrete mixes with the different strength capabilities were monitored for their 28 days curing period. Furthermore, the effects of aggregate size and cement type on the elastic properties will be studied by the MSR system. The MSR tests were carried out to evaluate elastic properties of wall and columns, in situ. The ability of the MSR system to measure concrete setting times in situ can be used as a means of quality control of the structures. The results of the body wave dynamic elastic moduli determinations were compared with the standard resonant frequency (RF) test described in ASTM C 215. The results from standard dynamic and static tests were compared with the results obtained by the MSR system. Also the ultrasonic velocities were compared with the stress waves generated by the MSR system. Finally, a concrete block was evaluated and the results of elastic moduli obtained by the MSR system were contoured.

8.2 SAMPLE PREPARATION

Compressive strength gain and development of elastic constants of six different types of concrete mixes were studied. Details of concrete mix used in this experiment are listed in Table 8-1. The curing condition was kept the same (air-dried curing) for all the mixes. The dynamic and static elastic properties of the mixes were obtained by various methods. The Grindosonic apparatus was used to obtain the dynamic elastic properties of the mixes by the RF technique. Prismatic samples, 400 mm × 100 mm × 100 mm, were cast in plexiglas molds designed to enable demolding without disturbing the concrete at an early vulnerable age. Concrete cylinders, 152 × 305 mm, were cast in special cardboard cylinder molds designed to enable demolding at very early ages without disturbing the concrete. The static tests, MSR tests, and UPV tests were conducted on the same types of samples (concrete cylinders with 152 × 305 mm dimensions). All of the cylinders were hand rodded in accordance with ASTM C 31 (1988). All of the specimens were covered with plastic sheets for 24 hours after casting and kept in the laboratory environment (i.e., ambient temperature of 22 ± 1^{o}C and relative humidity of 50 ± 10%). The specimens were demolded 24 hours after casting. Air-dried curing was achieved by leaving the specimens in the laboratory at normal temperature and humidity condition.

Table 8-1 Composition and properties of the six concrete mixes used in the experiments.

Characteristics	BN20	BN25	BN30	BN35	BN40	BN50
Cement (Type 10), kg/m^3	260	290	345	410	445	475
Fine aggregates, kg/m^3	1100	1060	1005	920	900	870
6 mm coarse aggregates, kg/m^3	640	655	675	675	710	720
12 mm coarse aggregates, kg/m^3	210	215	225	225	235	240
Total water, l/m^3	175	175	175	180	165	145
PDA 25 XL, ml/m^3 (water-reducing agent)	840	905	1080	1285	1393	1487
Superplasticizer, l/m^3	-	-	-	-	2.6	3.8-4
Density, kg/m^3	2230	2300	2320	2410	2360	2470
28th days UCS	10±1.0	15±0.5	20±1.0	30±1.5	54±2.0	60±2.2

8.3 DETERMINATION OF COMPRESSIVE STRENGTH, STATIC YOUNG'S MODULUS AND POISSON'S RATIO OF DIFFERENT CONCRETE MIXES

The compressive strength tests were carried out at frequent intervals during the first 28 days in order to determine the influence of early-age hydration on compressive strength and elasticity gain. After the first 24 hours, the cylinders were end faced by grinding (see Plate 8-1a). The compressive strength and the static dynamic elastic properties of the cylinders were determined using a standard compressive testing machine (MTS Model 315.03) with a maximum loading capacity of 4600 kN (see Plate 8-1b). The cylinders were tested under strain control as was advised by the ASTM C 39-86 (1988). The axial strain was measured by MTS extensometers (Model 632.94), with 200 mm gauge lengths, placed on opposite faces of the specimen. A total of about 200 cylinders were tested in compression for this study.

8.3.1 Compressive Strength

Figures 8-1 through 8-3 show the variations of average compressive strengths of BN20, BN25, BN30, BN35, BN40, and BN50 concretes with age for the air-dried curing condition. The average compressive strength gain at an early age is higher for the samples with higher compressive strengths, which can be due to higher rate of hydration. For the BN40 and BN50 concretes there is a retardation in compressive strength gain for the first 24 hours which is due to the presence of superplasticizer in their mixes. After this retardation period there is a rapid increase in strength gain for these two types of samples. Figure 8-4a illustrates that strength gain continues for all concrete batches after the 28 days testing period.

8.3.2 The Stress-Strain Response

Cylindrical samples were tested at ages of 1, 2, 3, 4, 5, 6, 7, 14, 21, and 28 days. Figures 8-1 through 8-3 illustrate the calculated stress-strain responses for the BN20, BN25, BN30, BN35, BN40 and BN50 concretes. At the very early stages the stress-strain responses indicate very low elastic moduli, low compressive strengths, and relatively high strains. The graphs exhibit a change of stress-strain response during the 28-day curing. Between the age of 1 day and 28 days strain changes slightly. The stress-strain curve changes to a more linear and steeper form as the compressive strength increases. The higher strength concretes (BN40 and BN50) have higher peak strains than the lower strength concretes.

8.3.3 Young's Moduli

The chord elastic modulus was calculated for the six different types of mixes from the measured stress-strain responses, in accordance with ASTM C 469-87 (1988). Figures 8-4b through 8-7b show the variation of the chord and initial tangent modulus for the various mixes at different ages for the six different concretes. Also in these figures the values of the modulus predicted are shown by using the expression given in the ACI Code (1983) and ACI Committee 363 (1992) (see Section 5.3, equations 5-1 and 5-2). In all six cases the modulus predicted is overestimated. This overestimation is particularly obvious in the case of BN30 and BN35 concretes. Nevertheless, the ACI 363 expression provides a reasonable estimate of the average modulus of elasticity for the low and high strength concretes. The data illustrates a rapid gain in chord and initial tangent modulus for the first seven days curing period. For the low-strength concrete batches (BN20 and BN25) the initial tangent modulus is higher than the chord modulus for the 28 days curing period. For the rest of the batches the gap between the two modulus values narrow. For the BN40 and BN50 the initial tangent moduli are in very good agreement with the predicted moduli. Figure 8-7b shows the variation of the average chord, initial tangent, and predicted modulus versus the average compressive strength from day 1 to an age of 28 days for all the batches. The data indicate a progressive increase in elastic moduli with compressive strength. Eventhough the elastic moduli increases with compressive strength, the relationship is not linear.

8.3.4 Poisson's Ratio

Figures 8-8 through 8-10 show the development of the Poisson's ratio with time for the six concrete batches. The axial and diametrical strains were measured by the MTS extensometers. For all the batches there is a rapid gain in Poisson's ratio between two to seven days of curing period. BN40 illustrates an unusual drop in Poisson's ratio between 6 to 14th days. After this dramatic gain, the Poisson's ratio reaches an stable and steady value throughout the rest of the curing period.

(a)

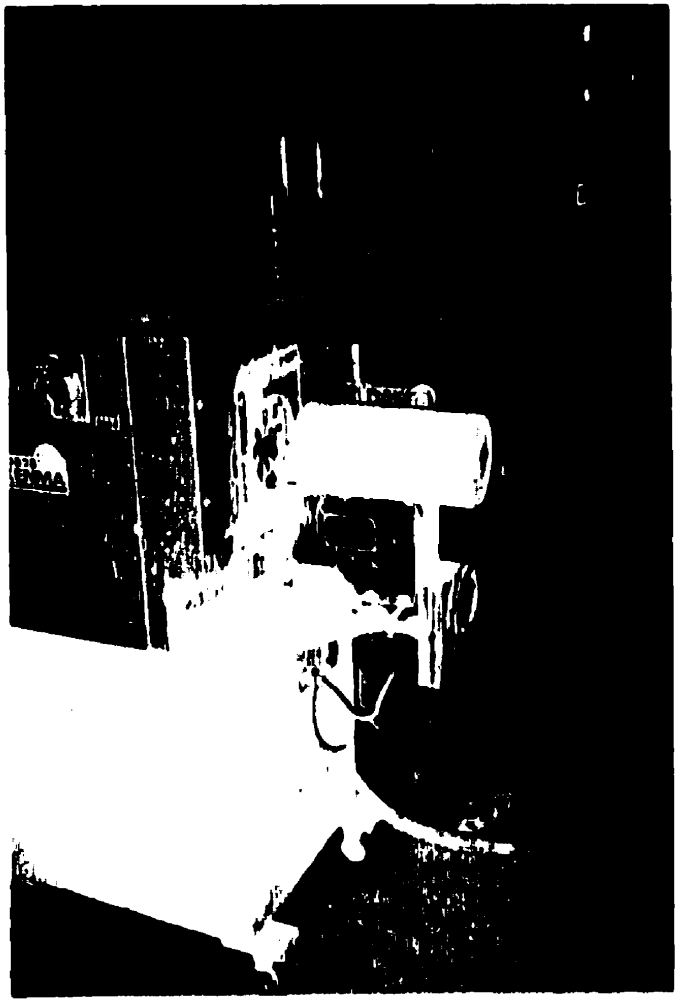

(b)

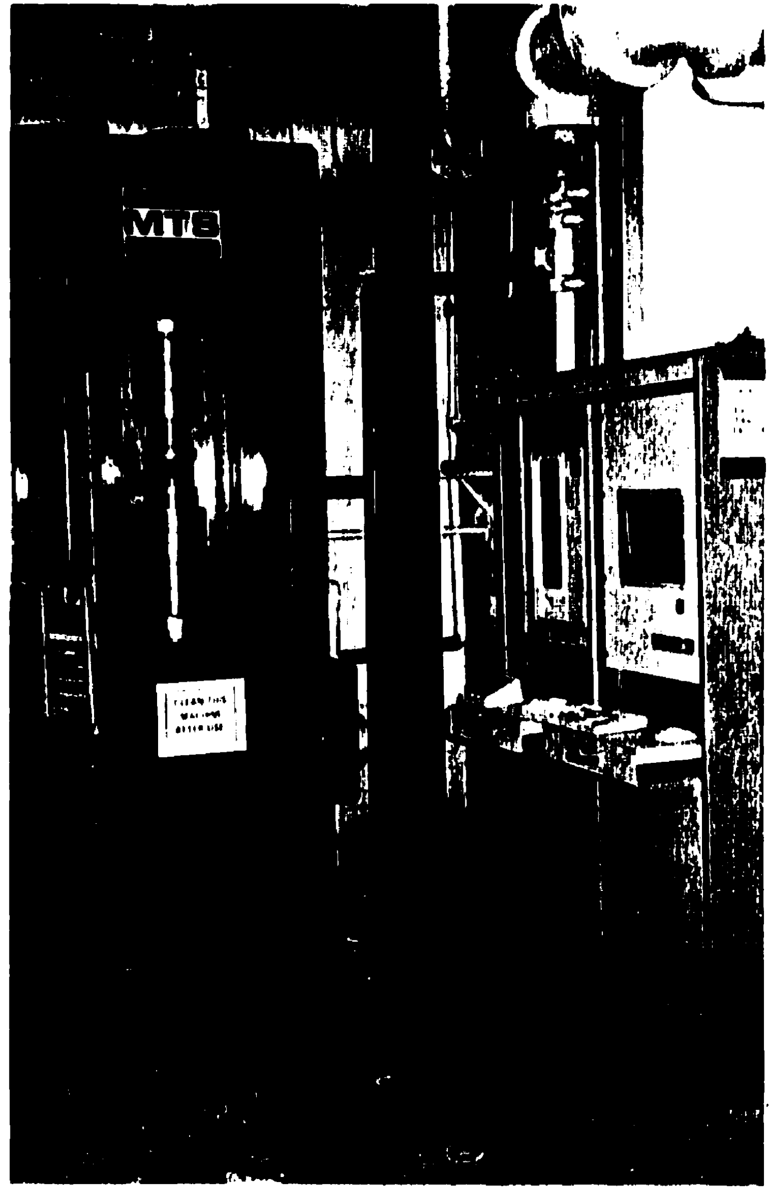

Plate 8-1 a) The grinding machine,
b) The MTS Model 315.03 compressive testing machine.

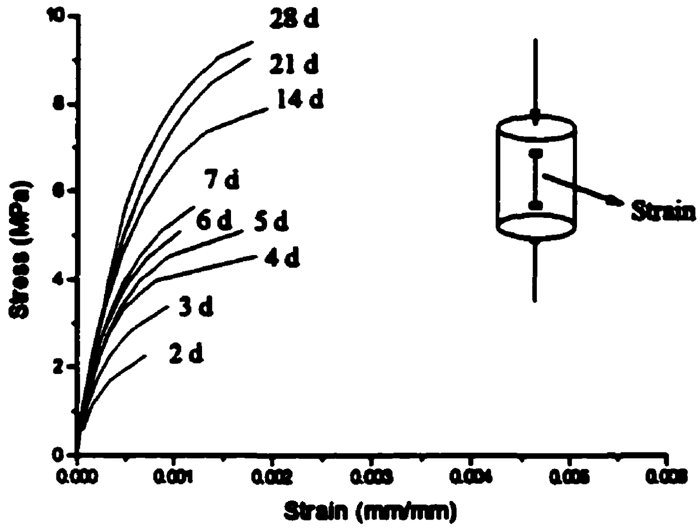

(a)

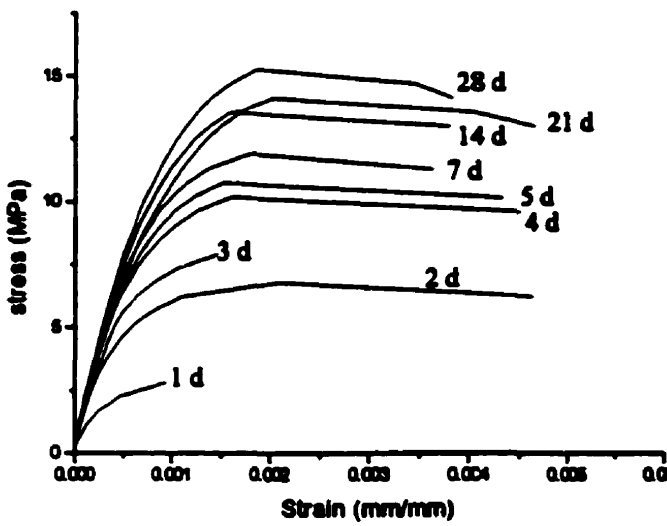

(b)

Figure 8-1 Compressive stress-strain responses of a) BN20 and b) BN25 concretes.

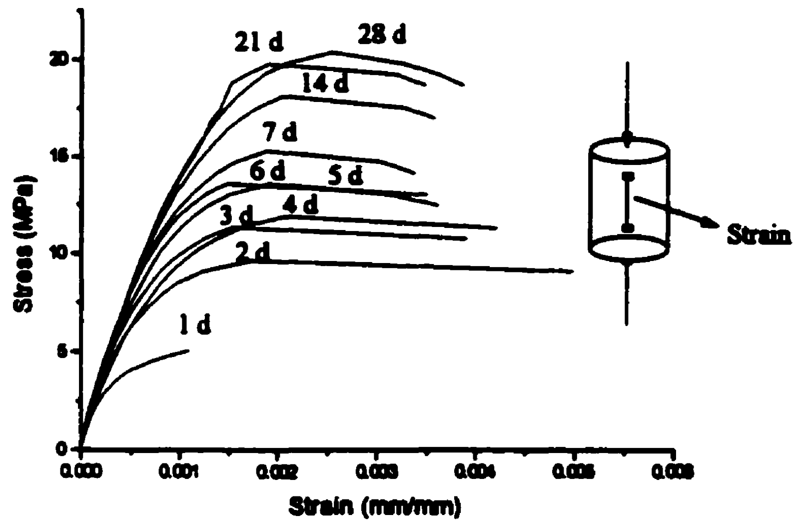

(a)

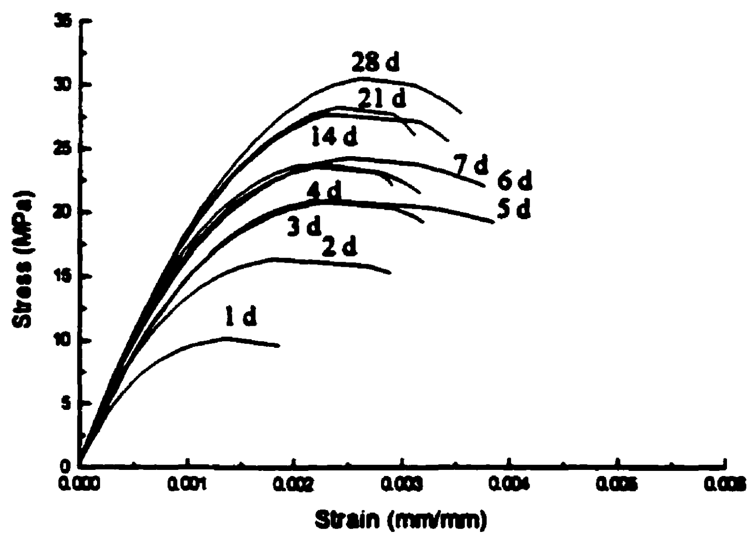

(b)

Figure 8-2 **Compressive stress-strain responses of a) BN30 and b) BN35 concretes.**

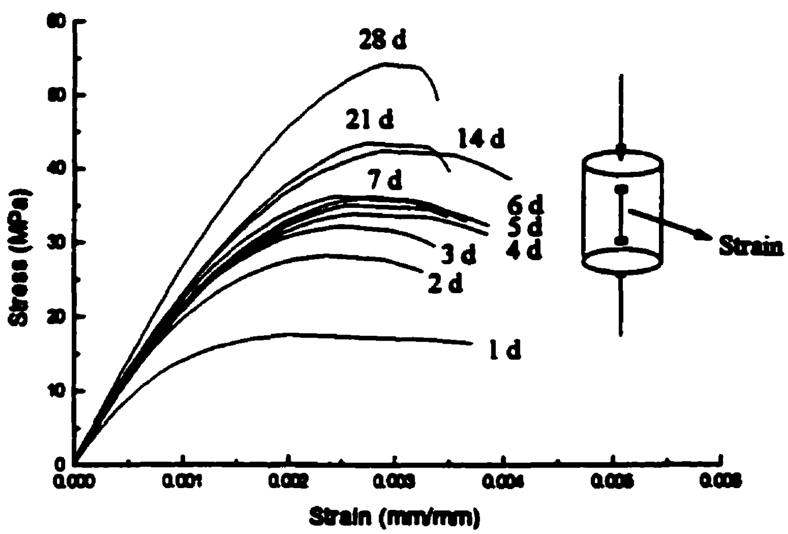

(a)

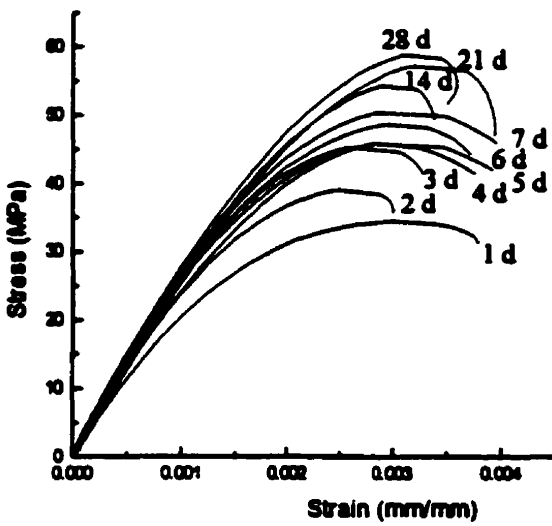

(b)

Figure 8-3 Compressive stress-strain responses of a) BN40 and b) BN50 concretes.

8.4 DETERMINATION OF DYNAMIC ELASTIC CONSTANTS OF CONCRETES

8.4.1 Determination of MSR Response

The 3.0 mm diameter spherical tip impact device was used as the impact source. Surface displacements were monitored by the vertical and tangential broadband transducers. The distance between the impact source and the vertical displacement transducer was kept at 5.0 cm for all tests (see Plate 8-2). The tangential displacement transducer was placed near the edge of the cylinders, approximately 7.0 cm away for all of the tests (see Plate 8-3). An A/D card was used for acquisition of the waveforms. Subsequently, the recorded waveforms were collected in a portable computer for further analysis. The A/D card was operating at a 2048 data points, recorded at a sampling frequency of 200 kHz (sampling intervals of 5 μs). Thus, the total duration of the record is 10240 μs. From equation 6-12, the frequency interval in the frequency spectrum is 0.098 kHz, which allows the wave velocities to be computed to the nearest 30 m/s. The effect of the low frequency (below 1000 Hz) transducer assembly resonance and the R-wave frequency were filtered out. The waveforms were difficult to interpret prior to the first 24 hours of setting time.

In Appendix C, Figures C-1 through C-20 show the frequency spectra for some of the MSR tests made on the six different types of mixes. The spectra on the left sides are measured from the waveforms captured by the vertical displacement transducer and the spectra on the right sides are measured from waveforms captured by the tangential displacement transducer. The frequency range shown in each spectrum is from 1000 to 10000 Hz, with the exception of P20d1 which ranges between 2000 to 3000 Hz. Note that on each frequency spectrum the frequency peak was used to compute the velocity plots in Figures 8-11 through 8-13.

In Appendix C, as can be seen in Figures C-1 through C-20, early frequency spectra are characterized by large amplitude low frequency peaks. As the concrete matures, the resonance frequency of the body waves in the cylindrical specimens increases. Hence, the frequency peak values increase with concrete maturity.

Once the peak corresponding to the resonance frequencies of P- and S-waves were identified, the development of the velocities can be easily followed. Equation 6-4 and the peak frequency values from the spectra generated by the vertical displacement transducer were used to calculate the P-wave velocities. Similarly, equation 6-9 and the peak frequency values from the spectra generated by the tangential displacement transducer were used to calculate S-wave velocities. Figures 8-11 through 8-13 show the development of the P- and S-wave velocities as the time progresses through the resulting frequency spectra. The MSR velocity determinations were attempted at an age as early as 24 hours (day 1). Prior to the first 24 hours most of the data, particularly in the case of S-waves, were scattered. For the early hours in the case of BN20, BN40, and BN50 it was impossible to determine which frequency in the spectrum corresponds to the resonance frequency of the waveforms. In this study to be able to compare all the data obtained from different techniques, all the values after the first 24 hours were considered. For all the six mixes, there is a rapid increase in P- and S-wave velocities for the early curing days. However, after the early dramatic increase in wave velocities, there is a decrease in the rate of velocity increase. This change in the rate of wave velocity increase occurs earlier for the S-waves. This means that the rapid rate increase in S-wave velocity drops faster than the P-wave. In the case of the S-waves the period for rapid gain of velocity varies between the shortest at second days (BN50) to longest at sixth days (BN20). For the P-waves this period of rapid gain of velocities ends between five to seven days.

At any given time the wave velocities are higher for the higher strength concretes. This difference can be attributed to the coarser aggregate content and cement content of the higher strength concretes. As it is evident in Table 8-1, the higher strength concretes contain higher amounts of coarse aggregates and cements in their mixes.

Once the elastic wave velocities were computed from the frequency spectra, they can be used to determine the mechanical properties of the six mixes for the curing period. Equations in Table 3-2 and the density values from Table 8-1 were used to calculated values of dynamic elastic constants for the concrete mixes.

In Chapter 3 it was seen that stress wave velocities within a solid depend upon the elastic moduli. The elastic moduli of early-age concrete increases with age as the cement paste matures. Figures 8-14 through 8-16 show the progressive gain of elastic parameters for the six concrete mixes with time. Overall, the gain in elastic parameters is similar to the gain in elastic wave velocities. More specifically, the increase in Young's modulus is similar to the increase in P-wave velocities with time. Also, the increase in shear modulus is similar to the increase in S-wave velocity with time. The bulk modulus shows a rapid increase for the first two days, followed by an adjusting period of two to three days, and finally a smooth linear relationship with time. In the case of BN25, BN40, and BN50 the adjusting period is shown by an early drop and later gain of bulk modulus within three days. For BN20, BN30, and BN35 the gain in bulk modulus is steady, however the values are slightly scattered.

In general, the elastic moduli of a composite depends on the elastic moduli of individual components in it. A concrete mix is composed of coarse and fine aggregates, cement paste and water. At an early age the concrete is a fluid-solid mixture. Later on as the chemical reactions between the coarse and fine aggregates start, a large number of water-filled pores are left behind. At this stage, stress wave velocities are low. The water in the pores is used eventually by the cement to create cement gel. Cement gel reacts with the aggregates and interlocks the components of the mix. As the volume of pores decrease the interlocking between cement and aggregates increase. Hence, the stress wave velocities and consequently the elastic moduli increase. The increase in elastic moduli as hydration proceeds is attributed to the reduction of porosity of the paste, and to the increase in the degree of interlocking between the cement paste and aggregates.

Figures 8-8 through 8-10 show the development of Poisson's ratio computed by the MSR system. The values of Poisson's ratio demonstrate scattering by sharp increases and decreases for the first seven days. After the first seven days the Poisson's ratio of the samples are almost consistent.

Over a period of 28 days the values for elastic wave velocities and elastic constants were monitored by the MSR system. The computed results clearly show the development of the elastic properties with concrete maturity. It was also observed that for the concretes having higher compressive strength values, the elastic wave velocities and the values of Young's, shear and bulk moduli are higher. However, the values for Poisson's ratio does not show a clear correlation with concrete stiffness.

Plate 8-2 Arrangement of vertical displacement transducer and the impact device on concrete cylinders.

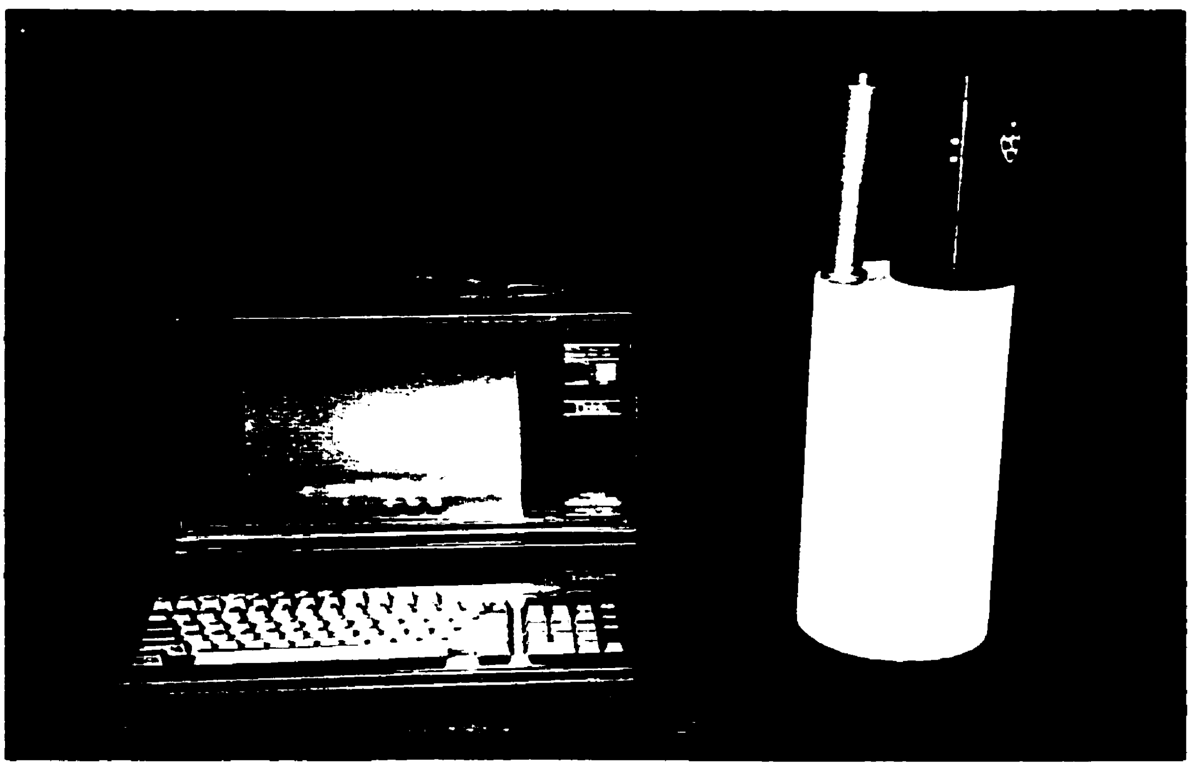

Plate 8-3 Arrangement of tangential displacement transducer and the impact device on concrete cylinders.

8.4.2 Determination of Resonant Frequency (RF) Response

The Grindosonic apparatus was used for testing the resonant frequency of the prismatic concrete specimens (see Plate 8-4). A more detail description of the Grindosonic instrument and testing methodology is given in Appendix A. The testing apparatus functions based on the ASTM C 215 (1986) requirements. The prismatic samples were 400 mm × 100 mm × 100 mm in dimension. Tests were conducted with samples resting on a foam rubber mat. The top face of each specimen was struck at its central point with a thin circular steel rod. The piezoelectric detector was held in contact with the samples at the center of one of the side faces. Dampening of the vibrations depends on the elastic properties of each sample. The flexural, torsional, and longitudinal frequencies of the six different concrete specimens were collected at regular daily intervals during the curing period. By utilizing the dimensions and density of the samples, dynamic Young's modulus, shear modulus, Poisson's ratio and bulk modulus were calculated for each sample at regular daily intervals.

Figures 8-14 through 8-16 show the development of elastic constants calculated by the RF technique. Similar to the MSR and the static values the values of elastic constants calculated by the RF technique increase rapidly for the first seven days. This sharp increase in elastic properties reduces its rate and the relationship becomes more smoother as the sample matures. Overall, the data obtained by the RF system are more scattered for the first seven days than for the rest of the curing period. This can be observed particularly in the case of BN50.

Figures 8-8 through 8-10 show the development of Poisson's ratio computed by the RF technique. For the Poisson's ratio, the values for the first seven days are scattered. For each batch the behavior of the Poisson's ratio is different. For BN20 there is a sharp increase up to the second day and then the Poisson's ratio drops gradually until it stabilizes at the 21st day. For BN25 there is a drop in Poisson's ratio from first to second day then it increases until the seventh day and then it stabilizes. For the BN30 there is a sharp increase in Poisson's ratio until the seventh day and then it stabilizes. BN35 behaves similar to the BN25. For BN40 there is a drop for the Poisson's ratio from first to second day, then there is a sharp increase followed by a drop and later it stabilizes by the 28th day. For the BN50 the Poisson's ratio increases by the second day then decreases and stabilizes by the 21st day. Over the 28-day curing period it was clearly observed that the values of elastic constants computed by the RF technique were increasing as the concrete batches matured. It was also observed that the Young's, shear and bulk modulus of the stronger batches were higher. However, the computed Poisson's ratio does not show a clear relationship with concrete stiffness.

8.4.3 Comparison of MSR and Resonant Frequency (RF) Results

Figures 8-14 through 8-16 show a comparison between the values of dynamic elastic parameters computed by the MSR system and RF technique. For all the six concrete mixes the gain in elastic properties, whether calculated by the MSR system or the RF technique, follows the same pattern with time. For BN25, BN30, BN35, BN40, and BN50 the values of Young's, shear and bulk moduli are higher when they were obtained by the RF technique than for the same parameters computed by the MSR system. In the case of BN20 the values computed by the MSR system are higher than the values obtained by the RF technique. In other words, in the case of very weak concrete, BN20, the values of MSR are higher than the values of RF. For the weak, intermediate and strong concretes RF values are higher than the MSR values. The discrepancy between the MSR values and the RF values are greatest for BN20. For BN25 the gap between the values obtained by the two system reduces. For BN30, BN35 and BN40 there is only an small gap between the values obtained by the two systems and the progress and gain of elasticity for the three batches can be seen to be almost identical. In the case of BN50 the gap between the results obtained by the MSR and the RF increases, particularly in the case of Young's and bulk moduli. Also, the elasticity values obtained by the RF show more scattering for the first five days of curing than the values obtained by the MSR system.

In case of monitoring the Poisson's ratios with time by the two systems, in Figures 8-8 through 8-10, the values obtained by the MSR system are less scattered than those obtained by the RF technique. However, for both techniques the Poisson's ratio values for the first seven days are not stable and do not follow a regular trend. Table 8-2 shows the comparison between the MSR and the RF data.

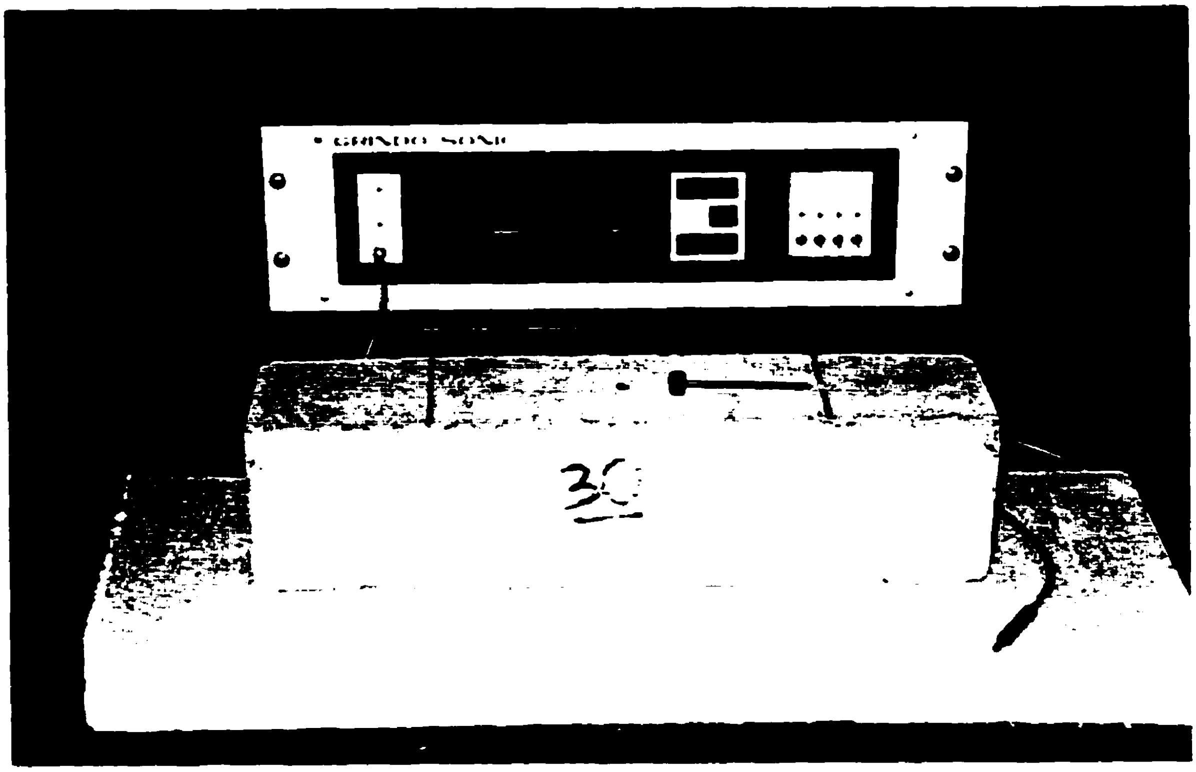

Plate 8-4 The resonance frequency test equipment used in monitoring the concrete samples.

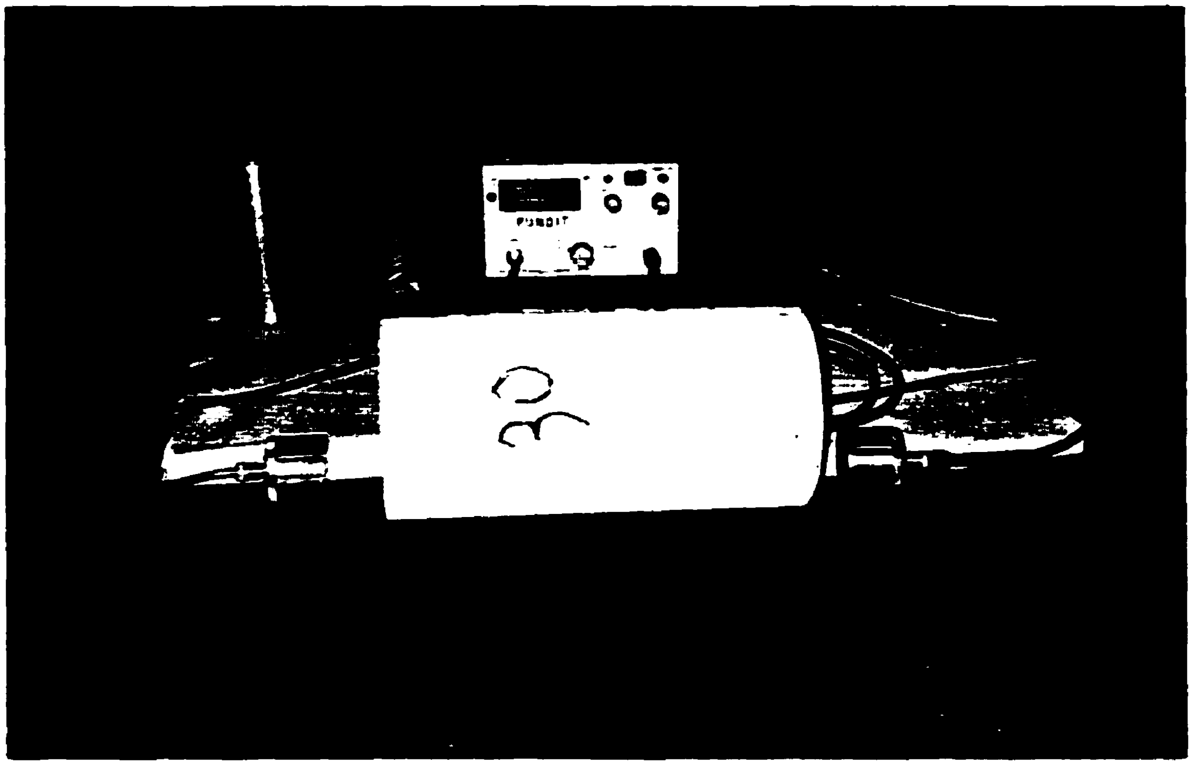

Plate 8-5 UPV test equipment used for monitoring the concrete cylinders.

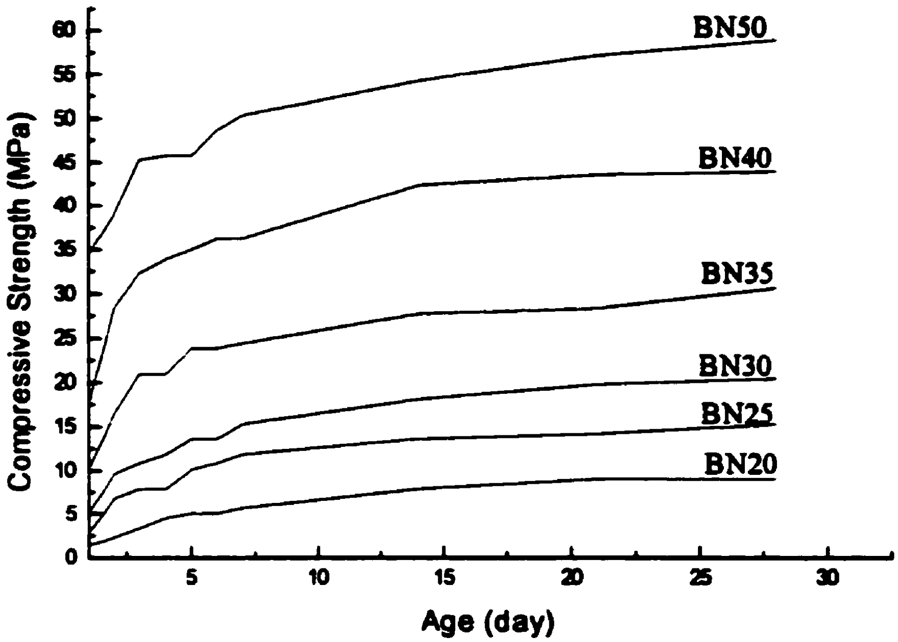

(a)

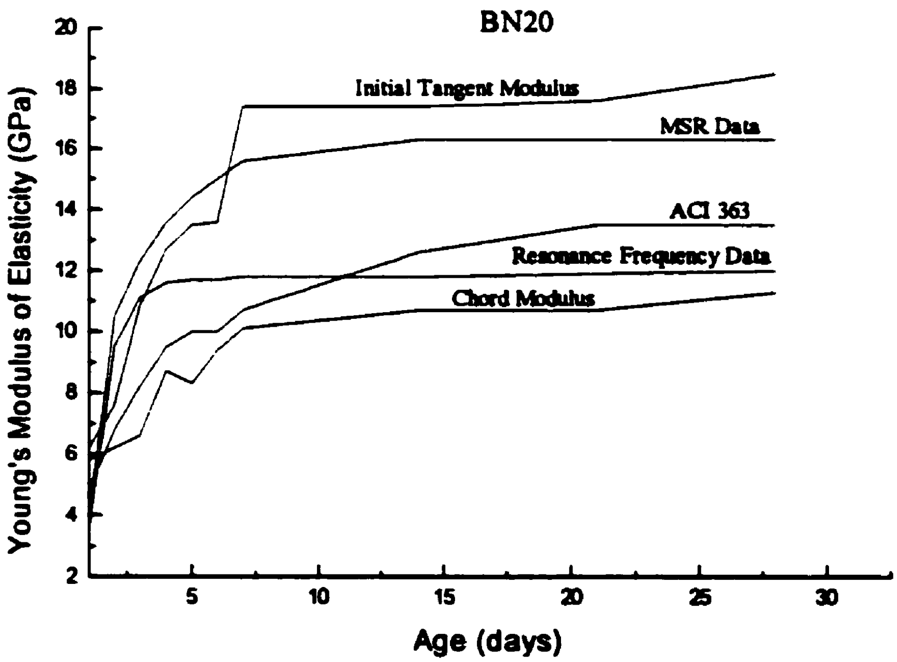

(b)

Figure 8-4 a) Compressive responses of six mixes with curing time, b) developments of Young's modulus by various techniques for BN20.

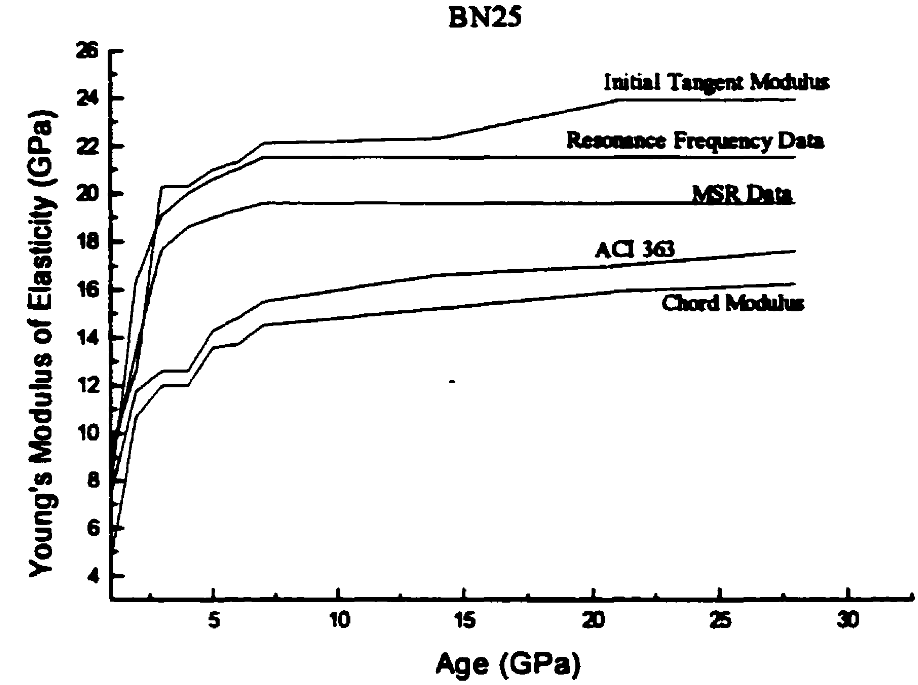

(a)

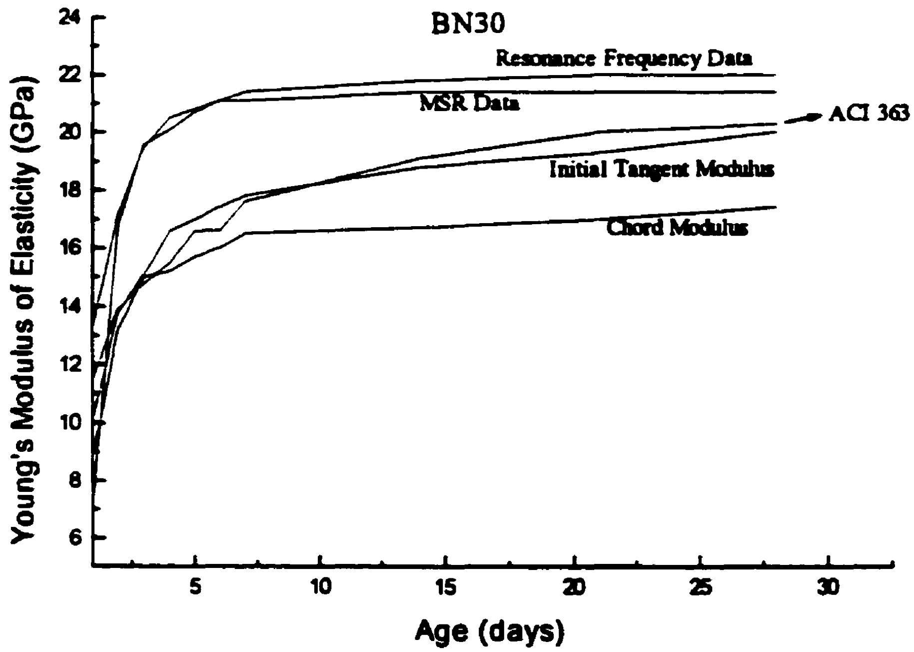

(b)

Figure 8-5 a) Developments of Young's modulus by various techniques for BN25, and b) for the BN30.

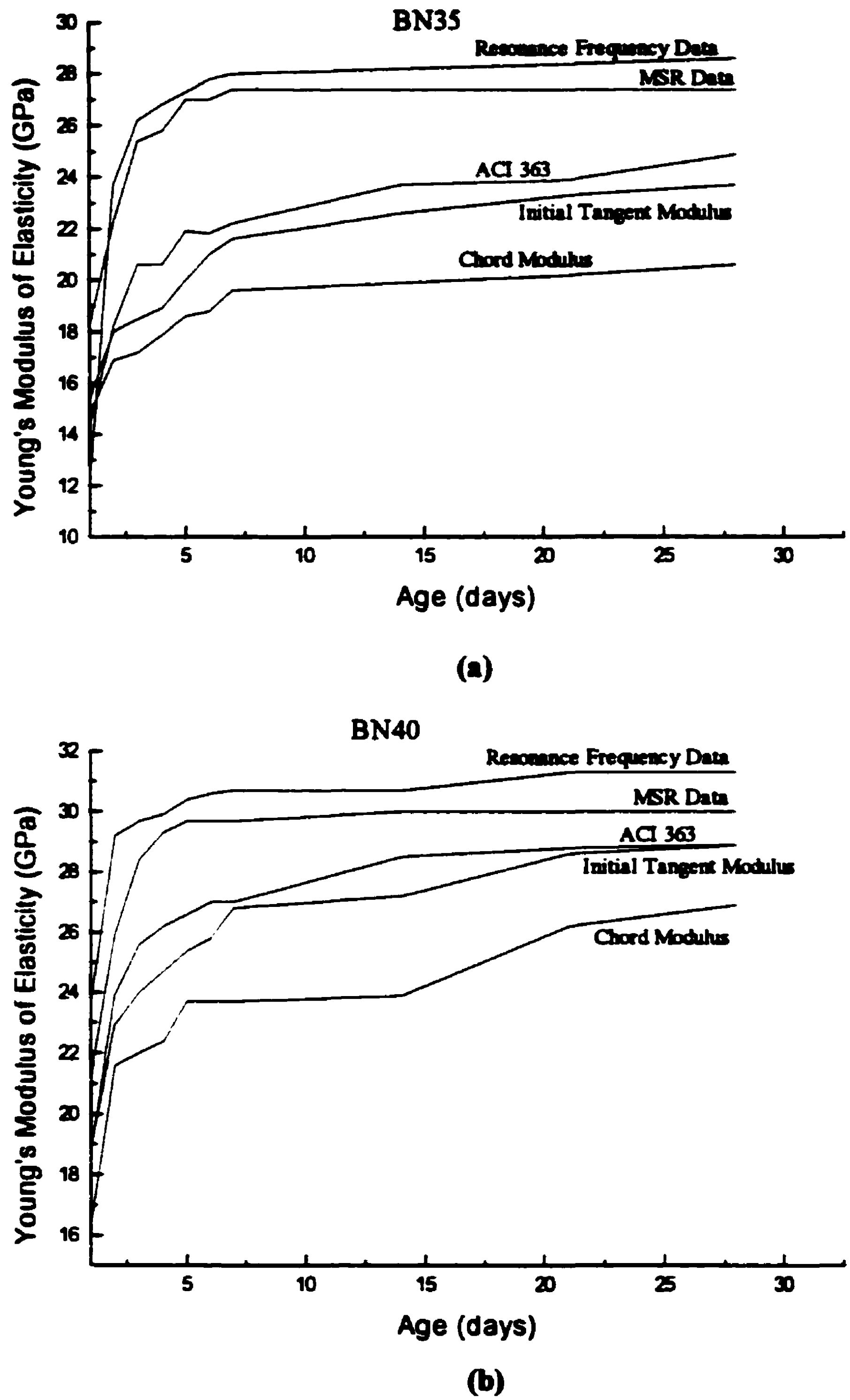

Figure 8-6 a) Developments of Young's modulus by various techniques for BN35, and b) for the BN40.

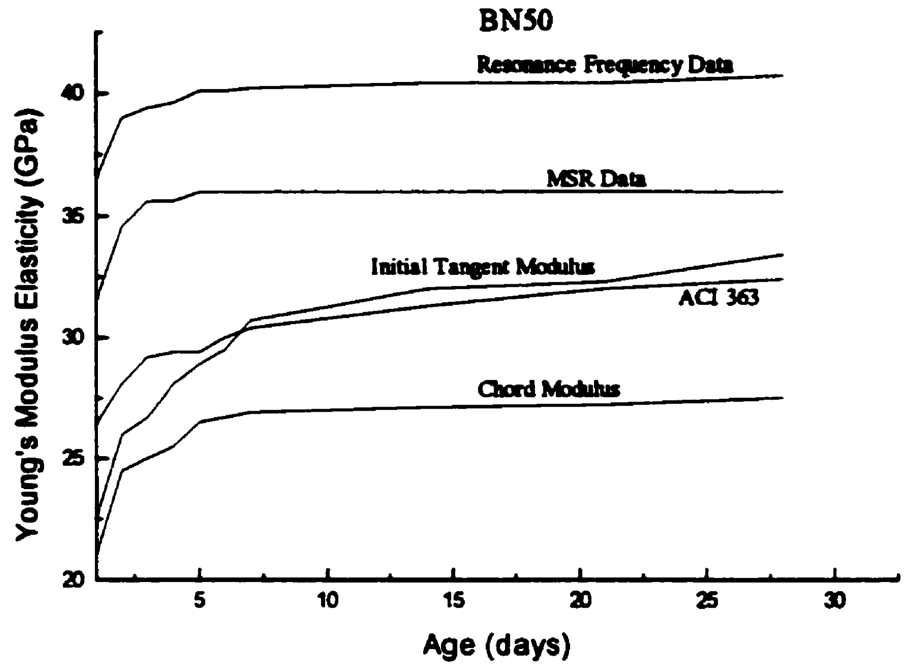

(a)

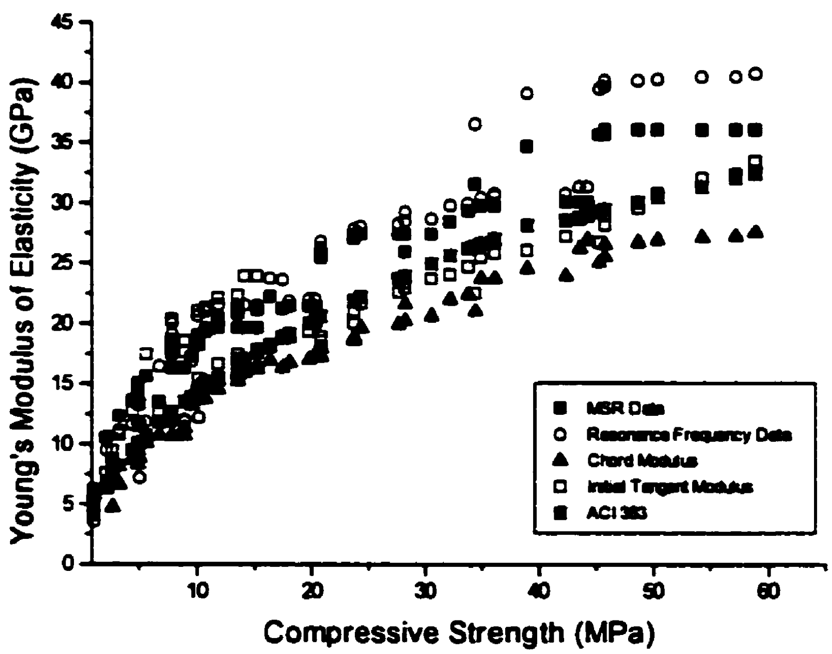

(b)

Figure 8-7 a) Developments of Young's modulus by various techniques for BN50, and b) the relationship between computed values of Young's modulus by various techniques and compressive strength.

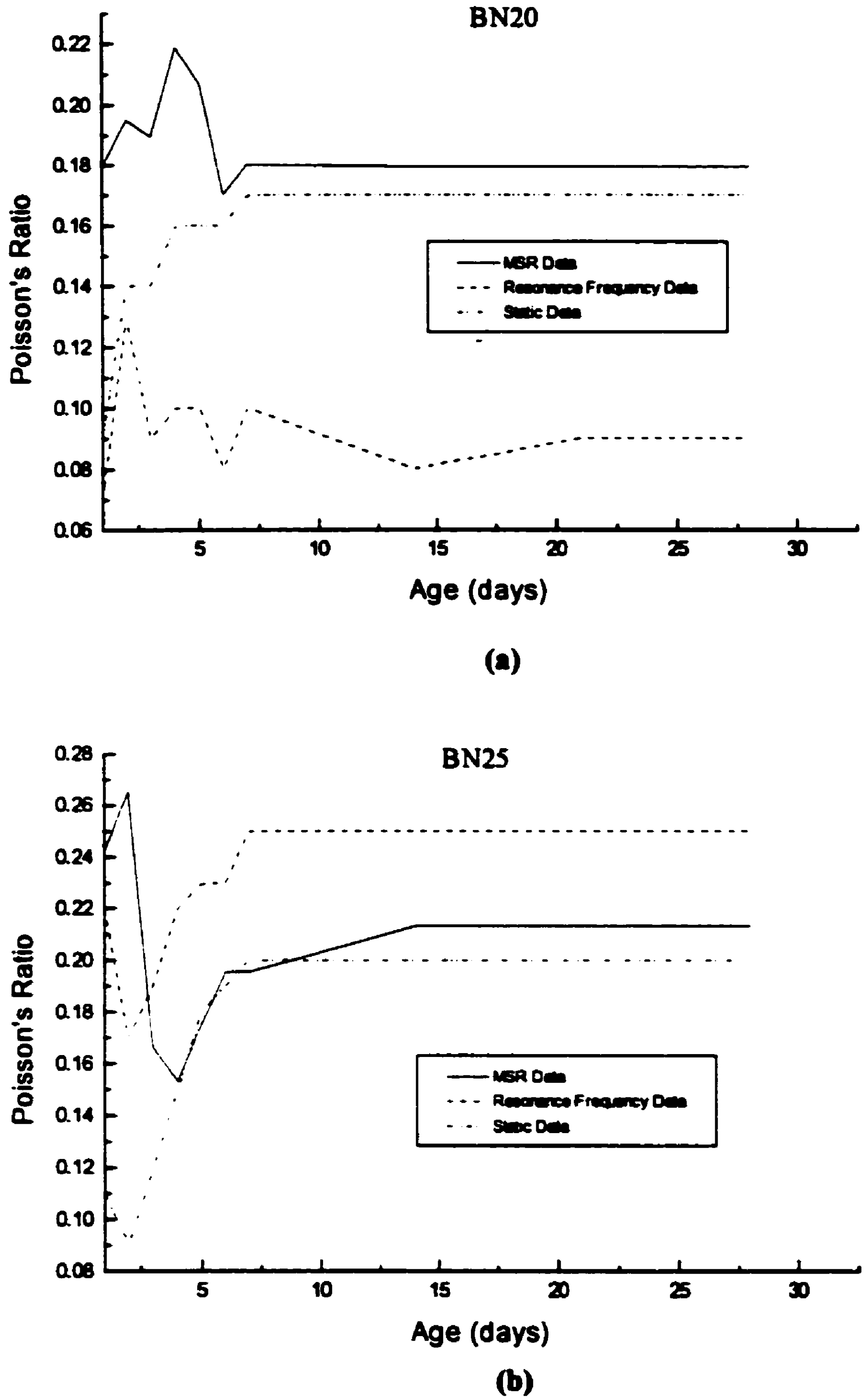

Figure 8-8 a) Developments of Poisson's ratio by various techniques for BN20, and b) for the BN25.

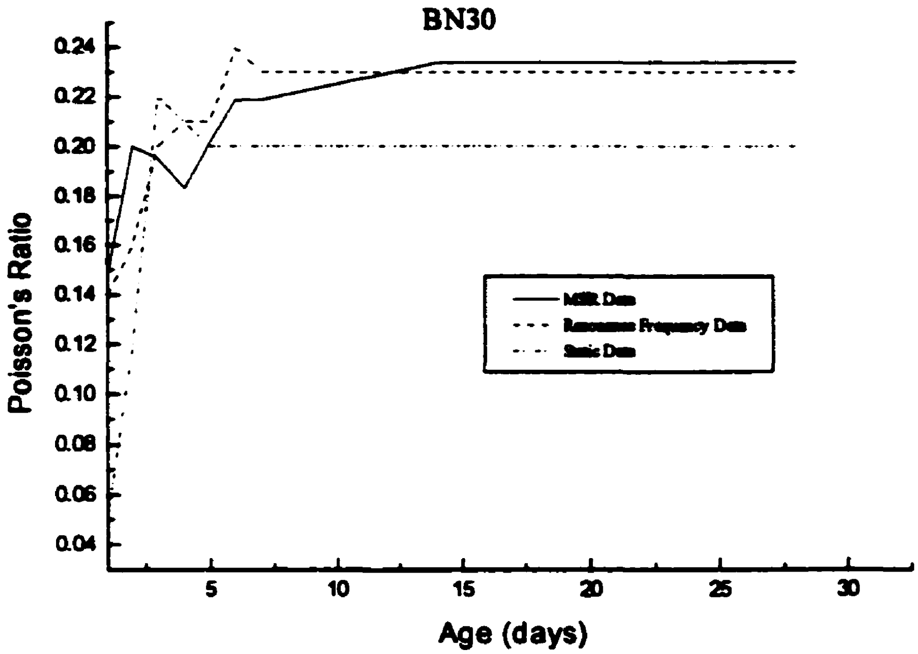

(a)

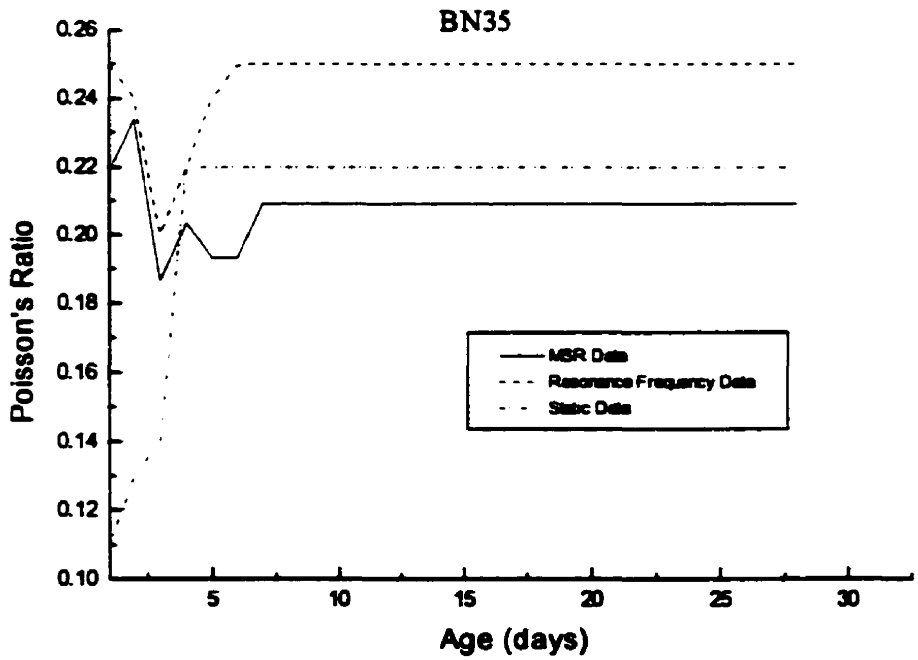

(b)

Figure 8-9 a) Developments of Poisson's ratio by various techniques for BN30, and b) for the BN35.

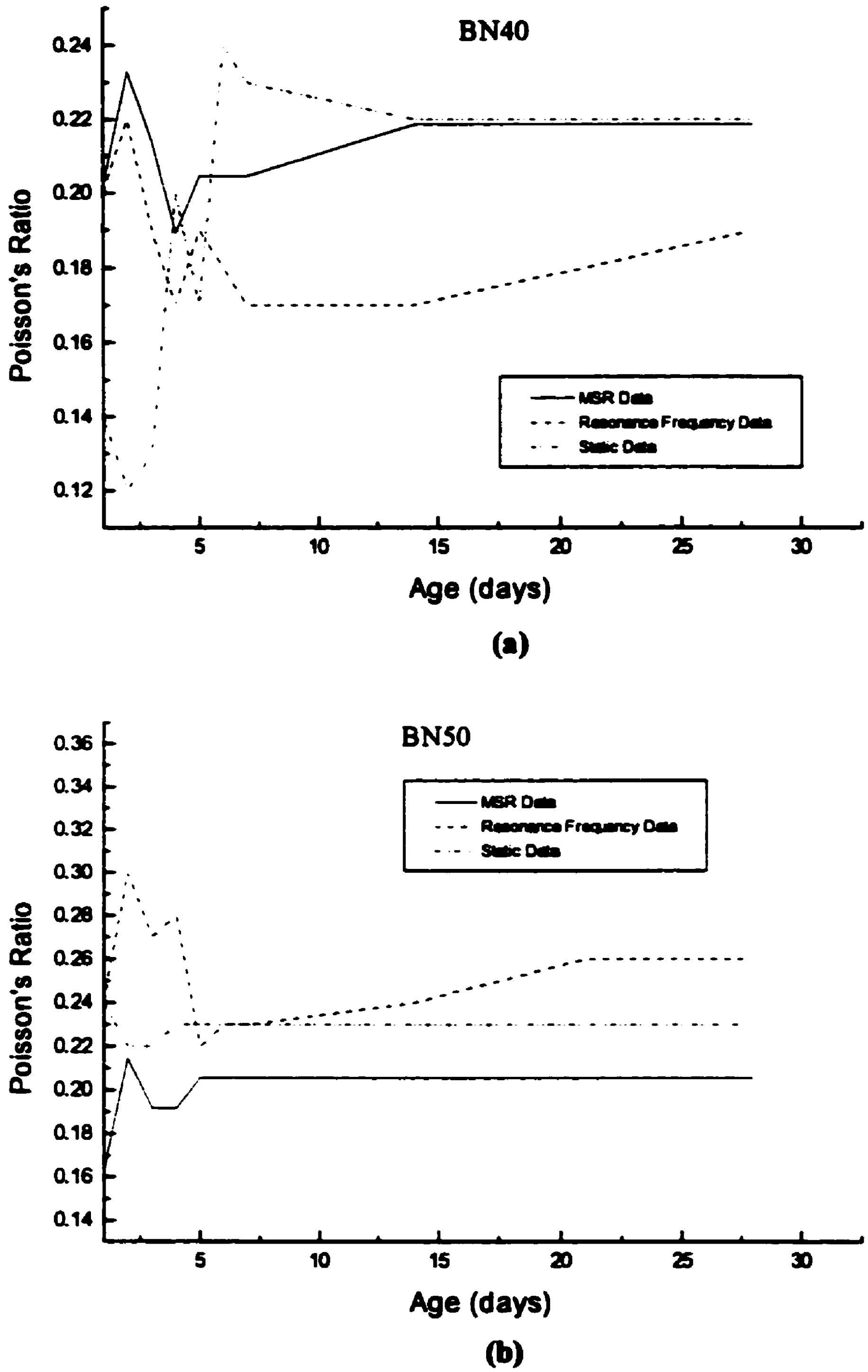

Figure 8-10 a) Developments of Poisson's ratio by various techniques for BN40, and b) for the BN50.

Table 8-2 A general comparison between MSR and RF data.

	υ	E GPa	G GPa	K GPa
BN20	MSR>RF	MSR>RF	MSR>RF	MSR>RF
BN25	MSR<RF	MSR<RF	MSR<RF	MSR<RF
BN30	MSR>RF	MSR<RF	MSR<RF	MSR<RF
BN35	MSR<RF	MSR<RF	MSR<RF	MSR<RF
BN40	MSR>RF	MSR<RF	MSR<RF	MSR>RF
BN50	MSR<RF	MSR<RF	MSR<RF	MSR<RF

As for the instrumentation, the RF testing requires access to the three surfaces of the testing area, while the MSR system only requires access to one side of the testing area. The RF technique provides the elastic characteristics of concrete depending on the size and shape of specimen. The MSR system on the other hand, only requires the knowledge of thickness of the specimen and the calculations can be done independent of shape of the samples.

8.4.4 Determination of Ultrasonic Pulse Velocity (UPV)

Measurements of UPV were made using a PUNDIT instrument with 50 kHz transducers (see Plate 8-5). A more detail description of the PUNDIT apparatus and testing methodology is given in Appendix B. The digital display of the equipment was used for recording the travel times in microseconds. Wave velocities were determined by measuring the time taken for an ultrasonic pulse to traverse the sample. The cylindrical samples were placed between the UPV transmitter and receiver. The 0.3 m length of the cylinders were the transmission length. The first measurements of the ultrasonic P-wave velocities were conducted 24 hours after initial mixing. Prior to the first 24 hours, most of the collected data were scattered. Figures 8-11 to 8-13 show the development of pulse velocities in the six different concrete mixes. The results indicate that the setting times are different for various types of concrete mixes. For all the batches the P-wave velocities increase rapidly for the first seven days. After this period of dramatic increase, there is a decrease in the rate of velocity increase. That is after the first seven days, the ultrasonic wave velocities for most of the batches reach a stable value. However in the case of BN20 and BN25 the UPV value still increases with time but the rate is very small. In the case of BN40 and BN50 due to presence of super-plasticizer the UPV values stabilize after the first four days of curing.

Over the 28-day curing period it was observed clearly that the UPV values for higher strength concrete batches are higher. The higher velocities can be attributed to coarser aggregate and cement contents of the higher strength concretes.

8.4.5 Comparison of MSR and UPV Results

Figures 8-11 through 8-13 show the increase of body wave velocities with curing time obtained by the UPV and MSR systems. For all the six concrete mixes the ultrasonic wave velocities are higher than the P-waves velocities determined by the MSR system. This difference between the P-wave velocities measured by the two techniques was expected, and has been demonstrated by others (Philleo, 1955; Sansalone, 1985, and Sadri, 1992). The reason for this difference is not well established yet. However, it is clear that the frequencies of the reflected stress waves generated by the impact can be used to monitor the development of P-and S-wave velocities.

Table 8-3 A general comparison between MSR and UPV P-wave velocity data.

	C_P m/s
BN20	MSR<UPV
BN25	MSR<UPV
BN30	MSR<UPV
BN35	MSR<UPV
BN40	MSR<UPV
BN50	MSR<UPV

One reason for this difference could be due to the propagation characteristics of the ultrasonic and stress waves. In making velocity measurements by the UPV and the MSR techniques, because of the fact that concrete contains about 75% aggregate by volume, the velocity is measured along a path three-quarters of which lies in aggregate and only one-quarter in cement paste. It is expected that the velocity measurements are mainly sensitive to the properties of aggregates rather than cement paste. Also, usually aggregates have higher elastic properties than the paste. The high frequency UPV travel along a narrow beamwidth, but the stress waves generated by the MSR system travel along a broader beamwidth. In the case of the ultrasonic pulses, the narrow beamwidth of the signal is more sensitive to the aggregate properties. On the other hand, the broader beamwidth stress pulses travel through a larger portion of the concrete and are more effected by either cement paste, voids and aggregates. One advantage of the MSR signals is their quality in seeing the properties of the specimens more globally than the ultrasonic pulses.

The UPV technique is fast and effective for measuring the P-wave velocities in the concrete where two sides of the test specimen are accessible. However, since the ultrasonic pulses are highly affected by the aggregate properties in a narrow beamwidth, elastic modulus values calculated by the ultrasonic wave velocities might not reflect the global properties of the concrete. The use of couplants such as petroleum gelly and grease in the case of UPV testing is essential while in the case of the MSR system no couplant is required to provide good contact between the transducers and the concrete surface. The relatively high-frequency ultrasonic pulses (50 kHz standard) are more severely attenuated than the lower frequency stress pulses of the MSR. This can limit the capability of the UPV systems in monitoring areas with a long pathlength (thick specimens or structures). Table 8-2 shows the comparison between the MSR and the UPV P-wave velocities.

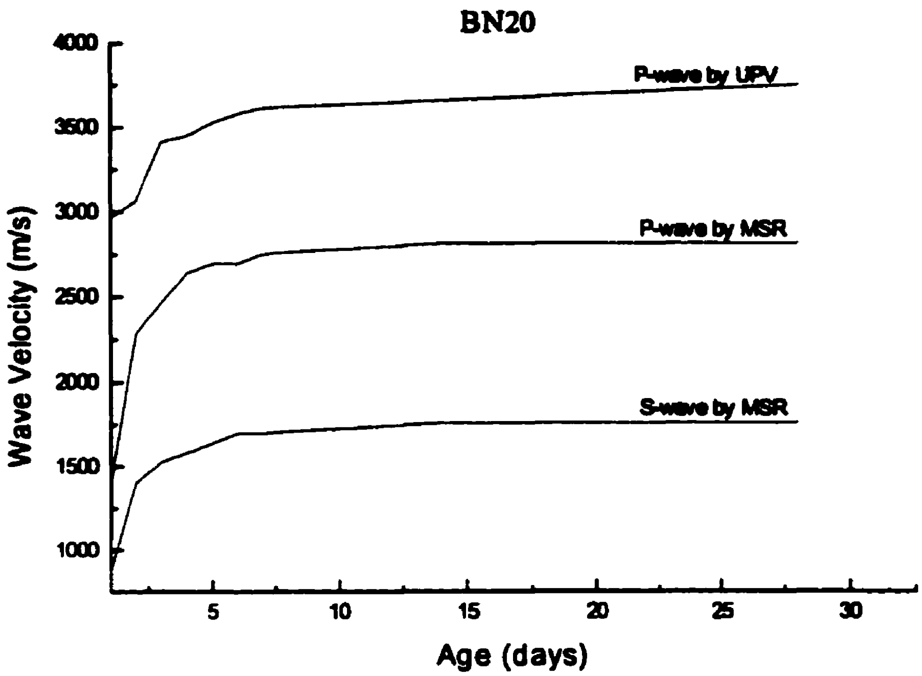

(a)

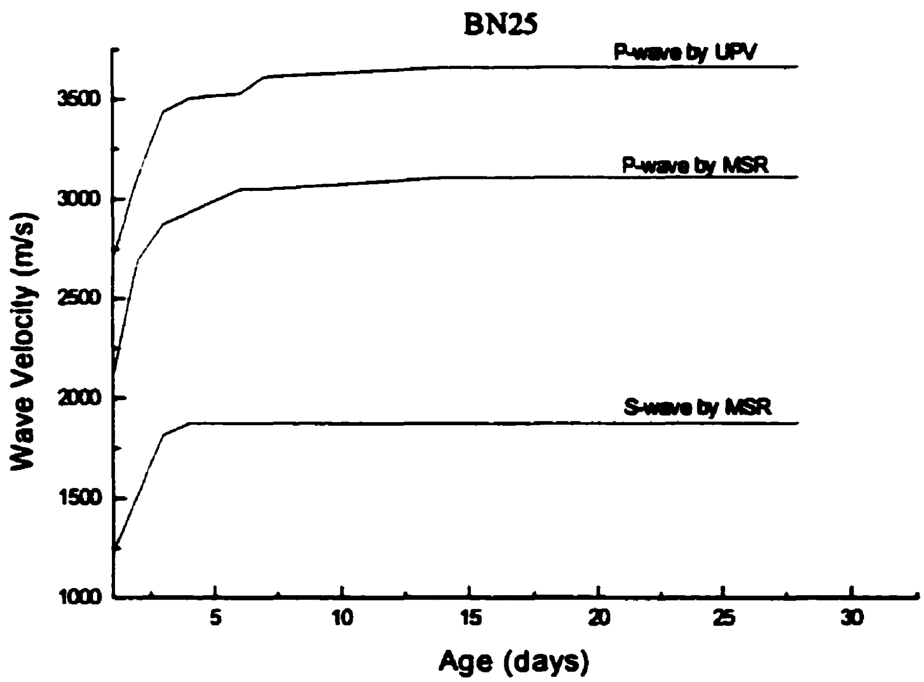

(b)

Figure 8-11 Developments of P- and S-wave velocities by the UPV and MSR systems for a) BN20 and b) BN25.

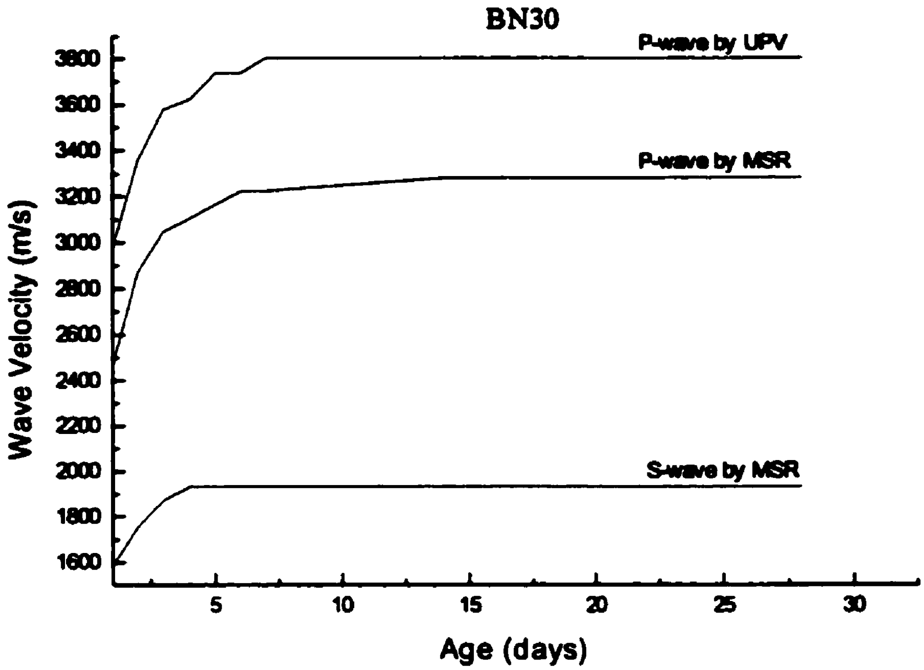

(a)

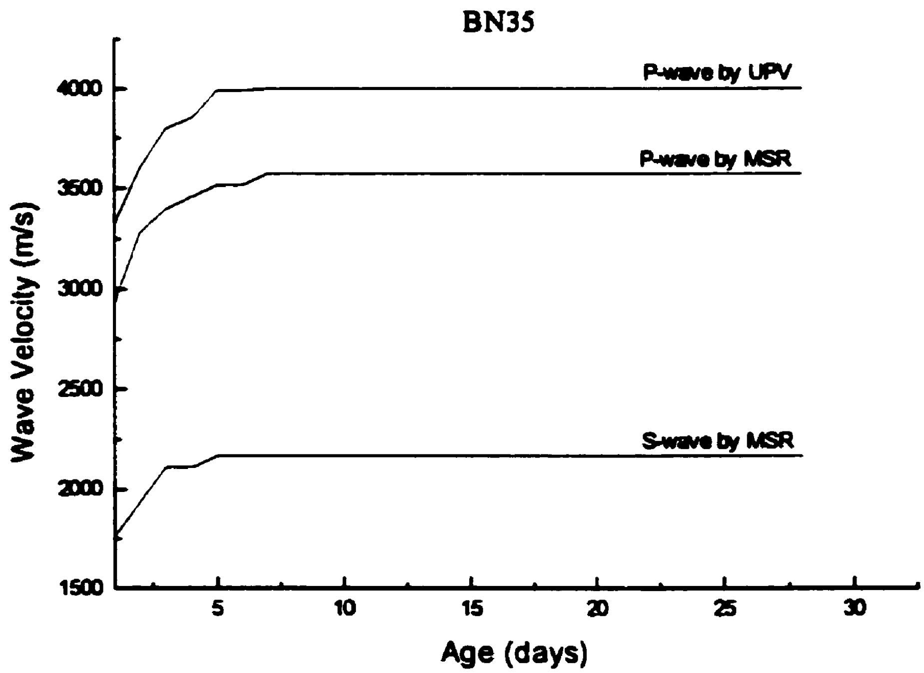

(b)

Figure 8-12 Developments of P- and S-wave velocities by the UPV and MSR systems for a) BN30 and b) BN35.

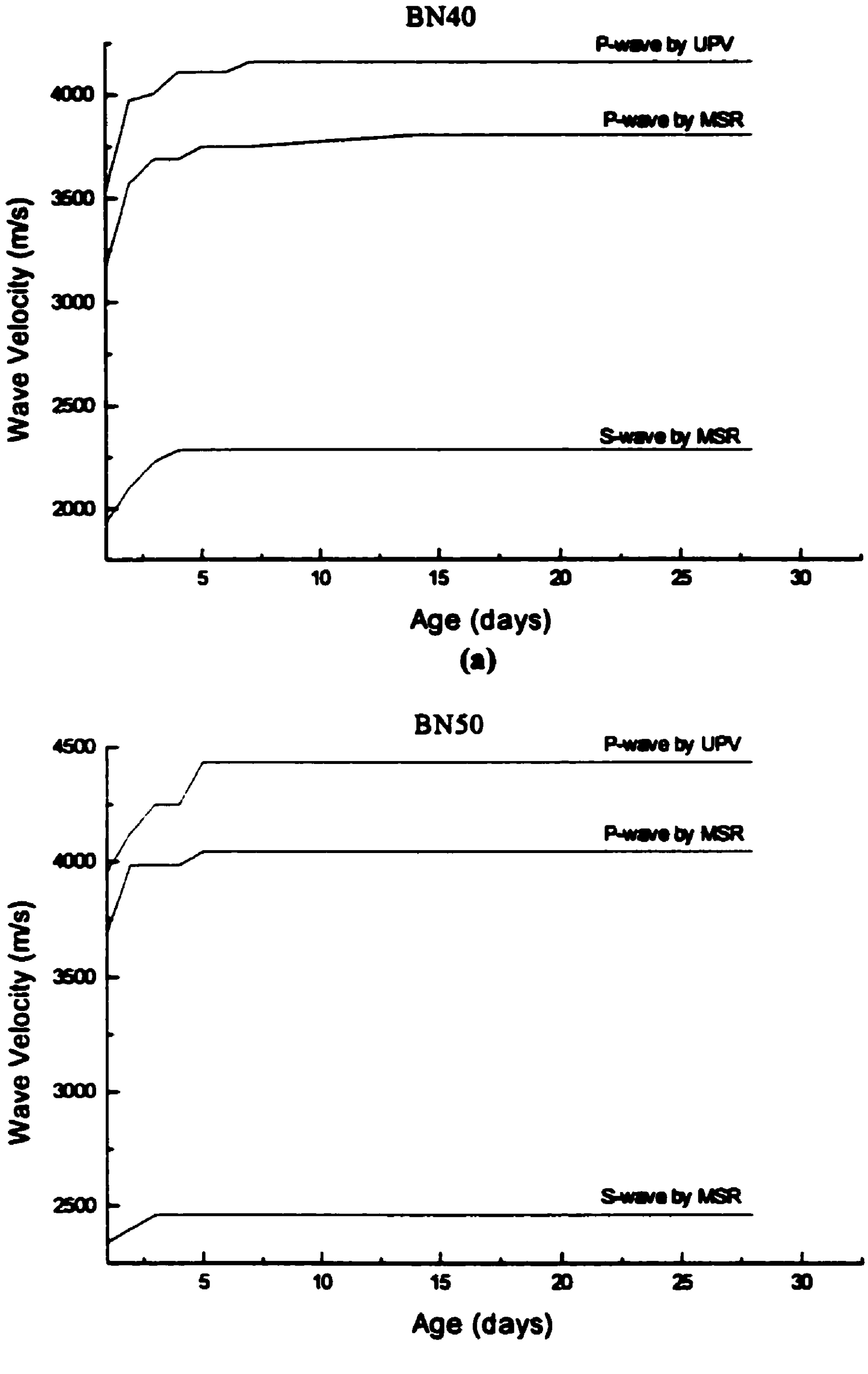

(b)

Figure 8-13 Developments of P- and S-wave velocities by the UPV and MSR systems for a) BN40 and b) BN50.

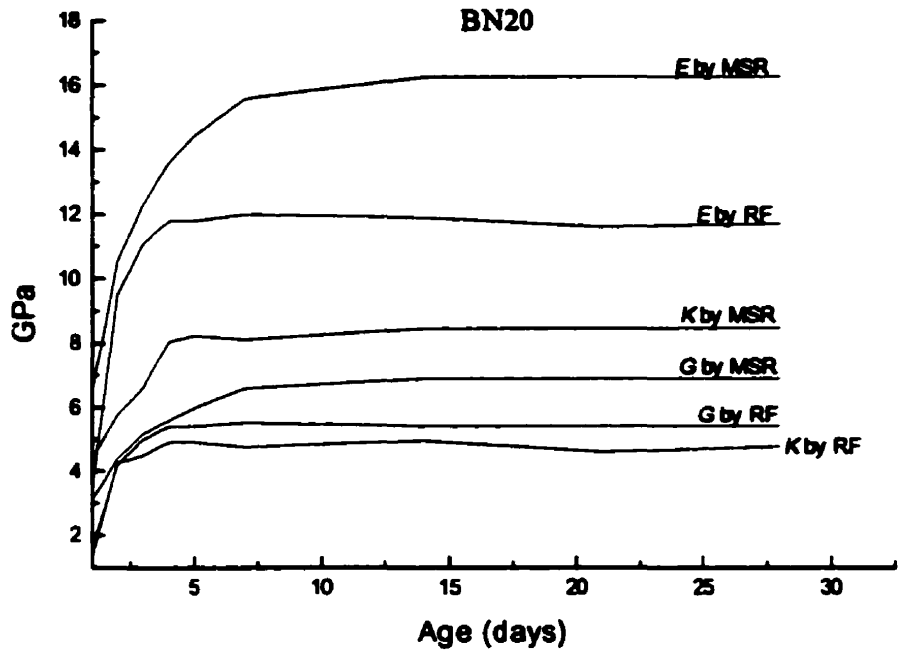

(a)

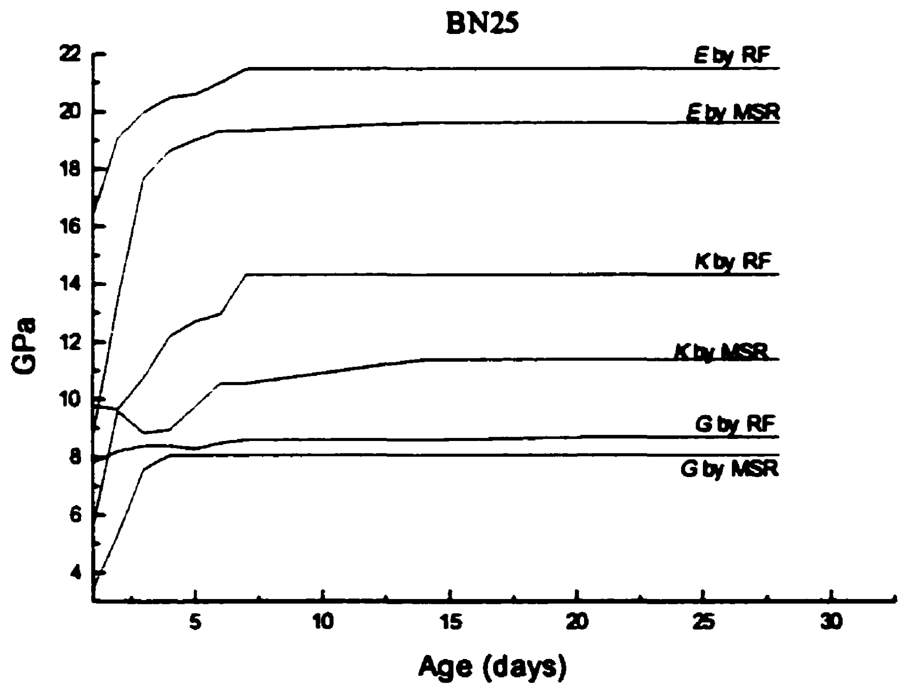

(b)

Figure 8-14 Developments of dynamic Young's, shear and bulk modulus by the MSR systems and resonance frequency technique, for a) BN20 and b) BN25.

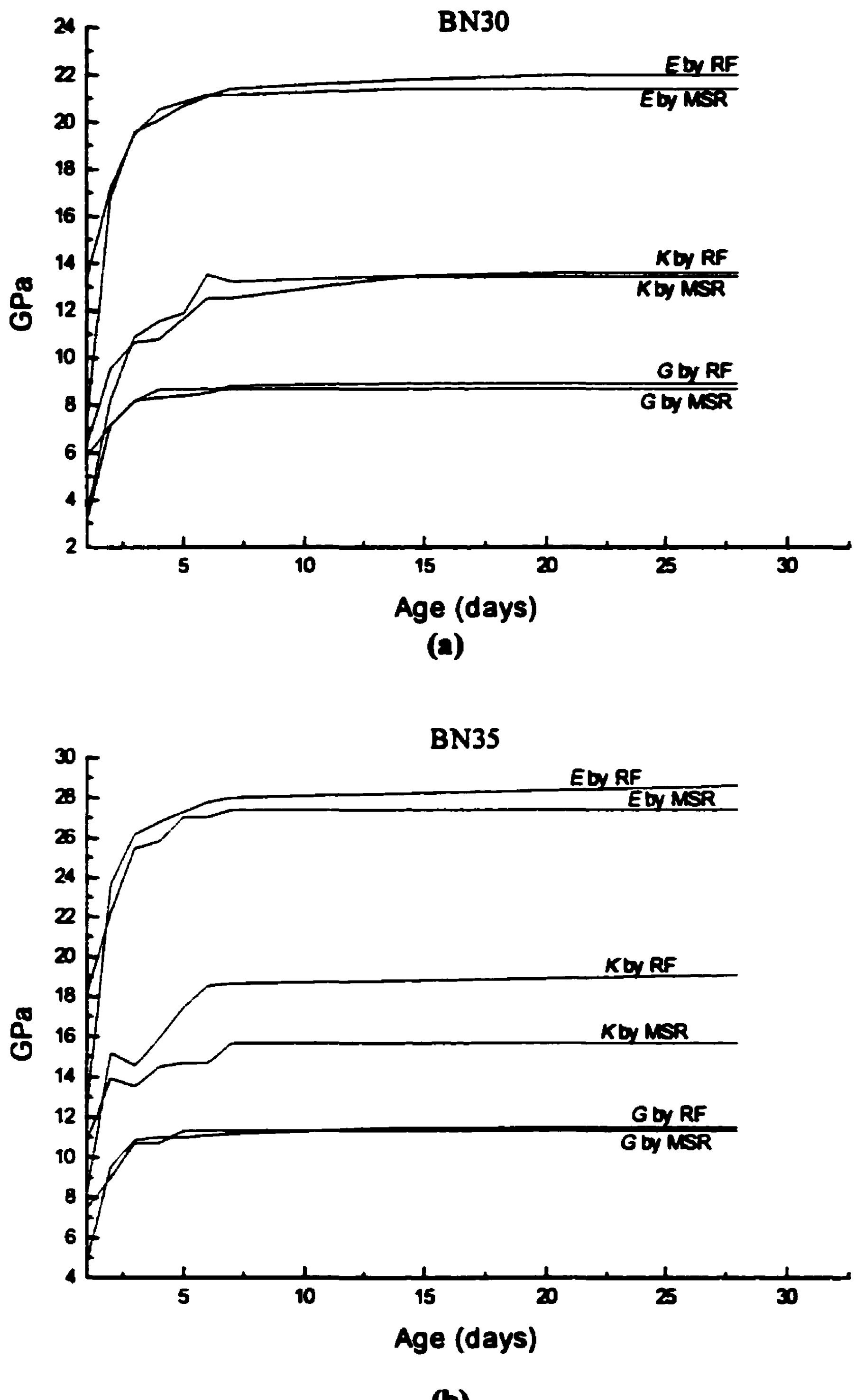

Figure 8-15 Developments of dynamic Young's, shear and bulk modulus by the MSR systems and resonance frequency technique, for a) BN30 and b) BN35.

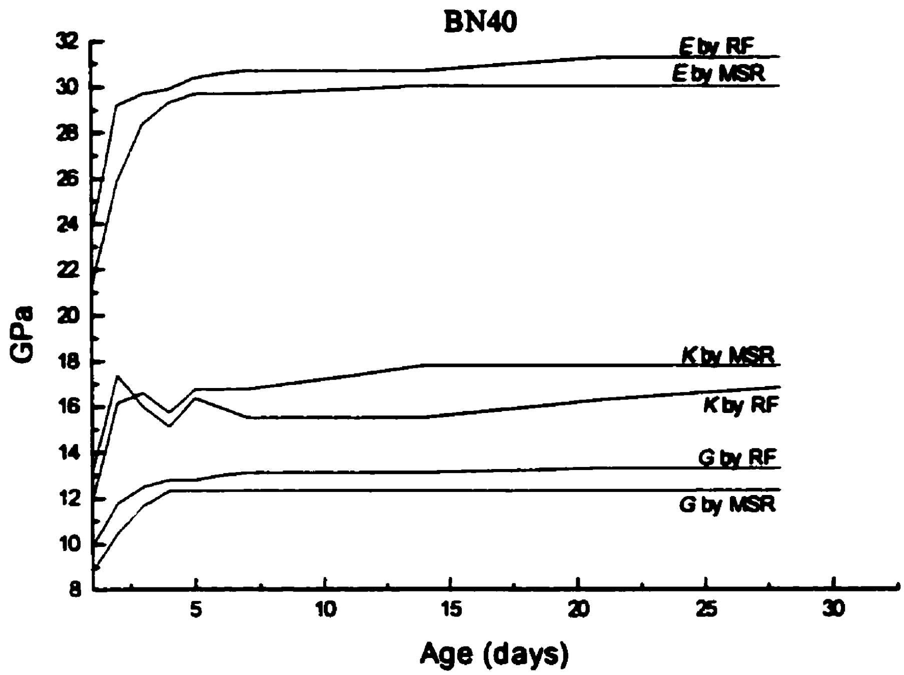

(a)

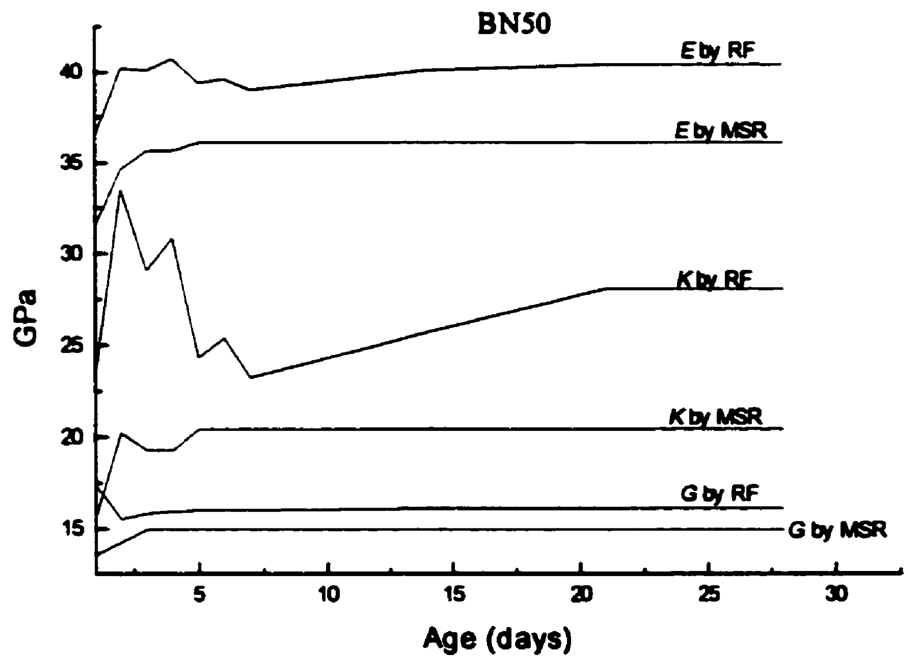

(b)

Figure 8-16 Developments of dynamic Young's, shear and bulk modulus by the MSR systems and resonance frequency technique, for a) BN40 and b) BN50.

8.4.6 Comparison of Static and Dynamic Elastic Constants

Figures 8-4b through 8-7a show the initial tangent and chord modulus, and the dynamic Young's modulus computed by the MSR and the RF systems. For all the batches the values of chord modulus is smaller than the dynamic Young's modulus. The discrepancies between the dynamic and static values were expected and the known explanations are given in detail in Section 5.7. The dynamic methods should not be used to check or evaluate the static methods. The two methods are independent of one another. The dynamic methods deal almost entirely with elastic parameters of concrete composition but the static measurements are complicated by inelastic deformations, microfractures and pores. Also, various methods are affected by the heterogeneity of concrete in different ways. However, it is important to compare the results of newly assembled MSR system with expected results obtained by various systems to evaluate the validity of the data computed by the MSR.

In comparing the results obtained in this study, except BN20, the Young's moduli obtained by the MSR are closer to the chord modulus than the RF values. This can be seen in the case of BN50 where the RF values are up to 38% higher than the chord modulus whereas the MSR values are 28% higher. This could be related to the fact that the strains generated by the MSR system is higher than that of the RF system.

The Poisson's ratio obtained by the MSR, for all the different concrete mix is in close agreement with the static values, compared to the Poisson's ratios obtained by the RF technique. The biggest discrepancy can be seen in the case of BN30. Only in this case, the RF values show better agreement with static values. Table 8-4 shows the comparison between the MSR, static and predicted data.

8.4.7 Comparison of Static and Dynamic Elastic Constants with Strength

Figure 8-7b shows all the values of Young's modulus versus compressive strength for the six concrete mixes obtained by various techniques. From the graph it can be seen that there is a clear correlation between the values of elastic moduli and the compressive strength. Both dynamic and static values obtained in this study constantly increase with the increase in compressive strength. The values of elastic moduli for the MSR and RF techniques are more scattered when the compressive strengths are above 40 MPa. From Figure 8-7b it can be concluded that the MSR data are well correlated with the values obtained by other standard techniques.

The graph in Figure 8-7b shows that the empirical relationship established by Pauw (1960) maybe used for the values obtained by the MSR system as well as other dynamic and static techniques. Pauw's relationship states that for mature concrete the modulus of elasticity of concrete, E_c, is proportional to the square root of compressive strength f_c, or

$$E_c = \alpha\sqrt{f_c} \tag{8-1}$$

The results from Figure 8-7b suggests that the above relationship is also true for immature concrete.

Table 8-4 A general comparison between MSR, static and predicted data.

	υ	E_{Chord} GPa	$E_{\epsilon.Tan.}$ GPa	E_{ACI363} GPa
BN20	MSR>Static	MSR>Static	MSR<Static	MSR>Static
BN25	MSR>Static	MSR>Static	MSR<Static	MSR>Static
BN30	MSR>Static	MSR>Static	MSR>Static	MSR>Static
BN35	MSR<Static	MSR>Static	MSR>Static	MSR>Static
BN40	MSR<Static	MSR>Static	MSR>Static	MSR>Static
BN50	MSR<Static	MSR>Static	MSR>Static	MSR>Static

8.5 EFFECT OF AGGREGATE SIZE AND CEMENT TYPE ON THE MSR

To study the effect of aggregate size and cement type on the MSR's body wave velocities, a series of tests was conducted. Two different concrete batches were mixed and cured in the same environment. Both concrete types were 30 MPa; however in order to see the effect of aggregate size on the wave velocities one of the batches was prepared having 20.0 mm size aggregates (BNA) and the other batch was prepared with 10.0 mm size aggregates. Cement type 30 was used in both mixes in order to compare the effect of fast curing on the changes in stress and ultrasonic wave velocities. The rest of the mix specifications were kept similar for both batches. The concrete mix specifications were:

BNA:

Cement type	30
Concrete type	30 MPa
Average aggregate size	20 mm
Slump	130 mm
Air content	6 to 8%
Water/cement ratio	0.47
Density	2260

BNB:

Cement type	30
Concrete type	30 MPa
Average aggregate size	10 mm
Slump	120 mm
Air content	6 to 8%
Water/cement ratio	0.47
Density	2175

Concrete cylinders with 152×305 mm dimensions were cast. A total of 72 concrete cylinders were cast, half of which were from BNA batch and the other half were from BNB batch. All of the cylinders were hand-rodded in accordance with ASTM C 31 (1988). All of the specimens were covered with plastic sheets for 24 hours after casting and kept in the laboratory environment (i.e., ambient temperature of 22 ± 1°C and relative humidity of $50 \pm 10\%$). The specimens were not demolded and were kept in the same condition for the 28-day curing period. Curing was achieved by leaving the specimens in the laboratory temperature and humidity condition. The curing conditions were kept the same, air-dried curing, for both mixes.

The 28-day unconfined compressive strengths of the cylinders were determined using a standard compressive testing machine (MTS Model 315.03) with a maximum loading capacity of 4600 kN. The cylinders were tested under strain control as was recommended by the ASTM C 39-86 (1988). The axial strain was measured by MTS extensometers (Model 632.94), with 200 mm gauge lengths, placed on opposite faces of the specimen. The maximum 28th day compressive strength of BNA was 38.0 ± 0.7 and for the BNB was 39.0 ± 0.5 MPa.

Figure 8-17a shows the stress-strain responses for the BNA and BNB concretes for the 28th day. The graphs exhibit a difference between the stress-strain response of the two batches for the 28th day curing. The stress-strain responses indicate similar compressive strengths for both batches. However, BNA demonstrates higher elastic moduli and relatively lower strains than BNB.

The UPV and MSR readings were collected at daily intervals. The testing specifications and instrumentation for both techniques were kept the same as in the previous exercise. The travel times of the ultrasonic waves were used along the 0.3 m length of the cylinders to calculate the P-wave velocities. The frequency responses of the body waves on the concrete cylinders were collected using vertical and tangential displacement transducers. The A/D card collected 2048 data points, recorded at a sampling frequency of 100 kHz (sampling intervals of 10 μs). Thus, the total duration of the record is 20480 μs. From equation 6-12, the frequency interval in the frequency spectrum is 0.049 kHz, which allows the wave velocities to be computed to the nearest 15 m/s. The stress wave velocities were calculated using equations 6-4 and 6-9 and the peak frequency values from the spectra generated by the vertical and tangential displacement transducers.

Figure 8-17b shows the development of the P-wave velocities obtained by the UPV and the MSR systems, and the S-wave velocities computed by the MSR system as the time progresses, from the resulting frequency spectra. The MSR and the UPV velocity determinations were attempted at an age as early as 24 hours (day 1) and the readings were collected for the next 28 days. As was expected from the previous study, the wave velocities increase as the concrete mixes cure during the 28 days period. Also similar to the results obtained from the previous study, the P-wave velocities computed by the UPV system are higher than the P-waves velocities derived by the MSR system. For all three wave types the velocities for the BNA are higher than the BNB concrete mix.

Notice that the size of coarse aggregates for the BNA batch are twice larger than for the BNB batch. Using the MSR system, at the 28th day the P-wave velocity of the BNA is 1.5% and the S-wave is 2.4% higher than BNB. For the same period, the ultrasonic waves computed for the BNA are 2.9% higher than the BNB.

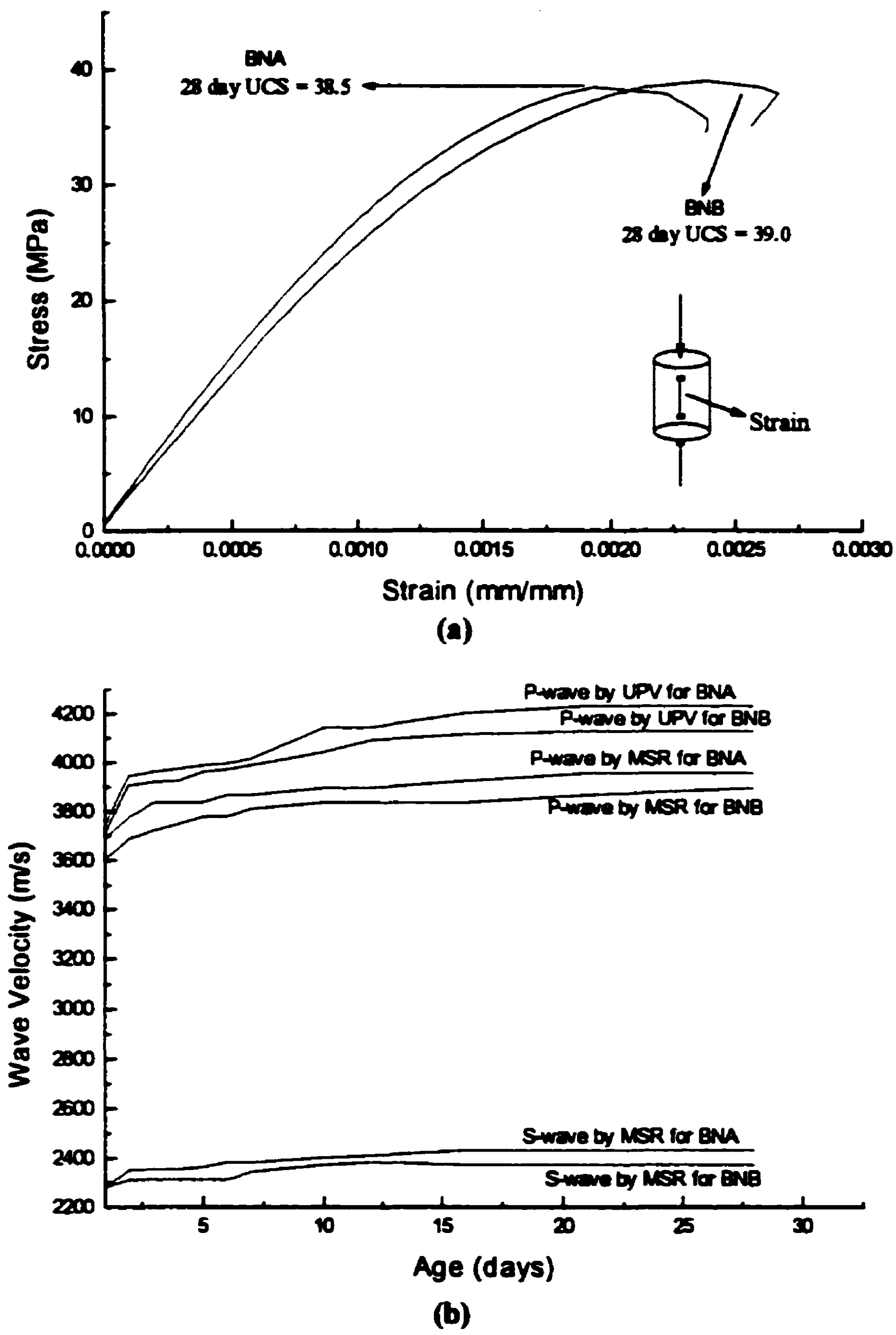

Figure 8-17 a) The stress-strain curve and maximum compressive strength for BNA and BNB at 28th day, b) the development of elastic wave velocities for BNA and BNB with maturity.

For the mixes in this study cement type 30 was used. Cement type 30 has quick setting properties. This means in comparison to the batches in the previous study, where cement type 10 was used, the BNA and BNB batches reach maturity in shorter time period. This change in cement type is detectable by the MSR and UPV systems. Comparing the velocity/age graphs from the previous study to the graphs obtained from BNA and BNB it can be seen that the period of dramatic increase in wave velocities is almost absent in Figure 8-17b. Because of the cement type, the rapid increase in wave velocities occur during the first 24 hours and prior to the testing period. However, in comparison between the UPV and MSR wave velocities, the UPV results are less affected by the cement type, having a sharp increase up to the second days.

Equations in Table 3-2 and the density values were used to compute the dynamic elastic properties of the two mixes having the body wave velocities were obtained by the MSR system.

Figure 8-18a shows the development of the Poisson's ratio for the two mixes with time. Similar to the results from the previous study, values of Poisson's ratio are scattered for the early-age concretes. The graphs indicate that the change in aggregate size and cement type does not have a substantial influence on the development characteristics of the Poisson's ratio. However, the Poisson's ratio of the BNB is slightly higher for the 28th day concrete than the BNA.

Figure 8-18b shows the development of the Young's, shear, and bulk moduli with maturity of the two concrete batches. As was expected from the previous study, the elastic parameters increase with curing time. Similar to the development of the P- and S-wave velocities in BNA and BNB, there is an absence of primary sharp increase in elastic parameters. This means that the use of fast-curing cement type 30 affects the development of the dynamic elastic parameters computed by the MSR system. For all cases, the elasticity values obtained for the BNA are larger than the BNB. These results confirm the relationship between stress-strain and elastic modulus for the two batches that was discussed previously.

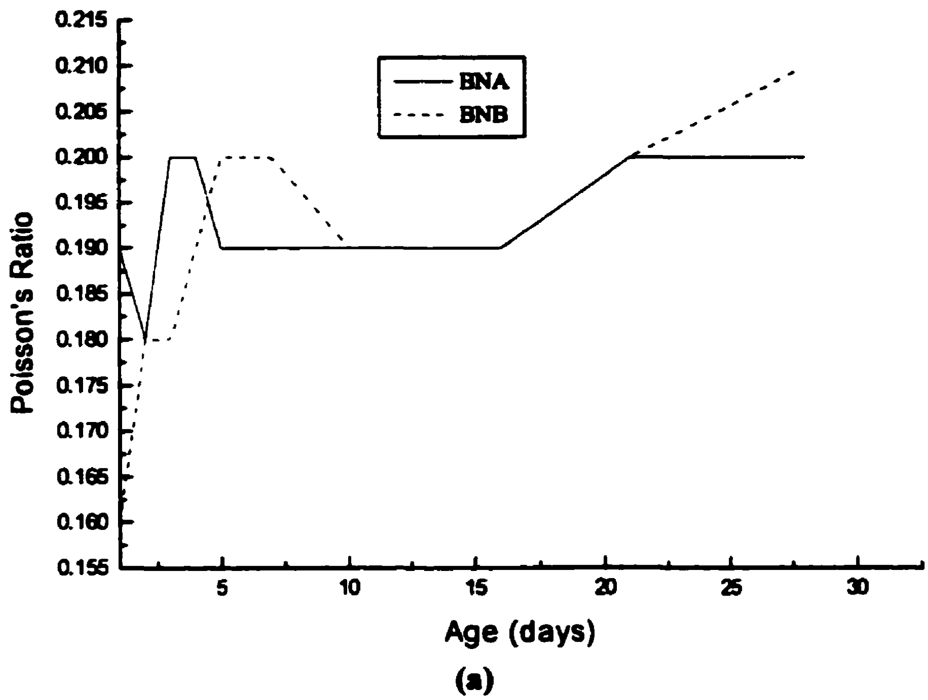

Figure 8-18 a) Development of Poisson's ratio for BNA and BNB with maturity and b) development of Young's, shear and bulk modulus for BNA and BNB with maturity.

From the results in this study it can be concluded that change in aggregate size influences the body wave velocities generated by the MSR system as well as the ultrasonic waves generated by the UPV technique. However, the ultrasonic wave velocities are more sensitive to the change in aggregate size. Evidently, the increase in aggregate size influences the density and consequently the values of elastic constants, which were also detected by the MSR system. This is clearly explained by the fact that for the same volume of mix there more coarse aggregates per volume in the cylinder. Since, the elastic properties of the coarse aggregates are higher than the cement paste, the wave velocities and elastic constants of the mix with larger aggregate size are higher. Also it can be concluded that the MSR readings are affected by the cement type of the mixes.

8.5.1 Comparing Cylindrical Values With Structural Values Obtained by the MSR

In order to understand the influence of shape and dimension on the MSR readings, one standing wall and a column were cast using the BNA and BNB mix proportions. The wall had a dimension 4.8 m × 1.55 m × 0.3 m. The column was 0.6 × 0.45 × 0.8 m in dimension. The wall was cast with the BNA mix and the column was cast with BNB mix. The frames were removed three days after casting. The MSR tests were conducted on the side of the wall where the thickness was 0.3 m. On the column the MSR system was placed on the side of the column where the thickness was 0.6 m. The 15.0 mm diameter impact device was used to generate the stress pulses. Both vertical and tangential displacement transducers were used to collect the surface displacements. The transducers and the impact device were placed on the same side of the structure. The distance between the impact source and the vertical displacement transducer was kept at 5.0 cm for all tests. The tangential displacement transducer was placed approximately 10.0 cm away from the impact device for all of the tests. Three points on each structure were tested at a 10.0 cm interval. An A/D card was used for acquisition of the waveforms. Subsequently, the recorded waveforms were collected in a portable computer for further analysis. The A/D card collected 2048 data points and recording at a sampling frequency of 200 kHz (sampling intervals of 5 μs). Thus, the total duration of the record is 10240 μs. From equation 6-12, the frequency interval in the frequency spectrum is 0.098 kHz, which allows the wave velocities to be computed to the nearest 30 m/s. The effect of the low frequency (below 1000 Hz) transducer assembly resonance and the R-wave frequency were filtered out.

In Appendix C, Figures C-21 and C-24 show the displacement waveforms and the computed frequency spectra for the tests conducted on the wall and the column after 21 days of curing. Figures C-25 and C-26 show the displacement waveforms and the computed frequency spectra for the tests conducted on the cylinders having the same mix proportions as of the wall and the column after 21 days of curing.

The highest peak value from each spectrum was used for velocity calculations. The spectra computed from the signals on the wall and column are as clear as the spectra obtained from the cylinders. The distinct high peak frequency values are the result of body wave resonance from the opposite side of the test specimens. However, the extra distinct peak values in the wall and column spectra are due to the presence of the steel reinforcement bars. The same peaks are not present in the spectra computed from cylinders.

Tables 8-5 and 8-6 represent the elastic wave velocities measured on the cylinders, the wall and the column. As it was expected from the previous study, in all cases the wave velocities for the BNA are higher than for the BNB. Comparing the results of wave velocities obtained from the wall with the cylindrical values of the same mix, the wall velocities are higher. For the wall, the value of P-wave is 5% higher than the cylinder, and the S-wave 4%. In the case of the column, the cylindrical values are higher: 5% for the P-wave and 11% for the S-wave.

Table 8-5 The sample calculations of velocity measurements obtained by the MSR on the cylinders.

Cylinder								
Age (day)	Mix: BNA				Mix: BNB			
	C_p (m/s)	C_s (m/s)	υ	E GPa	C_p (m/s)	C_s (m/s)	υ	E GPa
21	3955	2431	0.20	32.0	3838	2373	0.19	28.9

Table 8-6 The sample calculations of velocity measurements obtained by the MSR on the wall and the column.

Wall & Column								
Age (day)	Mix: BNA				Mix: BNB			
	C_p (m/s)	C_s (m/s)	υ	E GPa	C_p (m/s)	C_s (m/s)	υ	E GPa
21	4160	2519	0.21	34.7	3632	2108	0.25	23.9

The result on the BNA confirms the previous conclusions by Sansalone (1985) and Pessiki (1987), that the values of stress P-wave velocities in the structures are higher than the cylindrical values. In the case of the BNA, the P- and S-values for the wall are higher than the cylindrical values. The higher wave velocities of the BNA in the case of the wall could be due to the dimensions of the test specimen or better mixing and/or curing conditions. In the BNB case, the higher wave velocities of the cylinders could be the result of better mixing and/or curing condition in comparison with the velocities obtained in the column. The Poisson's ratio for the structures are higher than the cylindrical values at all the time but the trend in Young's modulus values follow the wave velocities: higher for the wall in the case of the BNA and higher for the cylinder in the case of BNB. However, from the results of this experiment we can conclude that the cylinder values are different than the in situ structural values. The difference between the cylindrical values and structural values is even higher when the concrete is cast in the field. The cylinders are cast and cured in laboratory conditions using skilled labor. The placing, consolidation and curing of concrete takes place in the field using labor which is relatively unskilled. The resulting field product is, by its very nature and construction method, highly variable. For this reason, a better evaluation of the mechanical properties of concrete structures should be carried out by the in situ testing. In the following chapter (Chapter 9) the MSR system will be used to evaluate mechanical properties of shaft and concrete linings in the field. This is to evaluate the capabilities of the MSR system, operating as an in situ nondestructive testing device.

8.6 CONTOURING OF A STRUCTURE BASED ON ELASTIC MODULI

In many cases due to poor mixing and curing conditions at casting time or later as a result of environmental changes, the strength and the load-bearing capacity of the concrete structures change. One way to evaluate the integrity of the structure is to evaluate its elastic moduli. In many cases a drop in elastic moduli means a drop in load bearing capacity and strength of the structure. Using the MSR system, concrete structures can be contoured based on their elastic moduli.

A 2.25 m × 1.0 m × 0.5 m plate was cast using a 40 MPa concrete mix. The average density of the concrete was calculated to be 2100 kg/m^3 throughout the plate. The preliminary studies indicated that there is a large variation of wave velocities throughout the plate.

A 0.1 × 0.1 cm grid was placed on the top surface of the concrete plate. Both vertical and tangential displacement transducers were used to determine the P- and S-wave velocities. Equations 6-4 and 6-9 were applied to calculate the reflected body wave velocities. The 3.0 mm diameter impact device was used to generate impacts with an average of 65 μs contact-time. Equations in Table 3-2 were used to calculate the dynamic modulus of elasticity for each testing point. The distance between the impact source and the receiver was kept constant at 0.1 m for both transducers. A total of 189 points on the surface were examined by the MSR system. Figure 8-19a shows a typical frequency spectrum generated from the waveform outputs captured by the vertical displacement transducer and Figure 8-19b illustrate a typical frequency spectrum generated from the waveform outputs captured by the tangential displacement transducer, on the 0.5 m thick concrete plate. Figure 8-20 shows contouring of a concrete plate based on its dynamic elastic moduli.

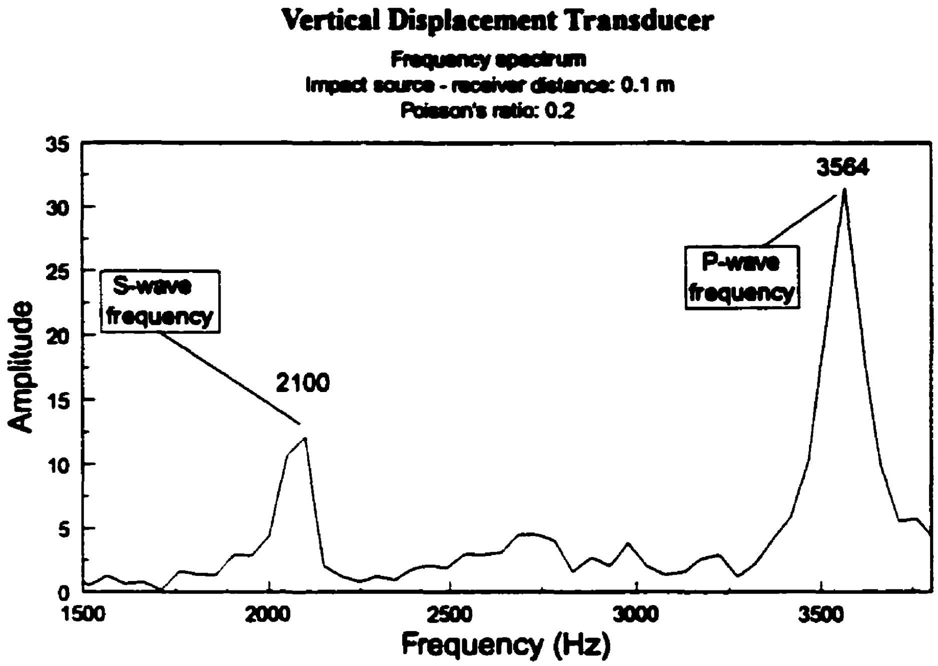

(a)

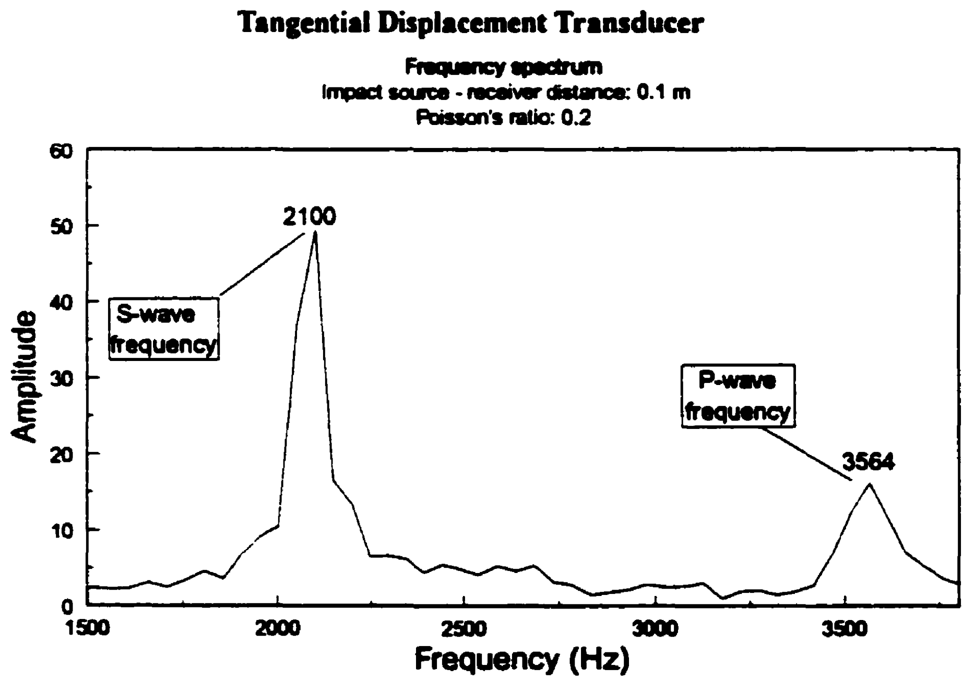

(b)

Figure 8-19 Typical frequency spectrum generated by the vertical displacement transducer on a 0.5 m thick concrete plate (a), and the frequency spectrum created from the waveforms captured by the tangential displacement transducer at the same station (b).

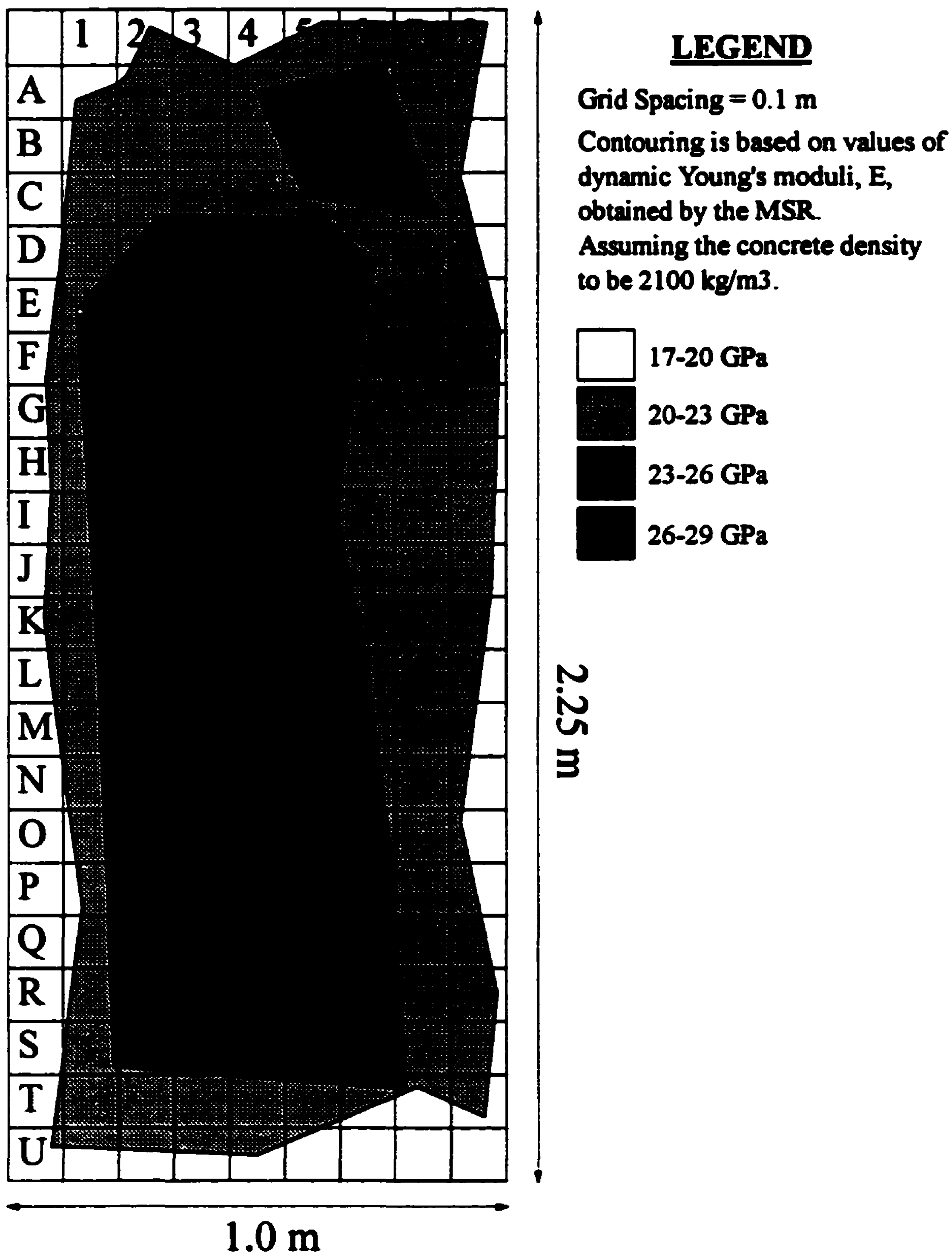

Figure 8-20 Contouring the concrete plate using the MSR system and dynamic elastic moduli.

8.7 SUMMARY AND CONCLUSIONS

The work presented in this chapter clearly demonstrates that the MSR system is a feasible means of measuring the setting time and dynamic elastic properties of concrete. The following conclusions are made from the laboratory work on different concrete specimens:

1. The development of the P- and S-wave velocities by the MSR system and the UPVs were monitored and related to the setting time of six different concrete mixes for a period of 28 days. It was shown that the UPV values are higher than the stress P-wave velocities at all times for the six different mixes. After the first day, the velocities began to increase dramatically and the development of velocities could be easily followed.

2. The dynamic and static moduli of elasticity were computed by the various techniques. The elastic parameters evaluated by MSR and RF techniques were higher than the results obtained by the static technique. However, the results obtained by the MSR system are in better agreement with the static values. It was shown that the values of Poisson's ratio for the early-age concrete is scattered and does not show a clear correlation with strength. The development of elastic parameters could be easily followed by the MSR system.

4. It was shown that for evaluation purposes, the MSR system only uses one surface of the testing specimen while the UPV system uses two surfaces and the RF technique uses three surfaces. This makes the MSR system more practical than the two other techniques.

5. It was shown that like the other dynamic and static methods, the results obtained by the MSR system can be correlated to the compressive strength.

6. The MSR system is sensitive to changes in setting time caused by the cement type. The use of fast curing cement was seen by the change in the rate of maturity which was reflected in the elastic wave velocities and elastic constants.

7. It was shown that the influence of aggregate size on the elastic parameters can be detected by the MSR system.

8. The elastic wave velocities and dynamic elastic constants were computed by the MSR system on actual structural elements such as a column and a wall. It was shown that the MSR system is capable of evaluating these structures' setting time as well as the cylindrical samples made from the same mix.

9. A poorly cast concrete block was monitored by the MSR system for the body wave velocities in a chessboard survey fashion. The global state of the block was represented by contouring dynamic elastic moduli which was shown to be an easy interpretation method for controlling the quality of the concrete block and possibly concrete structures.

CHAPTER 9

APPLICATION OF THE MSR SYSTEM ON SHAFT AND TUNNEL CONCRETE LININGS

9.1 INTRODUCTION

Assessment of the condition of concrete linings in underground excavations is difficult since most of the deterioration processes take place in the rock-side or blind-side (i.e. in the rock/concrete interface) of the lining. Groundwater and variations in stress conditions are the main cause for deterioration and damage to concrete linings.

The studies presented in this chapter demonstrate that the MSR system can be used for integrity testing of mine shaft and tunnel linings. In the first section, results obtained from experimental studies on two concrete shaft linings are presented. Various sections of shaft linings at different elevations were investigated and their elastic properties at each point are calculated. In the second section, thickness of tunnel lining was calculated. For both cases, the effect of surrounding rocks on the signals were studied.

The MSR outputs were compared with results obtained by independent laboratory testing of core samples extracted from the structures.

9.2 THE MSR SYSTEM

The field MSR system used in the projects throughout this chapter, includes a series of spherical tip, spring loaded impact devices (ranging between 0.5 mm and 25.4 mm in diameter), one broad band vertical displacement transducer and the associated amplifier, one broad band tangential displacement transducer and the associated amplifier, a data acquisition A/D board, and a portable computer. A sampling frequency of 100 kHz was used throughout the experiments, and a total signal length of 2048 points was used for the calculations. The analysis software program was developed on the GAUSS mathematical and statistical system using the time series analysis package to identify and measure P- and S-wave frequencies and velocities. In the frequency spectrums, the values below 1000 Hz were clipped (using a high pass filter), since they were related to the frequency of the R-wave, the electrical and mechanical vibrations of the structure and the resonance frequency of the transducers.

9.3 APPLICATION OF THE MSR ON TUNNEL SHAFT LINING

The main objective of this project was to study the capability of MSR for evaluating the quality of underground concrete linings. The quality of the linings were evaluated based on their mechanical properties, particularly the dynamic elastic constants. The shaft No.2 of CCP Mine [(Central Canada Potash Inc.) as of January 1995 (after completion of these tests) the CCP Mine was bought by the International Minerals & Chemicals Corp. (IMC)] and shaft No. 2 at the Allan Division of PCS (Potash Corporation of Saskatchewan Inc.) in Saskatchewan were considered ideal for this study. CCP and Allan mines are two of the nine potash mines in Saskatchewan. The potash ore is located in a depth of 1021 to 1036 meters within a potash deposit known as Patience Lake Member of the Prairie Evaporate Formation. The deposit is of a Devonian age (350 - 400 million years old) (Molavi, 1987). Figure 9-1 illustrates position of the two Mines and the geological stratification of the potash ore.

The vertical accessibility to the testing stations were provided by the personnel carrier cages. Both sites were production shafts, causing unique time constraints for MSR testing. The external ring of shaft No. 2 at the Allen mine is covered by various types of rocks, mainly of a sedimentary nature. The inner concrete surface was smooth in various sections and there was no evidence of spalling (Plate 9-1). By visual inspection, the concrete linings in both shafts appeared to be in good condition. The thickness of the linings for both shafts were known from the available plans. In the case of Allan's shaft No. 2 drilling was conducted to confirm the lining thickness at various levels.

9.3.1 CCP Mine

Shaft No. 2 of CCP Mine is a production shaft that extends down to 1090 m. The shaft was constructed in 1965. The concrete used for the lining was sulfate-resistant having a compressive strength of 34.47 MPa (AMC, 1965). The maximum size of the aggregate was 0.2 to 0.9 cm. The top 100.0 m of the shaft had a 0.51 m thick concrete lining. Thick reinforcement bars and mesh-form, positioned 5.1 cm from the inner surface and 5.1 cm from the outer ring (AMC, 1965) (Figure 9-2). The concrete has a bulk density of 2700 kg/m3 (AMC, 1965). The top 30.5 m of the concrete lining is surrounded by overburden consisting of glacial till. The MSR tests at CCP Mine were conducted in the top 9.1 m of the concrete shaft lining. In this exercise, the thickness of the shaft lining was taken from plans provided by the shaft personnel.

9.3.1.1 Experimental Setup

The equipment was placed on the top of the personnel career cage (Plate 9-2). The tests were conducted from the top of the cage. In this case both the semi-spherical tipped hammer and the mechanical impact devices were used to generate the initial stress pulse. The contact-time generated by the mechanical impact device was ranging between 40 to 75 μs (Figure 9-3b). The contact-time generated by the semi-spherical tipped hammer was ranging between 300 to 340 μs (Figure 9-3a). The MSR readings were taken from two different locations on the accessible side of the concrete lining. The vertical displacement transducer was placed 5 to 10 cm from the impact device for all the tests performed (Plate 9-3). To collect the reflected S-waves, the tangential displacement transducer was placed at a distance equal or half of the thickness of the lining (Plate 9-4). The analysis was done in frequency domain, taking the thickness values from the shaft plan. Two sets of equations were used, equations 6-4 and 6-9 were applied for evaluation of elastic wave velocities and equation 4-26 was used for detection of steel reinforcement bars within the concrete.

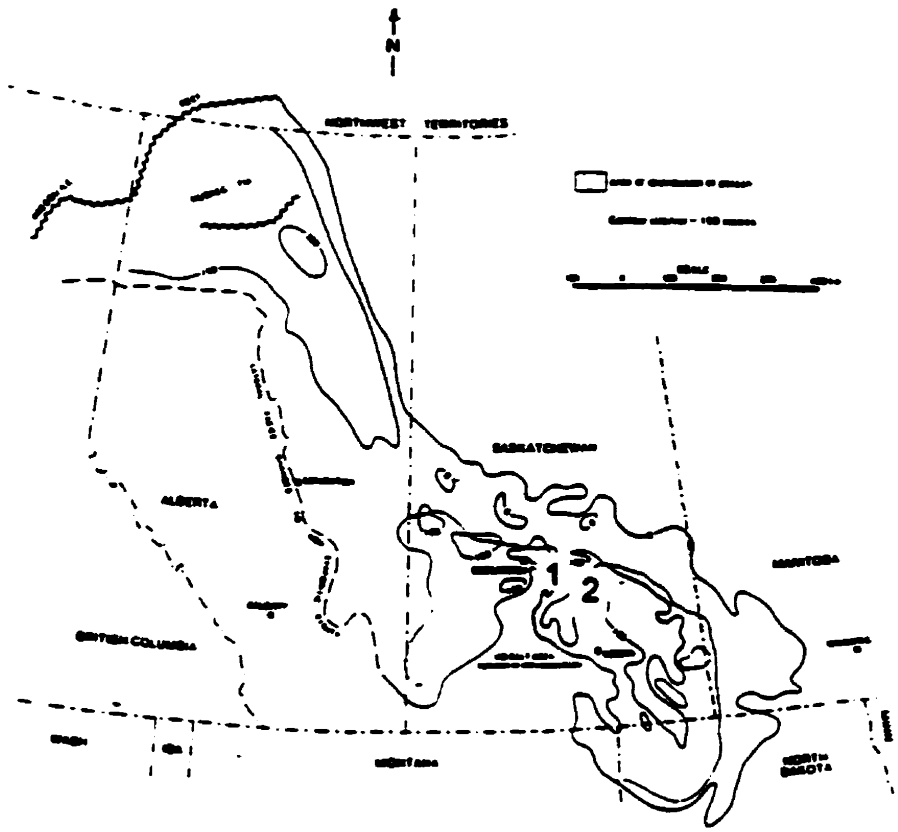

(a)

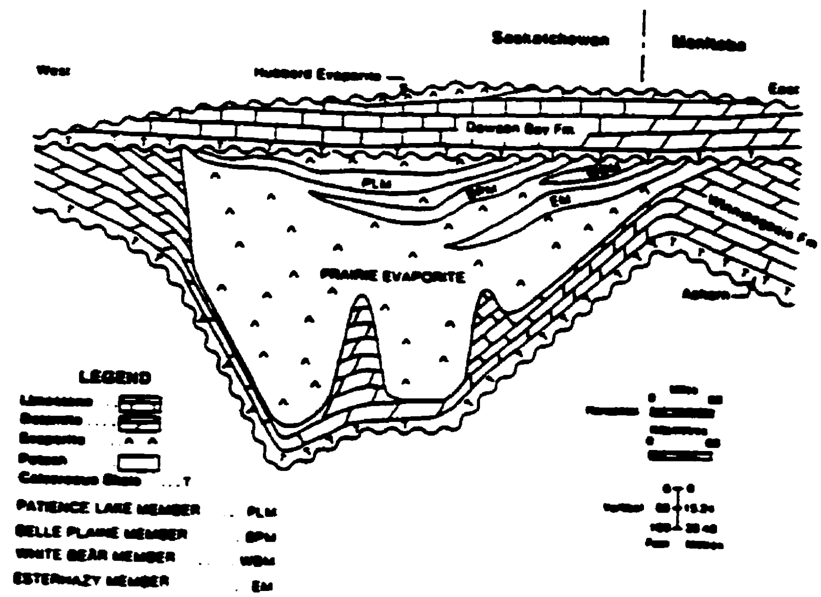

(b)

Figure 9-1 a) The position of the Allan (1) & CCP (2) mines in addition to the isopach map of Prairie Evaporite, b) The cross-section through Prairie Evaporite (After Molavi, 1987).

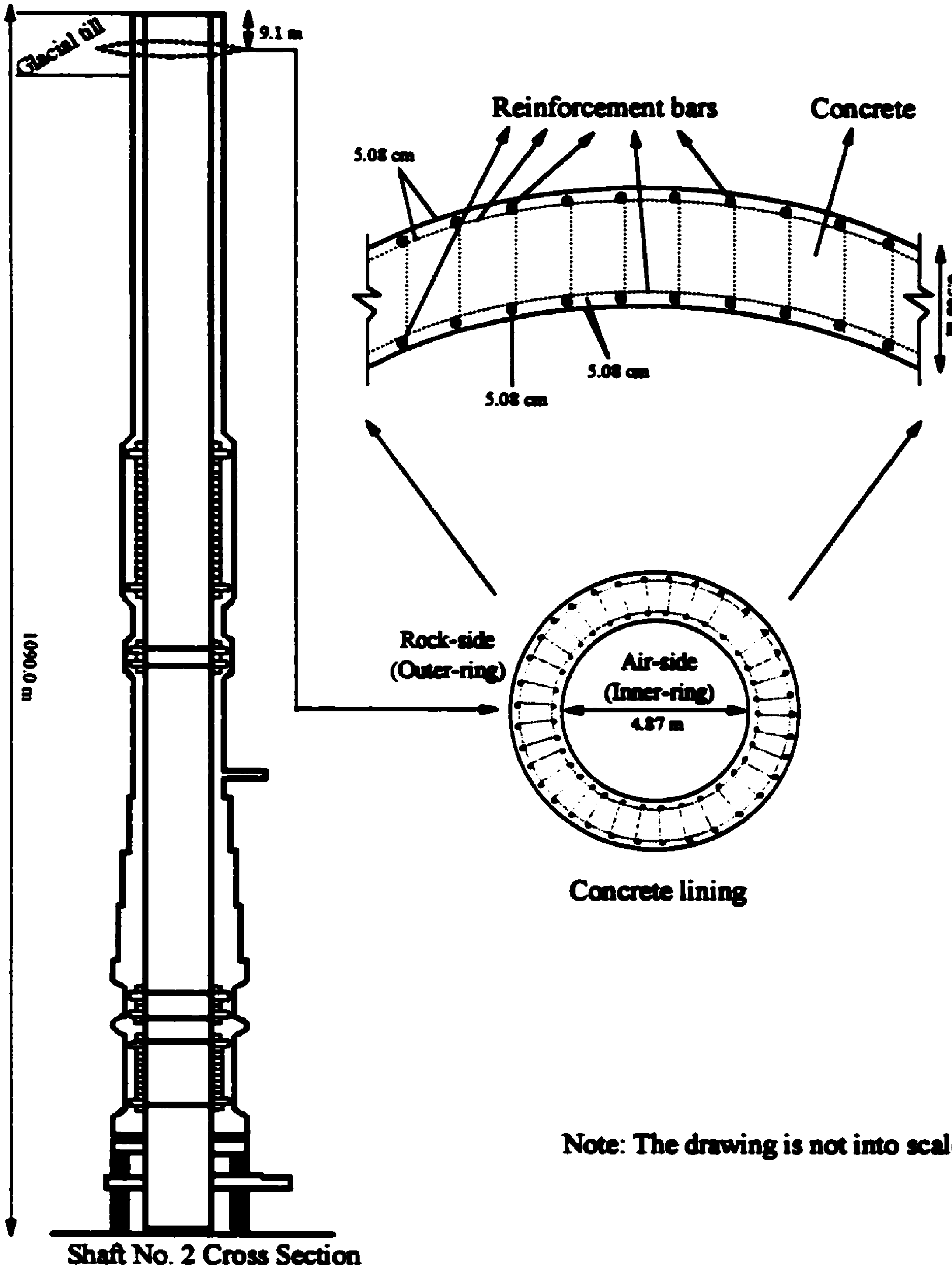

Figure 9-2 Schematic diagram of CCP Mine shaft depicting MSR testing location and the position of the reinforcement bars.

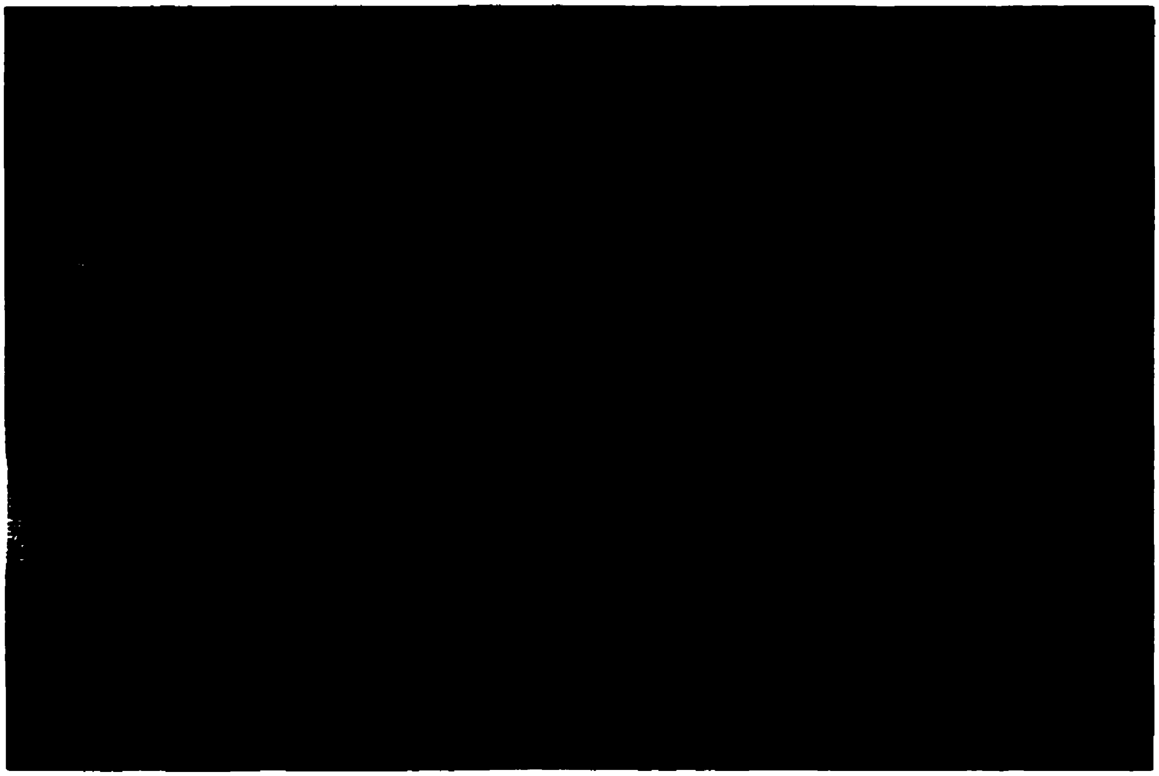

Plate 9-1 Concrete shaft lining.

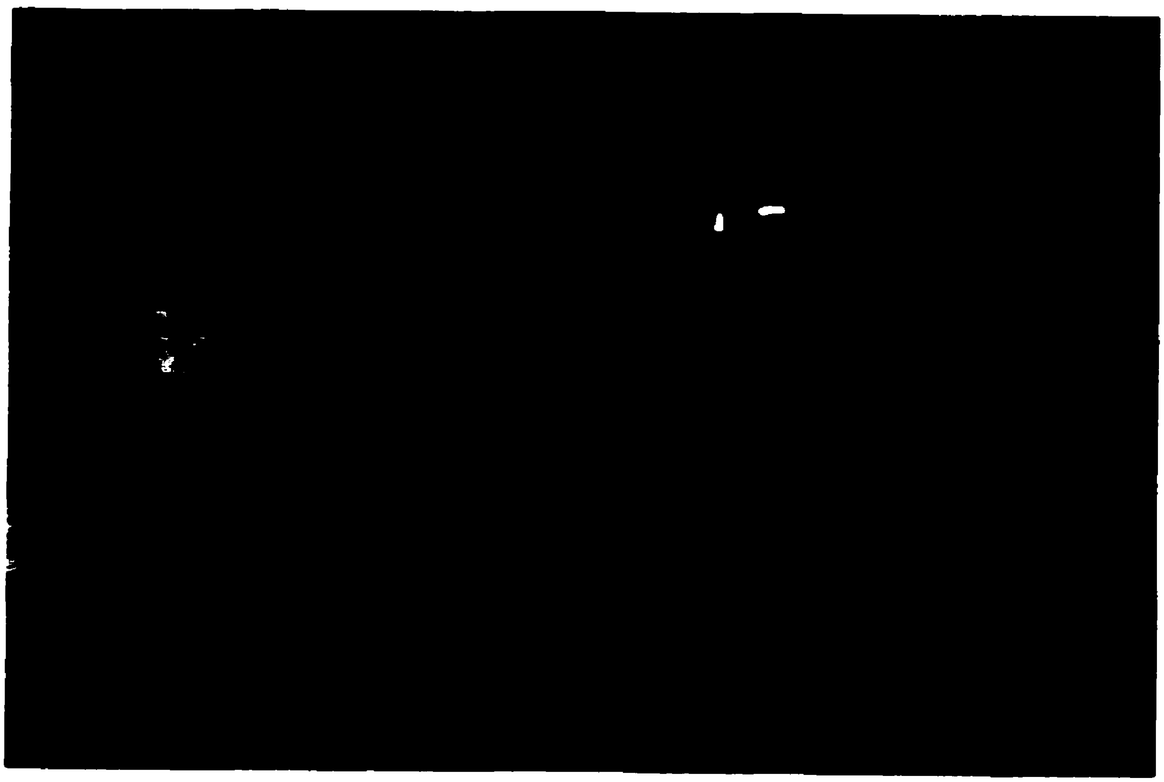

Plate 9-2 Personnel carrier cage.

Plate 9-3 Measurement of P-wave, using vertical displacement transducer, at CCP Mine.

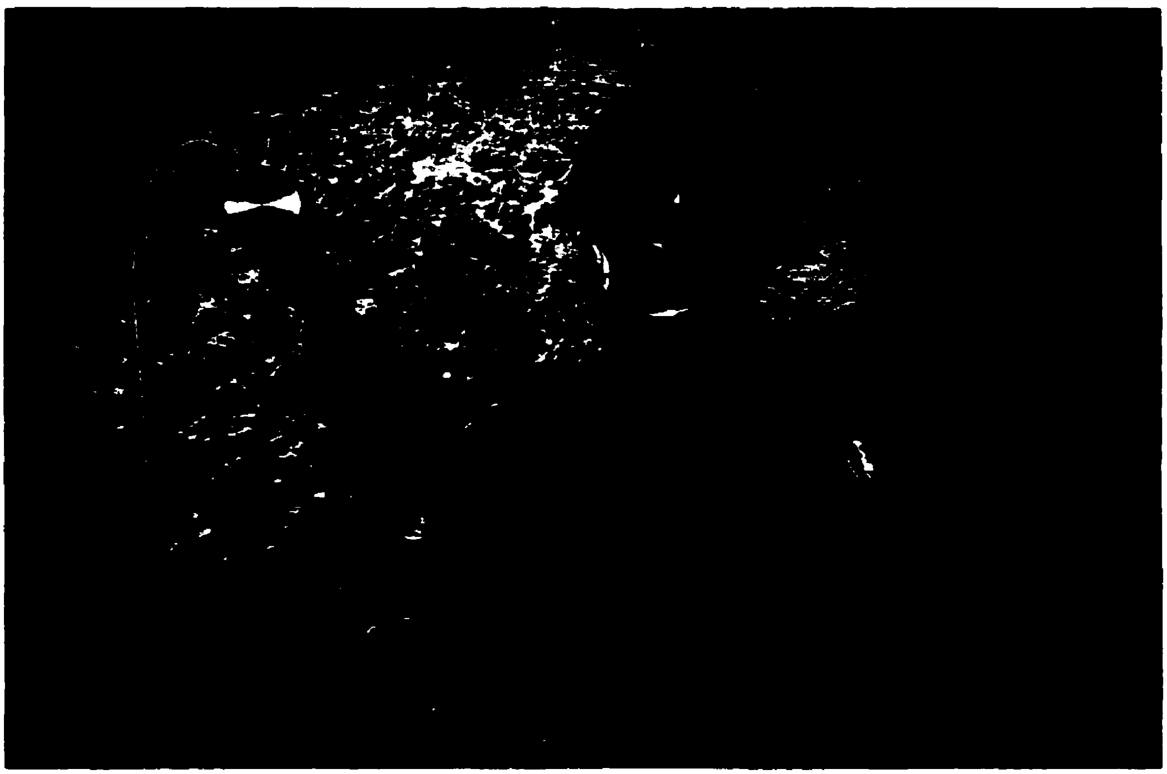

Plate 9-4 Measurement of S-wave, using tangential displacement transducer, at CCP Mine.

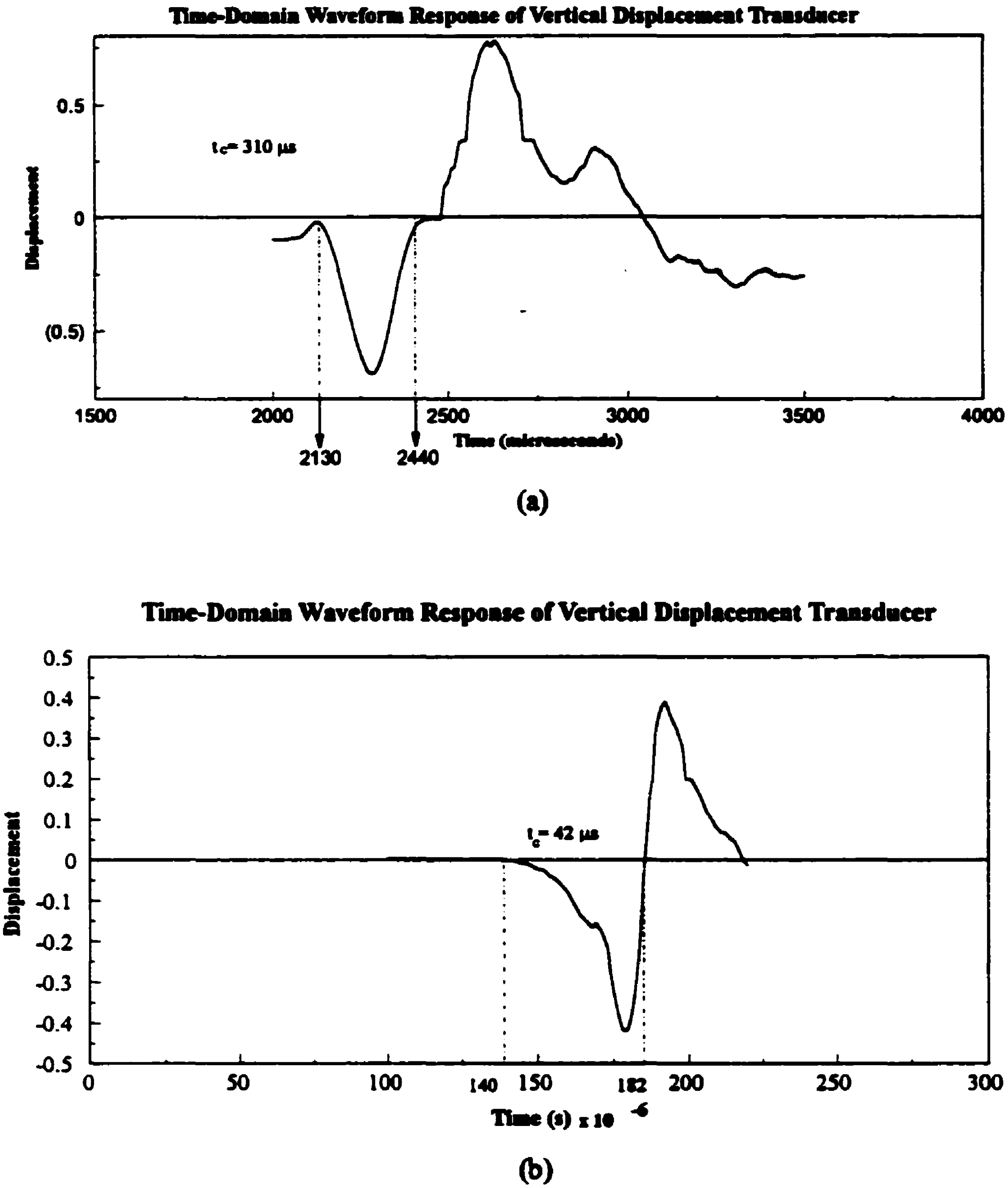

Figure 9-3 Estimating the contact time of impact on the concrete shaft lining., a) impact by a semi-spherical tip hammer, b) impact by an impact device.

9.3.1.2 Results and Discussion

Figures 9-4 and 9-5 show samples of collected waveforms by the vertical and tangential displacement waveforms and their calculated frequency spectra from the concrete shaft lining at the CCP Mine. The P- and S-wave velocities were calculated using the distinct peak value from frequency spectra determined using the time-domain signals collected by the vertical and tangential displacement transducers, respectively. The spectra were produced by transformation of time-domain signals to frequency domain, using FFT technique. The thickness frequency is clearly distinguishable in the frequency spectrum. The thickness frequency is related to the resonance of P- and S-wave signals between the two surfaces of concrete lining (Figures 9-4b and 9-5b). The frequency of the compressive wave signal for the 0.508 m thickness of the concrete lining was found to be 4345.0 Hz. The frequency of the shear wave signal for the 0.508 m thickness of the concrete lining was found to be 2490.0 Hz. In this case, the stress characteristics of reflected signals change at both interfaces. This means the concrete lining has a higher acoustic impedance than glacial till. When the waves reach the concrete/till boundary both P- and S-waves change sign, i.e. in the case of the P-wave the incident compression wave changes to tension wave and for the S-wave, the incident transverse-right (or left) changes polarity. For both waves, the changed waveforms reach the transducers, where reflection again occurs. The P-waves reflect back as compression wave and the S-wave reflects as transverse-right. The signs change to the same form as the incident waves. In this case, equations 6-4 and 6-9 are used for the velocity calculation. The P- and S-wave velocities were calculated to be 4415 m/s and 3535 m/s, respectively. Having the density (provided from the Associated Mining Construction Limited: the contractors for constructing the shaft) of the concrete and the P- and S-wave velocities, dynamic elastic properties of concrete lining could be calculated using the equations in Table 3-2. The dynamic elastic properties obtained by the MSR system at the CCP Mine are listed in Table 9-1.

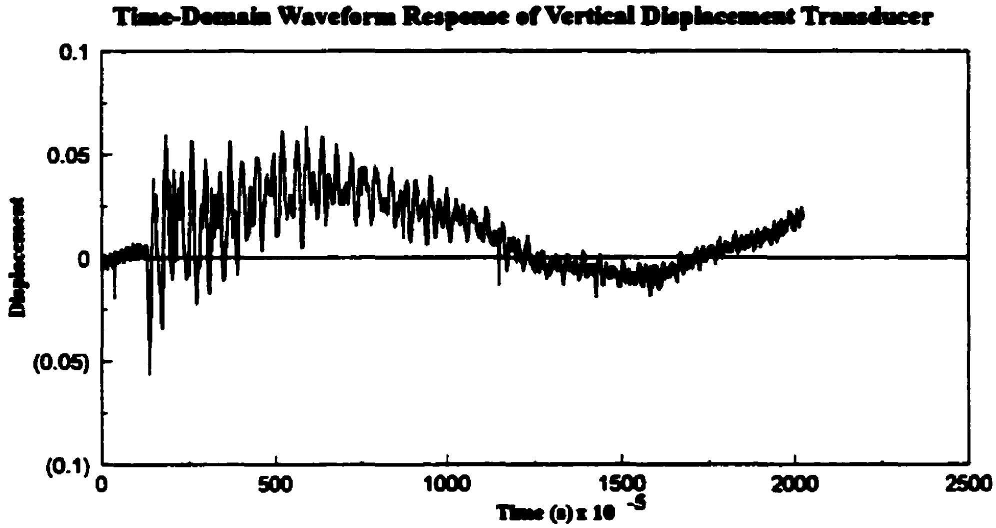

(a)

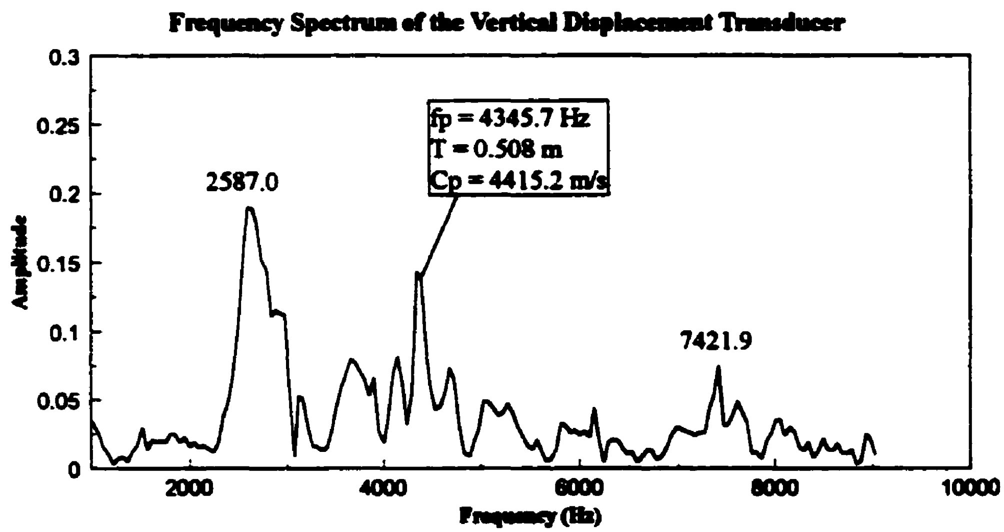

(b)

Figure 9-4 Sample of one a) time-domain and it's b) frequency spectrum collected by vertical displacement transducer in CCP Mine.

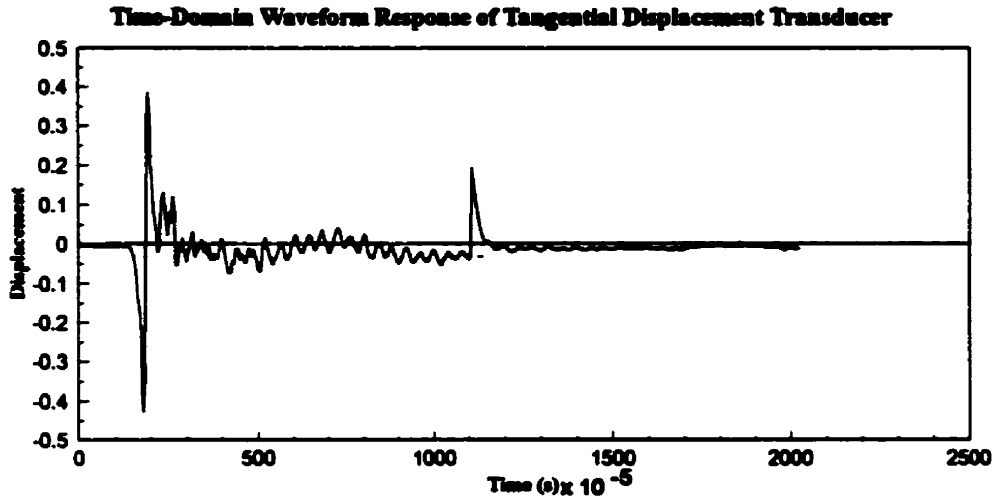

(a)

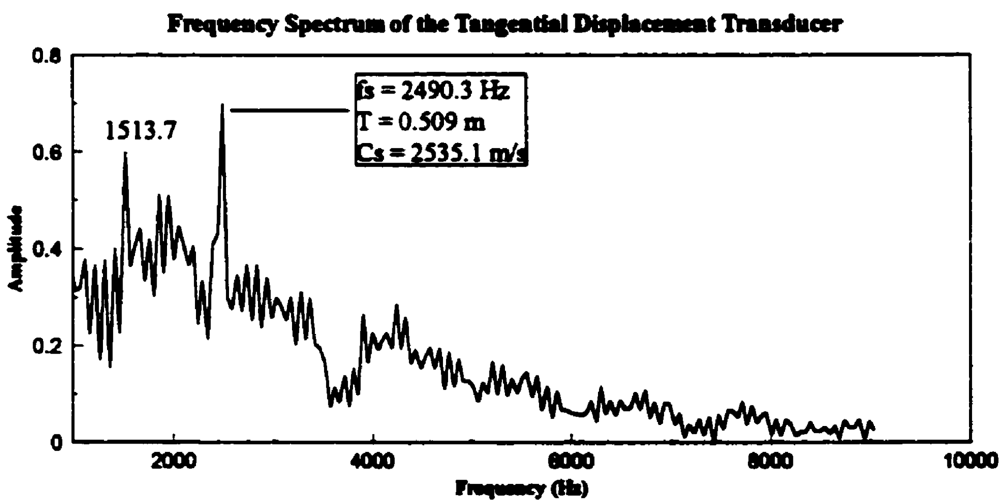

(b)

Figure 9-5 Sample of one a) time-domain and it's b) frequency spectrum collected by tangential displacement transducer in CCP Mine.

Table 9-1 The mass density and dynamic elastic properties of CCP Mine's concrete shaft lining calculated using MSR values.

Mass density	2700 kg/m^3
P-wave velocity	4415 m/s
S-wave velocity	3535 m/s
Young's modulus	44.0 GPa
Poisson's ratio	0.25
Shear modulus	17.4 GPa
Bulk modulus	29.3 GPa

Other frequency values in the tangential and vertical displacement spectra are related to either presence of reinforcement bars or flaws and delaminations within the concrete lining (Figures 9-4b and 9-5b). To detect the position of any object, the resulting spectra from the vertical displacement transducer was used. On the frequency spectrum obtained by the vertical displacement transducer, two other significant values exist (Figure 9-4b). Assuming that the frequency values are related to the reflections from the reinforcement bars, equation 4-26 was used for calculations. The two values at 2587.0 Hz and 7421.9 Hz mark the presence of the reinforcement bars within the concrete lining. The location of the two sets of inner and outer reinforcement bars were identified at 0.43 m and 0.15 m respectively. The position of the reinforcement bars for the outer mesh was documented to be at 0.46 m and the inner mesh to be at 0.05 m. Therefore, the other frequency amplitudes are related to the reinforcement bars and no voids or delaminations were detected.

9.3.2 Allan Mine

The MSR in the Allan Mine was used to evaluate the in situ dynamic elastic properties of the shaft lining at three stations. Shaft No. 2 of Allan Mine is a production shaft and extends down to 975.4 m, and is 4.9 m in diameter. The shaft was constructed in the 1960s. The concrete design specification for the Allan's shaft lining was sulfate-resistant with 34.47 MPa compressive strength and a density of 2590 kg/m3 (AMC, 1965).

Figure 9-6 illustrates a schematic diagram of Allan Mine's shaft No.2. The shaft lining was tested in three locations at 640.0 m, 823.0 m, and 914.4 m of the shaft with variable concrete thicknesses: 0.58 m, 0.58 m, and 0.57-0.61 m. The information about the position and thickness of the reinforcement bars were not available. The shaft is extended down to the depth of 975.4 m located in Prairie Evaporite Formation. Immediately overlaying the Prairie Evaporite formation is carbonates, shale and glacial till. The lining at the first two test sites at 640.0 m and 823.0 m was surrounded by limestone and the third site at 914.4 m was surrounded by halite. The P wave velocities of these rocks were calculated in the laboratory by the UPV technique and are listed in Table 9-6.

9.3.2.1 Experimental Setup

The equipment was placed on the top of the personnel career cage (Plate 9-5). The tests were conducted from the top of the cage. The semi-spherical tipped hammer with 2.54 cm diameter was used in all three locations to generate the initial stress pulses. The contact-times of impacts were calculated between 280 to 350μs. The MSR readings were taken from two different locations on the accessible side of the concrete lining at each station. For the detection of the P-wave displacements, the vertical displacement transducer was placed 5 to 10 cm away from the impact source (Plate 9-6). To detect the S-wave vibrations, the tangential displacement transducer was placed at a distance equal to the thickness of the lining (Plate 9-7). The signals were captured and stored in the portable computer for later analysis.

9.3.2.2 Results and Discussion

Figures 9-7 to 9-12 show examples of displacement waveforms and frequency spectra collected by the vertical and tangential displacement transducers at each station in Allan Mine's shaft No.2. The frequency spectra were calculated from the data collected by the vertical and tangential transducers at each station using FFT technique. The available thickness values from drilling were used in the calculations. Based on the distinct frequency values in each spectra, the P- and S-wave velocities were determined for the three stations and are listed in Table 9-2. Equation 6-4 and 6-9 were used to calculate P- and S-wave velocities. Having the mass density from the extracted cores and the P- and S-wave velocities, dynamic elastic constants of concrete lining were calculated using the equations in Table 3-2.

Table 9-2 The mass density and dynamic elastic properties of Allan Mine's concrete shaft lining calculated using MSR values at three stations.

	Cp Cs (m/s)	Concrete Thickness (m)	Poisson's Ratio	Density (kg/m3)	Young's Modulus (GPa)	Shear Modulus (GPa)	Bulk Modulus (GPa)
Station at 640.0 m	4418 2662	0.58	0.22	2595	44.4	18.4	26.4
Station at 823.0 m	4248 2209	0.58	0.31	2595	33.8	12.7	29.6
Station at 914.4	4050 2502	0.61	0.19	2565	38.3	16.0	20.6

If the concrete and rock have similar acoustic impedance (velocities and density), Z, little energy reflects back from the interface, provided there is a good contact between the rock and concrete ($Z_2 = Z_1$). When the rock has a higher acoustic impedance than concrete ($Z_2 > Z_1$), most of the energy enters the rock and little energy reflects back from the rock/concrete interface. In this case, the P- and S-wave signals do not change their polarity, i.e.in the case of P-wave, compression remains compression at the air-side (transducer side). The reflected signal, in this case, has the same characteristics as the signal reflected from concrete/steel interface. In areas where concrete has a higher acoustic impedance than rock ($Z_2 < Z_1$), or the concrete and rock do not have a good contact (bonding) most of the energy will be reflected from the interface. In this case, both P- and S-waves change signs at the air-side, i.e. for P-wave changes from compression to tension at the transducer side. The acoustic impedance (Z_2) of the rocks in contact with the concrete lining for the three testing stations were calculated and are listed in Table 9-3.

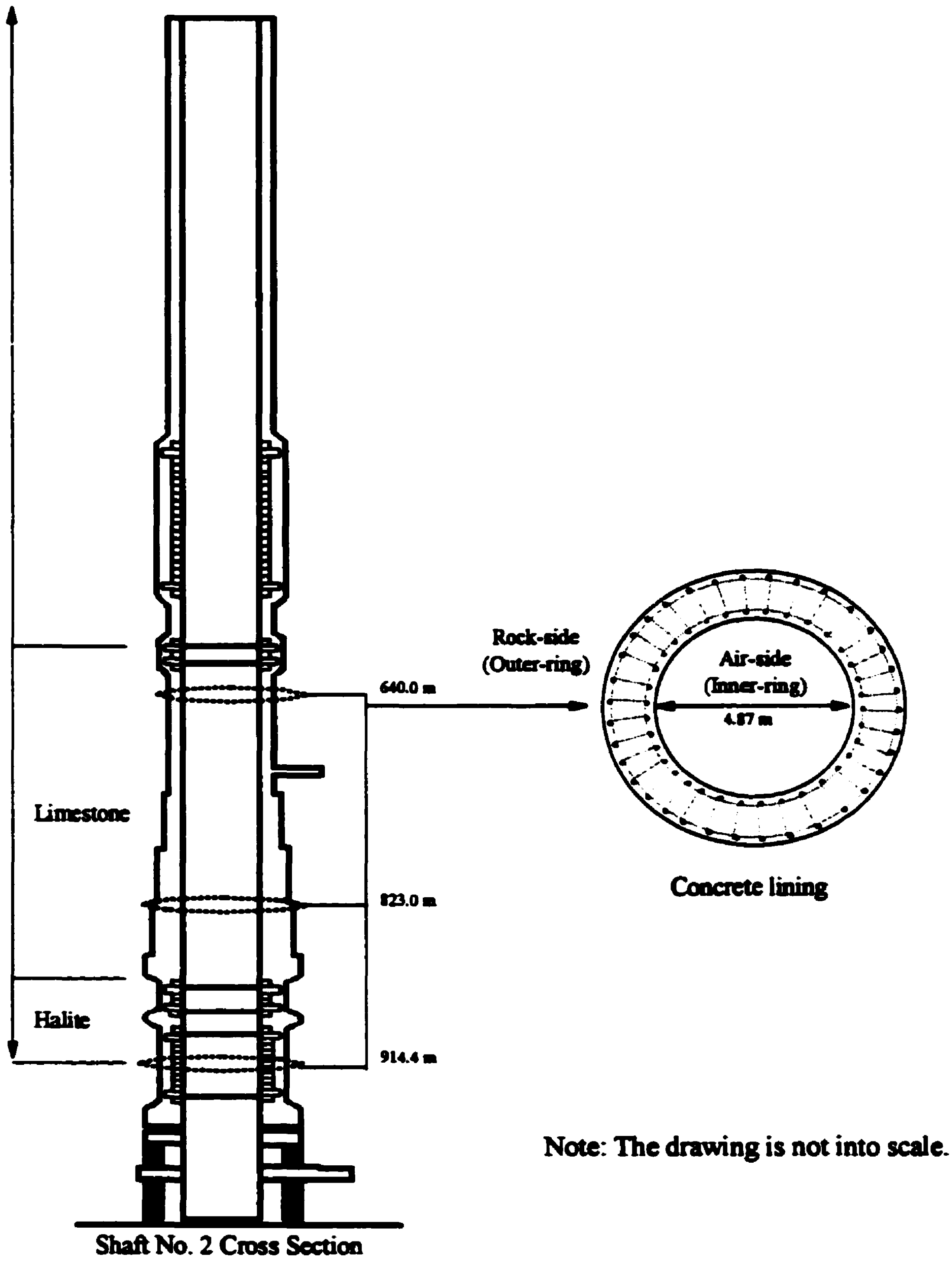

Figure 9-6 Schematic diagram of PCS Allan Mine shaft depicting the MSR testing locations.

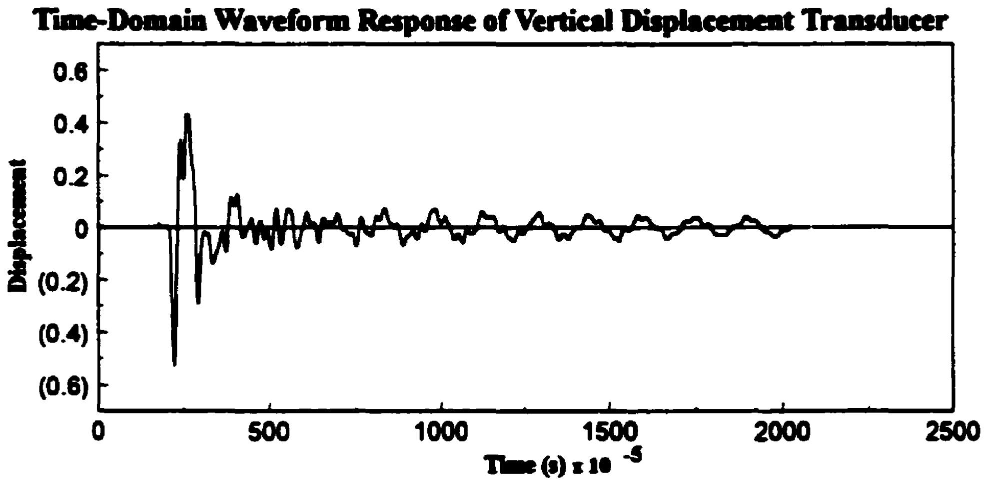

(a)

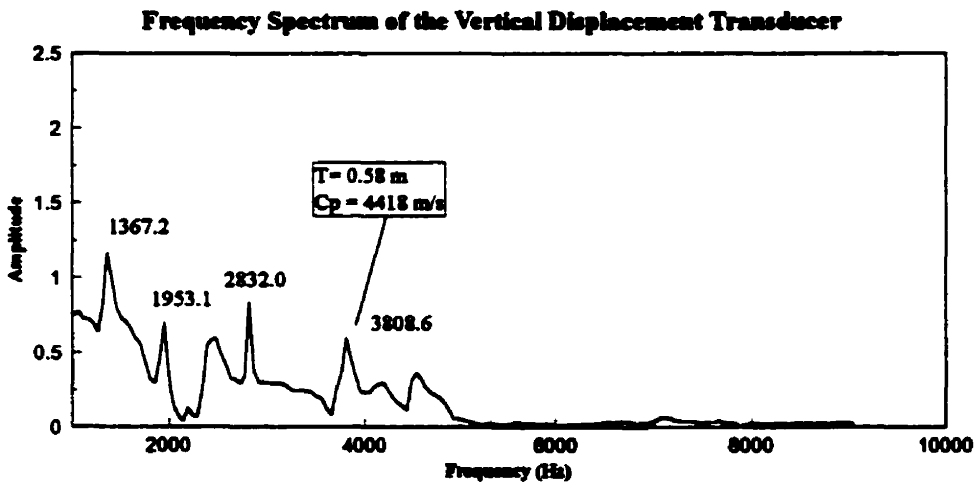

(b)

Figure 9-7 Example of a a) time domain and it's b) frequency spectrum by vertical displacement transducer in Allan Mine at 640.0 m station.

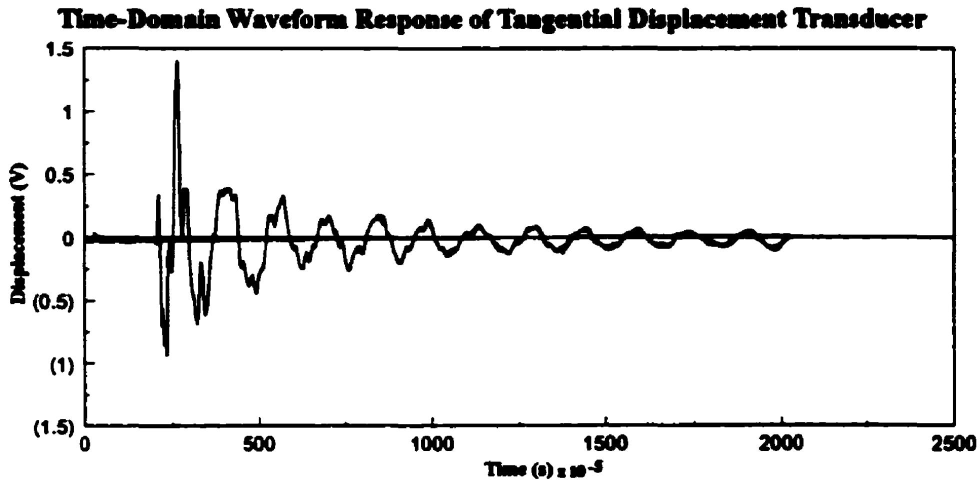

(a)

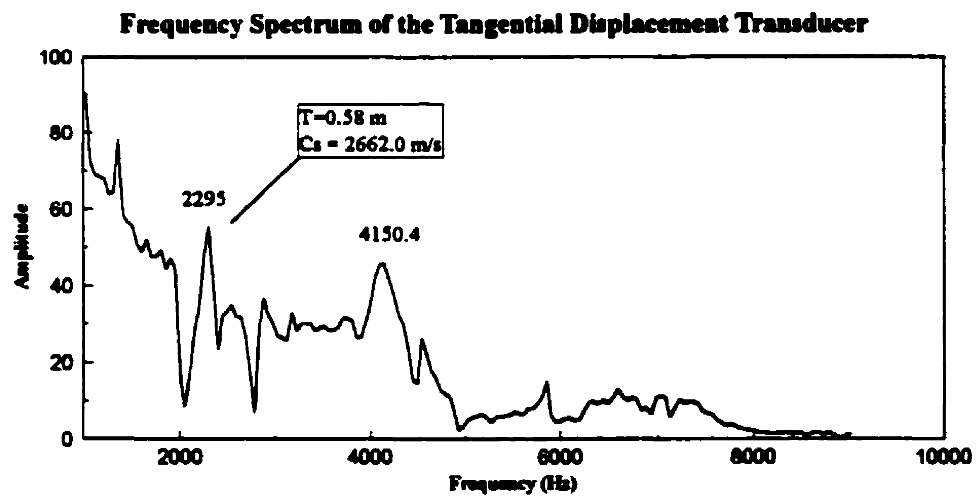

(b)

Figure 9-8 Example of a a) time domain and it's b) frequency spectrum by tangential displacement transducer in Allan Mine at 640.0 m station.

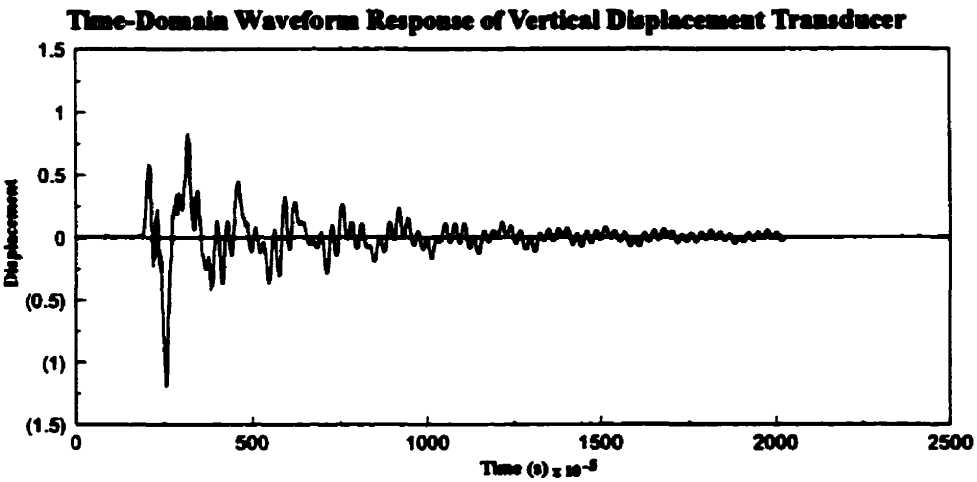

(a)

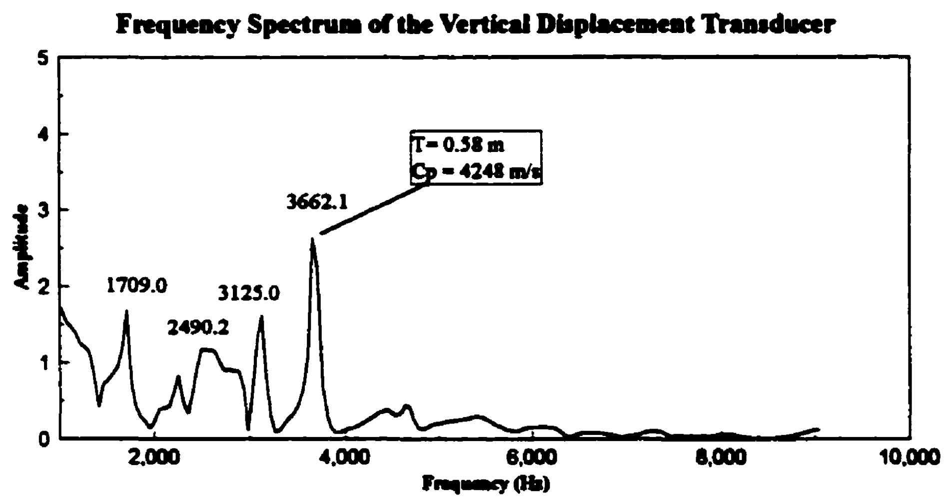

(b)

Figure 9-9 Example of a a) time domain and it's b) frequency spectrum by vertical displacement transducer in Allan Mine at 823.0 m station.

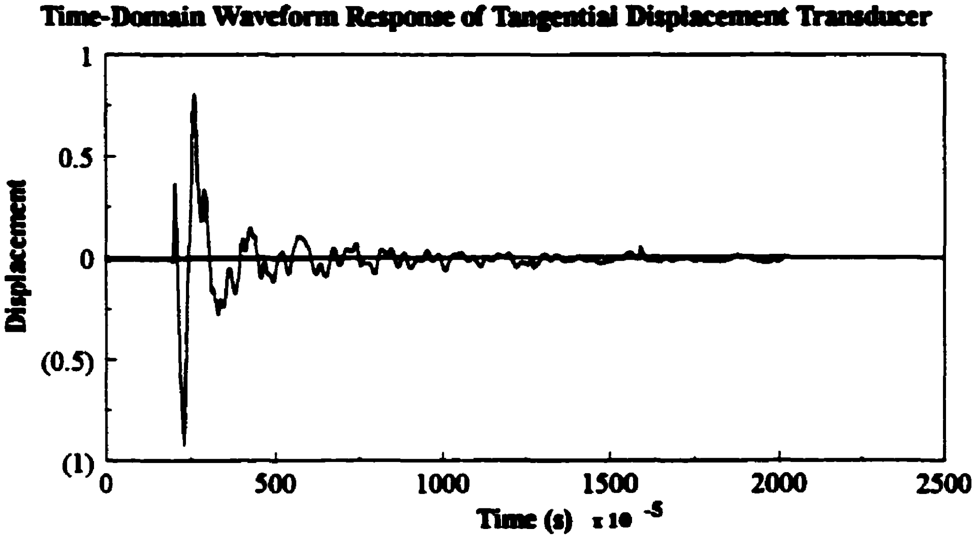

(a)

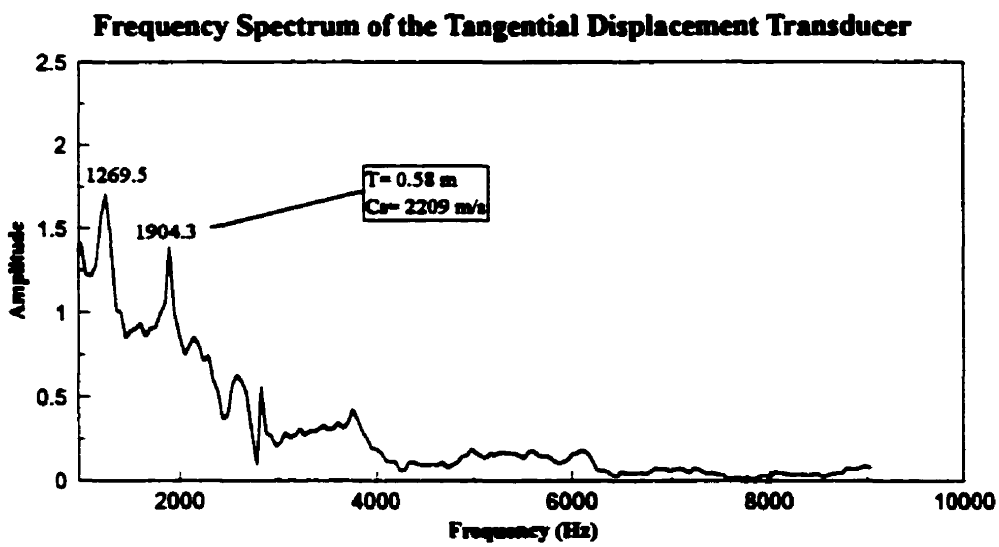

(b)

Figure 9-10 Example of a a) time domain and it's b) frequency spectrum by tangential displacement transducer in Allan Mine at 823.0 m station.

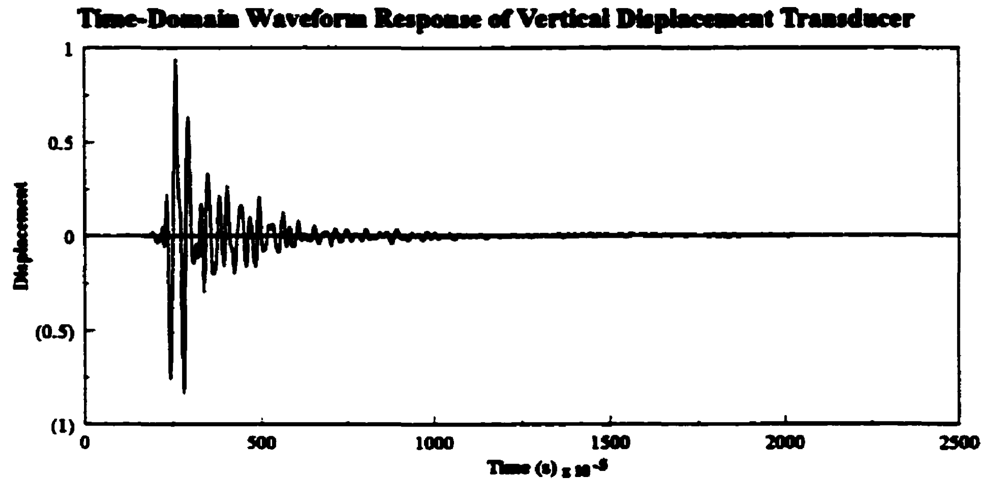

(a)

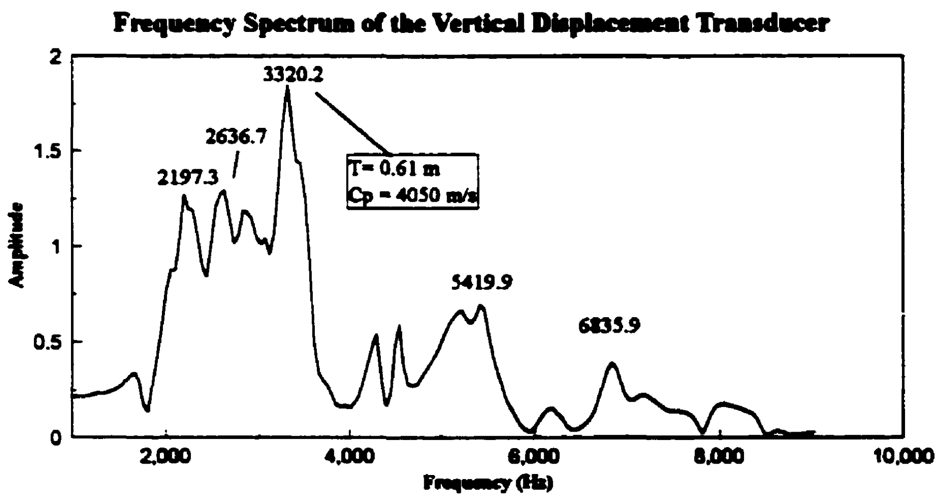

(b)

Figure 9-11 Example of a a) time domain and it's b) frequency spectrum by vertical displacement transducer in Allan Mine at 914.4 m station.

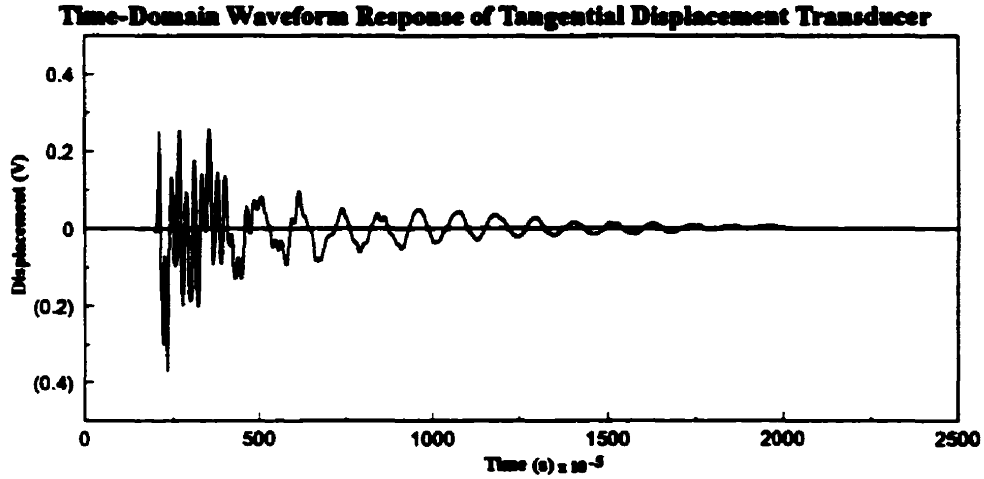

(a)

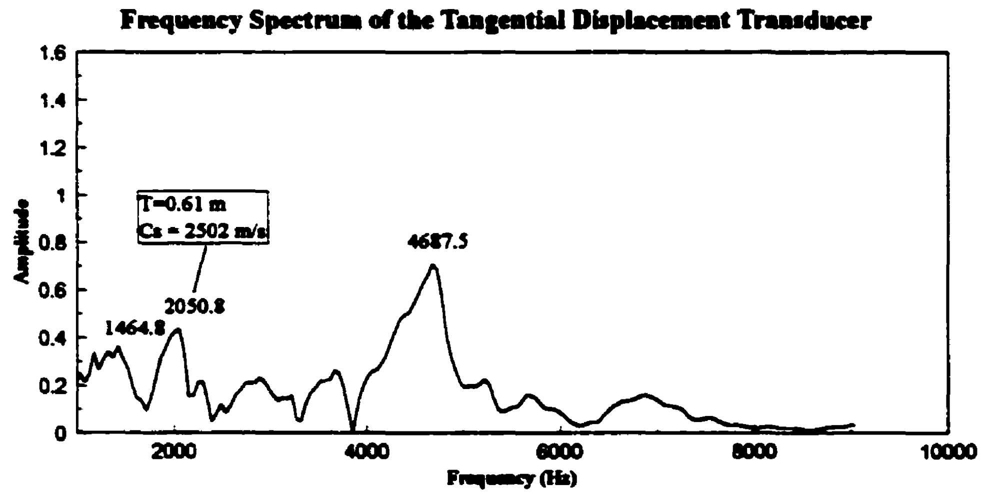

(b)

Figure 9-12 Example of a a) time domain and it's b) frequency spectrum by tangential displacement transducer in Allan Mine at 914.4 m station.

Table 9-3 The values of density, P-wave velocity and acoustic impedance for surroundings rocks at Allan Mine for the three station's and the concrete acoustic impedance.

Depth in m	Lithology	Density (kg/m^3)	Cp (m/s)	Rock Acoustic Impedance (Z_2) ($kg/m^2.s$)	Concrete Acoustic Impedance (Z_1) ($kg/m^2.s$)
640.0	Limestone	2370	3850	9.1×10^6	12.9×10^6
823.0	Limestone	2920	4750	13.9×10^6	12.0×10^6
914.4	Halite	2110	4200	8.8×10^6	11.5×10^6

The values of acoustic impedance for the concrete are higher than those of the surrounding rock at the 640.0 m and 914.4 m stations. For the testing station at 823.0 m the acoustic impedance of the rock is slightly higher than concrete. However, studying the frequency spectrums from the 823.0 m station indicates a strong signal reflection. The frequency values for both P- and S-waves can be used with the thickness and equations 6-4 and 6-9 to calculate velocity values. Knowing at this station the rock has higher acoustic impedance than concrete (see Table 9-3), it can be assumed that the concrete and rock in this area are not well bonded. As for the frequency spectrums obtained from the other two stations, the signals have been reflected from a boundary with lower acoustic impedance than of concrete ($Z_2 < Z_1$) (see Table 9-3). In all three cases equations 6-4 and 6-9 were used to calculate the elastic wave velocities.

Core samples of approximately 3.18cm in diameter were extracted from the lining from the same levels the MSR tests were conducted. The cores were tested at the Core Laboratories in Calgary for acoustic velocities (P- and S-waves), densities, porosity, permeability, and dynamic elastic constants. Two samples were taken from each level, one from the air-side of the concrete and one near the rock-side. Samples 21-1A, 1B were extracted from 640.0 m, 26-2A, 1B from 823.0 m, and 30-2A, 2B from 914.4 m. The system used by the Core Laboratory to measure elastic waves is an UPV device having automatic pore pressure and confining pressure controller.

The acoustic velocities are measured at the specific pressures (12.5, 16.5, and 19.5 MPa for samples extracted from 640.0 m, 823.0 m, and 914.4 m respectively and 0.5 MHz (500 kHz) frequency. Porosity, permeability, and grain density were measured at the same specific pressures. The porosity ranges from 6.8% to 10.6% in the cores, permeability ranges from 0.016 to 0.075 mD, while density only varies slightly between 2560 and 2600 kg/m^3. These data are listed in Table 9-4. The P-wave velocity in the cores range from 4496 m/s to 4641 m/s, while the S-wave velocity ranges from 2688 m/s to 2745 m/s. The Cp/Cs ratio, Poisson's ratio, bulk modulus, and shear modulus are calculated from the velocity and density data and are listed in the Table 9-4.

Table 9-4 The values obtained by the UPV technique from the concrete core samples.

Velocities and Mechanical Properties of PCS Concrete Cores (Temperature = 25 °C)

Sample No.	Overburden Pressure (MPa)	Porosity (%)	Permeability (mD)	Density (kg/m^3)	Cp (m/s)	Cs (m/s)
21-1A	12.5	7.67	0.016	2600	4817	2809
21-1B	12.5	9.24	0.075	2590	4425	2680
26-1B	16.5	8.24	0.048	2600	4428	2589
26-2A	16.5	6.80	0.032	2590	4853	2787
30-2A	19.5	8.07	0.017	2570	4609	2807
30-2B	19.5	10.62	0.024	2560	4383	2658

Sample No.	Cp/Cs Ratio	Poisson's Ratio	Young's Modulus (GPa)	Shear Modulus (GPa)	Bulk Modulus (GPa)
21-1A	1.715	0.24	51.2	18.9	30.5
21-1B	1.651	0.21	45.0	16.9	23.5
26-1B	1.710	0.24	43.3	16.0	25.5
26-2A	1.741	0.25	50.8	18.8	31.9
30-2A	1.642	0.21	48.5	18.7	25.4
30-2B	1.649	0.21	43.7	16.2	22.4

For comparison purposes, the results obtained by the MSR system and the laboratory UPV technique are listed in Table 9-5. It can be seen that the MSR results follow the trend of UPV values but that they are consistently lower except for the Poisson's ratio and bulk modulus values for the station at 823.0meters. Results obtained by MSR show that P-wave velocities obtained from the laboratory measurement are higher by 4.4% at the first station, 8.5% at the second station, and 10.0% higher at the third station. For S-waves the UPV values are higher by 3.2% at the first station, 17.6% at the second station, and 8.9% at third station. One reason for this could be that the MSR impact device generates higher strain rates in the concrete than the UPV high frequency pulse generator, which results in lower velocities and consequently lower elastic values. Both P- and S-wave velocities obtained in the laboratory and field drop progressively with increasing depth. However, the MSR readings are more consistent. The calculated dynamic elastic constants obtained by the MSR are generally lower than the values obtained by the UPV technique. Similar to the wave velocities, elastic constants decrease as the depth increases.

In the frequency spectrums obtained by the two transducers, other significant peaks exist (Figures 9-7b to 9-12b). These frequency values are related to the existence of reinforcement bars and potential discontinuities or voids within concrete structures. However, since the information about the location of the reinforcement bars in the concrete shaft lining at the Allan Mine was not available, the determination of position of these reinforcement bars and later comparison with the actual values was not possible.

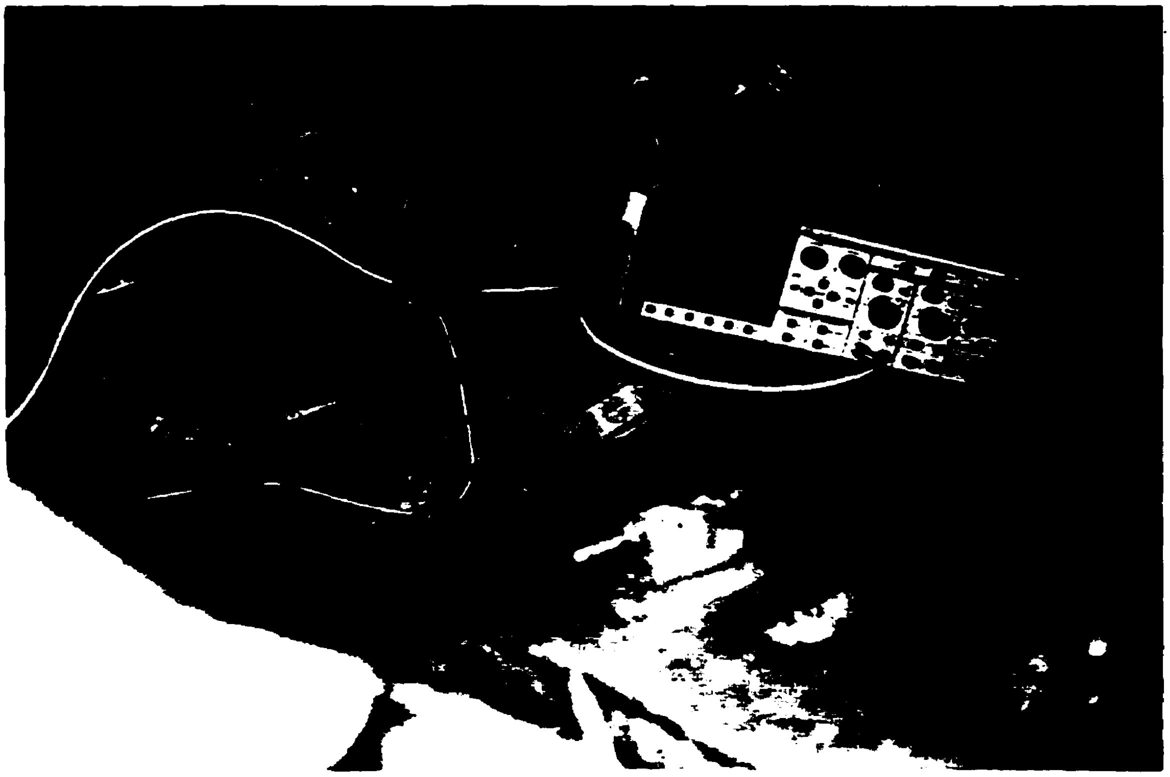

Plate 9-5 The MSR system setup on top of the cage.

Plate 9-6 Measurement of P-wave, using vertical displacement transducer, at Allan Mine.

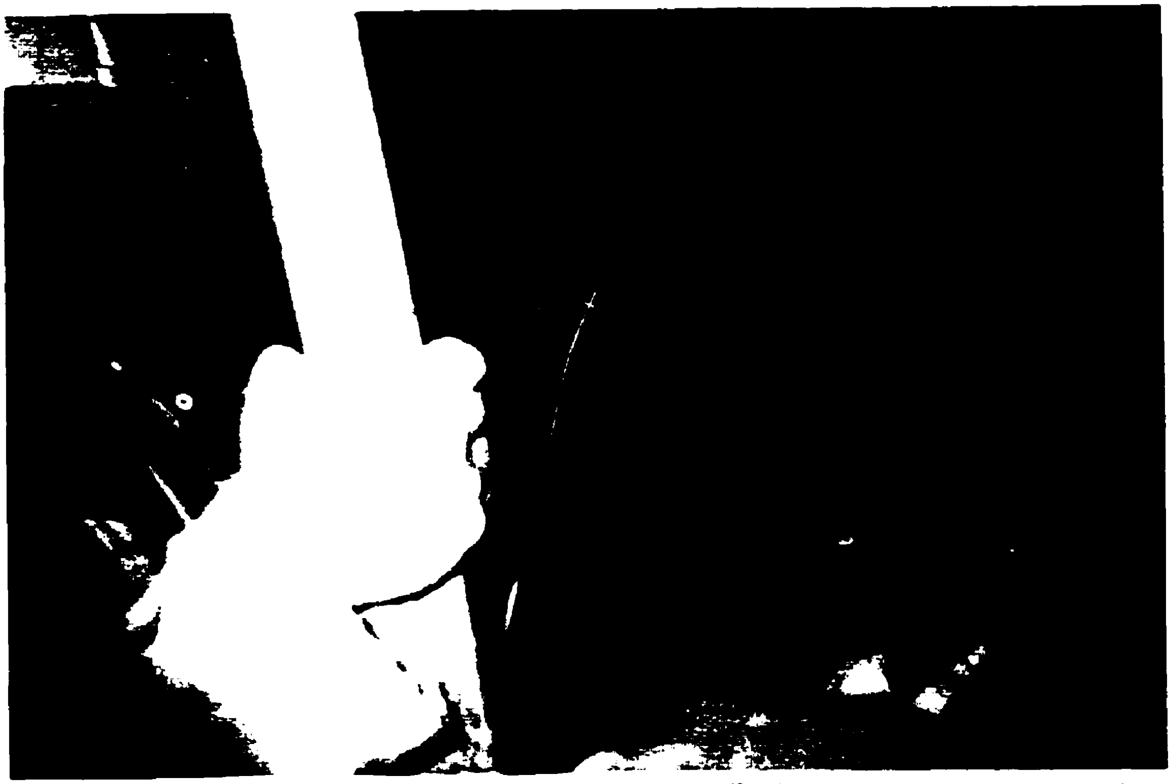

Plate 9-7 Measurement of S-wave, using tangential displacement transducer, at Allan Mine.

Plate 9-8 The S.T.C.U.M. underground tunnel system with concrete lining.

Table 9-5 A comparison between the values obtained by the MSR and laboratory measurements.

Depth m	Concrete Coring	Desktop Study	Laboratory Measurements		MSR Field Measurements	
	Observed Thickness (m)	Planed Thickness (m)	Measured Cp (m/s)	Measured Cs (m/s)	Measured Cp (m/s)	Measured Cs (m/s)
640.0	0.58	0.61	4620	2750	4418	2662
823.0	0.58 0.55	0.61 0.74	4640	2680	4248	2209
914.4	0.61 0.57 0.57	0.56 0.69	4500	2725	4050	2502

	Laboratory Measurements				MSR Field Measurements			
Depth m	υ	E (GPa)	G (GPa)	K (GPa)	υ	E (GPa)	G (GPa)	K (GPa)
640.0	0.23	48.1	17.9	27.0	0.22	44.4	18.4	26.4
823.0	0.25	47.0	17.4	28.7	0.31	33.8	12.7	29.6
914.4	0.21	46.1	17.5	23.9	0.19	38.3	16.0	20.6

9.4 APPLICATION OF THE MSR ON THE CONCRETE TUNNEL LININGS

In this section, the MSR system was used to examine the thickness of concrete tunnel linings of the Societe de Transport de la Communate Urbaine de Montreal (S.T.C.U.M.)underground subway (Metro). The tunnel was constructed in 1965 (see Figure 9-13). Since the construction of the subway system, due to the circulation of saline water, the outer section of the concrete lining has undergone extensive deterioration. Figure 9-14 shows a schematic diagram of the concrete lining and deterioration of the lining's outer ring. The deteriorated tunnel section is located about 30.0 meters below the surface (Plate 9-8). The reduction of the concrete thickness at the rock-side is not uniform. Most of the damage has been done at the rock/soil interface with the lining. Nevertheless, the concrete's deterioration has a great influence on the integrity of the tunnel lining system. As a solution, the thickness of the lining has to be identified and the damaged areas should be repaired and reinforced. However, to prevent extensive damage a continuous monitoring of the tunnel lining would be beneficial.

In order to estimate the lining's thickness, the average P-wave velocities in the concrete should be known. In this case, the vertical displacement transducer was used. An average P-wave velocity of 4330 ± 42 m/s for the concrete was calculated from the areas where the thickness is known. Knowing the velocity of the P-wave in the lining, and the frequency of the resonated waves between the two surfaces of the lining and using equation 6-5, the thickness of the lining was calculated at each survey station. To examine the results, the calculated thickness values were compared with a number of cores extracted from the concrete lining. The concrete core samples were extracted by the S.T.C.U.M.tunnel maintenance personnel and inspected in the laboratory for the thickness measurements, flaw detections, and mechanical properties. The results from the laboratory evaluation of the cored samples are listed in Table 9-6. The core values for the concrete thickness vary between 0.43 m to 0.74 m.

Table 9-6 The results from laboratory evaluation of concrete core samples from the tunnel lining.

Sample No.	Concrete Thickness (cm)	Concrete Segregation		Presence of Flaws in Concrete		Flaw Depth (m)	Separation of Rock/Concrete Interface	
		Yes	No	Yes	No		Yes	No
N-1	68.6		X	X			X	
N-2	50.8		X	X				X
N-3	72.4		X	X				X
L-3	63.5		X	X		0.27, 0.39		X
J-32	43.2		X	X		0.31		X
G-35	53.3		X	X		0.28, 0.48	X	
G-12	71.1		X	X		0.27, 0.43	X	
F-33	55.9	X		X		0.18, 0.31		X
E-21	58.4		X	X		0.31, 0.47	X	
C-12	73.7		X	X		0.31, 0.52		X

9.4.1 Experimental Setup

Access to the site was provided between 2 and 5 a.m., while the subway was not functioning. The testing site was halfway between Laurier and Mont-Royal stations on Line No. 2 (Plate 9-9 also see Figure 9-13). The concrete mix was cured for a 28 days 35.0 MPa strength. According to the original drawings, besides in the roof there is no indication of reinforcement bars in the structure (see Figure 9-14). This area of the lining was subjected to extensive damage caused by groundwater infiltration at the triple contact between the surrounding rock, overburden, and the concrete (Plate 9-10). Trenton limestone is the rock type surrounding the tunnel lining and the overburden is a mixture of post-glaicial sands and clays (Clark, 1952).

A hydraulic lift was used to provide easy access to the roof and the sides of the tunnel (Plate 9-11). There was evidence of spalling and the surface was rough.

For the thickness measurements only the vertical displacement transducer was used. The 3.0 mm impact device was used to introduce the transient stress signals into the lining. The contact-time of impacts were between 45 to 75 μs. The distance between the impact device and the receiver was kept less than 0.2 times the assumed thickness of the structure (5 to 10 cm) all the time. The collected waveforms captured by the vertical displacement transducer were stored in a portable computer. The frequency spectra were generated by using the FFT technique.

The thickness of the concrete tunnel lining was evaluated at 20 testing stations. Each station was 0.3 m apart, and in total an area of 2.50 m^2 on the upper east side of the tunnel was surveyed by the MSR system. Four parallel lines, Line A, B, C, and D were surveyed. On each line 4 to 6 stations were examined.

Table 9-7 The values of density, P-wave velocity and acoustic impedance for rock and soil surrounding the concrete tunnel lining and the concrete acoustic impedance.

Medium	Dry Density (kg/m^3)	Cp (m/s)	Rock Acoustic Impedance (Z_2) ($kg/m^2.s$)	Concrete Acoustic Impedance (Z_1) ($kg/m^2.s$)
Limestone	2690	2400	6.4×10^6	10.0×10^6
Sand & Clay	1601	800	1.2×10^6	10.0×10^6

9.4.2 Results and Discussion

Both surrounding materials (limestone, sand and clay) have lower acoustic impedance than the concrete. Therefore, the reflected signals from the concrete/rock and concrete/soil interfaces are strong and clear. In the frequency spectra, the single clear high peak corresponds to multiple reflections of P-wave signals from the concrete/rock or concrete/soil interface. Figures 9-15 and 9-16 illustrate the frequency spectra collected from the tunnel lining. A constant 4000 Hz narrow width signal in the spectra is related to the AC electrical current in the tunnel and is ignored in the calculations. Using the average P-wave velocity of 4330 ± 42 m/s (density 2310 kg/m^3), the distinct peak frequency from each spectra, and equation 6-5, thicknesses for the concrete lining in various areas were calculated and are listed in Tables 9-8 and 9-9. The values listed in Tables 9-8 and 9-9 suggest a thickness variation between 0.45 to 0.67 m.

A comparison between the calculated (0.45 to 0.67) and cored thickness values (0.43 to 0.74) indicates a reasonable correlation, considering the cores were not extracted at the same place where the MSR tests were conducted. The MSR results indicate that the concrete lining has an irregular outer shape at the contact with the surrounding rock. On the frequency spectra a number of distinct frequency peaks suggest the possibility of presence of voids and fractures in concrete (see Figure 9-15, Line A-1, 2, and 3; Line B-4 and 5; and Figure 9-16, Line C-1 and 4; and Line D-4) which can be confirmed by the cored samples. These points were identified from their high frequency distinct peaks in the frequency spectra, which is indicative of potential flaws. However, the exact position of the flaws can not be confirmed since the coring was not conducted at exact positions where the MSR tests were conducted. The results from this study suggests that the MSR system is capable of determining concrete thickness of the underground lining structures with considerable accuracy.

Table 9-8 The thickness and flaw measurements calculated by the MSR data for lines A and B.

Station No.	Thickness Frequency (Hz)	Calculated Thickness (m)	Flaw Depth (m)	Station No.	Thickness Frequency (Hz)	Calculated Thickness (m)	Flaw Depth (m)
A-1	4053	0.53	0.31	B-1	4346	0.50	-
A-2	3809	0.57	0.40	B-2	4053	0.53	-
A-3	4102	0.53	0.30	B-3	4199	0.52	-
A-4	3809	0.57	-	B-4	4004	0.54	0.33
A-5	3223	0.67	-	B-5	4541	0.48	0.28

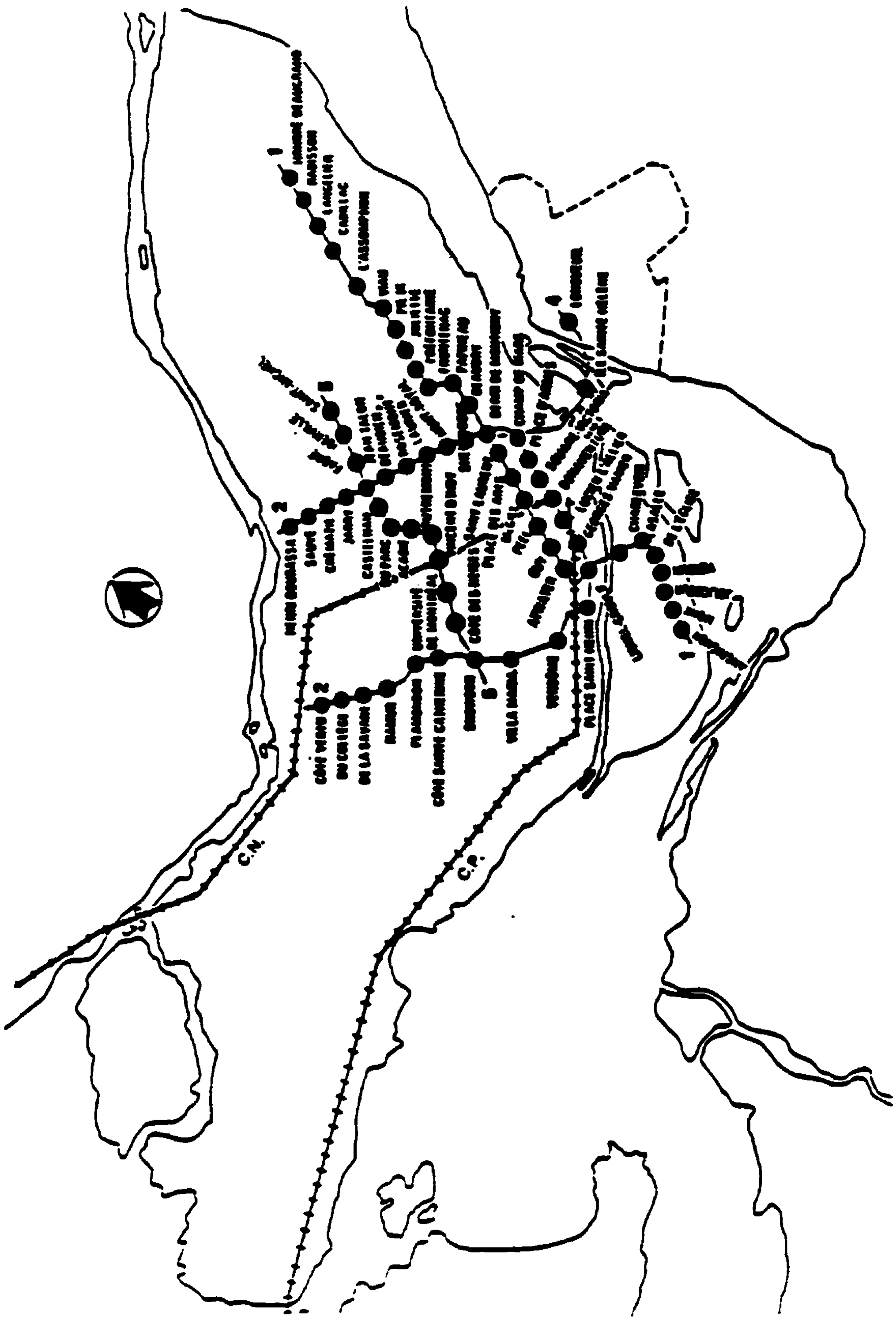

Figure 9-13 Montreal Metro and position of the Mont-Royal and Sherbrooke stations.

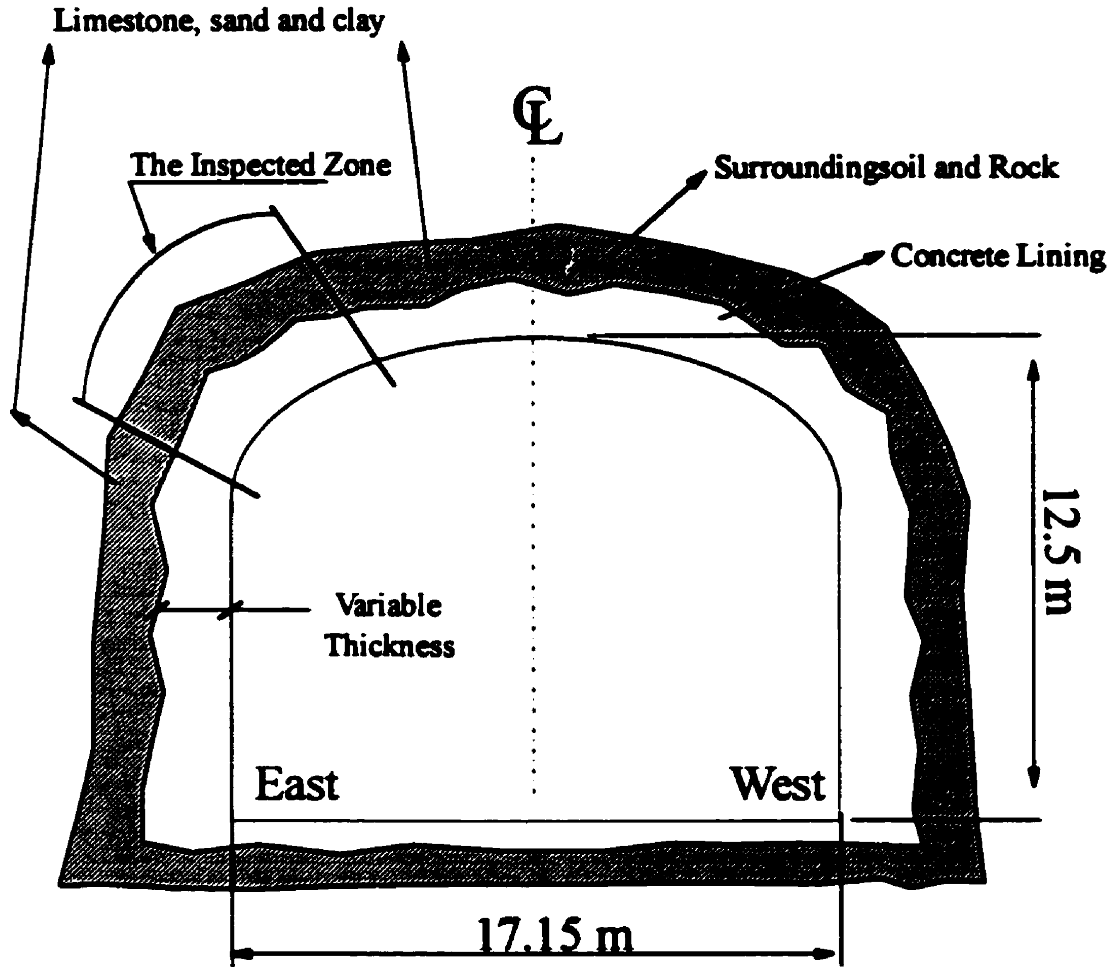

Figure 9-14 Schematic diagram of Montreal Metro concrete tunnel lining.
Note: The drawing is not into scale.

Plate 9-9 The survey zone: half way between Mont-Royal and Sherbrooke stations..

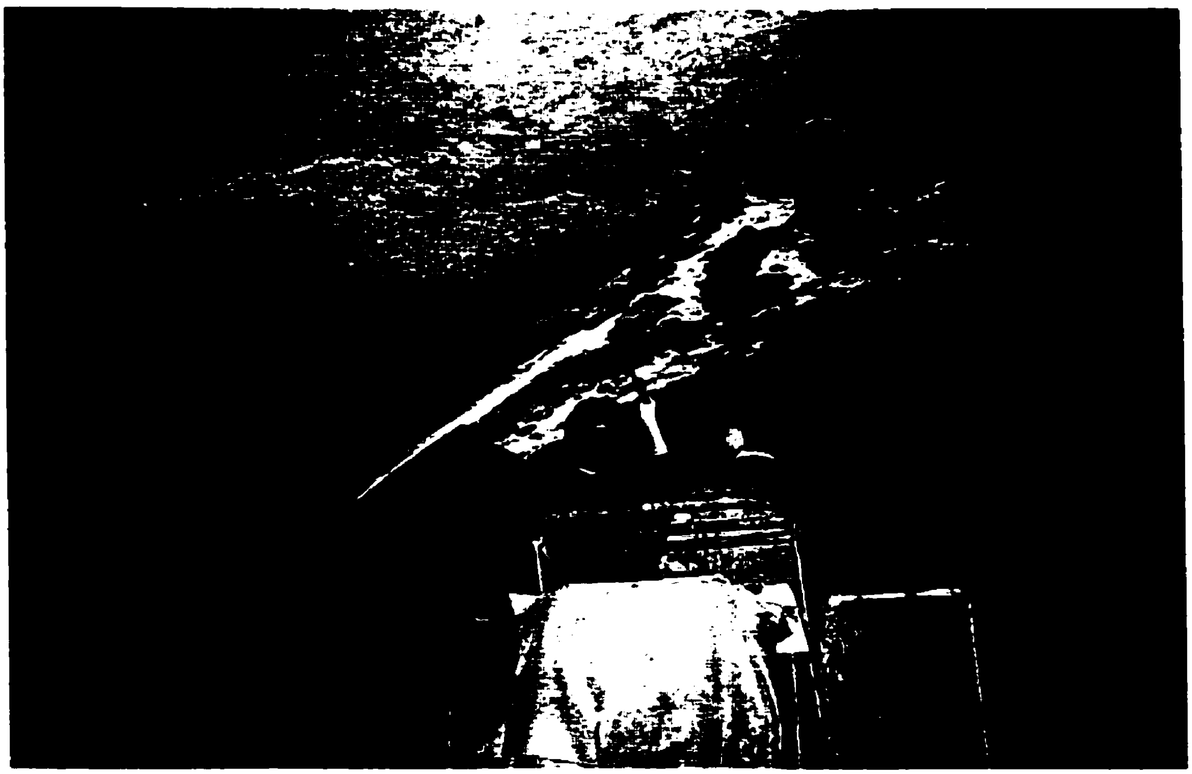

Plate 9-10 Extensive deterioration of the concrete tunnel lining.

Plate 9-11 The MSR testing of the concrete tunnel lining.

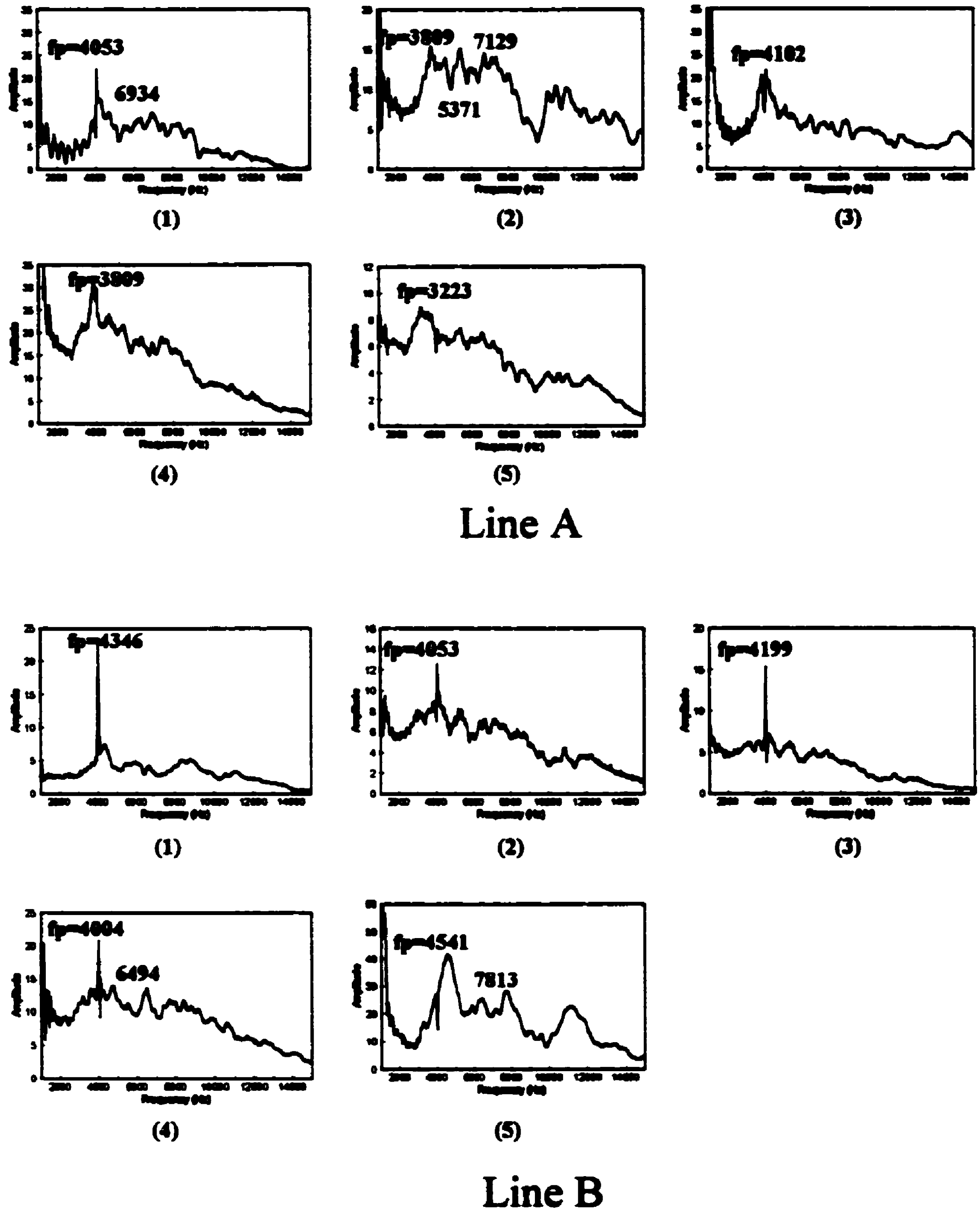

Figure 9-15 The frequency spectra calculated from the MSR survey on Lines A and B.

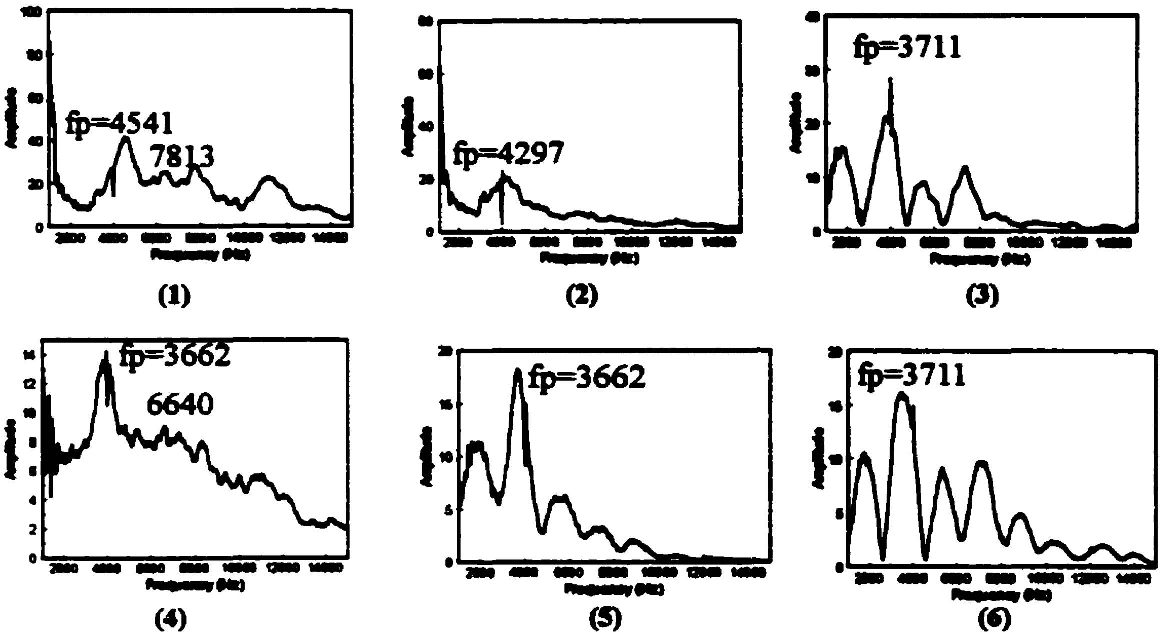

Line C

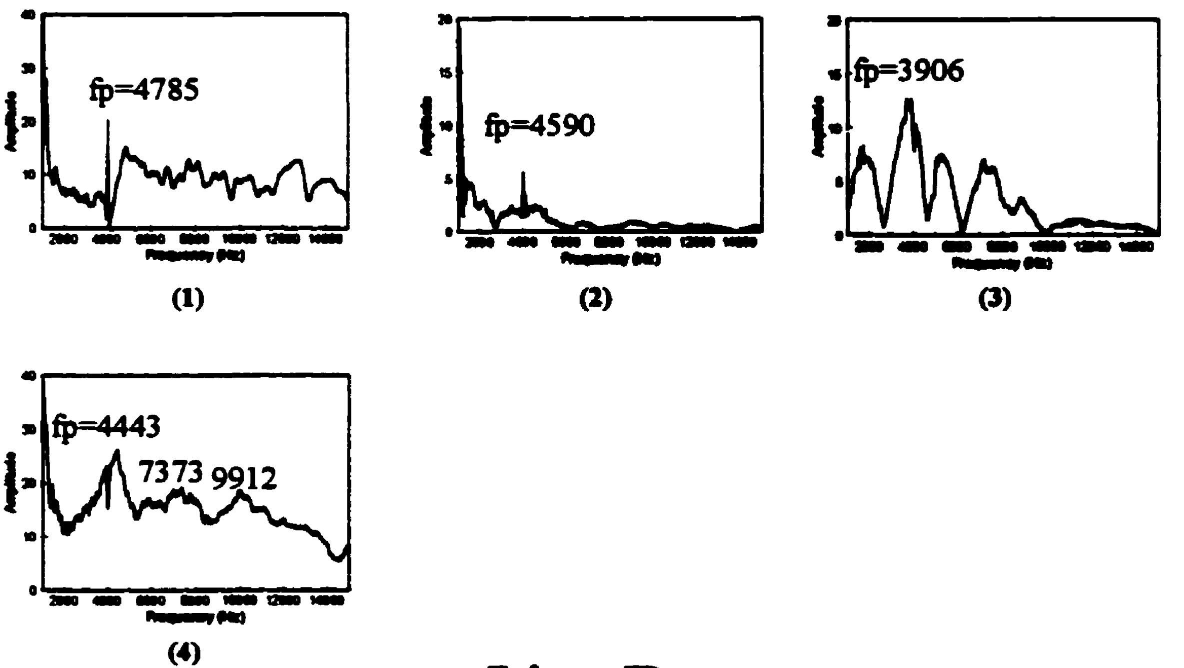

Line D

Figure 9-16 The frequency spectra calculated from the MSR survey on Lines C and D.

Table 9-9 The thickness and flaw measurements calculated by the MSR data for lines C and D.

Station No.	Thickness Frequency (Hz)	Calculated Thickness (m)	Flaw Depth (m)	Station No.	Thickness Frequency (Hz)	Calculated Thickness (m)	Flaw Depth (m)
C-1	4541	0.48	0.28	D-1	4785	0.45	-
C-2	4297	0.50	-	D-2	4590	0.47	-
C-3	3711	0.58	-	D-3	3906	0.55	-
C-4	3662	0.59	0.33	D-4	4443	0.49	0.33, 0.22
C-5	3662	0.59	-	-	-	-	
C-6	3711	0.58	-	-	-	-	-

9.5 SUMMARY AND CONCLUSIONS

A series of tests was conducted by the MSR system on the production shafts at the CCP and Allan Mines of Saskatchewan and concrete tunnel lining at Montreal's underground subway. The following conclusions are drawn from the field experimentations in this chapter:

1. For shaft linings, concrete thickness was known. Using the thickness values, the dynamic elastic properties of the concrete linings were evaluated at various locations. In the case of the CCP Mine, the position of the reinforcement bars was confirmed by MSR readings. In the case of the Allan Mine, due to lack of information, the location of the rebars or possible defects could not be determined. However, the dynamic elastic properties of concrete lining was evaluated. The in-situ results obtained by the MSR system were compared to the laboratory values calculated by the UPV technique on the extracted core samples at different levels. The trend of the results are similar, however, the MSR values are generally lower than the UPV readings. One advantage of the MSR technique over traditional methods such as resonant frequency or pulse velocity is that accurate readings may be obtained from a free face (in situ) regardless of the dimension and condition of the concrete structure. A continuous and periodic

survey of shaft linings by the MSR system can help detect the beginning and growth of a problem in a structure, and hence repairing can be done prior to expansion of the problems leading to a structural damage.

2. For the tunnel lining, the average P-wave velocity of the concrete was calculated in the areas with known thickness. The MSR results were analyzed to identify significant reflected P-wave peaks. Using the P-wave velocity and distinct peak from the frequency spectra, the concrete thickness was calculated at various positions. On the frequency spectra a number of flaws were identified. Both thickness and flaw measurements by the MSR system are within the acceptable range which were confirmed by the testing of extracted cores. The results in this field study showed the ability of the MSR system to evaluate concrete lining thickness and integrity. As for the concrete shaft lining, a continuous and periodical monitoring of the lining can foresee the deteriorations and help prevent structural damages.

3. The MSR equipment assembly is well suited for the underground testing environment. The method of analysis is accurate and rapid. One important advantage of the MSR system is its capability of measuring elastic wave velocities from the air-side of the shaft. The MSR results in these two projects were encouraging and confirmed that the system can be used as an in situ nondestructive testing technique in order to evaluate the thickness, elastic properties and integrity of the concrete linings in an underground environment.

CHAPTER 10

APPLICATION OF THE MSR SYSTEM FOR EVALUATING MECHANICAL PROPERTIES OF ROCKS

10.1 INTRODUCTION

The mechanical properties of rocks under different conditions must be taken into consideration in the design of mining and geotechnical structures. In general, estimates of the elastic constants are used to determine the load-bearing capacity of desired rock types. The purpose of this study is to investigate the capability of the MSR system to evaluate the elastic properties of rocks. Here the MSR system is used to determine the elastic constants of igneous rock blocks and cores. In order to confirm the MSR results and for comparison purposes, standard laboratory static and dynamic tests were conducted. In the case of dynamic methods, RF and UPV instruments were used. In addition, the cored rock samples were be loaded to failure in stepwise intervals. At each step, the samples loaded up to a percentage of the maximum strength and then unloaded to zero. At zero load the samples were tested by the MSR system to evaluate their elastic properties. For comparison purposes, the samples were also tested by the UPV instruments. The main objective of these tests was to study the sensitivity and applicability of the MSR system in relation to mechanical changes in the rocks. Finally, the MSR system was used in a field study to measure the thickness of separations on the back of a potash opening in an underground mine in Saskatchewan. The location of the discontinuities were confirmed by drilling.

10.2 TESTING OF ROCK SPECIMEN FOR ELASTIC PROPERTIES

The purpose of this research was to study the capability of the MSR system in evaluating the elastic properties of the rocks. This laboratory study was conducted in two parts. In the first part, five blocks of igneous rocks were tested by the MSR system. To study the effect of dimension and shape of the specimens on the results, the cored samples of the same rock types were also tested. The calculated results of elastic constants from the MSR readings were compared with the values of elastic constants calculated using standard UPV and RF methods. These results were also compared with the values of static elastic moduli and Poisson's ratio. In the second part of the laboratory study, cored rock specimens were cyclically loaded and unloaded. At each cycle, ten percent load was added until the sample failed. When the sample was unloaded the MSR and the UPV testings were conducted. The purpose of this experiment was to examine the capability of the MSR system in testing samples under dynamic conditions as well as to compare the behavior of the UPV and MSR systems under the same dynamic loading/unloading conditions.

10.2.1 Physical Properties of Rock Specimens

A total of five different intrusive igneous rock types, namely a white granite, a red granite, a charnokite, a diorite and a gabbro, were selected for testing (Plate 10-1). The rocks were isotropic, homogeneous and without any visible internal fractures. Dry density and porosity were determined for all the rock types following the procedure outlined in the standard laboratory techniques recommended by the International Society for Rock Mechanics Commission (ISRM) on "Standardization on Laboratory and Field Tests" (1981); the results are listed in Table 10-1.

10.2.2 Petrographic Analysis

One sample from each rock type was cut and polished, and thin-sections were prepared and studied under a light-transmitting microscope. Various magnifications were used to study the constituents of the rock sample.

White granite (UGIS Classification) is hollocrystaline, hypidiomorphic, medium grained and essentially equigranular. The rock consists of 30% plagioclase, 35% quartz, 25% K-feldspar, 8% biotite, and 2% trace minerals and opaques. The average crystal size is between 2 to 4 mm in diameter. The rock is also known as Stanstead granite, coming from the Bebee region of the province of Quebec.

Red granite (UGIS Classification) is hollocrystaline, hypidiomorphic, medium grained and essentially equigranular. The rock consists of 25% plagioclase, 35% quartz, 35% K-feldspar, 3% biotite, and 2% trace minerals and opaques. The average crystal size is between 2 to 5 mm in diameter. This red granite was originally extracted from the Canadian Shield in the northern part of the province of Ontario.

Charnokite (UGIS Classification) or amphibole rich granite is hollocrystaline, hypidiomorphic, large-medium grained and essentially inequigranular. Charnokite is also called: hypersthene granite. The rock is made of 5% plagioclase (0.5-4 mm), 35% K-feldspar (0.5-20 mm), 25% quartz (2-9 mm), 30% hornblende-amphibole (0.5-5 mm) and 3% biotite (0.5- 2 mm). This charnokite is from the Parc Laurentide region of the province of Quebec.

Diorite (UGIS Classification) is hollocrystaline, hypidiomorphic, medium-fine grained and essentially equigranular. The rock is made of 76% plagioclase, 8% quartz, 6% K-feldspar, 5% pyroxene, 3% amphibole, and 2% trace minerals and opaques. The average crystal size is between 2 to 7 mm in diameter. This diorite came from the south western region of the province of Ontario.

Gabbro (USGS Classification) is hollocrystaline, hypidiomorphic, medium-fine grained and essentially inequigranular. A more precise name for this rock is hornblende-pyroxene gabbronorite. The rock consists of 70% hornblende-amphibole (5-15 mm), 25% pyroxene (3-5 mm), 3% muscovite (0.5-1 mm), and 2% trace minerals and opaques. This gabbro is from the Ste. Xenon region of the province of Quebec.

Table 10-1 The physical characteristics of the rock specimens.

Rock Type	Bulk Density (Kg/m^3)	Dimensions l×w×h (m)	Maximum Crystal Size (cm)	Porosity (%)
White granite	2660	0.61×0.31×0.31	1.5	1.4
Red granite	2610	0.62×0.32×0.32	1.2	0.9
Charnokite	2700	0.62×0.32×0.21	4.4	2.1
Diorite	2930	0.62×0.32×0.30	0.5	0.5
Gabbro	2700	0.61×0.31×0.21	0.9	0.7

10.2.3 Observation of Dynamic and Static Elastic Moduli

10.2.3.1 The MSR System

The MSR tests were conducted both on the large block samples and cored specimen. The block dimensions are given in Table 10-1. Figure 10-1 shows schematic drawing of the MSR experimental setup on the rock blocks. The spherical tip spring loaded impact device having a diameter of 3.0 mm was used as the impact device. The impacts were responsible for generating a contact-time between 40 to 45 μs, which results in generating input frequencies between 18 to 25 kHz. The vertical displacement transducer was placed at a distance of 5.0 cm from the impact device for all the tests performed. To collect the reflected S-waves at their maximum amplitude, the tangential displacement transducer was placed at a distance equal to the thickness of the blocks. The A/D card was used for acquisition of the waveforms. Subsequently, the recorded waveforms were collected in a personal computer for further analysis. A sampling frequency of 100 kHz was used throughout the experiment and the total signal length retained for analysis was 2048 points, having 10 μs intervals. This value corresponds to a resolution of 0.0488 kHz in the frequency spectra. A high pass filter was used to remove the 1.0 kHz resonance frequency of the transducers and the effect of the R-wave signals.

The frequency content of the collected waveforms was determined by the FFT technique. The frequency spectra contain peaks at various frequency values. In the spectra for the waveforms collected with the vertical displacement transducer, the dominant frequency peak corresponds to the P-wave resonance between the top and the bottom of the blocks. In cases where the tangential displacement transducer was used, the dominant frequency peak corresponds to the S-wave resonance between the two surfaces. In Appendix D, Figures D-1 to D-3 show examples of the captured waveforms and the corresponding frequency spectra on the rock blocks. Equations 6-4 and 6-9 were used to calculate the P- and S-wave velocities. The equations in Table 3-2 were used with the calculated wave velocities to determine the dynamic elastic constants of each rock block. Table 10-2 shows the values of body wave velocities, elastic moduli and Poisson's ratio of the rock blocks. The values of the P-wave velocities of the five different rock blocks for the comparison purposes with the cored samples and UPV values are listed in Table 10-4.

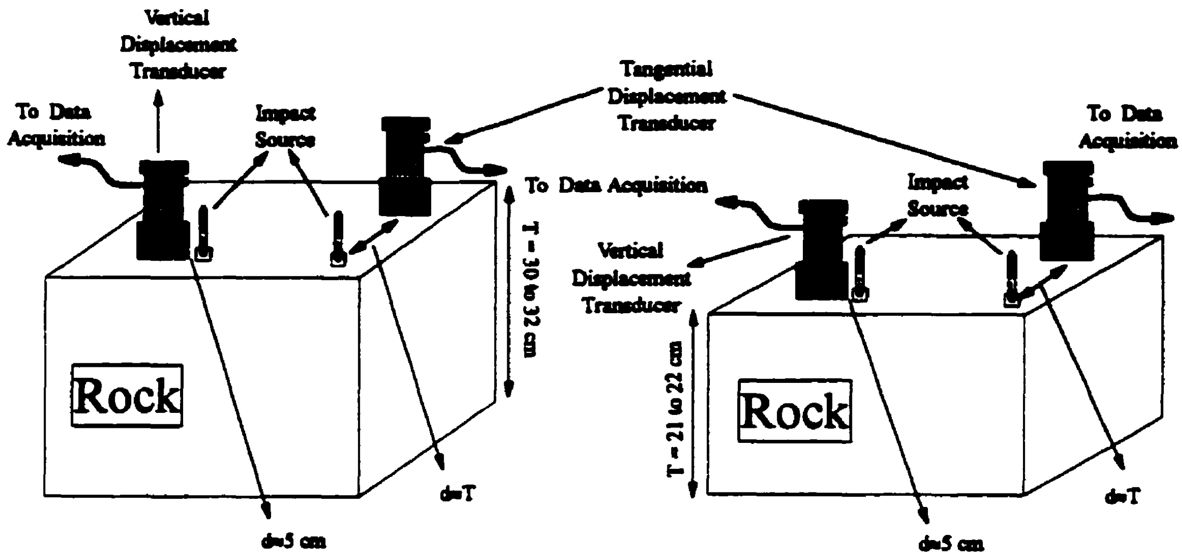

Figure 10-1 Schematic representation of experimental setup used to evaluate the P- and S-wave parameters in rock blocks.

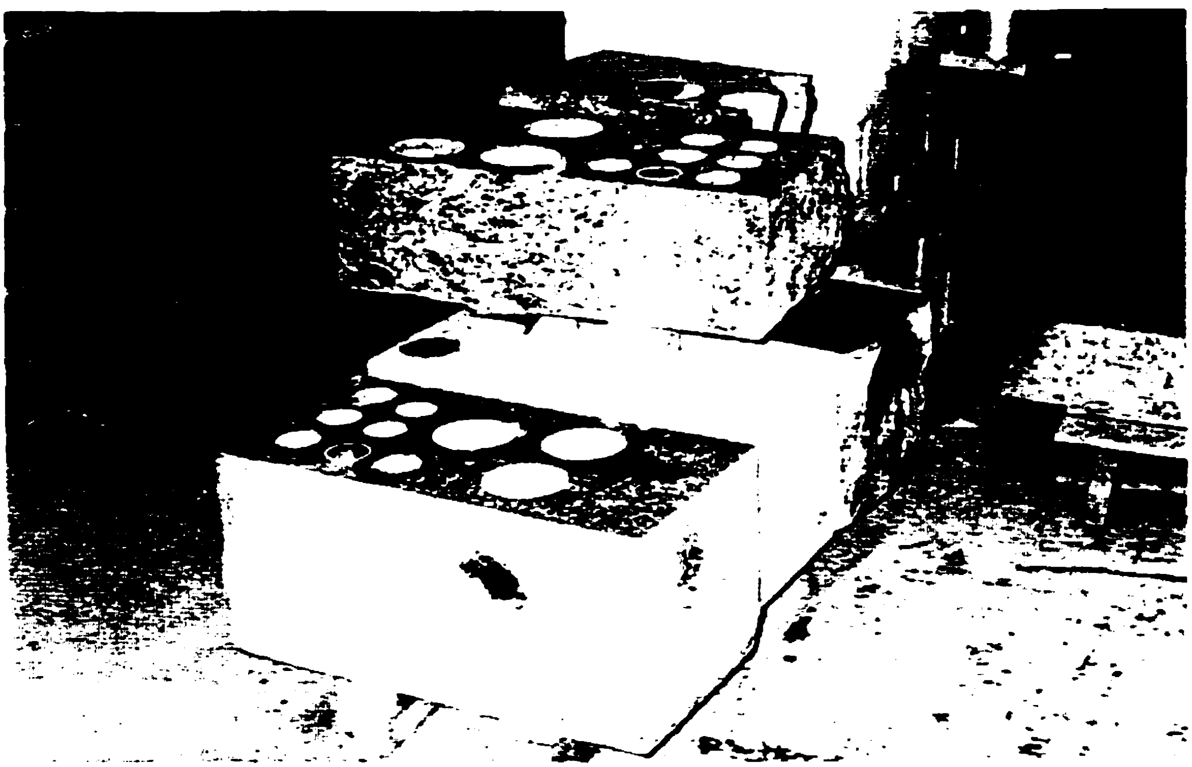

Plate 10-1 The Five different igneous rock specimens.

Table 10-2 The dynamic modulus of elasticity and Poisson's ratio data derived by the MSR technique on the block size samples.

Rock Type	P-wave Velocity	S-wave Velocity	Dynamic Young's Modulus of Elasticity MSR (GPa)	Poisson's Ratio
White granite	4481±86	2565±98	43.6±1.3	0.26±0.01
Red granite	5281±74	3138±41	62.8±2.5	0.23±0.01
Charnokite	4881±22	3134±49	61.0±1.8	0.15±0.02
Diorite	4863±64	3056±38	64.4±2.8	0.17±0.03
Gabbro	5500±12	3330±54	66.9±0.5	0.21±0.02

Three 9.6 cm diameter samples from each rock type were cored. The vertical and tangential displacement transducers were used to collect P- and S-wave parameters. Figure 10-2 shows the schematic drawing of the MSR test setup on the rock cores. Both the transducers and the impact source were placed on the same sides of the cored samples. Dominant frequency peaks were representatives of the P-wave and S-wave reflections from back of the cores detected by the vertical and tangential displacement transducers, respectively. In Appendix D, Figures D-4, D-7, D-11, D-15, and D-20, at the top show the captured waveforms and the calculated frequency spectra for the rock cores were there was zero applied load. Knowing the thickness of the cored samples, equations 6-4 and 6-9 were used to calculate the body wave velocities from the resulting maximum amplitude peaks at the frequency spectra. The P-wave velocities of the cored samples obtained by the MSR system are listed in Table 10-4 for the comparison purposes with rock block and UPV values.

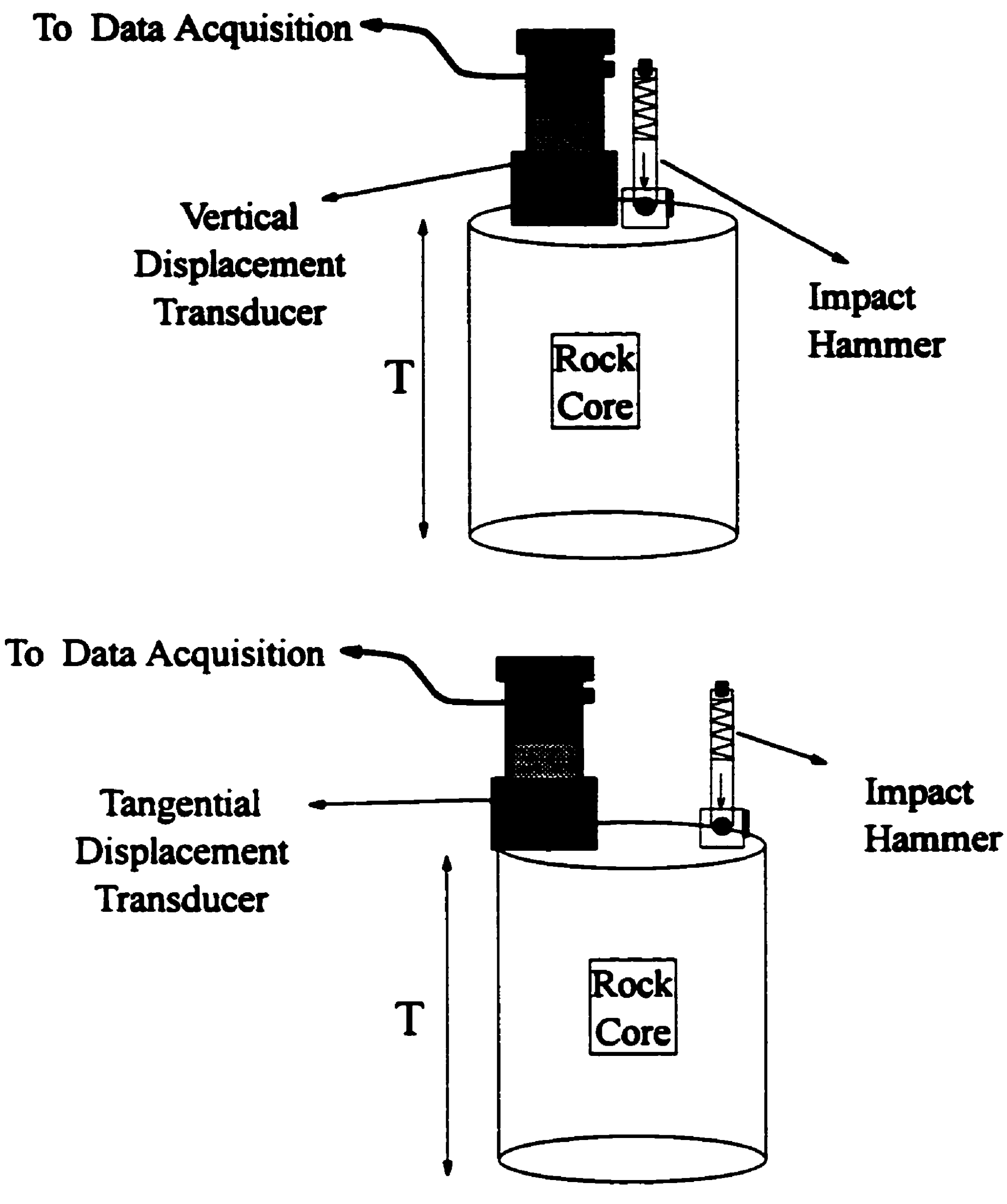

Figure 10-2 Schematic representation of experimental setup used to evaluate the P- and S-wave parameters in rock cores.

Table 10-3 The dynamic modulus of elasticity and Poisson's ratio data derived by the MSR technique on the core samples.

Rock Type	P-wave Velocity	S-wave Velocity	Dynamic Young's Modulus of Elasticity MSR (GPa)	Poisson's Ratio
White granite	4026±70	2750±84	35.0±0.5	0.26±0.01
Red granite	4645±66	2741±32	48.3±1.1	0.24±0.01
Charnokite	4155±5	2551±51	42.0±2.0	0.19±0.02
Diorite	5395±42	3183±52	63.1±2.6	0.23±0.01
Gabbro	5172±36	3166±53	64.9±1.2	0.20±0.03

10.2.3.2 The Ultrasonic Pulse Velocity (UPV) Technique

The UPV tests were carried out both on the block and core specimens. Ultrasonic P-wave velocities were obtained by direct method using the Pundit system (C.N.S. Electronics Ltd.). A more detail description of the instrumentation and the testing technique is given in Appendix B. The samples were placed between two P-wave piezoelectric transducers operating at 50.0 kHz (direct method). Petroleum jelly was used at the contact between the rock specimens and the transducers, in order to establish good acoustic coupling. The ultrasonic pulse was created at one end of the samples and detected at the other end by a receiving transducer. The time that pulse travels from the initial point to the destination transducer was measured by the instrument. Knowing the length of the core samples, the P-wave velocities of cores and block samples were determined. The P-wave velocities were obtained for the three samples from each rock type and are listed in Table 10-4.

Table 10-4 A comparison between the ultrasonic compressional wave velocity values and compression wave velocity values obtained by the MSR system.

Rock type	Blocks		Cores	
	UPV PUNDIT (direct method) (m/s)	MSR system (m/s)	UPV PUNDIT (direct method) (m/s)	MSR system (m/s)
White granite	4112±124	4481±86	4196±82	4026±70
Red granite	4800±106	5281±74	4891±75	4645±66
Charnokite	4596±55	4881±22	4693±24	4155±5
Diorite	5748±87	4863±64	5783±66	5395±42
Gabbro	5401±59	5500±12	6207±48	5172±36

10.2.3.3 The Resonant Frequency (RF) Technique

The RF tests were conducted on prismatic specimens cut and prepared with specific dimensions. The dynamic modulus of elasticity and Poisson's ratio were obtained using the Grindosonic RF instrument (J.W. Lemmens Inc.). A detail description of the instrumentation and testing technique is presented in Appendix A. The dimensions of rock samples were 50 × 50 × 240 mm. The samples were struck by a rubber tip steel rod in order to generate mechanical vibrations in the prisms. The samples were placed on a dampening rubber pad. The piezoelectric receiver was held in contact with the sample's surface. The detected signals were amplified and transferred to the instrument. The instrument's output is related to the elastic and dampening properties of each specimen; therefore the instrument output (*r*-value) was used to calculate the elastic properties of each rock type. The values of dynamic elastic moduli calculated by RF method are listed in Table 10-5.

Table 10-5 Dynamic modulus of elasticity and Poisson's ratio using the Grindosonic instrument (RF) technique.

Rock type	Dynamic Young's modulus of elasticity by Grindosonics (GPa)	Poisson's ratio
White granite	42.2±3.4	0.24±0.04
Red granite	57.4±2.1	0.23±0.03
Charnokite	48.2±2.9	0.25±0.04
Diorite	84.9±8.1	0.20±0.03
Gabbro	75.6±1.6	0.25±0.02

10.2.3.4 Static Testing

The procedure recommended by the International Society for Rock Mechanics (ISRM, 1981) was used to calculate the modulus of elasticity and Poisson's ratios for each specimen. Three samples were extracted from the specimens listed in Table 10-1 for uniaxial testing. The samples were prepared to be 50.8 mm in diameter and 101.3 mm in length. The ends were lapped flat and parallel to each other and normal to the core axis. Strain gauges, two parallel and two perpendicular to the longitudinal axis of the specimen, were installed to measure the amount of axial and diametrical strains. The strain values were used to calculate Poisson's ratio for each sample. The installation procedure was carried out following the manufacturer's recommended guideline (Micro-Measurements Group, Inc.). For all the specimens, type CEA-06-12UN-120 strain gauges were used. The strains were monitored and recorded by a computer based measuring equipment. The maximum unconfined compressive strength and Young's modulus of elasticity were calculated by analyzing the data collected by the RDP 2500 kN servo-controlled hydraulic stiff testing machine using a loading rate of 0.7 MPa/sec (see Plate 10-2). All of the specimens were tested under strain control, as recommended by the ISRM. The stress-strain curves were plotted for each sample and used to compute three values for Young's modulus, the tangent modulus (E_t), secant modulus (E_{sec}) and the average modulus (E_{av}). Table 10-6 shows the average values of unconfined compressive strengths for the five rock types. Figures 10-3 to 10-5 show examples of stress-strain curves for the five rock types. Table 10-7 shows the calculated static modulus of elasticity and Poisson's ratio for the five rock types.

Table 10-6 The values of unconfined compressive strength for the rock samples tested samples.

Rock type	Uniaxial compressive strength (MPa)
White granite	143.3±6
Red granite	205.2±4
Charnokite	131.4±3
Diorite	216.5±6
Gabbro	235.2±5

Table 10-7 The static modulus of elasticity and Poisson's ratio of the five rock types.

Rock type	E_t (GPa)	E_{av} (GPa)	E_{sec} (GPa)	Poisson's ratio
White granite	53.2±2.5	56.2±0.8	37.2±3.3	0.27±0.03
Red granite	61.3±2.4	61.5±1.1	45.7±3.1	0.27±0.02
Charnokite	54.7±1.9	50.9±0.9	32.7±2.1	0.17±0.01
Diorite	67.2±2.4	65.3±1.7	48.4±2.6	0.26±0.01
Gabbro	62.7±2.1	64.3±1.4	49.1±2.3	0.22±0.01

10.2.3.5 Results and Discussion

The analysis of the data is concentrated on two aspects: first, the relationship between the P-wave velocities obtained by the UPV and the MSR systems from the rock samples, and second, a comparison between the dynamic elastic properties obtained by the MSR system and the RF technique with static elastic constants. Tables

10-1, 10-2, 10-3, 10-4, 10-5 and 10-7 present the results of the velocity measurement and the determination of static and dynamic modulus of elasticity and Poisson's ratio using traditional techniques and the MSR technique.

With the exception of diorite, the P-wave velocities obtained by the MSR system on the rock blocks are higher than the P-wave velocities of the same samples when they were cored. The UPV values obtained from the cored samples are higher in all cases than the velocities obtained from the rock blocks.

A comparison between UPV and MSR compressive wave velocity values shows that in the case of cored samples the ultrasonic values are higher than MSR value between 4 to 16%. In the case of block specimens, with the exception of diorite (UPV values are higher up to 15%), the MSR values are higher than the UPV values between 2 to 9%.

By comparing the frequency spectra obtained by the MSR system it is evident that the interpretation of the results from cores samples are much simpler than interpretation of rock blocks. For the cores, the multiple reflected P- and S-waves dominates the response of the specimen, and therefore the corresponding frequency appears as the highest peak in the frequency spectrum. In the block specimen, the corresponding P- and S-wave frequency amplitudes are not as strong and clear as in the case of cored specimens.

As was expected, the dimensions, type and physical properties of rock specimen have a significant influence on the P-wave velocities. However, these effects are not equally shared by the UPV and MSR systems. The signal attenuation rate for the ultrasonic pulse is greater than the MSR pulse. The confined dimensions of the cored specimens positively enhance the amplitudes in frequency spectra generated by the MSR signals. In the case of UPV values, shorter cored samples provide higher velocity values than unconfined long block specimens. This is due to higher rate of attenuation in the block samples, which is a result of their large dimensions, in relation to the short cored samples. The UPV results on the cored samples are higher than the MSR values. The reason is due to the difference in strain rate, the higher pulse frequency of the PUNDIT in comparison with MSR impact pulses, and higher sensitivity of the MSR transducers. The PUNDIT uses the threshold approach to trigger its time of arrival measurement unit.

Despite the good overall correlation obtained between the dynamic and static Young's moduli, a reliable value for the ratio between the static and dynamic values cannot be inferred from there. The fact that the difference between the static and dynamic values obtained by various methods are large in some cases indicates that there are a number of effects influencing the behavior of the rocks. Most likely these include the stress-strain rate, chemical weakening of the bonds along grain boundaries, presence of microfractures, and the shape and orientation of voids and pores.

A comparison of the values for the modulus of elasticity obtained from the dynamic methods shows that both Grindosonic and MSR produce estimates that are within an acceptable range. If one considers the results of the static tests, however, it can be seen that for stronger rock types (i.e. gabbro, diorite and red granite), the values of the Young's modulus obtained from the MSR are closer to their static counterparts (E_t and E_{av}). The same comparison cannot be made for the values measured with the Grindosonic instrument.

Using the MSR system, in most cases the values of dynamic Young's moduli taken from the block specimens are higher than the values calculated for the cored samples.

Poisson's ratios from the MSR system are close to the static values. The largest discrepancy in the Poisson's ratios from the Grindosonic compared to the static values is from the charnokite samples.

The results of this comparative study suggest that the MSR technique can be used to assess the elastic properties of the rocks. The MSR system offers an advantage over the UPV and RF techniques in that only one side of the test object needs to be accessible. Another advantage of the MSR testing technique is the ease by which the tests can be carried out to a high degree of repeatability on an particular sample. The tests by the MSR system require minimum sample preparation as it is in the case of RF, and do not require any couplants as is required in the case of UPV testing. It is, therefore, possible to use the system for in situ testing of a rock sample over a long period of time, without any detrimental (e.g. microfracturing) effects being caused by the propagation of the low energy level stress pulses through the samples.

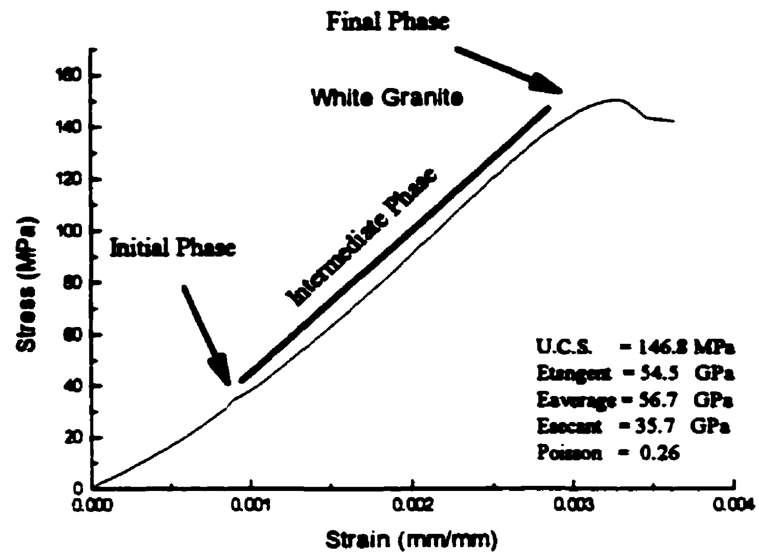

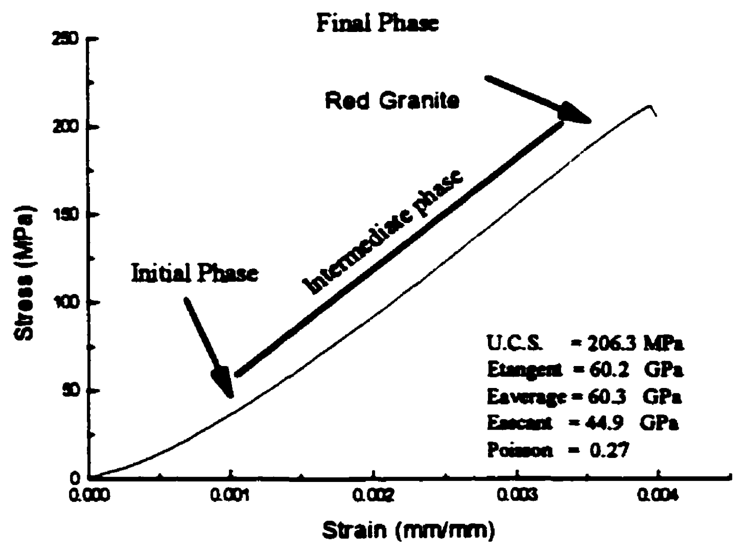

Figure 10-3 Samples of stress-strain curves for the white and red granite.

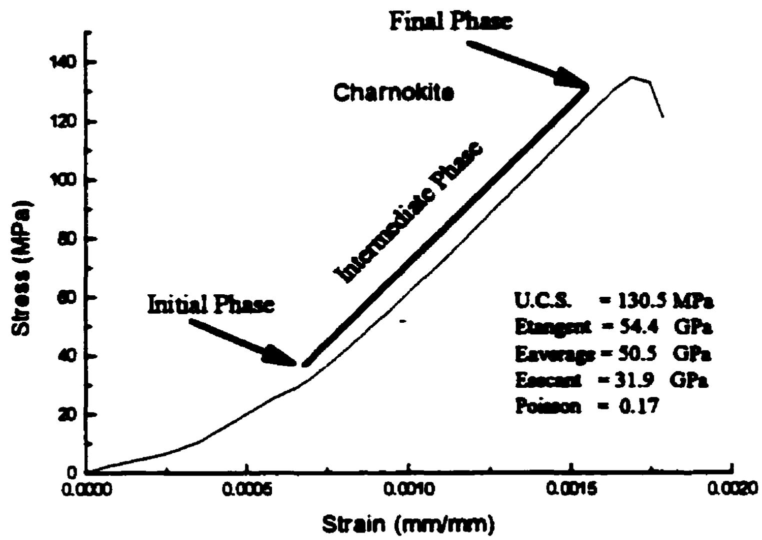

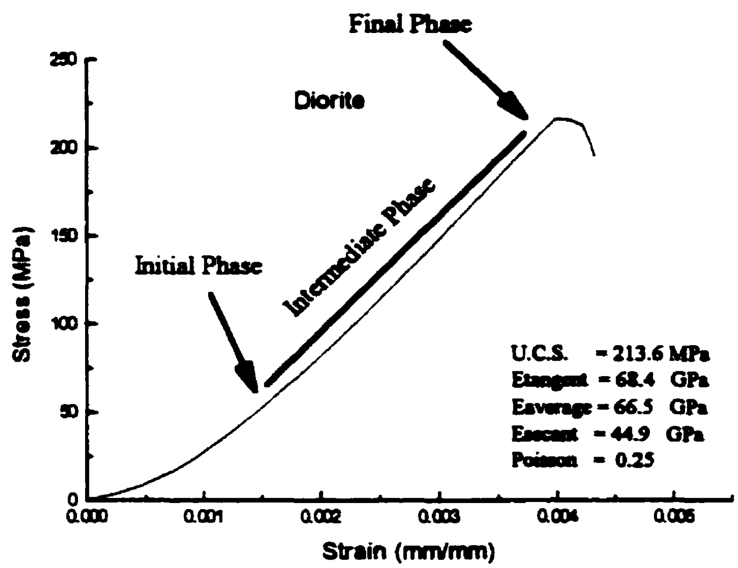

Figure 10-4 Samples of stress-strain curves for the charnokite and diorite.

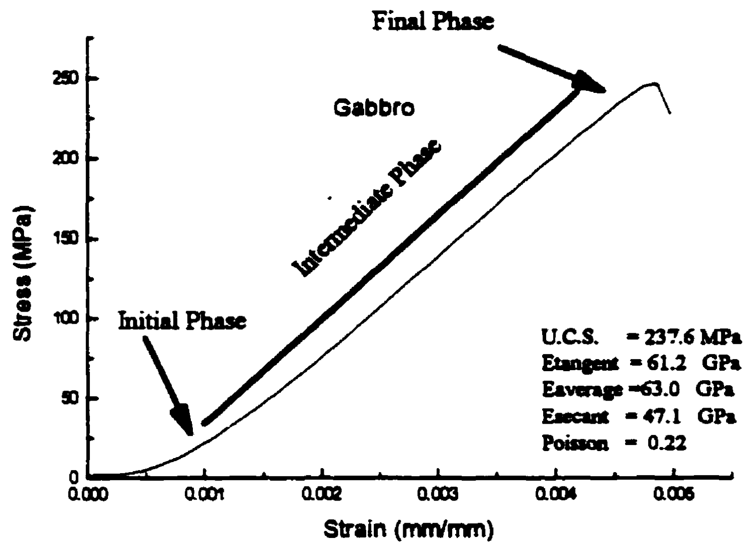

Figure 10-5 Samples of stress-strain curves for the gabbro.

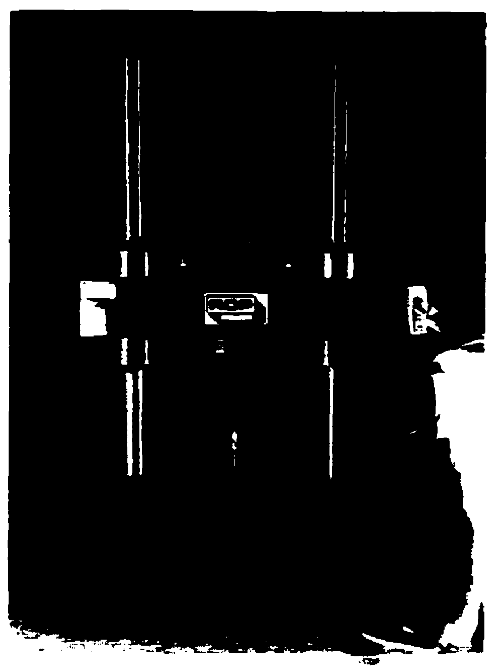

Plate 10-2 The RDP servo-controlled hydraulic stiff testing machine.

10.2.4 Effect of Loading/Unloading Cycles on Elastic Constants

10.2.4.1 Experimental Technique

This study was based on the assumption that compressive stress would damage rock specimens and thus change the modulus of elasticity, strain, and elastic waves characteristics. Beside permanent strain, elastic constants and elastic wave velocities were determined using the MSR system. For the purposes of comparison, compressive wave velocities were also calculated by the UPV technique. To evaluate the efficiency of the MSR system as a tool to detect the critical state of the rock, the specimens were subjected to compressive loading and then tested with the UPV technique and the MSR system. The critical state occurs when the rock is extensively fractured as a result of stress and it is very unstable. Five intrusive igneous rock types - white granite, red granite, charnokite, gabbro, and diorite - were used in this study.

The 2500 kN, RDP servo-controlled rock mechanics test system was used for the cyclic testing (see Plate 10-2). The machine is programmed to apply loading to a specimen by controlling the stress. The maximum load to be applied on the sample along with the frequency of loading/unloading process was determined based on the maximum load-bearing capacity of each rock type. For each cycle the load was increased by 10%. The 9.6 cm diameter cylindrical core samples are used for the tests. The length of the samples varied from 19.5 to 22.7 cm. The ends of the cores were ground flat and parallel.

The elastic wave velocities were determined at the end of each cycle (zero load), using the MSR system in order to determine the corresponding dynamic moduli. A 3.0 mm diameter spherical tip impact device was used to generate stress pulses on the samples. The impact device was kept the same for all performed measurements. The contact-time of the impact was measured to be between 40 to 45 μs, responsible for generating input frequencies between 18 to 25 kHz and wavelengths less than 0.2 meters. Both vertical and tangential displacement transducers were used to collect P- and S-wave displacements. Respectively the transducers were placed 5.0 cm away from the impact source on the same surface. The limited shape and dimensions of the specimens accommodated the detection of the reflected waves, particularly the S-waves. As in the previous exercise, the A/D card was used for acquiring the waveforms. The recorded waveforms were collected in a personal computer for further analysis. A sampling frequency of 100 kHz was used throughout the experiment and the total signal length retained for analysis was 2048 points, having 10 μs intervals. Hence, a resolution of 0.0488 kHz in the frequency spectra was established. A high pass filter was used to remove the 1.0 kHz resonance frequency of the transducers and undesirable R-wave frequencies. The P-wave velocities were measured using the UPV technique. The readings were taken after each unloading, directly, were the 50.0 kHz transmitting and receiving transducers were placed at two opposite sides of the specimen toward the longitudinal direction. Tests for all rock types have been repeated at least three times in order to check the repeatability of the results.

10.2.4.2 Results and Discussion

The vertical and tangential output signals' frequency spectra were derived from each readings. The frequency spectra were different depending on the rock type and the state of loading/unloading cycle. For each specimen, the frequency spectra had multiple peaks, however the highest amplitude corresponded with the P- or S-wave displacements reflected from the bottom surface. In the Appendix D, Figures D-4 to D-25 show examples of the captured waveforms and the corresponding frequency spectra for the rock samples evaluated by the MSR system at the end of each unloading cycle. As the load increases, the number of fractures in the rocks increase and the body wave velocities decrease. Slower velocities cause resonance of the waves from top to bottom of the cores to decrease. The frequency values in the spectra particularly drops after 65% of maximum compressive strength of the samples. The presented data exhibit a consistent trend concerning decrease of frequency values with increasing load.

Figures 10-6 to 10-10 shows the accumulated results of body wave velocities and elastic constants for the rock samples. In general, both P- and S-wave velocities decrease with increasing load. However, depending on the rock type, this decrease varies. It can be seen that both P- and S-wave velocities have a nonlinear dependence on axial stress. Figures 10-11 to 10-13 show the effect of the loading/unloading cycles on the P-wave velocities of the rock samples detected by the UPV technique. There is a difference between the trend of P-wave velocities collected by the MSR and UPV techniques. For the ultrasonic readings, the data describe three distinct phases. At the first phase or the pore closure stage, there is a sharp increase in wave velocities as the load increases. This increase in velocity is due to the closure of voids and micro-fractures at the beginning of stress-strain curve which is caused by the axial load. In the second phase or the elastic stage, the velocity decreases slightly, which indicates the creation of new fractures. In the third phase or the failure stage, the velocity decreases sharply, particularly after 90% of the maximum uniaxial strength of the rocks. For the MSR readings, the pore closure stage reflecting the increase of velocity values is absent. The absence of the first phase in MSR data is due to the fact that the input frequency of the impact device is lower than that of the UPV transmitter. The high frequency ultrasonic pulse is sensitive to the initial fractures and voids in the rocks. The MSR signals have lower range of frequencies and view the samples more globally; therefore small voids and fractures do not effect the output frequencies as much as with ultrasonic pulses. The velocities determined by the pulse velocity technique are more dispersed than the velocities determined by the MSR system, due to the fact that the ultrasonic pulses have smaller wavelengths than the stress pulses. The shorter wavelength ultrasonic pulses are more sensitive to the small changes that occurs along their raypath therefore in the case of rocks the velocity values exhibit a more scatter nature than the MSR velocity readings.

The Young's modulus and shear modulus decrease with the increasing load. The changes in the two moduli are well recorded by the MSR system. The bulk modulus increases in the failure stage where the volume of samples expands. The Poisson's ratio at the failure stage also increased drastically since the ratio of the longitudinal to diametrical strains changes more rapidly as a result of uniaxial loading. For all rock types the modulus values suggest that the beginning of a critical stage (failure stage) to be between 60 to 70% of the maximum load-bearing capacity of the samples. Based on the ultrasonic P-wave velocity values this critical stage is only evident after 75 to 80% of the maximum load-bearing capacity of the samples. The discrepancy can be explained based on the areas the UPV and MSR signals cover when they propagate in a sample. MSR signals cover a wider area than UPV signals; therefore MSR signals are more sensitive to the physical changes occur in a sample.

Based on the result of this study it is concluded that the MSR system can be used to determine the P- and S-wave parameters and the dynamic elastic constants in a dynamic loading/unloading conditions. The MSR signals view a broader area than UPV signals; therefore they can detect the critical stage (failure stage) at an earlier time. Nevertheless, the MSR signals are not very sensitive to the presence of pores and voids at the early loading/unloading cycle.

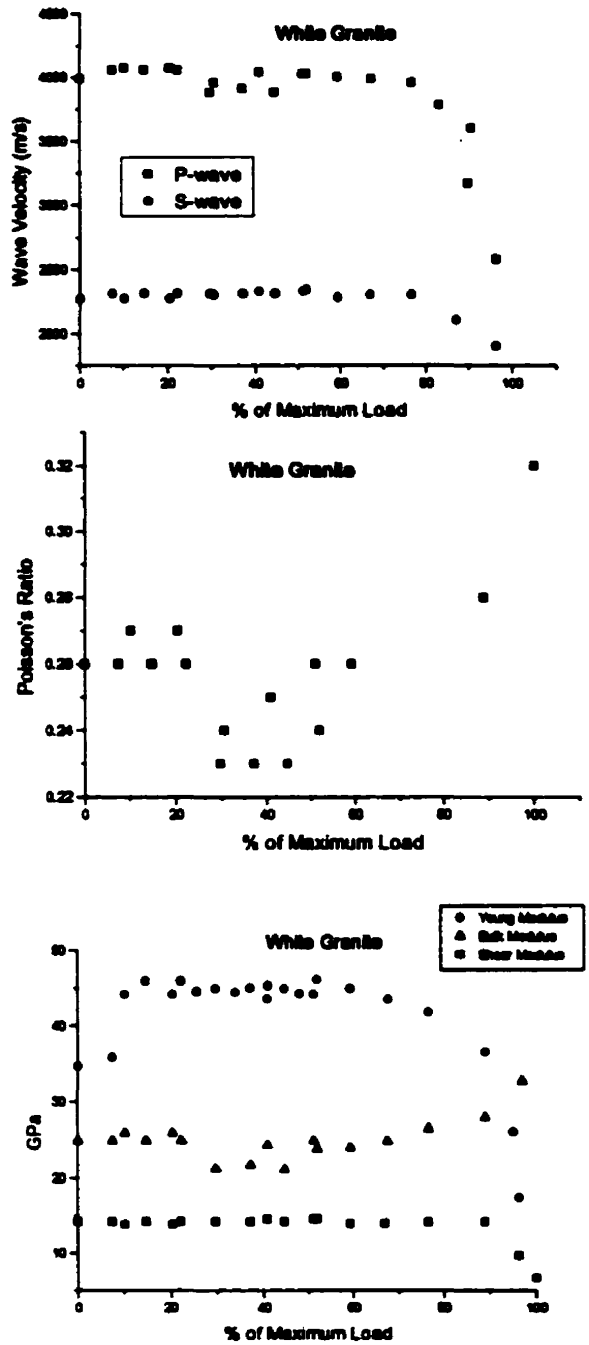

Figure 10-6 Effect of loading/unloading tests on wave velocities and elastic properties using the MSR system.

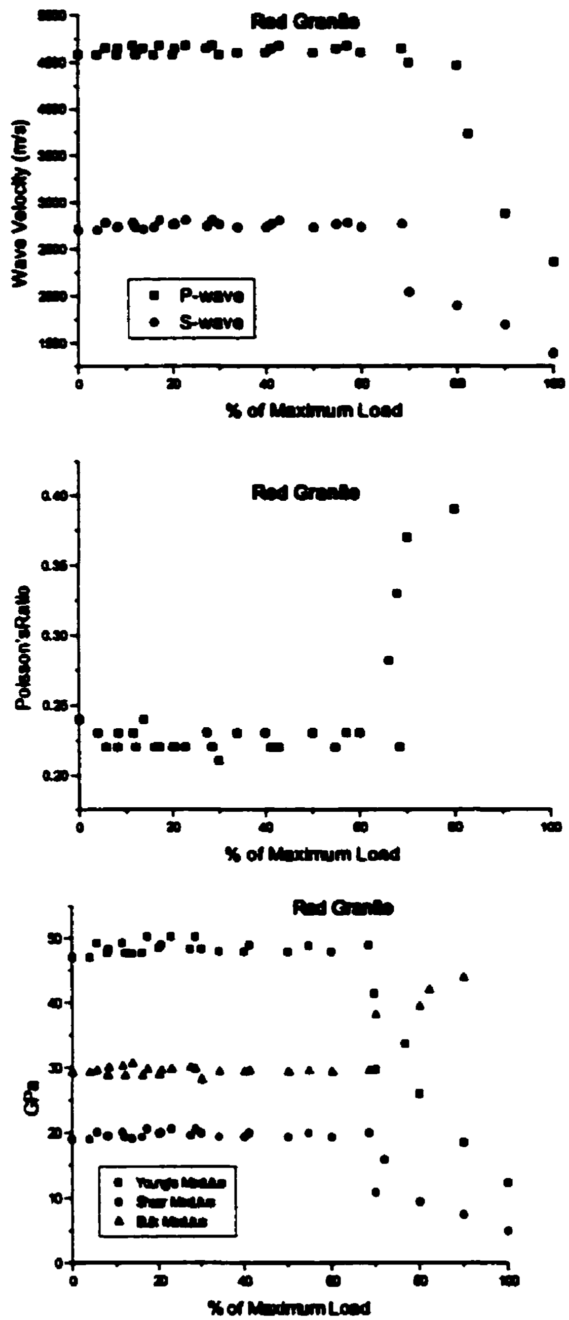

Figure 10-7 Effect of loading/unloading tests on wave velocities and elastic properties using the MSR system.

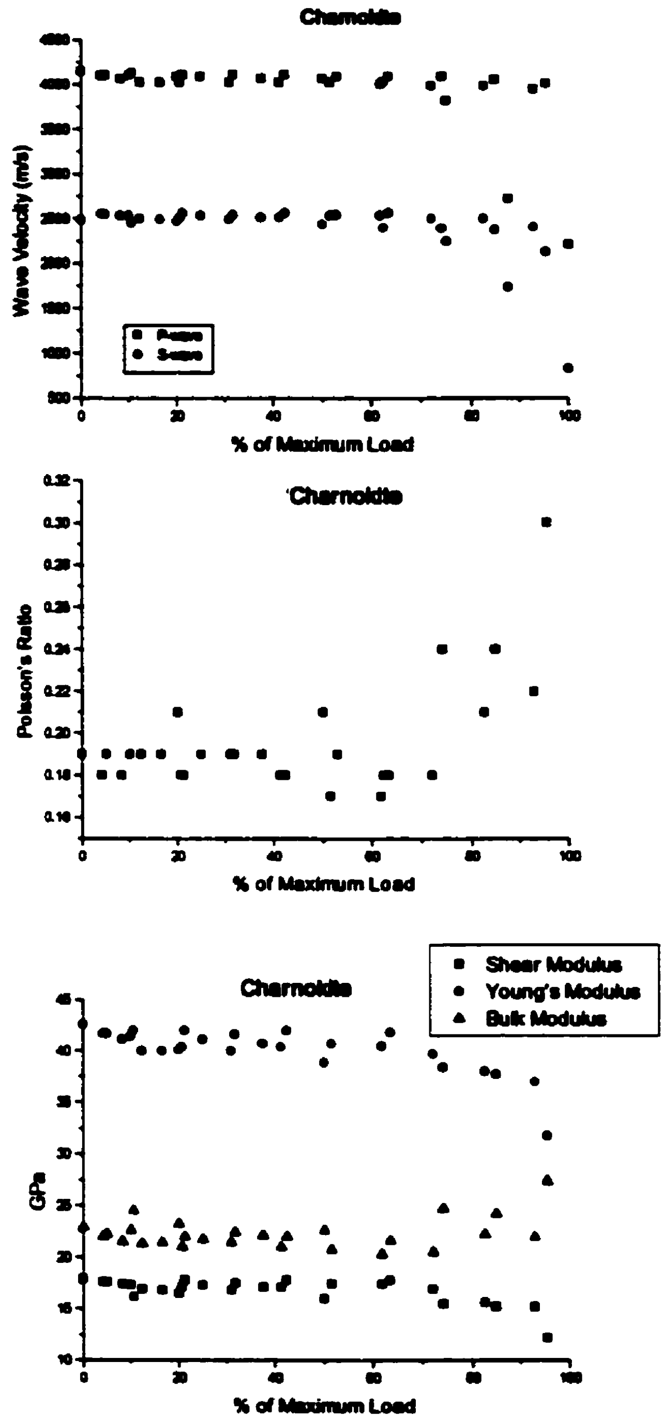

Figure 10-8 Effect of loading/unloading tests on wave velocities and elastic properties using the MSR system.

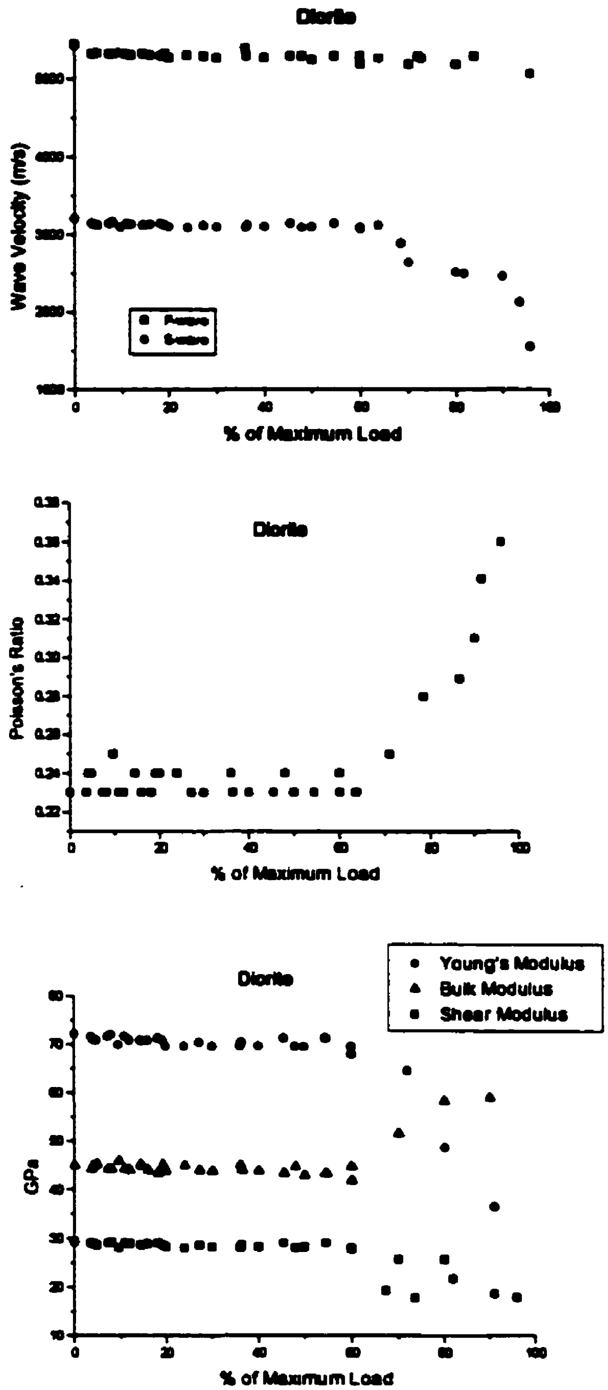

Figure 10-9 Effect of loading/unloading tests on wave velocities and elastic properties using the MSR system.

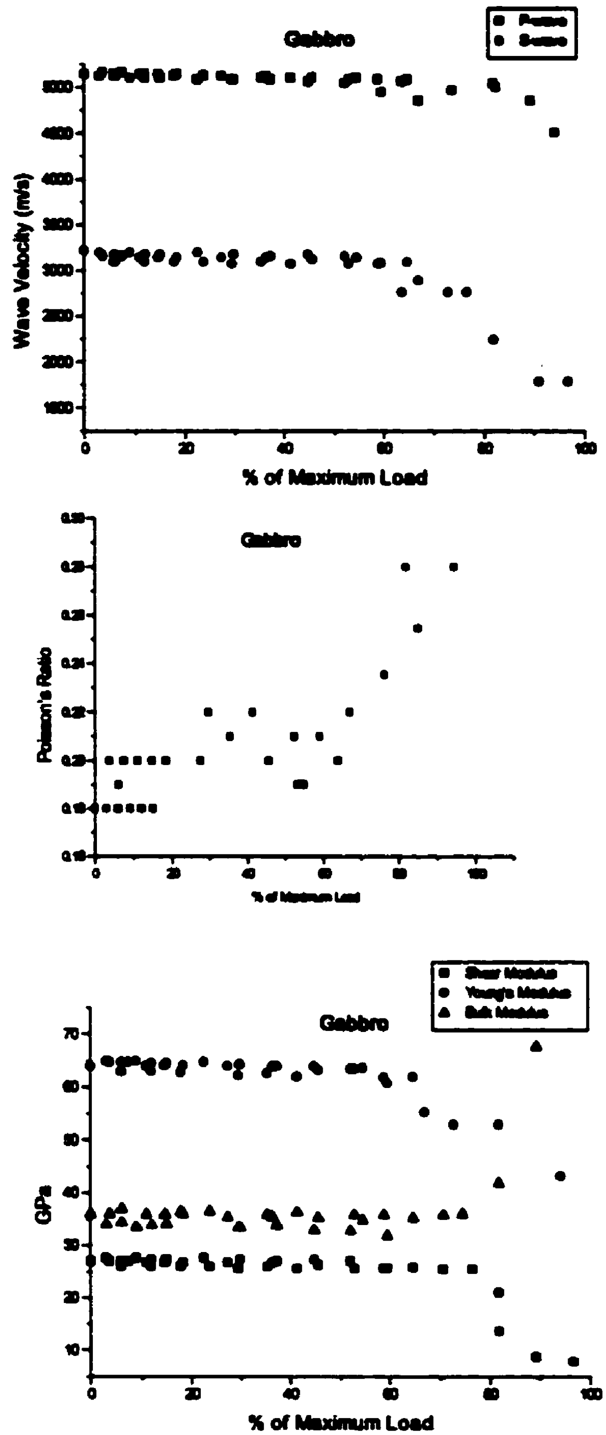

Figure 10-10 Effect of loading/unloading tests on wave velocities and elastic properties using the MSR system.

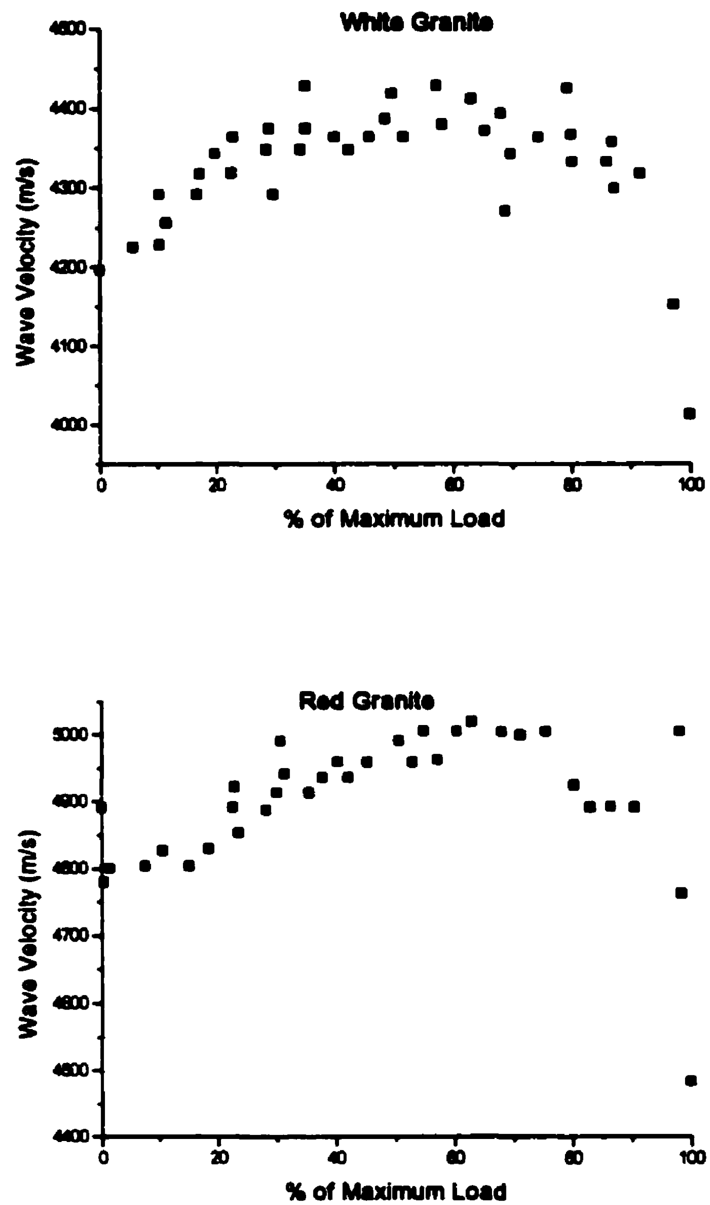

Figure 10-11 Effect of loading/unloading tests on P-wave velocities taken by UPV technique.

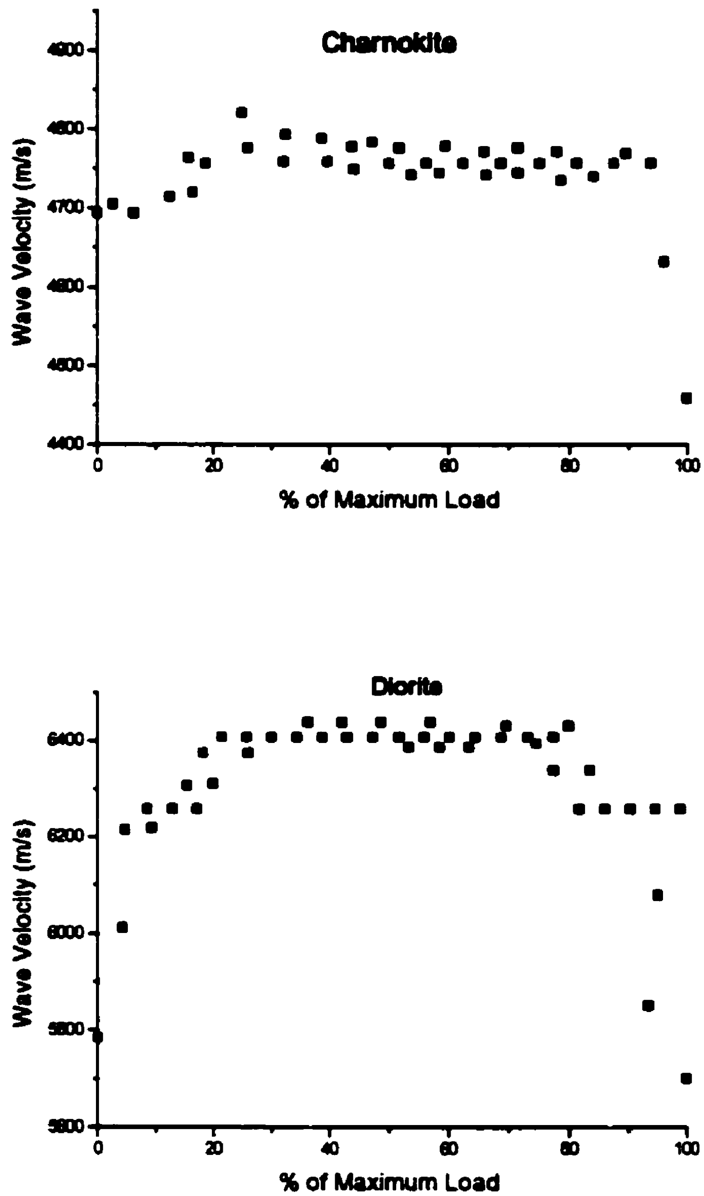

Figure 10-12 Effect of loading/unloading tests on P-wave velocities taken by UPV technique.

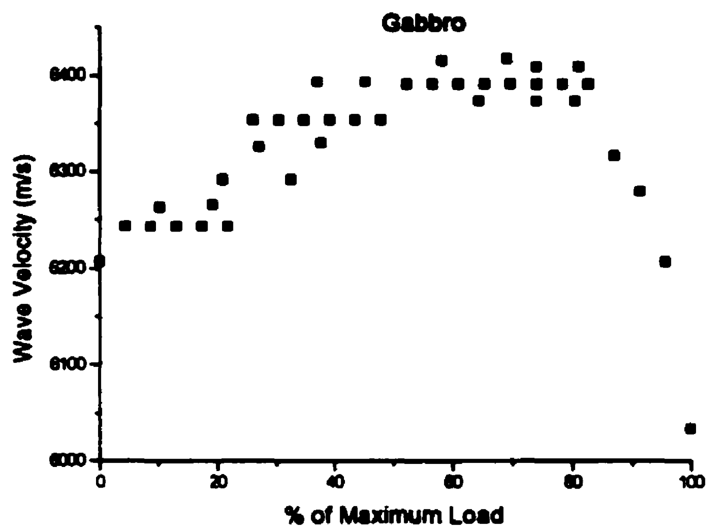

Figure 10-13 Effect of loading/unloading tests on P-wave velocities taken by UPV technique.

10.3 FIELD EXPERIMENTS

In this section, a two-layer separation of potash ore in one of the openings in an underground potash mine was studied by the MSR system. The results of these tests located the precise position of the discontinuities which was confirmed subsequently by drilling. Both the velocities of P- and S-waves were obtained and the dynamic elastic properties of the ore was calculated.

10.3.1 Detection and Evaluation in Underground Potash Mine

Two discontinuities were identified in the back of an opening in the Allan Division of PCS (Potash Corporation of Saskatchewan Inc.) potash mine. Drilling located the position of these fractures to be at 45.7 cm and 86.4 cm. The mineralogy of the potash ore was identified as 33.7% halite, 63.1% sylvite, and 3.2% clay size minerals. The mass density of the potash ore was calculated from the cored sample in the laboratory and was 2130 kg/m^3.

Plate 10-3 and Figure 10-14 show the MSR test configuration on the back of an opening in the Allan potash mine. A spherical tip hammer of 2.54 cm diameter was used as the impact source. Vertical and horizontal surface displacements were monitored with the broadband vertical and tangential displacement transducers. The sensitive piezoelectric elements were placed in direct contact with the rock surface. The surface displacement signals were captured, processed and stored using a A/D card and a portable computer. A high pass filter was used to remove the 1.0 kHz resonance frequency of the transducers. A sampling frequency of 100 kHz was used throughout the experiment and the total signal length retained for analysis was 2048 points, having $10\mu s$ intervals which corresponds to a resolution of 0.0488 kHz in the frequency spectra.

10.3.2 Results and Discussion

Figures 10-15 to 10-20 show captured waveforms by the vertical and tangential displacement transducers and their frequency spectra for the potash ore. In order to evaluate the accuracy of the MSR, the thickness of the first fracture at 45.7 cm was known from the drilling. Using the frequency peak value and the thickness, the velocity of the P-wave was calculated using equation 6-4. For the second fracture the P-wave velocity from the first layer was used and the thickness of the second layer was calculated. The thickness of the second layer was calculated at 85.0 cm using equation 6-5. Measurement of the second discontinuity by drilling at 86.4 cm correlates with the calculated values at 85.0 cm. The discrepancy between the actual position of the discontinuity and the calculated value by the MSR is only 1.4 cm (1.6% error). Having the accuracy of the MSR data being confirmed, the values of P- and S-wave velocities were collected on three nearby locations and the values of elastic constants were calculated. Table 10-8 shows the values of the P- and S-wave velocities and also values of elastic constants calculated by the MSR system.

Table 10-9 presents the results of velocity measurements and the determination of dynamic elastic constants in the laboratory using the UPV technique. In the case of potash ore the ultrasonic wave velocities are 5 to 9% higher than the values obtained by the MSR. The MSR system was used successfully to determine the position of the second discontinuity and the potash ore's dynamic elastic properties, in situ.

Table 10-8 The value of P- and S-wave velocities and elastic constants measured on the potash ore by the MSR system.

P-wave velocity S-wave velocity (m/s)	Density (kg/m^3)	Young's Modulus (GPa)	Shear Modulus (GPa)	Poisson's Ratio	Bulk Modulus (GPa)
4043 2490	2310	31.7	13.2	0.19	17.0
4067 2505	2310	32.0	13.4	0.19	17.2
3985 2241	2310	27.0	10.7	0.27	19.6

Table 10-9 The value of P- and S-wave velocities and dynamic elastic constants measured on the various salt rocks using UPV technique in the laboratory.

Rock Type	P-wave velocity S-wave velocity (m/s)	Density (kg/m^3)	Young's Modulus (GPa)	Shear Modulus (GPa)	Poisson's Ratio	Bulk Modulus (GPa)
Potash Ore	4280 2530	2310	36.5	14.8	0.23	22.5
Rock Salt	4530 2600	2160	36.9	14.6	0.25	24.6
Pure Halite	4450 2430	2090	31.6	12.3	0.29	25.0

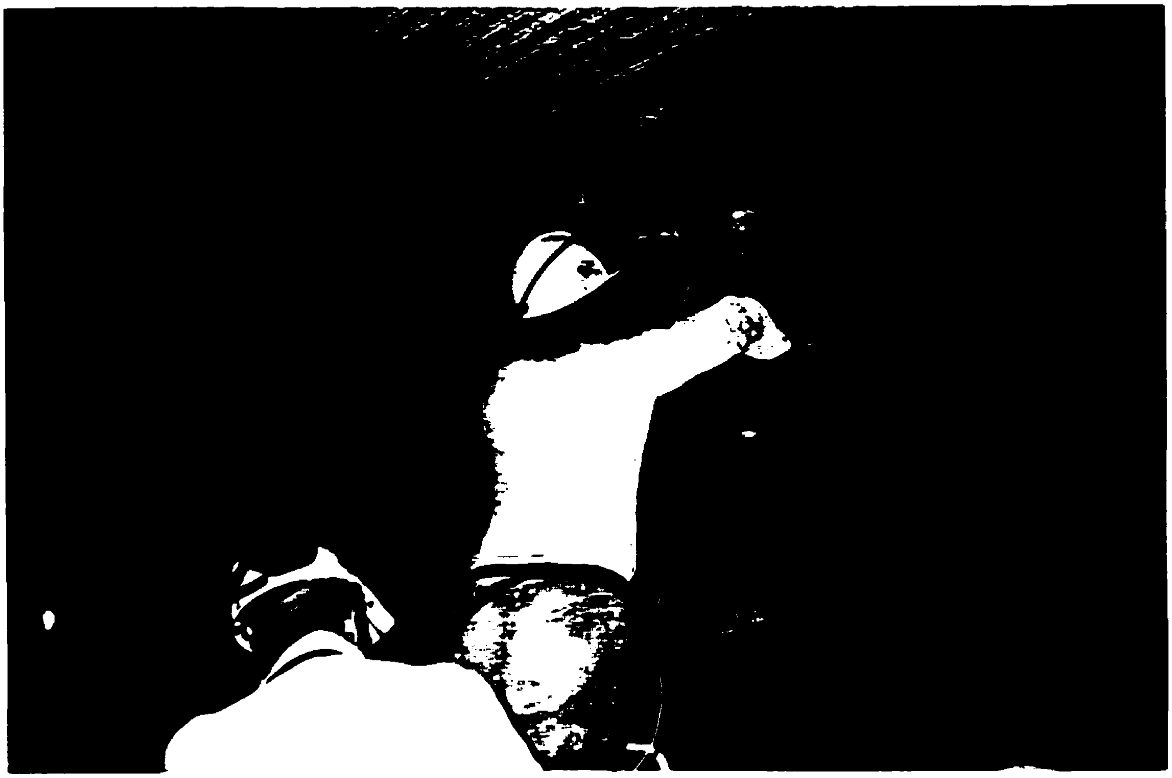

Plate 10-3 Measurement of P- and S-wave parameters on the potash ore at Allan Mine.

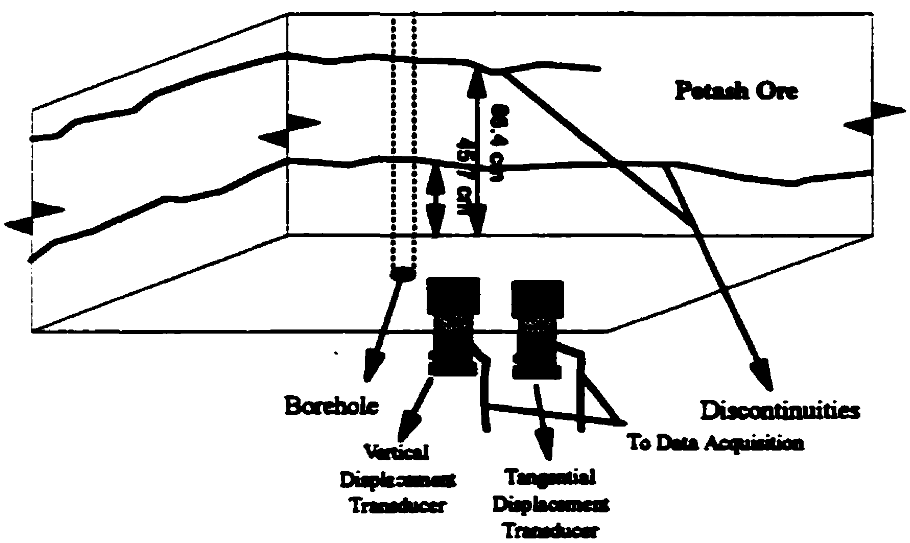

Figure 10-14 Schematic diagram of MSR test configuration on the potash ore at Allan Mine.

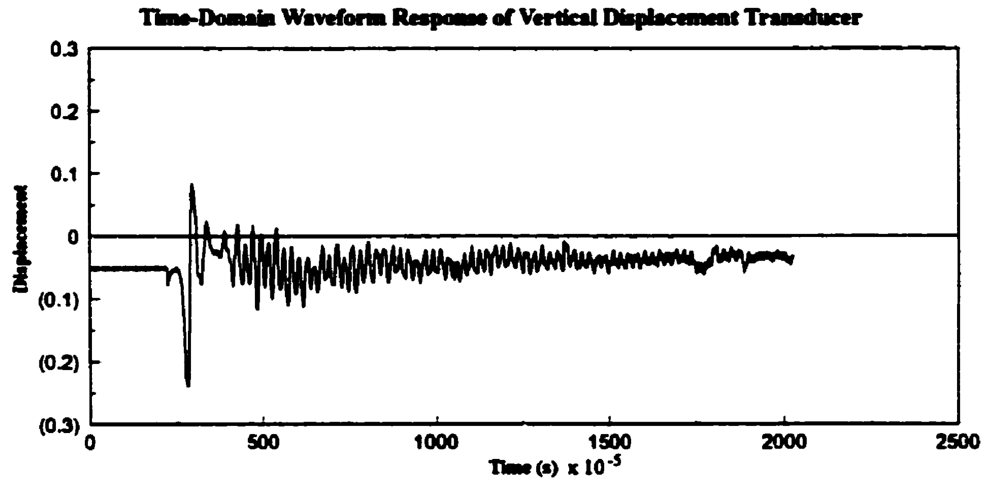

(a)

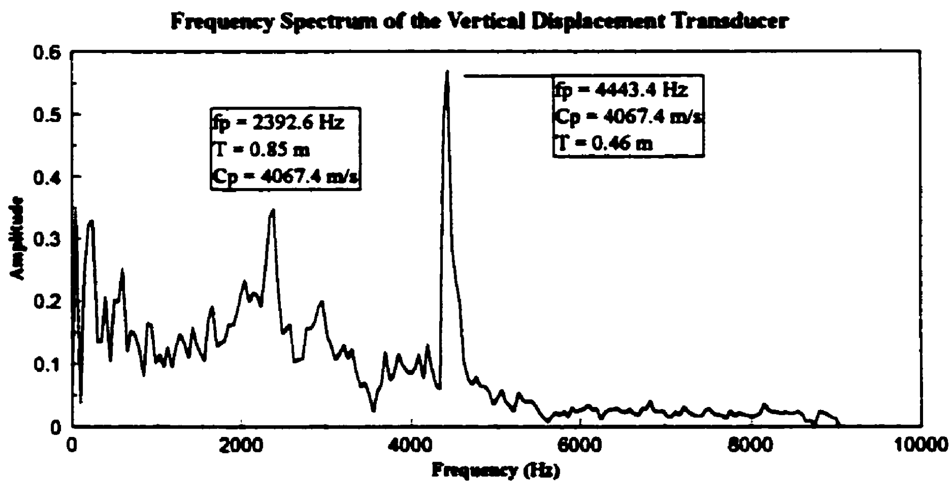

(b)

Figure 10-15 Example of a time domain and it's b) frequency spectrum collected by vertical displacement transducer collected from the potash ore in Allan Mine.

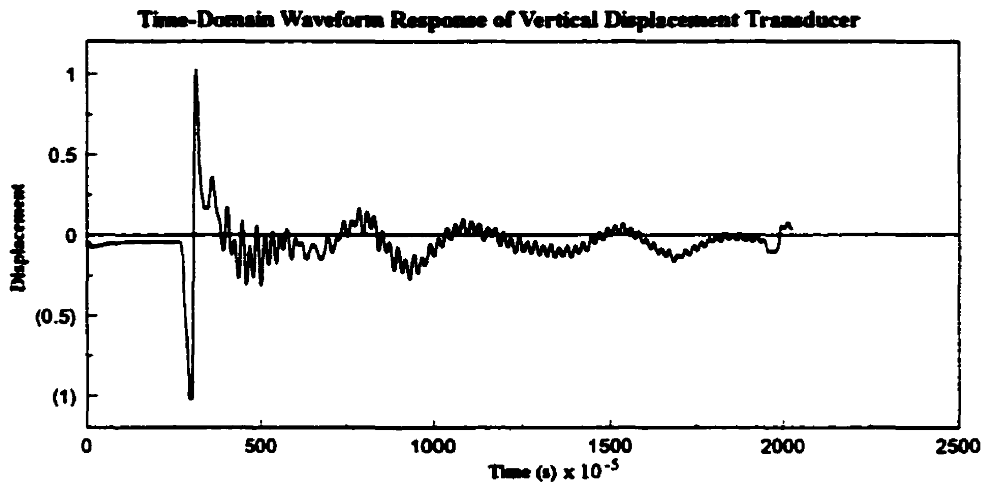

(a)

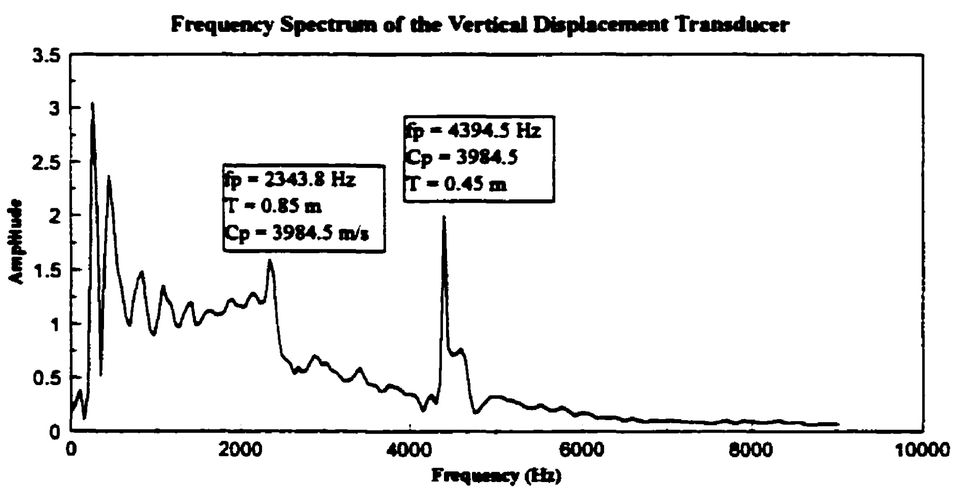

(b)

Figure 10-16 Example of a time domain and it's b) frequency spectrum collected by vertical displacement transducer collected from the potash ore in Allan Mine.

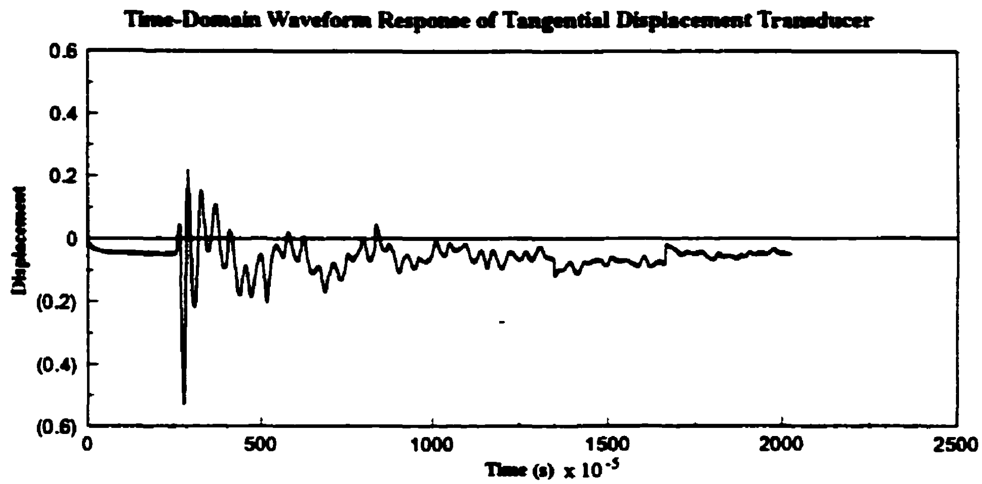

(a)

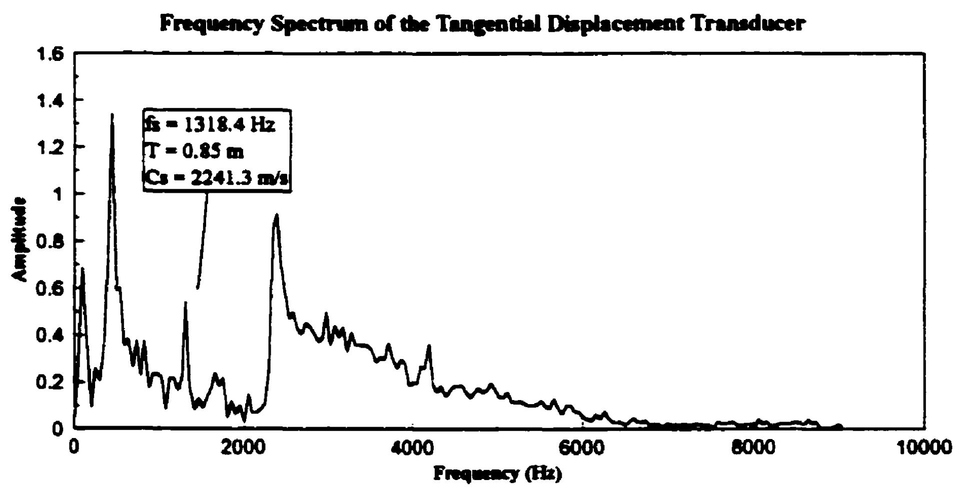

(b)

Figure 10-17 Example of a time domain and it's b) frequency spectrum collected by tangential displacement transducer collected from the potash ore in Allan Mine.

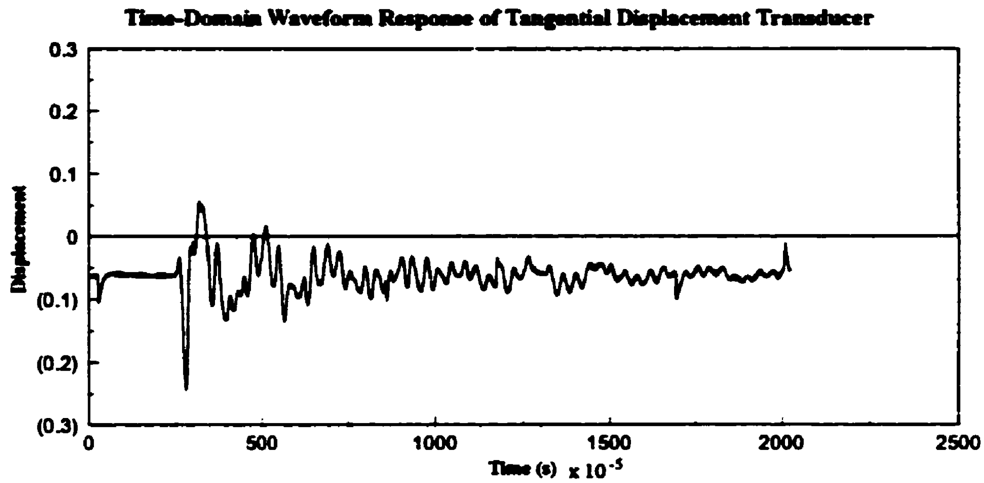

(a)

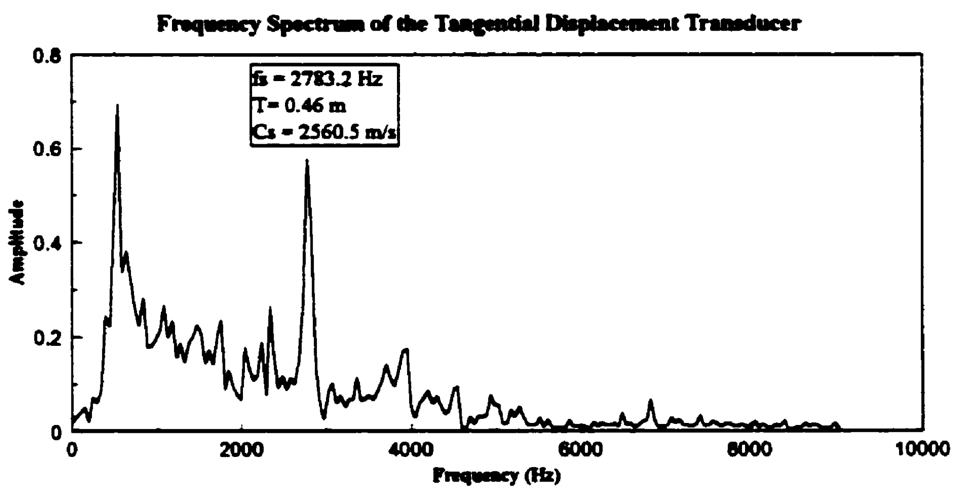

(b)

Figure 10-18 Example of a time domain and it's b) frequency spectrum collected by tangential displacement transducer collected from the potash ore in Allan Mine.

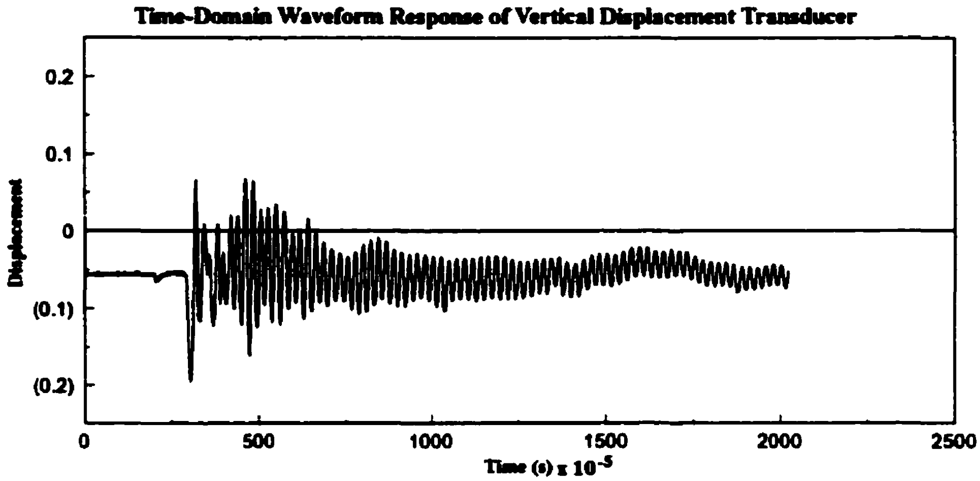

(a)

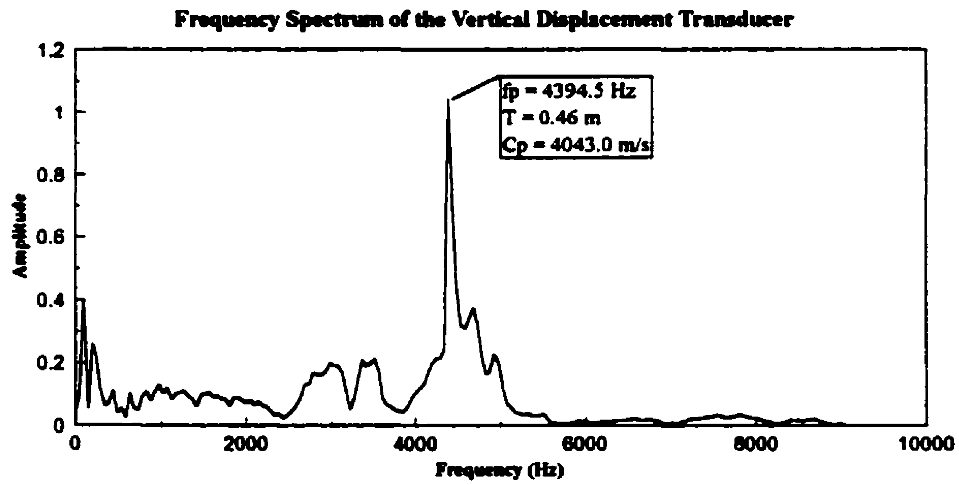

(b)

Figure 10-19 Example of a time domain and it's b) frequency spectrum collected by vertical displacement transducer collected from the potash ore in Allan Mine.

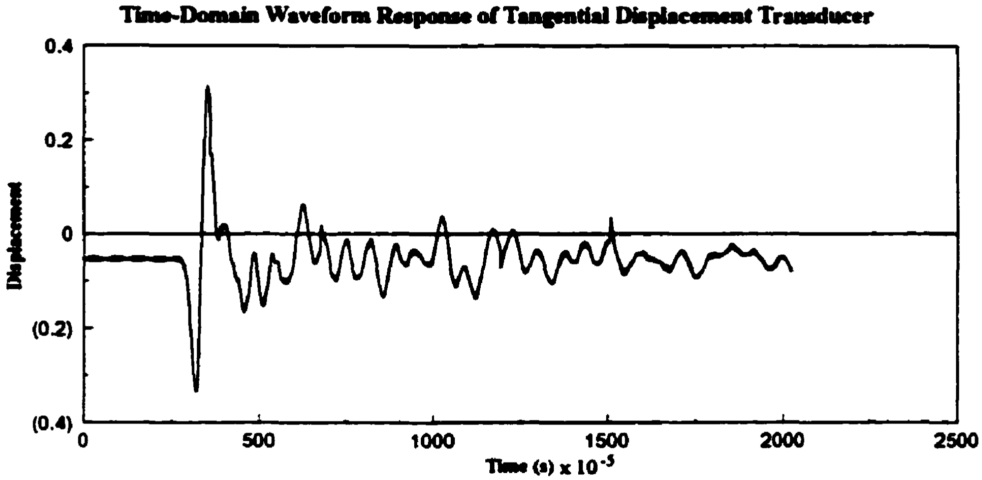

(a)

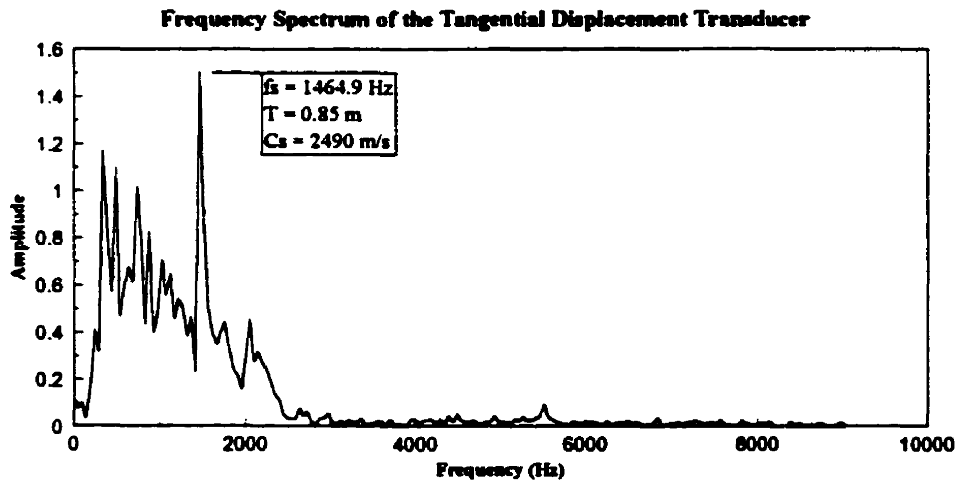

(b)

Figure 10-20 Example of a time domain and it's b) frequency spectrum collected by tangential displacement transducer collected from the potash ore in Allan Mine.

10.4 SUMMARY AND CONCLUSIONS

The work presented in this chapter clearly demonstrates that the MSR system is a viable means of measuring the elastic properties of rocks in the laboratory and in the field. It was also demonstrated that the MSR system can be used to determine the position of discontinuities in a rock mass. From the results presented in this chapter the following specific conclusions can be drawn:

1. The MSR system can be used to evaluate the elastic properties of rock blocks and cores. Comparing the results obtained by the MSR system on the rock blocks with the cored rocks suggests that the body wave velocities are faster in the blocks. The frequency spectra generated as a result of the MSR tests on the cored samples are higher in amplitudes than the calculated spectra from the rock blocks. This is mainly due to higher signal attenuations in the case of rock blocks. Comparing the results of the MSR tests with standard static tests and accepted dynamic tests such as UPV and RF, it is shown that the MSR data produce the most consistent set of values for elastic constants.

2. In a series of experiments on five igneous rock types, by loading and unloading the cored samples to their maximum unconfined compressive strength, the MSR system was successfully used to evaluate the sample's elastic properties in regular intervals. The P-wave velocities calculated by the MSR system were compared to the P-wave velocities obtained by the UPV technique. In this comparison it was indicated that the UPV values are more scattered than the MSR values and the lower frequency MSR signals see the sample more globally than the higher frequency UPV signals.

3. In an attempt to locate the position of discontinuities in an underground rock mass, it was demonstrated that the vertical displacement transducer can successfully be used to evaluate the thickness of a rock mass within less than 2% error. It was also demonstrated that the MSR system can be used to calculate the elastic properties of the rock mass in situ.

4. In addition, the MSR data were obtained in a fraction of the time required by other testing methods because of minimal sample preparation requirements and data processing techniques.

CHAPTER 11

CONCLUSIONS AND RECOMMENDATIONS FOR FURTHER RESEARCH

11.1 SUMMARY

This thesis describes the development of a new nondestructive testing system for evaluating the integrity of concrete shaft and tunnel linings. The new system functions based on the miniature seismic reflection (MSR) principle which has been inspired from the well-established impact-echo nondestructive testing technique. The MSR system includes a series of spherical tip mechanically triggered impact devices and a pair of vertical and tangential displacement transducers. The signals are transformed from time domain waveforms to frequency domain spectra. Laboratory and field testing programmes were conducted to establish the capabilities of the new system. The laboratory programme consisted of the following:

i) Assembly of an experimental MSR system, including manufacturing of a tangential displacement transducer and a series of impact devices for finding delaminations, defects and reinforcement bars in concrete and assessing the quality of concrete elements based on their dynamic elastic properties.

ii) Direct and indirect measurements of P-wave velocity in concrete.

iii) Studying the effect of interface materials on the reflection mechanism of P- and S-waves.

iv) Detection and location of simulated planar and vertical discontinuities and steel reinforcement bars in concrete.

v) Investigating the curing and maturity of various concrete cylindrical samples for a 28-day period based on the changes registered by the MSR system on their P- and S-wave velocities and elastic properties.

vi) Comparison of the concrete curing results obtained by the MSR system to the results obtained by standard dynamic and static tests.

vii) Studying the effects of cement type and aggregate size on concrete curing based on the MSR system.

viii) Studying the effect of shape and dimension of concrete testing specimens on the wave velocities and dynamic elastic properties obtained by the MSR system.

ix) Investigating the capabilities of the MSR system in determining the dynamic elastic properties of various rock types with variable core and block dimensions.

x) Comparison of the results obtained by the MSR system on the rock samples to the values obtained by the standard static and dynamic techniques.

xi) Studying the effects of stress increase on the rock samples by the changes in elastic wave velocities obtained by the MSR system.

The laboratory tests were followed by in situ field measurements using the MSR system. The objectives of the field programme consisted of the following:

i) Investigating the capabilities of the MSR system in evaluating the integrity of shaft linings based on their computed dynamic elastic properties. The results of these experiments were compared to independent laboratory studies.

ii) Studying the capabilities of the MSR system in measuring the thickness of a concrete tunnel lining. The results of this experiment were compared with the extracted cores from the lining.

iii) Measuring the thickness of discontinuities in a rock mass in an underground mining environment.

11.2 CONCLUSIONS

The following conclusions were reached based on the results of the comprehensive laboratory and field studies.

11.2.1 Instrumentation

A transient point impact on a surface causes the generation of P-, S- and R-waves. P- and S-waves travel on the surface and into the tested object. An abrupt change along the raypath of the P- and S-waves causes signals to reflect back to the original surface. On the original surface, the arriving waveforms generate displacements indicating the characteristic particle motions of each wave type. The velocity of the P- and S-waves are controlled by the material properties of the tested object. With the MSR system, which includes a pair of broadband piezoelectric transducers, a series of spherical tip mechanically triggered impact devices, and an A/D data acquisition card, the quality of the concrete specimens and structures can be determined by analyzing the P- and S-wave parameters.

The broadband piezoelectric vertical displacement transducer is the best detector of the P-wave signals. This transducer is manufactured so that it is sensitive to normal surface displacements. It is capable of detecting S-wave signals as well. The broadband piezoelectric tangential displacement transducer is, however, mainly sensitive to surface horizontal motions. Nevertheless, the later transducer is also capable of detecting vertical surface displacements.

The contact-time of the impact is a key element of the MSR system. Contact-time mainly depends on the diameter of the spherical impact device. However, the stiffness of the testing object and the force of impact affects the time duration of impact. Contact-time controls the frequency content of the waves generated by the impact. Therefore, contact-time controls the wavelength of the P- and S-wave signals. For the results to be valid, the wavelength of the signals must be smaller than half the path length of the signals. Therefore, instead of one, a series of impact devices were included in the MSR system with different impact head diameters capable of generating a range of contact-times on the testing objects.

The efficient assembly of the MSR system was proven to be capable of operating in both laboratory and field environments.

11.2.2 Determination of P-Wave Velocity

It was established that for interpretation purposes the P-wave velocity or the thickness of the test specimens must be known prior to any accurate determination. In the case in which the thickness of the tested specimen is known, the P-wave velocity can be determined directly using equation 6-4. In cases in which the thickness of the testing specimen is not known, P-wave velocity can be calculated by indirect methods. The indirect methods include: a) estimate of the P-wave velocity based on the R-wave parameters, and b) calculation of the surface P-wave velocity based on the travel-time graph.

11.2.3 Principles Governing the MSR System

The frequency spectrum analysis based on the application of the FFT technique on the waveforms simplifies signal interpretation significantly. In a flawless test specimen, for the signals captured by the vertical displacement transducer, the peak amplitude in the frequency spectrum represents the frequency of the resonated P-waves. For the signals captured by the tangential displacement transducer, the peak amplitude in the frequency spectrum represents the frequency of the resonated S-waves. The reflected P-waves in an infinite plate are best captured when the distance between the impact source and the receiver are minimum [i.e. not more than 0.2 times the thickness of the plate (Sansalone, 1985)]. The S-waves in an infinite plate are best captured at a distance away from the impact source. The optimum distance between the impact source and the tangential displacement transducer is calculated based on the elastic properties of tested objects. In the case of concretes having an estimated Poisson's ratio between 0.15 to 0.25, the optimum distance between the impact source and the receiver is from 0.8 to 1.0 times the thickness of the plate.

The shape and dimensions of the testing specimen can affect the propagation of the signals. In finite cylindrical samples having a length/diameter ratio of 2:1, the amplitude of the arriving signals are magnified. The sides of the samples act as guiding channels for the waveforms. In this case, the distance relationship between the impact source and the receiver is not critical and they can be placed in any respective positions.

11.2.4 Detection and Location of Objects

The results of laboratory investigations show that the MSR system is capable of detecting and locating planar flaws, steel reinforcement bars, and depth of vertical surface opening cracks. It was also shown that the vertical displacement transducer based on the P-wave reflections is a suitable sensor for detection of discontinuities and defects.

The results of the laboratory investigations indicate that the reflection characteristics of the P- and S-wave signals relies on the acoustic characteristics of the reflecting interface. For material interfaces with higher acoustic stiffness than concrete, the period of arriving signals is twice as long as that of material interfaces with lower acoustic stiffness.

11.2.5 Concrete Maturity

A strong correlation was found between the curing of concrete cylindrical samples and the wave velocities and dynamic elastic constants computed by the MSR system. The results presented in this thesis clearly indicate that the MSR system is a feasible means of measuring the dynamic elastic properties and quality of the early-aged concrete.

In a comparison between the P-wave signals generated by the MSR system and the P-wave signals generated by the UPV techniques, it was shown that ultrasonic wave velocities are higher than the MSR wave velocities. It was also concluded that the signals generated by the MSR system view the testing objects more globally than the ultrasonic signals.

It was also shown that in most cases the dynamic elastic constants computed by the resonance frequency technique are higher than the values generated by the MSR system.

The difference between the wave velocities obtained by the MSR system and UPV technique could be explained based on the time lags in the strains (see Section 5.7). The time lag of the strains behind that of the applied stresses generated by the MSR system are shorter than the time lag of the strains behind that of the applied stresses in the case of the UPV technique. Therefore, the wave velocities generated by the MSR system are slower than the wave velocities generated by the UPV technique. The same explanation is valid in comparison of the time lag of the strains generated by the MSR system and the RF technique. Therefore, the elastic constants computed by the MSR system are lower than the elastic constants computed by the RF technique. Also it has to be noted that the wave velocities in heterogeneous media are frequency dependent and in the case of the UPV technique the signal frequencies are higher than of those generated by the MSR system.

In general, the static elastic moduli were lower than the dynamic elastic moduli.

The MSR system was also shown to be sensitive to the influence of aggregate size and cement type in the mix.

Overall, it was proven that the MSR system is capable of monitoring the curing and setting time of early-aged concrete. The curing of the concrete elements are recorded by the MSR system based on progressive changes in P- and S-wave velocities and dynamic elastic constants.

11.2.6 Concrete Shaft and Tunnel Linings

The MSR equipment assembly is well suited for an underground testing environment. The method of analysis is accurate and rapid. One important advantage of MSR is its capability of measuring elastic wave velocities and dynamic elastic properties directly from the air-side of the shaft.

It was also shown that the MSR system is capable of measuring thickness variations in the tunnel lining with reasonable accuracy.

11.2.7 Application of the MSR System on Rocks

The MSR system was used to evaluate various rock types in the laboratory. It was shown that the MSR system is capable of determining dynamic elastic properties of rocks when they are in cored or block shapes. The values of elastic wave velocities were shown to be higher in the block-shaped rock samples than in the cylindrical samples.

The MSR system was used to monitor the changes that occur as a result of uniaxial load on rock cores. These changes were recorded based on the elastic wave velocities and elastic constants. It was shown that in comparison with the UPV values, the MSR values are less scattered and indicate the failure stage earlier.

The MSR system was successfully used to locate a two layer separation of potash ore in an underground environment. The results from the recent tests located the position of discontinuities which was confirmed by drilling.

The P- and S-wave velocities were also used to evaluate the elastic properties of potash ore in situ.

11.3 FURTHER RESEARCH

The experimental assembly of the MSR system was designed to operate in both laboratory and field situations. However, a more rugged and field oriented design is needed for long term in situ tests.

The major drawback of the MSR system is its limited speed in collecting data. At this time the MSR system is capable of collecting 3 to 5 readings per minute. An improved version of the MSR system should be assembled in order to scan shaft and tunnel linings more rapidly.

In this thesis the application of the MSR system was limited to only a number of rock types with no visible structures. A more comprehensive testing program is needed to study the application of the MSR system on different rock types and structures.

BIBLIOGRAPHY

ACI Committee 318, 1983.
"Building Code Requirements for Reinforced Concrete (ACI 318-83)."
American Concrete Institute, Detroit, 118 pp.

ACI Committee 363, 1984.
"State-of-the-Art Report on High-Strength Concrete."
ACI Journal, Proceedings Vol. 81, No. 4, July-August, pp. 364-411.

Allison, R.J., 1987.
"Nondestructive Determination of Young's Modulus and its Relationship with Compressive Strength, Porosity and Density."
Jones, M.F. & Prestar, R.M.F (eds), 1987, Deformation of Sediments and Sedimentary Rocks., Geological Society Special Publication., No. 29., pp. 63-69.

AMC: Associated Mining Construction Ltd., 1965.
"The Report on Shaft Construction and Details"
AMC, Engineering Report, Saskatoon, 38 pp.

Arni, H.T., 1972.
"Impact and Penetration Tests of Portland Cement Concrete."
Highway Research HRB No. 378, pp. 55-67.

ASTM Test Designation C215-85.
"Standard Test Method for Fundamental Transverse, Longitudinal, and Torsional Frequencies of Concrete Specimens."
Annual Book of ASTM Standards, Vol 04.02, Philadephia, 1991.

ASTM Test Designation C31-88.
"Standard Practice for Making and Curing Concrete Test Specimens in the Field."
Annual Book of ASTM Standards, Vol. 04.02, Philadelphia, 1991.

ASTM Test Designation C39-86.
"Standerd Test Method for Compressive Strength of Concrete Specimens."
Annual Book of ASTM Standards, Vol. 04.02, Philadelphia, 1988.

ASTM Test Designation C469-87.
"Standerd Test Method for Static Modulus of Elasticity and Poisson's Ratio of Concrete in Compression."
Annual Book of ASTM Standards, Vol. 04.02, Philadelphia, 1988.

ASTM Test Designation C597-83.
"Standerd Test Method for Pulse Velocity Through Concrete."
Annual Book of ASTM Standards, Vol. 04.02, Philadelphia, 1991.

Banks, B., Oldfield, G., and Rawding, H., 1962.
"Ultrasonic Flaw Detection in Metals."
Prentice-Hall, Inc., New Jersey, 1962, 256 pp.

Beer, F.P. and Johnston Jr. E.R., 1985.
"Mechanics of Materials."
Copyright McGraw-Hill Inc., 610 pp.

Belesky, R.M., Bieniawski, Z.T., and Greenfield, R.J., 1984.
"Latest Research Findings from Petite Sismique Trials."
Proc. of the 3rd Conference on Acoustic Emissions/Microseismic Activity in Geologic Structures and Materials, Trans Tech Publications, Rockport, pp. 223-238.

Bieniawski, Z.T., 1978.
"The 'Petite Sismique' - A Review of Current Developments."
Proc. of the 2nd Conference on Acoustic Emissions/ Microseismic Activity in Geologic Structures and Materials, Trans Tech Publication, 1979, pp. 305-318.

Blitz, J., 1971.
"Ultrasonics: Methods And Applications."
Butterworth Publication, first edition, 1971, 148 pp.

Blitz, J. and Simpson G., 1996.
"Ultrasonic Methods of Non-destructive Testing."
Chapman & Hall, 2-6 Boundary Row, London, UK, 203 pp.

Brady, B.H.G., and Brown, E.T., 1985.
"Rock Mechanics for Underground Mining."
Published by George Allen & Unwin Australia Pty Ltd., 1985, 527 pp.

C.N.S. Electronics Ltd, 1985.
"Pundit Manual."
C.N.S. Electronics Ltd., 61-63 Holmes Road, London, NW5., 51 pp.

Canadian Portland Cement Association, 1985.
"Concrete Design Handbook."
Canadian Portland Cement Association (CPCA).

Carino, N.J., and Sansalone, M., 1988.
"Impact-Echo: A New Method for Inspecting Construction Materials."
Presented at Conference on NDT & E for Manufacturing and Construction, 15 pp.

Carino, N.J., and Sansalone, M., 1992.
"Detection of Voids in Grouted Ducts Using the Impact-Echo Method".
ACI Materials Journal, May/June 1992, pp. 296-303.

Carino, N.J., Sansalone, M., and Hsu, N.N., 1986.
"Flaw Detection in Concrete by Frequency Spectrum Analysis of Impact-Echo Waveforms."
International Advances in Nondestructive Testing, 12th Edition, 1986, Vol. 12, pp. 117-146.

Carino, N.J., Sansalone, M., and Hsu, N.N., 1986.
"A Point Source-Point Receiver, Pulse-Echo Technique for Flaw Detection in Concrete."
ACI Journal, March-April 1986, Title no. 83-20, pp. 199-208.

Chenevert, M.E., 1964.
"The Deformation Failure Characteristics of Laminated Sedimentary Rocks with Frequency."
Ph. D. Thesis, University of Texas, 1964, 203 pp.

Cheng, C.C. and Sansalone, M., 1993.
"Effects on Impact-Echo Signals Caused by Steel Reinforcing Bars and Voids Around Bars."
ACI Materials Journal, September/October 1993, pp. 421-434.

Cheng, C.C. and Sansalone, M., 1993.
"The Impact-Echo Response of Concrete Plates Containing Delaminations: Numerical, Experimental and Field Studies."
Materials and Structures, Vol. 26, 1993, pp. 274-285.

Chiou, C.P. and Schmerr, 1990.
"Quasi Pulse-Echo Ultrasonic Technique for Flaw Classification."
Ultrasonics, Vol. 29, November 1991, pp. 471-479.

Clark, T.H., 1952.
"Geological Report 46: Montreal Area, Laval and Lachine Map-Areas."
Department of Mines, Province of Quebec, 159 pp.

Collins M.P. and Mitchell D., 1987.
"Prestressed Concrete Basics."
Canadian Prestressed Concrete Institute., pp. 54-114.

Coon, R., 1968.
"Correlation of Engineering Behavior with Classification of in Situ Rocks."
Ph. D. Thesis, University of Illinois, 1968.

Core Laboratories Canada., 1991.
"Acoustic Velocities and Mechanical Properties of Potash Concrete Cores."
File Number: 52132-91-021, Reported by Dr. Zhijing Wang, 10 pp.

Crice, D., 1978.
"Shear Waves: Techniques and Systems."
Geometric/Nimbus, Sunnyvale, Ca., 94086, 27 pp.

Dohr, G.P., 1985.
"Seismic Shear Waves, Part B: Applications."
Geophysical Press, Vol. 15B, 272 pp.

Dvorak, A., 1957.
"Field Test of Rocks on Dam Sites."
Proc. 4th Int. Conf. Soil Mech. Found. Eng., London, 1957, pp. 221-224.

Fenner, T., 1995.
"Ground Penetrating Radar for Identification of Mine Tunnels and Abandoned Mine Stopes."
Mining Engineering, Vol. 47, No. 3, March 1995, pp. 280-284.

Filipczynski, L., 1966.
"Ultrasonic Methods of Testing Materials."
London, Butterworths, 280 pp.

Fintel Mark., 1985.
"Handbook of Concrete Engineering."
Canadian Concrete Society, Second edition., pp. 176-186.

Franklin, J.A. and Dausseault, M.B., 1989.
"Rock Engineering."
McGraw-Hill, Inc. Publisher, 600 pp.

Gaidis, J.M. and Rosenburg, M., 1986.
"New Test for Determining Fundamental Frequencies of Concrete."
Cement, Concrete and Aggregates, CCAGDP, Vol. 8, No. 2, 1986, pp. 117.

Ghorbanpoor, Al., and Shew, Theodore E., 1991.
"Workshop on Nondestructive Testing and Evaluation of Concrete: Detection of Flaws in Bars and Cables in Concrete Bridge Structures."
Sponsored by Center for By-product and Utilization (CBU)., Oct. 17 & 18, 1991., pp. 84-91.

Ghorbanpoor, Al. 1991.
"Workshop on Nondestructive Testing and Evaluation of Concrete: Monitoring Steel Bridges by Acoustic Emission."
Sponsored by Center for By-product and Utilization (CBU)., Oct. 17 & 18, 1991., pp. 148-155.

Goodman, R.E., 1989.
"Introduction to Rock Mechanics."
Published by John Wiley & Sons, Second Edition, 1989, pp. 562.

Hassani, F.P., Momayez, M., and Wang, E., 1989.
"Concrete Shaft Lining: Thickness Measurement and Quality Control."
Department of Mining and Metallurgical Engineering, McGill University, Montreal, March 1989, pp 356.

Helbig, K., 1987.
"Shear-Waves: What They are and How They Can be Used."
Presented at the Society of Exploration Geophysicists Shear Wave Symposium, Midland, 1984, 18 pp.

Helbig, K., and Mesdag, C.S., 1982.
"The Potential of Shear-Wave Observations."
Geophysical Prospecting, 1982, Vol. 30, pp. 413-431.

Higgs, J., 1979.
"Integrity Testing of Piles by the Shock Method."
Concrete, October 1979, 31 pp.

Hornibrook, F.B., 1939.
"Application of Sonic Method to Freezing and Thawing Studies of Concrete."
ASTM Bulletin, Vol. 5, No. 101, December 1939.

Hucka, V., 1965.
"A Rapid Method of Determining the Strength of Rocks in Situ."
International Journal of Rock Mechanics and Mining Science, Vol. 2, 1965, pp. 127-134.

Hussbaumer, H.J., 1990.
"Fast Fourier Transform and Convolution Algorithms."
1990, 254 pp.

Ide, J.M., 1936.
"The Velocity of Sound in Rocks and Glasses as a Function of Temperature."
Journal of Geology, Vol. 45, 1937, pp. 689-716.

ISRM, 1979.
"Suggested Methods for Determining in Situ Deformability of Rocks."
ISRM Comission on Standardization of Laboratory and Field Tests, Int. Jor. Rock Mech. Min. Sci. Geomech. Vol. 16, No. 3, pp. 195-214.

ISRM, 1981.
"Suggested Methods for Rock Characterization, Testing and Monitoring."
ISRM Comission on Testing Methods, E.T. Brown, Ed. (Oxford, 1981), 211 pp.

J.W. Lemmens Inc., 1989.
"Grindo-Sonic: Measurement and Calculation Of Elastic Properties of Concrete Test Pieces."
J.W. Lemmens Inc., 1989, 8 pp.

J.W. Lemmens Inc., 1989.
"Grindosonic: Measurement and Calculation of Elastic Properties of Concrete Test Pieces."
J.W. Lemmens Inc., 1989, 8 pp.

Jolly, R.N., 1956.
"Investigation of Shear Waves."
Geophysics, 1956, Vol. 21, pp. 905-938.

Jones, R., 1948.
"The Application of Ultrasonics to the Testing of Concrete."
Research (London), May 1948, 383 pp.

Jones, R., and Facaoaru, I., 1969.
"Recommendations for Testing Concrete by the Ultrasonic Pulse Method."
Materials and Structures Research and Testing (Paris) Vol. 2, No. 19, 275 pp.

Kahler, S. and Meissner, R., 1983.
"Radiation and Receiver Pattern of Shear and Compressional Waves as a Function of Poisson's Ratio."
Geophisical Prospecting, Vol. 31, 1983, pp. 421-435.

Kat, M.P., 1988.
"Comparative Studies of Microsesmic Source Location Techniques."
Master of Engineering Thesis, McGill University, Department of Mining and Metallurgical Engineering, 411 pp.

Kesler, C.E. and Higuchi, Y., 1954.
"Problems in the Sonic Testing of Plan Concrete."
Proc. Int. Symp. on Nondestructive Testing of Materials and Structures, Vol. 1, RILEM, Paris, 45 pp.

Kim, Y.H., Lee, S. and Kim, H.C., 1990.
"Quantitative Vibration Mode Analysis of Mortar and Concrete Blocks Containing Flaws."
NDT International., Vol. 23, No. 2., April 1990, pp. 67-74.

Kolek, J., 1958.
"An Appreciation of the Schmidt Rebound Hammer."
Magazine of Concrete Research (London), Vol. 10., No. 28., March 1958, pp. 27-36.

Koller, M.G., and Kolsky, H., 1987.
"Waves Produced by the Elastic Impact of Sphere on Thick Plates."
International Journal of Solids Structures, Vol. 23, No. 10, 1987, pp. 1387-1400.

Lama, R.D., 1970.
"In Situ and Laboratory Strength of Coal."
Proc. 12th Symp. Rock Mec., Rolla, 1970, pp. 265-300.

Lama, R.D., and Vutukuri, V.S., 1978.
"Handbook on Mechanical Properties of Rocks."
Trans Tech Publications, Vol. 2, First Print, 1978, 481 pp.

Leeb, D., 1979.
"Dynamic Hardness Testing of Metallic Materials."
NDT International, December 1979, pp. 274-278.

Lin, J.M. and Sansalone, M., 1994.
"Impact-Echo Response of Hollow Cylindrical Concrete Structures Surrounded by Soil and Rock: Part I - Numerical Studies."
Geotechnical Testing Journal, Vol. 17, No. 2, June 1994, pp. 207-219.

Lin, J.M. and Sansalone, M., 1994.
"Impact-Echo Response of Hollow Cylindrical Concrete Structures Surrounded by Soil and Rock: Part II - Experimental Studies."
Geotechnical Testing Journal, Vol. 17, No. 2, June 1994, pp. 220-226.

Lin, Y., and Sansalone, M., 1991.
"Transient Response of Thick Circular and Square Bars Subjected to Transverse Elastic Impact."
Journal of the Acoustical Society of America, February 1992.

Lin, Y., Sansalone, M., and Carino, N.J., 1991.
"Finite Element Studies of the Transient Response of Plates Containing Thin Layers and Flaws."
Journal of Nondestructive Evaluation, Vol. 9, No. 1, 1991.

Malhotra, V.M., 1984.
"In Situ Nondestructive Testing of Concrete."
American Concrete Institute (ACI), Publication SP-82. 1984, 825 pp.

Malhotra, V.M., and Sivasundaram, V., 1991.
"CRC Handbook On Nondestructive Testing Of Concrete: Resonance Frequency Methods."
CRC press, editors, V.M. Malhotra, N.J. Carino., pp. 147-168.

Mehta, P.K. and Monteiro, P.J.M., 1993.
"Concrete: Structure, Properties, and Materials."
Published by Prentice-Hall, Inc., Second Edition, 1993, 548 pp.

Meissner, R., 1985.
"Wave-Front Diagrams From Uphole Shooting."
Geophisical Prospecting, Vol. 9, pp. 533-543.

Miller, Ronnie K. and McIntire, Paul., 1987.
"Nondestructive Testing Handbook, Volume 5: Acoustic Emission Testing."
American Society for Nondestructive Testing., pp. 92-122.

Mindess, Sidney., 1991.
"CRC Handbook on Nondestructive Testing of Concrete: Acoustic Emission Methods."
CRC press, editors, V.M. Malhotra, N.J. Carino., pp. 317-334.

Molavi, M.A., 1987.
"A Study of Potash Mining Methods Related to Ground Control Criteria."
Master of Engineering Thesis, McGill University, Department of Mining and Metallurgical Engineering, pp. 1-19.

Momayez, M., Hara, A., Hassani, F.P., and Sadri, A., 1994.
"Application of Ground Penetrating Radar for More Efficient Mine Planning."
GPR International Conference, Waterloo, 1994, pp. 907-913.

Momayez, M., Sadri, A., and Hassani, F.P., 1995.
"Impact-Echo: A Technique for Determining Mechanical Properties of Rocks."
The 35th U.S. Rock Mechanics Symposium, Lake Tahoe, 1995, 6 pp.

Momayez, M., Sadri, A. and Hassani, F.P., 1994.
"A Comparitive Study of GPR and Impact-Echo Nondestructive Testing Techniques For Detection of Buried Objects."
GPR International Conference, Waterloo, 1994, pp. 433-448.

Mooney, H.M., 1974.
"Seismic Shear Waves in Engineering."
Journal of the Geotechnical Engineering division, ASCE, Vol. 100, No. GT8, pp. 905-923.

Mooney, H.M., 1980.
"Handbook of Engineering Geophysics Volume 1: Seismic."
Bison Inc., Vol. 1., 1981, pp. 1-25.

Mooney Harold M., 1976.
"The Seismic Wave System from a Surface Impact."
Geophysics, Vol. 41, No. 2; pp. 243-265.

Naik, T.R., 1979.
"The Ultrasonic Testing of Concrete."
Published by ACI, Sabnis, G.M, and Fitzsimons, N., Eds., October 1979.

Nazarin, S. and Stokoe, K.H.II, 1983.
"Use of the Spectrum Analysis of Surface Wave Method for Determination of Moduli and Thicknesses of Pavement Systems."
Transportation Research Record, 930, 1983, 38 pp.

Nazarin, S. and Stokoe, K.H.II, 1986.
"Use of Surface Waves in Pavement Evaluation."
Transportation Research Rec., 1986, 1070 pp.

Nazarin, S. and Stokoe, K.H.II, 1986.
"In Situ Determination of Elastic Moduli of Pavement Systems by Spectral Analysis of Surface Waves Method (Theoretical Aspects)."
Res. Rep. 437-2, Center for Transportation Research, 1986, University of Texas at Austin.

Neville, A.M., 1981.
"Properties of Concrete."
Pitman Publishing Pty Ltd., 1981, 779 pp.

Nicholls, H.R., 1961.
"In Situ Determination of the Dynamic Properties of Rocks."
Proc. Int. Symp. Min. Res., Rolla, 1961, Vol. 2, pp. 727-738.

Obert, L., 1939.
"Sonic Method of Determining the Modulus of Elasticity by Means of Sonic Vibrations."
Proceeding of ASTM, Vol. 39, 1939, 987 pp.

Obert, L., and Duvall, W.I., 1967.
"Rock mechanics and the Design of Structures in Rock."
New York, Wiley, 1967, 670 pp.

Obert, L., Windes, S.L. and Duvall, W.I., 1967.
"Standardised Tests for Determining the Physical Properties of Mine Rocks."
U.S.B.M.R.I. 3891, 1946, 67 pp.

Obert, L. and Duvall, W.L., 1941.
Discussion of Dynamic Methods of Testing Concrete with Suggestions for Standardization."
Proceeding ASTM, 41, 1053 pp.

Olson, L.D., Sack, D.A., Stokoell, K.H., and Buchinski, K.W., 1995.
"Stress-Wave Nondestructive Testing of Tunnels and Shafts."
Transportation Research Record 1415, pp. 88-94.

Olson, L.D. and Wright, C.C., 1990.
"Seismic, Sonic, and Vibration Methods for Quality Assurance and Forensic Investigation of Geotechnical, Pavement, and Structural Systems."
Proceedings Conference on Nondestructive Testing and Evaluation for Manufacturing and Construction, R.H.L.M., Ed., Hemisphere, 1990, 263 pp.

Oppenheium, Alan V., and Schafer Ronald W., 1989.
"Discrete-Time Signal Processing."
Published by Pretice-Hall inc.

Pao, Y.H., Gajewski, R.R., and Ceranoglu, A.N., 1979.
"Acoustic Emission and Transient Waves in an Elastic Plate."
Journal of Acoustic Society of America, Vol. 65, No. 1, January 1979, pp. 96-104.

Pauw, A., 1960.
"Static Modulus of Elasticity of Concrete as Affected by Density."
Journal of the American Concrete Institute, Vol. 32, No. 6, Dec., pp. 679-687.

Pessiki, S.P., and Carino, N.J., 1987.
"Measurement of the Setting Time and Strength of Concrete by the Impact-Echo Method."
Report No. NBSIR 87-3575, National Bureau of Standards, Washington, D.C., July, pp 109.

Pessiki, S.P. and Carino, N.J., 1988.
"Setting Time and Strength of Concrete Using the Impact-Echo Method."
ACI Material Journal, September/October 1988, pp. 389-399.

Pessiki, S.P. and Johnson, M., 1995.
"In-Place Determination of Concrete Strength by the Impact-Echo Method." Structures Congress XII Proceedings of Structural Congress 1994, Published by ASCE, New York, NY, USA., pp. 1340-1345.

Philleo, R.E., 1955.
"Comparison of Results of Three Methods for Determining Young's Modulus of Elasticity of Concrete."
Journal of the American Concrete Institute, Vol. 26, No. 5, Jan., pp. 461-472.

Popovics, R, and Cvetkovic, M., 1972.
"Determination of the Dynamic Parameters of Elasticity for Rocksalt Using Resonant and Ultrasonic Techniques."
In Serbo-Croat. Proc. 3rd Yugoslav. Symp. Rock Mech. Underground Excavations, 6 pp.

Powers, T.C. 1938.
"Measuring Young's Modulus of Elasticity by Means of Sonic Vibrations."
Proc. ASTM, Vol. 38, Part II, 460 pp.

Proctor, T.M. Jr., 1982.
"Some Details of the NBS Conical Transducer."
Journal of Acoustic Emission, Vol. 31 No. 3, pp. 173-178.

Proctor, Thomas M., 1986.
"More Recent Improvement on the NBS Conical Transducer."
Journal of Acoustic Emission, Vol. 5, No. 4, pp. 134-142.

Proctor, Thomas M., 1988.
"A High Fidelity Piezoelectric Tangential Displacement Transducer for Acoustic Emission."
Journal of Acoustic Emission, Vol. 7, No. 5, pp. 41-47.

Ramana, Y.V. and Venkatanarayana, B., 1973.
"Laboratory Studies on Kolar Rocks."
Journal of Rock Mechanics and Mining Sciences, Vol. 10, 1973, pp. 465-489.

Rayleigh, J.W., 1945.
"Theory of Sound."
Second Edition, Dover Press, New York, 1945.

Sadri, A, 1992.
"An Investigation of the Impact-Echo Technique."
Master of Engineering Thesis, McGill University, Department of Mining and Metallurgical Engineering, 146 pp.

Sansalone, M., and Carino, N.J., 1986.
"Impact-Echo: A Method For Flaw Detection in Concrete Using Transient Stress Waves."
NBSIR 86-3452, NTIS PB#87-104444/AS, Springfield, Virginia, September, 1986, 222 pp.

Sansalone, M., and Carino, N.J., 1988.
"Impact-Echo Method".
ACI Journal, April 1988., pp. 38-46.

Sansalone, M., and Carino, N.J., 1989a.
"Detecting Delaminations in Concrete Slabs With and Without Overlays Using the Impact-Echo Method."
Submitted for publication in the ACI Material Journal, Contribution of the National Bureau of standards, 31 pp.

Sansalone, M., and Carino, N.J., 1989b.
"Detecting Honeycombing, the Depth of Surface opening Cracks, and Ungrouted Ducts Using the Impact-Echo Method."
Concrete International, April 1988, pp. 34-46.

Sansalone, M., and Carino, N.J., 1989c.
"CRC Handbook On Nondestructive Testing Of Concrete: Stress Wave propagation Methods."
CRC Press, Inc., editors, V.M. Malhotra, N.J. Carino., pp. 147-168.

Sansalone, M., and Carino, N.J., 1990.
"Finite Element Studies of the Impact-Echo Response of Layered Plates Containing Flaws."
International Advances in Nondestructive testing, 15th Edittion, McGonnagle, Ed., Gordon & Breach Science Publishers, New York, 1990.

Sansalone, M., and Carino, N.J. and Hsu, N.N., 1987.
"A Finite Element Study of the Transient Wave Propagation in Plates."
NBS Journal of Research, July/August 1987, pp. 267-278.

Sansalone, M., and Carino, N.J. and Hsu, N.N., 1987.
"A Finite Element Study of the Interaction of Transient Wave with Planar Flaws."
NBS Journal of Research, July/August 1987, pp. 279-290.

Sansalone, M.J., 1985.
"Flaw Detection in Concrete Using Transient Stress Wave."
PH.D. Thesis, Cornell University, 220 pp.

Schmidt, E., 1954.
"The Concrete Sclerometer."
Proceedings, International Symposium on Nondestructive Testing on Materials and Structures, Vol. 2, RILEM, Paris, pp. 310-319.

Sharma, P.V., 1986.
"Geophysical Methods in Geology."
Elsevier Science Publishers, second edition, 442 pp.

Stead, D., and Lu, C., 1992.
"Results of Acoustic Velocity, Porosity, and Density Measurements."
IMC GERALD: Borehole No. 10d-13-20-32W1, Rock Mechanics Laboratory, University of Saskatchewan.

Sturrup, V.R., Vecchio, F.J., and Caratin, H. 1984.
"Pulse Velocity as a Measure of Concrete Compressive Strength."
ACI SP 82-11, 1984, 201 pp.

Sutherland, R.B., 1961.
"A Comparison Between the Sonic and Static Elastic Moduli of Rocks."
Master of Engineering Thesis, McGill University, Department of Mining Engineering, 175 pp.

Swamy, N.R. and Al-Hamed, A.H., 1984.
"The Use of Pulse Velocity Measurments to Estimate Strength of Air Dried Cubesand Hence In Situ Strength of Concrete."
ACI SP 82, Malhotra, V.M.., Ed. 247 pp.

Tarun, R. Naik and Malhotra, V.M., 1991.
"CRC Handbook on Nondestructive Testing of Concrete: The Ultrasonic Pulse Velocity Method."
CRC press, editors, V.M. Malhotra, N.J. Carino., pp. 169-189.

Telford, W.M., Geldart L.P. and Sheriff R.E., 1990.
"Applied Geophysics."
Cambridge University Press. second edition, pp. 136-273.

Thomson, W.T., 1940.
"Measuring Changes in Physical Properties of Concrete by the Dynamic Method."
Proceeding ASTM, 40, 1113 pp.

Tselentis, G.A., Sofianos, A., Paliatsas, D., Makropoulos, K., and Drakopoulos, J., 1988.
"A Rock Mass Assessment Experiment in the Artemission Tunnel (Central Greece) Using Seismic Attenuation Measurments."
Geoexploration, Vol. 25, 1988, pp. 219-228.

Weil, G., 1991.
"CRC Handbook on Nondestructive Testing of Concrete: Infrared Thermographic Techniques."
CRC press, editors, V.M. Malhotra, N.J. Carino., pp. 305-316.

Yiching, L. and Sansalone, M., 1992a.
"Transient Response of Thick Rectangular Bars Subjected to Transverse Elastic Impact."
Journal of Acoustic Society of America, Vol. 91, No. 5, May 1992, pp. 2674-2685.

Yiching, L. and Sansalone, M., 1992b.
"Detecting Flaws in Concrete Beams and Columns Using the Impact-Echo Method."
ACI Materials Journal, July/August 1992, pp. 394-405.

Youash, Y.Y., 1970.
"Dynamic Phisical Properties of Rocks."
Proc. second Cong. Int. Soc. Rock Mec., Belgrade, 1970, Vol. 4, pp. 204-205.

Yu, T.R., Henning, J.G. and Croxall, J.E., 1990.
"Loose Rock Detection with Infrared Thermography."
CIM Bulletin, Vol. 83. No. 937, pp. 46-52.

Zisman, W.A., 1933.
"A Comparison of the statistically and Seismologically Determined Elastic Constants of Rock."
Proc. Nat. Acad. Sci. U.S.A., Vol. 19, pp. 680-686.

APPENDIXES

GRINDOSONIC

The description of the Grindosonic apparatus was taken from *"Nondestructive Determination of Young's Modulus and Its Relationship with Compressive Strength, Porosity and Density" by R. J. Allison (1987) and **"Grindosonic Measurement & Calculations of Elastic Properties of Concrete Test Pieces" by J. W. Lemmens, Inc. (1989).

1 The Basic Principle

"The Grindosonic apparatus (Figure A-1) is a new device capable of determining rock, concrete, and composite strength. It utilizes the principle that elasticity theory can be applied to the solid masses, and it directly measures the fundamental vibration frequency of a sample of known dimensions following shock excitation. The measured elastic material properties can be calibrated to determine the material's hardness and strength. The device, an example of ultrasonic pulse velocity testing equipment (Neville, 1981), analyses the transient vibration of test a specimen. The sample is struck to set up a mechanical vibration pattern rather than being subjected to continuous flexure. This pattern is converted to an electronic signal via a piezoelectric detector held in contact with the test piece surface. The signal is amplified by the apparatus before being fed by the instrument input. If it exceeds the predetermined minimum level required for analysis, the time of eight wave passes is measured. A short interval between striking the sample and measurement prevents the analysis of spurious initial wave patterns which have complex harmonics and which occur when the test piece is initially struck. The lapsed time appears in the equipment display panel and is known as the *r*-value."**

"The vibrating sample experiences dampening relative to its elastic properties. The decay of a vibration pattern set up in a hard, rigid test piece will take much longer than the same flexure in a soft material of similar dimensions. The result given by Grindosonic therefore constitutes a direct measure of sample rigidity or hardness. However, the natural frequency of vibration is determined by specimen shape and several other physical constants. Consequently, by utilizing detail of the dimensions and weight of a specimen together with its *r*-value determined by the Grindosonic, Young's modulus of elasticity, shear modulus, Poisson's ratio, bulk density, seismic velocity and a variety of other parameters can be calculated."**

2 Sample Preparation and Constraints

"Grindosonic testing relies on accurate sample preparation. Test pieces can be cut to a variety of shapes including bars, cylinders and circular discs. Some variables used in the analysis do have specific nominal limits. For example, when preparing bar-shaped samples the length-to-thickness ratio should be greater than three and the width of the bar should be less than one-third the length (Figure A-2). Beyond these limits the calculations gradually lose accuracy. Careful sample preparation is of the utmost importance because the variations in cross-sectional area and non-square edges cause significant changes in the vibration pattern." *

3 Apparatus

The test apparatus consists of a compact electronic instrument and a suitable vibration detector.

3.1 Compact Electronic Instrument

The electronic part of the instrument consists of amplifier, electronic analyzer, digital display, the selector features and a serial output port.

3.2 Vibration Detector

"The piezoelectric vibration detector is made of a sensitive piezoelectric element and electronic preamplifier. It will cover the entire frequency range of the Grindosonic and will be used almost exclusively by manual operation. A white dot indicates the direction of maximum sensitivity, which should be observed during the measurement. The dot is always held in the direction of the vibration."**

4 Measurement of Fundamental Vibration Frequencies

"The position of the transducer and the receiver in order to measure flexural, torsional and longitudinal vibration are shown in Figure A-3. The test specimens were placed on rubber strips in order to avoid excessive external dampening. A small plastic hammer or a screwdriver handle could be used to generate various desirable vibrations."**

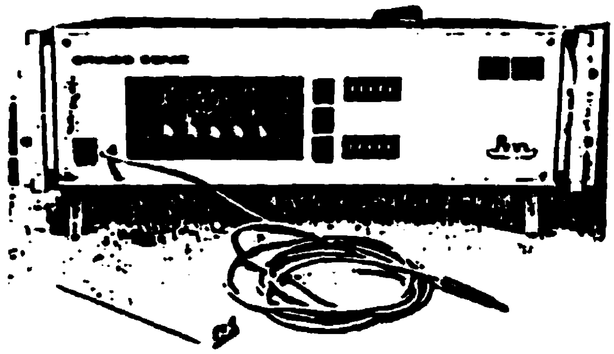

Figure A-1 The Grindosonic apparatus.

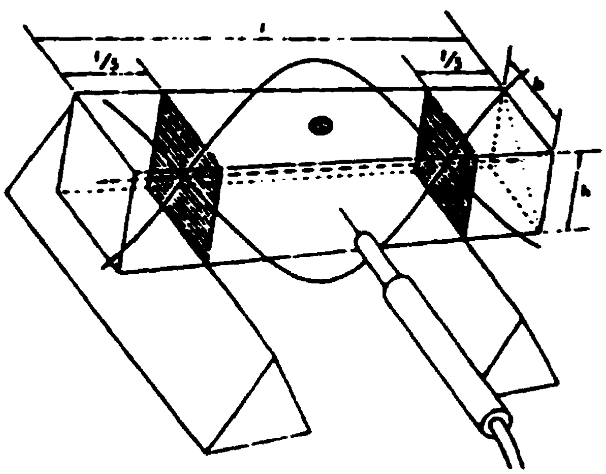

Figure A-2 The experimental setup for Grindosonic.

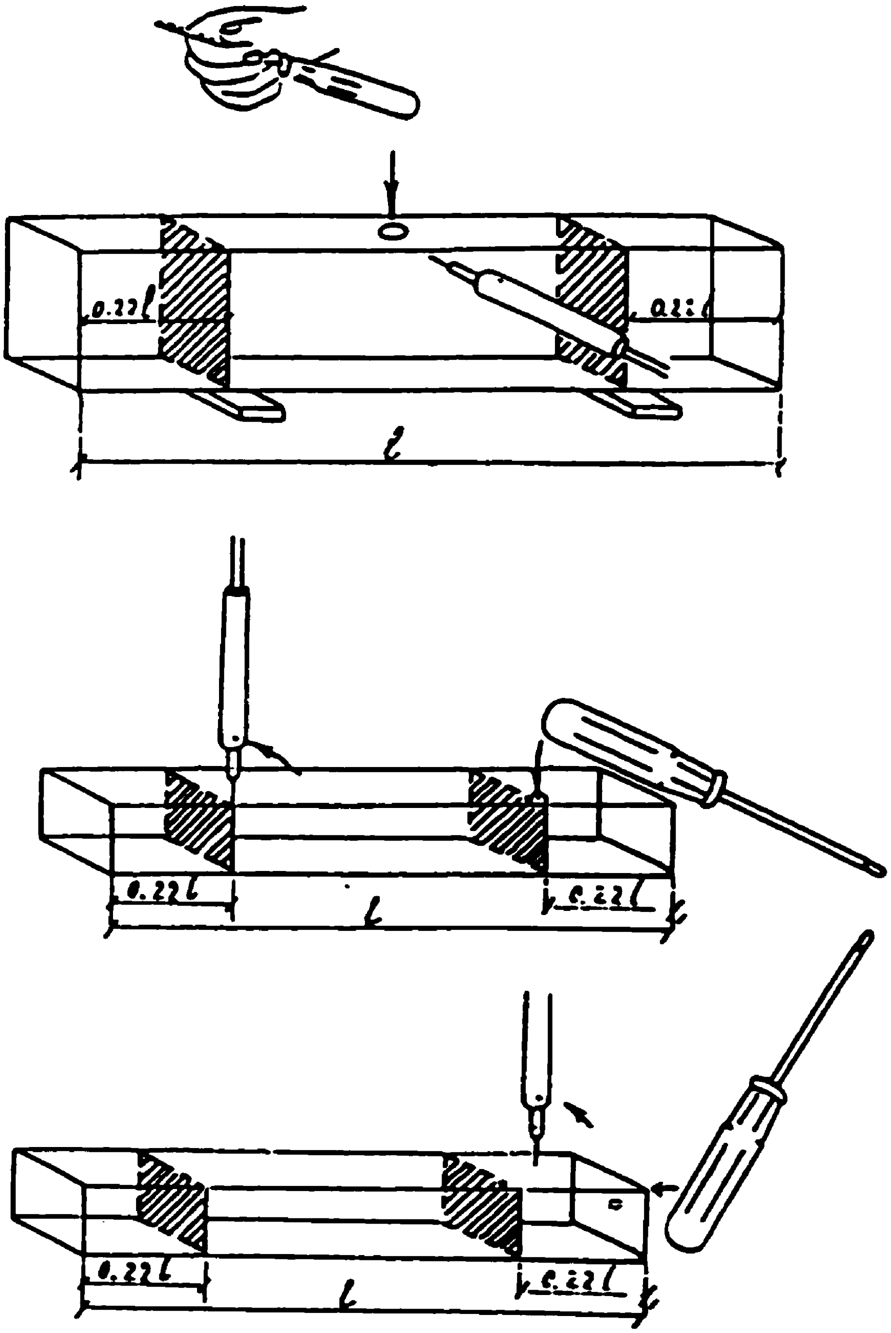

Figure A-3 The position of the impact source and receiver in order to measure flexural, torsional, and longitudinal (from top to bottom) vibrations.

PUNDIT (Portable Ultrasonic Nondestructive Digital Indicating Tester)

The description of PUNDIT apparatus was taken from *"The Ultrasonic Pulse Velocity Method" by Tarun R. Naik and V. M. Malhotra (1991) and **"PUNDIT Manual" by C.N.S. electronics Ltd. (1985)

"PUNDIT consists of a mean of producing and introducing a pulse into the concrete (pulse generator and transmitter), and a means of accurately measuring the time taken by the pulse to travel through the concrete. The equipment may also be connected to a cathode ray (CR) oscilloscope. The equipment is portable and simple to operate."* The PUNDIT carrying case is 180 × 110 × 160 mm and it weighs 3.2 kg. It is included with rechargeable batteries and carrying case. The range for operating ambient temperature for PUNDIT is between 0° to 45°C (Figure B-1).

"The transit time is displayed on a 4 digit, 12.7 mm Transflective Liquid Crystal: Two ranges of time measurements are available on the instrument, namely-

a) 0.1 to 999.9 microsecs in units of 0.1 microseconds.
b) 1 to 9999 microsecs in units of 1 microsecond."**

The PUNDIT comes with two transducers, one to transmit and one to receive the ultrasonic pulse. Both transducers are 50 mm in diameter and 42 mm long. "They have a typical resonant frequency of 54000 cycles per second (cps) for concrete testing. These consist of lead zirconate totanite ceramic (PZT-4) piezoelectric elements housed in stainless steel cases."* Other transducers with different resonance frequencies are also available for special applications. These would be high frequency transducers with 150000 cps and low frequency transducers with 24000 cps. "The instrument comes with an internal, rechargeable, nickel-cadmium battery, which can provide power for about 6 h of continuous operation. A constant current charger is built into the instrument to allow the battery to be recharged from an A.C. power supply." *

1 The Basic Principle

"The velocity of ultrasonic pulses travelling in a solid material depends on the density and elastic properties. The quality of some materials is sometimes related to their elastic stiffness so that the measurement of the ultrasonic pulse velocity in such materials can often be used to indicate their quality as well as to determine their elastic properties."**

2 Applications

"The pulse velocity method of testing may be applied to the testing of plain, reinforced and prestressed concrete, whether it is precast or cast in situ. The measurement of pulse velocity may be used to determine:

a) the homogenity of the concrete,
b) the presence of voids, cracks or other imperfections,
c) changes in the concrete which may occur with time (i.e. due to the cement hydration) or through the action of fire, frost or chemical attack,
d) the quality of the concrete in relation to specified standard requirements, which generally refers to its strength."*

3 Coupling

"Accuracy of transit time measurement can only be assured if good acoustic coupling between the transducer face and the concrete surface can be achieved." * Various types of couplants are available in the market: petroleum jelly, grease, liquid soap, and kaolin-glycerol paste.

4 Transducer Arrangement

"There are three possible ways in which the transducer may be arranged, as shown in Figure B-2, A through C. These are (a) direct transmission; (b) semi-direct transmission; and (c) indirect or surface transmission.

The direct transmission method, Figure B-2 'A', is the most desirable and the most satisfactory arrangement because maximum energy of the pulse is transmitted and received with this arrangement. The semi-direct transmission method, Figure B-2 'B', can also be quit satisfactory. However, care should be exercised that these transducers are not too far apart, otherwise the transmitted pulse might attenuate and a pulse might not be received. This method is useful in avoiding concentrations of reinforcements. The indirect or surface transmission method, Figure B-2 'C', is least satisfactory because the amplitude of the receiving signal may only be 3% or less than that received by the direct transmission method."*

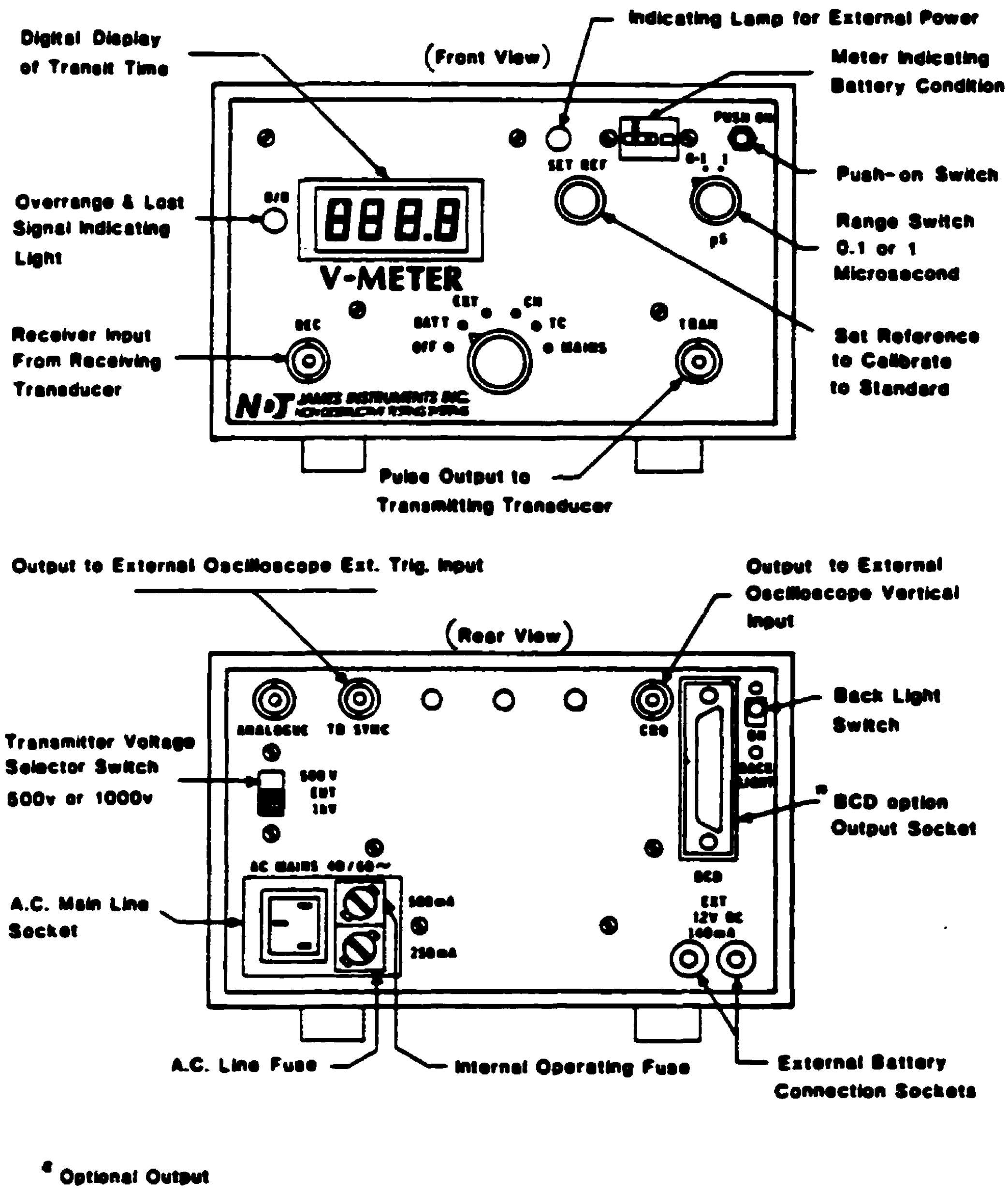

Figure B-1 The PUNDIT apparatus.

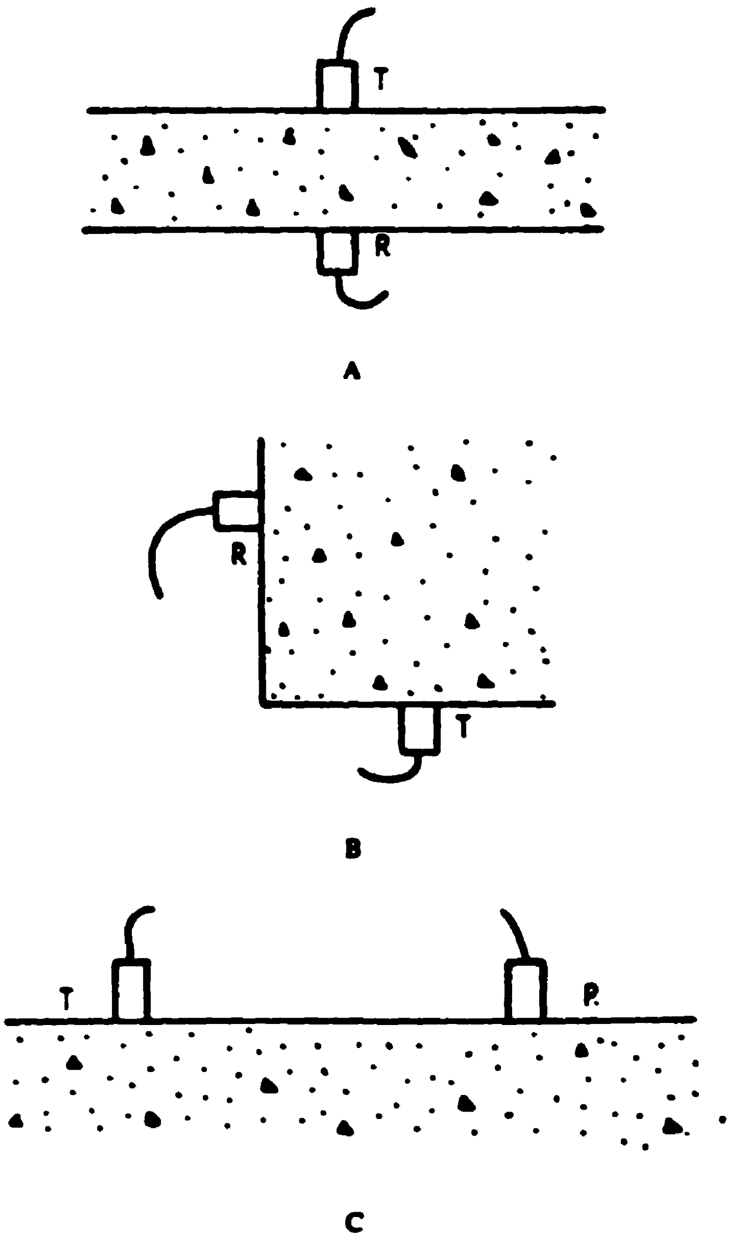

Figure B-2 Various types of transducer arrangements for PUNDIT: A) direct, B) semi-direct, and C) indirect.

BATCH No. 1

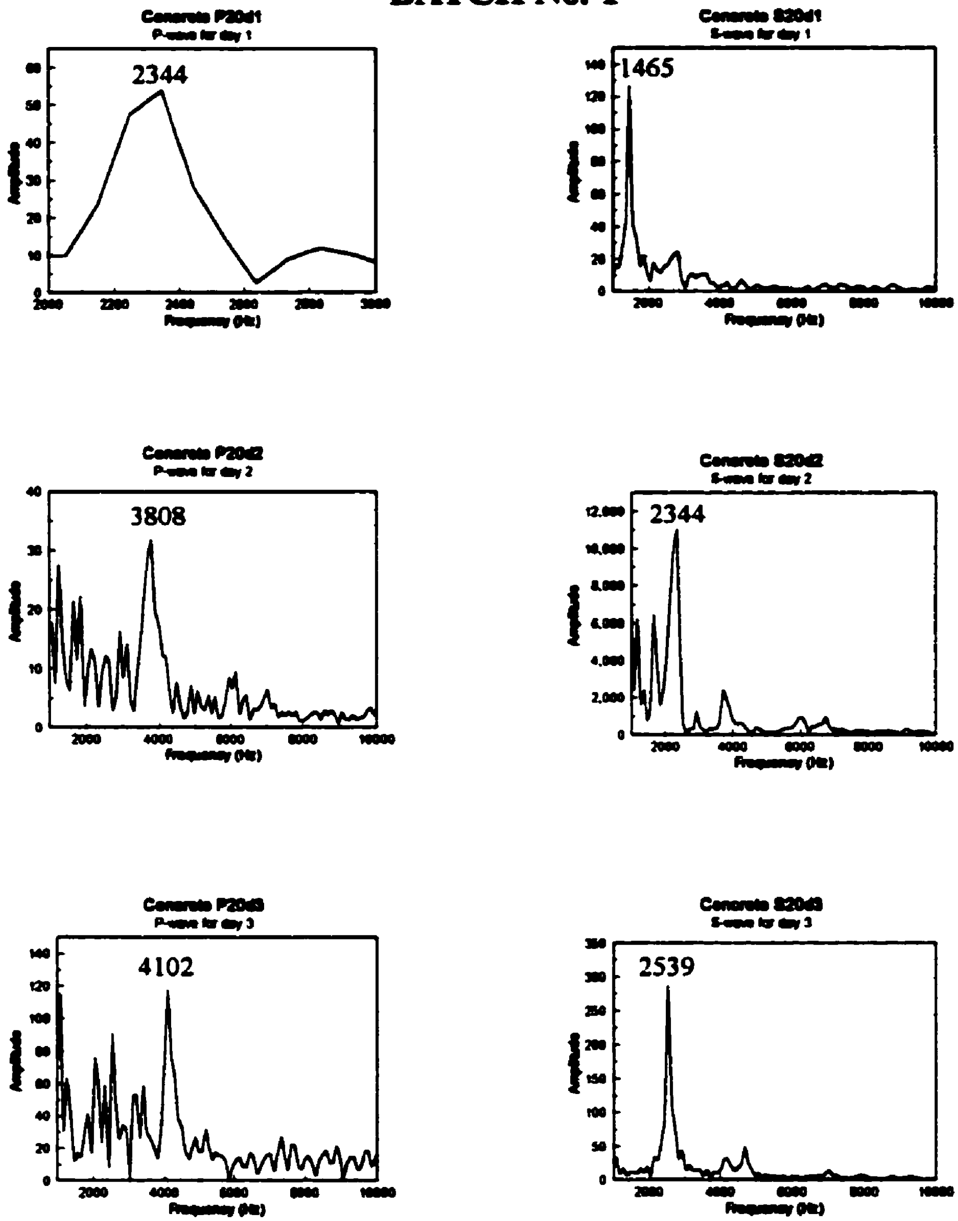

Figure C-1 The MSR computed frequency spectra for the BN20, day 1 to day 3.

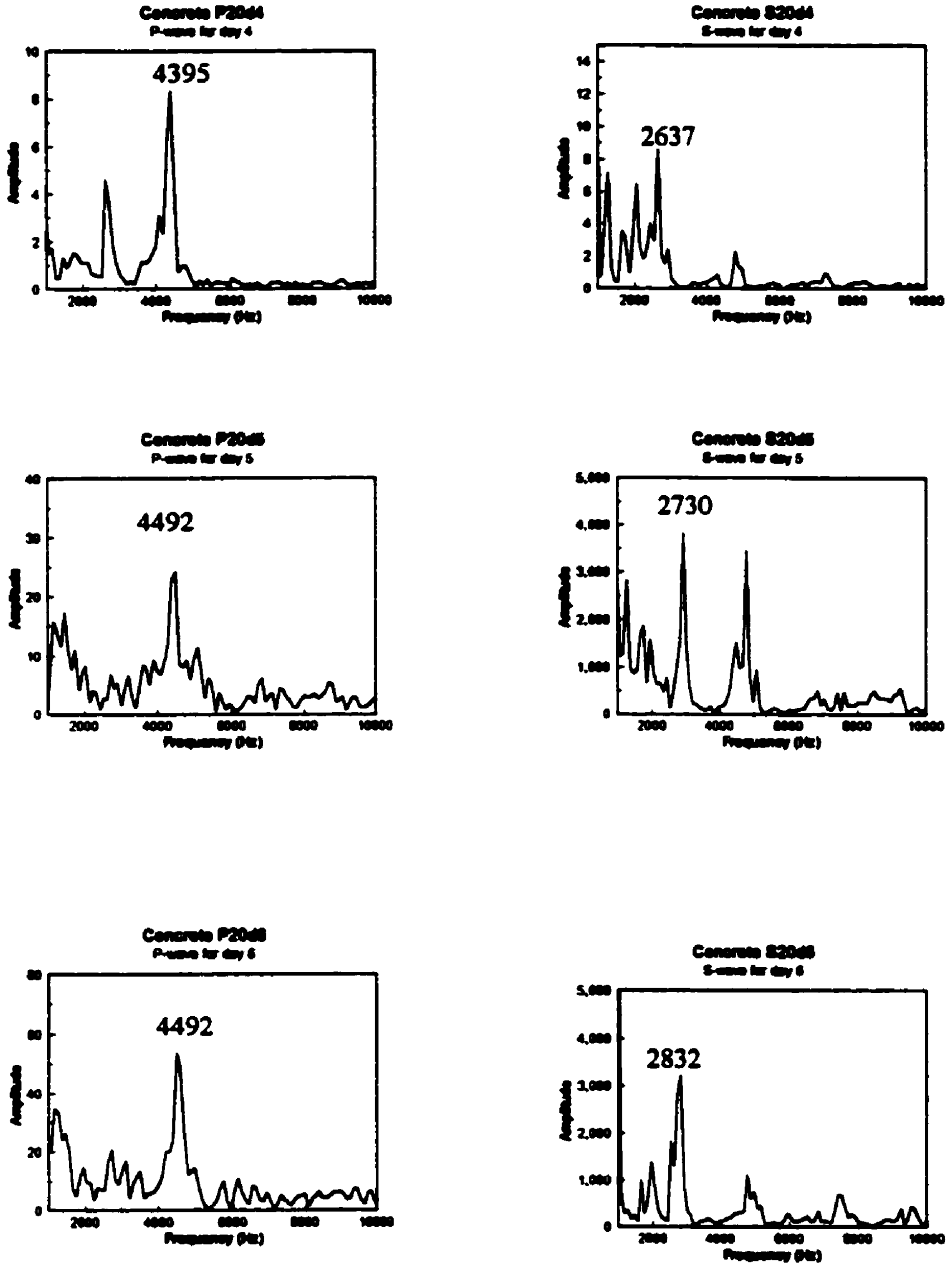

Figure C-2 The MSR computed frequency spectra for the BN20, day 4 to day 6.

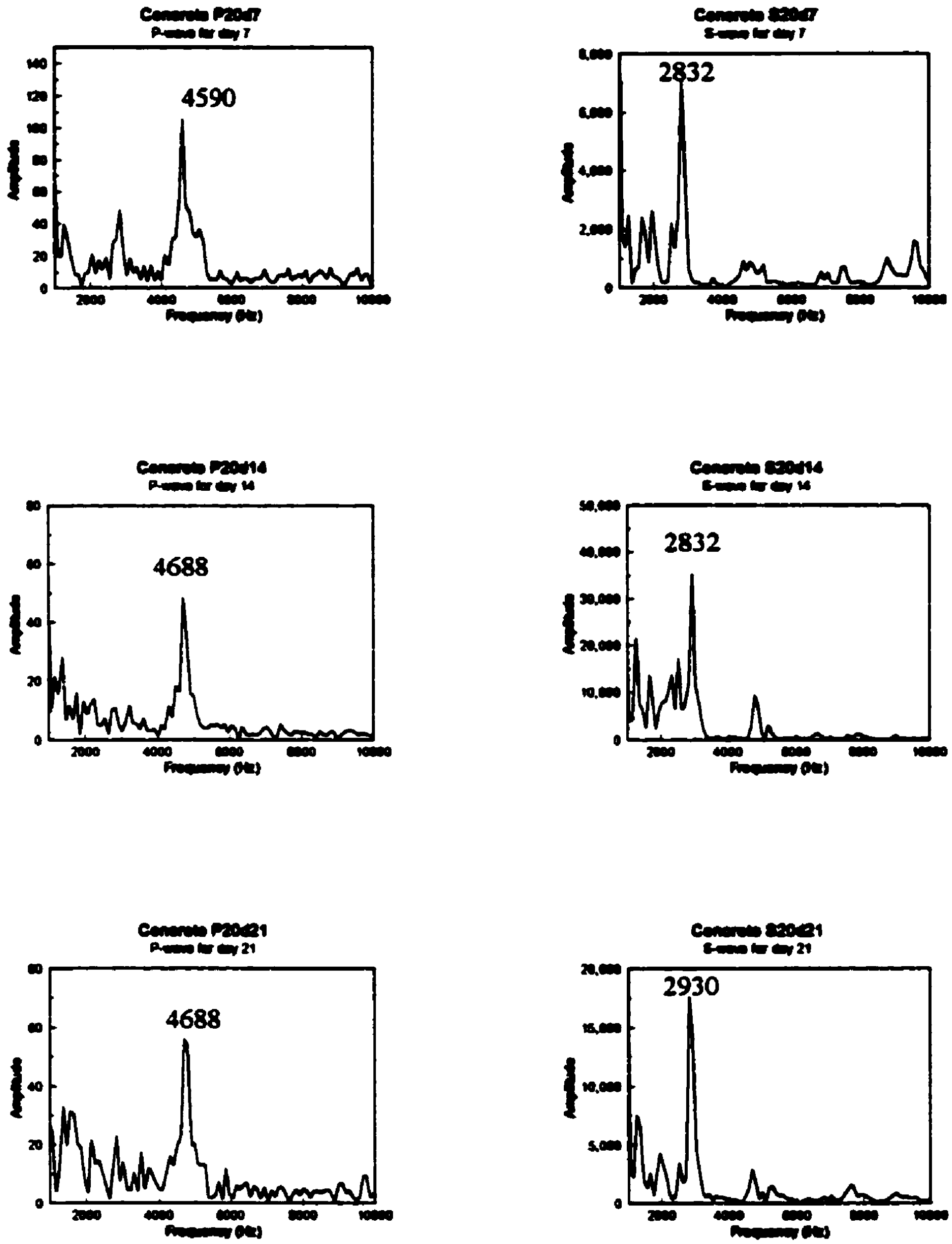

Figure C-3 The MSR computed frequency spectra for the BN20, day 7 to day 21.

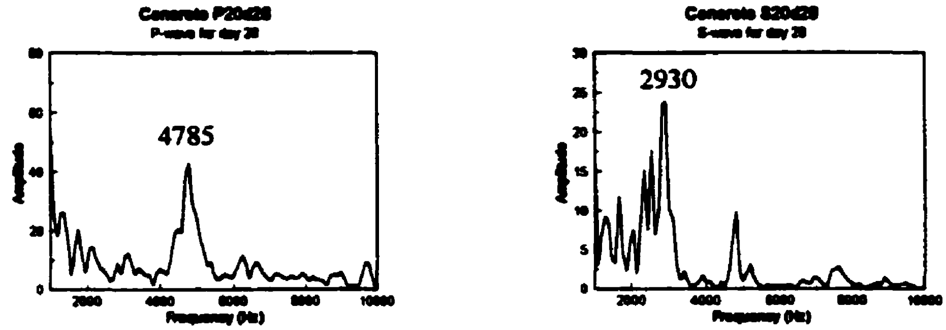

BATCH No. 2

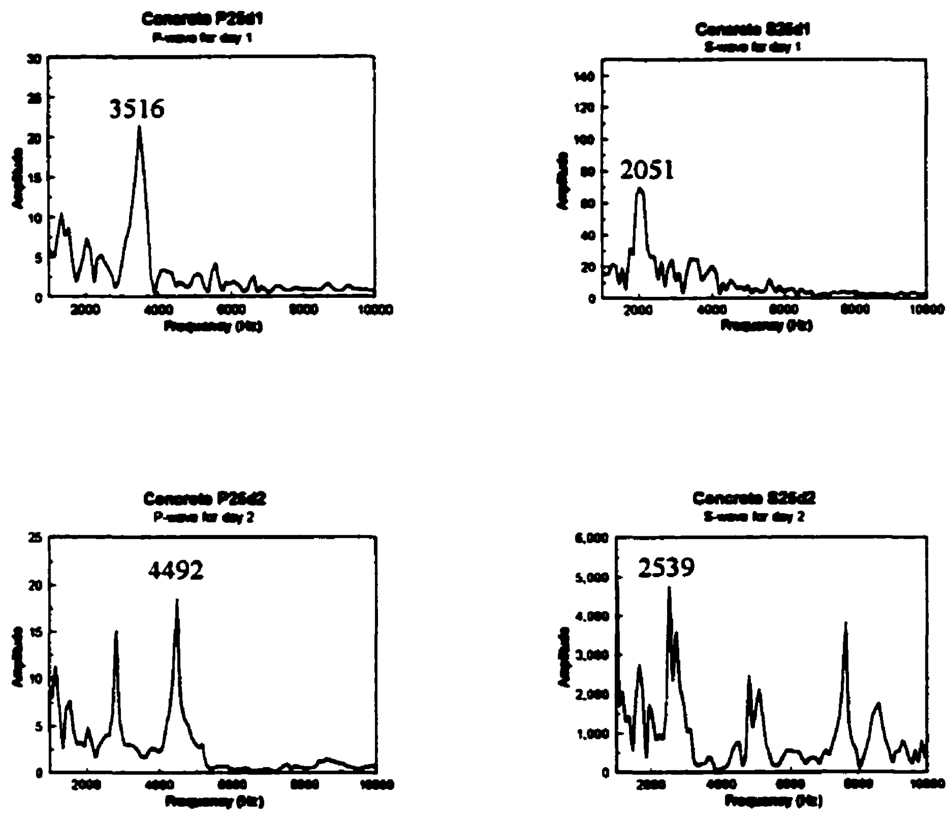

Figure C-4 The MSR computed frequency spectra for the BN20 day 28 and for the BN25 day 1 to day 2.

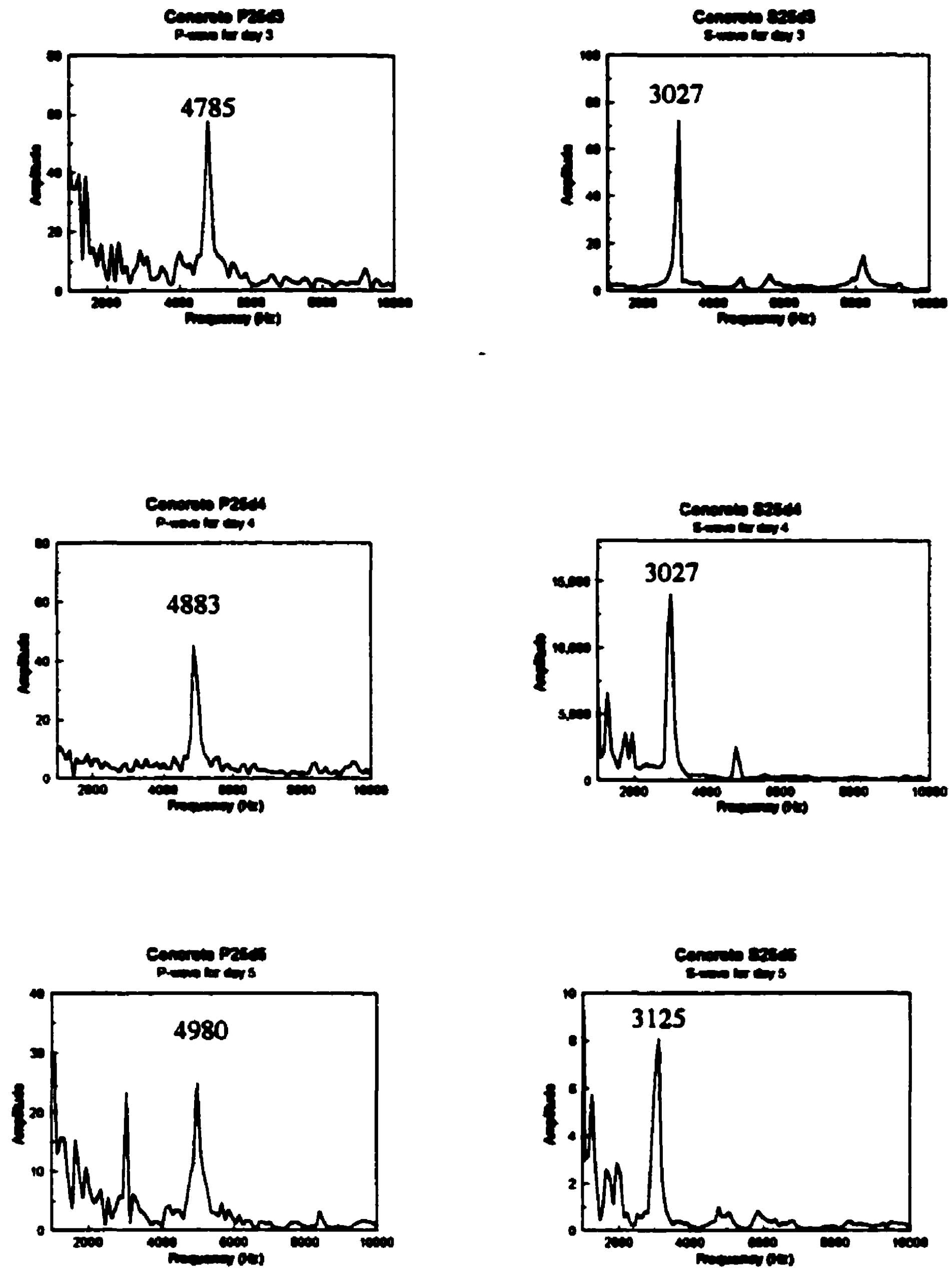

Figure C-5 The MSR computed frequency spectra for BN25, day 3 to 5.

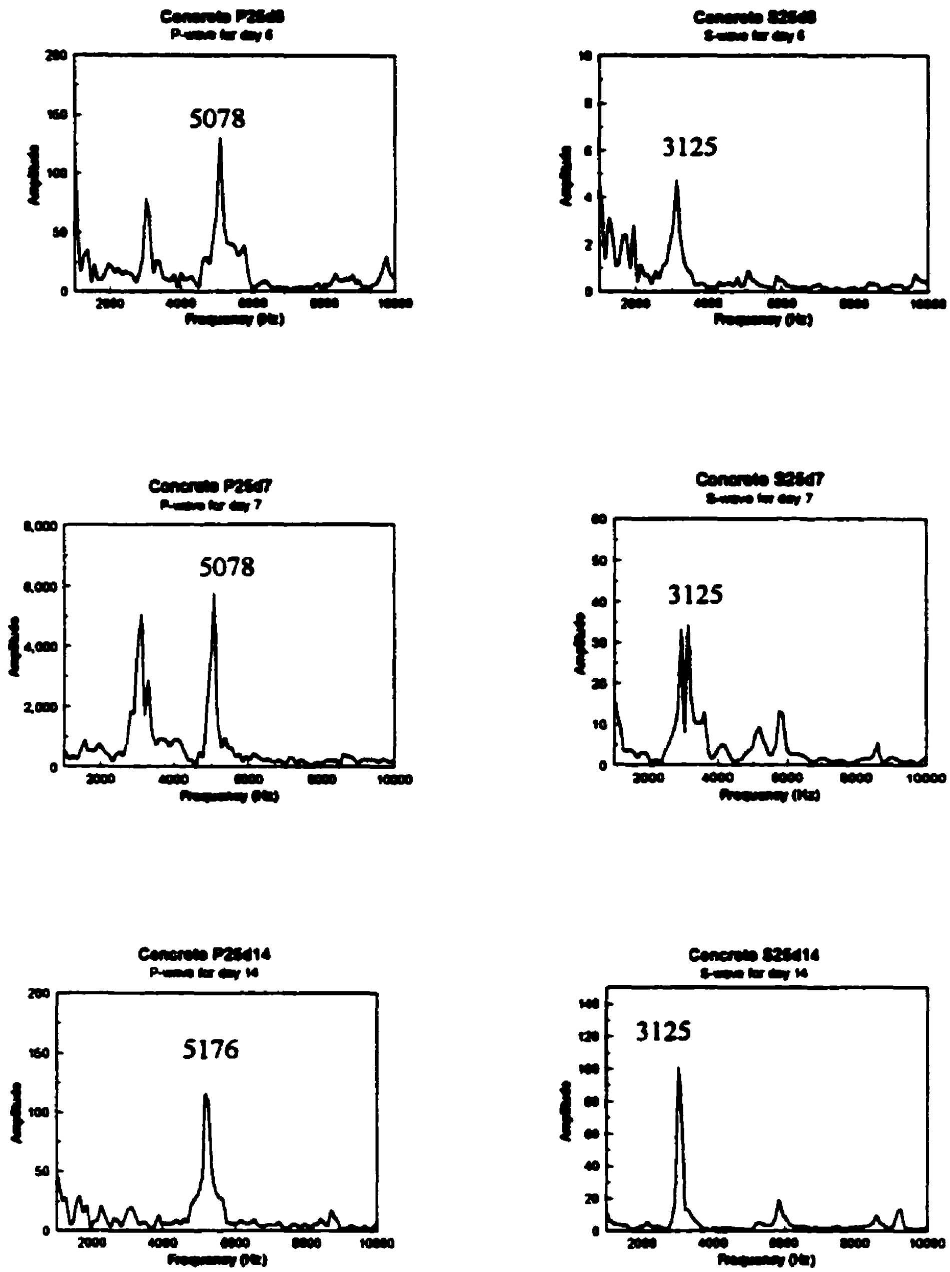

Figure C-6 The MSR computed frequency spectra for BN25, day 6 to 14.

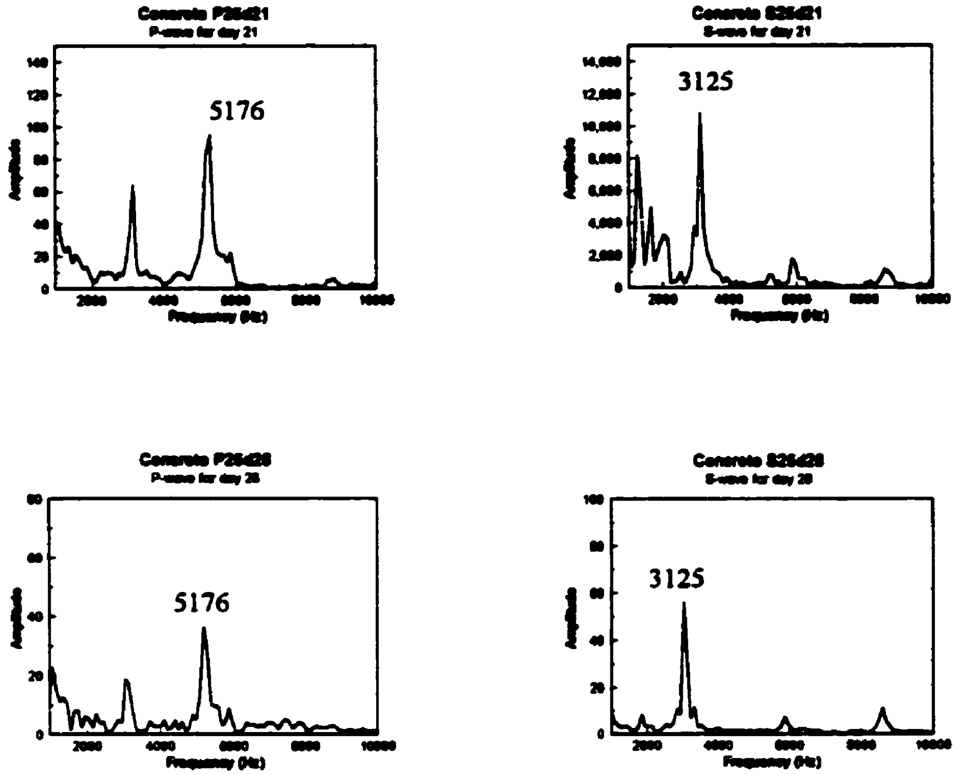

BATCH No. 3

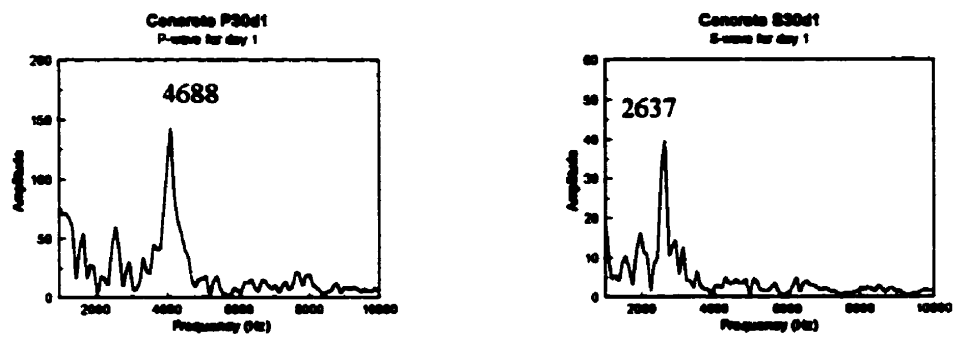

Figure C-7 The MSR computed frequency spectra for BN25, day 21 and 28, and BN30 day 1.

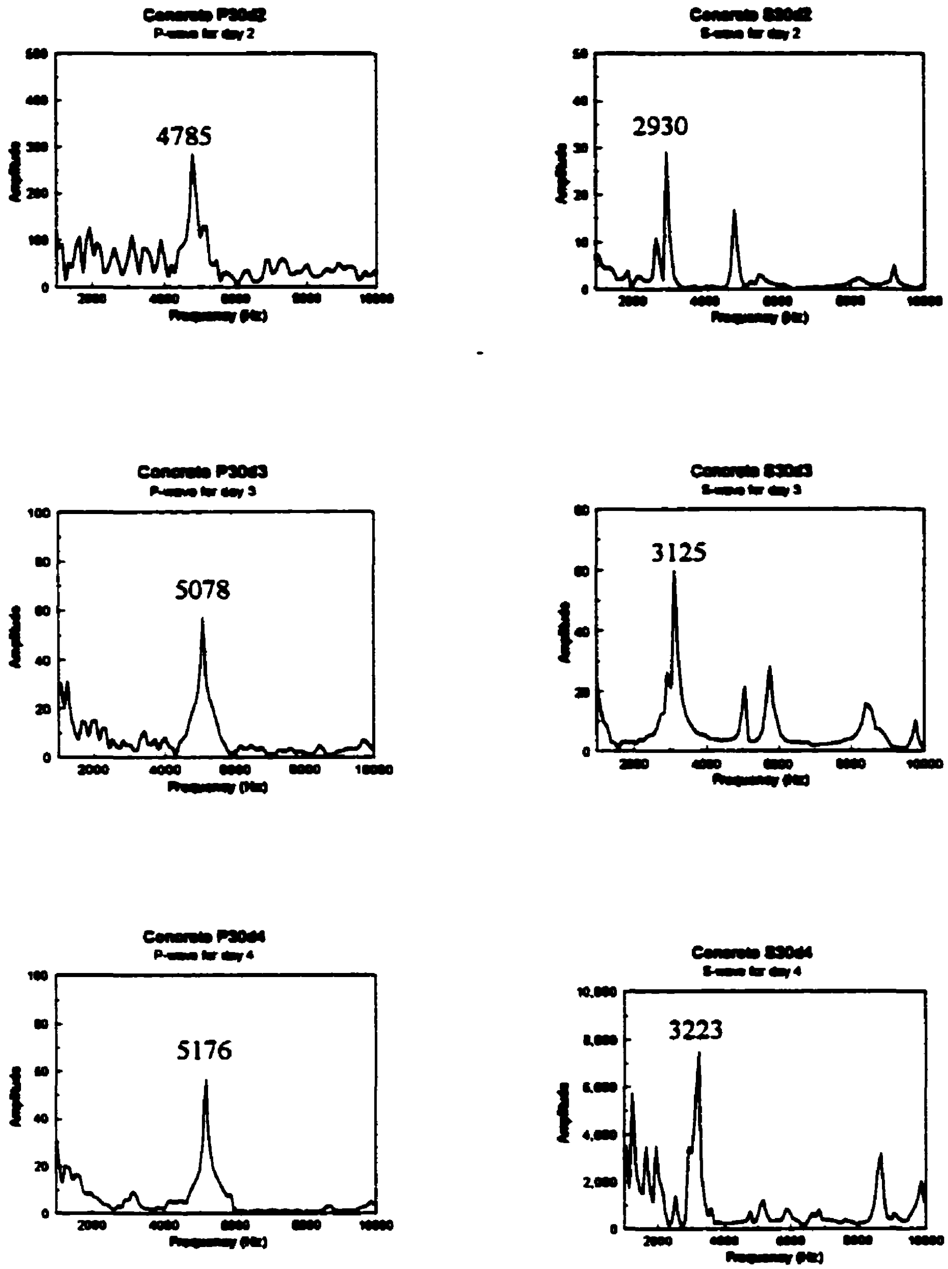

Figure C-8 The MSR computed frequency spectra for BN30, day 2 to 4.

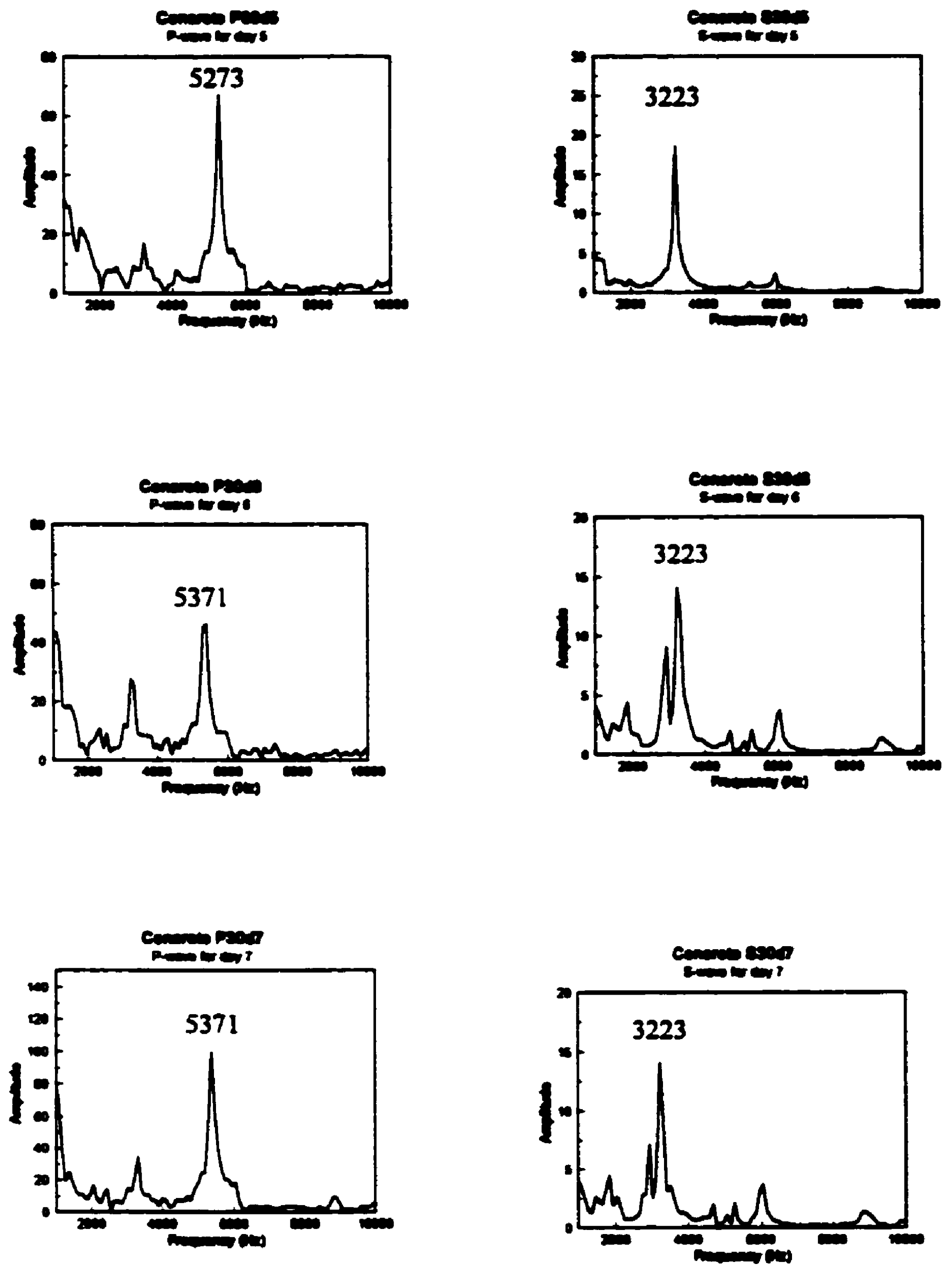

Figure C-9 The MSR computed frequency spectra for BN30, day 5 to 7.

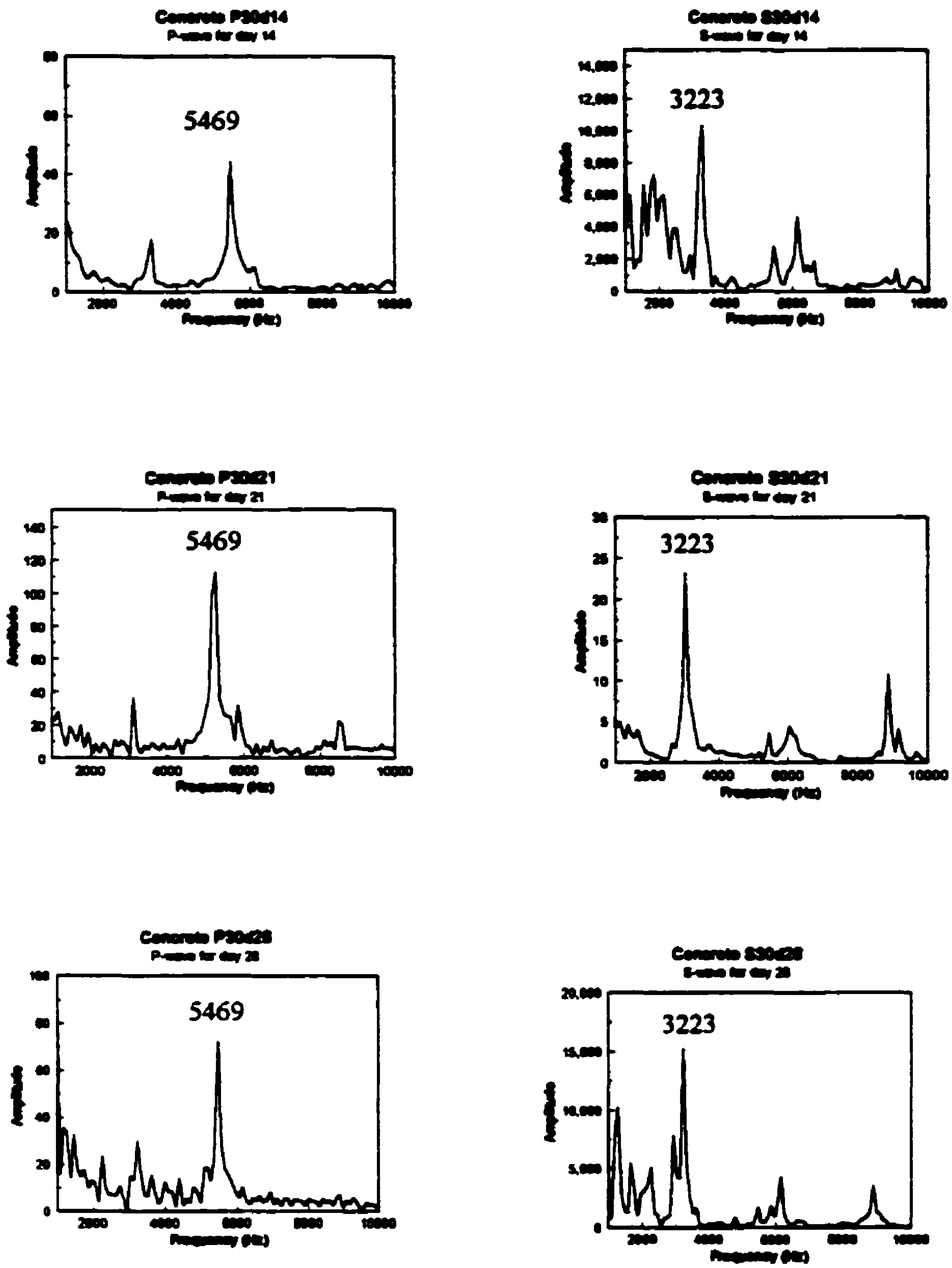

Figure C-10 The MSR computed frequency spectra for BN30, day 14 to 28.

BATCH No. 4

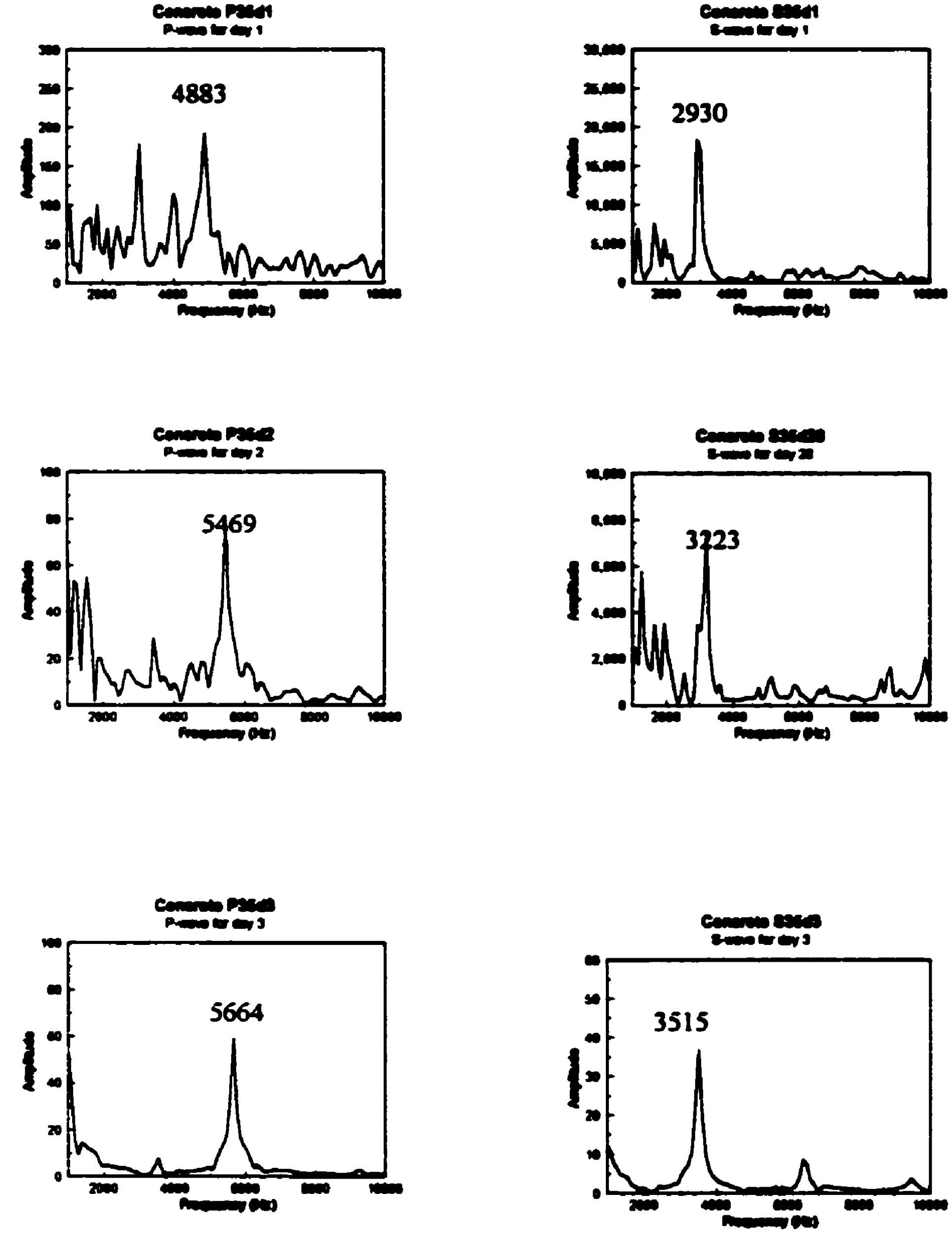

Figure C-11 The MSR computed frequency spectra for BN35, day 1 to 3.

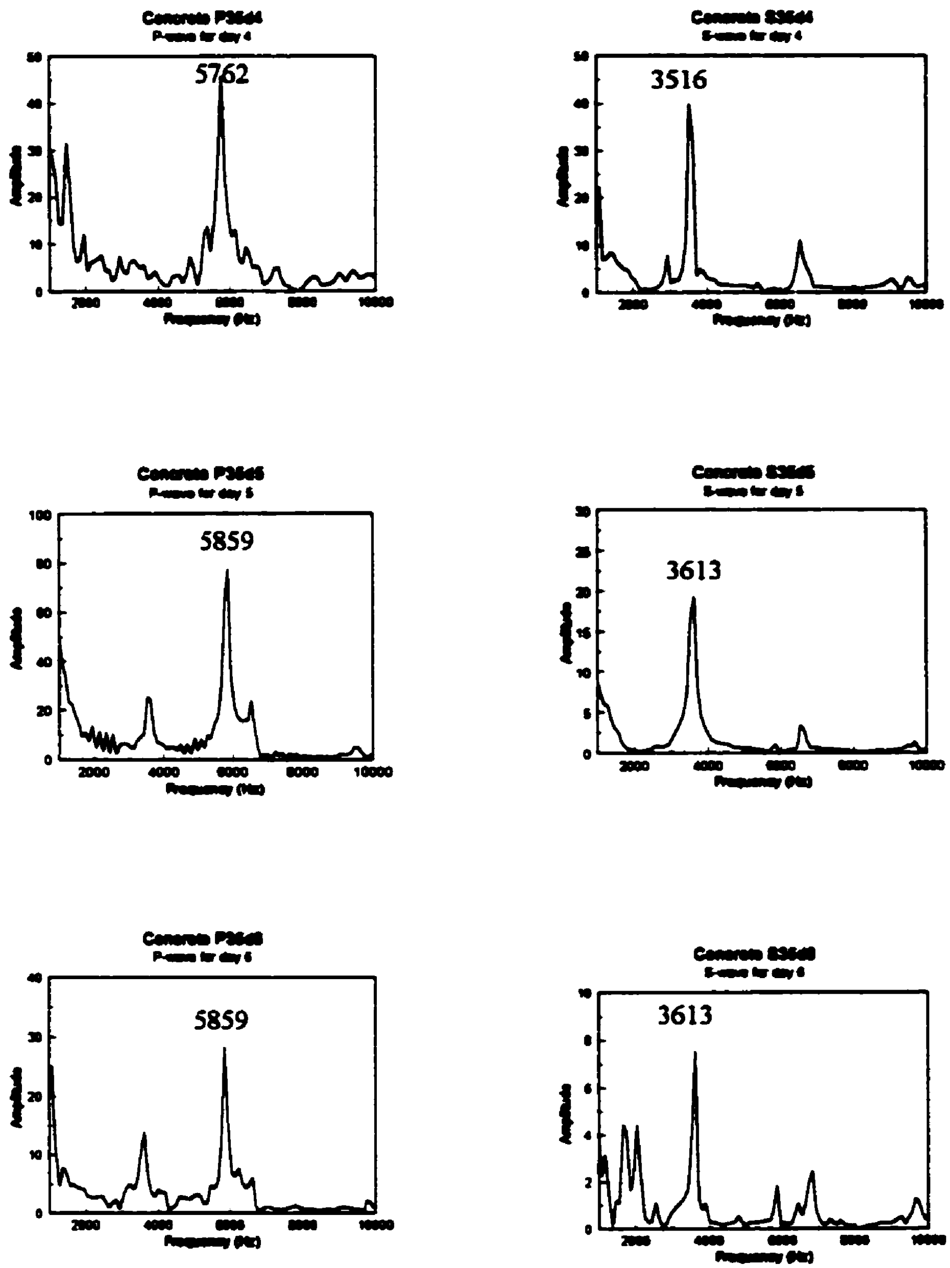

Figure C-12 The MSR computed frequency spectra for BN35, day 4 to 6.

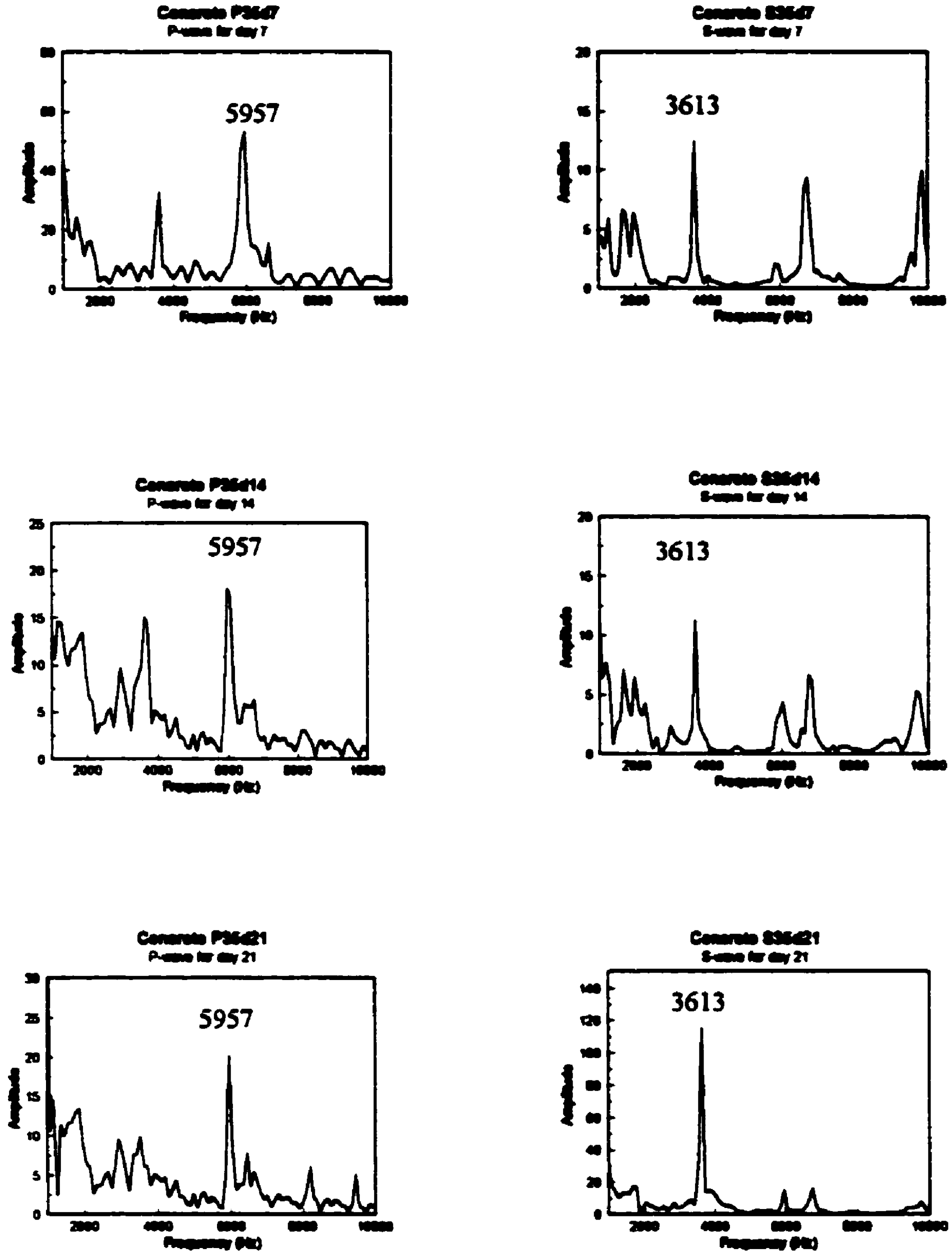

Figure C-13 The MSR computed frequency spectra for BN35, day 7 to 21.

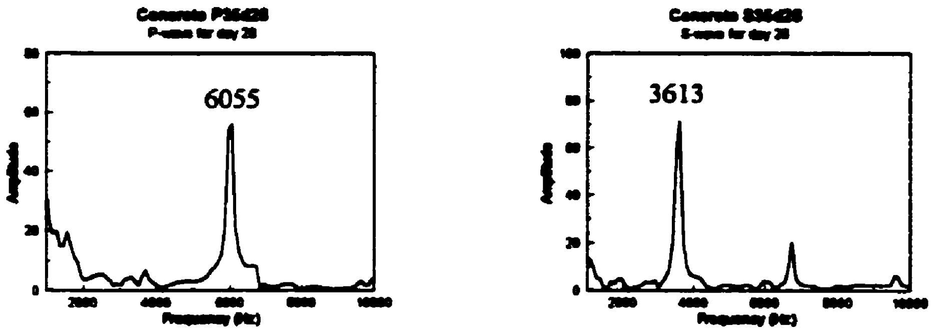

BATCH No. 5

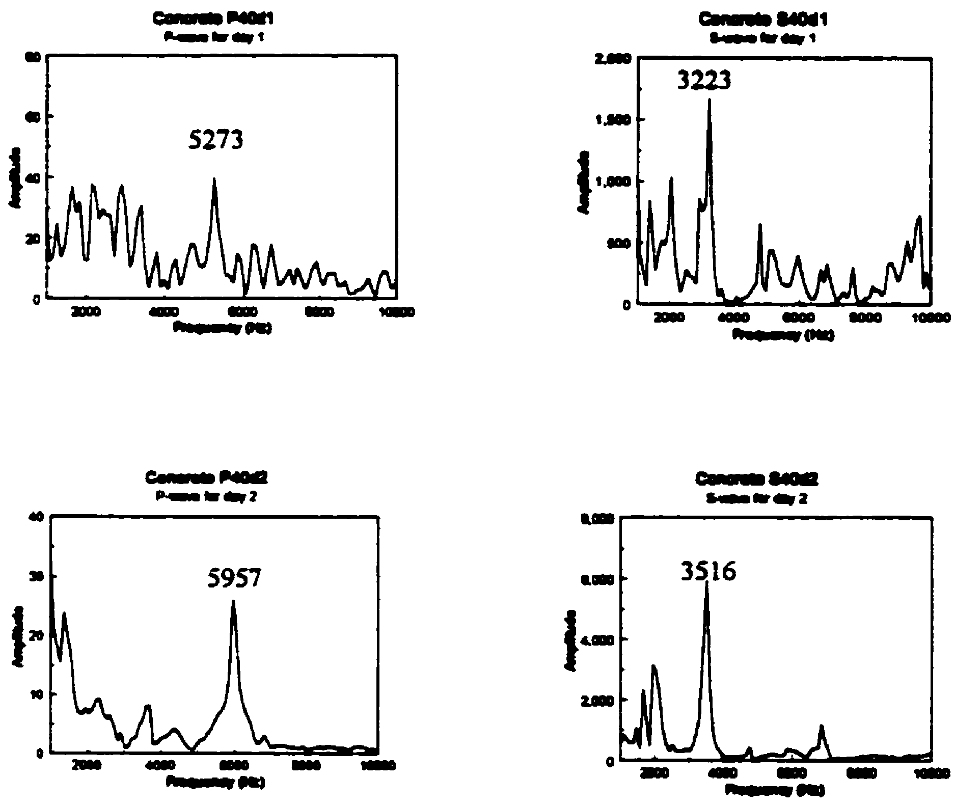

Figure C-14 The MSR computed frequency spectra for BN35 day 28 and for BN40, day 1 and 2.

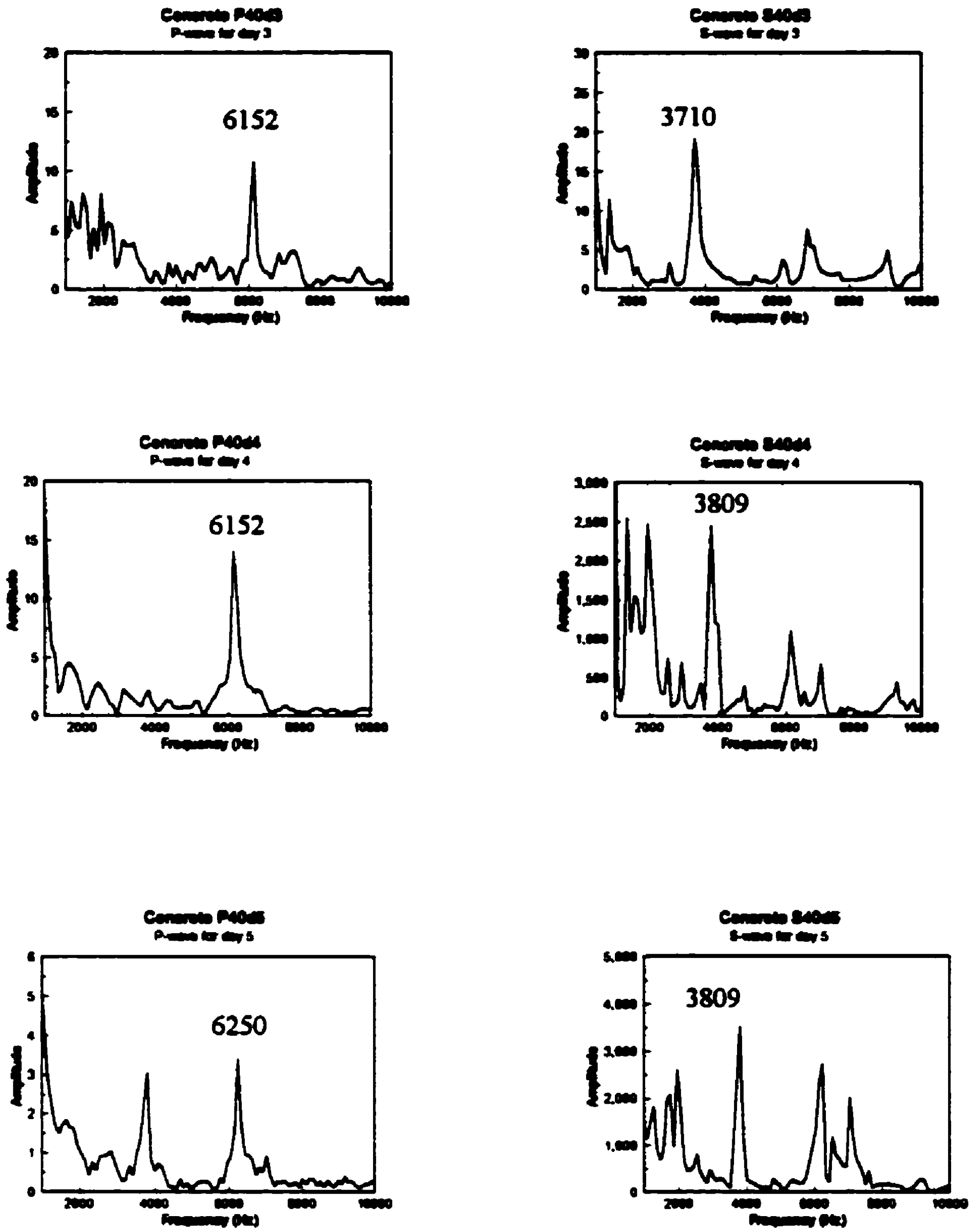

Figure C-15 The MSR computed frequency spectra for BN40, day 3 to 5.

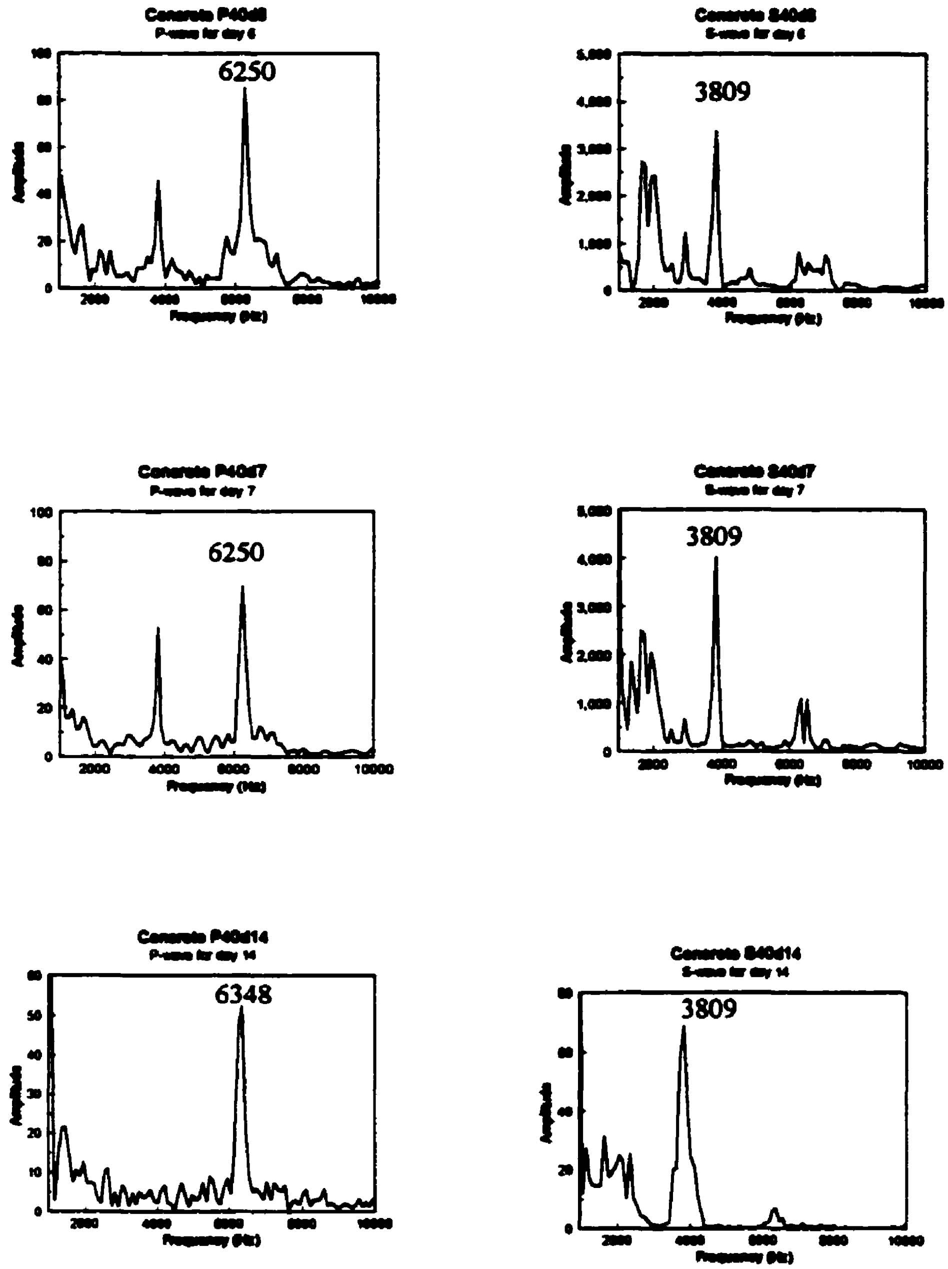

Figure C-16 The MSR computed frequency spectra for BN40, day 6 to 14.

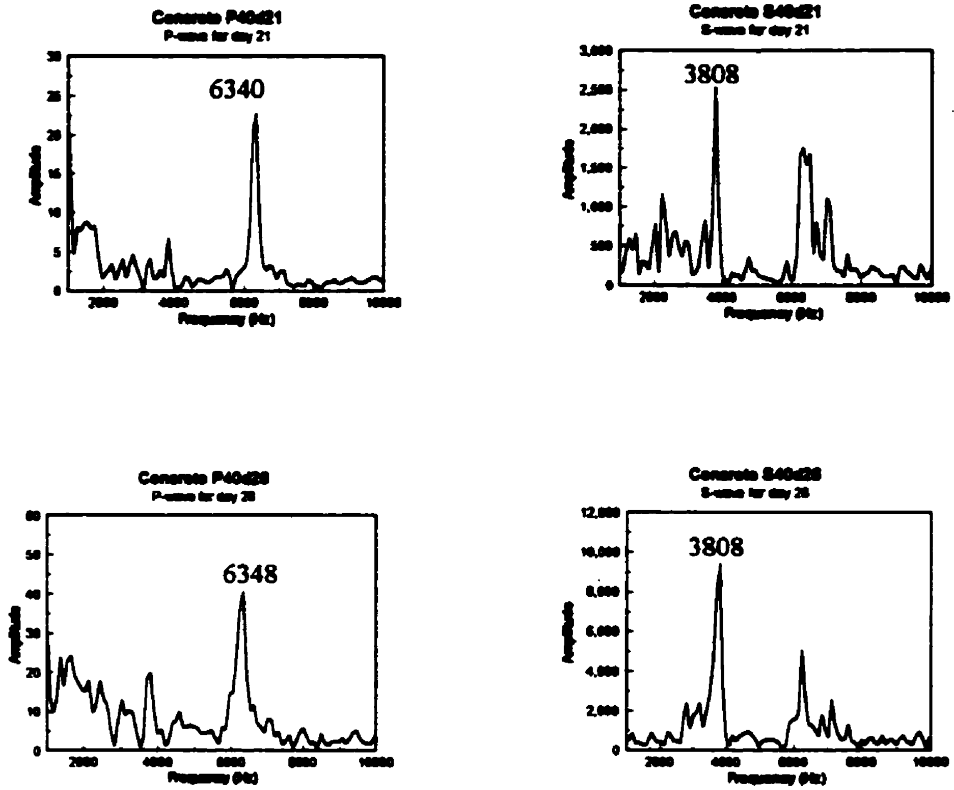

BATCH No. 6

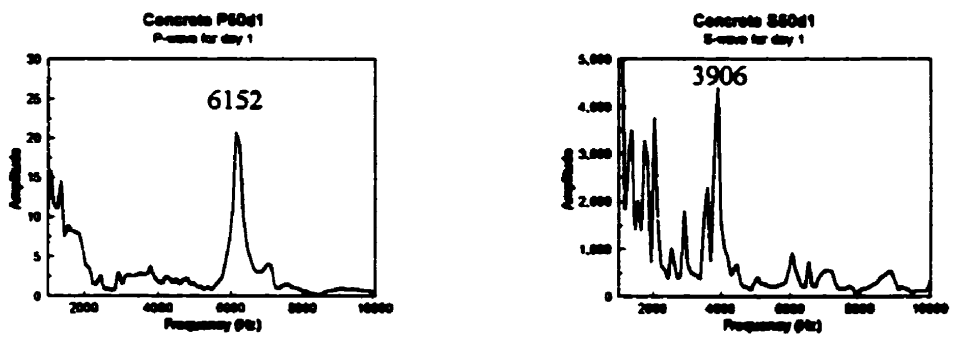

Figure C-17 The MSR computed frequency spectra for BN40 day 21 and 28 and for BN50 day1.

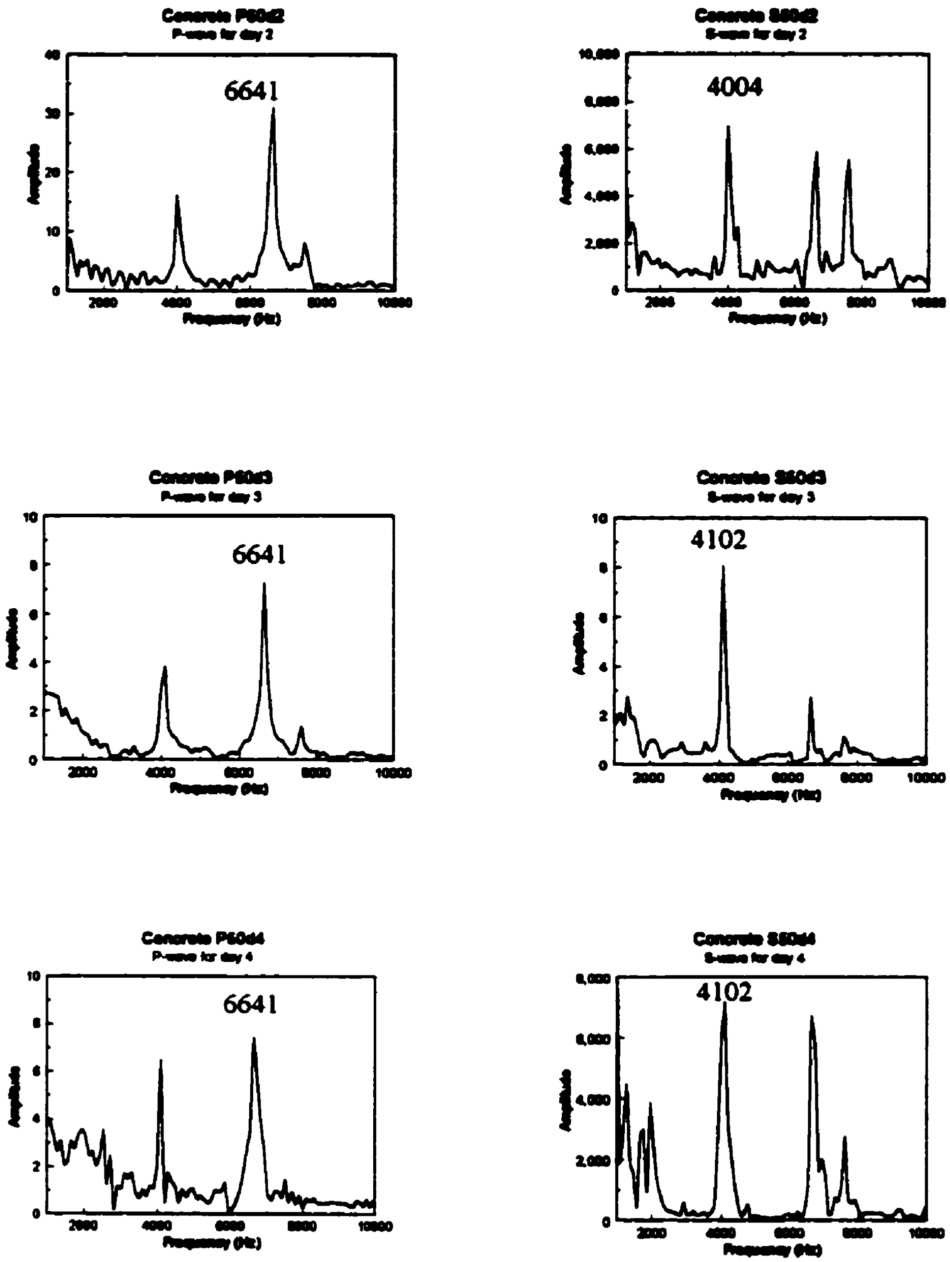

Figure C-18 The MSR computed frequency spectra for BN50, day 2 to 4.

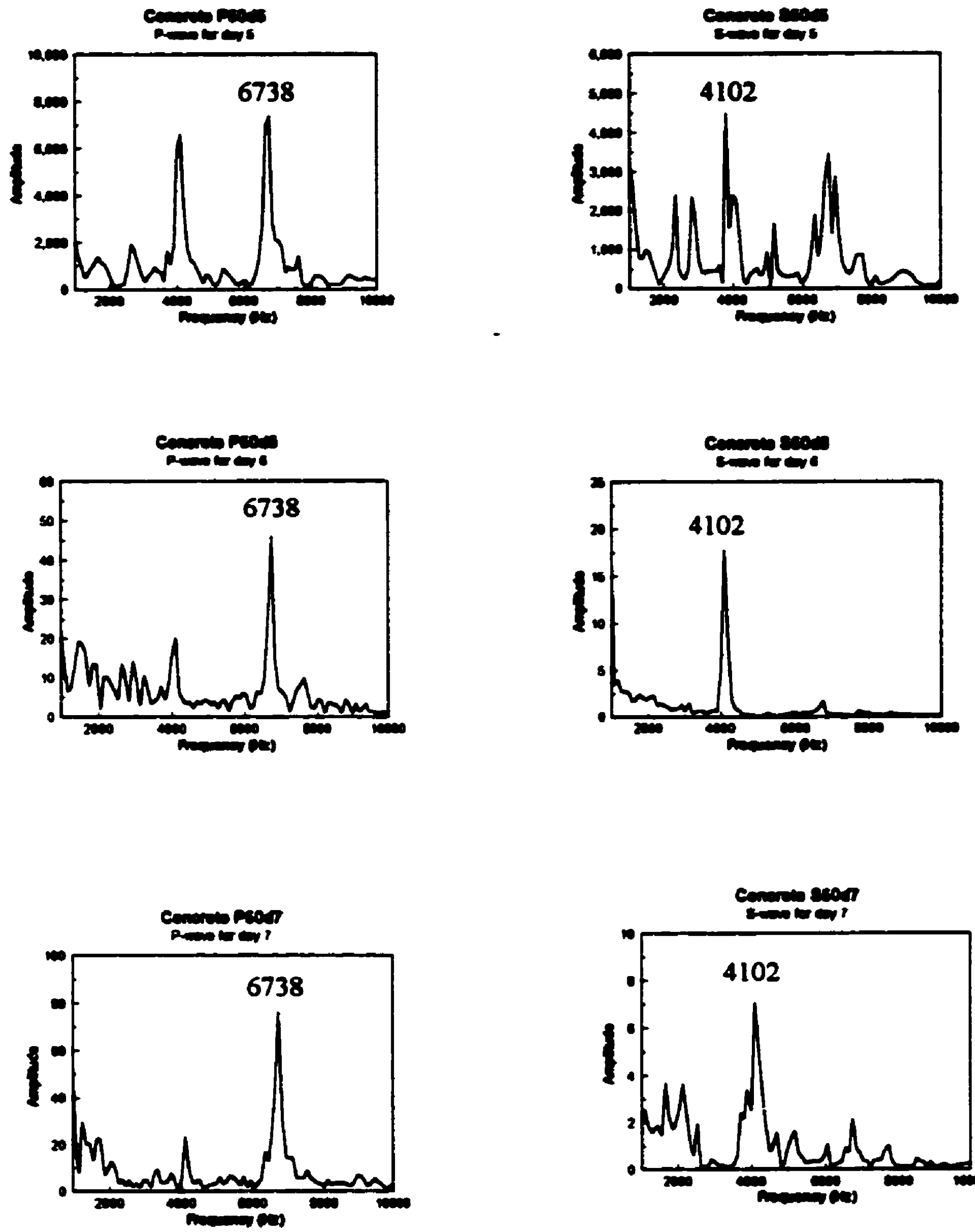

Figure C-19 The MSR computed frequency spectra for BN50, day 5 to 7.

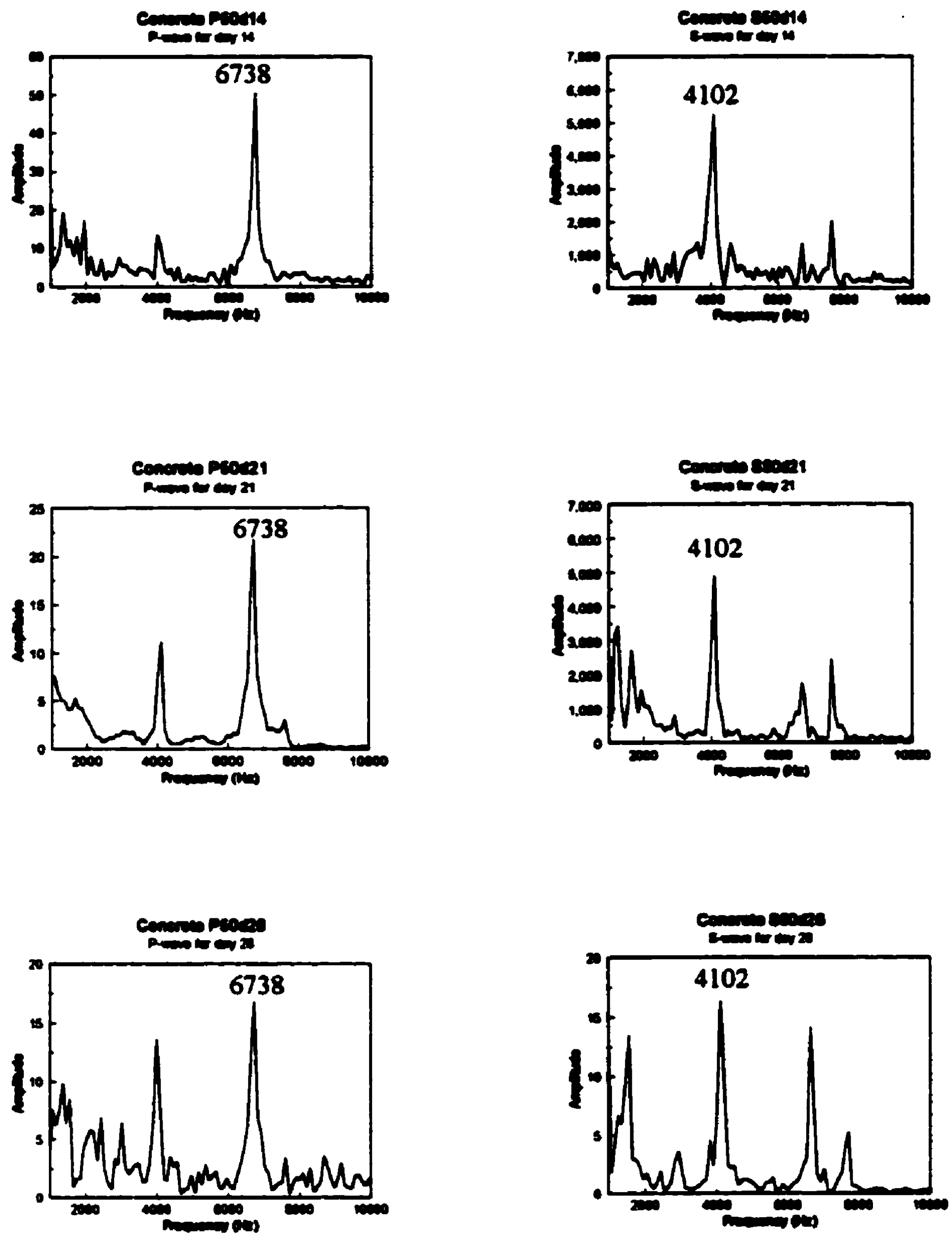

Figure C-20 The MSR computed frequency spectra for BN50, day 14 to 28.

BNA Mix for the Wall

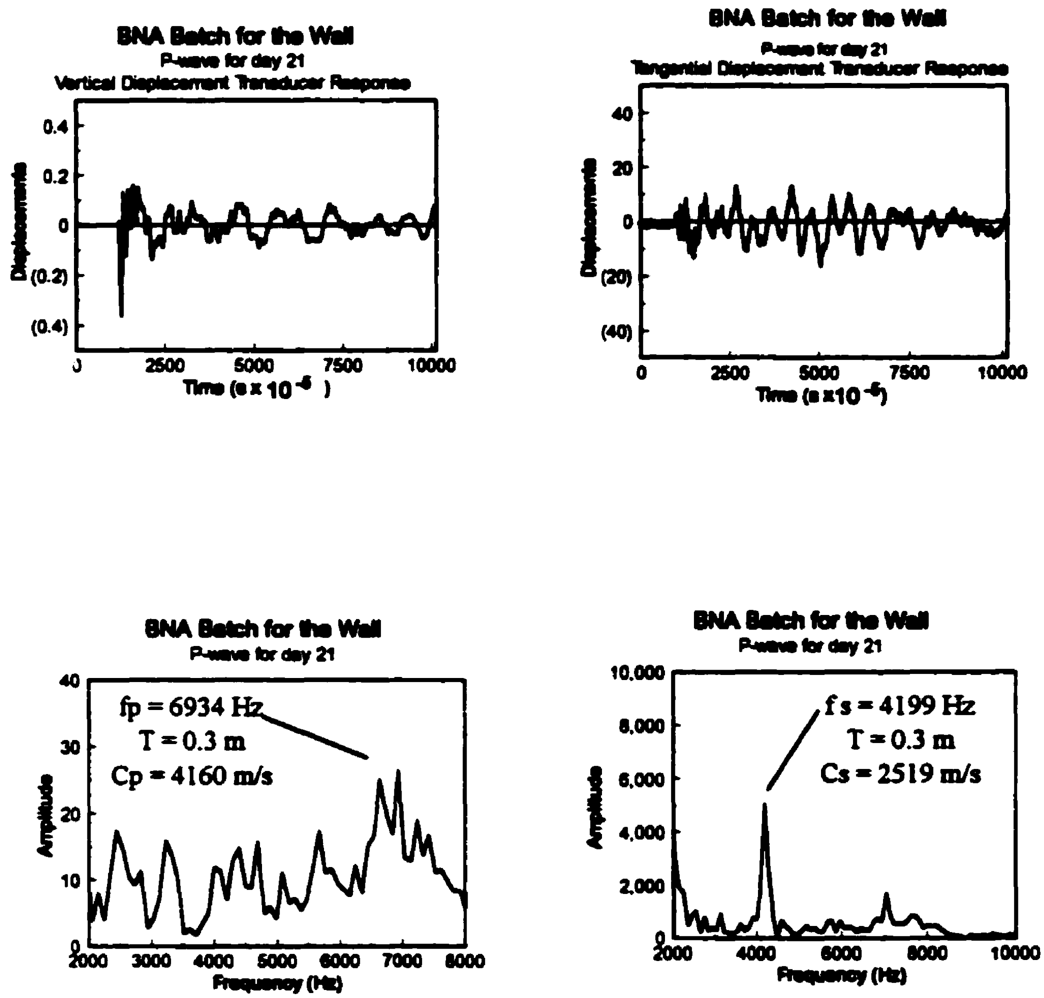

Figure C-21 The displacement waveforms and the frequency spectra for the wall with BNA mix composition, generated by the MSR.

BNB Mix for the Column

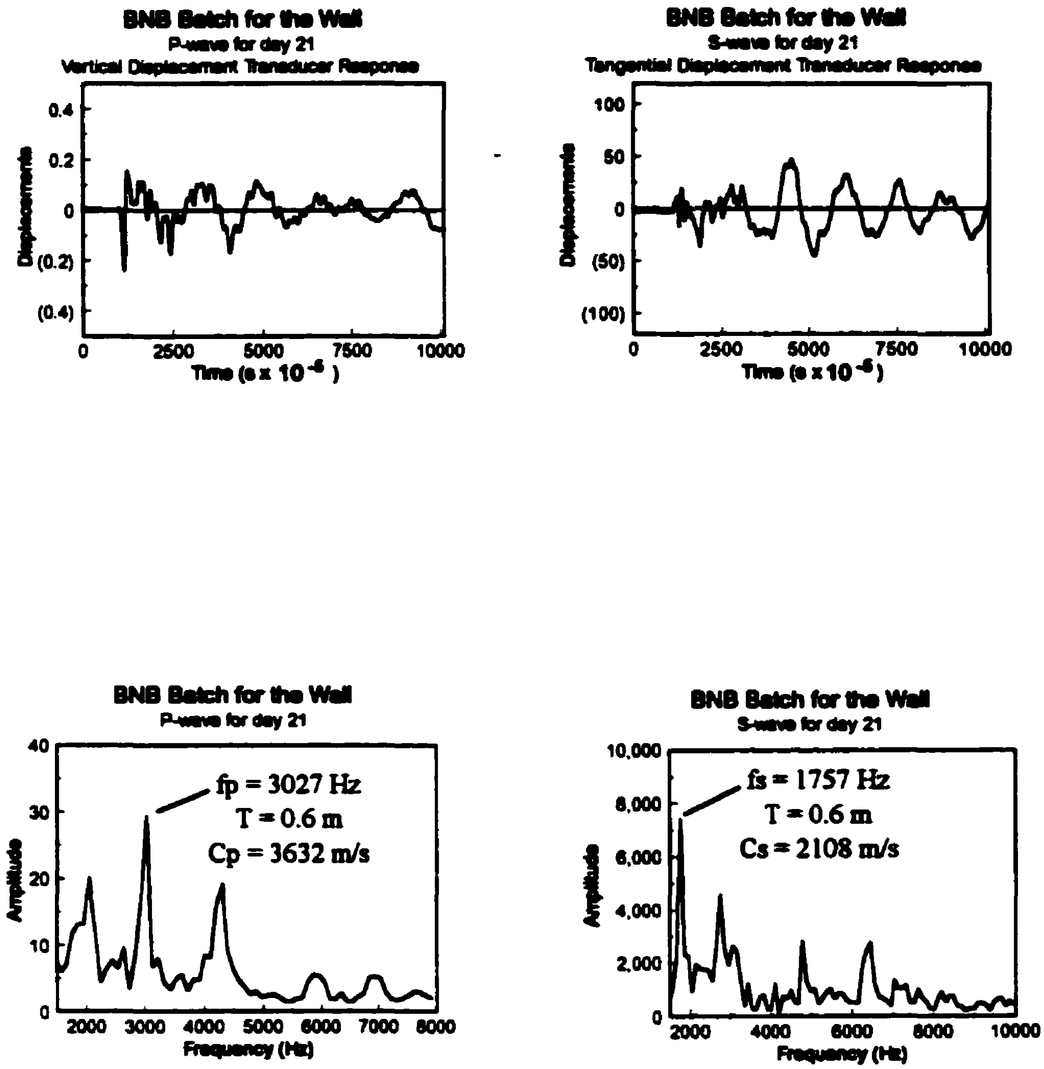

Figure C-22 The displacement waveforms and the frequency spectra for the column with BNB mix composition, generated by the MSR.

BNA Mix for the Cylinder

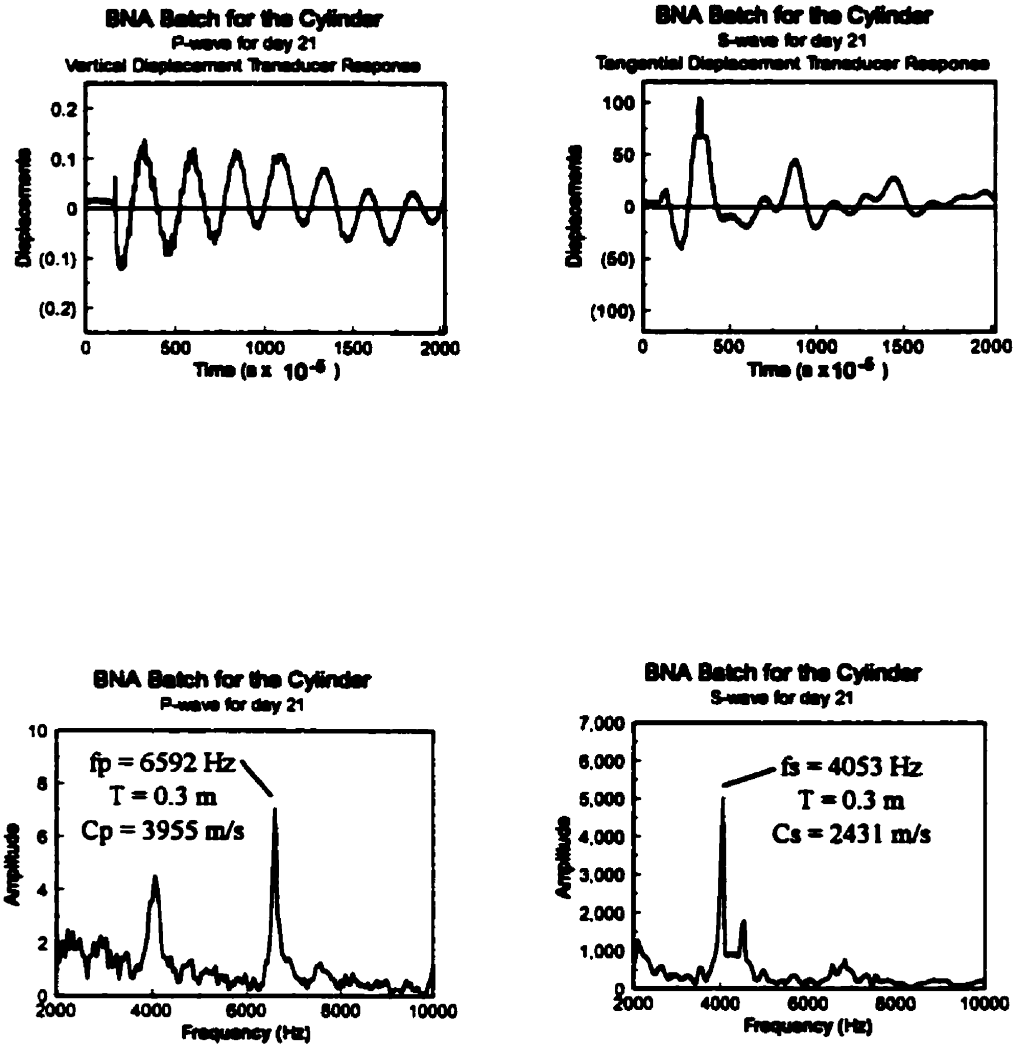

Figure C-23 The displacement waveforms and the frequency spectra for the cylinders with BNA mix composition, generated by the MSR.

BNB Mix for the Cylinder

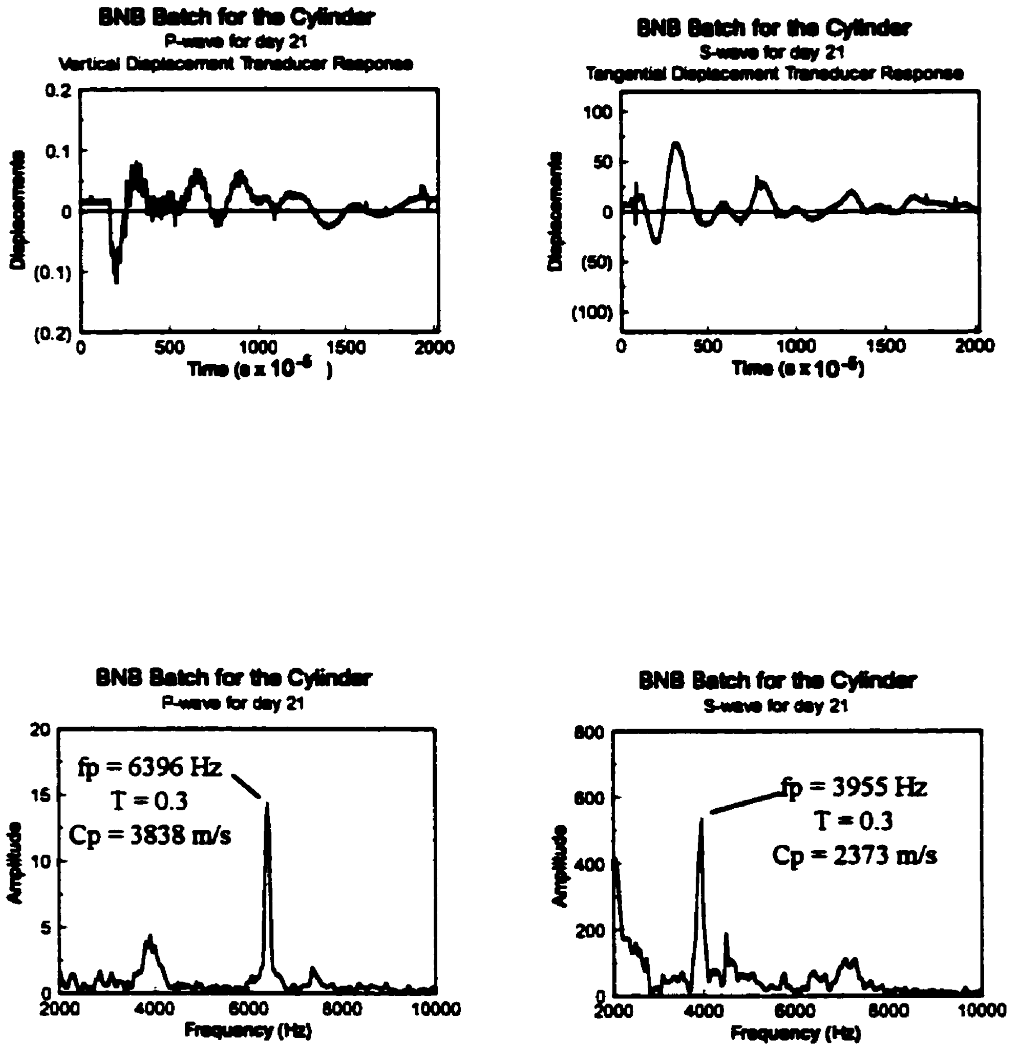

Figure C-24 The displacement waveforms and the frequency spectra for the cylinders with BNB mix composition, generated by the MSR.

Table C-1 The sample calculation of compressive strength, initial tangent modulus, chord modulus and Poisson's ratio.

Age (days)	BN20			
	Compressive Strength (MPa)	Initial Tangent (GPa)	Chord Modulus (GPa)	Poisson's ratio
1	-	-	-	0.09
2	2.3	7.6	6.2	0.14
3	3.4	10.8	6.6	0.17
4	4.5	12.7	8.3	0.12
5	5.0	13.5	8.7	0.14
6	5.0	13.6	9.4	0.14
7	5.7	17.4	10.1	0.16
14	7.9	17.4	10.7	0.16
21	9.0	17.6	10.7	0.17
28	9.0	18.5	11.3	0.17

Table C-2 The sample calculation of compressive strength, initial tangent modulus, chord modulus and Poisson's ratio.

Age (days)	BN25			
	Compressive Strength (MPa)	Initial Tangent (GPa)	Chord Modulus (GPa)	Poisson's ratio
1	2.8	9.4	4.7	0.11
2	6.8	12.6	10.7	0.09
3	7.9	20.2	12.0	0.06
4	7.9	20.3	12.0	0.11
5	10.1	21.3	13.6	0.12
6	10.8	22.1	13.7	0.16
7	11.9	22.3	14.0	0.18
14	13.6	23.9	15.2	0.20
21	14.2	23.9	15.9	0.20
28	15.3	23.9	16.2	0.20

Table C-3 The sample calculation of compressive strength, initial tangent modulus, chord modulus and Poisson's ratio.

Age (days)	BN30			
	Compressive Strength (MPa)	Initial Tangent (GPa)	Chord Modulus (GPa)	Poisson's ratio
1	5.1	10.1	8.8	0.05
2	9.6	13.8	13.2	0.12
3	10.8	15.1	15.0	0.19
4	11.9	16.6	15.2	0.13
5	13.6	17.0	15.7	0.17
6	13.6	17.4	16.0	0.17
7	15.3	17.8	16.5	0.19
14	18.1	18.8	16.6	0.20
21	19.8	19.3	16.7	0.20
28	20.4	20.0	17.0	0.22

Table C-4 The sample calculation of compressive strength, initial tangent modulus, chord modulus and Poisson's ratio.

Age (days)	BN35			
	Compressive Strength (MPa)	Initial Tangent (GPa)	Chord Modulus (GPa)	Poisson's ratio
1	10.2	15.4	14.8	0.11
2	16.4	18.0	16.9	0.24
3	20.9	18.5	17.2	0.14
4	20.9	18.9	17.9	0.17
5	23.8	20.0	18.6	0.22
6	23.8	21.0	18.8	0.22
7	24.4	21.6	19.6	0.22
14	27.7	22.6	19.9	0.22
21	28.3	23.3	20.2	0.22
28	30.6	23.7	20.6	0.22

Table C-5 The sample calculation of compressive strength, initial tangent modulus, chord modulus and Poisson's ratio.

Age (days)	BN40			
	Compressive Strength (MPa)	Initial Tangent (GPa)	Chord Modulus (GPa)	Poisson's ratio
1	17.5	22.9	20.0	0.14
2	28.3	24.0	21.6	0.12
3	32.3	24.0	22.0	0.22
4	33.9	24.7	22.4	0.17
5	35.0	25.4	23.4	0.13
6	36.2	25.8	23.7	0.17
7	36.2	27.2	23.7	0.20
14	42.4	28.6	23.9	0.22
21	43.6	28.9	26.2	0.23
28	54.3	28.9	26.9	0.24

Table C-6 The sample calculation of compressive strength, initial tangent modulus, chord modulus and Poisson's ratio.

Age (days)	BN50			
	Compressive Strength (MPa)	Initial Tangent (GPa)	Chord Modulus (GPa)	Poisson's ratio
1	34.5	20.6	21.0	0.24
2	39.0	26.0	24.5	0.22
3	45.3	28.1	25.0	0.22
4	45.8	28.9	26.5	0.23
5	45.8	29.5	26.7	0.23
6	48.7	30.7	26.9	0.23
7	50.4	32.0	27.1	0.23
14	54.3	32.3	27.2	0.23
21	57.2	33.3	27.5	0.23
28	58.9	34.2	28.3	0.23

Table C-7 The sample calculation of elastic constants obtained by the MSR system.

Age (days)	BN20			
	Young's modulus (GPa)	Shear modulus (GPa)	Bulk modulus (GPa)	Poisson's ratio
1	4.0	1.7	2.1	0.18
2	10.5	4.4	5.8	0.19
3	12.3	5.1	6.6	0.19
4	13.6	5.6	7.6	0.21
5	14.4	6.0	8.0	0.20
6	15.0	6.4	8.1	0.17
7	15.6	6.6	8.2	0.18
14	16.3	6.9	8.5	0.18
21	16.3	6.9	8.5	0.18
28	16.3	6.9	8.5	0.18

Table C-8 The sample calculation of elastic constants obtained by the MSR system.

Age (days)	BN25			
	Young's modulus (GPa)	Shear modulus (GPa)	Bulk modulus (GPa)	Poisson's ratio
1	8.7	3.5	5.6	0.24
2	13.5	5.3	9.6	0.26
3	17.7	7.6	8.8	0.17
4	18.6	8.0	9.0	0.15
5	19.0	8.0	9.75	0.18
6	19.3	8.0	10.6	0.20
7	19.3	8.0	10.6	0.20
14	19.6	8.0	11.4	0.21
21	19.6	8.0	11.4	0.21
28	19.6	8.0	11.4	0.21

Table C-9 The sample calculation of elastic constants obtained by the MSR system.

Age (days)	BN30			
	Young's modulus (GPa)	Shear modulus (GPa)	Bulk modulus (GPa)	Poisson's ratio
1	13.3	5.8	4.0	0.20
2	17.2	7.2	9.6	0.20
3	19.5	8.2	10.7	0.18
4	20.5	8.7	10.8	0.20
5	20.9	8.7	11.7	0.20
6	21.1	8.7	12.5	0.22
7	21.1	8.7	12.5	0.22
14	21.4	8.7	13.4	0.23
21	21.4	8.7	13.4	0.23
28	21.4	8.7	13.4	0.23

Table C-10 The sample calculation of elastic constants obtained by the MSR system.

Age (days)	BN35			
	Young's modulus (GPa)	Shear modulus (GPa)	Bulk modulus (GPa)	Poisson's ratio
1	18.1	7.4	10.8	0.22
2	22.2	9.0	13.9	0.23
3	25.5	10.7	13.5	0.19
4	25.8	10.7	14.5	0.20
5	27.0	11.3	14.7	0.19
6	27.0	11.3	14.7	0.19
7	27.4	11.3	15.7	0.21
14	27.4	11.3	15.7	0.21
21	27.4	11.3	15.7	0.21
28	27.4	11.3	15.7	0.21

Table C-11 The sample calculation of elastic constants obtained by the MSR system.

Age (days)	BN40			
	Young's modulus (GPa)	Shear modulus (GPa)	Bulk modulus (GPa)	Poisson's ratio
1	21.2	8.9	11.9	0.20
2	25.9	10.5	16.1	0.23
3	28.4	11.7	16.6	0.21
4	29.3	12.3	15.7	0.19
5	29.7	12.3	16.8	0.20
6	29.7	12.3	16.8	0.20
7	29.7	12.3	16.8	0.20
14	30.0	12.3	17.8	0.22
21	30.0	12.3	17.8	0.22
28	30.0	12.3	17.8	0.22

Table C-12 The sample calculation of elastic constants obtained by the MSR system.

Age (days)	BN50			
	Young's modulus (GPa)	Shear modulus (GPa)	Bulk modulus (GPa)	Poisson's ratio
1	31.5	13.6	15.6	0.16
2	34.6	14.3	20.2	0.21
3	35.7	15.0	19.3	0.19
4	35.7	15.0	19.3	0.19
5	36.0	15.0	20.4	0.21
6	36.0	15.0	20.4	0.21
7	36.0	15.0	20.4	0.21
14	36.0	15.0	20.4	0.21
21	36.0	15.0	20.4	0.21
28	36.0	15.0	20.4	0.21

Table C-13 The sample calculation of elastic constants obtained by the RF technique.

Age (days)	BN20			
	Young's modulus (GPa)	Shear modulus (GPa)	Bulk modulus (GPa)	Poisson's ratio
1	3.5	1.6	1.4	0.07
2	9.5	4.2	4.3	0.13
3	11.1	5.0	4.5	0.09
4	11.6	5.4	4.6	0.10
5	11.7	5.4	4.8	0.10
6	12.8	5.4	4.8	0.08
7	11.8	5.4	4.8	0.09
14	11.8	5.4	4.9	0.09
21	11.9	5.5	4.9	0.09
28	12.0	5.5	4.9	0.09

Table C-14 The sample calculation of elastic constants obtained by the RF technique.

Age (days)	BN25			
	Young's modulus (GPa)	Shear modulus (GPa)	Bulk modulus (GPa)	Poisson's ratio
1	7.8	3.2	4.8	0.23
2	16.4	7.8	9.7	0.22
3	19.1	8.3	9.6	0.17
4	20.0	8.4	10.8	0.19
5	20.5	8.4	12.2	0.22
6	20.6	8.5	12.7	0.23
7	21.5	8.6	13.0	0.23
14	21.5	8.6	14.3	0.25
21	21.5	8.7	14.3	0.25
28	21.5	8.9	14.3	0.25

Table C-15 The sample calculation of elastic constants obtained by the RF technique.

Age (days)	BN30			
	Young's modulus (GPa)	Shear modulus (GPa)	Bulk modulus (GPa)	Poisson's ratio
1	7.17	1.6	1.4	0.14
2	16.8	4.2	4.3	0.16
3	19.6	5.0	4.5	0.20
4	20.1	5.4	4.6	0.21
5	20.7	5.4	4.8	0.21
6	21.1	5.4	4.8	0.24
7	21.4	5.4	4.8	0.23
14	21.8	5.4	4.9	0.23
21	22.0	5.5	4.9	0.23
28	22.0	5.5	4.9	0.23

Table C-16 The sample calculation of elastic constants obtained by the RF technique.

Age (days)	BN35			
	Young's modulus (GPa)	Shear modulus (GPa)	Bulk modulus (GPa)	Poisson's ratio
1	12.2	4.8	8.1	0.25
2	23.7	9.6	15.2	0.24
3	26.2	10.9	14.6	0.20
4	26.8	11.0	16.0	0.22
5	27.3	11.0	17.5	0.24
6	27.8	11.1	18.5	0.25
7	28.0	11.2	18.7	0.25
14	28.2	11.5	18.8	0.25
21	28.4	11.5	18.9	0.25
28	28.6	11.5	19.0	0.25

Table C-17 The sample calculation of elastic constants obtained by the RF technique.

Age (days)	BN40			
	Young's modulus (GPa)	Shear modulus (GPa)	Bulk modulus (GPa)	Poisson's ratio
1	23.6	9.9	13.1	0.20
2	29.2	11.8	17.4	0.22
3	29.7	12.5	16.0	0.19
4	29.9	12.8	15.0	0.17
5	30.4	12.8	15.1	0.19
6	30.6	13.0	15.5	0.18
7	30.7	13.1	15.5	0.17
14	30.7	13.1	15.9	0.17
21	31.3	13.1	16.3	0.18
28	31.3	13.3	16.8	0.19

Table C-18 The sample calculation of elastic constants obtained by the RF technique.

Age (days)	BN50			
	Young's modulus (GPa)	Shear modulus (GPa)	Bulk modulus (GPa)	Poisson's ratio
1	36.5	13.6	15.6	0.24
2	39.0	14.3	20.2	0.30
3	39.4	15.0	19.3	0.27
4	39.6	15.0	19.3	0.28
5	40.1	15.0	20.4	0.23
6	40.1	15.0	20.4	0.24
7	40.2	15.0	20.4	0.24
14	40.4	15.0	20.4	0.24
21	40.4	15.0	20.4	0.26
28	40.7	15.0	20.4	0.26

Table C-19 The sample calculation of elastic wave velocities obtained by the MSR and UPV systems.

Age (days)	BN20			BN25		
	C_p(m/s) MSR	C_s(m/s) MSR	C_p(m/s) UPV	C_p(m/s) MSR	C_s(m/s) MSR	C_p(m/s) UPV
1	1406	1406	2970	2110	1231	2704
2	2285	1523	3061	2695	1523	3110
3	2461	1582	3409	2871	1816	3433
4	2637	1638	3448	2930	1875	3502
5	2695	1699	3530	2988	1875	3515
6	2695	1699	3580	3047	1875	3525
7	2754	1758	3614	3047	1875	2610
14	2823	1758	3659	3106	1875	3658
21	2813	1758	3703	3106	1875	3658
28	2813	1758	3750	3106	1875	3658

Table C-20 The sample calculation of elastic wave velocities obtained by the MSR and UPV systems.

Age (days)	BN30			BN35		
	C_p(m/s) MSR	C_s(m/s) MSR	C_p(m/s) UPV	C_p(m/s) MSR	C_s(m/s) MSR	C_p(m/s) UPV
1	2461	1582	2970	2461	1758	3320
2	2871	1758	3358	2930	1934	3602
3	3047	1875	3580	3281	2110	3798
4	3106	1934	3623	3398	2168	3855
5	3164	1934	3736	3457	2168	3990
6	3223	1934	3736	3515	2168	3990
7	3223	1934	3805	3515	2168	4000
14	3281	1934	3805	3574	2168	4000
21	3281	1934	3805	3574	2168	4000
28	3281	1934	3805	3574	2168	4000

Table C-21 The sample calculation of elastic wave velocities obtained by the MSR and UPV systems.

Age (days)	BN40			BN50		
	C_p(m/s) MSR	C_s(m/s) MSR	C_p(m/s) UPV	C_p(m/s) MSR	C_s(m/s) MSR	C_p(m/s) UPV
1	3164	1934	3530	3691	2344	3954
2	3574	2109	3975	3985	2402	4125
3	3691	2226	4005	3985	2461	4250
4	3691	2285	4110	3985	2461	4250
5	3750	2285	4110	4043	2461	4432
6	3750	2285	4110	4043	2461	4432
7	3750	2285	4160	4043	2461	4432
14	3809	2285	4160	4043	2461	4432
21	3809	2285	4160	4043	2461	4432
28	3809	2285	4160	4043	2461	4432

Table C-22 The sample calculation of elastic wave velocities obtained by the MSR and UPV systems.

Age (days)	BNA			BNB		
	C_p(m/s) MSR	C_s(m/s) MSR	C_p(m/s) UPV	C_p(m/s) MSR	C_s(m/s) MSR	C_p(m/s) UPV
1	3691	2285	3745	3603	2285	3712
2	3779	2353	3945	3691	2314	3907
3	3837	2353	3960	3721	2314	3920
4	3837	2353	3973	3750	2314	3920
5	3837	2363	3987	3779	2314	3960
6	3867	2383	3996	3779	2314	3971
7	3867	2383	4016	3809	2344	3987
10	3896	2402	4141	3837	2373	4042
12	3896	2411	4141	3837	2383	4089
16	3925	2432	4202	3837	2373	4115
21	3955	2432	4228	3867	2373	4125
28	3955	2432	4228	3896	2490	4125

Table C-23 The sample calculation of elastic constants obtained by the MSR system.

Age (days)	BNA			
	Young's Modulus (GPa)	Shear Modulus (GPa)	Bulk Modulus (GPa)	Poisson's ratio
1	28.0	11.8	15.0	0.19
2	29.6	12.5	15.6	0.18
3	30.0	12.5	16.6	0.20
4	30.0	12.5	16.6	0.20
5	30.1	12.6	16.7	0.19
6	30.6	12.8	16.7	0.19
7	30.6	12.8	16.9	0.19
10	31.1	13.0	17.0	0.20
12	31.2	13.1	17.0	0.20
16	31.7	13.4	17.5	0.20
21	32.0	13.4	17.5	0.20
28	32.0	13.4	17.5	0.20

Table C-24 The sample calculation of elastic constants obtained by the MSR system.

Age (days)	BNB			
	Young's Modulus (GPa)	Shear Modulus (GPa)	Bulk Modulus (GPa)	Poisson's ratio
1	26.4	11.4	13.6	0.16
2	27.4	11.7	14.7	0.18
3	27.6	11.7	15.1	0.18
4	27.8	11.7	15.7	0.19
5	27.9	11.7	16.1	0.20
6	27.9	11.7	16.2	0.20
7	28.6	12.0	16.2	0.20
10	29.1	12.3	16.3	0.20
12	29.1	12.3	16.3	0.20
16	29.3	12.3	16.8	0.20
21	29.4	12.3	16.8	0.21
28	29.5	12.3	17.3	0.21

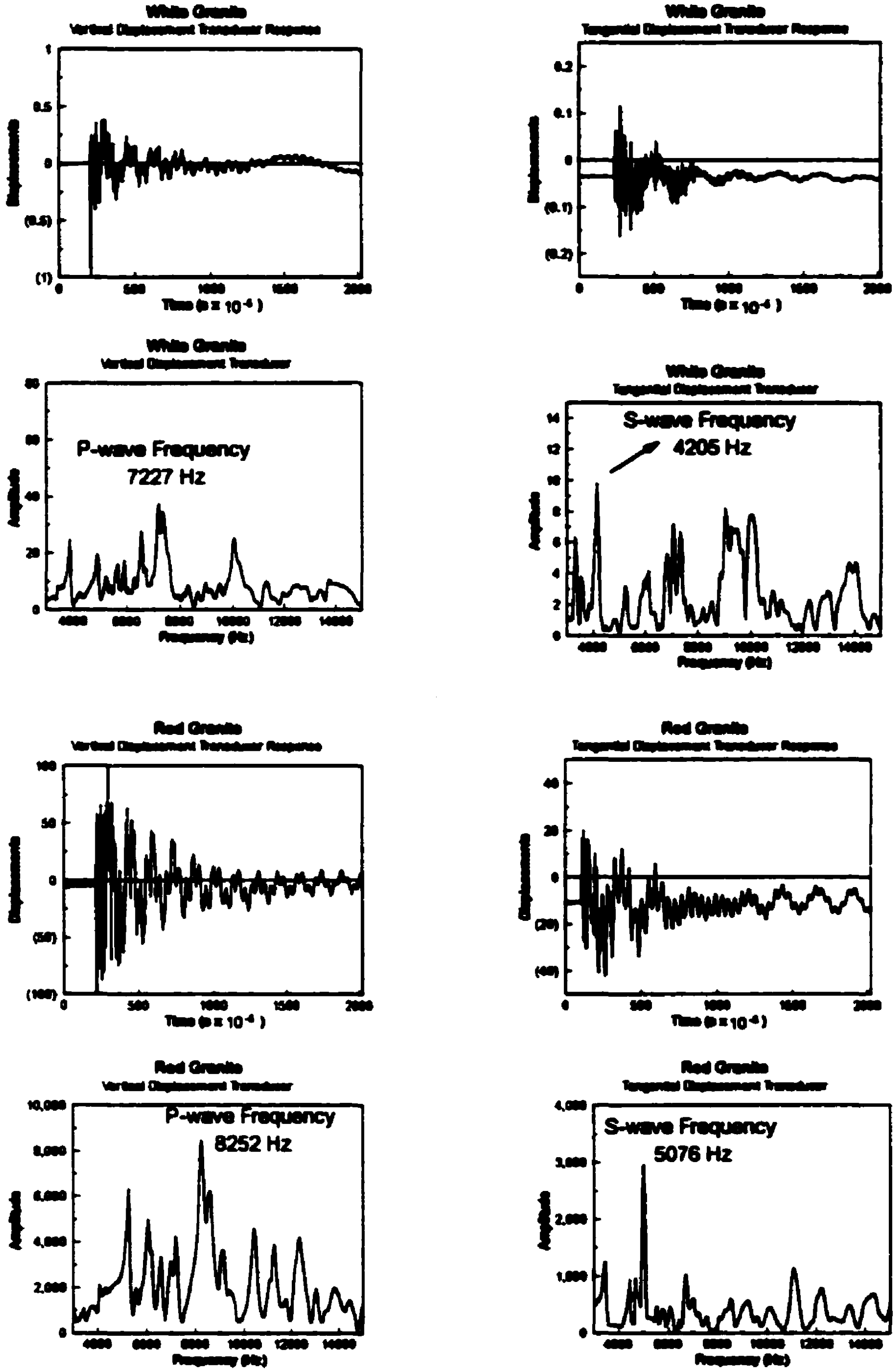

Figure D-1 **Samples of collected waveforms and the corresponding frequency spectra for the vertical and tangential displacement transducers on white and red granite blocks.**

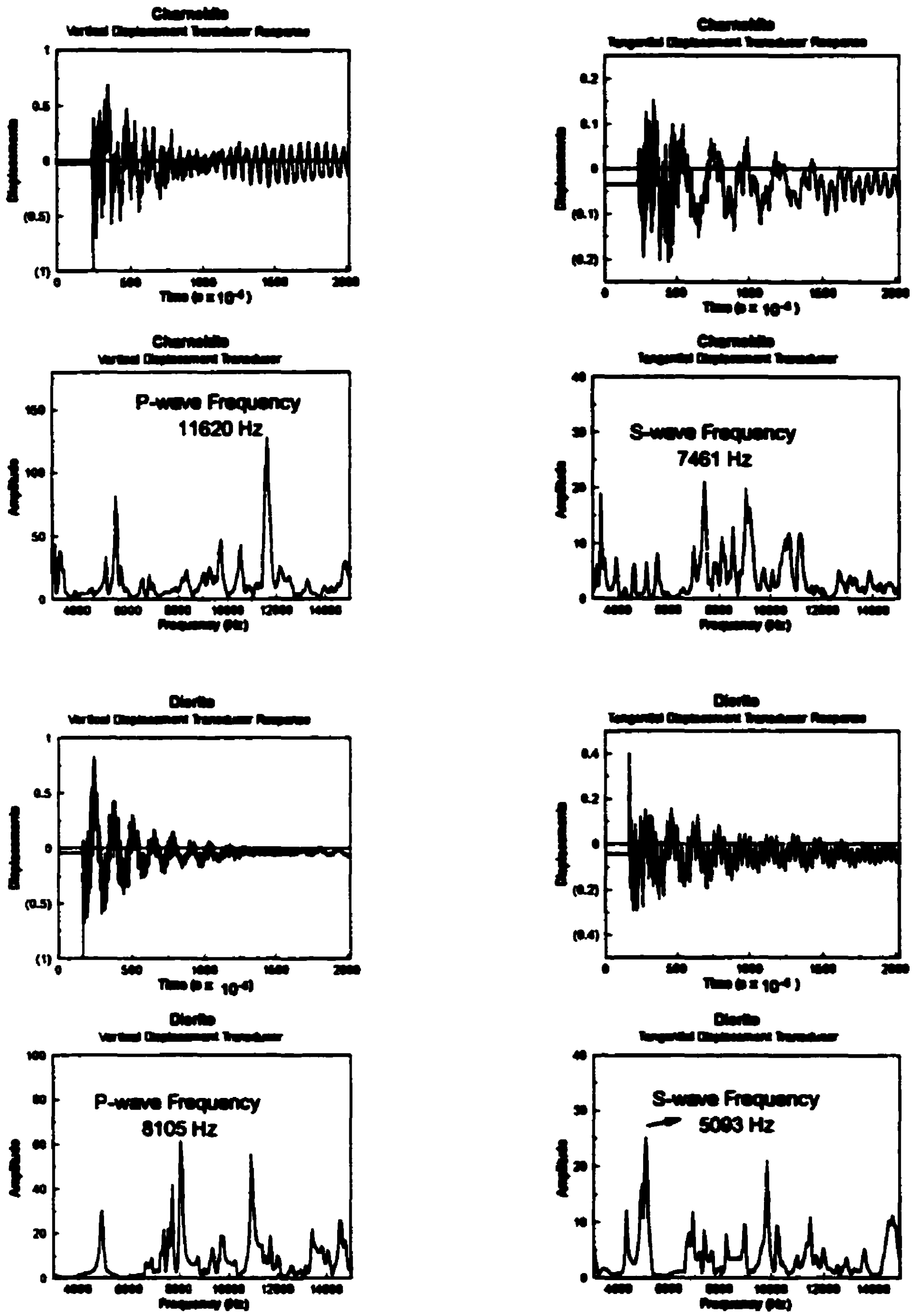

Figure D-3 Samples of collected waveforms and the corresponding frequency spectra for the vertical and tangential displacement transducers on charnokite and diorite blocks.

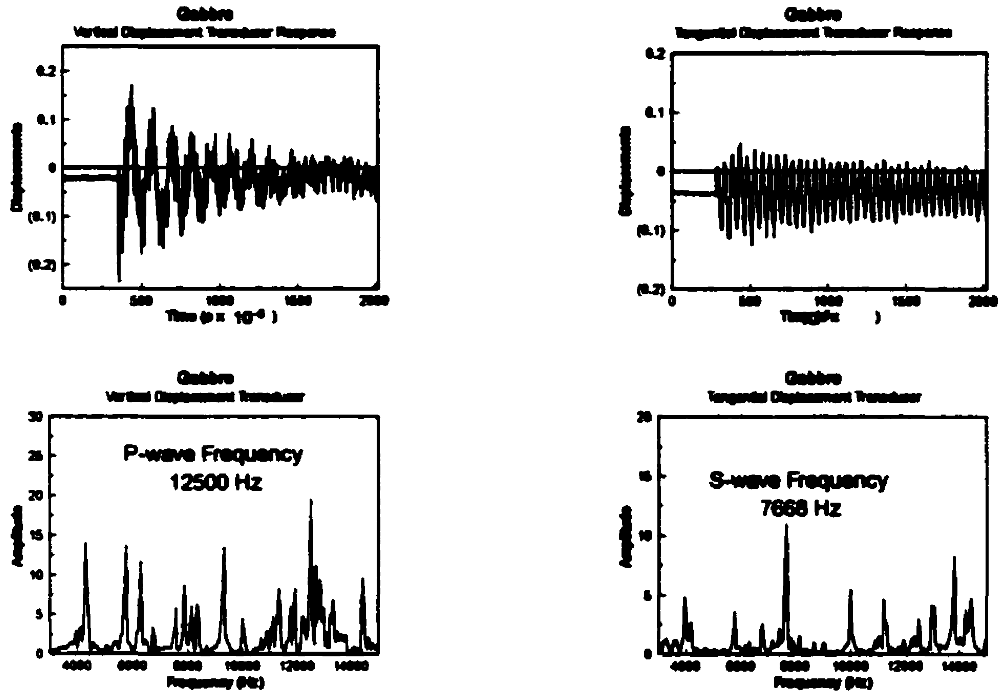

Figure D-3 Samples of collected waveforms and the corresponding frequency spectra for the vertical and tangential displacement transducers on gabbro block.

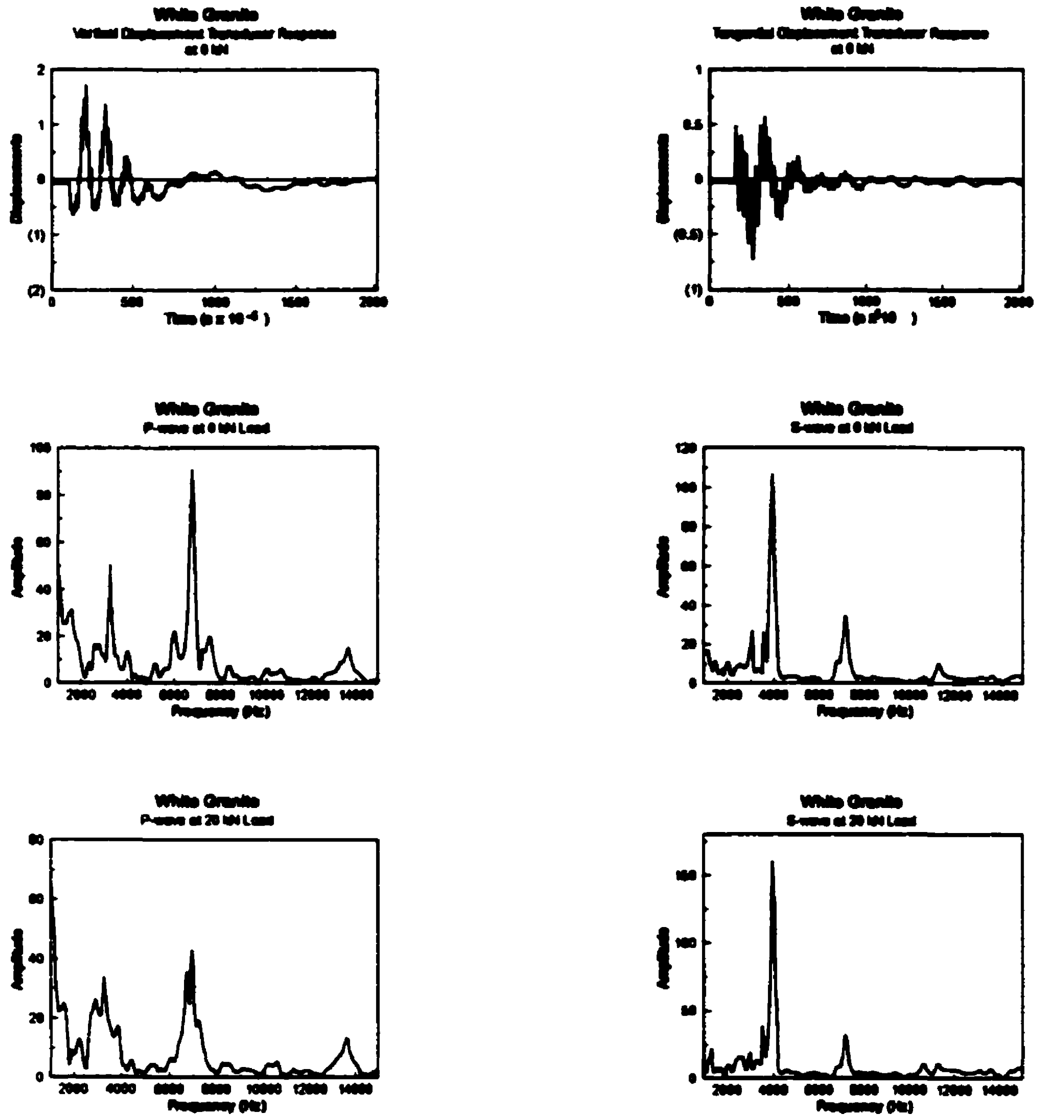

Figure D-4 The samples of waveforms collected by the vertical and tangential displacement transducers and the corresponding frequency spectra for the load/unloading cycles of white granite.

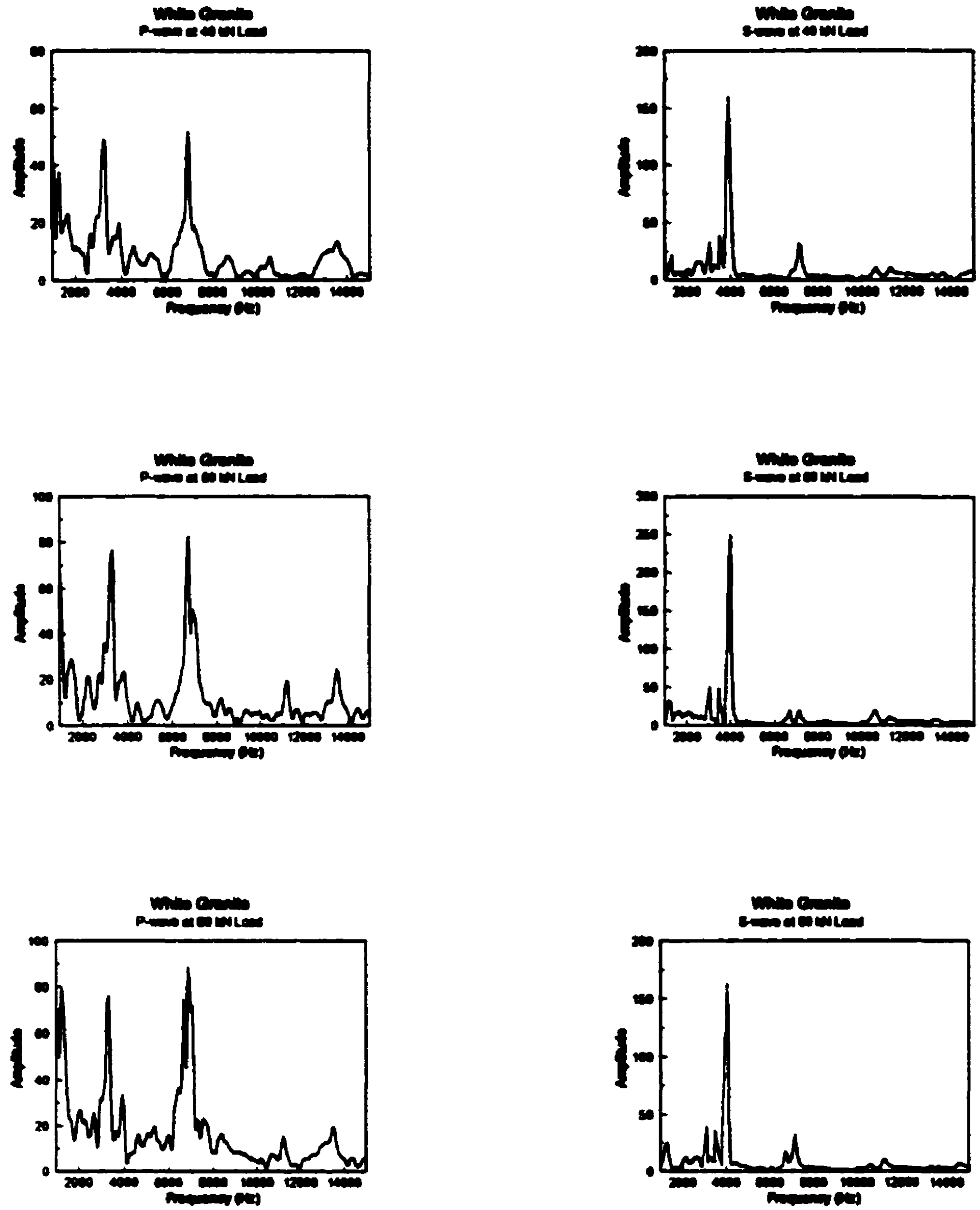

Figure D-5 The samples of the corresponding frequency spectra for the loading and unloading cycles collected by the vertical and tangential displacement transducers for the white granite.

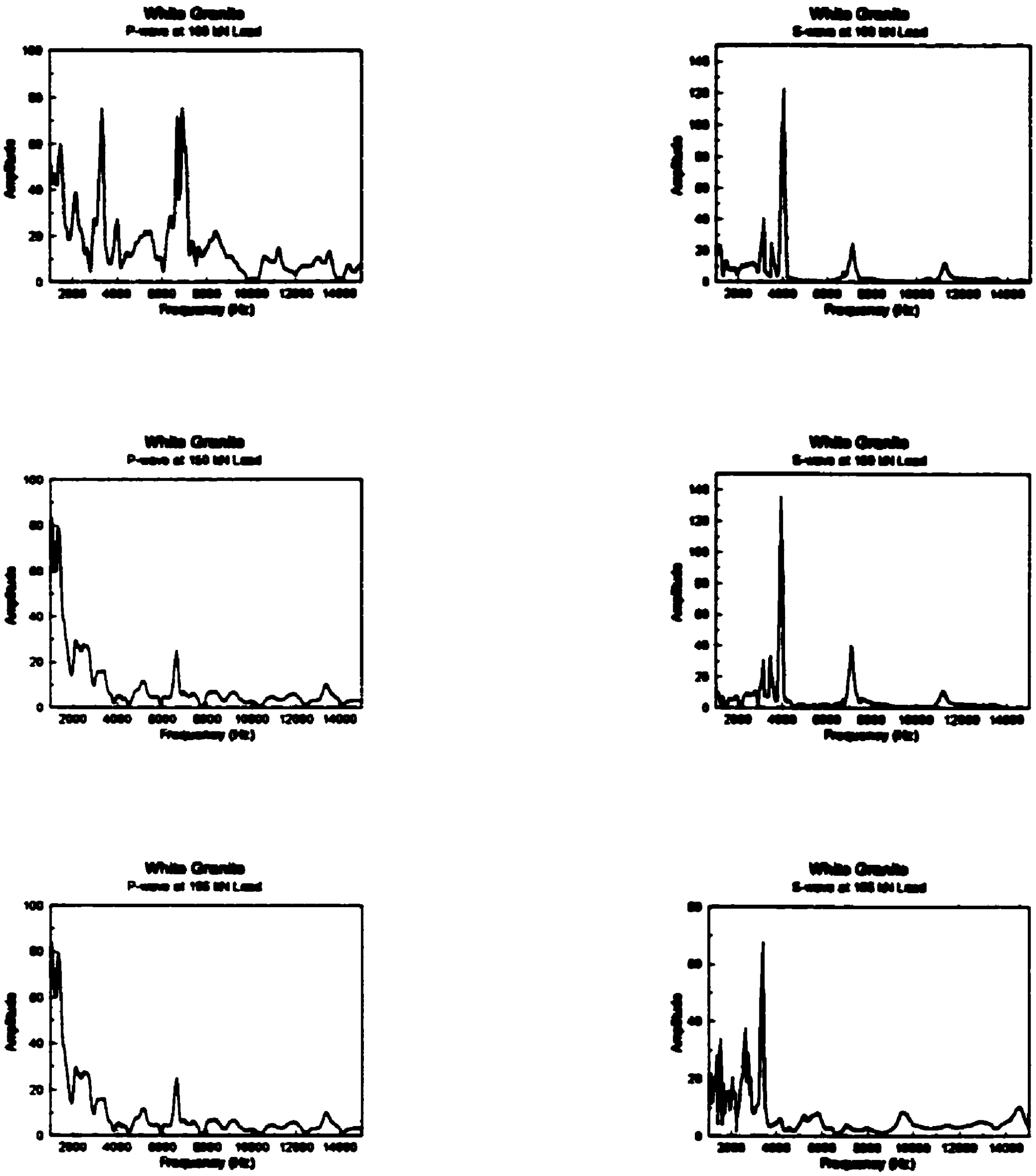

Figure D-6 The samples of the corresponding frequency spectra for the loading and unloading cycles collected by the vertical and tangential displacement transducers for the white granite.

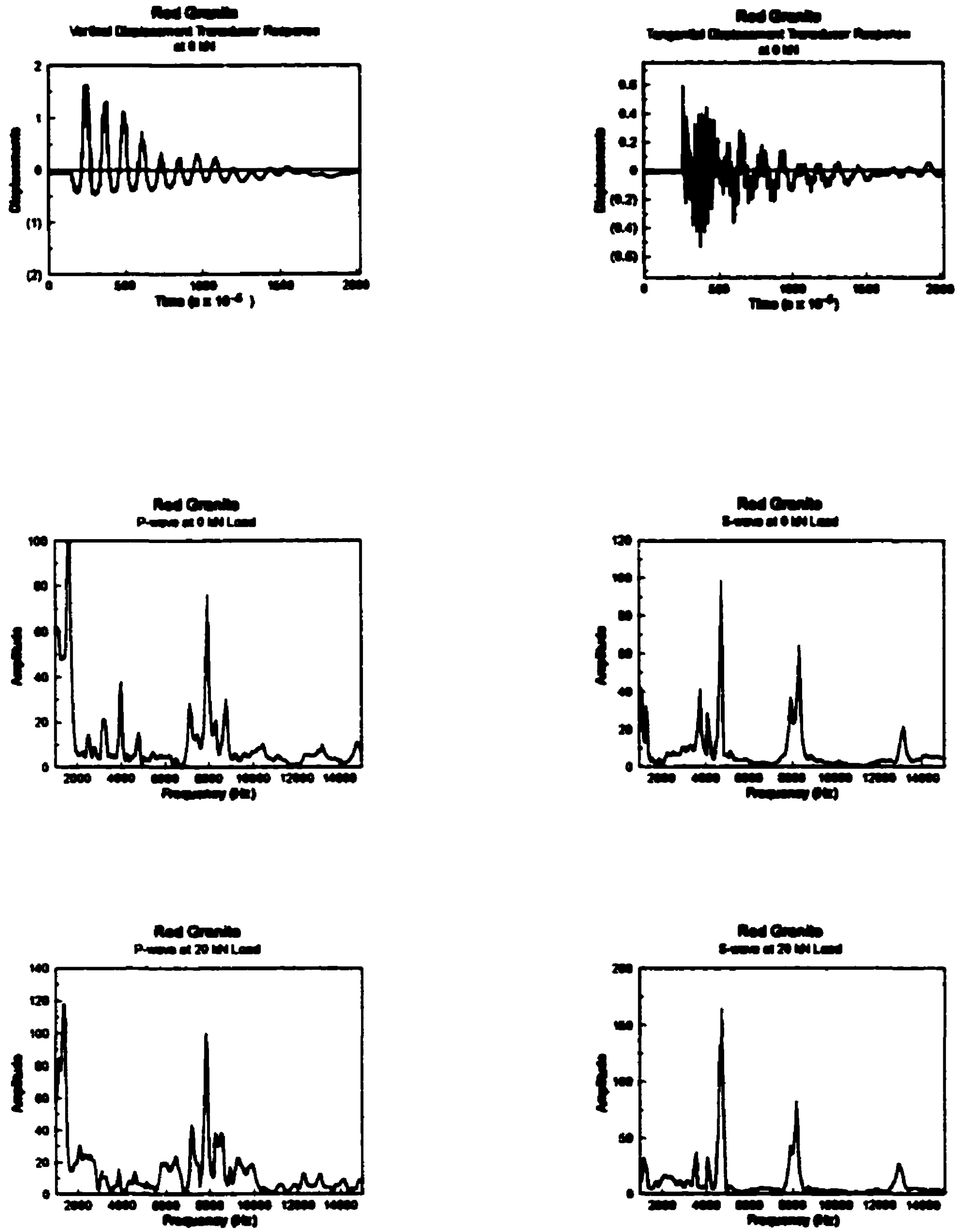

Figure D-7 The samples of waveforms collected by the vertical and tangential displacement transducers and the corresponding frequency spectra for the load/unloading cycles of red granite.

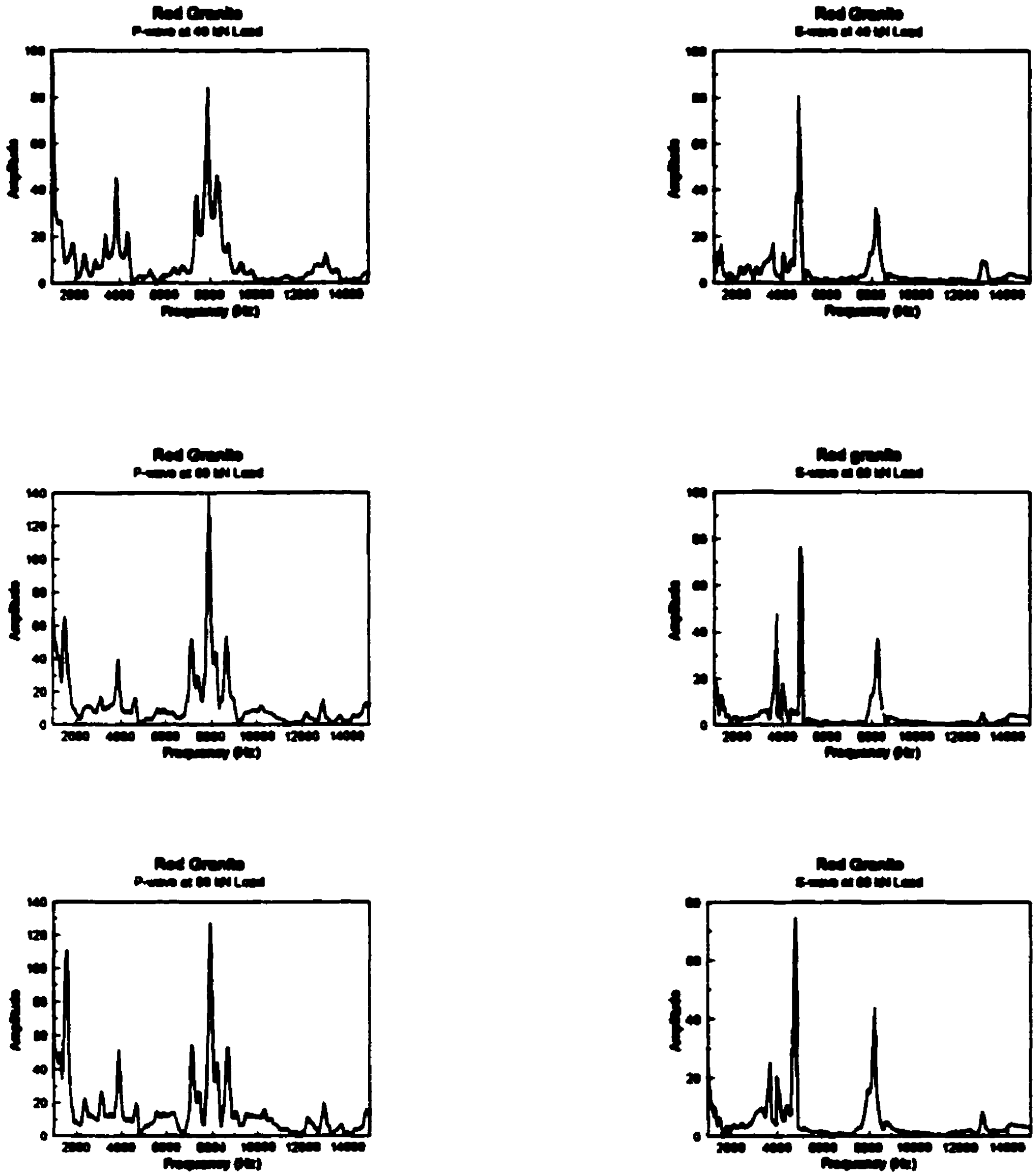

Figure D-8 The samples of the corresponding frequency spectra for the loading and unloading cycles collected by the vertical and tangential displacement transducers for the red granite.

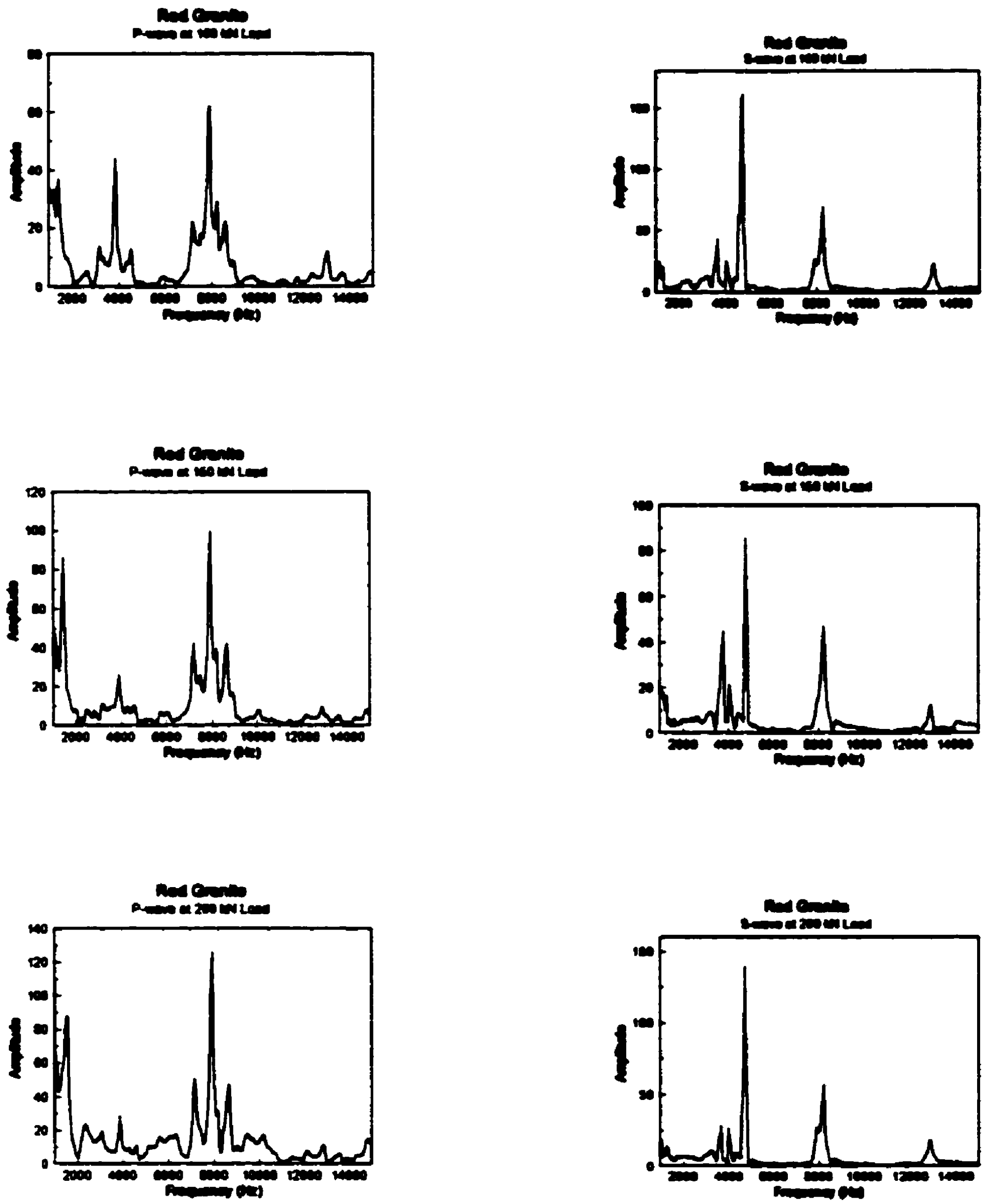

Figure D-9 The samples of the corresponding frequency spectra for the loading and unloading cycles collected by the vertical and tangential displacement transducers for the red granite.

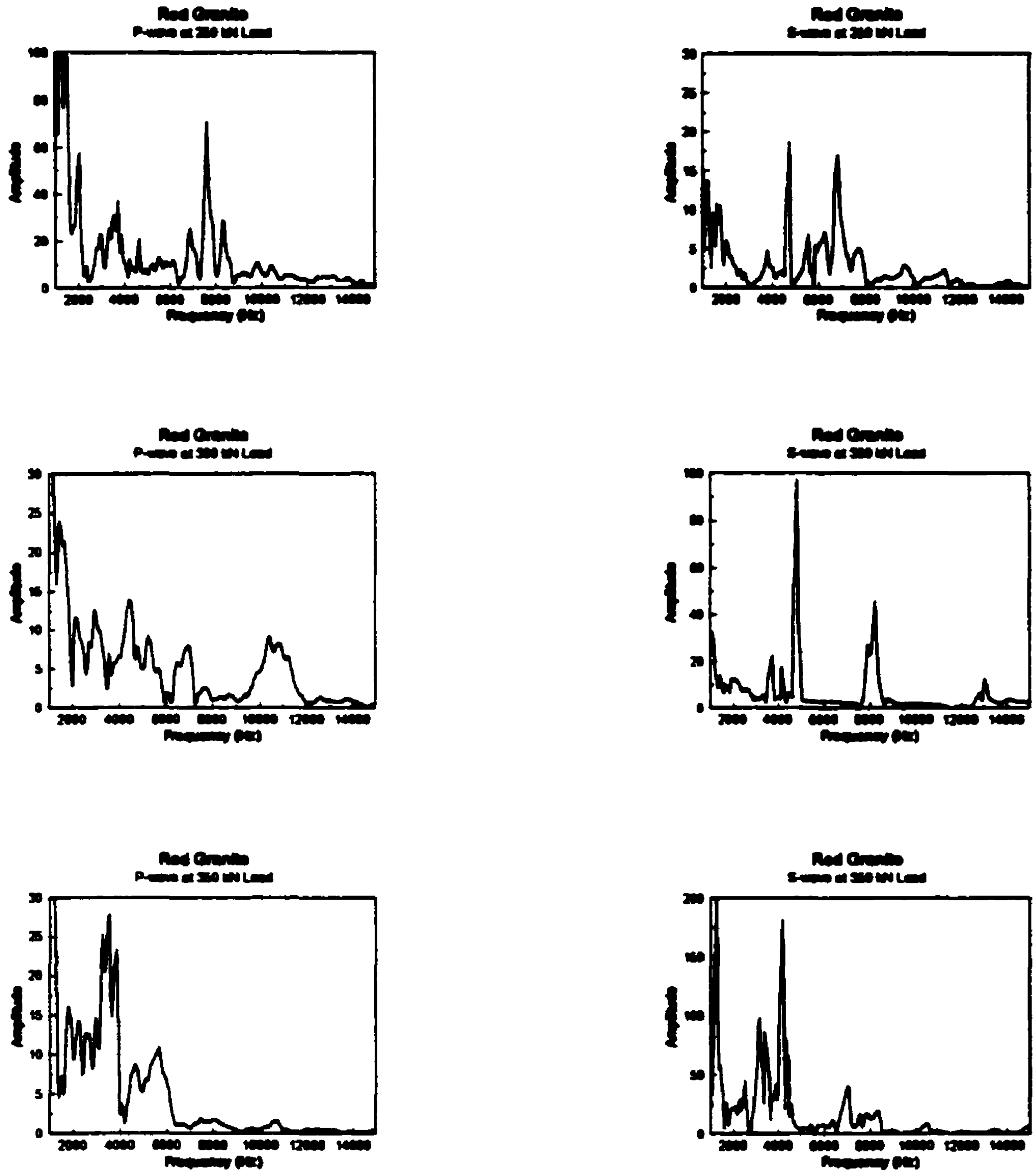

Figure D-10 The samples of the corresponding frequency spectra for the loading and unloading cycles collected by the vertical and tangential displacement transducers for the red granite.

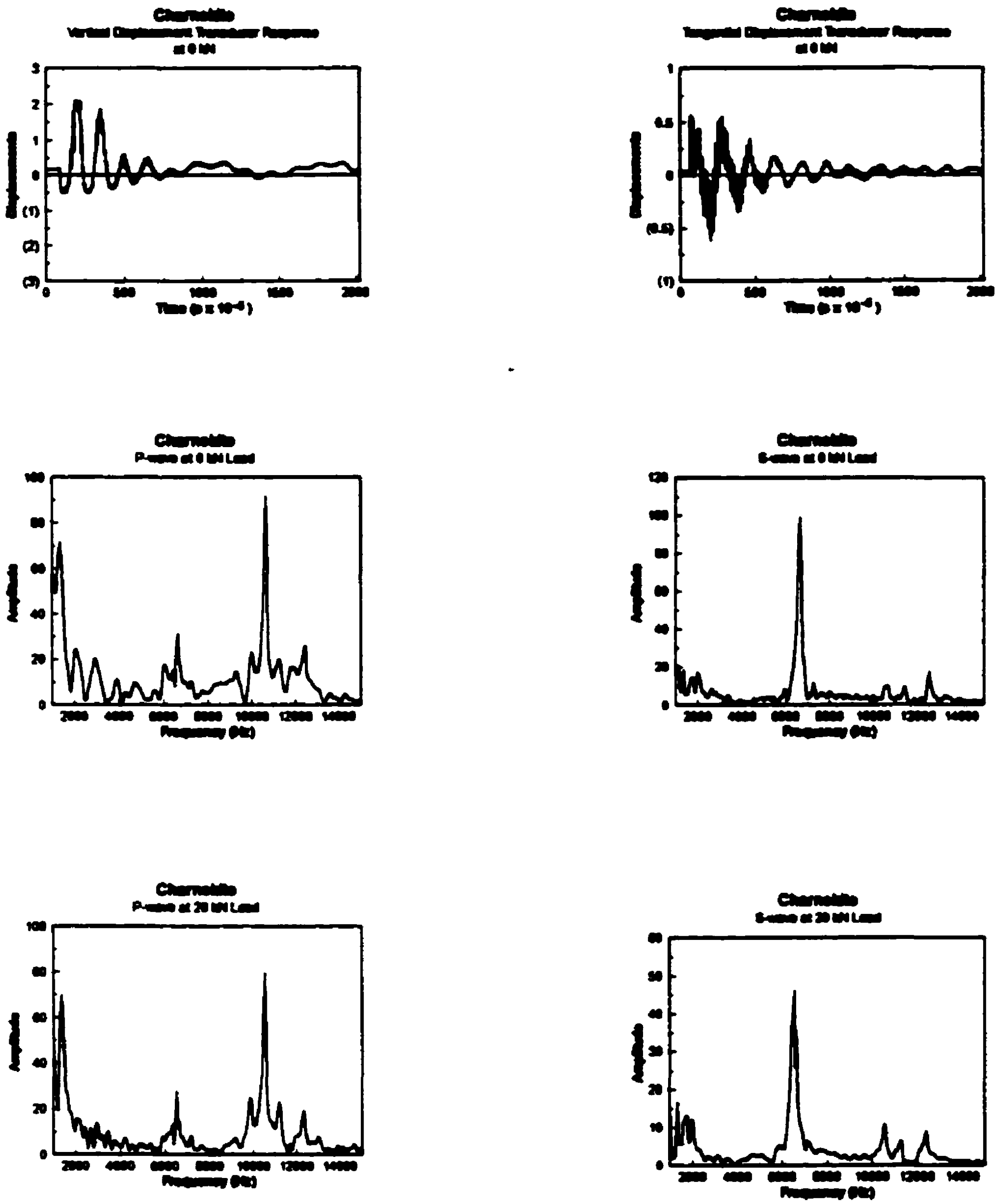

Figure D-11 The samples of waveforms collected by the vertical and tangential displacement transducers and the corresponding frequency spectra for the load/unloading cycles of charnokite.

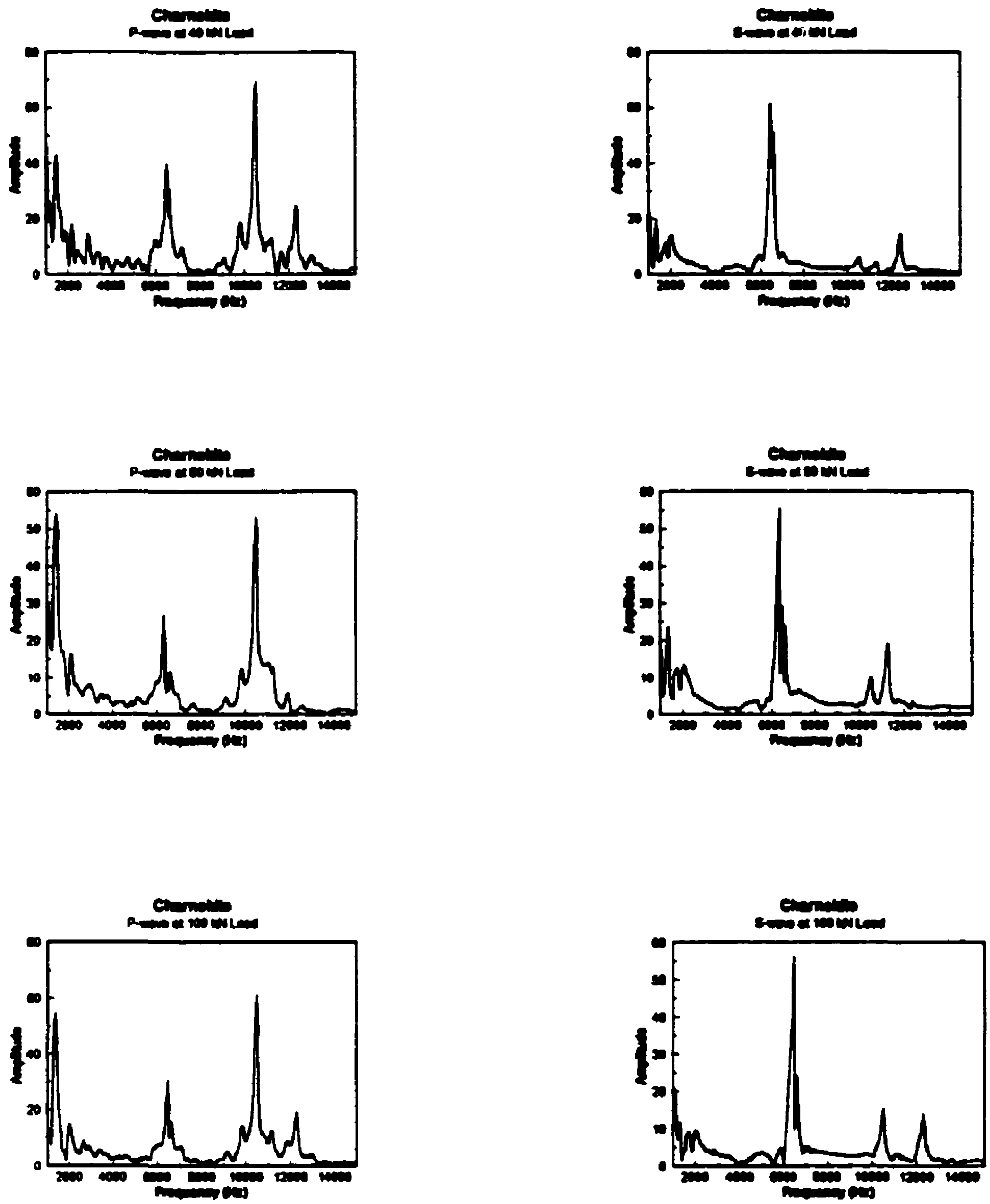

Figure D-12 The samples of the corresponding frequency spectra for the loading and unloading cycles collected by the vertical and tangential displacement transducers for the charnokite.

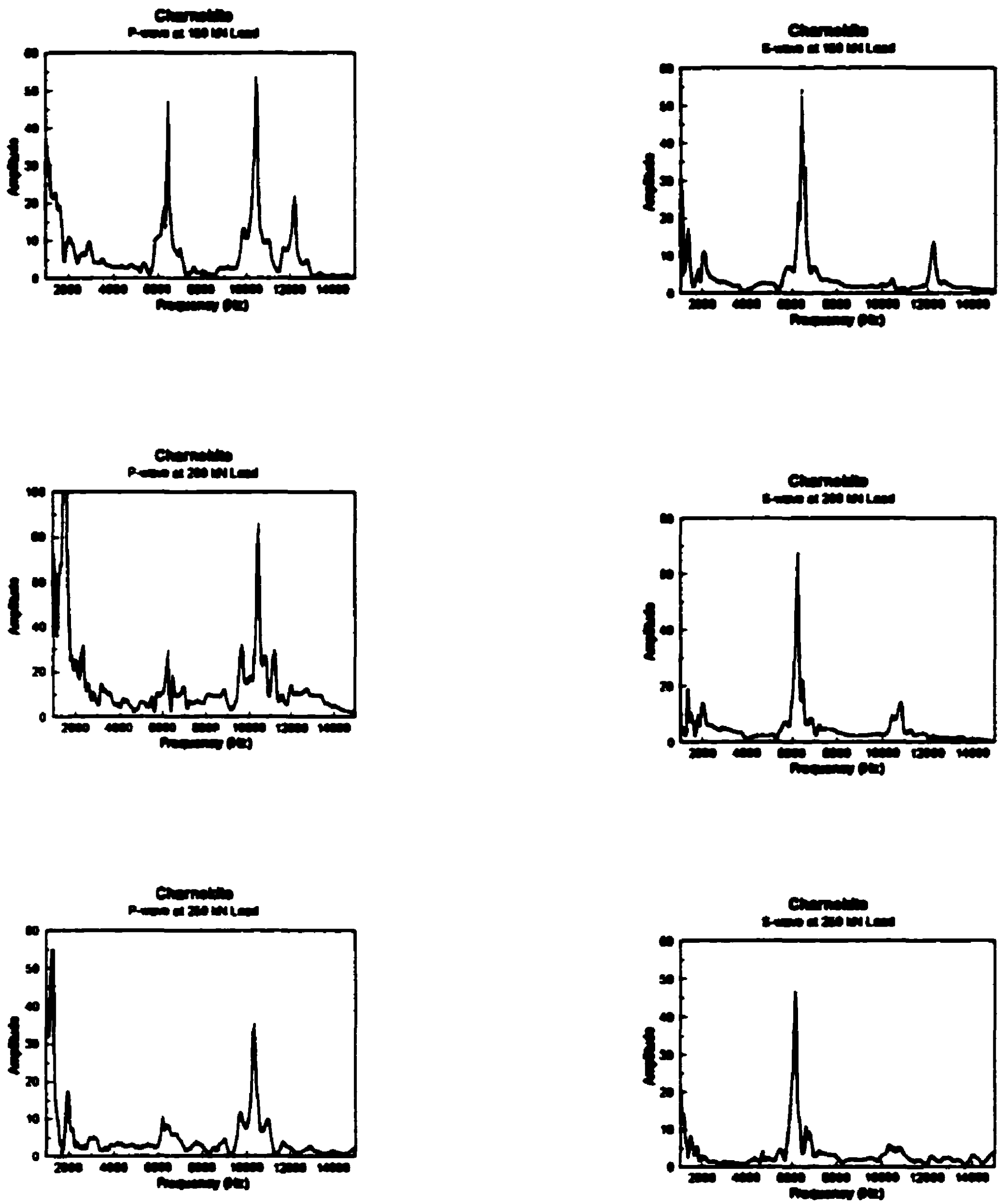

Figure D-13 The samples of the corresponding frequency spectra for the loading and unloading cycles collected by the vertical and tangential displacement transducers for the charnokite.

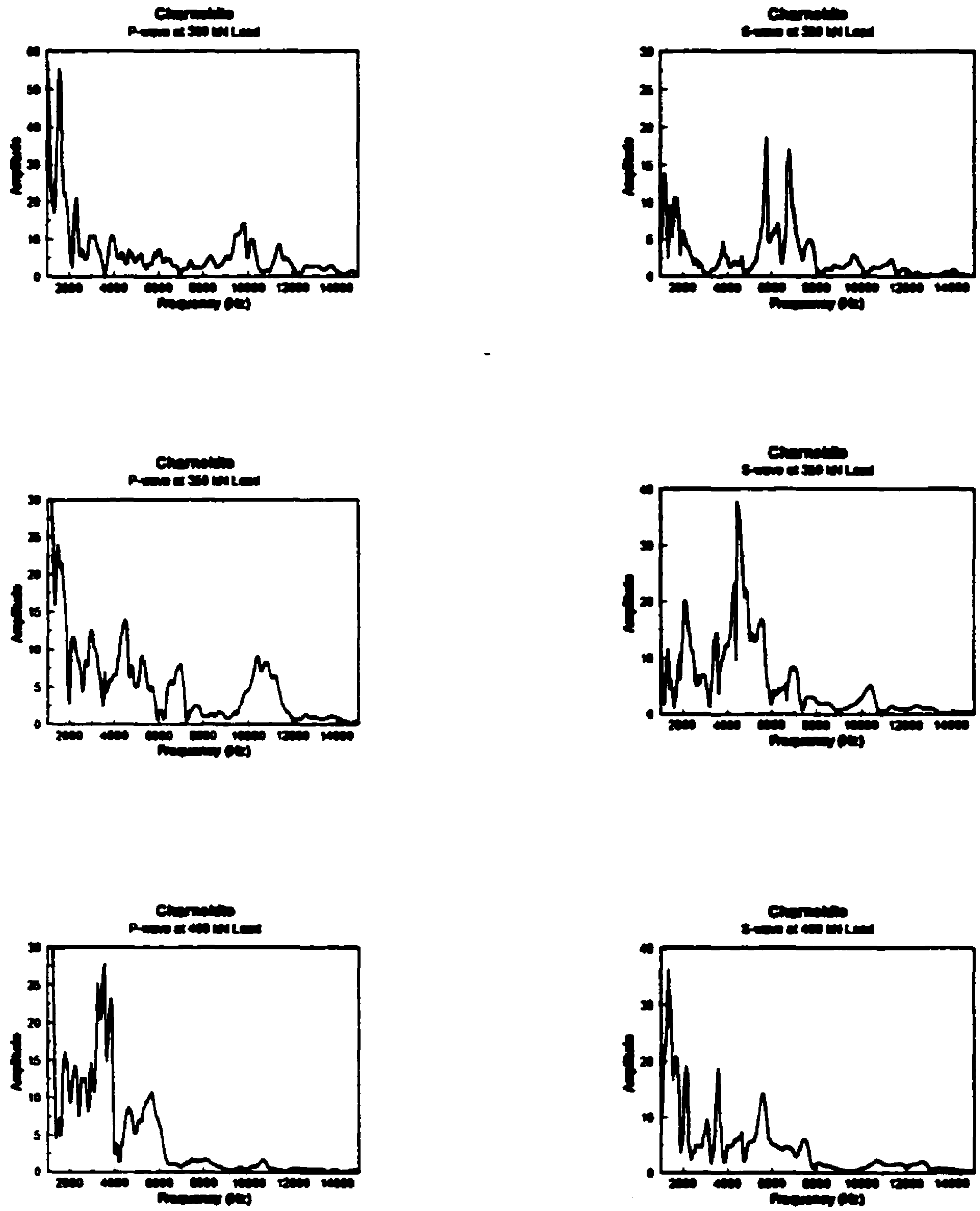

Figure D-14 The samples of the corresponding frequency spectra for the loading and unloading cycles collected by the vertical and tangential displacement transducers for the charnokite.

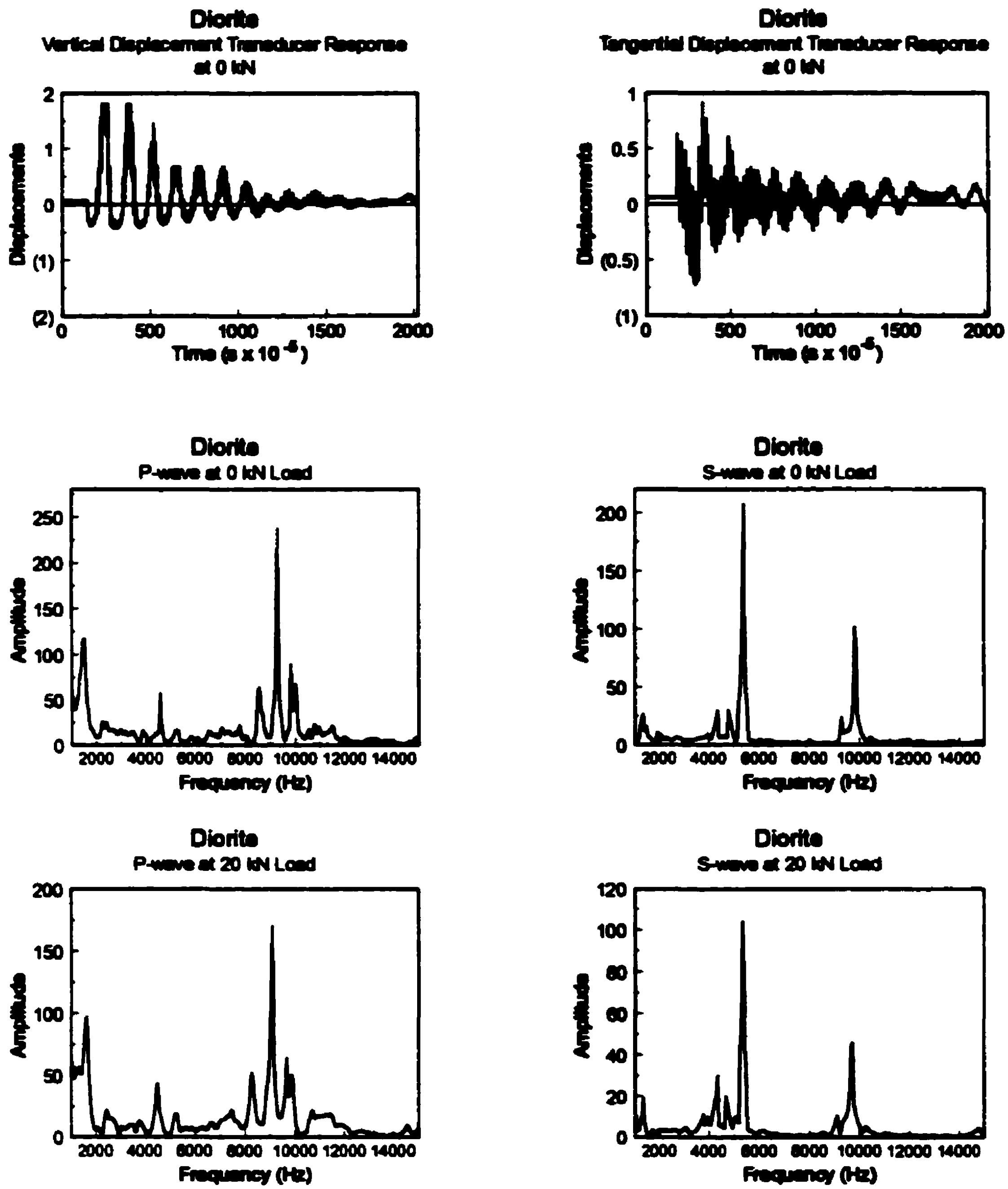

Figure D-15 The samples of waveforms collected by the vertical and tangential displacement transducers and the corresponding frequency spectra for the load/unloading cycles of diorite.

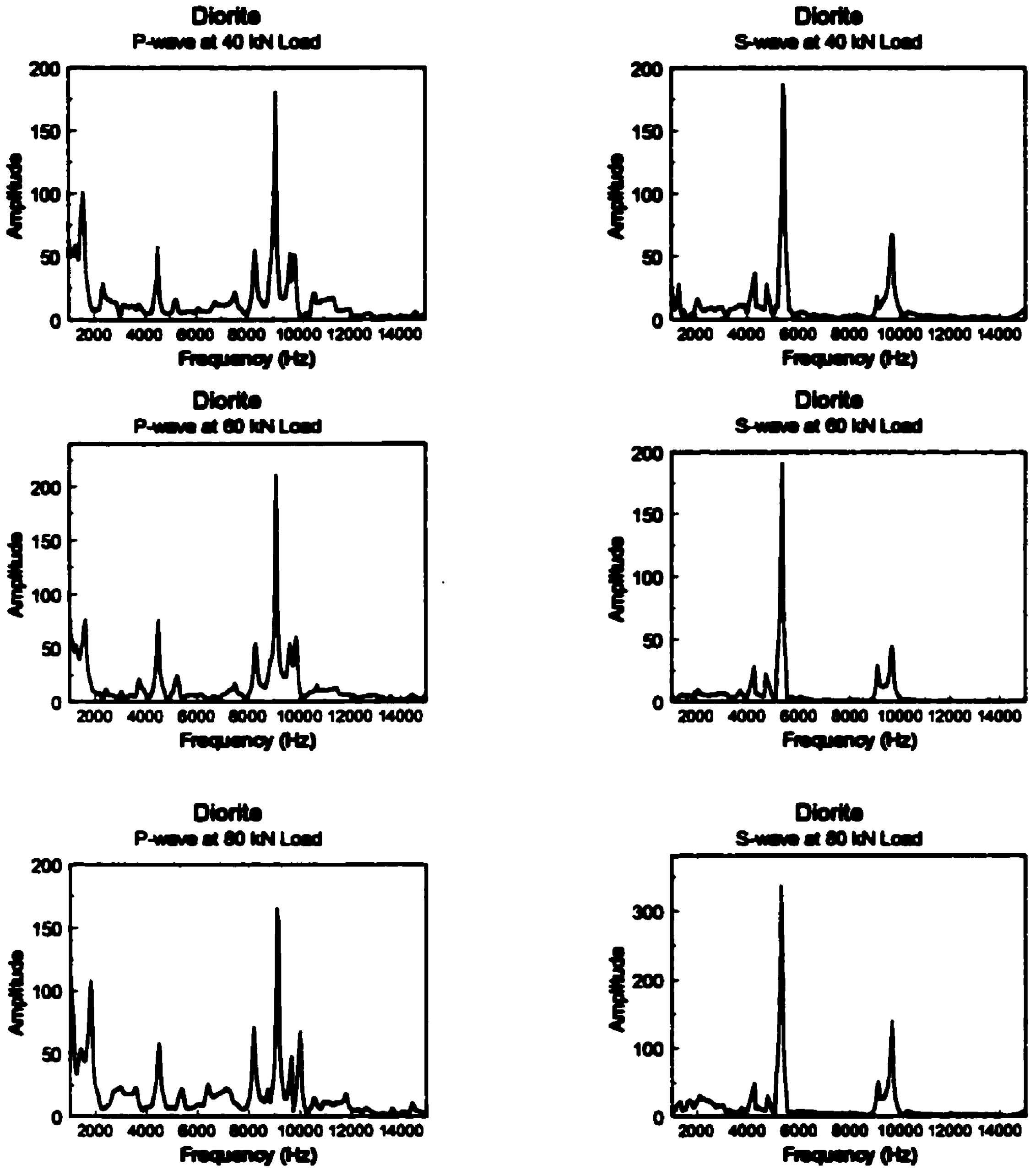

Figure D-16 The samples of the corresponding frequency spectra for the loading and unloading cycles collected by the vertical and tangential displacement transducers for the diorite.

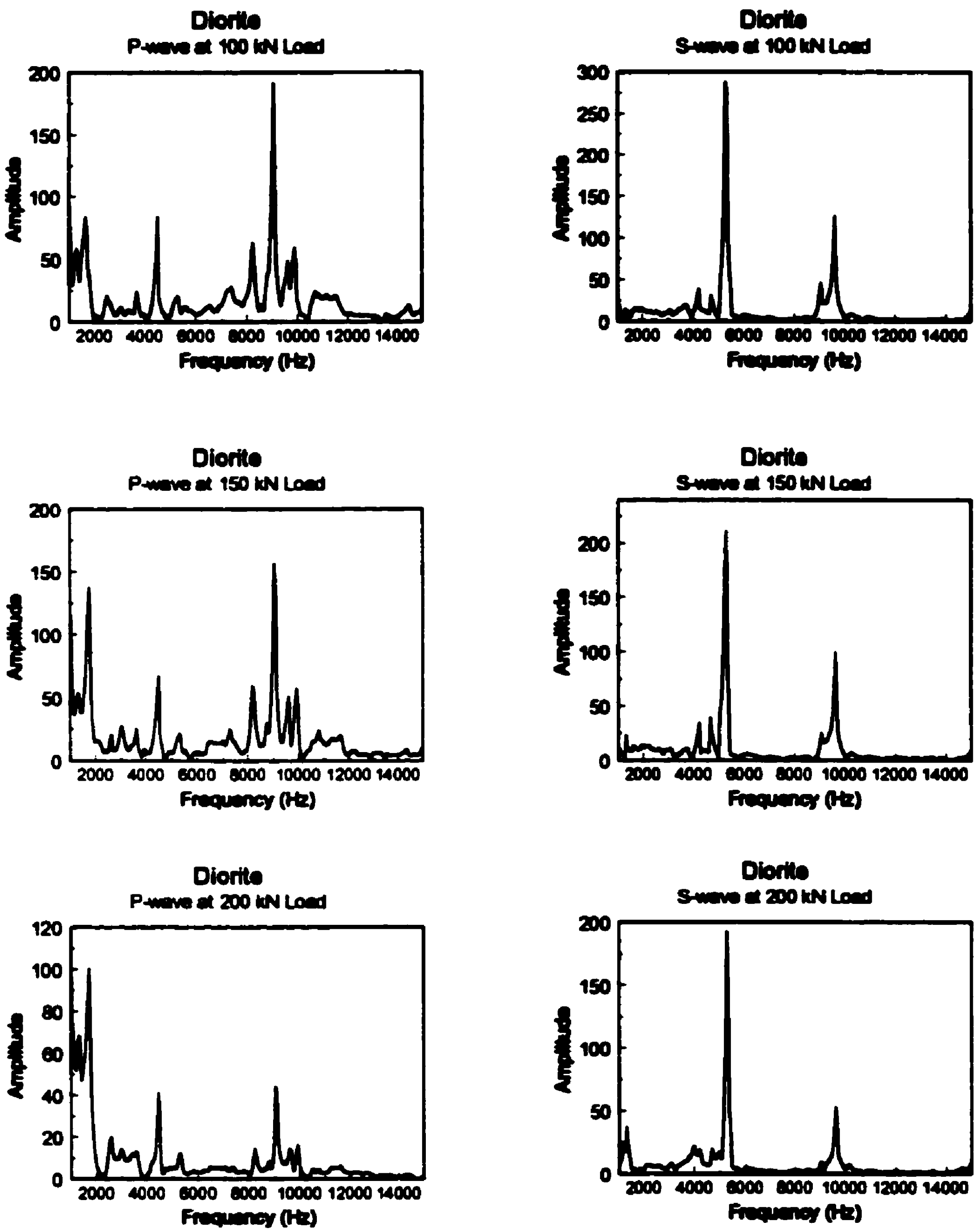

Figure D-17 The samples of the corresponding frequency spectra for the loading and unloading cycles collected by the vertical and tangential displacement transducers for the diorite.

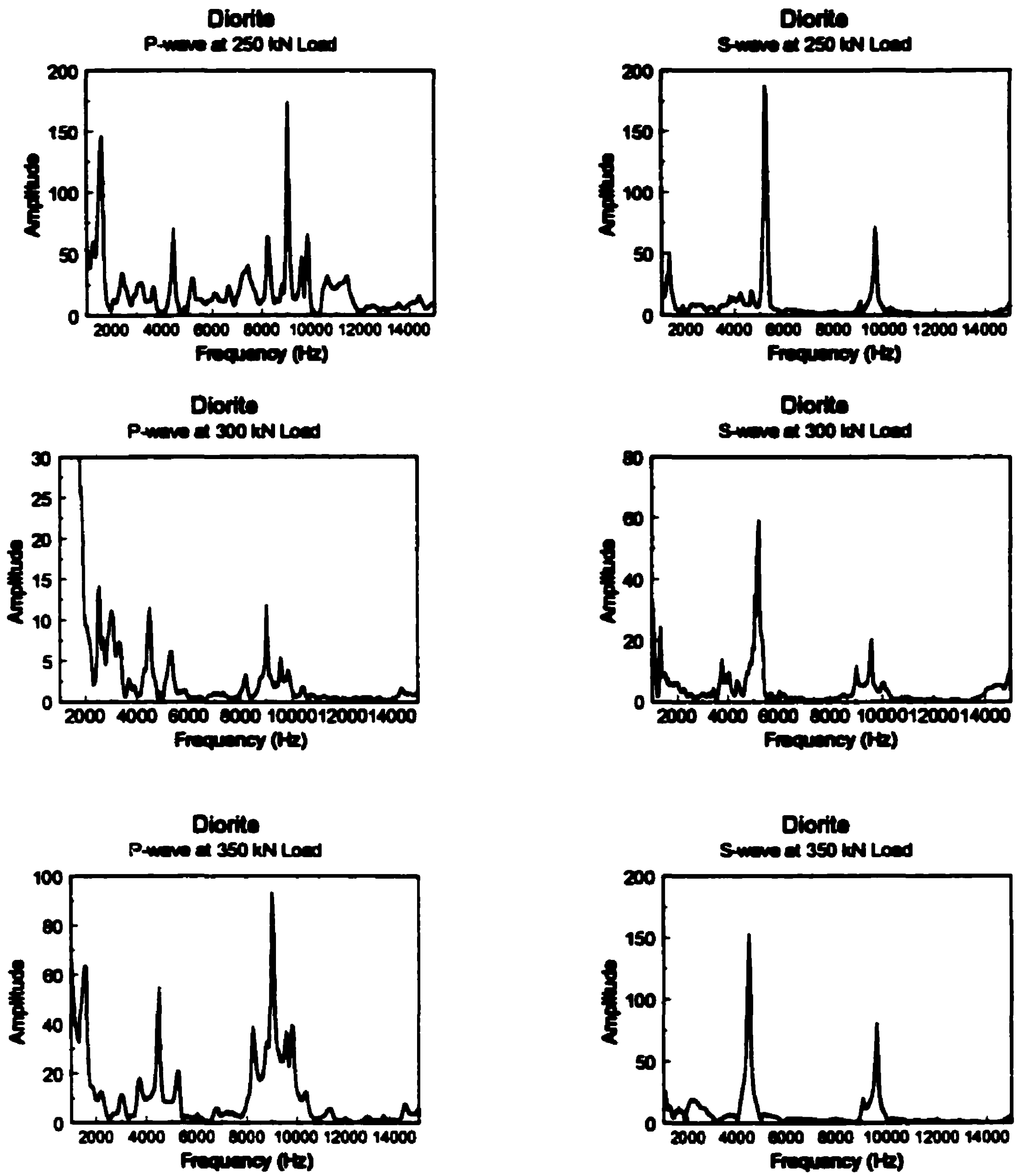

Figure D-18 The samples of the corresponding frequency spectra for the loading and unloading cycles collected by the vertical and tangential displacement transducers for the diorite.

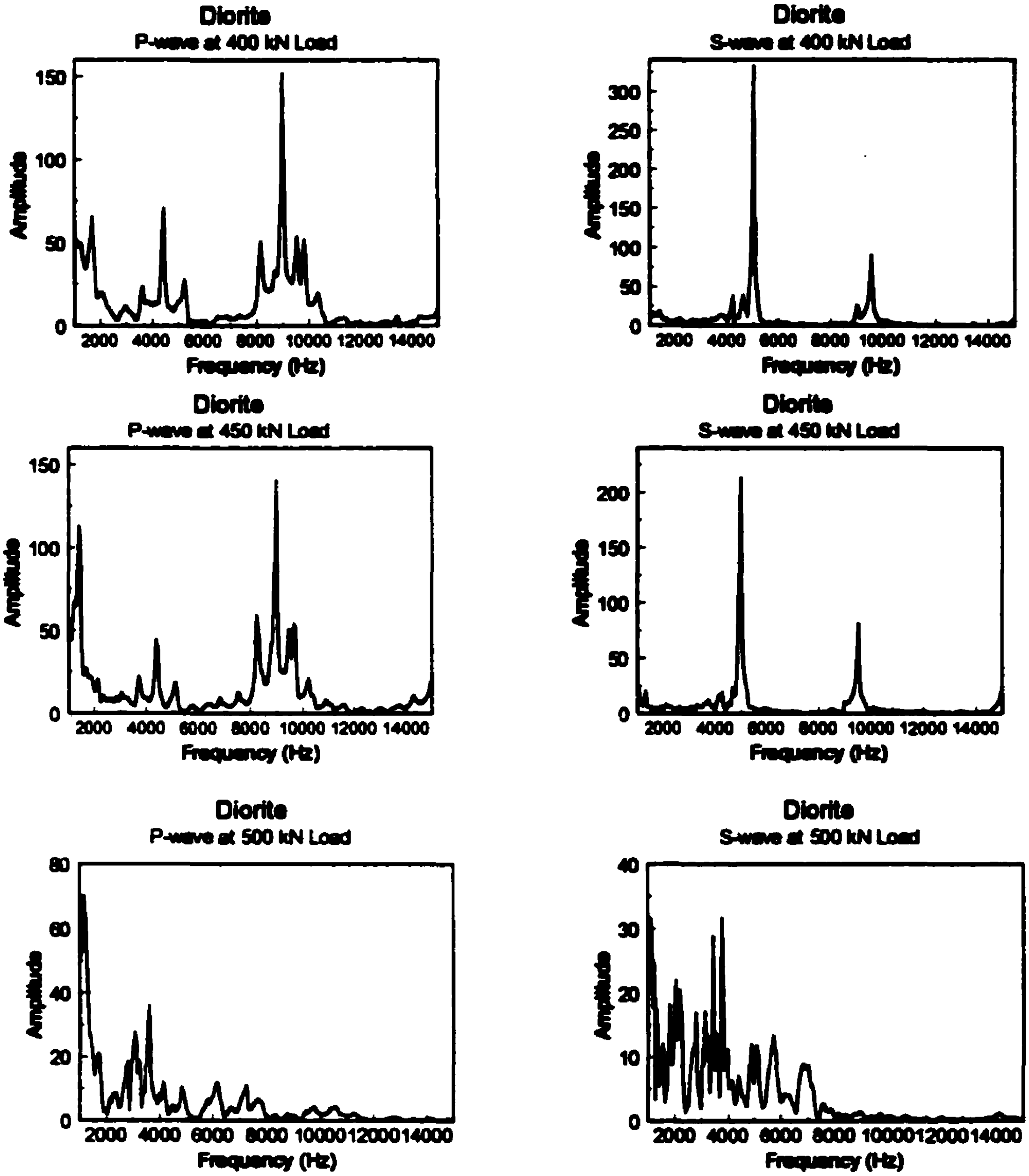

Figure D-19 The samples of the corresponding frequency spectra for the loading and unloading cycles collected by the vertical and tangential displacement transducers for the diorite.

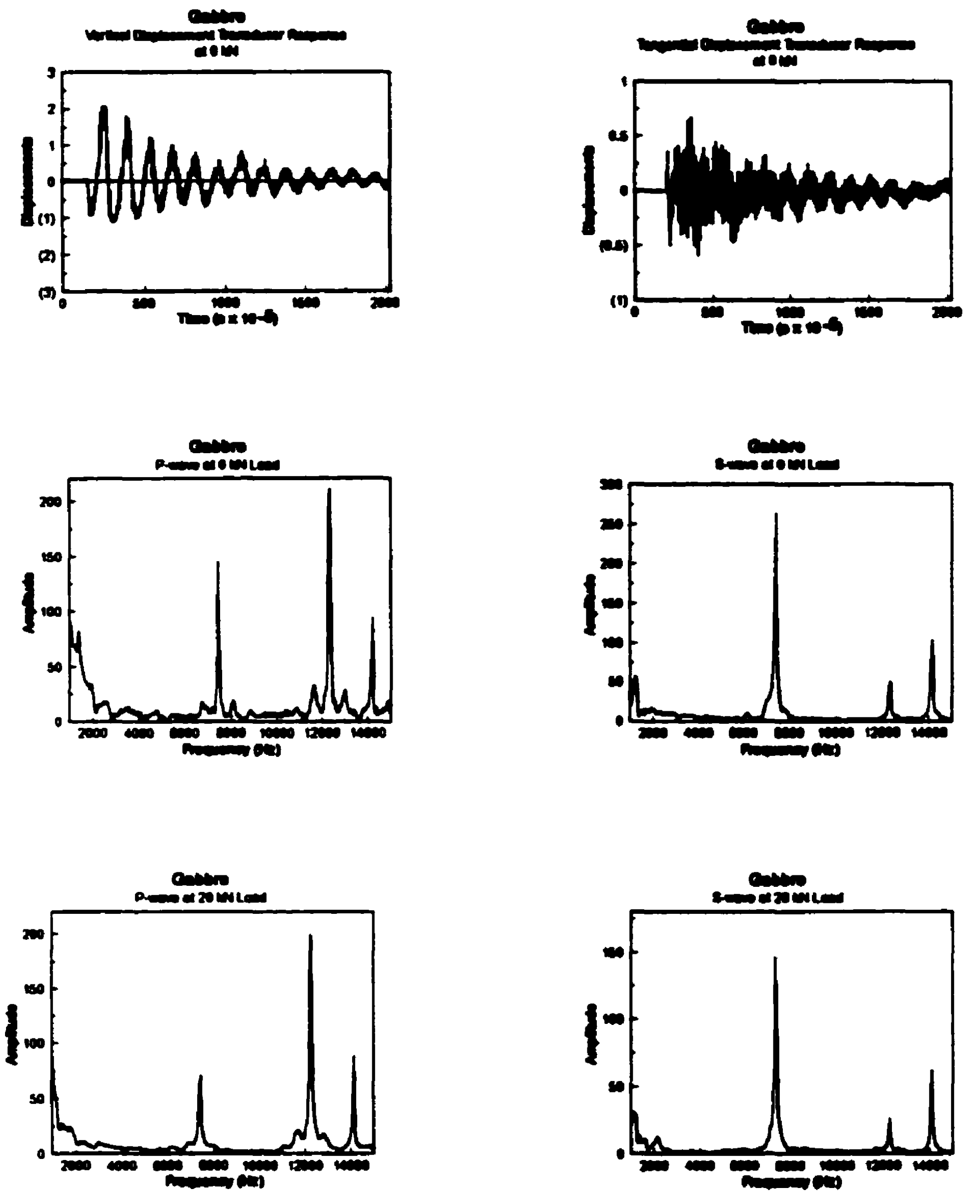

Figure D-20 The samples of waveforms collected by the vertical and tangential displacement transducers and the corresponding frequency spectra for the load/unloading cycles of gabbro.

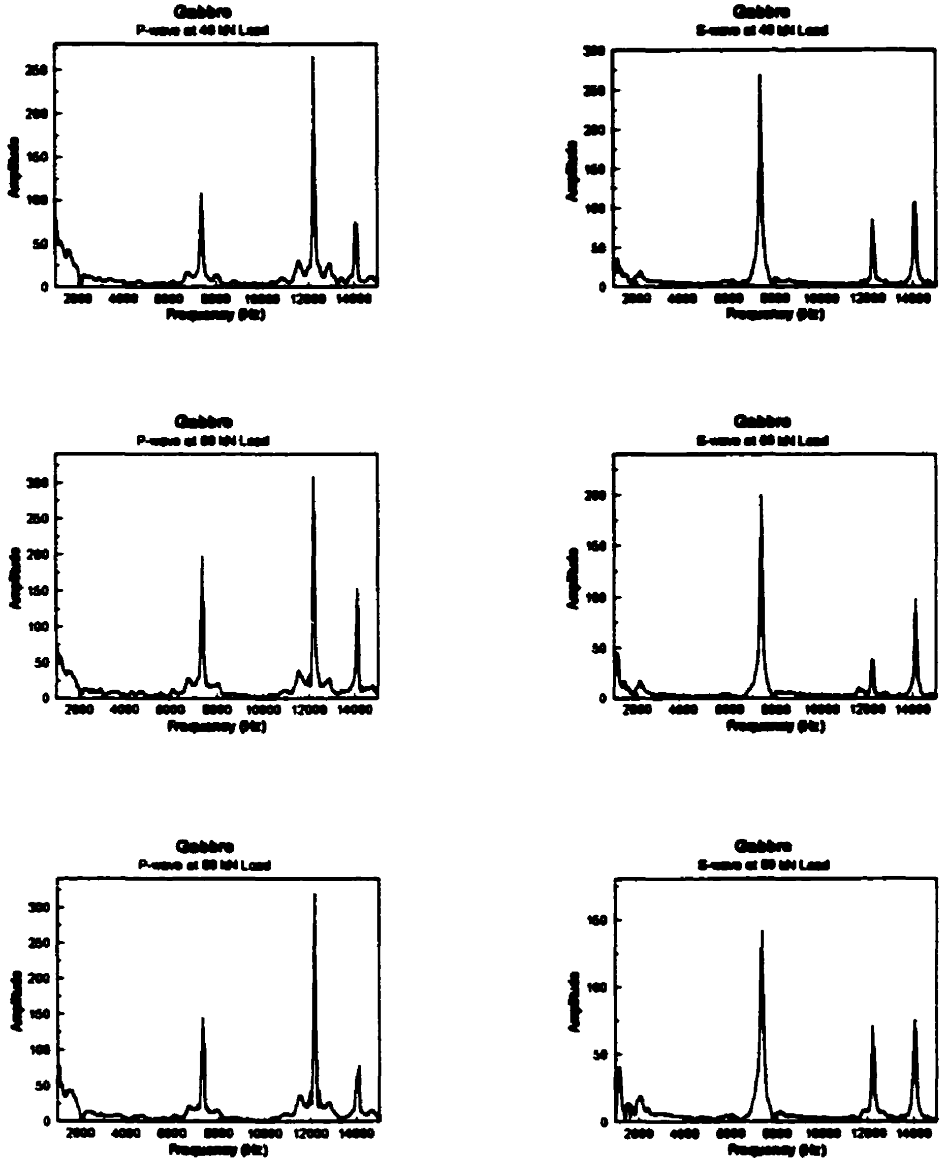

Figure D-21 The samples of the corresponding frequency spectra for the loading and unloading cycles collected by the vertical and tangential displacement transducers for the gabbro.

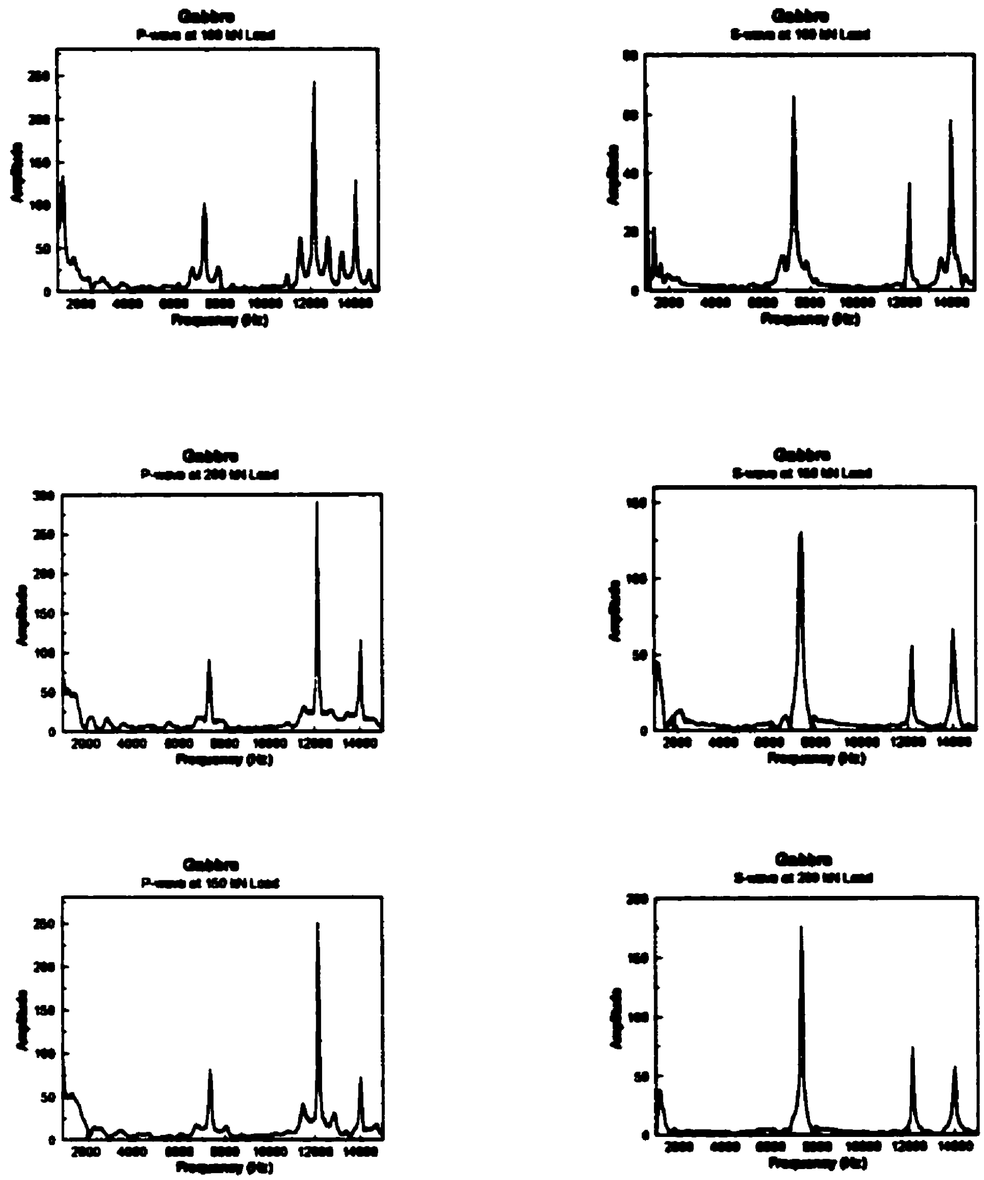

Figure D-22 The samples of the corresponding frequency spectra for the loading and unloading cycles collected by the vertical and tangential displacement transducers for the gabbro.

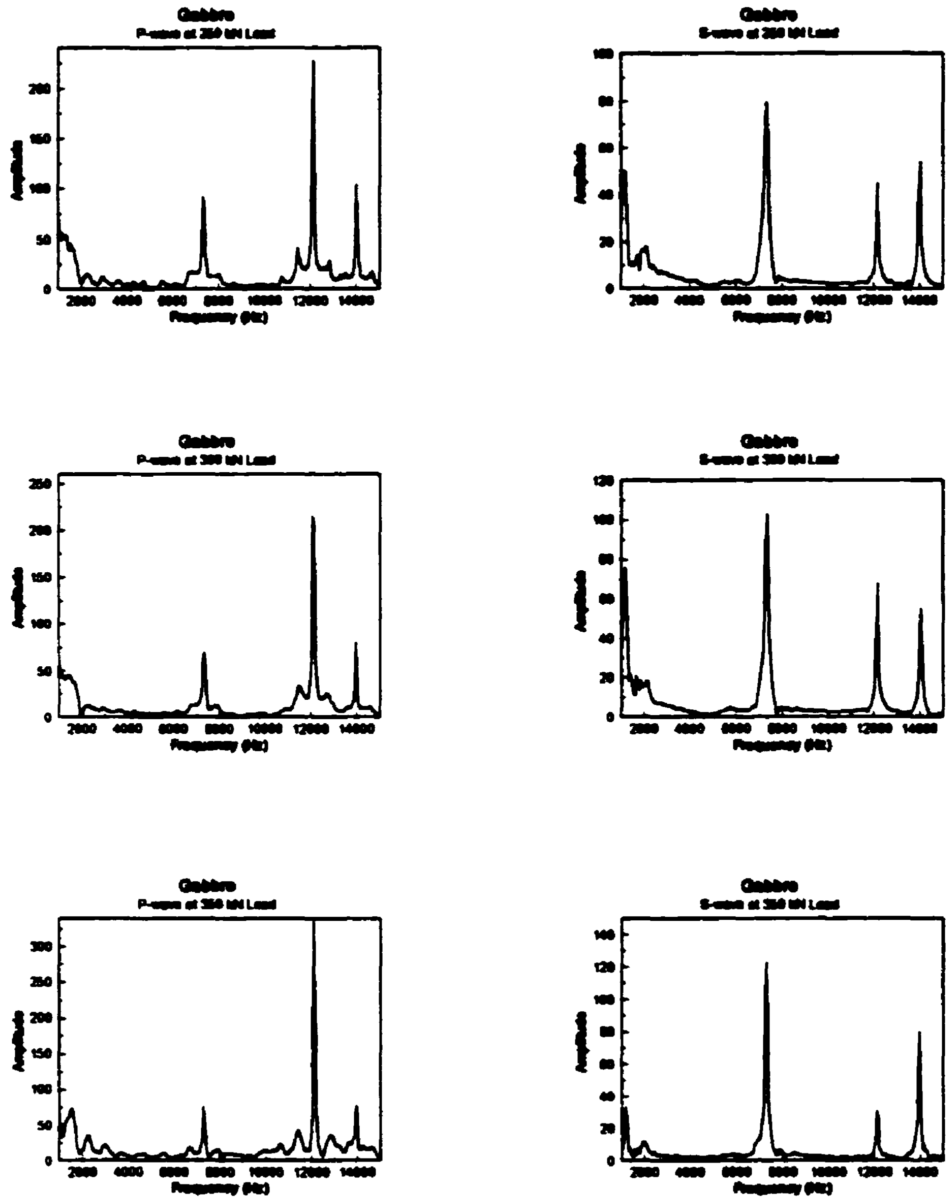

Figure D-23 The samples of the corresponding frequency spectra for the loading and unloading cycles collected by the vertical and tangential displacement transducers for the gabbro.

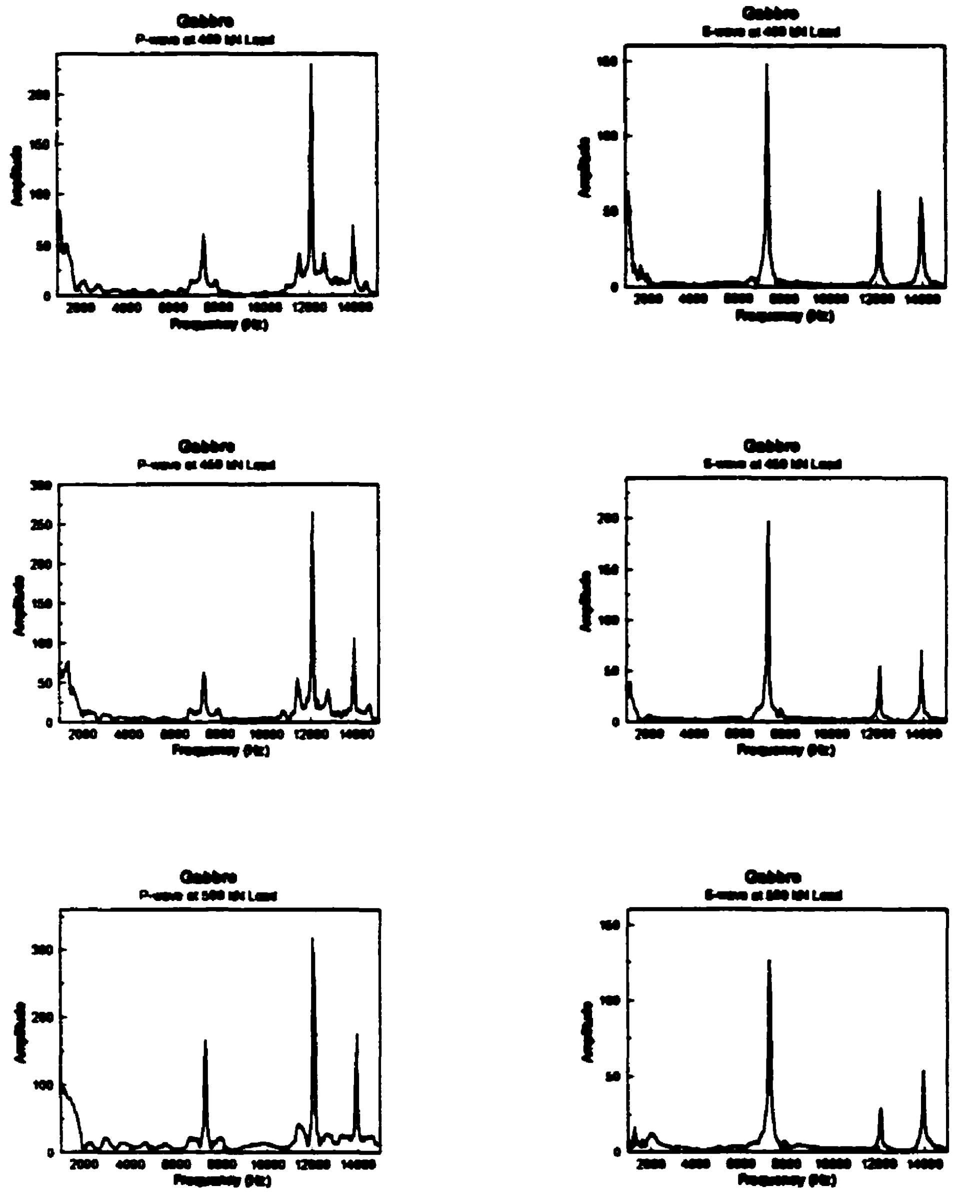

Figure D-24 The samples of the corresponding frequency spectra for the loading and unloading cycles collected by the vertical and tangential displacement transducers for the gabbro.

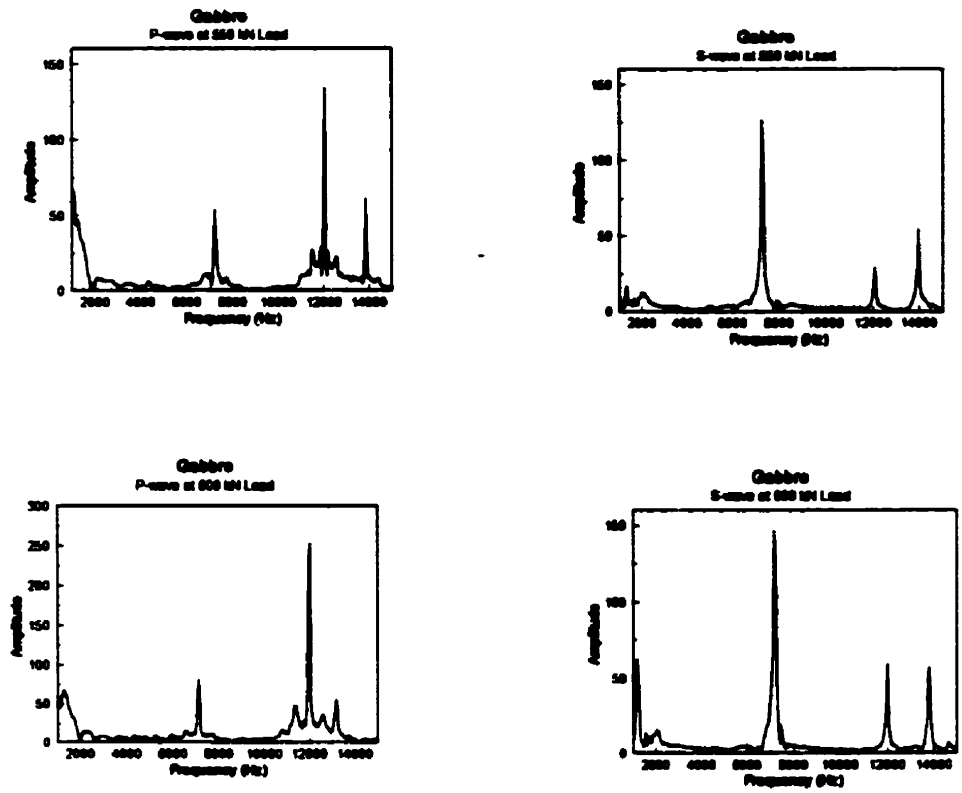

Figure D-25 The samples of the corresponding frequency spectra for the loading and unloading cycles collected by the vertical and tangential displacement transducers for the gabbro.

Table D-1 Examples of values computed by the MSR system for white granite.

Load (kN)	% Load	Cp (m/s)	Cs (m/s)	Poisson	E (GPa)	K (GPa)	G (GPa)
0	0.00	3990.8	2274.8	0.26	34.67	24.01	13.76
20	10.20	4077	2274.8	0.27	35.07	25.86	13.76
40	20.41	4077	2274.8	0.27	35.07	25.86	13.76
60	30.61	3962.1	2303.7	0.24	35.14	22.94	14.12
80	40.82	4048.3	2332.2	0.25	36.22	24.30	14.47
100	51.02	4077	2332.2	0.26	36.37	24.92	14.47
150	76.53	3962.1	2305.7	0.24	35.18	22.90	14.14
196	100.00	3904.7	1987.7	0.33	27.85	26.54	10.51

Load (kN)	% Load	Cp (m/s)	Cs (m/s)	Poisson	E (GPa)	K (GPa)	G (GPa)
0	0.00	4060.6	2314.5	0.26	35.89	24.86	14.25
20	7.41	4060.6	2314.5	0.26	35.89	24.86	14.25
40	14.81	4060.6	2314.5	0.26	35.89	24.86	14.25
60	22.22	4060.6	2314.5	0.26	35.89	24.86	14.25
80	29.63	3886.6	2314.5	0.23	34.92	21.18	14.25
100	37.04	3915.6	2314.5	0.23	35.10	21.78	14.25
120	44.44	3886.6	2314.5	0.23	34.92	21.18	14.25
140	51.85	4031.5	2343.5	0.24	36.37	23.75	14.61
160	59.26	4002.6	2285.4	0.26	34.96	24.09	13.89
240	88.89	4205.6	2314.5	0.28	36.56	28.05	14.25
260	96.30	2581.3	1908	-0.10	17.39	4.81	9.68
270	100		1589.4	1.00	#DIV/0!	-8.96	6.72

Table D-2 Examples of values computed by the MSR system for red granite.

Load (kN)	% Load	Cp (m/s)	Cs (m/s)	Poisson	E (GPa)	K (GPa)	G (GPa)
0	0	4580.6	2702.6	0.23	47.01	29.34	19.06
20	4	4580.6	2702.6	0.23	47.01	29.34	19.06
40	8	4580.6	2731.2	0.22	47.67	28.80	19.47
60	12	4580.6	2731.2	0.22	47.67	28.80	19.47
80	16	4580.6	2731.2	0.22	47.67	28.80	19.47
100	20	4609.4	2760.1	0.22	48.54	28.94	19.88
150	30	4580.6	2731.2	0.22	47.67	28.80	19.47
170	34	4609.4	2731.2	0.23	47.87	29.49	19.47
200	40	4609.4	2731.2	0.23	47.87	29.49	19.47
250	50	4609.4	2731.2	0.23	47.87	29.49	19.47
300	60	4609.4	2731.2	0.23	47.87	29.49	19.47
350	70	4494.1	2040.2	0.37	29.77	38.23	10.86
400	80	4465.4	1896.1	0.39	26.09	39.53	9.38
450	90	2880.9	1695.5	0.24	18.53	11.66	7.50
500	100	2361.8	1388.5	0.24	12.44	7.85	5.03

Load (kN)	% Load	Cp (m/s)	Cs (m/s)	Poisson	E (GPa)	K (GPa)	G (GPa)
0	0.00	4711.7	2779.9	0.23	49.74	31.05	20.17
20	5.71	4653.9	2779.9	0.22	49.32	29.64	20.17
40	11.43	4682.4	2779.9	0.23	49.53	30.33	20.17
60	17.14	4682.4	2808.8	0.22	50.20	29.77	20.59
80	22.86	4682.4	2808.8	0.22	50.20	29.77	20.59
100	28.57	4682.4	2808.8	0.22	50.20	29.77	20.59
150	42.86	4682.4	2808.8	0.22	50.20	29.77	20.59
200	57.14	4682.4	2779.9	0.23	49.53	30.33	20.17
250	71.43	4671.6	2808.8	0.22	50.12	29.51	20.59
300	85.71	4653.9	2837.7	0.20	50.61	28.51	21.02
350	100.00	4509.4	2490.9	0.28	41.47	31.48	16.19

Table D-3 Examples of values computed by the MSR system for charnokite.

Load (kN)	% Load	Cp (m/s)	Cs (m/s)	Poisson	E (GPa)	K (GPa)	G (GPa)
0	0.00	4153.5	2488.3	0.22	40.79	24.29	16.72
50	10.59	4134.4	2450	0.23	39.85	24.54	16.21
100	21.19	4115.2	2564.9	0.18	42.00	22.04	17.76
150	31.78	4115.2	2545.7	0.19	41.65	22.39	17.50
200	42.37	4115.2	2564.9	0.18	42.00	22.04	17.76
250	52.97	4096	2545.7	0.19	41.48	21.97	17.50
300	63.56	4096	2564.9	0.18	41.83	21.62	17.76
350	74.15	4096	2392.4	0.24	38.36	24.69	15.45
400	84.75	4058	2373.4	0.24	37.72	24.18	15.21
450	95.34	4019.6	2124.6	0.31	31.84	27.37	12.19
472	100.00	0	0	#DIV/0!	#DIV/0!	0.00	0.00

Load (kN)	% Load	Cp (m/s)	Cs (m/s)	Poisson	E (GPa)	K (GPa)	G (GPa)
0	0.00	4151.4	2589.8	0.18	42.79	22.39	0.00
20	5.00	4113.3	2551.8	0.19	41.74	22.24	0.00
40	10.00	4113.3	2532.7	0.19	41.38	22.59	0.00
80	20.00	4094.2	2475.6	0.21	40.11	23.20	0.00
100	25.00	4094.2	2532.7	0.19	41.44	22.17	0.00
150	37.50	4075.2	2513	0.19	40.69	22.10	0.00
200	50.00	4075.2	2437.5	0.21	39.66	23.45	0.00
250	62.50	4037.1	2399.4	0.18	40.68	23.28	0.00
300	75.00	3827.7	2247	-0.57	23.33	21.38	0.00
350	87.50	2723.1	1733	-0.30	17.24	9.21	0.00
400	100.00	2208.9	837.9	1.00	#DIV/0!	10.65	0.00

Load (kN)	% Load	Cp (m/s)	Cs (m/s)	Poisson	E (GPa)	K (GPa)	G (GPa)
0	0.00	4159.5	2574	0.19	42.56	22.86	17.89
20	4.12	4103.5	2555.4	0.18	41.72	21.96	17.63
40	8.25	4066.2	2536.8	0.18	41.05	21.47	17.38
60	12.37	4028.9	2499.4	0.19	40.05	21.34	16.87
80	16.49	4028.9	2494.4	0.19	39.96	21.43	16.80
100	20.62	4028.9	2518.1	0.18	40.39	21.00	17.12
150	30.93	4028.9	2494.4	0.19	39.96	21.43	16.80
200	41.24	4028.9	2518.1	0.18	40.39	21.00	17.12
250	51.55	4028.9	2536.7	0.17	40.71	20.66	17.37
300	61.86	4010.2	2536.7	0.17	40.53	20.26	17.37
350	72.16	3991.6	2499.4	0.18	39.72	20.53	16.87
400	82.47	3991.6	2406.1	0.21	37.97	22.18	15.63
450	92.78	3954.3	2368.8	0.22	36.97	22.02	15.15
485	100.00	0	1305.7	1.00	#DIV/0!	-6.14	4.60

Table D-4 Examples of values computed by the MSR system for diorite.

Load (kN)	% Load	Cp (m/s)	Cs (m/s)	Poisson	E (GPa)	K (GPa)	G (GPa)
0	0.00	5358.4	3161.5	0.23	72.22	45.08	29.29
20	4.00	5329.5	3132.7	0.24	71.08	44.88	28.75
40	8.00	5329.5	3161.5	0.23	71.96	44.18	29.29
60	12.00	5300.8	3132.7	0.23	70.83	43.99	28.75
80	16.00	5300.8	3132.7	0.23	70.83	43.99	28.75
100	20.00	5272	3103.9	0.23	69.71	43.80	28.23
150	30.00	5272	3103.9	0.23	69.71	43.80	28.23
200	40.00	5272	3103.9	0.23	69.71	43.80	28.23
250	50.00	5243.1	3103.9	0.23	69.45	42.91	28.23
300	60.00	5185.5	3075	0.23	68.09	41.85	27.70
350	70.00	5185.5	2642.9	0.32	54.22	51.50	20.47
400	80.00	5185.5	2959.9	0.26	64.60	44.56	25.67
450	90.00	5616.8	2930.9	0.31	66.09	58.88	25.17
500	100.00	5070.4	2498.9	0.34	49.02	50.93	18.30

Load (kN)	% Load	Cp (m/s)	Cs (m/s)	Poisson	E (GPa)	K (GPa)	G (GPa)
0	0.00	5436.5	3107.5	0.26	71.15	48.87	28.29
20	3.64	5322	3150.3	0.23	71.55	44.22	29.08
40	7.27	5322	3150.3	0.23	71.55	44.22	29.08
60	10.91	5322	3150.3	0.23	71.55	44.22	29.08
80	14.55	5322	3121.7	0.24	70.68	44.92	28.55
100	18.18	5293.5	3150.3	0.23	71.29	43.33	29.08
150	27.27	5293.5	3121.7	0.23	70.43	44.03	28.55
200	36.36	5293.5	3121.7	0.23	70.43	44.03	28.55
250	45.45	5293.5	3150.3	0.23	71.29	43.33	29.08
300	54.55	5293.5	3150.3	0.23	71.29	43.33	29.08
350	63.64	5264.9	3121.7	0.23	70.18	43.15	28.55
400	72.73	5264.9	3121.7	0.23	70.18	43.15	28.55
450	81.82	3605.3	2721.3	-0.16	36.36	9.15	21.70
500	90.91		2520.9	1.00	#DIV/0!	-24.83	18.62
550	100.00		2520.9	1.00	#DIV/0!	-24.83	18.62

Load (kN)	% Load	Cp (m/s)	Cs (m/s)	Poisson	E (GPa)	K (GPa)	G (GPa)
0	0.00	5389.4	3179.7	0.23	73.05	45.61	29.62
20	4.80	5332.4	3123	0.24	70.81	45.21	28.58
40	9.59	5332.4	3094.5	0.25	69.93	45.90	28.06
60	14.39	5332.4	3123	0.24	70.81	45.21	28.58
80	19.18	5332.4	3123	0.24	70.81	45.21	28.58
100	23.98	5303.9	3094.5	0.24	69.69	45.01	28.06
150	35.97	5303.9	3094.5	0.24	69.69	45.01	28.06
200	47.96	5293.5	3094.5	0.24	69.61	44.69	28.06
250	59.95	5293.5	3094.5	0.24	69.61	44.69	28.06
300	71.94	5293.5	2467.2	0.36	48.56	58.32	17.84
350	83.93	5293.5	2467.2	0.36	48.56	58.32	17.84
400	95.92		2467.2	1.00	#DIV/0!	-23.78	17.84
417	100.00		1554.6	1.00	#DIV/0!	-9.44	7.08

Table D-5 Examples of values computed by the MSR system for gabbro

Load (kN)	% Load	Cp (m/s)	Cs (m/s)	Poisson	E (GPa)	K (GPa)	G (GPa)
0	0.00	5208	3117.2	0.22	64.06	38.25	26.24
50	5.88	5147.1	3096.6	0.22	62.98	37.01	25.89
100	11.76	5147.1	3096.6	0.22	62.98	37.01	25.89
150	17.65	5126.9	3096.6	0.21	62.80	36.45	25.89
200	23.53	5127	3096.6	0.21	62.80	36.45	25.89
250	29.41	5127	3076	0.22	62.27	36.91	25.55
300	35.29	5106.4	3096.6	0.21	62.61	35.88	25.89
350	41.18	5106.4	3076	0.22	62.09	36.34	25.55
400	47.06	5106.4	3076	0.22	62.09	36.34	25.55
450	52.94	5085.8	3076	0.21	61.90	35.77	25.55
500	58.82	5085.8	3076	0.21	61.90	35.77	25.55
550	64.71	5085.8	3097.5	0.21	62.44	35.30	25.91
600	70.59	5085.8	3076	0.21	61.90	35.77	25.55
650	76.47	5065.2	3076	0.21	61.71	35.21	25.55
700	82.35	5065.2	3035.1	0.22	60.68	36.11	24.87
750	88.24	5044.9	3014.6	0.22	59.98	36.00	24.54
800	94.12	4511.7	2501.9	0.28	43.20	32.43	16.90
850	100.00		2091.8		0.00	-15.75	11.81

Load (kN)	%Load	Cp (m/s)	Cs (m/s)	Poisson	E (GPa)	K (GPa)	G (GPa)
0	0.00	5141.6	3218.3	0.18	65.88	34.09	27.97
20	2.98	5122.6	3199.2	0.18	65.23	34.01	27.63
40	5.95	5122.6	3180.2	0.19	64.80	34.44	27.31
60	8.93	5103.6	3199.2	0.18	65.02	33.48	27.63
80	11.90	5103.6	3180.2	0.18	64.59	33.92	27.31
100	14.88	5103.6	3180.2	0.18	64.59	33.92	27.31
150	22.32	5084.4	3199.2	0.17	64.79	32.95	27.63
200	29.76	5084.4	3180.2	0.18	64.37	33.39	27.31
250	37.20	5084.4	3161.2	0.18	63.94	33.82	26.98
300	44.64	5065.4	3180.2	0.17	64.15	32.87	27.31
350	52.08	5046.4	3161.2	0.18	63.52	32.78	26.98
400	59.52	4951.2	3085	0.18	60.78	31.93	25.70
450	66.96	4856	2894.6	0.22	55.40	33.50	22.62
500	74.40	5008.3	2434	0.35	43.04	46.40	16.00
550	81.85		2247	1.00	#DIV/0!	-18.18	13.63
600	89.29		1790.1	1.00	#DIV/0!	-11.54	8.65
650	96.73		1790.1	1.00	#DIV/0!	-11.54	8.65
672	100.00		1694.9	1.00	#DIV/0!	-10.34	7.76

Table D-6 Examples of values computed by the MSR system for gabbro

Load (kN)	%Load	Cp (m/s)	Cs (m/s)	Poisson	E (GPa)	K (GPa)	G (GPa)
0	0.00	5165	3163	0.20	64.83	36.01	27.01
20	3.64	5165	3163	0.20	64.83	36.01	27.01
40	7.27	5165	3163	0.20	64.83	36.01	27.01
60	10.91	5145	3143	0.20	64.14	35.91	26.67
80	14.55	5145	3143	0.20	64.14	35.91	26.67
100	18.18	5145	3143	0.20	64.14	35.91	26.67
150	27.27	5125	3143	0.20	63.94	35.35	26.67
200	36.36	5125	3143	0.20	63.94	35.35	26.67
250	45.45	5104.9	3123	0.20	63.25	35.25	26.33
300	54.55	5104.9	3143	0.19	63.73	34.80	26.67
350	63.64	5064.9	2762.7	0.29	53.10	41.79	20.61
400	72.73	5064.9	2762.7	0.29	53.10	41.79	20.61
450	81.82	5064.9	2782.7	0.28	53.68	41.39	20.91
500	90.91		1701.6	1.00	#DIV/0!	-10.42	7.82
550	100.00		1581.5	1.00	#DIV/0!	-9.00	6.75

Table D-7 Examples of values computed by the UPV.

White granite

Load (kN)	% Load	Cp (m/s)
0	0.0	4195.8
15	5.7	4225.4
30	11.5	4255.3
45	17.2	4316.5
60	22.9	4363.6
75	28.6	4347.8
90	34.4	4347.8
105	40.1	4363.6
120	45.8	4363.6
135	51.5	4363.6
150	57.3	4428.0
165	63.0	4411.8
180	68.7	4270.5
195	74.4	4363.6
210	80.2	4332.1
225	85.9	4332.1
240	91.6	4316.5
255	97.3	4152.2
262	100.0	4013.4

Charnokite

Load (kN)	% Load	Cp (m/s)
0	0.0	4693.0
15	6.3	4693.0
30	12.5	4713.7
45	18.8	4755.6
60	25.0	4819.8
75	31.3	4908.3
90	37.5	4908.3
105	43.8	4776.8
120	50.0	4755.6
135	56.3	4755.6
150	62.5	4755.6
165	68.8	4755.6
180	75.0	4755.6
195	81.3	4755.6
210	87.5	4755.6
225	93.8	4755.6
240	100.0	4458.3

Red granite

Load (kN)	% Load	Cp (m/s)
0	0.0	4890.9
20	7.5	4803.6
40	15.1	4803.6
60	22.6	4890.9
80	30.2	4913.2
100	37.7	4935.8
120	45.3	4958.5
140	52.8	4958.5
160	60.4	5004.7
180	67.9	5004.7
200	75.5	5004.7
220	83.0	4890.9
240	90.6	4890.9
260	98.1	5004.7
265	100.0	4483.3

Diorite

Load (kN)	% Load	Cp (m/s)
0	0.0	5783.8
20	4.3	6011.2
40	8.6	6257.3
60	12.9	6257.3
80	17.2	6257.3
100	21.5	6407.2
120	25.8	6407.2
140	30.1	6407.2
160	34.4	6407.2
180	38.7	6407.2
200	43.0	6407.2
220	47.3	6407.2
240	51.6	6407.2
260	55.9	6407.2
280	60.2	6407.2
300	64.5	6407.2
320	68.8	6407.2
340	73.1	6407.2
360	77.4	6407.2
380	81.7	6257.3
400	86.0	6257.3
420	90.3	6257.3
440	94.6	6257.3
460	98.9	6257.3
465	100.0	5700.0

Table D-8 Examples of values computed by the UPV.

Gabbro

Load (kN)	% Load	Cp (m/s)
0	0.0	6206.9
20	4.3	6242.8
40	8.7	6242.8
60	13.0	6242.8
80	17.4	6242.8
100	21.7	6242.8
120	26.1	6352.9
140	30.4	6352.9
160	34.8	6352.9
180	39.1	6352.9
200	43.5	6352.9
220	47.8	6352.9
240	52.2	6390.5
260	56.5	6390.5
280	60.9	6390.5
300	65.2	6390.5
320	69.6	6390.5
340	73.9	6390.5
360	78.3	6390.5
380	82.6	6390.5
400	87.0	6315.8
420	91.3	6279.1
440	95.7	6206.9
460	100.0	6033.5